RECENT ADVANCES ON MYOCARDIUM PHYSIOLOGY

EDITED BY: Norio Fukuda, Henk Granzier, Shin'Ichi Ishiwata and Sachio Morimoto
PUBLISHED IN: Frontiers in Physiology

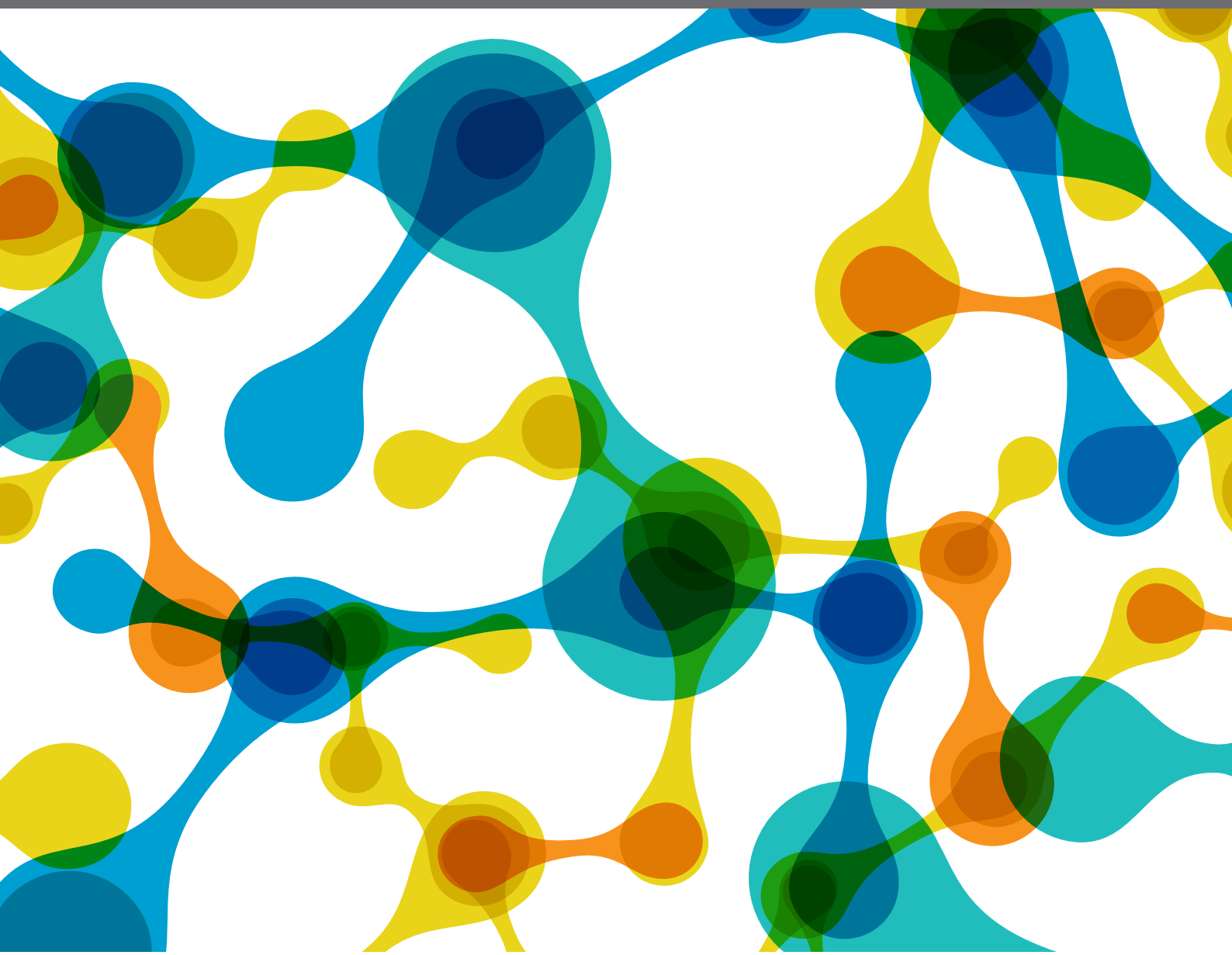

frontiers Research Topics

ISSN 1664-8714
ISBN 978-2-88971-086-7
DOI 10.3389/978-2-88971-086-7

About Frontiers

Frontiers is more than just an open-access publisher of scholarly articles: it is a pioneering approach to the world of academia, radically improving the way scholarly research is managed. The grand vision of Frontiers is a world where all people have an equal opportunity to seek, share and generate knowledge. Frontiers provides immediate and permanent online open access to all its publications, but this alone is not enough to realize our grand goals.

Frontiers Journal Series

The Frontiers Journal Series is a multi-tier and interdisciplinary set of open-access, online journals, promising a paradigm shift from the current review, selection and dissemination processes in academic publishing. All Frontiers journals are driven by researchers for researchers; therefore, they constitute a service to the scholarly community. At the same time, the Frontiers Journal Series operates on a revolutionary invention, the tiered publishing system, initially addressing specific communities of scholars, and gradually climbing up to broader public understanding, thus serving the interests of the lay society, too.

Dedication to Quality

Each Frontiers article is a landmark of the highest quality, thanks to genuinely collaborative interactions between authors and review editors, who include some of the world's best academicians. Research must be certified by peers before entering a stream of knowledge that may eventually reach the public - and shape society; therefore, Frontiers only applies the most rigorous and unbiased reviews.
Frontiers revolutionizes research publishing by freely delivering the most outstanding research, evaluated with no bias from both the academic and social point of view. By applying the most advanced information technologies, Frontiers is catapulting scholarly publishing into a new generation.

What are Frontiers Research Topics?

Frontiers Research Topics are very popular trademarks of the Frontiers Journals Series: they are collections of at least ten articles, all centered on a particular subject. With their unique mix of varied contributions from Original Research to Review Articles, Frontiers Research Topics unify the most influential researchers, the latest key findings and historical advances in a hot research area! Find out more on how to host your own Frontiers Research Topic or contribute to one as an author by contacting the Frontiers Editorial Office: frontiersin.org/about/contact

RECENT ADVANCES ON MYOCARDIUM PHYSIOLOGY

Topic Editors:
Norio Fukuda, Jikei University School of Medicine, Japan
Henk Granzier, University of Arizona, United States
Shin'Ichi Ishiwata, Waseda University, Japan
Sachio Morimoto, International University of Health and Welfare (IUHW), Japan

Citation: Fukuda, N., Granzier, H., Ishiwata, S., Morimoto, S., eds. (2021). Recent Advances on Myocardium Physiology. Lausanne: Frontiers Media SA. doi: 10.3389/978-2-88971-086-7

Table of Contents

frontiers in Physiology

EDITORIAL
published: 26 May 2021
doi: 10.3389/fphys.2021.697852

Editorial: Recent Advances on Myocardium Physiology

Norio Fukuda[1], Henk Granzier[2], Shin'ichi Ishiwata[3] and Sachio Morimoto[4]*

[1] Department of Cell Physiology, The Jikei University School of Medicine, Tokyo, Japan, [2] Department of Cellular and Molecular Medicine, University of Arizona, Tucson, AZ, United States, [3] Department of Physics, Faculty of Science and Engineering, Waseda University, Tokyo, Japan, [4] Department of Health Sciences at Fukuoka, International University of Health and Welfare, Fukuoka, Japan

Keywords: heart, cardiomyopathy, calcium, muscle, sarcomere, titin (connectin), troponin

Editorial on the Research Topic

Recent Advances on Myocardium Physiology

Myocardial activity reflects a multitude of signals that regulate the ability of cardiomyocytes to produce active and passive force. These mechanical activities originate in the sarcomeres highly ordered structures, composed of three filaments [thick and thin filaments, and the giant elastic protein titin (connectin)]. Early on, sarcomeres were thought to have little or no role in the regulation of the heart's pump function beyond being active force producers, in either the "*on*" or "*off*" state, simply responding to a change in the intracellular Ca^{2+} concentration [$[Ca^{2+}]_i$]. Since the turn of the 21st century, cardiac researchers have applied new molecular biological and optical technologies for elucidating the detailed mechanisms of myocardial contraction. Employing these new technologies revealed that the sarcomeres are much more complex than simple "*on-off*" machines; they are actively involved in the processes regulating the dynamics, growth, and remodeling of the heart. Likewise, these new technologies have provided new prospects to the diagnosis and treatment of heart disease. This Research Topic in *Frontiers in Physiology* is a collection of 16 original research and review papers on the physiology and pathophysiology of the myocardium, which provide compelling evidence of the rapid evolution in the field, and in particular on the roles of sarcomere proteins in health and disease.

Five of the 16 papers focus on titin, demonstrating that titin is a "hot topic" in this area of research. Before introducing each published paper in this Research Topic, we briefly summarize the current general knowledge of titin. Within the physiological sarcomere length (SL) range, titin predominantly bears passive force in mammalian myocardium (e.g., Granzier and Labeit, 2004; Fukuda et al., 2008). Titin comprises two portions: (1) the A-band portion is composed of immunoglobulin (Ig)-like and fibronectin type 3 repeats and binds to the rod segment of myosin and myosin-binding protein C (MyBP-C), and (2) the I-band portion which is the basis of viscoelasticity, has a complex sequence with distinct extensible segments: the tandem Ig segments, the PEVK segment and the segment that has a unique amino acid sequence (N2B or N2A, or both). Within the normal physiological SL range, the PEVK and unique sequences are stretched in response to SL elongation, resulting in the production of passive force. In the myocardium, the titin transcripts i.e., stiff N2B titin (containing the N2B segment) and compliant N2BA titin (containing both N2B and N2A segments) are processed differently. In the ventricle of large animals, including humans, both titin isoforms are similarly expressed, whereas N2B titin is predominantly expressed in the ventricle of small animals (e.g., small rodents).

Tharp et al. provide an informative review on titin, focusing especially on its role in dilated cardiomyopathy (DCM). DCM, a leading cause of heart failure which frequently results in sudden cardiac death, is inherited in ∼50% of cases; the most frequent genetic defects are associated with

OPEN ACCESS

Edited and reviewed by:
Paul M. L. Janssen, The Ohio State University, United States

****Correspondence:***
Norio Fukuda
noriof@jikei.ac.jp

Specialty section:
This article was submitted to Striated Muscle Physiology, a section of the journal Frontiers in Physiology

Received: *20 April 2021*
Accepted: *26 April 2021*
Published: *26 May 2021*

Citation:
Fukuda N, Granzier H, Ishiwata S and Morimoto S (2021) Editorial: Recent Advances on Myocardium Physiology. Front. Physiol. 12:697852. doi: 10.3389/fphys.2021.697852

truncation variants of the titin gene (*TTN*). Tharp et al. discuss the role of *TTN* mutations in the development of DCM, differential expressions of titin isoforms relating to DCM pathophysiology, and the effects of post-translational modifications of titin on cardiomyocyte functions. Future studies should be directed to elucidate whether missense variants are specifically associated with various types of cardiac disease, and the mechanism by which transcriptional and post-translational modifications contribute to DCM. As suggested by Tharp et al., altered forms of *TTN* can represent potential therapeutic targets for genetic and acquired heart disease.

Titin can be phosphorylated by various kinases. In particular, the N2B segment has physiologically important phosphorylation events mediated by various kinases, such as protein kinase A (PKA), protein kinase G (PKG), extracellular signal-regulated kinase 2 (ERK2), and calcium/calmodulin-dependent protein kinase type II delta (CaMKIIδ). Phosphorylation of the N2B segment results in a decrease in titin-based passive force, via, presumably, lengthening of the segment and as a result the whole molecule. Conversely, phosphorylation of the PEVK segment by protein kinase C alpha (PKCα) increases passive force. Although relatively lesser known to researchers in the field, recent studies have shown that protein kinase D (PKD) plays crucial roles in regulating contraction, hypertrophy and remodeling in the heart. Herwig et al. performed experiments using specimens from mice and humans, and reported that titin is a substrate of PKD, and titin-based passive force is decreased following PKD-dependent phosphorylation. Phosphosites were found in titin's various segments, including the proximal Ig region, the N2B segment and the PEVK segment. Lengthening of either the N2B segment or the PEVK segment, or both, likely underlies the PKD-dependent passive force reduction.

A sedentary lifestyle is related to increased cardiovascular risk factors and reduced ventricular wall compliance, as compared to an exercise-rich lifestyle. Chung et al. showed in rats that sedentary conditions are associated with a reduction in the content of the N2BA isoform relative to the N2B isoform in the ventricle, with no significant change in the total phosphorylation level. Likewise, the gene expression of a titin mRNA splicing factor, RNA Binding Motif 20 protein, was negatively correlated with the N2BA/N2B isoform ratio. It is therefore suggested that a sedentary lifestyle in humans reduces the N2BA/N2B isoform ratio, thereby reducing ventricular compliance. Because reduced ventricular wall compliance results in a decrease in ventricular filling and the ensuing reduction in cardiac output, the findings by Chung et al. confirm the importance of exercise in daily life activities.

Although other regions in the I-band portion of titin have been widely studied, its N2A segment, which assembles a signalosome with cardiac ankyrin repeat protein (CARP), has attained lesser attention. Lanzicher et al. investigated the effects of PKA-dependent phosphorylation and CARP on the N2A segment. They found that the N2A segment was phosphorylated by PKA, the phosphorylation did not alter the mechanical properties of the N2A segment, and that CARP blocked phosphorylation. A PKA phosphosite was revealed at the border between the N2A segment and immunoglobulin domain I81. Based on these findings, they proposed that the compliance of the N2A segment has local effects on the binding of signaling molecules and that it contributes to strain- and phosphorylation-dependent mechano-signaling.

Titin can be a therapeutic target in the treatment of heart disease associated with stiffening of ventricular muscle. Kolijn et al. provided evidence showing that nitric oxide-independent activation of soluble guanylyl cyclase (sGC) reduces myocyte passive force from the ventricles of rats and humans by improving the activities of PKA and PKG. They studied the effects of nitric oxide-independent activation of sGC on cardiomyocyte function in a hypertensive rat model with diastolic dysfunction and in biopsies from human heart failure with preserved ejection fraction (HFpEF). Passive force was increased in cardiomyocytes from Dahl salt-sensitive rats as well as in those from human myocardial biopsies. The increase in passive force was related to hypophosphorylation of the total titin and to deranged site-specific phosphorylation of titin's elastic segments, accompanied by reduced levels of PKG and PKA activity, along with dysregulation of hypertrophic pathway markers such as CaMKII, PKC, and ERK2. It was shown that sGC activator improved cardiomyocyte function, reduced inflammation and oxidative stress, improved sGC-PKG signaling and normalized hypertrophic kinases, suggesting that it is a potential treatment option for HFpEF patients and, presumably, for cases with increased hypertrophic signaling.

Hypertrophic cardiomyopathy (HCM) is a genetic disorder caused by mutations in different genes but mainly encoding myofilament proteins. While mutations in sarcomere proteins were discovered ∼30 years ago, the cellular and molecular mechanisms for the development of HCM remain unclarified. Many efforts have been made to treat HCM in the clinical setting; however, they have largely been unsuccessful, and no curative treatment has been developed. Chowdhury et al. shed light on this issue by providing important evidence that acceleration of the sarcoplasmic reticulum function prevents progression of cardiac troponin (Tn) T (cTnT)-linked HCM. They investigated a mouse model expressing the mutant cTnT-R92Q (which is linked to HCM and induces an increase in myofilament Ca^{2+} sensitivity and diastolic dysfunction), and they found that early amelioration of the diastolic dysfunction via enhanced $[Ca^{2+}]_i$ reduction by phospholamban knockout prevented the development of the HCM phenotype in this mouse model.

Regulation of cardiac physiology occurs via kinases that reversibly phosphorylate ion channels, Ca^{2+} handling machinery and signaling effectors. Essandoh et al. reviewed zDHHC enzymes and substrate S-acylation in myocardium physiology. Palmitoylation or S-acylation, the post-translational modification of cysteines with saturated fatty acids, plays roles in regulating various functions of proteins in cardiomyocytes. S-acylation

Abbreviations: $[Ca^{2+}]_i$, intracellular Ca^{2+} concentration; CaMKII, calcium/calmodulin-dependent protein kinase type II; DCM, dilated cardiomyopathy; ERK2, extracellular signal-regulated kinase 2; HCM, hypertrophied cardiomyopathy; MyBP-C, myosin-binding protein C; PKA, protein kinase A; PKC, protein kinase C; PKD, protein kinase D; PKG, protein kinase G; SL, sarcomere length; SR, sarcoplasmic reticulum; sGC, soluble guanylyl cyclase; Tn, troponin.

is catalyzed by the zDHHC family of S-acyl transferases that localize to intracellular organelle membranes or the sarcolemma. Recent works have revealed the functions of S-acylation in the heart, particularly in the regulation of cardiac excitation-contraction coupling. Although the dynamics and functions of these modifications in myocardium physiology have not been interrogated, proteins with critical signaling roles in the heart are likewise S-acylated, including receptors and G-proteins. Proteomic studies to interrogate alterations in cardiac palmitoylome in models with manipulated zDHHC enzyme activities will facilitate the discovery of novel molecular mechanisms giving rise to cardiac disease.

Four papers have added to the recent advances in the understanding of cardiomyopathies. Copeland et al. investigated whether TnI and MyBP-C phosphorylation levels are decreased in myocardium from non-HCM patients with aortic stenosis. Previous studies indicated that phosphorylation levels of these proteins are extremely low in patients with hypertrophic obstructive cardiomyopathy (HOCM), an obstructive variant of HCM with aortic stenosis, compared to in patients with non-obstructive HCM. They found that the phosphorylation levels of TnI and MyBP-C were significantly lower in aortic stenosis patients' hearts than in donor hearts, suggesting that left ventricular pressure overload is a major factor in inducing the secondary phenotype of HOCM hearts. The mechanisms of low phosphorylation await further investigations. However, as Copeland et al. pointed out, such mechanisms are likely coupled with downregulation of β adrenoceptors and the ensuing reduction of PKA activity as well as with increased phosphatase activities.

McDonald et al. analyzed the myofibrillar basis for contractile dysfunction in failing human myocardium. They introduced the novel parameter "peak power output normalized to isometric force (PNPO)," and measured the contractile properties in cardiac myocytes from left ventricular mid-wall biopsies of donor and failing human hearts. It was found that maximal Ca^{2+}-activated isometric force, maximal force development rates (k_{tr}), and Ca^{2+} activation dependence of k_{tr} were similar between the groups. The Ca^{2+} activation dependence of loaded shortening and power output were then examined. PNPO was decreased by ∼10% from maximal Ca^{2+} to half-maximal Ca^{2+} activations in both donor and failing groups. The SL dependence of PNPO was diminished in failing myocytes. Their findings suggest that the altered SL-dependent regulation of myofilament function impairs ventricular performance in failing human hearts.

Groen et al. compared the effects of mutations associated with HCM or DCM. In their study, the native Tn complex in skinned trabecular fibers of guinea pigs was replaced with recombinant human cardiac troponin complexes containing different human cardiac TnT (hcTnT); i.e., HCM-associated $hcTnT^{R130C}$, DCM-associated $hcTnT^{\Delta K210}$ or wild type hcTnT. They found that lengthening the fibers from 1.1 slack length (L_0) to 1.25 L_0 increased Ca^{2+} sensitivity in fibers containing $hcTnT^{R130C}$, did not alter Ca^{2+} sensitivity in the wild type, and decreased Ca^{2+} sensitivity in fibers containing $hcTnT^{\Delta K210}$. As they noted, the findings with the wild type and $hcTnT^{\Delta K210}$ were unexpected. As an exemplification, Mashali et al. (2021) recently reported that length-dependent activation is preserved and virtually identical in large numbers of failing and non-failing human hearts. Nevertheless, the findings by Groen et al. may be important in the primary effects of mutations on length-dependent activation that contribute to the development of the diverging phenotypes in HCM and DCM in humans.

Pioner et al. reviewed DCM associated with mutations in the Duchenne muscular dystrophy (DMD) gene encoding dystrophin. They discussed the physiological roles of dystrophin in myocardial functions in cardiac development, as well as in the progression of the disease. Dystrophin is localized at the cytoplasmic face of the muscle cell plasma membrane, or at the sarcolemma, and particularly at the components within a cytoskeletal lattice (costameres). Costameres couple the sarcolemma with the Z disk of myofibrils via interacting proteins. Recently, studies using human induced pluripotent stem cells (hiPSCs) have advanced to reveal the pathogenesis of DMD. It has been suggested that the pathogenic mechanisms appear early in the disease progression as a combination of the developmental consequences of the absence of full-length dystrophin in cardiomyocytes. Gene therapies have been emerged as a promising approach for DMD; i.e., a gene therapy with micro dystrophin, up-regulation of utrophin or exon skipping approaches are currently the most promising ways to rescue or at least mitigate the DMD phenotype.

Experimentations using living isolated single cardiomyocytes have dramatically advanced our understanding of myocardium physiology and pathophysiology. Wright et al. reported a new approach using the novel CytoCypher High-Throughput System (CC-HTS). This system allows for assessment of shortening of sarcomeres, cell length, Ca^{2+} handling and cellular morphology of nearly four cells per minute. They explored basic morphological and functional characteristics of rat, mouse, guinea pig, and human cells. Likewise, they analyzed the effects of agents that affect actomyosin interaction involved in cardiomyocyte contraction. The introduction of HTS methodology for myocytes has dramatically increased the speed of measurement and improved the statistical power while reducing the number of myocyte isolations needed for a study.

The chambers of the heart fulfill different hemodynamic functions. By taking advantage of the high-throughput contractility set-up, Nollet et al. measured the contractile function of >2,000 cultured cells from the atrium, right ventricle (RV), left ventricle (LV) and interventricular septum (IVS) of the healthy rat. They report two important findings. First, compared to ventricular cardiomyocytes, atrial cells showed a twofold lower shortening amplitude and ∼1.5-fold slower kinetics of shortening and lengthening. The interventricular differences were much smaller; RV cells displayed 12–13% less fractional shortening and 5–9% slower shortening and 3–15% slower lengthening kinetics compared to LV / IVS cells. These findings are in line with the contractile differences observed at the atrioventricular level in traditional studies. Their study highlights the importance of extensive, unbiased sampling when performing studies on cardiomyocyte contractility.

Two papers review important basic characteristics of myocardial functions. Ishii et al. discussed the effects of

temperature on the contractile performance of mammalian striated muscle. In myocardium, either a decrease or an increase in temperature enhances its contractility: First, a rapid decrease in solution temperature generates contraction in intact cardiac muscle, a phenomenon known as "rapid cooling contracture (RCC)." RCC is caused by Ca^{2+} release from the sarcoplasmic reticulum (SR) through ryanodine receptors. Second, rapid heating induces reversible cardiomyocyte shortening (Oyama et al., 2012). It is important that this heating-induced contraction is regulated at the sarcomere level. Ishii et al. discussed their previous work (Ishii et al., 2019) demonstrating that reconstituted cardiac thin filaments exhibit sliding movements at $>\sim 35^{\circ}$C in the absence of Ca^{2+}. One possible mechanism for the "thermal activation" of thin filaments is partial dissociation of the Tn-tropomyosin complex from F-actin, thereby allowing the actomyosin interaction.

Myocardial cells exhibit spontaneous beating. Most notably, pacemaker cells beat at a relatively fixed frequency, and similar spontaneous beating likewise occurs in embryonic and neonatal cardiomyocytes. Ryanodine receptors (RyR) in the SR play an important role in spontaneous beating, coupled with rhythmic changes in $[Ca^{2+}]_i$. Cohen and Safran focused on the role of RyR channels and SR Ca^{2+} pump functions in the cytoplasmic $[Ca^{2+}]$ cycles, and constructed a minimal mathematical model based on the Van-der-Pol equation. Accordingly, the dynamics of spontaneous beating, as well as paced isolated cardiomyocytes, were simulated as derived from Ca^{2+} pumps and channels dynamics. Spontaneous contraction-relaxation cycles in normal ventricular myocytes may result in fatal arrythmias. Therefore, understanding not only the biology but also the physics behind cardiomyocyte beating can facilitate the design of better treatments for arrhythmias.

Washio et al. add a mathematical simulation paper based on the bio-hierarchy of the heart, i.e., sarcomeres, myofibrils, cells, muscle fibers and the organ. Namely, by taking into account the fiber reorientation in the heart, they refined their UT-Heart model (e.g., Sugiura et al., 2012). From the viewpoint of myocardium physiology, they provided three important findings. First, the force-velocity relationship is crucial in transferring the fiber shortening strain to active force in myofiber reorientation. Second, the algorithm developed in their study facilitates assessment of homogeneity in active force and fiber shortening strain, and results in near-optimal pumping performance. Third, the reorientation mechanism may degrade the heart's pumping performance if myocardial contractility becomes inhomogeneous. Future studies are warranted to investigate the effects of changes in the dynamics of a component in the heart's bio-hierarchy on its physiological and pathophysiological functions.

This Research Topic that although many challenges remain, considerable progress has been made in understanding the physiology and pathophysiology of the heart. As revealed by the authors, by taking advantage of current technologies as well as developing new techniques and approaches, obstacles toward elucidating the physiology and pathophysiology of the heart can be overcome, bringing us closer toward understanding and ultimately treating disorders of the heart.

AUTHOR CONTRIBUTIONS

All authors listed have made a substantial, direct and intellectual contribution to the work, and approved it for publication.

FUNDING

This work was supported by the Ministry of Education, Culture, Sports, Science, and Technology of Japan Grants-in-Aid for Scientific Research (B) (to NF: 20H03421).

ACKNOWLEDGMENTS

We thank Drs. Kotaro Oyama and Shuya Ishii (National Institutes for Quantum and Radiological Science and Technology, Gunma, Japan) for helpful discussions.

REFERENCES

Fukuda, N., Granzier, H. L., Ishiwata, S., and Kurihara, S. (2008). Physiological functions of the giant elastic protein titin in mammalian striated muscle. *J. Physiol. Sci.* 58, 151–159. doi: 10.2170/physiolsci.RV005408

Granzier, H. L., and Labeit, S. (2004). The giant protein titin: a major player in myocardial mechanics, signaling, and disease. *Circ. Res.* 94, 284–295. doi: 10.1161/01.RES.0000117769.88862.F8

Ishii, S., Oyama, K., Arai, T., Itoh, H., Shintani, S. A., Suzuki, M., et al. (2019). Microscopic heat pulses activate cardiac thin filaments. *J. Gen. Physiol.* 151, 860–869. doi: 10.1085/jgp.201812243

Mashali, M. A., Saad, N. S., Canan, B. D., Elnakish, M. T., Milani-Nejad, N., Chung, J. H., et al. (2021). Impact of etiology on force and kinetics of left ventricular end-stage failing human myocardium. *J. Mol. Cell. Cardiol.* 156, 7–19. doi: 10.1016/j.yjmcc.2021.03.007

Oyama, K., Mizuno, A., Shintani, S. A., Itoh, H., Serizawa, T., Fukuda, N., et al. (2012). Microscopic heat pulses induce contraction of cardiomyocytes without calcium transients. *Biochem. Biophys. Res. Commun.* 417, 607–612. doi: 10.1016/j.bbrc.2011.12.015

Sugiura, S., Washio, T., Hatano, A., Okada, J., Watanabe, H., and Hisada, T. (2012). Multi-scale simulations of cardiac electrophysiology and mechanics using the University of Tokyo heart simulator. *Prog. Biophys. Mol. Biol.* 110, 380–389. doi: 10.1016/j.pbiomolbio.2012.07.001

Conflict of Interest: The authors declare that the research was conducted in the absence of any commercial or financial relationships that could be construed as a potential conflict of interest.

frontiers in Physiology

REVIEW
published: 28 November 2019
doi: 10.3389/fphys.2019.01436

The Giant Protein Titin's Role in Cardiomyopathy: Genetic, Transcriptional, and Post-translational Modifications of TTN and Their Contribution to Cardiac Disease

*Charles A. Tharp[1], Mary E. Haywood[1], Orfeo Sbaizero[2], Matthew R. G. Taylor[1] and Luisa Mestroni[1]**

[1] Adult Medical Genetics Program and Cardiovascular Institute, University of Colorado Anschutz Medical Campus, Aurora, CO, United States, [2] Department of Engineering and Architecture, University of Trieste, Trieste, Italy

Dilated cardiomyopathy (DCM) is a leading cause of heart failure, sudden cardiac death and heart transplant. DCM is inherited in approximately 50% of cases, in which the most frequent genetic defects are truncation variants of the titin gene (*TTN*tv). *TTN* encodes titin, which is the largest protein in the body and is an essential component of the sarcomere. Titin serves as a biological spring, spanning half of the sarcomere and connecting the Z-disk to the M-line, with scaffold and signaling functions. Truncations of titin are believed to lead to either haploinsufficiency and loss-of-function, or to a "poison peptide" effect. However, other titin mechanisms are postulated to influence cardiac function including post-translational modifications, in particular changes in titin phosphorylation that alters the stiffness of the protein, and diversity of alternative splicing that generates different titin isoforms. In this article, we review the role of *TTN* mutations in development of DCM, how differential expression of titin isoforms relate to DCM pathophysiology, and discuss how post-translational modifications of titin can affect cardiomyocyte function. Current research efforts aim to elucidate the contribution of titin to myofibril assembly, stability, and signal transduction, and how mutant titin leads to cardiac dysfunction and human disease. Future research will need to translate this knowledge toward novel therapeutic approaches that can modulate titin transcriptional and post-translational defects to treat DCM and heart failure.

OPEN ACCESS

Edited by:
Henk Granzier, University of Arizona, United States

Reviewed by:
Ralph Knöll, AstraZeneca, Sweden
Zoltán Papp, University of Debrecen, Hungary

***Correspondence:**
Luisa Mestroni
luisa.mestroni@cuanschutz.edu

Specialty section:
This article was submitted to Striated Muscle Physiology, a section of the journal Frontiers in Physiology

Received: *27 August 2019*
Accepted: *07 November 2019*
Published: *28 November 2019*

Citation:
Tharp CA, Haywood ME, Sbaizero O, Taylor MRG and Mestroni L (2019) The Giant Protein Titin's Role in Cardiomyopathy: Genetic, Transcriptional, and Post-translational Modifications of TTN and Their Contribution to Cardiac Disease. Front. Physiol. 10:1436. doi: 10.3389/fphys.2019.01436

HIGHLIGHTS

- Titin (TTN) truncation variants are the most frequent cause of dilated cardiomyopathy, one of the main causes of heart failure and heart transplant. Titin is a giant protein, and the mechanisms causing the disease are both complex and still incompletely understood.
- This review discusses the role of titin in myocardial function and in disease. In particular, we discuss TTN gene structure, the complexity of genotype-phenotype correlation in human disease, the physiology of TTN and the role of post-translation modification.

- Additional studies will be required to clarify whether missense variants are associated with cardiac disease. While initial studies suggested a role of non-synonymous variants in arrhythmogenic cardiomyopathy, confirmatory investigations have been hampered by the complexity of the protein structure and function.

Keywords: titin, dilated cardiomyopathy, sarcomere, truncation variants, proportion-spliced-in, RBM20, phosphorylation, phosphosites

INTRODUCTION

The sarcomere is the basic structural unit that facilitates contraction of striated muscle. An essential component of the sarcomere is the giant filament protein titin (TTN). TTN is the largest protein in the human body, which is encoded by 364 exons of the *TTN* gene that produce a protein of between 27,000 and 33,000 amino acids in length with a molecular weight ranging between 2,900 and 3,800 kDa (Freiburg et al., 2000; LeWinter et al., 2007). Structurally, TTN serves as a biological spring, spanning half of the sarcomere and connecting the Z-disk to the M-line. It is composed of four structural subunits (**Figure 1**). The Z-line is the N-terminal region that embeds and anchors TTN to the sarcomere Z-disk. The I-band is composed of repetitive immunoglobulin (Ig) regions that can extend when mechanical force is applied, providing the extensible or "spring-like" function of TTN. The A-band is composed of Ig regions alternating with fibronectin and is a non-extensible rigid region that serves as a stable anchor for myosin binding during muscle contraction. The M-band is the C-terminal domain containing serine/threonine kinase domains and forms a scaffold with myomesin to link myosin to thick filaments at the M-line of the sarcomere. In addition to the essential structural role that TTN provides within the sarcomere it is also important for sarcomere formation, mechanosensing, and signal transduction.

Alternative splicing is a major feature of *TTN* and produces three major isoforms: N2A, N2B, and N2BA which predominately differ in the lengths of the extensible I-band domains. N2B and N2BA are isoforms expressed within adult cardiomyocytes and differ based on their length and extensibility, with N2BA being a longer, less rigid protein compared to N2B (Freiburg et al., 2000). *TTN* mutations are associated with cardiac diseases, particularly dilated cardiomyopathy (DCM) that presents with ventricular enlargement and systolic dysfunction in the absence of alternative etiologies of cardiomyopathy such as valvular, hypertensive, congenital, or ischemic causes (Bozkurt et al., 2016). DCM has an estimated prevalence of 1:250–1:500. DCM accounts for up to one half of heart failure cases (Hershberger et al., 2013; LeWinter and Granzier, 2013). With the advent of next generation sequencing, many gene mutations that cause DCM have been discovered with 50 genes causing genetic DCM (Hershberger et al., 2010, 2013; Pinto et al., 2016; McNally and Mestroni, 2017). Of the known genetic mutations that cause DCM, *TTN* mutations are the most common accounting for 20–25% of cases (LeWinter and Granzier, 2013). Specifically, TTNtv are highly associated with development of DCM (Herman et al., 2012; Merlo et al., 2013). In recent years, the mechanisms for how *TTN* and potential modifier genes contribute to cardiomyopathy have been more clearly elucidated. The purpose of this article is to review the role of *TTN* mutations in development of DCM. Specifically, we will discuss how location of TTNtv lead to DCM, review mechanisms for TTNtv leading to phenotypes, consider how differential expression of TTN isoforms relates to DCM pathophysiology, and discuss how post-translational modifications of TTN can affect cardiomyocyte function.

Abbreviations: NMD, Non-sense mRNA decay; PSI, proportion-spliced-in; TTN, titin; TTNtv, titin truncation variation.

ASSOCIATION OF TTN TRUNCATION POSITION AND HUMAN HEART DISEASE

Although *TTN*tvs are associated with a large proportion of DCM, it is interesting that TTNtvs are also found in 2–3% of the general population who are asymptomatic (Golbus et al., 2012; Herman et al., 2012; Roberts et al., 2015). While some healthy TTNtv carriers may later develop DCM, the heterogeneity of pathogenicity of TTNtv has prompted efforts to better understand how mutational position influences phenotype. Roberts et al. completed *TTN* sequencing in a diverse cohort of >5,000 persons whose cardiac phenotypes were known (including healthy persons) to correlate truncation location position with phenotype. The data demonstrated that a key predictor of pathogenicity of a TTNtv is whether the affected exon is expressed in cardiac tissue (Roberts et al., 2015). TTNtv located in constitutive exons were more often pathogenic; whereas those located in exons that are minimally expressed in heart tissue or that can be rescued, or "bypassed," by differential splicing had a lower risk of DCM. A score to predict whether a truncation mutation in TTN is pathogenic has been proposed as the PSI. The PSI calculates a percentage of TTN transcripts in which a given exon is spliced into an expressed transcript based on RNA sequencing data from human left-ventricular tissue. Therefore, a high PSI score suggests a high proportion of the total transcripts include a given exon in cardiac tissue. This study found that a TTNtv located in exons with a PSI >0.9 were associated with at 93% probability of pathogenicity (likelihood ratio-14) if discovered in a patient with a DCM phenotype (Roberts et al., 2015).

Specific *TTN* variants may also be position-dependent with respect to proximal or distal ends of the protein with a correlation of pathogenicity to distance from N-terminal (Roberts et al., 2015; Schafer et al., 2017). This correlation of position to pathology however, is more likely a reflection of alternative splicing than true positional location, as TTNtv in DCM are overrepresented

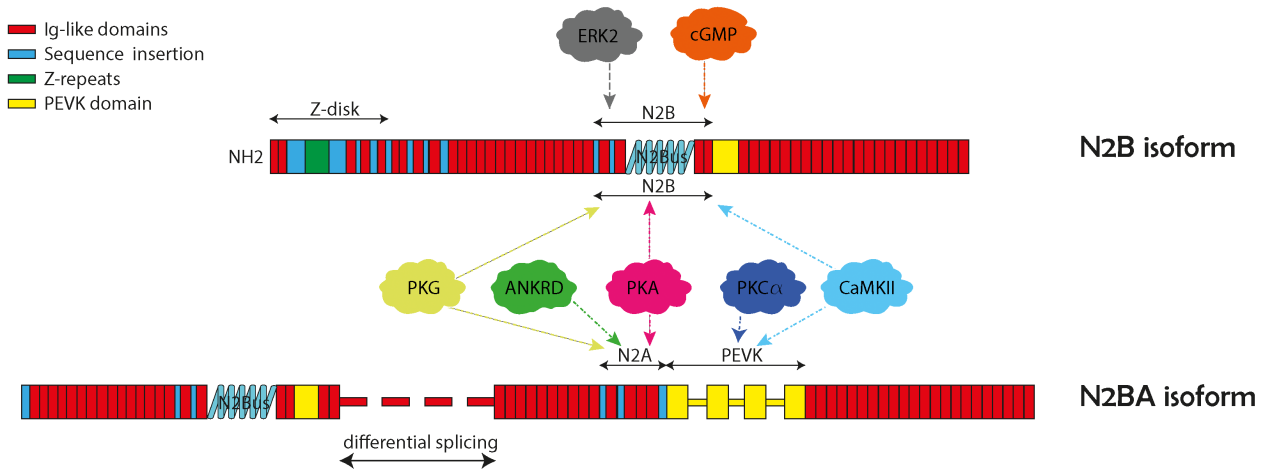

FIGURE 1 | Structure and domains of titin N2B and N2BA isoforms. The two cardiac isoforms and their protein kinase phosphorylation N2B and N2BA are illustrated here with their specific protein regions. Both isoforms contain the N2B unique sequence (N2Bus), and the PEVK region (titin region rich in proline, glutamate, valine, and lysine). The N2BA isoform also contains the N2A unique sequence (N2Aus). The various protein kinase binding partners are indicated in the balloons with arrows pointing to their general binding regions.

in the more distal A-band which has a higher proportion of constitutively expressed exons. In contrast, mutations in the more proximal exons are more likely to undergo alternative splicing (Roberts et al., 2015; Schafer et al., 2017). As an example, a large portion of TTNtv found in healthy controls are found in a single exon that represents an alternative 3′ exon that is exclusively expressed in the Novex-3 isoform which does not span the sarcomere and has very low expression in cardiomyocytes (Herman et al., 2012; Roberts et al., 2015; Schafer et al., 2017). The association of clinically relevant TTNtv with their expression is further demonstrated in **Figure 2** where pathogenic mutations from the ClinVar database are clustered in the highly constitutively expressed A-band region located at the carboxy terminus.

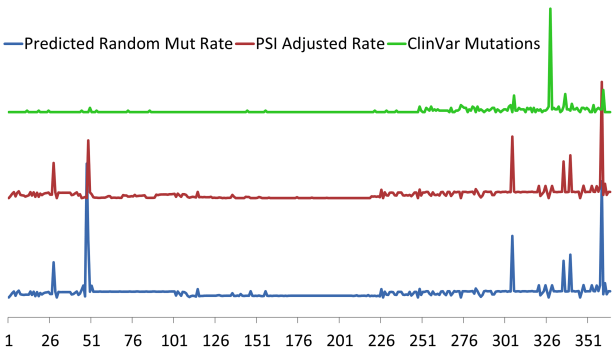

FIGURE 2 | Relative predicted rates of purely random mutations in TTN based on exon size (bottom, blue) and adjusted for cardiac exon expression (middle red) using Proportion Spliced In (PSI) approach of Roberts et al. (2015). Regions of where PSI is generally <50% include exons 51–69, 78–89, and 124–220. Exon location of 327 clinically relevant TTN truncation variants from ClinVar (top, green) demonstrates clustering toward the carboxy terminus of TTN in the region of the A-band where most of the constitutively expressed exons are located. Exons indicated on horizontal axis.

MECHANISMS OF TTNTV CARDIAC PATHOGENICITY

The exact mechanisms for how TTNtv lead to the DCM phenotype have not been clearly demonstrated. In families with inherited TTNtvs, the heritability follows an autosomal dominant pattern, however, there is clearly incomplete and age-dependent penetrance, evidenced by patients who carry predicted pathogenic TTNtv who do not acquire the DCM phenotype, or do not develop DCM until later in life, respectively (Herman et al., 2012; Franaszczyk et al., 2017). The molecular mechanism for how TTNtv causes DCM has been controversial with several models proposed. It has been conjectured that TTNtv may lead to abnormally shortened TTN proteins that cause harm to sarcomere function and cardiomyocytes through a "poison peptide" mechanism. In order to support this model, identification of truncated TTN proteins and their association with sarcomere and cardiomyocyte dysfunction would be required, which has proven difficult. One model of the "poison peptide" has been suggested by the discovery of a specific missense mutation in *TTN* leading to a truncated protein that was discovered in two separate families with autosomal dominant inheritance of DCM. This CMD1G mutation was predicted to affect a highly conserved immunoglobulin fold at the Z-disc I-band transition (Gerull et al., 2002). In another example, induced pluripotent stem cell-derived cardiomyocytes (hiPS-CM) were made from a DCM patient with an A-band TTNtv. In this model, truncated TTN protein was isolated from the sarcomere and it was demonstrated that disorganization of the sarcomere led to reduction of contractile force by more than 50% (Hinson et al., 2015). Additionally, Chopra et al. described a direct mechanism by which TTNtvs affect sarcomere

assembly related to loss of a binding site. Using hiPS-CM, it was shown that cells with heterozygous A-band TTNtv did not effectively form sarcomeres due to loss of binding site for β-cardiac myosin on TTN. This appeared to prevent formation of protocostameres and Z-disks leading to a reduction in diastolic tension (Chopra et al., 2018). These two studies support disease models by which TTNtv lead to abnormally shortened TTN protein and directly affect sarcomere function. Interestingly, changes in contractile force that were seen in hiPS-CM studies could not be recapitulated in a study of isolated cardiomyocytes derived from human hearts with TTNtvs (Vikhorev et al., 2017). This discrepancy in contractility between hiPS-CM and adult cardiomyocytes may be related to the relative developmental immaturity of hiPS-CM.

While there may be circumstances where some TTNtvs cause dominant negative effects on the sarcomere, an alternative model is haploinsufficiency. In this model, TTNtv leads to abnormal mRNA transcripts that are degraded by NMD (Zhou et al., 2015). From this, follows a reduction in allelic expression of TTN and this reduction could increase metabolic stress leading to compensatory changes in the cardiomyocyte and eventual phenotype of DCM (Tabish et al., 2017; Ware and Cook, 2018). Data supporting this model come from a study where A-band and I-band TTNtv in rats do not affect amount of TTN protein, however, increase NMD (Schafer et al., 2017). Furthermore it has been shown that TTNtv in A-band and I-band similarly affect cardiac metabolism by reducing medium and long chain fatty acids as nutritional substrates, instead of preferring branched-chain amino acids and glycolytic intermediates similar to metabolic changes seen in other models of heart failure (Shibayama et al., 2015; Schafer et al., 2017). It has been further proposed that changes in metabolism lead to activation of mTOR complex 1 signaling which causes pathogenic responses related to protein synthesis and autophagy (Ramos et al., 2012; Neishabouri et al., 2015; Schisler et al., 2015; Yano et al., 2016). Activation of the mTOR complex and associated pathways has been found in other forms of DCM suggesting they represent terminal maladaptive pathways (Yano et al., 2016; Sweet et al., 2018).

This model of haploinsufficiency leading to increased metabolic stress is also in keeping with the clinical presentation of DCM in patients with TTNtv who have incomplete penetrance and generally present later in life, and often in conjunction with additional cardiac stressors (Herman et al., 2012; Franaszczyk et al., 2017). In a recent prospective observational study of patients with DCM, patients with TTNtv presented at an advanced median age of 49, which is similar to other studies of TTNtv in DCM (Herman et al., 2012; Franaszczyk et al., 2017; Tayal et al., 2017). Compared to other etiologies of DCM, patients with TTNtvs had similar clinical prognosis with respect to a combined outcome of cardiovascular mortality, major arrhythmia, and major heart failure events (Tayal et al., 2017). This study also demonstrated no significant phenotype differences among TTNtvs in regards to mutation location suggesting TTNtvs similarly affected cardiac stress leading to DCM, arguing for a mutation independent haploinsufficiency model (Tayal et al., 2017). Interestingly, even without a phenotype of DCM, changes in LV size are seen in asymptomatic patients with TTNtv suggesting that TTNtv affect cardiac function in ostensibly healthy persons and that also there could be significant compensation prior to development of DCM (Schafer et al., 2017). Animal models similarly demonstrate this delayed or incomplete DCM phenotype. This is evidenced by a murine model described by Gramlich et al. (2015) where heterozygous TTNtv mutants did not develop DCM unless exposed to cardiac stress. This study also described a potential therapeutic target in treating TTNtvs by alternatively splicing out the mutant exon. It was demonstrated that heterozygous mice that developed DCM with cardiac stress could be rescued by antisense oligonucleotides that induce exon skipping of the mutant exon. By skipping the frameshift mutation containing exon, premature termination was avoided and a majority of the TTN protein was translated. In this model, the DCM phenotype was rescued as demonstrated by sarcomere formation and contractile performance (Gramlich et al., 2015). This study represents an intriguing proof of concept for therapy to treat patients with TTNtvs with antisense oligonucleotides.

TTN TRANSCRIPTIONAL ISOFORM SWITCHING ALTERS PASSIVE TENSION OF THE SARCOMERE

Titin has many roles, including signal transduction and mechanosensing, which are reviewed elsewhere (Gautel, 2011; Tabish et al., 2017). In the context of DCM pathophysiology, as a large protein that bridges half of the sarcomere, TTN is essential for sarcomere stabilization and maintenance of passive and active tension. Within the I-band, Ig-domains serve as springs and provide elasticity to TTN and the sarcomere. Understandably, the role of TTN's spring functions in diastolic relaxation is of interest. When the sarcomere is not stretched, the Ig-domains are relaxed and highly folded. When tension is applied, the domains extend to provide passive tension. Initial tensile forces stretch the distal Ig-domains followed by stretching of the PEVK segment with the N2B element providing the highest level of passive resistance (Trombitas et al., 1998; Kontrogianni-Konstantopoulos et al., 2009; Tabish et al., 2017). These four unique domains provide increased passive force as TTN is more highly extended. This tension-force relationship contributes to the physiologic function described in the Frank-Starling curve where increased diastolic volume leads to increased contractility (Fukuda and Granzier, 2005; Tabish et al., 2017).

One of the most important ways passive resistance is modulated in cardiomyocytes is through alternative expression of TTN isoforms. In healthy hearts, the TTN N2B isoform is predominant and the TTN N2BA isoform is less expressed (Nagueh et al., 2004). N2B is a comparatively shorter protein with fewer exons expressed from the I-band, and has less elasticity as a result of less Ig-like domains compared to the N2BA. Due to its larger size and increased elasticity, N2BA has less passive stiffness compared to N2B. In DCM, there is reduced systolic function and enlargement of the ventricles, which may be partially explained by decreased passive tension leading to less diastolic forces and resultant dilation of the heart. Experimentally it has been shown

that heart tissue extracted from patients with DCM exhibit less passive tension when compared to controls (Nagueh et al., 2004). More interestingly in the same study, patients with DCM also had an increased ratio of N2BA:N2B TTN isoforms suggesting that reduced passive force from TTN isoform switching is a feature of DCM. The N2BA:N2B isoform ratios also correlated with echocardiographic findings of increased end diastolic volume, increased end systolic volume, and decreased systolic ejection fraction (Nagueh et al., 2004).

It has been conjectured that switching to the longer N2BA isoform is initially physiologic and improves diastolic function; however, it is likely that as the myocardium continues to fail, systolic function worsens due to decreased passive tension and diastolic pressure (Makarenko et al., 2004).

While regulation of isoform switching in TTN is likely complex, there has clearly been an association with the splicing factor RNA binding motif protein RBM20 (Guo et al., 2012). RBM20 is a splicing factor specific to muscle cells that is involved in formation of the spliceosome, which regulates mRNA splicing. Notably, mutations in *RBM20* are associated with a clear DCM phenotype in humans (Brauch et al., 2009; Li et al., 2010; Refaat et al., 2012). In a rat model, knockout of *RBM20* causes DCM and these rats have increased ratio of N2BA:N2B isoforms suggesting that RBM20 regulates isoform expression of TTN (Guo et al., 2012). Interestingly, in the same RBM20 knockout rats, viral expression of *RBM20* decreased the N2BA:N2B ratio (Guo et al., 2012). This suggests that upregulation of RBM20 can favor production of the shorter, stiffer N2B isoform and possibly rescue a DCM phenotype. These results were recapitulated in iPSC derived cardiomyocytes from a patient with an RBM20 missense mutation. These cells demonstrated a reduction in the amount of N2B expression leading to reduction in active and passive force when studied in engineered heart muscle (Streckfuss-Bomeke et al., 2017). Based on these results, control of RBM20 to alter N2BA:N2B may represent a potential therapeutic target for treating patients afflicted with DCM. Several cell signaling pathways have been implicated in regulation of RBM20 which subsequently leads to altered N2BA:N2B ratios. Recently, in neonatal rat cardiomyocytes, insulin was shown to activate the mTOR kinase axis leading to RBM20 dependent increase in N2B isoform expression (Zhu et al., 2017). Interestingly, the mTOR pathway is associated with development of DCM caused by TTNtv as described above. In addition, thyroid hormone, specifically T3, has been shown to upregulate N2B isoform expression via RBM20 in neonatal rat cardiomyocytes (Zhu et al., 2015).

One proposed mechanism by which RBM20 affects TTN alternative splicing is via regulation of circular RNA (circRNA) (Khan et al., 2016). CircRNA is formed during transcription when the spliceosome covalently binds the 5′ and 3′ ends of an exon forming a stable RNA molecule (Memczak et al., 2013). It is thought that circRNAs are co-generated with mRNAs and their formation regulates gene expression by competing with mRNA transcription to decrease availability of linear mRNAs (Ashwal-Fluss et al., 2014). In their paper, Khan et al. (2016) used ribosomal depleted RNA from human hearts and demonstrated significant circRNA from *TTN*. Furthermore, they showed that RBM20 knockout mice lack the TTN circRNA (Ashwal-Fluss et al., 2014). This study suggests that RBM20 is essential for formation of TTN circRNA and that circRNA is a pathway by which RBM20 modulates expression of alternative isoforms of TTN.

Control of RBM20 and subsequent expression of TTN N2BA:N2B ratios is also important in the development of diastolic dysfunction. It is conjectured that decreasing the N2BA:N2B ratio results in stiffening of TTN and a more rigid sarcomere. This in turn may lead to impaired relaxation and a less compliant ventricle consistent with heart failure with preserved ejection fraction (HFpEF). This is seen in a small group of patients who required heart transplantation due to heart failure. The patients with failing hearts but normal systolic function suggestive of diastolic dysfunction had a lower N2BA:N2B ratio compared to patients with failing hearts and reduced systolic function (Borbely et al., 2009). Furthermore in a mouse model of diastolic dysfunction, inhibition of RBM20 and increase in N2BA:N2B TTN expression led to improvement of HFpEF resulting in normalization of function by echocardiogram and exercise tolerance (Bull et al., 2016). This suggests that control of TTN stiffness is an important therapeutic target for patients with systolic as well as diastolic dysfunction.

POST-TRANSLATION MODIFICATION OF TITIN

In addition to transcriptional modifications, TTN function is also highly regulated by post-translational modifications. These alterations of TTN allow the cardiomyocyte and sarcomere to rapidly adjust to environmental changes within the heart. The most well described modification to TTN involves phosphorylation and de-phosphorylation at unique sites within the protein. Due its size, TTN may have the most phosphorylation sites of any protein. Hundreds of phosphorylation sites on TTN have been predicted based on proteomic analysis. These are listed on online databases: http://gygi.med.harvard.edu/phosphomouse/index.php (Huttlin et al., 2010), http://www.phosphosite.org/ (Hornbeck et al., 2015) or http://cpr1.sund.ku.dk/cgi-bin/PTM.pl (Lundby et al., 2012). While much effort has been made to understand how phosphorylation of TTN affects its function within the cardiomyocyte, only a few of these phosphosites have been associated with changes in the structure and function of TTN (Linke and Hamdani, 2014; Krysiak et al., 2018). The effect that phosphorylation has on the function of TTN depends on the unique structural domain that is being altered. Phosphorylation on TTN can be categorized based on which domain is being altered. Most of the biologically significant phosphosites that have been described within TTN are located in "spring-like" I-domain. This is likely due to the dynamic properties of this domain, where phosphorylation has the most significant effects on the passive and active

tension of the sarcomere. Within the I-domain, there are two specific elements where differential phosphorylation has been shown to directly alter the length and tension of cardiomyocytes.

The PEVK element within the I-band is highly extensible and is characterized by richness in proline, glutamate, valine, and lysine (Freiburg et al., 2000). Phosphorylation of this element by the kinase PKCα in mouse and pig cardiomyocytes has been shown to increase cardiomyocyte passive tension by 20–30% (Hidalgo et al., 2009). Similarly, human cardiomyocytes treated with PKCα demonstrated increased passive stiffness compared to controls (Rain et al., 2014). It is hypothesized that addition of the positively charged phosphate in the negatively charged PEVK element increases electrostatic attraction making it less extensible and increasing passive force (Hamdani et al., 2017). In humans with failing hearts, it has been shown that there is increased PKC mediated phosphorylation of the PEVK element, which corresponds with increased passive tension (Hamdani et al., 2013). This study was done in patients with both hypertrophic and DCM who likely have very different diastolic pressures. It may be interesting to observe phosphorylation of the PEVK element in only DCM patients, where it may be hypothesized that there would be reduced phosphorylation leading to reduced passive tension and a dilated phenotype.

In addition to phosphorylation of the PEVK element, there are several phosphorylation sites within the cardiac specific N2B element. The N2B element is expressed on both cardiac TTN isoforms N2B and N2BA and is composed of three Ig domains as well as a unique sequence, named N2Bus that has many phosphosites (Linke et al., 1999). This element has been shown to have biologically significant phosphorylation events mediated by several different kinases including PKA (Yamasaki et al., 2002), PKG (Kruger et al., 2009), ERK2 (Raskin et al., 2012), and CaMKIIδ (Hamdani et al., 2013). Both *in vitro* and *in vivo* studies where the N2Bus element is phosphorylated demonstrate filament lengthening, reduction in TTN stiffness and reduction in passive tension of the sarcomere and cardiomyocyte (Hidalgo et al., 2009; Kruger et al., 2009; Perkin et al., 2015; Hamdani et al., 2017). While kinases that phosphorylate TTN at the N2Bus have been extensively studied, there has been less research on the effects of dephosphorylation via phosphatases. In a recent study, protein phosphatase 5 (PP5) was demonstrated to dephosphorylate TTN at the N2Bus element resulting in increased passive tension of cardiomyocytes. This study is complimentary to research in kinases that passive tension of TTN can be differentially regulated via phosphorylation and dephosphorylation of the N2Bus region. It is known that the N2Bus region is acidic and carries a positive charge. Therefore, addition of a positively charged phosphate in this element increases propulsion forces that lengthens the domain and decreases stiffness of TTN (Hamdani et al., 2017).

Post-translational modification of TTN via phosphorylation can alter its stiffness and passive tension so that cardiomyocytes can respond to physiologic changes. These alterations may also become pathologic in heart failure where alterations in TTN phosphorylation may lead to worsening of passive and active forces reducing the ability of the heart to function normally. It is likely that in addition to phosphorylation, TTN is modified by many other post-translational pathways. Research is ongoing to identify additional post-translational modifications of TTN and therapeutic targets. In one recent trial, it was suggested that in a mouse model of diastolic dysfunction, metformin improved HFpEF by increasing phosphorylation the N2B element via PKA. It was conjectured that phosphorylation increased TTN compliance and improved diastolic dysfunction as measured by echocardiogram, pressure volume analysis, and exercise tolerance (Slater et al., 2019).

CONCLUSION

As the largest protein in the human body, the extent of TTN's role in cardiac physiology and disease is not yet completely understood. We are still learning how TTN contributes to myofibril assembly, stability, and signal transduction, and how perturbations in these processes can lead to cardiac dysfunction and human disease. We have reviewed how modification of TTN at the genetic, transcriptional, and post-translational levels can affect cardiac function by altering the passive and active forces of the sarcomere and cardiomyocyte. Undoubtedly, future research will continue to elucidate TTN's large role in cardiac physiology and how transcriptional and post-translational modifications may contribute to DCM as well as normal cardiac physiology. Alteration of TTN represents potential therapeutic targets for genetic and acquired cardiomyopathies.

AUTHOR CONTRIBUTIONS

CT wrote the manuscript with contributions of MH and OS. MT, LM, and OS contributed figures and grant support. MH, OS, MT, and LM provided critical insights and editing of the final manuscript.

FUNDING

This work was supported by the National Institutes of Health grants R01 HL69071, HL116906, and AHA17GRNT33670495 (to LM); National Institutes of Health grants 1K23HI067915 and R01HL109209 (to MT), and in part by the TransAtlantic Network of Excellence 14-CVD 03 grant from the Leducq Foundation (to OS, MT, and LM).

ACKNOWLEDGMENTS

The authors are grateful to the family members for their participation in these studies that allowed the advancement of understanding the disease mechanism and management.

REFERENCES

Ashwal-Fluss, R., Meyer, M., Pamudurti, N. R., Ivanov, A., Bartok, O., Hanan, M., et al. (2014). circRNA biogenesis competes with pre-mRNA splicing. *Mol. Cell.* 56, 55–66. doi: 10.1016/j.molcel.2014.08.019

Borbely, A., Falcao-Pires, I., van Heerebeek, L., Hamdani, N., Edes, I., Gavina, C., et al. (2009). Hypophosphorylation of the Stiff N2B titin isoform raises cardiomyocyte resting tension in failing human myocardium. *Circ. Res.* 104, 780–786. doi: 10.1161/CIRCRESAHA.108.193326

Bozkurt, B., Colvin, M., Cook, J., Cooper, L. T., Deswal, A., Fonarow, G. C., et al. (2016). Current diagnostic and treatment strategies for specific dilated cardiomyopathies: a scientific statement from the american heart association. *Circulation* 134, e579–e646.

Brauch, K. M., Karst, M. L., Herron, K. J., de Andrade, M., Pellikka, P. A., Rodeheffer, R. J., et al. (2009). Mutations in ribonucleic acid binding protein gene cause familial dilated cardiomyopathy. *J. Am. Coll. Cardiol.* 54, 930–941. doi: 10.1016/j.jacc.2009.05.038

Bull, M., Methawasin, M., Strom, J., Nair, P., Hutchinson, K., and Granzier, H. (2016). alternative splicing of titin restores diastolic function in an HFpEF-like genetic murine model (TtnDeltaIAjxn). *Circ. Res.* 119, 764–772. doi: 10.1161/CIRCRESAHA.116.308904

Chopra, A., Kutys, M. L., Zhang, K., Polacheck, W. J., Sheng, C. C., Luu, R. J., et al. (2018). Force generation via beta-cardiac myosin, Titin, and alpha-actinin drives cardiac sarcomere assembly from cell-matrix adhesions. *Dev. Cell* 44:87-96.e5. doi: 10.1016/j.devcel.2017.12.012

Franaszczyk, M., Chmielewski, P., Truszkowska, G., Stawinski, P., Michalak, E., Rydzanicz, M., et al. (2017). Titin truncating variants in dilated cardiomyopathy - prevalence and genotype-phenotype correlations. *PLoS One* 12:e0169007. doi: 10.1371/journal.pone.0169007

Freiburg, A., Trombitas, K., Hell, W., Cazorla, O., Fougerousse, F., Centner, T., et al. (2000). Series of exon-skipping events in the elastic spring region of titin as the structural basis for myofibrillar elastic diversity. *Circ. Res.* 86, 1114–1121. doi: 10.1161/01.res.86.11.1114

Fukuda, N., and Granzier, H. L. (2005). Titin/connectin-based modulation of the frank-starling mechanism of the heart. *J. Muscle Res. Cell Motil.* 26, 319–323. doi: 10.1007/s10974-005-9038-1

Gautel, M. (2011). Cytoskeletal protein kinases: titin and its relations in mechanosensing. *Pflugers. Arch.* 462, 119–134. doi: 10.1007/s00424-011-0946-1

Gerull, B., Gramlich, M., Atherton, J., McNabb, M., Trombitas, K., Sasse-Klaassen, S., et al. (2002). Mutations of TTN, encoding the giant muscle filament titin, cause familial dilated cardiomyopathy. *Nat. Genet.* 30, 201–204. doi: 10.1038/ng815

Golbus, J. R., Puckelwartz, M. J., Fahrenbach, J. P., Dellefave-Castillo, L. M., Wolfgeher, D., and McNally, E. M. (2012). Population-based variation in cardiomyopathy genes. *Circ. Cardiovasc. Genet.* 5, 391–399. doi: 10.1161/CIRCGENETICS.112.962928

Gramlich, M., Pane, L. S., Zhou, Q., Chen, Z., Murgia, M., Schotterl, S., et al. (2015). Antisense-mediated exon skipping: a therapeutic strategy for titin-based dilated cardiomyopathy. *EMBO Mol. Med.* 7, 562–576. doi: 10.15252/emmm.201505047

Guo, W., Schafer, S., Greaser, M. L., Radke, M. H., Liss, M., Govindarajan, T., et al. (2012). RBM20, a gene for hereditary cardiomyopathy, regulates titin splicing. *Nat. Med.* 18, 766–773. doi: 10.1038/nm.2693

Hamdani, N., Herwig, M., and Linke, W. A. (2017). Tampering with springs: phosphorylation of titin affecting the mechanical function of cardiomyocytes. *Biophys. Rev.* 9, 225–237. doi: 10.1007/s12551-017-0263-9

Hamdani, N., Krysiak, J., Kreusser, M. M., Neef, S., Dos Remedios, C. G., Maier, L. S., et al. (2013). Crucial role for Ca2(+)/calmodulin-dependent protein kinase-II in regulating diastolic stress of normal and failing hearts via titin phosphorylation. *Circ. Res.* 112, 664–674. doi: 10.1161/CIRCRESAHA.111.300105

Herman, D. S., Lam, L., Taylor, M. R., Wang, L., Teekakirikul, P., Christodoulou, D., et al. (2012). Truncations of titin causing dilated cardiomyopathy. *N. Engl. J. Med.* 366, 619–628. doi: 10.1056/NEJMoa1110186

Hershberger, R. E., Hedges, D. J., and Morales, A. (2013). Dilated cardiomyopathy: the complexity of a diverse genetic architecture. *Nat. Rev. Cardiol.* 10, 531–547. doi: 10.1038/nrcardio.2013.105

Hershberger, R. E., Morales, A., and Siegfried, J. D. (2010). Clinical and genetic issues in dilated cardiomyopathy: a review for genetics professionals. *Genet. Med.* 12, 655–667. doi: 10.1097/GIM.0b013e3181f2481f

Hidalgo, C., Hudson, B., Bogomolovas, J., Zhu, Y., Anderson, B., Greaser, M., et al. (2009). PKC phosphorylation of titin's PEVK element: a novel and conserved pathway for modulating myocardial stiffness. *Circ. Res.* 105, 631–638. doi: 10.1161/CIRCRESAHA.109.198465

Hinson, J. T., Chopra, A., Nafissi, N., Polacheck, W. J., Benson, C. C., Swist, S., et al. (2015). Titin mutations in iPS cells define sarcomere insufficiency as a cause of dilated cardiomyopathy. *Science* 349, 982–986. doi: 10.1126/science.aaa5458

Hornbeck, P. V., Zhang, B., Murray, B., Kornhauser, J. M., Latham, V., and Skrzypek, E. (2015). PhosphoSitePlus, 2014: mutations, PTMs and recalibrations. *Nucleic Acids Res.* 43, D512–D520. doi: 10.1093/nar/gku1267

Huttlin, E. L., Jedrychowski, M. P., Elias, J. E., Goswami, T., Rad, R., Beausoleil, S. A., et al. (2010). A tissue-specific atlas of mouse protein phosphorylation and expression. *Cell* 143, 1174–1189. doi: 10.1016/j.cell.2010.12.001

Khan, M. A., Reckman, Y. J., Aufiero, S., van den Hoogenhof, M. M., van der Made, I., Beqqali, A., et al. (2016). RBM20 regulates circular RNA production from the titin gene. *Circ. Res.* 119, 996–1003. doi: 10.1161/circresaha.116.309568

Kontrogianni-Konstantopoulos, A., Ackermann, M. A., Bowman, A. L., Yap, S. V., and Bloch, R. J. (2009). Muscle giants: molecular scaffolds in sarcomerogenesis. *Physiol. Rev.* 89, 1217–1267. doi: 10.1152/physrev.00017.2009

Kruger, M., Kotter, S., Grutzner, A., Lang, P., Andresen, C., Redfield, M. M., et al. (2009). Protein kinase G modulates human myocardial passive stiffness by phosphorylation of the titin springs. *Circ. Res.* 104, 87–94. doi: 10.1161/CIRCRESAHA.108.184408

Krysiak, J., Unger, A., Beckendorf, L., Hamdani, N., von Frieling-Salewsky, M., Redfield, M. M., et al. (2018). Protein phosphatase 5 regulates titin phosphorylation and function at a sarcomere-associated mechanosensor complex in cardiomyocytes. *Nat. Commun.* 9:262. doi: 10.1038/s41467-017-02483-3

LeWinter, M. M., and Granzier, H. L. (2013). Titin is a major human disease gene. *Circulation* 127, 938–944. doi: 10.1161/circulationaha.112.139717

LeWinter, M. M., Wu, Y., Labeit, S., and Granzier, H. (2007). Cardiac titin: structure, functions and role in disease. *Clin. Chim. Acta* 375, 1–9. doi: 10.1016/j.cca.2006.06.035

Li, D., Morales, A., Gonzalez-Quintana, J., Norton, N., Siegfried, J. D., Hofmeyer, M., et al. (2010). Identification of novel mutations in RBM20 in patients with dilated cardiomyopathy. *Clin. Transl. Sci.* 3, 90–97. doi: 10.1111/j.1752-8062.2010.00198.x

Linke, W. A., and Hamdani, N. (2014). Gigantic business: titin properties and function through thick and thin. *Circ. Res.* 114, 1052–1068. doi: 10.1161/CIRCRESAHA.114.301286

Linke, W. A., Rudy, D. E., Centner, T., Gautel, M., Witt, C., Labeit, S., et al. (1999). I-band titin in cardiac muscle is a three-element molecular spring and is critical for maintaining thin filament structure. *J. Cell Biol.* 146, 631–644. doi: 10.1083/jcb.146.3.631

Lundby, A., Secher, A., Lage, K., Nordsborg, N. B., Dmytriyev, A., Lundby, C., et al. (2012). Quantitative maps of protein phosphorylation sites across 14 different rat organs and tissues. *Nat. Commun.* 3:876. doi: 10.1038/ncomms1871

Makarenko, I., Opitz, C. A., Leake, M. C., Neagoe, C., Kulke, M., Gwathmey, J. K., et al. (2004). Passive stiffness changes caused by upregulation of compliant titin isoforms in human dilated cardiomyopathy hearts. *Circ. Res.* 95, 708–716. doi: 10.1161/01.res.0000143901.37063.2f

McNally, E. M., and Mestroni, L. (2017). Dilated cardiomyopathy: genetic determinants and mechanisms. *Circ. Res.* 121, 731–748. doi: 10.1161/circresaha.116.309396

Memczak, S., Jens, M., Elefsinioti, A., Torti, F., Krueger, J., Rybak, A., et al. (2013). Circular RNAs are a large class of animal RNAs with regulatory potency. *Nature* 495, 333–338. doi: 10.1038/nature11928

Merlo, M., Sinagra, G., Carniel, E., Slavov, D., Zhu, X., Barbati, G., et al. (2013). Poor prognosis of rare sarcomeric gene variants in patients with dilated cardiomyopathy. *Clin. Transl. Sci.* 6, 424–428. doi: 10.1111/cts.12116

Nagueh, S. F., Shah, G., Wu, Y., Torre-Amione, G., King, N. M., Lahmers, S., et al. (2004). Altered titin expression, myocardial stiffness, and left ventricular function in patients with dilated cardiomyopathy. *Circulation* 110, 155–162. doi: 10.1161/01.cir.0000135591.37759.af

Neishabouri, S. H., Hutson, S. M., and Davoodi, J. (2015). Chronic activation of mTOR complex 1 by branched chain amino acids and organ hypertrophy. *Amino. Acids* 47, 1167–1182. doi: 10.1007/s00726-015-1944-y

Perkin, J., Slater, R., Del Favero, G., Lanzicher, T., Hidalgo, C., Anderson, B., et al. (2015). Phosphorylating titin's cardiac N2B element by ERK2 or CaMKIIdelta lowers the single molecule and cardiac muscle force. *Biophys. J.* 109, 2592–2601. doi: 10.1016/j.bpj.2015.11.002

Pinto, Y. M., Elliott, P. M., Arbustini, E., Adler, Y., Anastasakis, A., Bohm, M., et al. (2016). Proposal for a revised definition of dilated cardiomyopathy, hypokinetic non-dilated cardiomyopathy, and its implications for clinical practice: a position statement of the ESC working group on myocardial and pericardial diseases. *Eur. Heart J.* 37, 1850–1858. doi: 10.1093/eurheartj/ehv727

Rain, S., Bos Dda, S., Handoko, M. L., Westerhof, N., Stienen, G., Ottenheijm, C., et al. (2014). Protein changes contributing to right ventricular cardiomyocyte diastolic dysfunction in pulmonary arterial hypertension. *J. Am. Heart. Assoc.* 3:e000716. doi: 10.1161/JAHA.113.000716

Ramos, F. J., Chen, S. C., Garelick, M. G., Dai, D. F., Liao, C. Y., Schreiber, K. H., et al. (2012). Rapamycin reverses elevated mTORC1 signaling in lamin A/C-deficient mice, rescues cardiac and skeletal muscle function, and extends survival. *Sci. Transl. Med.* 4:144ra103. doi: 10.1126/scitranslmed.3003802

Raskin, A., Lange, S., Banares, K., Lyon, R. C., Zieseniss, A., Lee, L. K., et al. (2012). A novel mechanism involving four-and-a-half LIM domain protein-1 and extracellular signal-regulated kinase-2 regulates titin phosphorylation and mechanics. *J. Biol. Chem.* 287, 29273–29284. doi: 10.1074/jbc.M112.372839

Refaat, M. M., Lubitz, S. A., Makino, S., Islam, Z., Frangiskakis, J. M., Mehdi, H., et al. (2012). Genetic variation in the alternative splicing regulator RBM20 is associated with dilated cardiomyopathy. *Heart Rhythm* 9, 390–396. doi: 10.1016/j.hrthm.2011.10.016

Roberts, A. M., Ware, J. S., Herman, D. S., Schafer, S., Baksi, J., Bick, A. G., et al. (2015). Integrated allelic, transcriptional, and phenomic dissection of the cardiac effects of titin truncations in health and disease. *Sci. Transl. Med.* 7:270ra6. doi: 10.1126/scitranslmed.3010134

Schafer, S., de Marvao, A., Adami, E., Fiedler, L. R., Ng, B., Khin, E., et al. (2017). Titin-truncating variants affect heart function in disease cohorts and the general population. *Nat. Genet.* 49, 46–53. doi: 10.1038/ng.3719

Schisler, J. C., Grevengoed, T. J., Pascual, F., Cooper, D. E., Ellis, J. M., Paul, D. S., et al. (2015). Cardiac energy dependence on glucose increases metabolites related to glutathione and activates metabolic genes controlled by mechanistic target of rapamycin. *J. Am. Heart Assoc.* 4:e001136. doi: 10.1161/JAHA.114.001136

Shibayama, J., Yuzyuk, T. N., Cox, J., Makaju, A., Miller, M., Lichter, J., et al. (2015). Metabolic remodeling in moderate synchronous versus dyssynchronous pacing-induced heart failure: integrated metabolomics and proteomics study. *PLoS One* 10:e0118974. doi: 10.1371/journal.pone.0118974

Slater, R. E., Strom, J. G., Methawasin, M., Liss, M., Gotthardt, M., Sweitzer, N., et al. (2019). Metformin improves diastolic function in an HFpEF-like mouse model by increasing titin compliance. *J. Gen. Physiol.* 151, 42–52. doi: 10.1085/jgp.201812259

Streckfuss-Bomeke, K., Tiburcy, M., Fomin, A., Luo, X., Li, W., Fischer, C., et al. (2017). Severe DCM phenotype of patient harboring RBM20 mutation S635A can be modeled by patient-specific induced pluripotent stem cell-derived cardiomyocytes. *J. Mol. Cell Cardiol.* 113, 9–21. doi: 10.1016/j.yjmcc.2017.09.008

Sweet, M. E., Cocciolo, A., Slavov, D., Jones, K. L., Sweet, J. R., and Graw, S. L. (2018). Transcriptome analysis of human heart failure reveals dysregulated cell adhesion in dilated cardiomyopathy and activated immune pathways in ischemic heart failure. *BMC Genomics* 19:812. doi: 10.1186/s12864-018-5213-9

Tabish, A. M., Azzimato, V., Alexiadis, A., Buyandelger, B., and Knoll, R. (2017). Genetic epidemiology of titin-truncating variants in the etiology of dilated cardiomyopathy. *Biophys. Rev.* 9, 207–223. doi: 10.1007/s12551-017-0265-7

Tayal, U., Newsome, S., Buchan, R., Whiffin, N., Halliday, B., Lota, A., et al. (2017). Phenotype and clinical outcomes of titin cardiomyopathy. *J. Am. Coll. Cardiol.* 70, 2264–2274. doi: 10.1016/j.jacc.2017.08.063

Trombitas, K., Greaser, M., Labeit, S., Jin, J. P., Kellermayer, M., Helmes, M., et al. (1998). Titin extensibility in situ: entropic elasticity of permanently folded and permanently unfolded molecular segments. *J. Cell Biol.* 140, 853–859. doi: 10.1083/jcb.140.4.853

Vikhorev, P. G., Smoktunowicz, N., Munster, A. B., Copeland, O., Kostin, S., Montgiraud, C., et al. (2017). Abnormal contractility in human heart myofibrils from patients with dilated cardiomyopathy due to mutations in TTN and contractile protein genes. *Sci. Rep.* 7:14829. doi: 10.1038/s41598-017-13675-8

Ware, J. S., and Cook, S. A. (2018). Role of titin in cardiomyopathy: from DNA variants to patient stratification. *Nat. Rev. Cardiol.* 15, 241–252. doi: 10.1038/nrcardio.2017.190

Yamasaki, R., Wu, Y., McNabb, M., Greaser, M., Labeit, S., and Granzier, H. (2002). Protein kinase A phosphorylates titin's cardiac-specific N2B domain and reduces passive tension in rat cardiac myocytes. *Circ. Res.* 90, 1181–1188. doi: 10.1161/01.res.0000021115.24712.99

Yano, T., Shimoshige, S., Miki, T., Tanno, M., Mochizuki, A., Fujito, T., et al. (2016). Clinical impact of myocardial mTORC1 activation in nonischemic dilated cardiomyopathy. *J. Mol. Cell Cardiol.* 91, 6–9. doi: 10.1016/j.yjmcc.2015.12.022

Zhou, Q., Kesteven, S., Wu, J., Aidery, P., Gawaz, M., Gramlich, M., et al. (2015). Pressure overload by transverse aortic constriction induces maladaptive hypertrophy in a titin-truncated mouse model. *Biomed. Res. Int.* 2015:163564. doi: 10.1155/2015/163564

Zhu, C., Yin, Z., Ren, J., McCormick, R. J., Ford, S. P., and Guo, W. (2015). RBM20 is an essential factor for thyroid hormone-regulated titin isoform transition. *J. Mol. Cell Biol.* 7, 88–90. doi: 10.1093/jmcb/mjv002

Zhu, C., Yin, Z., Tan, B., and Guo, W. (2017). Insulin regulates titin pre-mRNA splicing through the PI3K-Akt-mTOR kinase axis in a RBM20-dependent manner. *Biochim. Biophys. Acta Mol. Basis Dis.* 1863, 2363–2371. doi: 10.1016/j.bbadis.2017.06.023

Conflict of Interest: The authors declare that the research was conducted in the absence of any commercial or financial relationships that could be construed as a potential conflict of interest.

frontiers in Physiology

ORIGINAL RESEARCH
published: 05 February 2020
doi: 10.3389/fphys.2020.00015

Compliant Titin Isoform Content Is Reduced in Left Ventricles of Sedentary Versus Active Rats

Charles S. Chung†, Mark A. Hiske, Arjun Chadha and Patrick J. Mueller†*

Department of Physiology, Wayne State University, Detroit, MI, United States

A sedentary lifestyle is associated with increased cardiovascular risk factors and reduced cardiac compliance when compared to a lifestyle that includes exercise training. Exercise training increases cardiac compliance in humans, but the mechanisms underlying this improvement are unknown. A major determinant of cardiac compliance is the compliance of the giant elastic protein titin. Experimentally reducing titin compliance in animal models reduces exercise tolerance, but it is not known whether sedentary versus chronic exercise conditions cause differences in titin isoform content. We hypothesized that sedentary conditions would be associated with a reduction in the content of the longer, more compliant N2BA isoform relative to the stiffer N2B isoform (yielding a reduced N2BA:N2B ratio) compared to age-matched exercising controls. We obtained left ventricles from 16-week old rats housed for 12 weeks in standard (sedentary) or voluntary running wheel (exercised) housing. The N2BA:N2B ratio was decreased in the hearts of sedentary versus active rats ($p = 0.041$). Gene expression of a *titin* mRNA splicing factor, RNA Binding Motif 20 protein (RBM20), correlated negatively with N2BA:N2B ratios ($p = 0.006$, $r = -0.449$), but was not different between groups, suggesting that RBM20 may be regulated post-transcriptionally. Total phosphorylation of cardiac titin was not different between the active and sedentary groups. This study is the first to demonstrate that sedentary rats exhibit reduced cardiac titin N2BA:N2B isoform ratios, which implies reduced cardiac compliance. These data suggest that a lack of exercise (running wheel) reduces cardiac compliance and that exercise itself increases cardiac compliance.

Keywords: heart, diastole, passive stiffness, exercise, inactivity, titin

OPEN ACCESS

Edited by:
Henk Granzier,
The University of Arizona,
United States

Reviewed by:
Marion Lewis Greaser,
University of Wisconsin–Madison,
United States
Nazha Hamdani,
Ruhr University Bochum, Germany

****Correspondence:***
Charles S. Chung
cchung@med.wayne.edu

†ORCID:
Charles S. Chung
orcid.org/0000-0001-9180-3236
Patrick J. Mueller
orcid.org/0000-0002-7720-1519

Specialty section:
This article was submitted to Striated Muscle Physiology, a section of the journal Frontiers in Physiology

Received: *08 November 2019*
Accepted: *13 January 2020*
Published: *05 February 2020*

Citation:
Chung CS, Hiske MA, Chadha A and Mueller PJ (2020) Compliant Titin Isoform Content Is Reduced in Left Ventricles of Sedentary Versus Active Rats. Front. Physiol. 11:15. doi: 10.3389/fphys.2020.00015

INTRODUCTION

Sedentary behavior is a major risk factor for premature death, and prolonged periods of sedentary behavior are considered a medical hazard (Blair et al., 1995; Bassett et al., 2010; Lavie et al., 2019). Sedentary behavior is also associated with reduced cardiac compliance (inverse of passive stiffness), which itself is an important index of cardiac health (Lalande et al., 2017; Howden et al., 2018). Cardiac compliance is primarily determined by titin, the giant elastic protein present in the sarcomeres of striated muscles, including cardiac myocytes (Granzier and Irving, 1995; Granzier and Labeit, 2004; Chung and Granzier, 2011). Increasing titin's compliance reduces the slope of the pressure–volume relationship during diastole, providing the heart with a greater capacity to fill

during increases in venous return that occur during exercise (Lalande et al., 2017). Reducing titin compliance (increasing passive stiffness) impairs diastolic filling and the ability of the left ventricle to increase stroke volume during exercise.

Titin is encoded by a single gene (*titin*, *ttn*), but can be alternatively spliced. Increased splicing of *titin* mRNA reduces the length of the elastic region of the protein, which resides in the I-band of the sarcomere (Granzier and Labeit, 2004; Guo et al., 2012). Alternative splicing of *titin* is an important mechanism to modify titin's properties and thus cardiac compliance (Granzier and Labeit, 2004). Cardiac muscle expresses two classes of splice isoforms: the longer, more compliant N2BA isoform and the shorter, less compliant N2B isoform. The two isoforms are distributed throughout the myofibrils so that the ratio of their relative contents defines the compliance of a given myocyte (Trombitas et al., 2001). Increases in the relative content ratio of the N2BA to N2B isoform (N2BA:N2B) is associated with increased ventricular compliance. The relative content of these two isoforms is primarily controlled by RNA Binding Motif 20 protein (RBM20) (Guo et al., 2012, 2013). An increased RBM20 content is consistent with a reduced N2BA:N2B ratio, as additional exons of *titin* mRNA are spliced out to form the shorter, stiffer, N2B protein isoform (Guo et al., 2012, 2013; Methawasin et al., 2016; Zhu et al., 2017). RBM20's activity may be inhibited by the Polypyrimidine Tract Binding protein 4 (PTB4) (Dauksaite and Gotthardt, 2018). Thus, multiple mechanisms to modify titin isoform content have been proposed.

While our current knowledge of the relationship between titin and exercise tolerance is limited, experimentally reduced titin compliance is associated with reduced exercise tolerance (Lalande et al., 2017). This relationship is based primarily on studies using transgenic and knockout mouse models that modified the size of the *titin* gene to modify titin compliance. Reducing RBM20 expression or activity has been shown to increase the content of compliant titin isoforms and increase exercise tolerance (Methawasin et al., 2016; Slater et al., 2017). In humans, there are fewer studies directly relating N2BA:N2B ratios and exercise tolerance. In heart failure patients with a reduced ejection fraction, exercise tolerance correlated positively ($r = 0.8$) with the N2BA:N2B ratio but not with ejection fraction (Nagueh et al., 2004). This correlation was possible only because the myocardial tissues were made available for biochemical study after an explant of a heart during transplant. The remainder of the human studies use measures of cardiac compliance without direct measure of titin properties but report a stronger correlation between exercise tolerance and cardiac compliance than between exercise tolerance and heart failure status (Meyer et al., 2004). While these data imply that titin compliance predicts exercise tolerance, there are no data to indicate whether sedentary versus physical activity conditions result in differences in titin isoform content.

In humans, exercise training increases both exercise tolerance (Edelmann et al., 2011; Fujimoto et al., 2012) and clinical measures of cardiac compliance (Howden et al., 2018). These data indicate that cardiac compliance differs between sedentary and active groups. However, it is unknown if titin isoform content shifted to an increase in the compliant isoform (N2BA) in response to exercise. In mice, moderate duration exercise protocols (i.e., $\leq$1 month) have been reported to modify titin compliance via post-translational modifications but did not appear to alter titin isoform content (Hidalgo et al., 2014; Muller et al., 2014; Slater et al., 2017). It is possible that the short-duration of the studies and the use of mouse models might have masked changes in the N2BA:N2B ratio. Thus, it remains unknown whether sedentary conditions reduce titin compliance (or whether more chronic activity (exercise) increases titin compliance), which would provide a mechanism for exercise training-induced increases in exercise tolerance in sedentary individuals.

This study sought to evaluate titin isoform content in left ventricular tissue from established rat models that promote inactivity or voluntary exercise. The models utilize chronic (12 weeks) voluntary running wheel access to mimic exercise activity and sedentary housing conditions to mimic inactivity (Mischel and Mueller, 2011). In small animal models, standard laboratory conditions are increasingly associated with un-natural sedentary conditions. Sedentary lifestyles reflect a form of inactivity and are considered by some to be a pathophysiologic state associated with numerous diseases including cardiac dysfunction (Booth et al., 2017). Further, voluntary running wheel activity in wild mice is comparable to that of lab-mice (Meijer and Robbers, 2014). These data suggest that sedentary housing conditions for laboratory rodents is actually an unnatural condition, and voluntary running wheel activity would reflect a more natural, control state for the rats. We hypothesized that the titin N2BA:N2B ratio would be lower in rat hearts after 12 weeks of sedentary conditions compared to chronic voluntary wheel running conditions. We also hypothesized that changes in the titin isoform ratio would be dependent on *titin* mRNA splicing factors such as RBM20.

MATERIALS AND METHODS

Animal Model and Samples

Vertebrate animal procedures were approved by the Institutional Animal Care and Use Committee of Wayne State University and conducted in accordance with the American Physiological Society's "Guiding Principles in the Care and Use of Animals." Rat samples were collected using an established exercise protocol as previously described (Mischel and Mueller, 2011). Briefly, 75–100 g male Sprague Dawley rats, approximately 4 weeks of age, were obtained (Envigo, Indianapolis, IN, United States). Thirty-nine rats were randomly distributed into two groups. Active rats performing voluntary exercise (EX, $n = 20$) were housed in $9'' \times 18'' \times 9''$ cages containing a commercially available running wheel (Techniplast, Eaton, PA, United States; wheel diameter 47 cm). Bicycle computers (Sigma Sport, Olney, IL, United States) recorded daily and cumulative running distances. Voluntary exercised rats had 24-h access to the running wheel. Rats in the sedentary group (SED, $n = 19$) were housed in identically sized cages that lacked a running wheel, which mimics typical laboratory conditions for rats. All animals were individually housed and received food and water *ad libitum*. After 12 weeks

of housing under sedentary or exercising conditions (16 weeks of age), running wheels were removed from the cages of exercising animals 24 h prior to sacrifice to prevent acute exercise from impacting the results (Muller et al., 2014). The rats were sacrificed via decapitation under deep anesthesia (Fatal Plus, 50 mg/kg body weight (BW), i.p.; Vortech, Dearborn, MI, United States). The left ventricle was dissected, weighed, and flash-frozen in a container of isopentane chilled with dry ice and subsequently stored at −80°C. Two segments of left ventricular free wall were isolated under liquid nitrogen for protein analysis (∼15 mg) and RNA isolation (∼150 mg).

Tissue Solubilization

The small (∼15 mg) segments of the left ventricular wall used for protein analysis were pulverized using Kontes Dounce homogenizers (Kimble Chase, Rockwood, TN, United States) cooled in liquid nitrogen, as previously described (Lahmers et al., 2004; Chung et al., 2013). Subsequently, all samples were solubilized in a solution containing equal amounts of solubilization buffer (8 M Urea, 2 M thiourea, 0.05 M Tris–HCl, 0.075 M DTT, 3% sodium dodecyl sulfate (SDS), and 0.03% Bromophenol Blue all adjusted to pH 6.8) and glycerol with protease inhibitors [50% glycerol, 0.008% Leupeptin, 0.04 mM E-64, and 0.5 mM phenylmethylsulfonyl fluoride (PMSF)] at 60°C. Solubilized samples were centrifuged, aliquoted, flash-frozen in liquid nitrogen, and stored at −80°C.

Titin Isoform and Phosphorylation Analysis

To determine titin isoform content, 1% Agarose gels (agarose with 0.005 M tris base, 0.039 M glycine, 2% SDS, 30% glycerol) were prepared in a large-format gel system (Hoeffer SE600X, Hoefer, Inc., Holliston, MA, United States) (Lahmers et al., 2004; Chung et al., 2013; Zhu and Guo, 2017). Briefly, solubilized samples were loaded, and gel electrophoresis was run at 15 mA/gel for 3 h and 20 min. Gels were stained using Coomassie Brilliant Blue and scanned using a commercially available scanner (Epson V850, Epson America, Inc., Long Beach, CA, United States) with a calibrated Optical Density step tablet (Stouffer Industries, Mishawaka, IN, United States). The scan was normalized for Optical Density using a custom MATLAB script (MathWorks, Natick, MA, United States) and analyzed using ImageQuant TL (GE Healthcare Bio-Sciences Corp., Marlborough, MA, United States). Relative titin mobility was evaluated by loading and co-electrophoresing rat ventricular and soleus muscle reference samples. Relative mobility was calculated using ImageQuant TL as previously described using rat soleus N2A titin isoform, Nebulin, and Myosin Heavy Chain as mobility references (Granzier and Irving, 1995; Buck et al., 2010; Li et al., 2012). Relative titin isoform content (N2BA:N2B ratio) was evaluated by loading individual samples in a range of five volumes (3–9 μL) at dilutions pre-determined to be within the linear range of detection. Background subtraction was performed using the Rolling Ball function (Sternberg, 1983). Relative content was determined using the slope of the optical density versus volume loading for MHC and all titin bands (N2BA, N2B, and T2, the titin degradation band). Two minor bands representing the N2BA isoform were summed to determine the N2BA content (Freiburg et al., 2000).

To determine the total titin phosphorylation status, 2–12% gradient acrylamide gels (2–12% Acrylamide, (1:50) Bis-acrylamide, 0.1% SDS, 5% glycerol, 10× Fairbanks buffer (400 mM Tris Base, 200 mM Sodium Acetate, 20 mM EDTA, pH adjusted to 7.5 with glacial acetic acid), 0.0625% Ammonium Persulfate, and 0.0875% TEMED) were prepared in Mini-PROTEAN Cassettes (BioRad) and allowed to polymerize. Electrophoresis was pre-run with running buffer (10× Fairbanks buffer, 0.1% SDS, and 11.44 mM βME) at 60 V for 3 min without sample. Solubilized samples were then loaded and gel electrophoresis was run at 60 V for 68 min and then 90 V for 70 min. Gels were fixed overnight in 50% methanol and 10% acetic acid, washed three times using ultrapure water, and stained for total phosphate content using a rapid protocol for Pro-Q Diamond staining (Thermo Fisher Scientific, Waltham, MA, United States). Gels were destained using Pro-Q Diamond Destain Solution and washed twice with ultrapure water before scanning with a Typhoon Trio + scanner at 532-nm excitation and 560-nm emission. Gels were then stained for total protein content with Sypro Ruby Gel Stain using the rapid protocol, washed, and scanned with a Typhoon Trio + scanner at 488-nm excitation and 610-nm emission. Bands were quantified using ImageQuant TL (GE Healthcare Bio-Sciences Corp., Marlborough, MA, United States).

Rat Cardiac mRNA Expression Analysis

To determine the mRNA expression of titin-splicing proteins RBM20 and PTB, frozen left ventricular tissue segments were placed in pre-chilled (−80°C) RNAlater-ICE (Ambion) and allowed to transition from −80°C to −20°C for at least 16 h. RNA was extracted from samples weighing approximately 150 mg using the Trizol method (Rio et al., 2010). The RNA concentration was measured in duplicate using a Tecan microplate reader and averaged; all samples had a concentration >100 ng/μL or were re-isolated. RT-PCR was performed using an Applied Biosystems 7300 Real-Time PCR System (Foster City, CA, United States). The following custom primers were obtained from Integrated DNA Technologies, Inc (Coralville, IA, United States): *rbm20* Forward: 5′-CTCAGCTCACCCTCCACC-3′; *rbm20* Reverse: 5′-GTTGAAGAGAGGCTGGGAC-3′; *ptb* Forward 5′-AAAGCCTCTTTATTCTCTTCGGCGTCTAC-3′; *ptb* Reverse 5′-TGAAGCCTTTGACCACACCACCGTTGCTGG-3′; β-*actin* Forward: 5′-AGTGCTGTGGGTGTAGGTA-3′; β-*actin* Reverse: 5′-TTTAGATGGAGAAGGGATGAGAC-3′. All samples were run in triplicate for each primer, then averaged. The $2^{-\Delta\Delta Ct}$ method was used to quantify mRNA expression; ΔCt was calculated between *rbm20* or *ptb* and β-*actin* (Livak and Schmittgen, 2001). Fold change was calculated against the SED group. Two samples were excluded from analysis of each primer set because data suggested poor amplification (e.g., average Ct > 20, or $2^{-\Delta\Delta Ct}$ was 3 standard deviations outside the mean of all samples).

Statistics

Data are presented as individual data points or mean ± SD. Statistics were calculated in SPSS (Ver 25, IBM Corporation, Armonk, NY, United States). Normality was tested using the Shapiro–Wilk test. For normally distributed data sets, unpaired *t*-tests were performed. For non-normally distributed data sets, a Mann–Whitney *U* test was used. Linear regression was also performed. A *p*-value of less than 0.05 was considered significant.

RESULTS

Rat Chronic Exercise and Titin

Voluntary exercise rats (EX) ran a mean cumulative distance of 130 ± 47 km over 12 weeks (n = 19, excluding one sample that was a statistical outlier with a distance of 607 km over 12 weeks). **Table 1** shows body and organ weight data from sedentary and active rats. As expected, the BW differed between groups ($p < 0.001$). The BW was larger in the 16-week old sedentary (SED) versus the exercise (EX) group. Left ventricular weights (LVW) of the SED animals were not statistically different than the EX group ($p = 0.795$). The LVW:BW ratio was significantly larger in the EX group compared to the SED groups ($p = 0.012$).

Cardiac titin isoform analysis is shown in **Figure 1**. The N2BA:N2B ratio for the SED group was significantly smaller than the EX group ($p = 0.041$). Relative mobility, which indicates titin size, was not different for either the N2BA nor N2B isoforms in the 16-week groups ($p = 0.18$, data not shown), suggesting otherwise normal titin splicing. The ratio between relative content of degraded titin to total titin (T2:TTN) and the ratio between total titin and myosin heavy chain content (TTN:MHC) were not different between groups.

Cardiac *rbm20* mRNA expression tended to be less in ventricular tissue from the EX versus SED group (**Figure 2A**), but this difference did not reach statistical significance ($p = 0.65$ by Mann–Whitney *U* test). However, *rbm20* expression was significantly and negatively correlated with N2BA:N2B ratios for all 16-week samples ($p = 0.006$, $r = -0.449$) (**Figure 2B**). Cardiac *ptb* mRNA expression was not different between SED and EX groups ($p = 0.314$ by *t*-test) (**Figure 3A**), and there was no correlation between *ptb* mRNA expression and N2BA:N2B ratios ($p = 0.645$, $r = -0.078$) in the 16 week rat hearts (**Figure 3B**).

TABLE 1 | Physiologic measures from rats.

Parameter	Sedentary control (SED)	Exercise (EX)	*p*-value
n	19	20	
BW (g)	419 ± 23	379 ± 40	*0.001*
LV Weight (mg)	869 ± 53	828 ± 83	0.079
LV:BW (mg/g)	2.07 ± 0.10	2.19 ± 0.14	*0.012*

Sample numbers (n) are biological replicates for individual rats. Listed p-values for SED versus EX via t-test for BW and LVW, Mann–Whitney U test for LVW:BW; italics denotes p < 0.05. Body weight (BW); left ventricular (LV) weight; LV weight to body weight ratio (LV:BW).

Total phosphorylation of titin was evaluated using ProQ Diamond staining (**Figure 4**). No significant difference was observed in the total phosphorylation of titin between the exercised and sedentary groups ($p = 0.95$ by Mann–Whitney *U* test).

DISCUSSION

Sedentary aging is associated with an increase in both cardiovascular and general health risks (Blair et al., 1995; Bassett et al., 2010; Booth et al., 2017; Lavie et al., 2019) and reduced cardiac compliance (Howden et al., 2018). Exercise is thought to alleviate these changes and increase cardiac compliance (Howden et al., 2018). To date, the mechanisms underlying exercise-dependent increases in cardiac compliance have not been fully elucidated. The current study is the first to show that the titin N2BA:N2B ratio, which correlates with cardiac compliance, is reduced in a sedentary animal model.

Titin Isoform Content

Titin is well known to be the major determining factor of cardiac passive stiffness (Granzier and Irving, 1995; Chung and Granzier, 2011) and is known to be able to predict exercise tolerance (Lalande et al., 2017). It is less well understood how exercise impacts titin's compliance. Specifically, there have been only limited studies on how short-term (≤4 weeks) differences in activity/exercise modifies titin, despite evidence that exercise increases myocardial compliance (Edelmann et al., 2011; Howden et al., 2018).

In animal models, the relationship between titin and exercise has historically been focused on how titin compliance can predict exercise tolerance (Lalande et al., 2017). For example, when transgenic methods were used to delete exons that code for several proximal Ig domains of the I-band of titin, titin's passive stiffness increased by approximately 25% (Chung et al., 2013). This reduced compliance was coincident with a 30% reduction in exercise tolerance. More recent studies have further confirmed that reduced titin compliance (increased stiffness) leads to reduced exercise tolerance; whereas, increased titin compliance increases exercise tolerance (see Lalande et al., 2017 for a recent review). Titin isoform expression (and thereby compliance) has also been modified by interfering with the *titin* mRNA splicing factor RBM20. A reduction in RBM20 content or RBM20 activity increases the content of the larger N2BA isoform, and potentially allows for the expression of an unusually large "N2BA-G" isoforms that result in very high titin compliance (Guo et al., 2012). In such studies, reducing the content of functioning RBM20 led to increased titin compliance and improved exercise tolerance (Methawasin et al., 2016; Slater et al., 2017). In humans, cardiac compliance also appears to be a strong predictor of exercise tolerance and predicts exercise tolerance better than heart failure status or ejection fraction (Meyer et al., 2004; Nagueh et al., 2004). However, with the exception of one study directly correlating the N2BA:N2B ratio with exercise tolerance in heart failure patients who later underwent a heart transplant (Nagueh et al., 2004), studies

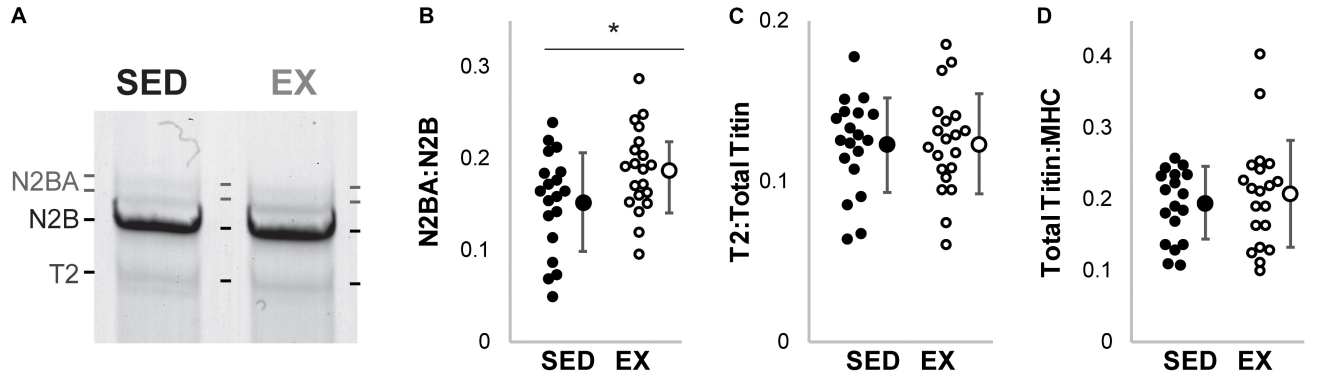

FIGURE 1 | Titin protein analysis. **(A)** Example gel electrophoresis for an exercise and sedentary sample. (Linear contrast adjustment applied to the original image for visualization.) **(B)** The ratio of the longer more compliant N2BA isoform of titin to its shorter N2B isoform (N2BA:N2B) was decreased in hearts from rats housed in sedentary conditions (SED; black circles filled, $n = 19$), versus exercise conditions (EX, open circles, $n = 20$, * denotes $p = 0.041$ by t-test). **(C)** Titin degradation (T2) versus total titin (TTN) and **(D)** TTN to Myosin Heavy Chain (MHC) ratio were not different ($p = 0.95$ and $p = 0.54$, respectively) between the SED and EX groups.

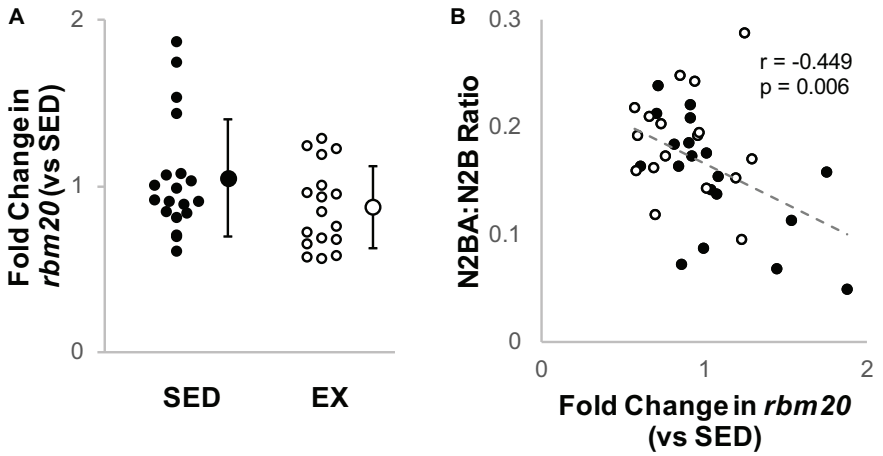

FIGURE 2 | Analysis of Titin Splicing factor RBM20. **(A)** Fold change ($2^{-\Delta\Delta Ct}$) in relative *RNA Binding Motif 20* (*RBM20*) mRNA expression in the exercise group (EX, open circles, $n = 17$) compared to sedentary controls (SED, black circles, $n = 19$); the difference was not statistically significant ($p = 0.65$ by Mann–Whitney U test). Individual samples shown as circles, mean ± SD shown at the right of individual data. **(B)** Titin isoform ratio negatively correlated (gray dashed line, $r = -0.449$, $p = 0.006$, linear regression) with *RBM20* mRNA expression for all samples, which is consistent with prior work that *RBM20* expression is the primary driver of changes in N2BA:N2B ratio.

in humans are limited mechanistically due to constraints on gathering human tissues.

Clinical studies in humans continue to produce evidence that cardiac compliance is increased by exercise training and reduced by sedentary behaviors. The relationship between sedentary behaviors and cardiac compliance is observed in both patients with heart failure and otherwise healthy individuals (Edelmann et al., 2011; Howden et al., 2018). The molecular mechanisms underlying the increased compliance in these human studies have not been elucidated. Previous studies in small animal models have reported that the N2BA:N2B ratio does not differ between exercising and sedentary conditions. Thus, our data (**Figure 1**) is the first biochemical evidence that sedentary conditions reduce the titin N2BA:N2B ratio. The modest change in isoform ratios may be important, given that significant improvements in hazard ratios are observed only with modest amounts of activity and do not improve with increasing activity (Lavie et al., 2019).

The methodology may indicate why a difference in titin isoform content between sedentary and active rodents was not previously revealed. First, the exercise-related activity in the prior studies lasted just 4 weeks or less (Hidalgo et al., 2014; Muller et al., 2014; Slater et al., 2017). In contrast, the current study compared the hearts of rats that underwent 12 weeks of housing in sedentary conditions or active conditions with unrestricted access to a voluntary running wheel. Second, while both mice and rats show high content of the stiff N2B isoform, mice appear to have very low amounts of N2BA naturally, and the N2BA isoform is only observed in mice under extreme stress, such as in heart failure models (Wu et al., 2000). Third, the natural variances in the N2BA:N2B ratios in ours and previous studies suggest that the small sample sizes observed in

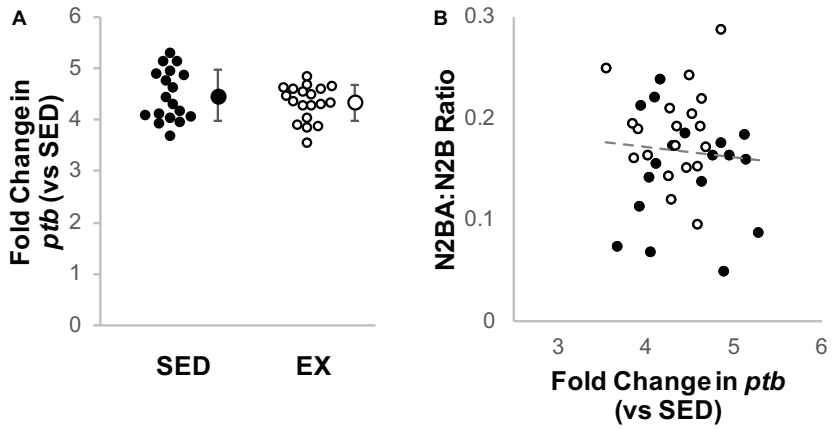

FIGURE 3 | Analysis of titin splicing factor PTB. **(A)** Fold change ($2^{-\Delta\Delta Ct}$) in relative *Polypyrimidine Tract Binding protein* (*PTB*) mRNA expression in the exercise group (EX, open circles, $n = 19$) compared to sedentary controls (SED, black circles, $n = 18$); the difference was not statistically significant ($p = 0.314$ by t-test). Individual samples shown as circles, mean ± SD shown at the right of individual data. **(B)** Titin isoform ratio did not correlate with *PTB* expression (gray dashed line, $r = 0.078$, $p = 0.645$, linear regression).

previous studies (typically $n = 6$) were underpowered to observe any effect. Sampling analysis of our data suggests that more than 10 hearts per group were required to observe significant differences. Thus, the current study may be the first that provides both a sufficiently long intervention and sufficient sample size to report that sedentary conditions were associated with a decrease in the titin N2BA:N2B isoform ratio.

Mechanisms to Modify Titin Isoform Content

The titin protein is encoded by a single gene, so investigating *titin* gene expression does not provide insight into mechanisms that alter isoform expression. However, the change in the N2BA:N2B ratio is likely driven by the splicing factor RBM20 (RNA Binding Motif 20 protein). Increasing content of RBM20 is associated with reductions in the proportions of the N2BA isoform (Guo et al., 2012, 2013; Methawasin et al., 2016; Zhu et al., 2017). Loss of RBM20 activity in rodent models results in increases in the content of the N2BA isoform or the induction of unusually large titin isoforms (Guo et al., 2012). RBM20 has been suggested as a therapeutic target to improve left ventricular stiffness and exercise tolerance (Methawasin et al., 2016). For example, a heterozygous, conditional disruption of RBM20 in mice increased titin-based compliance, which improved exercise tolerance (Methawasin et al., 2016). In contrast, homozygous mutant rats have reduced exercise tolerance compared to wild-type control rats (Guo et al., 2013), suggesting a J-curve in the relationship between exercise tolerance and RBM20 expression.

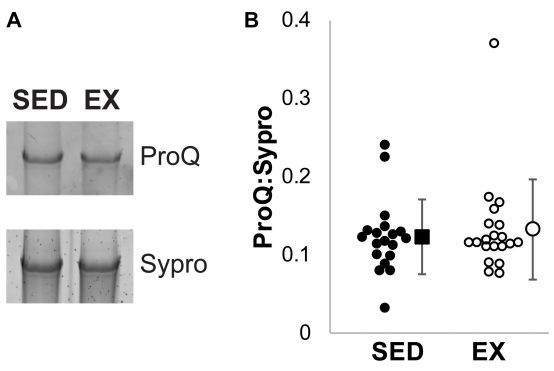

FIGURE 4 | ProQ Diamond Phosphorylation analysis. **(A)** Example ProQ Diamond and Sypro Ruby staining of titin, contrast adjusted. **(B)** The total phosphorylation to protein ratio was not statistically significant ($p = 0.95$ by Mann–Whitney U test) between the SED (black filled, $n = 19$) and EX (open circles, $n = 20$) groups. Individual samples shown as circles, mean ± SD shown at the right of individual data.

We investigated gene expression of both RBM20 and PTB4 (Guo et al., 2012; Dauksaite and Gotthardt, 2018) to evaluate if transcription of these proteins related to titin isoform content. We did not observe a significant decrease in *rbm20* mRNA expression in the hearts of exercising rats versus the sedentary controls (**Figure 2A**). *Rbm20* mRNA expression level did, however, correlate with the titin N2BA:N2B ratio (**Figure 2B**), suggesting that RBM20 may still contribute to the change in N2BA:N2B ratio, but that the expression level changes are modest. RBM20 activity might also be influenced by PTB4, which was recently proposed as an inhibitor of RBM20's splicing of *titin* mRNA (Dauksaite and Gotthardt, 2018). We found no change in *ptb* gene expression. While our data suggest that chronic exercise does not alter *ptb* expression, it is possible that our inability to observe changes is limited by the primer used, since it cannot differentiate between the PTB isoforms (Wollerton et al., 2001).

Other regulators of RBM20 might also be important to analyze in future studies. For example, RBM20 is downstream of the insulin signaling pathway (Zhu et al., 2017). Exercise itself can modify insulin sensitivity and glucose uptake (Kirwan et al., 2009) so changes in RBM20 may be dependent on subtle changes on this PI3K/AKT dependent pathway. Similarly, exercise might modify the phosphorylation of RBM20 or alter its splicing activity (Zhu

et al., 2017; Murayama et al., 2018). Thus, while we have reported a correlation between *rbm20* gene expression and the titin N2BA:N2B ratio, the precise activity-dependent mechanism(s) that might modify titin isoform expression is not fully elucidated. Thus, future studies into protein content and activity of splicing factors such as RBM20 and PTB4 may be warranted.

Post-translational Modifications

Titin compliance can be directly modified by a wide array of post-translational modifications (Koser et al., 2019), of which phosphorylation is the most well characterized. For example, a single bout of treadmill exercise reduced compliance by increasing PKC and reducing PKA phosphorylation of titin (Muller et al., 2014). A 3- or 4-week exposure to voluntary running wheel exercise results in the reverse, i.e., reductions in PKC phosphorylation and increases in PKA phosphorylation, which is consistent with an increase in compliance (Hidalgo et al., 2014; Slater et al., 2017). PKG, ERK, and CaMKII are other known modifiers of cardiac stiffness (Koser et al., 2019). When PKG, ERK, and CaMKII bind to the N2B element of titin, compliance increases, and CaMKII can play a dual role by also phosphorylating the PEVK element to increase passive tension like PKC. In mice, PKG was not shown to be different after 4-weeks of exercise (Hidalgo et al., 2014), but the effect of long term exercise on ERK and CamKII phosphorylation targets on titin is not yet described. Similarly, the effect of exercise on other modifiers of titin such as oxidative stress (including disulphide bonding and glutathionylation) (Alegre-Cebollada et al., 2014; Koser et al., 2019) are not known.

In the current study, we assessed total phosphorylation using ProQ Diamond staining, which has previously helped identify titin phosphorylation sites, but we observed no difference between the sedentary and active group. Two challenges of ProQ Diamond staining are first that it may not reflect PKC phosphorylation of the PEVK element of titin (Hudson et al., 2011) and second that more than 300 total putative phosphorylation sites on titin have been detected by mass spectrometry (Koser et al., 2019) meaning it is not specific. Nonetheless, we might speculate that, consistent with results reported in 4-week studies, exercise is likely to be associated with a reduction in PKC phosphorylation of the PEVK element, along with trends in increases of PKA of the N2B element (Hidalgo et al., 2014; Slater et al., 2017). Further, exercise has been associated with increasing activity of ERK and CaMKII (Hamdani et al., 2013; Perkin et al., 2015; Koser et al., 2019), supporting a role for post-translational modifications to increase compliance. While not feasible with the current samples, direct measurement of myocardial compliance and its response to kinase specific (de)phosphorylation would be a reasonable future study.

The current study focused on chronic changes to titin isoform switching. It is not known if non-titin related phosphorylation impacts chronic changes in stiffness such as with the phosphorylation of RBM20, as noted above (Murayama et al., 2018). The resultant change in titin isoform content by RBM20 regulation may itself modulate the impact of phosphorylation on titin compliance. Published works suggest that the two isoforms may be differentially phosphorylated and that phosphorylation by PKA has a reduced effect in tissues with more N2BA (Fukuda et al., 2005; Borbely et al., 2009; Koser et al., 2019). Thus, even a modest increase in the content of the more compliant N2BA isoform may cause a multiplicative increase in compliance because of changes in the phosphorylation status.

Perspective and Summary

Sedentary behavior is associated with significant general and cardiovascular health risks and reduced exercise tolerance (Blair et al., 1995; Bassett et al., 2010; Martin et al., 2010; Lalande et al., 2017; Howden et al., 2018; Lavie et al., 2019). In laboratory animals, voluntary wheel running is more equivalent to the natural active state whereas standard caging is more similar to sedentary behaviors (Meijer and Robbers, 2014; Booth et al., 2017). We evaluated whether titin isoform content might be modified by sedentary conditions in rats. Our study is the first to report that sedentary conditions reduce the content of long, compliant titin isoforms in rat left ventricles. This result suggests that reduced cardiac compliance, which is associated with sedentary behavior, may be alleviated by chronic exercise by altering the titin isoform content.

NOMENCLATURE

SED Samples from rats after 12 weeks of sedentary housing
EX Samples from rats after 12 weeks of voluntary exercise housing
N2B The smaller, less compliant cardiac isoform of the giant titin protein
N2BA The larger, more compliant isoform of the giant titin protein
N2BA:N2B Ratio of titin isoform content
MHC Myosin Heavy Chain
RBM20 RNA binding motif 20; splicing factor for *titin* mRNA
PTB Polypyrimidine Tract Binding protein; a putative splicing factor for *titin* mRNA

DATA AVAILABILITY STATEMENT

The datasets generated for this study are available on request to the corresponding author.

ETHICS STATEMENT

The animal study was reviewed and approved by the Institutional Animal Care and Use Committee Wayne State University.

AUTHOR CONTRIBUTIONS

All authors contributed to data acquisition, data analysis, manuscript writing and editing, and approved the submitted version of the manuscript.

FUNDING

This work was supported by the American Heart Association (14SDG20100063 and 18TPA34170169 to CC; AHA25810010 to PM), the National Institutes of Health (NIH) (R01HL096787 to PM) and a Pilot and Feasibility Grant from the Michigan Diabetes Research Center (NIH Grant P30-DK020572) to CC.

ACKNOWLEDGMENTS

We gratefully acknowledge Toni Azar and Bozena Fyk-Kolodziej for collection of rat tissues and running wheel data, and the Wayne State University, Department of Physiology Quantitative PCR Core for assistance in qRT-PCR methodology and analysis.

REFERENCES

Alegre-Cebollada, J., Kosuri, P., Giganti, D., Eckels, E., Rivas-Pardo, J. A., Hamdani, N., et al. (2014). S-glutathionylation of cryptic cysteines enhances titin elasticity by blocking protein folding. *Cell* 156, 1235–1246. doi: 10.1016/j.cell.2014.01.056

Bassett, D. R. Jr., Freedson, P., and Kozey, S. (2010). Medical hazards of prolonged sitting. *Exerc. Sport Sci. Rev.* 38, 101–102. doi: 10.1097/jes.0b013e3181e373ee

Blair, S. N., Kohl, HW 3rd, Barlow, C. E., Paffenbarger, R. S. Jr., Gibbons, L. W., and Macera, C. A. (1995). Changes in physical fitness and all-cause mortality. a prospective study of healthy and unhealthy men. *JAMA* 273, 1093–1098. doi: 10.1001/jama.273.14.1093

Booth, F. W., Roberts, C. K., Thyfault, J. P., Ruegsegger, G. N., and Toedebusch, R. G. (2017). Role of inactivity in chronic diseases: evolutionary insight and pathophysiological mechanisms. *Physiol. Rev.* 97, 1351–1402. doi: 10.1152/physrev.00019.2016

Borbely, A., Falcao-Pires, I., Van Heerebeek, L., Hamdani, N., Edes, I., Gavina, C., et al. (2009). Hypophosphorylation of the stiff N2B titin isoform raises cardiomyocyte resting tension in failing human myocardium. *Circ. Res.* 104, 780–786. doi: 10.1161/CIRCRESAHA.108.193326

Buck, D., Hudson, B. D., Ottenheijm, C. A., Labeit, S., and Granzier, H. (2010). Differential splicing of the large sarcomeric protein nebulin during skeletal muscle development. *J. Struct. Biol.* 170, 325–333. doi: 10.1016/j.jsb.2010.02.014

Chung, C. S., and Granzier, H. L. (2011). Contribution of titin and extracellular matrix to passive pressure and measurement of sarcomere length in the mouse left ventricle. *J. Mol. Cell. Cardiol.* 50, 731–739. doi: 10.1016/j.yjmcc.2011.01.005

Chung, C. S., Hutchinson, K. R., Methawasin, M., Saripalli, C., Smith, J. E. III, Hidalgo, C. G., et al. (2013). Shortening of the elastic tandem immunoglobulin segment of titin leads to diastolic dysfunction. *Circulation* 128, 19–28. doi: 10.1161/CIRCULATIONAHA.112.001268

Dauksaite, V., and Gotthardt, M. (2018). Molecular basis of titin exon exclusion by RBM20 and the novel titin splice regulator PTB4. *Nucleic Acids Res.* 46, 5227–5238. doi: 10.1093/nar/gky165

Edelmann, F., Gelbrich, G., Dungen, H. D., Frohling, S., Wachter, R., Stahrenberg, R., et al. (2011). Exercise training improves exercise capacity and diastolic function in patients with heart failure with preserved ejection fraction: results of the Ex-DHF (Exercise training in Diastolic Heart Failure) pilot study. *J. Am. Coll. Cardiol.* 58, 1780–1791. doi: 10.1016/j.jacc.2011.06.054

Freiburg, A., Trombitas, K., Hell, W., Cazorla, O., Fougerousse, F., Centner, T., et al. (2000). Series of exon-skipping events in the elastic spring region of titin as the structural basis for myofibrillar elastic diversity. *Circ. Res.* 86, 1114–1121. doi: 10.1161/01.res.86.11.1114

Fujimoto, N., Prasad, A., Hastings, J. L., Bhella, P. S., Shibata, S., Palmer, D., et al. (2012). Cardiovascular effects of 1 year of progressive endurance exercise training in patients with heart failure with preserved ejection fraction. *Am. Heart J.* 164, 869–877. doi: 10.1016/j.ahj.2012.06.028

Fukuda, N., Wu, Y., Nair, P., and Granzier, H. L. (2005). Phosphorylation of titin modulates passive stiffness of cardiac muscle in a titin isoform-dependent manner. *J. Gen. Physiol.* 125, 257–271. doi: 10.1085/jgp.200409177

Granzier, H. L., and Irving, T. C. (1995). Passive tension in cardiac muscle: contribution of collagen, titin, microtubules, and intermediate filaments. *Biophys. J.* 68, 1027–1044. doi: 10.1016/s0006-3495(95)80278-x

Granzier, H. L., and Labeit, S. (2004). The giant protein titin: a major player in myocardial mechanics, signaling, and disease. *Circ. Res.* 94, 284–295. doi: 10.1161/01.res.0000117769.88862.f8

Guo, W., Pleitner, J. M., Saupe, K. W., and Greaser, M. L. (2013). Pathophysiological defects and transcriptional profiling in the RBM20-/- rat model. *PLoS One* 8:e84281. doi: 10.1371/journal.pone.0084281

Guo, W., Schafer, S., Greaser, M. L., Radke, M. H., Liss, M., Govindarajan, T., et al. (2012). RBM20, a gene for hereditary cardiomyopathy, regulates titin splicing. *Nat. Med.* 18, 766–773. doi: 10.1038/nm.2693

Hamdani, N., Krysiak, J., Kreusser, M. M., Neef, S., Dos Remedios, C. G., Maier, L. S., et al. (2013). Crucial role for Ca2(+)/calmodulin-dependent protein kinase-II in regulating diastolic stress of normal and failing hearts via titin phosphorylation. *Circ. Res.* 112, 664–674. doi: 10.1161/CIRCRESAHA.111.300105

Hidalgo, C., Saripalli, C., and Granzier, H. L. (2014). Effect of exercise training on post-translational and post-transcriptional regulation of titin stiffness in striated muscle of wild type and IG KO mice. *Arch. Biochem. Biophys.* 552-553, 100–107. doi: 10.1016/j.abb.2014.02.010

Howden, E. J., Sarma, S., Lawley, J. S., Opondo, M., Cornwell, W., Stoller, D., et al. (2018). Reversing the cardiac effects of sedentary aging in middle age-a randomized controlled trial: implications for heart failure prevention. *Circulation* 137, 1549–1560. doi: 10.1161/CIRCULATIONAHA.117.030617

Hudson, B., Hidalgo, C., Saripalli, C., and Granzier, H. (2011). Hyperphosphorylation of mouse cardiac titin contributes to transverse aortic constriction-induced diastolic dysfunction. *Circ. Res.* 109, 858–866. doi: 10.1161/CIRCRESAHA.111.246819

Kirwan, J. P., Solomon, T. P., Wojta, D. M., Staten, M. A., and Holloszy, J. O. (2009). Effects of 7 days of exercise training on insulin sensitivity and responsiveness in type 2 diabetes mellitus. *Am. J. Physiol. Endocrinol. Metab.* 297, E151–E156. doi: 10.1152/ajpendo.00210.2009

Koser, F., Loescher, C., and Linke, W. A. (2019). Posttranslational modifications of titin from cardiac muscle: how, where, and what for? *FEBS J.* 286, 2240–2260. doi: 10.1111/febs.14854

Lahmers, S., Wu, Y., Call, D. R., Labeit, S., and Granzier, H. (2004). Developmental control of titin isoform expression and passive stiffness in fetal and neonatal myocardium. *Circ. Res.* 94, 505–513. doi: 10.1161/01.res.0000115522.52554.86

Lalande, S., Mueller, P. J., and Chung, C. S. (2017). The link between exercise and titin passive stiffness. *Exp. Physiol.* 102, 1055–1066. doi: 10.1113/EP086275

Lavie, C. J., Ozemek, C., Carbone, S., Katzmarzyk, P. T., and Blair, S. N. (2019). Sedentary behavior, exercise, and cardiovascular health. *Circ. Res.* 124, 799–815. doi: 10.1161/CIRCRESAHA.118.312669

Li, S., Guo, W., Schmitt, B. M., and Greaser, M. L. (2012). Comprehensive analysis of titin protein isoform and alternative splicing in normal and mutant rats. *J. Cell. Biochem.* 113, 1265–1273. doi: 10.1002/jcb.23459

Livak, K. J., and Schmittgen, T. D. (2001). Analysis of relative gene expression data using real-time quantitative PCR and the 2(-Delta Delta C(T)) Method. *Methods* 25, 402–408. doi: 10.1006/meth.2001.1262

Martin, B., Ji, S., Maudsley, S., and Mattson, M. P. (2010). "Control" laboratory rodents are metabolically morbid: why it matters. *Proc. Natl. Acad. Sci. U.S.A.* 107, 6127–6133. doi: 10.1073/pnas.0912955107

Meijer, J. H., and Robbers, Y. (2014). Wheel running in the wild. *Proc. Biol. Sci.* 281:20140210. doi: 10.1098/rspb.2014.0210

Methawasin, M., Strom, J. G., Slater, R. E., Fernandez, V., Saripalli, C., and Granzier, H. (2016). Experimentally increasing the compliance of titin through RNA binding Motif-20 (RBM20) inhibition improves diastolic function in a mouse model of heart failure with preserved ejection fraction. *Circulation* 134, 1085–1099. doi: 10.1161/circulationaha.116.023003

Meyer, T. E., Karamanoglu, M., Ehsani, A. A., and Kovacs, S. J. (2004). Left ventricular chamber stiffness at rest as a determinant of exercise capacity in

heart failure subjects with decreased ejection fraction. *J. Appl. Physiol.* 97, 1667–1672. doi: 10.1152/japplphysiol.00078.2004

Mischel, N. A., and Mueller, P. J. (2011). (In)activity-dependent alterations in resting and reflex control of splanchnic sympathetic nerve activity. *J. Appl. Physiol.* 111, 1854–1862. doi: 10.1152/japplphysiol.00961.2011

Muller, A. E., Kreiner, M., Kotter, S., Lassak, P., Bloch, W., Suhr, F., et al. (2014). Acute exercise modifies titin phosphorylation and increases cardiac myofilament stiffness. *Front. Physiol.* 5:449. doi: 10.3389/fphys.2014.00449

Murayama, R., Kimura-Asami, M., Togo-Ohno, M., Yamasaki-Kato, Y., Naruse, T. K., Yamamoto, T., et al. (2018). Phosphorylation of the RSRSP stretch is critical for splicing regulation by RNA-binding motif protein 20 (RBM20) through nuclear localization. *Sci. Rep.* 8:8970. doi: 10.1038/s41598-018-26624-w

Nagueh, S. F., Shah, G., Wu, Y., Torre-Amione, G., King, N. M., Lahmers, S., et al. (2004). Altered titin expression, myocardial stiffness, and left ventricular function in patients with dilated cardiomyopathy. *Circulation* 110, 155–162. doi: 10.1161/01.cir.0000135591.37759.af

Perkin, J., Slater, R., Del Favero, G., Lanzicher, T., Hidalgo, C., Anderson, B., et al. (2015). Phosphorylating titin's cardiac N2B element by ERK2 or CaMKIIdelta lowers the single molecule and cardiac muscle force. *Biophys. J.* 109, 2592–2601. doi: 10.1016/j.bpj.2015.11.002

Rio, D. C., Ares, M. Jr., Hannon, G. J., and Nilsen, T. W. (2010). Purification of RNA using TRIzol (TRI reagent). *Cold Spring Harb. Protoc.* 2010:dbrot5439. doi: 10.1101/pdb.prot5439

Slater, R. E., Strom, J. G., and Granzier, H. (2017). Effect of exercise on passive myocardial stiffness in mice with diastolic dysfunction. *J. Mol. Cell. Cardiol.* 108, 24–33. doi: 10.1016/j.yjmcc.2017.04.006

Sternberg, S. R. (1983). Biomedical image processing. *Computer* 16, 22–34.

Trombitas, K., Wu, Y., Labeit, D., Labeit, S., and Granzier, H. (2001). Cardiac titin isoforms are coexpressed in the half-sarcomere and extend independently. *Am. J. Physiol. Heart Circ. Physiol.* 281, H1793–H1799.

Wollerton, M. C., Gooding, C., Robinson, F., Brown, E. C., Jackson, R. J., and Smith, C. W. (2001). Differential alternative splicing activity of isoforms of polypyrimidine tract binding protein (PTB). *RNA* 7, 819–832. doi: 10.1017/s1355838201010214

Wu, Y., Cazorla, O., Labeit, D., Labeit, S., and Granzier, H. (2000). Changes in titin and collagen underlie diastolic stiffness diversity of cardiac muscle. *J. Mol. Cell. Cardiol.* 32, 2151–2162.

Zhu, C., Yin, Z., Tan, B., and Guo, W. (2017). Insulin regulates titin pre-mRNA splicing through the PI3K-Akt-mTOR kinase axis in a RBM20-dependent manner. *Biochim. Biophys. Acta Mol. Basis Dis.* 1863, 2363–2371. doi: 10.1016/j.bbadis.2017.06.023

Zhu, C. Q., and Guo, W. (2017). Detection and quantification of the giant protein titin by SDS-agarose gel electrophoresis. *Methodsx* 4, 320–327. doi: 10.1016/j.mex.2017.09.007

Conflict of Interest: The authors declare that the research was conducted in the absence of any commercial or financial relationships that could be construed as a potential conflict of interest.

frontiers in Physiology

REVIEW
published: 19 February 2020
doi: 10.3389/fphys.2020.00108

Palmitoylation: A Fatty Regulator of Myocardial Electrophysiology

*Kobina Essandoh[1], Julie M. Philippe[1], Paul M. Jenkins[1,2] and Matthew J. Brody[1,3]**

[1] Department of Pharmacology, University of Michigan, Ann Arbor, MI, United States, [2] Department of Psychiatry, University of Michigan, Ann Arbor, MI, United States, [3] Department of Internal Medicine, University of Michigan, Ann Arbor, MI, United States

Regulation of cardiac physiology is well known to occur through the action of kinases that reversibly phosphorylate ion channels, calcium handling machinery, and signaling effectors. However, it is becoming increasingly apparent that palmitoylation or S-acylation, the post-translational modification of cysteines with saturated fatty acids, plays instrumental roles in regulating the localization, activity, stability, sorting, and function of numerous proteins, including proteins known to have essential functions in cardiomyocytes. However, the impact of this modification on cardiac physiology requires further investigation. S-acylation is catalyzed by the zDHHC family of S-acyl transferases that localize to intracellular organelle membranes or the sarcolemma. Recent work has begun to uncover functions of S-acylation in the heart, particularly in the regulation of cardiac electrophysiology, including modification of the sodium-calcium exchanger, phospholemman and the cardiac sodium pump, as well as the voltage-gated sodium channel. Elucidating the regulatory functions of zDHHC enzymes in cardiomyocytes and determination of how S-acylation is altered in the diseased heart will shed light on how these modifications participate in cardiac pathogenesis and potentially identify novel targets for the treatment of cardiovascular disease. Indeed, proteins with critical signaling roles in the heart are also S-acylated, including receptors and G-proteins, yet the dynamics and functions of these modifications in myocardial physiology have not been interrogated. Here, we will review what is known about zDHHC enzymes and substrate S-acylation in myocardial physiology and highlight future areas of investigation that will uncover novel functions of S-acylation in cardiac homeostasis and pathophysiology.

Keywords: S-acylation, palmitoylation, zDHHC enzymes, cardiac physiology, electrophysiology, post-translational modifications, ion channels, myocardium

OPEN ACCESS

Edited by:
Sachio Morimoto, International University of Health and Welfare (IUHW), Japan

Reviewed by:
Luke Chamberlain, University of Strathclyde, United Kingdom
Darren Boehning, Cooper Medical School of Rowan University, United States

***Correspondence:**
Matthew J. Brody
majbrody@umich.edu

Specialty section:
This article was submitted to Striated Muscle Physiology, a section of the journal Frontiers in Physiology

Received: *19 December 2019*
Accepted: *30 January 2020*
Published: *19 February 2020*

Citation:
Essandoh K, Philippe JM, Jenkins PM and Brody MJ (2020) Palmitoylation: A Fatty Regulator of Myocardial Electrophysiology. Front. Physiol. 11:108. doi: 10.3389/fphys.2020.00108

INTRODUCTION

S-acylation or palmitoylation is the post-translational modification of protein cysteines with saturated fatty acids that imparts spatiotemporal regulation of protein hydrophobicity and thereby can modulate many aspects of protein function including localization, activity, interactions with cofactors, membrane topology, and stability (Linder and Deschenes, 2007;

Greaves and Chamberlain, 2011; Chamberlain and Shipston, 2015). S-acylation is unique amongst lipid modifications on proteins in that it is a highly regulated and reversible process controlled by 23 Asp-His-His-Cys (DHHC) S-acyltransferases (Fukata et al., 2004; Greaves and Chamberlain, 2011; Gottlieb and Linder, 2017). Certain serine hydrolases, including acyl protein thioesterase-1 and -2 and α/β-Hydrolase domain-containing proteins (ABHD10, 17A, 17B, and 17C) exhibit thioesterase activity and function as protein S-deacylases (Hirano et al., 2009; Tomatis et al., 2010; Lin and Conibear, 2015a,b; Yokoi et al., 2016; Cao et al., 2019). This tight enzymatic control enables S-acylation to be acutely altered in response to stimuli or changes in cellular environment and rapidly regulate cellular and physiological responses.

The term palmitoylation is frequently used interchangeably with S-acylation and while the 16-carbon fatty acid palmitate (16:0) is most commonly attached to protein cysteines, some zDHHC enzymes are more promiscuous and will transfer shorter (14:0) or longer (18:0) length acyl chains onto substrates (Chamberlain and Shipston, 2015; Greaves et al., 2017; Rana et al., 2018). zDHHC S-acyltransferases are polytopic transmembrane proteins, many of which localize to the Golgi or endoplasmic reticulum (ER) but with some also localizing to the plasma membrane, endomembrane system, or intracellular vesicles (Ohno et al., 2006; Korycka et al., 2012). Although some zDHHCs have overlapping substrates, they exhibit a high degree of substrate specificity that is mediated in part by protein sequence recognition elements on the substrate and zDHHC enzymes, tissue- and temporal-specific expression patterns, and subcellular localization (Linder and Deschenes, 2007; Tsutsumi et al., 2008; Howie et al., 2014; Lemonidis et al., 2014; Plain et al., 2017; Shah et al., 2019). Catalysis of S-acylation by zDHHC enzymes occurs via a "ping-pong" kinetic mechanism in which the zDHHC enzyme undergoes transient autoacylation on its DHHC domain cysteine residue and subsequently transfers the fatty acid onto the cysteine of the protein substrate (Jennings and Linder, 2012; Rana et al., 2018; **Figure 1**). Importantly, many zDHHC enzymes are abundantly expressed in heart (Howie et al., 2014), suggesting vital regulatory functions in myocardial physiology. S-deacylating thioesterases are predominantly cytoplasmic enzymes and are also expressed in the heart, but far less is known regarding their substrate specificity and physiological functions (Davda and Martin, 2014; Chamberlain and Shipston, 2015).

While some substrates exhibit relatively stable S-acylation to mediate trafficking to and/or association with specific membrane domains, other proteins, including signaling molecules such as G-proteins and small GTPases, undergo rapid cycles of S-acylation and deacylation that can control movement to specific intracellular membrane microdomains with remarkable temporal resolution (Martin and Cravatt, 2009; Tsutsumi et al., 2009; Martin et al., 2012; Won and Martin, 2018). Indeed, the functional effects and kinetics of protein S-acylation are substrate and context specific. For example, the tyrosine kinase c-Met is S-acylated in the ER shortly after biosynthesis as a stable modification to promote anterograde trafficking to the plasma membrane (Coleman et al., 2016) while S-acylation of the ER-resident chaperone calnexin occurs several hours after synthesis to enhance protein stability and thereby deploy nascent calnexin protein at the ER membrane (Lakkaraju et al., 2012; Dallavilla et al., 2016). In contrast, H-Ras and N-Ras undergo rapid minute timescale cycles of deacylation/reacylation to regulate shuttling between the Golgi apparatus and signaling domains at the plasma membrane (Rocks et al., 2005) underscoring the need for further investigation of protein S-acylation dynamics and functional consequences, especially in physiologically relevant cell types such as cardiomyocytes. Recent studies demonstrate a critical role for S-acylation in many pathologies including several cancers (Liu et al., 2016; Runkle et al., 2016; Chen et al., 2017; Kharbanda et al., 2017; Chen S. et al., 2019), inflammatory diseases (Beard et al., 2016; Mukai et al., 2016; Hansen et al., 2019), and neurological disorders (Mukai et al., 2004; Cho and Park, 2016; Sanders et al., 2016; Kouskou et al., 2018). Moreover, mutations in *ZDHHC9* are associated with X-linked intellectual disability (Raymond et al., 2007; Han et al., 2017), suggesting a direct link between defective S-acylation and human disease. Here we will focus on the functions of S-acylation, zDHHC enzymes, and modified substrates in the heart, but comprehensive reviews can be found elsewhere (Chamberlain and Shipston, 2015; Jiang et al., 2018).

Cardiomyocytes, which comprise 70–90% of the volume fraction of the heart (Reiss et al., 1996; Zhou and Pu, 2016), are very specialized, electrically excitable contractile cells that mediate the predominant cardiac function of pumping blood to the peripheral tissues and organs. Importantly, the cardiomyocyte cytoplasm is packed full with myofilaments and mitochondria, which occupy approximately 60% and 30% of the intracellular milieu, respectively (Barth et al., 1992; Piquereau et al., 2013), leaving limited free cytoplasmic space for signaling molecules and membrane proteins to navigate and traffic. It is within this complex cytoarchitecture that membrane proteins, including ion channels and receptors, must traffic to the appropriate membrane microdomains, and signaling molecules must navigate to assemble into signaling complexes that nucleate at specific intracellular membranes. Beyond providing lipid-based molecular instructions to direct proteins to specific membranes, S-acylation can also locally alter how strongly a protein interacts with membranes or the topology of a membrane protein within a given cellular membrane, which dramatically affects protein activity as has been demonstrated for many ion channels (Chaube et al., 2014; Reilly et al., 2015; Pei et al., 2016; Duncan et al., 2019), receptors (Runkle et al., 2016; Chen et al., 2017; Kharbanda et al., 2017), and kinases (Barylko et al., 2009; Zhou et al., 2014; Akimzhanov and Boehning, 2015; **Figure 1**).

zDHHC mouse models suggest important roles for these enzymes in the heart. Deletion of the ER- and Golgi-localized enzyme zDHHC16 results in defects in eye development and perinatal cardiomyopathy and lethality (Zhou et al., 2015; Abrami et al., 2017). In contrast, cardiac muscle lacking the plasma membrane enzyme zDHHC5 exhibits enhanced recovery of contractile function following anoxia (Lin et al., 2013). Moreover, mutation of an S-acylation site (C981) in the cardiac voltage-gated sodium channel ($Na_v1.5$) is associated with cardiac

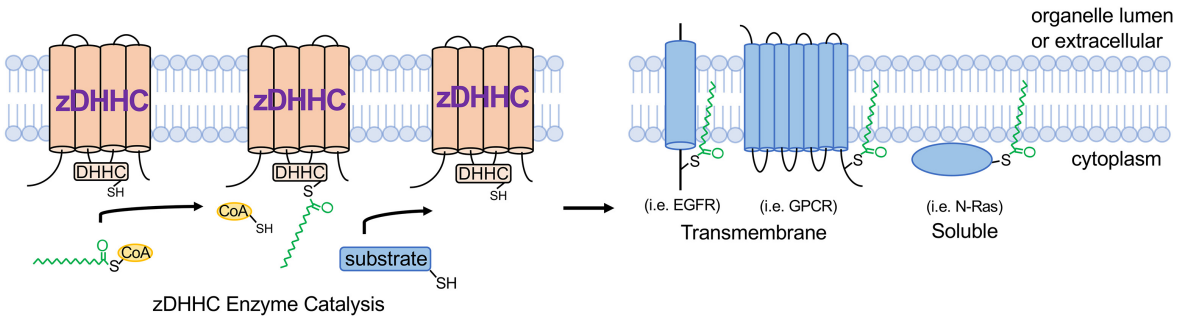

FIGURE 1 | zDHHC S-acyltransferase-mediated substrate modification. zDHHC enzymes modify substrates through a "ping-pong" kinetic mechanism (Jennings and Linder, 2012) whereby the enzyme transiently accepts an acyl chain on its DHHC Cys from acyl-CoA and then transfers the acyl group onto the substrate Cys residue. zDHHCs are transmembrane proteins with their enzymatic DHHC motif on the cytoplasmic loop and substrates are S-acylated on cytoplasmic juxtamembrane or membrane-associated Cys residues. *GPCR*, G-protein-coupled receptor; *EGFR*, epidermal growth factor receptor; *CoA*, coenzyme A.

arrhythmia in human patients (Kapplinger et al., 2009; Pei et al., 2016). Although genetic deletion of both acyl protein thioesterase-1 and -2 in mice did not result in an overt phenotype, cardiac function was not evaluated (Won and Martin, 2018). Pharmacological or genetic strategies to inhibit or augment specific S-acylation events in cardiomyocytes could provide novel therapeutic interventions for the treatment of heart disease.

S-acylation undoubtedly plays fundamental roles in cardiac function and disease, including modulation of ion channel function and signal transduction in cardiac myocytes. Here, we will review how S-acylation modulates myocardial physiology with a focus on the substrates and modifications demonstrated to impact cardiomyocyte electrophysiology as well as highlight other areas of cardiac physiology regulated by S-acylation that warrant future investigation.

MYOCARDIAL ELECTROPHYSIOLOGY

Despite the lack of knowledge of the functions of S-acylation in cardiomyocytes relative to other cell types such as neurons (Fukata and Fukata, 2010; Matt et al., 2019), recent studies demonstrate cardiomyocyte electrophysiology is highly regulated by this modification. Cardiomyocyte function is principally regulated by local ion concentrations that establish membrane potential and stimulate myofilament contraction. Rapid influx of Na^+ ions depolarizes the cardiomyocyte and is followed by Ca^{2+} influx through voltage-dependent L-type calcium channels ($Ca_v1.2$) that stimulate ryanodine receptor 2 (RyR2) to release Ca^{2+} from internal stores in the sarcoplasmic reticulum (SR). This, in turn, raises cytosolic Ca^{2+} levels by an order of magnitude to directly activate myofilament contraction in a process termed excitation-contraction coupling (MacLennan and Kranias, 2003; Fearnley et al., 2011; Ljubojevic and Bers, 2015). Cytosolic Ca^{2+} is returned to basal diastolic levels by reuptake back into the SR through the sarco ER ATPase (SERCA2a), and to a lesser extent, extrusion of Ca^{2+} outside the cell by the Na^+/Ca^{2+}-exchanger (NCX) (MacLennan and Kranias, 2003; Lytton, 2007; **Figure 2**). Cardiomyocyte electrophysiological properties are highly regulated by a number of ion channels, pumps, and auxiliary proteins each optimally positioned within the cardiomyocyte to impart precise spatiotemporal control of intracellular Na^+, Ca^{2+}, and K^+ ion concentrations (MacLennan and Kranias, 2003; Lytton, 2007; Fuller et al., 2013; Brody and Lee, 2016; Edokobi and Isom, 2018; Woon et al., 2018). Here we will highlight S-acylation-dependent mechanisms controlling ion channel homeostasis and excitation-contraction coupling in cardiomyocytes.

VOLTAGE-GATED SODIUM CHANNEL ($Na_v1.5$)

Inward Na^+ current provides the membrane depolarization responsible for action potential generation in cardiomyocytes. This occurs through voltage-gated sodium channels composed of the pore-forming $Na_v1.5$ α-subunit, which contains four homologous domains of six transmembrane domains each, and two auxiliary β subunits containing a single transmembrane domain and extracellular immunoglobulin loop (Detta et al., 2015; Edokobi and Isom, 2018). $Na_v1.5$ (encoded by *SCN5A*) is the major regulator of cardiac excitation and mutations in $Na_v1.5$ are associated with a number inherited arrhythmogenic channelopathies and disorders including Brugada syndrome, long QT syndrome, and atrial fibrillation (Abriel, 2007; Detta et al., 2015). A C981F mutation in $Na_v1.5$ was reported in a patient with long QT syndrome (Kapplinger et al., 2009; Pei et al., 2016), which corresponds to an intracellular loop cysteine on the domain II-III linker region (**Figure 2**), a location ideally situated to regulate pore activity. $Na_v1.5$ is S-acylated in the heart and mutation of four cysteines (including Cys981) in this region abrogated S-acylation (Pei et al., 2016), suggesting $Na_v1.5$ may by lipidated at multiple sites on this intracellular loop. More importantly, the C981F mutation or pharmacological inhibition of $Na_v1.5$ S-acylation did not affect cell surface expression but instead augmented closed-state inactivation and reduced channel availability and cardiomyocyte excitability (Pei et al., 2016). In contrast, increasing S-acylation of $Na_v1.5$ prolonged action potential duration and induced early after depolarizations

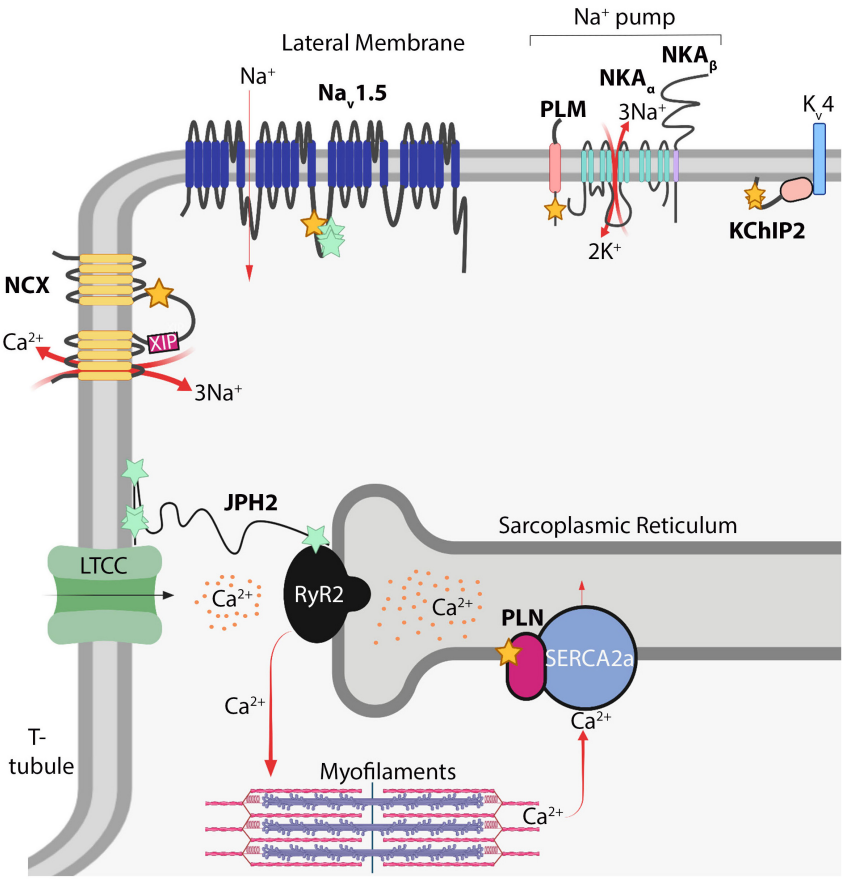

FIGURE 2 | S-acylation in myocardial electrophysiology. Schematic of S-acylated ion channels, transporters, and auxiliary proteins in cardiomyocytes. Yellow stars denote cysteines modified by S-acylation; turquoise stars denote potential modification sites. *NCX*, Na^+/Ca^{2+}-exchanger; *XIP*, exchanger inhibitory peptide; *$Na_v1.5$*, voltage-gated Na^+ channel; *PLM*, phospholemman; *NKA*, Na^+/K^+-ATPase; *KChIP2*, K^+ channel interacting protein 2; *K_v4*, delayed rectifier voltage-gated K^+ channel; *PLN*, phospholamban; *RyR2*, ryanodine receptor 2; *SERCA2A*, sarcoendoplasmic reticulum ATPase 2A; *JPH2*, junctophilin-2; *LTCC*, voltage-gated L-type Ca^{2+} channel. Image created with BioRender (www.biorender.com).

(Pei et al., 2016), revealing S-acylation functions as a rheostat for $Na_v1.5$ channel gating and cardiac excitability.

Na^+ PUMP (Na^+/K^+-ATPase)

The Na^+ pump establishes the resting membrane potential in cardiomyocytes through energy-dependent extrusion of three Na^+ ions concomitant with import of two K^+ ions. This homeostatic maintenance of intracellular Na^+ and K^+ concentrations sets the electrochemical gradient for $Na_v1.5$, other Na^+-dependent transporters, and NCX (Howie et al., 2013; Pavlovic et al., 2013). The cardiac Na^+ pump consists of the Na^+/K^+-ATPase catalytic α subunit (α1 or α2), the β1 subunit, and an ancillary FXYD protein called phospholemman (Fuller et al., 2013; **Figure 2**). The α and β subunits of the Na^+ pump are S-acylated in non-cardiac cells (Kang et al., 2008; Forrester et al., 2011; Martin et al., 2012; Howie et al., 2013), yet targeted studies investigating the functional consequences of these modifications or whether they occur in the heart have not been reported. However, recent studies have uncovered a vital role for S-acylation of phospholemman in regulating cardiac Na^+ pump activity. Phospholemman, a small 72 amino acid transmembrane protein that negatively regulates Na^+ pump activity, is palmitoylated on its intracellular membrane proximal residues, Cys40 and Cys42, adjacent to the Na^+/K^+-ATPase α subunit (Tulloch et al., 2011). In cardiomyocytes, S-acylation of phospholemman occurs predominantly at Cys40 (**Figure 2**) by the action of the sarcolemmal enzyme zDHHC5, which is required for phospholemman-mediated repression of Na^+ pump activity (Howie et al., 2014). Thus, regulation of phospholemman by zDHHC5 provides an S-acylation-dependent mechanism to acutely fine tune the cardiac Na^+ pump.

Na^+/Ca^{2+}-EXCHANGER (NCX)

The NCX is a sarcolemmal ion transporter containing 10 transmembrane domains that extrudes Ca^{2+} into the extracellular space in exchange for import of three Na^+ ions, which along with reuptake of Ca^{2+} into the SR by SERCA2a, restores cytosolic Ca^{2+} levels following myofilament

contraction (**Figure 2**). NCX activity thus is an important homeostatic regulator of excitation-contraction coupling. Reduced NCX activity and consequent diminished removal of systolic Ca^{2+} can elevate SR Ca^{2+} stores and be a source of arrhythmogenesis (Lytton, 2007; Voigt et al., 2012; Fuller et al., 2016). In contrast, enhanced NCX expression, which occurs in heart failure, can hasten diminished contractile function by reducing SR Ca^{2+} stores available for excitation-contraction coupling and contribute to arrhythmogenic delayed after depolarizations triggered by increased NCX-mediated Na^{+} influx concomitant with Ca^{2+} efflux (Lytton, 2007; Ottolia et al., 2013). NCX can also function in reverse-mode depending on Na^{+} and Ca^{2+} concentration gradients, thereby extruding Na^{+} and importing Ca^{2+}, which can exacerbate Ca^{2+} overload-induced cardiomyocyte necrosis during ischemia (Chen and Li, 2012; Fuller et al., 2016). Therefore, tight regulation of NCX activity is required for proper cardiomyocyte contraction, electrophysiology, and prevention of cardiac arrhythmias. NCX1, the only isoform expressed in cardiomyocytes, is S-acylated in the heart, brain and kidney (Reilly et al., 2015). NCX1 is S-acylated at the Golgi exclusively on Cys739 on the intracellular regulatory f-loop between the fifth and sixth transmembrane domains (**Figure 2**), tethering the cytoplasmic f-loop to the membrane (Reilly et al., 2015; Fuller et al., 2016). While S-acylation does not modulate localization or trafficking of NCX1 to the sarcolemma, it is required for effective inactivation in response to reduced intracellular Ca^{2+} or phosphatidylinositol 4,5-bisphosphate (PIP2) levels (Reilly et al., 2015; Fuller et al., 2016), physiological cues that trigger NCX1 inactivation (Lytton, 2007). Inactivation of NCX1 requires the action of an autoinhibitory peptide, the exchanger inhibitory peptide (XIP), located at the juxtamembrane N-terminal side of the cytosolic regulatory f-loop (amino acids 219-238) of NCX1 (**Figure 2**). S-acylation of NCX1 at Cys739 on the C-terminal side of this f-loop appears to modify its structure to enhance XIP-mediated inactivation of NCX1 (Molinaro et al., 2015; Reilly et al., 2015; Fuller et al., 2016; **Figure 2**). Therefore, S-acylation of NCX1 at the cardiomyocyte Golgi modulates its activity at the sarcolemma by controlling its propensity for inactivation in response to physiological stimuli (Reilly et al., 2015; Fuller et al., 2016). Since roughly 60% of NCX1 is S-acylated in the heart (Reilly et al., 2015; Fuller et al., 2016), the stoichiometry and dynamics of NCX1 S-acylation are likely to have important consequences for cardiac contractile function and arrhythmogenesis.

KChIP2

In addition to Na^{+} and Ca^{2+} currents, K^{+} currents mediated by voltage-gated K^{+} channels (K_v channels) are precisely regulated and make up an instrumental regulatory component of cardiac electrophysiology. K^{+} channel interacting protein 2 (KChIP2) primarily functions as an accessory K_v4 channel protein and is required for trafficking and cell surface expression of $K_v4.2$ and Kv4.3 and the generation of the transient outward K^{+} current in cardiomyocytes (Kuo et al., 2001; Takimoto et al., 2002; Shibata et al., 2003; Grubb et al., 2012). KChIP2 is a cytoplasmic protein with four EF hand motifs that bind Ca^{2+} and S-acylation sites at Cys45 and Cys46 that are required for its localization to the cell membrane in HEK cells (Takimoto et al., 2002; Grubb et al., 2012; **Figure 2**). Importantly, Cys45 and Cys46 of KChIP2 are also required for sarcolemmal localization in adult atrial and ventricular myocytes (Murthy et al., 2019), although direct effects of KChIP2 S-acylation on K^{+} current in cardiomyocytes have not been evaluated.

PHOSPHOLAMBAN

Phospholamban is a small 52 amino acid SR membrane protein that interacts with and represses the activity SERCA2a, thereby reducing transport of cytosolic Ca^{2+} back into the SR. Upon phosphorylation by cAMP-dependent protein kinase (PKA) downstream of β-adrenergic stimulation, phospholamban relieves its inhibition of SERCA2a resulting in enhanced Ca^{2+} reuptake into the SR, restoration of diastolic cytosolic Ca^{2+} levels, and myofilament relaxation (MacLennan and Kranias, 2003; **Figure 2**). Thus, phospholamban functions as an instrumental regulator of cardiac contraction and relaxation. In COS7 cells, phospholamban is S-acylated at Cys36 (**Figure 2**) by zDHHC16, a predominantly ER-localized enzyme (Li et al., 2002; Abrami et al., 2017), which enhances its phosphorylation by PKA and oligomerization (Zhou et al., 2015). Deletion of zDHHC16 in mice results in developmental defects of the eye and heart, including ventricular non-compaction cardiomyopathy and abnormal cardiomyocyte nuclear morphology, and mortality at 1 day of age in *Zdhhc16*$^{-/-}$ pups that are born alive (Zhou et al., 2015). Importantly, *Zdhhc16*$^{-/-}$ hearts have reduced phospholamban interaction with PKA and phospholamban phosphorylation (Zhou et al., 2015). Moreover, deletion of phospholamban partially rescues cardiomyocyte nuclear dysmorphology in postnatal *Zdhhc16*$^{-/-}$ hearts (Zhou et al., 2015), suggesting zDHHC16 functionally regulates phospholamban *in vivo*. Further studies are needed to substantiate regulation of phospholamban by zDHHC16 in the adult heart and test effects on Ca^{2+} handling and cardiac contractility, which would be greatly aided by generation of mice with cardiomyocyte-specific zDHHC16 deletion or a knock-in mutation of the PLN S-acylation site (Cys36) to further interrogate phospholamban modification *in vivo*.

JUNCTOPHILIN-2

Junctophilin-2 is a structural protein that tethers portions of the T-tubule sarcolemma to the SR membrane thereby forming junctional membrane complexes that enable efficient coupling of Ca^{2+} influx from the T-tubular L-type voltage-dependent Ca^{2+} channel ($Ca_v1.2$) to activate RyR2 and evoke SR Ca^{2+} release and subsequent myofilament contraction (Takeshima et al., 2015; **Figure 2**). Junctophilin-2 is required to maintain T-tubule structure, RyR2 function, and is a requisite component of the excitation-contraction coupling machinery (Van Oort et al., 2011; Chen et al., 2013; Guo et al., 2014;

Zhang et al., 2014). Not surprisingly, mutations in junctophilin-2 are associated with cardiomyopathy, arrhythmia, and heart failure (Beavers et al., 2013; Takeshima et al., 2015; Vanninen et al., 2018; Jones et al., 2019). Junctophilin-2 is a large, nearly 700 amino acid, predominantly cytoplasmic protein containing N-terminal MORN domains that associate with the plasma membrane and a C-terminal transmembrane domain embedded in the SR (Takeshima et al., 2015; **Figure 2**). However, mechanisms underlying junctopilin-2-dependent regulation of dyad architecture are not known. A recent study suggests junctophilin-2 is S-acylated in cardiomyocytes (Jiang et al., 2019; **Figure 2**). In COS7 cells, this allows for association with lipid-rafts in the plasma membrane and stabilizes ER-plasma membrane junctions (Jiang et al., 2019). Future studies are needed to determine which cysteines of junctophilin-2 are modified in cardiomyocytes and how this alters its association with the SR and sarcolemma, Ca^{2+} cycling, and T-tubule morphology.

OTHER ION CHANNELS AND REGULATORS

Recent studies have uncovered S-acylation of a number of ion channels and regulatory proteins in cardiomyocytes with divergent effects on protein function and electrophysiology, suggesting additional unidentified S-acylation events contribute to regulation of cardiac electrophysiology. Although $Na_v1.5$ activity is regulated by S-acylation (Pei et al., 2016), it is not known whether any of its auxiliary β subunits are S-acylated. Na_v-β1 (encoded by *SCN1B*) contains a putative S-acylation site at its intracellular juxtamembrane Cys162 (Brackenbury and Isom, 2011; Edokobi and Isom, 2018) that warrants further investigation into potential effects on $Na_v1.5$ activity. In contrast, there is intricate knowledge of how S-acylation of the auxiliary protein phospholemman modulates Na^+ pump activity (Howie et al., 2014), yet it is not clear if the α and β subunits of Na^+/K^+-ATPase themselves are S-acylated in cardiomyocytes and if this affects pump activity. Despite recent evidence that KChIP2 is S-acylated in cardiomyocytes (Murthy et al., 2019) and the importance of K_v4 channels in cardiomyocyte electrophysiology, it is not known if K_v4 or other K^+ channels, such as the rapidly activating delayed rectifier K^+ channel (I_{Kr}), undergo S-acylation and whether this impacts trafficking, recycling, gating, or inactivation. Coupling of large conductance calcium- and voltage- activated potassium channels (BK channels) is regulated by S-acylation (Duncan et al., 2019), yet the role of this in the mechanosensing functions of BK channels in ventricular myocytes (Zhao et al., 2017) is not clear. Moreover, except for phospholamban (Zhou et al., 2015), modification of SR Ca^{2+} handling proteins by S-acylation in cardiac myocytes has not been reported, although SERCA1a, RyR1, and $Ca_v1.1$ undergo S-acylation in skeletal muscle (Chaube et al., 2014), suggesting SERCA2a, RyR2, and/or $Ca_v1.2$ could be similarly regulated in the heart. Additionally, in HEK cells, S-acylation of Cys3 and Cys4 of the β_{2a} subunit of the L-type calcium channel is required for its plasma membrane targeting and modulation of $Ca_v1.2$ current (Chien et al., 1996, 1998), suggesting this mechanism could regulate L-type calcium channel current and excitation-contraction coupling in cardiomyocytes.

Several chaperones and cytoskeletal proteins critical for trafficking and localization of ion channels to the cell surface are modified and functionally regulated by S-acylation and it is unclear if this contributes to cardiac physiology or pathogenesis of arrhythmogenic channelopathy disorders. For example, ankyrin-G is a large cytoskeletal protein whose membrane localization and function are dictated by S-acylation in epithelial cells (He et al., 2012, 2014). Ankyrin-G is required for proper targeting of $Na_v1.5$ to the cardiomyocyte intercalated disc and loss of ankyrin-G results in lethal dilated cardiomyopathy, bradycardia, and hypersensitivity to cardiac arrhythmia (Makara et al., 2014, 2018). Moreover, the highly homologous scaffolding protein ankyrin-B, which contains a homologous Cys to the ankyrin-G acylation site, is necessary for targeting Na^+/K^+-ATPase and NCX to the cardiomyocyte T-tubule. Mutations in ankyrin-B result in "ankyrin-B syndrome" characterized by arrhythmogenic cardiomyopathy and sudden death (Mohler et al., 2003, 2004; Roberts et al., 2019). However, it is unclear if S-acylation regulates ankyrins or other ion channel targeting proteins in the heart.

Recent work has characterized a cargo-dependent, adaptor-independent endocytosis pathway termed massive endocytosis (MEND) in which large portions of the plasma membrane are internalized in response to reoxygenation of anoxic cardiac muscle (Lin et al., 2013). This unique form of endocytosis requires the activity of the plasma membrane enzyme zDHHC5 downstream of metabolic stress and mitochondrial-mediated activation of programed necrosis (Lin et al., 2013). Interestingly, S-acylation of both phospholemman and NCX1 promote MEND in response to pharmacological activation of G-protein signaling or mitochondrial Ca^{2+} overload, suggesting the presence of specific S-acylated cargo in sarcolemmal microdomains may induce this unique endocytic pathway (Lin et al., 2013; Reilly et al., 2015; Fuller et al., 2016). Further examination is required to determine the extent to which MEND occurs in the heart and participates in the response to ischemia-reperfusion injury and the activity and/or internalization cardiomyocyte ion channels, transporters, and regulatory proteins *in vivo*.

SIGNALING PROTEINS

S-acylation is emerging as a potent regulator of intracellular signal transduction with implications for many pathophysiologies. For example, the epidermal growth factor receptor (EGFR) is regulated by S-acylation (Runkle et al., 2016; **Figure 1**), which directly modulate signal transduction in cancer cells. Signaling by G-protein coupled receptors (GPCRs) mediates many critical cardiac physiological responses, including contractility and hypertrophic signaling (Bristow et al., 1990; Feldman and Bristow, 1990; D'Angelo et al., 1997; Paradis et al., 2000). S-acylation of many GPCRs functionally regulates G-protein signaling *in vivo* (Liu et al., 2012; Adachi et al., 2016; Chen et al., 2017; Chen S. et al., 2019; **Figure 1**), yet the effects

of GPCR S-acylation on receptor trafficking and signaling in cardiac physiology and disease have not been fully elucidated. Moreover, the majority of G-protein α subunits that transduce signals from activated GPCRs are S-acylated on their N-terminus (Linder et al., 1993; Oldham and Hamm, 2008) and a recent study suggests the plasma membrane-localized enzyme zDHHC5 regulates $G\alpha_s$ and $G\alpha_i$ S-acylation in cardiomyocytes in response to β-adrenergic stimulation (Chen J.J. et al., 2019). However, previous reports indicate that Gα protein S-acylation is catalyzed by Golgi-localized zDHHC enzymes (Tsutsumi et al., 2009). Thus, the kinetics and putative regulation of S-acylation of the many G-protein α subunits by the several zDHHC enzymes expressed in cardiomyocytes and resultant effects on transducing GPCR signals, cardiac contractility, and hypertrophy require further investigation. Furthermore, the role of acyl protein thioesterases in regulating dynamic S-acylation of signaling proteins in cardiomyocytes is virtually unexplored. Many other important cardiac signaling proteins, including regulator of G-protein signaling (RGS) proteins (Zhang and Mende, 2011), small GTPases (Navarro-Lerida et al., 2012; Modica et al., 2017; **Figure 1**), and kinases (Shenoy-Scaria et al., 1994; Runkle et al., 2016) are also regulated by S-acylation, warranting further investigation into the potential functions of these modifications in cardiac signal transduction and physiology. Thus, future studies into the modulation of receptors, kinases, GTPases, and other signaling molecules by S-acylation in the heart will aid in the discovery of novel signal transduction mechanisms that contribute to cardiac homeostasis and pathogenesis.

DISCUSSION

S-acylation represents a new frontier in post-translational modifications that can acutely and dynamically control membrane protein function and signal transduction. Its wide-ranging physiological effects clearly extend to cardiomyocytes and myocardial physiology. It is becoming increasingly evident that S-acylation plays instrumental roles in cardiac physiology although more *in vivo* data on cardiac function and disease in the context of genetic or pharmacological manipulation of zDHHC enzymes, acyl protein thioesterases, or specific S-acylation modifications will greatly enhance our understanding of S-acylation-mediated regulation in the heart. Recent advances in techniques to detect S-acylation (Forrester et al., 2011; Zaballa and Van Der Goot, 2018), including in tissue samples, will propel this field going forward. Protein cysteines can also undergo oxidation and other post-translational modifications such as glutathionylation and S-nitrosylation that can reciprocally and competitively regulate substrate function (Ho et al., 2011; Burgoyne et al., 2012; Shipston, 2014), which also necessitates careful interpretation of studies using cysteine mutagenesis. Indeed, much research remains to be conducted to understand how specific S-acyl modifications modulate protein function in cardiomyocytes and the broader impact on cardiac physiology and disease.

Pharmacological tools to manipulate zDHHC enzymes and substrate S-acylation will prove incredibly useful for basic science and potentially as novel therapeutics. The development of small molecule inhibitors with specificity for individual zDHHCs and *in vivo* efficacy continues to be a challenge but would facilitate the interrogation of the role of these enzymes in specific cell types, signaling pathways, cellular processes, and diseases and ultimately have potential for translation to the clinic. Recently, nitro-containing compounds (nitrofurans and nitro-fatty acids) have been discovered that irreversibly alkylate S-acylation sites on stimulator of interferon genes (STING) thereby inhibiting S-acylation and activation of STING (Haag et al., 2018; Hansen et al., 2018). These compounds are being pursued clinically for the treatment of autoinflammatory diseases (Haag et al., 2018; Hansen et al., 2019) and represent a new paradigm for targeted inhibition of substrate S-acylation with small molecule inhibitors.

Genetic tools and proteomics will greatly advance our understanding of the roles of S-acylation in cardiac biology and disease. Generation of *in vivo* mouse models including LoxP-targeted alleles to delete specific zDHHC enzymes in cardiac myocytes and non-myocyte cell populations (i.e., fibroblasts, immune cells) of the heart, cardiac-specific zDHHC gain-of-function transgenic mice, and knock-in mutations for specific substrate S-acylation sites, will prove invaluable in elucidating functional effects of S-acylation-dependent regulation on cardiac electrophysiology, protein trafficking, and signal transduction in cardiac physiology and disease. Moreover, proteomic studies to interrogate alterations in the cardiac palmitoylome in models with manipulated zDHHC enzyme activity and models of cardiac disease will identify novel S-acylated proteins in the heart, their cognate zDHHC enzymes, and modifications that are altered in the hypertrophied and failing heart, which will facilitate the discovery of novel molecular mechanisms participating in cardiac disease. Thus, future work will combine biochemical and molecular analyses of S-acylation modifications in cardiac cells with *in vivo* assessment of cardiac physiology and disease, which will ultimately enable a comprehensive understanding of mechanisms and functions of S-acylation in cardiac pathophysiology.

AUTHOR CONTRIBUTIONS

All authors contributed to the conception, writing, and editing of the manuscript.

FUNDING

This work was supported by the National Heart, Lung, and Blood Institute grant R00HL136695 to MB and the University of Michigan Pharmacology Charles W. Edmunds Predoctoral Fellowship to JP.

ACKNOWLEDGMENTS

The authors would like to thank Dr. Will Fuller (University of Glasgow) for his critical review and feedback on the manuscript.

REFERENCES

Abrami, L., Dallavilla, T., Sandoz, P. A., Demir, M., Kunz, B., Savoglidis, G., et al. (2017). Identification and dynamics of the human ZDHHC16-ZDHHC6 palmitoylation cascade. *Elife* 6:e27826. doi: 10.7554/eLife.27826

Abriel, H. (2007). Roles and regulation of the cardiac sodium channe Na v 1.5: *recent insights from experimental studies*. *Cardiovasc. Res.* 76, 381–389. doi: 10.1016/j.cardiores.2007.07.019

Adachi, N., Hess, D. T., Mclaughlin, P., and Stamler, J. S. (2016). S-Palmitoylation of a novel site in the beta2-adrenergic receptor associated with a novel intracellular itinerary. *J. Biol. Chem.* 291, 20232–20246. doi: 10.1074/jbc.M116.725762

Akimzhanov, A. M., and Boehning, D. (2015). Rapid and transient palmitoylation of the tyrosine kinase Lck mediates Fas signaling. *Proc. Natl. Acad. Sci U.S.A.* 112, 11876–11880. doi: 10.1073/pnas.1509929112

Barth, E., Stammler, G., Speiser, B., and Schaper, J. (1992). Ultrastructural quantitation of mitochondria and myofilaments in cardiac muscle from 10 different animal species including man. *J. Mol. Cell Cardiol.* 24, 669–681. doi: 10.1016/0022-2828(92)93381-s

Barylko, B., Mao, Y. S., Wlodarski, P., Jung, G., Binns, D. D., Sun, H. Q., et al. (2009). Palmitoylation controls the catalytic activity and subcellular distribution of phosphatidylinositol 4-kinase II{alpha}. *J. Biol. Chem.* 284, 9994–10003. doi: 10.1074/jbc.M900724200

Beard, RS Jr, Yang, X., Meegan, J. E., Overstreet, J. W., Yang, C. G., Elliott, J. A., et al. (2016). Palmitoyl acyltransferase DHHC21 mediates endothelial dysfunction in systemic inflammatory response syndrome. *Nat. Commun.* 7:12823. doi: 10.1038/ncomms12823

Beavers, D. L., Wang, W., Ather, S., Voigt, N., Garbino, A., Dixit, S. S., et al. (2013). Mutation E169K in junctophilin-2 causes atrial fibrillation due to impaired RyR2 stabilization. *J. Am. Coll Cardiol.* 62, 2010–2019. doi: 10.1016/j.jacc.2013.06.052

Brackenbury, W. J., and Isom, L. L. (2011). Na Channel beta subunits: overachievers of the ion channel family. *Front. Pharmacol.* 2:53. doi: 10.3389/fphar.2011.00053

Bristow, M. R., Hershberger, R. E., Port, J. D., Gilbert, E. M., Sandoval, A., Rasmussen, R., et al. (1990). Beta-adrenergic pathways in nonfailing and failing human ventricular myocardium. *Circulation* 82, I12–I25.

Brody, M. J., and Lee, Y. (2016). the role of leucine-rich repeat containing protein 10 (lrrc10) in dilated cardiomyopathy. *Front. Physiol.* 7:337.

Burgoyne, J. R., Haeussler, D. J., Kumar, V., Ji, Y., Pimental, D. R., Zee, R. S., et al. (2012). Oxidation of HRas cysteine thiols by metabolic stress prevents palmitoylation in vivo and contributes to endothelial cell apoptosis. *FASEB J.* 26, 832–841. doi: 10.1096/fj.11-189415

Cao, Y., Qiu, T., Kathayat, R. S., Azizi, S. A., Thorne, A. K., Ahn, D., et al. (2019). ABHD10 is an S-depalmitoylase affecting redox homeostasis through peroxiredoxin-5. *Nat .Chem. Biol.* 15, 1232–1240. doi: 10.1038/s41589-019-0399-y

Chamberlain, L. H., and Shipston, M. J. (2015). The physiology of protein S-acylation. *Physiol. Rev.* 95, 341–376. doi: 10.1152/physrev.00032.2014

Chaube, R., Hess, D. T., Wang, Y. J., Plummer, B., Sun, Q. A., Laurita, K., et al. (2014). Regulation of the skeletal muscle ryanodine receptor/Ca2+-release channel RyR1 by S-palmitoylation. *J. Biol. Chem.* 289, 8612–8619. doi: 10.1074/jbc.M114.548925

Chen, B., Guo, A., Zhang, C., Chen, R., Zhu, Y., Hong, J., et al. (2013). Critical roles of junctophilin-2 in T-tubule and excitation-contraction coupling maturation during postnatal development. *Cardiovasc. Res.* 100, 54–62. doi: 10.1093/cvr/cvt180

Chen, J. J., Marsden, A. N., Scott, C. A., Akimzhanov, A. M., and Boehning, D. (2019).). DHHC5 mediates beta-adrenergic signaling in cardiomyocytes by targeting galpha proteins. *Biophys J.*. S0006-3495, 30715–30715. doi: 10.1016/j.bpj.2019.08.018

Chen, S., Han, C., Miao, X., Li, X., Yin, C., Zou, J., et al. (2019). Targeting MC1R depalmitoylation to prevent melanomagenesis in redheads. *Nat. Commun.* 10:877. doi: 10.1038/s41467-019-08691-3

Chen, S., and Li, S. (2012). The Na+/Ca(2)+ exchanger in cardiac ischemia/reperfusion injury. *Med. Sci. Monit.* 18, RA161–RA165.

Chen, S., Zhu, B., Yin, C., Liu, W., Han, C., Chen, B., et al. (2017). Palmitoylation-dependent activation of MC1R prevents melanomagenesis. *Nature* 549, 399–403. doi: 10.1038/nature23887

Chien, A. J., Carr, K. M., Shirokov, R. E., Rios, E., and Hosey, M. M. (1996). Identification of palmitoylation sites within the L-type calcium channel beta2a subunit and effects on channel function. *J. Biol. Chem.* 271, 26465–26468. doi: 10.1074/jbc.271.43.26465

Chien, A. J., Gao, T., Perez-Reyes, E., and Hosey, M. M. (1998). Membrane targeting of L-type calcium channels. Role of palmitoylation in the subcellular localization of the beta2a subunit. *J. Biol. Chem.* 273, 23590–23597. doi: 10.1074/jbc.273.36.23590

Cho, E., and Park, M. (2016). Palmitoylation in Alzheimer's disease and other neurodegenerative diseases. *Pharmacol. Res.* 111, 133–151. doi: 10.1016/j.phrs.2016.06.008

Coleman, D. T., Gray, A. L., Kridel, S. J., and Cardelli, J. A. (2016). Palmitoylation regulates the intracellular trafficking and stability of c-Met. *Oncotarget* 7, 32664–32677. doi: 10.18632/oncotarget.8706

D'Angelo, D. D., Sakata, Y., Lorenz, J. N., Boivin, G. P., Walsh, R. A., Liggett, S. B., et al. (1997). Transgenic Galphaq overexpression induces cardiac contractile failure in mice. *Proc. Natl. Acad .Sci. U.S.A.* 94, 8121–8126. doi: 10.1073/pnas.94.15.8121

Dallavilla, T., Abrami, L., Sandoz, P. A., Savoglidis, G., Hatzimanikatis, V., and Van Der Goot, F. G. (2016). Model-driven understanding of palmitoylation dynamics: regulated acylation of the endoplasmic reticulum chaperone calnexin. *PLoS Comput. Biol.* 12:e1004774. doi: 10.1371/journal.pcbi.1004774

Davda, D., and Martin, B. R. (2014). Acyl protein thioesterase inhibitors as probes of dynamic S-palmitoylation. *Medchemcomm* 5, 268–276. doi: 10.1039/c3md00333g

Detta, N., Frisso, G., and Salvatore, F. (2015). The multi-faceted aspects of the complex cardiac Nav1.5 protein in membrane function and pathophysiology. *Biochim. Biophys. Acta* 1854, 1502–1509. doi: 10.1016/j.bbapap.2015.07.009

Duncan, P. J., Bi, D., Mcclafferty, H., Chen, L., Tian, L., and Shipston, M. J. (2019). S-Acylation controls functional coupling of BK channel pore-forming alpha-subunits and beta1-subunits. *J. Biol. Chem.* 294, 12066–12076. doi: 10.1074/jbc.RA119.009065

Edokobi, N., and Isom, L. L. (2018). Voltage-GATED SODIUM CHANNEL beta1/beta1B subunits regulate cardiac physiology and pathophysiology. *Front. Physiol.* 9:351. doi: 10.3389/fphys.2018.00351

Fearnley, C. J., Roderick, H. L., and Bootman, M. D. (2011). Calcium signaling in cardiac myocytes. *Cold Spring Harb. Perspect. Biol.* 3:a004242. doi: 10.1101/cshperspect.a004242

Feldman, A. M., and Bristow, M. R. (1990). The beta-adrenergic pathway in the failing human heart: implications for inotropic therapy. *Cardiology* 77(Suppl. 1), 1–32. doi: 10.1159/000174645

Forrester, M. T., Hess, D. T., Thompson, J. W., Hultman, R., Moseley, M. A., Stamler, J. S., et al. (2011). Site-specific analysis of protein S-acylation by resin-assisted capture. *J. Lipid Res.* 52, 393–398. doi: 10.1194/jlr.D011106

Fukata, M., Fukata, Y., Adesnik, H., Nicoll, R. A., and Bredt, D. S. (2004). Identification of PSD-95 palmitoylating enzymes. *Neuron* 44, 987–996. doi: 10.1016/j.neuron.2004.12.005

Fukata, Y., and Fukata, M. (2010). Protein palmitoylation in neuronal development and synaptic plasticity. *Nat. Rev. Neurosci.* 11, 161–175. doi: 10.1038/nrn2788

Fuller, W., Reilly, L., and Hilgemann, D. W. (2016). S-palmitoylation and the regulation of NCX1. *Channels* 10, 75–77. doi: 10.1080/19336950.2015.1099329

Fuller, W., Tulloch, L. B., Shattock, M. J., Calaghan, S. C., Howie, J., and Wypijewski, K. J. (2013). Regulation of the cardiac sodium pump. *Cell Mol. Life Sci.* 70, 1357–1380. doi: 10.1007/s00018-012-1134-y

Gottlieb, C. D., and Linder, M. E. (2017). Structure and function of DHHC protein S-acyltransferases. *Biochem Soc. Trans.* 45, 923–928. doi: 10.1042/BST20160304

Greaves, J., and Chamberlain, L. H. (2011). DHHC palmitoyl transferases: substrate interactions and (patho)physiology. *Trends Biochem. Sci.* 36, 245–253. doi: 10.1016/j.tibs.2011.01.003

Greaves, J., Munro, K. R., Davidson, S. C., Riviere, M., Wojno, J., Smith, T. K., et al. (2017). Molecular basis of fatty acid selectivity in the zDHHC family of S-acyltransferases revealed by click chemistry. *Proc. Natl. Acad. Sci. U.S.A.* 114, E1365–E1374. doi: 10.1073/pnas.1612254114

Grubb, S., Calloe, K., and Thomsen, M. B. (2012). Impact of KChIP2 on cardiac electrophysiology and the progression of heart failure. *Front. Physiol.* 3:118. doi: 10.3389/fphys.2012.00118

Guo, A., Zhang, X., Iyer, V. R., Chen, B., Zhang, C., Kutschke, W. J., et al. (2014). Overexpression of junctophilin-2 does not enhance baseline function but attenuates heart failure development after cardiac stress. *Proc. Natl. Acad. Sci. U.S.A.* 111, 12240–12245. doi: 10.1073/pnas.1412729111

Haag, S. M., Gulen, M. F., Reymond, L., Gibelin, A., Abrami, L., Decout, A., et al. (2018). Targeting STING with covalent small-molecule inhibitors. *Nature* 559, 269–273. doi: 10.1038/s41586-018-0287-8

Han, J. Y., Lee, I. G., Shin, S., Kim, M., Jang, J. H., and Park, J. (2017). The first patient with sporadic X-linked intellectual disability with de novo ZDHHC9 mutation identified by targeted next-generation sequencing. *Eur. J. Med. Genet.* 60, 499–503. doi: 10.1016/j.ejmg.2017.07.002

Hansen, A. L., Buchan, G. J., Ruhl, M., Mukai, K., Salvatore, S. R., Ogawa, E., et al. (2018). Nitro-fatty acids are formed in response to virus infection and are potent inhibitors of STING palmitoylation and signaling. *Proc. Natl. Acad. Sci. U.S.A.* 115, E7768–E7775. doi: 10.1073/pnas.1806239115

Hansen, A. L., Mukai, K., Schopfer, F. J., Taguchi, T., and Holm, C. K. (2019). STING palmitoylation as a therapeutic target. *Cell Mol. Immunol.* 16, 236–241. doi: 10.1038/s41423-019-0205-5

He, M., Abdi, K. M., and Bennett, V. (2014). Ankyrin-G palmitoylation and betaII-spectrin binding to phosphoinositide lipids drive lateral membrane assembly. *J. Cell Biol.* 206, 273–288. doi: 10.1083/jcb.201401016

He, M., Jenkins, P., and Bennett, V. (2012). Cysteine 70 of ankyrin-G is S-palmitoylated and is required for function of ankyrin-G in membrane domain assembly. *J. Biol Chem.* 287, 43995–44005. doi: 10.1074/jbc.M112.417501

Hirano, T., Kishi, M., Sugimoto, H., Taguchi, R., Obinata, H., Ohshima, N., et al. (2009). Thioesterase activity and subcellular localization of acylprotein thioesterase 1/lysophospholipase 1. *Biochim. Biophys. Acta Mol. Cell Biol. Lipids* 1791, 797–805. doi: 10.1016/j.bbalip.2009.05.001

Ho, G. P., Selvakumar, B., Mukai, J., Hester, L. D., Wang, Y., Gogos, J. A., et al. (2011). S-nitrosylation and S-palmitoylation reciprocally regulate synaptic targeting of PSD-95. *Neuron* 71, 131–141. doi: 10.1016/j.neuron.2011.05.033

Howie, J., Reilly, L., Fraser, N. J., Walker, J. M. V., Wypijewski, K. J., Ashford, M. L. J., et al. (2014). Substrate recognition by the cell surface palmitoyl transferase DHHC5. *Pro. Natl. Acad. Sci. U. S. A.* 111, 17534–17539. doi: 10.1073/pnas.1413627111

Howie, J., Tulloch, L. B., Shattock, M. J., and Fuller, W. (2013). Regulation of the cardiac Na(+) pump by palmitoylation of its catalytic and regulatory subunits. *Biochem. Soc. Trans.* 41, 95–100. doi: 10.1042/BST20120269

Jennings, B. C., and Linder, M. E. (2012). DHHC protein S-acyltransferases use similar ping-pong kinetic mechanisms but display different acyl-CoA specificities. *J. Biol. Chem.* 287, 7236–7245. doi: 10.1074/jbc.M111.337246

Jiang, H., Zhang, X., Chen, X., Aramsangtienchai, P., Tong, Z., and Lin, H. (2018). Protein Lipidation: occurrence. *Mech.Biol. Func.Enab. Technol.Chem. Rev.* 118, 919–988. doi: 10.1021/acs.chemrev.6b00750

Jiang, M., Hu, J., White, F. K. H., Williamson, J., Klymchenko, A. S., Murthy, A., et al. (2019). S-Palmitoylation of junctophilin-2 is critical for its role in tethering the sarcoplasmic reticulum to the plasma membrane. *J. Biol. Chem.* 294, 13487–13501. doi: 10.1074/jbc.RA118.006772

Jones, E. G., Mazaheri, N., Maroofian, R., Zamani, M., Seifi, T., Sedaghat, A., et al. (2019). Analysis of enriched rare variants in JPH2-encoded junctophilin-2 among Greater Middle Eastern individuals reveals a novel homozygous variant associated with neonatal dilated cardiomyopathy. *Sci. Rep.* 9, 9038. doi: 10.1038/s41598-019-44987-6

Kang, R., Wan, J., Arstikaitis, P., Takahashi, H., Huang, K., Bailey, A. O., et al. (2008). Neural palmitoyl-proteomics reveals dynamic synaptic palmitoylation. *Nature* 456, 904–909. doi: 10.1038/nature07605

Kapplinger, J. D., Tester, D. J., Salisbury, B. A., Carr, J. L., Harris-Kerr, C., Pollevick, G. D., et al. (2009). Spectrum and prevalence of mutations from the first 2,500 consecutive unrelated patients referred for the FAMILION long QT syndrome genetic test. *Heart Rhythm.* 6, 1297–1303. doi: 10.1016/j.hrthm.2009.05.021

Kharbanda, A., Runkle, K., Wang, W., and Witze, E. S. (2017). Induced sensitivity to EGFR inhibitors is mediated by palmitoylated cysteine 1025 of EGFR and requires oncogenic Kras. *Biochem. Biophys. Res. Commun.* 493, 213–219. doi: 10.1016/j.bbrc.2017.09.044

Korycka, J., Lach, A., Heger, E., Boguslawska, D. M., Wolny, M., Toporkiewicz, M., et al. (2012). Human DHHC proteins: a spotlight on the hidden player of palmitoylation. *Eur. J. Cell Biol.* 91, 107–117. doi: 10.1016/j.ejcb.2011.09.013

Kouskou, M., Thomson, D. M., Brett, R. R., Wheeler, L., Tate, R. J., Pratt, J. A., et al. (2018). Disruption of the Zdhhc9 intellectual disability gene leads to behavioural abnormalities in a mouse model. *Exp. Neurol.* 308, 35–46. doi: 10.1016/j.expneurol.2018.06.014

Kuo, H. C., Cheng, C. F., Clark, R. B., Lin, J. J., Lin, J. L., Hoshijima, M., et al. (2001). A defect in the Kv channel-interacting protein 2 (KChIP2) gene leads to a complete loss of I(to) and confers susceptibility to ventricular tachycardia. *Cell* 107, 801–813. doi: 10.1016/s0092-8674(01)00588-8

Lakkaraju, A. K., Abrami, L., Lemmin, T., Blaskovic, S., Kunz, B., Kihara, A., et al. (2012). Palmitoylated calnexin is a key component of the ribosome-translocon complex. *EMBO J.* 31, 1823–1835. doi: 10.1038/emboj.2012.15

Lemonidis, K., Gorleku, O. A., Sanchez-Perez, M. C., Grefen, C., and Chamberlain, L. H. (2014). The Golgi S-acylation machinery comprises zDHHC enzymes with major differences in substrate affinity and S-acylation activity. *Mol. Biol. Cell* 25, 3870–3883. doi: 10.1091/mbc.E14-06-1169

Li, B., Cong, F., Tan, C. P., Wang, S. X., and Goff, S. P. (2002). Aph2, a protein with a zf-DHHC motif, interacts with c-Abl and has pro-apoptotic activity. *J. Biol. Chem.* 277, 28870–28876. doi: 10.1074/jbc.m202388200

Lin, D. T., and Conibear, E. (2015a). ABHD17 proteins are novel protein depalmitoylases that regulate N-Ras palmitate turnover and subcellular localization. *Elife* 4:e11306. doi: 10.7554/eLife.11306

Lin, D. T., and Conibear, E. (2015b). Enzymatic protein depalmitoylation by acyl protein thioesterases. *Biochem. Soc. Trans.* 43, 193–198. doi: 10.1042/bst20140235

Lin, M. J., Fine, M., Lu, J. Y., Hofmann, S. L., Frazier, G., and Hilgemann, D. W. (2013). Massive palmitoylation-dependent endocytosis during reoxygenation of anoxic cardiac muscle. *Elife* 2:e01295. doi: 10.7554/eLife.01295

Linder, M. E., and Deschenes, R. J. (2007). Palmitoylation: policing protein stability and traffic. *Nat. Rev. Mol. Cell Biol.* 8, 74–84. doi: 10.1038/nrm2084

Linder, M. E., Middleton, P., Hepler, J. R., Taussig, R., Gilman, A. G., and Mumby, S. M. (1993). Lipid modifications of G proteins: alpha subunits are palmitoylated. *Proc. Natl. Acad. Sci. U.S.A.* 90, 3675–3679. doi: 10.1073/pnas.90.8.3675

Liu, P., Jiao, B., Zhang, R., Zhao, H., Zhang, C., Wu, M., et al. (2016). Palmitoylacyltransferase Zdhhc9 inactivation mitigates leukemogenic potential of oncogenic Nras. *Leukemia* 30, 1225–1228. doi: 10.1038/leu.2015.293

Liu, R., Wang, D., Shi, Q., Fu, Q., Hizon, S., and Xiang, Y. K. (2012). Palmitoylation regulates intracellular trafficking of beta2 adrenergic receptor/arrestin/phosphodiesterase 4D complexes in cardiomyocytes. *PLoS One* 7:e42658. doi: 10.1371/journal.pone.0042658

Ljubojevic, S., and Bers, D. M. (2015). Nuclear calcium in cardiac myocytes. *J. Cardiovasc. Pharmacol.* 65, 211–217. doi: 10.1097/FJC.0000000000000174

Lytton, J. (2007). Na+/Ca2+ exchangers: three mammalian gene families control Ca2+ transport. *Biochem. J.* 406, 365–382. doi: 10.1042/bj20070619

MacLennan, D. H., and Kranias, E. G. (2003). Phospholamban: a crucial regulator of cardiac contractility. *Nat. Rev. Mol. Cell Biol.* 4, 566–577. doi: 10.1038/nrm1151

Makara, M. A., Curran, J., Little, S. C., Musa, H., Polina, I., Smith, S. A., et al. (2014). Ankyrin-G coordinates intercalated disc signaling platform to regulate cardiac excitability in vivo. *Circ. Res.* 115, 929–938. doi: 10.1161/CIRCRESAHA.115.305154

Makara, M. A., Curran, J., Lubbers, E. R., Murphy, N. P., Little, S. C., Musa, H., et al. (2018). Novel Mechanistic Roles for Ankyrin-G in Cardiac Remodeling and Heart Failure. *JACC Basic Transl. Sci.* 3, 675–689. doi: 10.1016/j.jacbts.2018.07.008

Martin, B. R., and Cravatt, B. F. (2009). Large-scale profiling of protein palmitoylation in mammalian cells. *Nat. Methods* 6, 135–138. doi: 10.1038/nmeth.1293

Martin, B. R., Wang, C., Adibekian, A., Tully, S. E., and Cravatt, B. F. (2012). Global profiling of dynamic protein palmitoylation. *Nat. Methods* 9, 84–89. doi: 10.1038/nmeth.1769

Matt, L., Kim, K., Chowdhury, D., and Hell, J. W. (2019). Role of Palmitoylation of Postsynaptic Proteins in Promoting Synaptic Plasticity. *Front. Mol. Neurosci.* 12:8. doi: 10.3389/fnmol.2019.00008

Modica, G., Skorobogata, O., Sauvageau, E., Vissa, A., Yip, C. M., Kim, P. K., et al. (2017). Rab7 palmitoylation is required for efficient endosome-to-TGN trafficking. *J. Cell Sci.* 130, 2579–2590. doi: 10.1242/jcs.199729

Mohler, P. J., Schott, J. J., Gramolini, A. O., Dilly, K. W., Guatimosim, S., Dubell, W. H., et al. (2003). Ankyrin-B mutation causes type 4 long-QT cardiac arrhythmia and sudden cardiac death. *Nature* 421, 634–639. doi: 10.1038/nature01335

Mohler, P. J., Splawski, I., Napolitano, C., Bottelli, G., Sharpe, L., Timothy, K., et al. (2004). A cardiac arrhythmia syndrome caused by loss of ankyrin-B function. *Proc. Natl. Acad. Sci. U.S.A.* 101, 9137–9142. doi: 10.1073/pnas.0402546101

Molinaro, P., Pannaccione, A., Sisalli, M. J., Secondo, A., Cuomo, O., Sirabella, R., et al. (2015). A new cell-penetrating peptide that blocks the autoinhibitory XIP domain of NCX1 and enhances antiporter activity. *Mol. Ther.* 23, 465–476. doi: 10.1038/mt.2014.231

Mukai, J., Liu, H., Burt, R. A., Swor, D. E., Lai, W. S., Karayiorgou, M., et al. (2004). Evidence that the gene encoding ZDHHC8 contributes to the risk of schizophrenia. *Nat. Genet.* 36, 725–731. doi: 10.1038/ng1375

Mukai, K., Konno, H., Akiba, T., Uemura, T., Waguri, S., Kobayashi, T., et al. (2016). Activation of STING requires palmitoylation at the Golgi. *Nat. Commun.* 7:11932. doi: 10.1038/ncomms11932

Murthy, A., Workman, S. W., Jiang, M., Hu, J., Sifa, I., Bernas, T., et al. (2019). Dynamic palmitoylation regulates trafficking of K channel interacting protein 2 (KChIP2) across multiple subcellular compartments in cardiac myocytes. *J. Mol. Cell Cardiol.* 135, 1–9. doi: 10.1016/j.yjmcc.2019.07.013

Navarro-Lerida, I., Sanchez-Perales, S., Calvo, M., Rentero, C., Zheng, Y., Enrich, C., et al. (2012). A palmitoylation switch mechanism regulates Rac1 function and membrane organization. *EMBO J.* 31, 534–551. doi: 10.1038/emboj.2011.446

Ohno, Y., Kihara, A., Sano, T., and Igarashi, Y. (2006). Intracellular localization and tissue-specific distribution of human and yeast DHHC cysteine-rich domain-containing proteins. *Biochim. Biophys. Acta* 1761, 474–483. doi: 10.1016/j.bbalip.2006.03.010

Oldham, W. M., and Hamm, H. E. (2008). Heterotrimeric G protein activation by G-protein-coupled receptors. *Nat. Rev. Mol. Cell Biol.* 9, 60–71. doi: 10.1038/nrm2299

Ottolia, M., Torres, N., Bridge, J. H., Philipson, K. D., and Goldhaber, J. I. (2013). Na/Ca exchange and contraction of the heart. *J. Mol. Cell Cardiol.* 61, 28–33. doi: 10.1016/j.yjmcc.2013.06.001

Paradis, P., Dali-Youcef, N., Paradis, F. W., Thibault, G., and Nemer, M. (2000). Overexpression of angiotensin II type I receptor in cardiomyocytes induces cardiac hypertrophy and remodeling. *Proc. Natl. Acad. Sci. U.S.A.* 97, 931–936. doi: 10.1073/pnas.97.2.931

Pavlovic, D., Fuller, W., and Shattock, M. J. (2013). Novel regulation of cardiac Na pump via phospholemman. *J. Mol. Cell Cardiol.* 61, 83–93. doi: 10.1016/j.yjmcc.2013.05.002

Pei, Z., Xiao, Y., Meng, J., Hudmon, A., and Cummins, T. R. (2016). Cardiac sodium channel palmitoylation regulates channel availability and myocyte excitability with implications for arrhythmia generation. *Nat. Commun.* 7:12035. doi: 10.1038/ncomms12035

Piquereau, J., Caffin, F., Novotova, M., Lemaire, C., Veksler, V., Garnier, A., et al. (2013). Mitochondrial dynamics in the adult cardiomyocytes: which roles for a highly specialized cell? *Front. Physiol.* 4:102. doi: 10.3389/fphys.2013.00102

Plain, F., Congreve, S. D., Yee, R. S. Z., Kennedy, J., Howie, J., Kuo, C. W., et al. (2017). An amphipathic alpha-helix directs palmitoylation of the large intracellular loop of the sodium/calcium exchanger. *J. Biol. Chem.* 292, 10745–10752. doi: 10.1074/jbc.M116.773945

Rana, M. S., Kumar, P., Lee, C. J., Verardi, R., Rajashankar, K. R., and Banerjee, A. (2018). Fatty acyl recognition and transfer by an integral membrane S-acyltransferase. *Science* 359:eaao6326. doi: 10.1126/science.aao6326

Raymond, F. L., Tarpey, P. S., Edkins, S., Tofts, C., O'meara, S., Teague, J., et al. (2007). Mutations in ZDHHC9, which encodes a palmitoyltransferase of NRAS and HRAS, cause X-linked mental retardation associated with a Marfanoid habitus. *Am. J. Hum. Genet.* 80, 982–987. doi: 10.1086/513609

Reilly, L., Howie, J., Wypijewski, K., Ashford, M. L., Hilgemann, D. W., and Fuller, W. (2015). Palmitoylation of the Na/Ca exchanger cytoplasmic loop controls its inactivation and internalization during stress signaling. *FASEB J.* 29, 4532–4543. doi: 10.1096/fj.15-276493

Reiss, K., Cheng, W., Ferber, A., Kajstura, J., Li, P., Li, B., et al. (1996). Overexpression of insulin-like growth factor-1 in the heart is coupled with myocyte proliferation in transgenic mice. *Proc. Natl. Acad. Sci. U.S.A.* 93, 8630–8635. doi: 10.1073/pnas.93.16.8630

Roberts, J. D., Murphy, N. P., Hamilton, R. M., Lubbers, E. R., James, C. A., Kline, C. F., et al. (2019). Ankyrin-B dysfunction predisposes to arrhythmogenic cardiomyopathy and is amenable to therapy. *J. Clin. Invest* 129, 3171–3184. doi: 10.1172/JCI125538

Rocks, O., Peyker, A., Kahms, M., Verveer, P. J., Koerner, C., Lumbierres, M., et al. (2005). An acylation cycle regulates localization and activity of palmitoylated Ras isoforms. *Science* 307, 1746–1752. doi: 10.1126/science.1105654

Runkle, K. B., Kharbanda, A., Stypulkowski, E., Cao, X. J., Wang, W., Garcia, B. A., et al. (2016). Inhibition of DHHC20-Mediated EGFR palmitoylation creates a dependence on EGFR signaling. *Mol. Cell* 62, 385–396. doi: 10.1016/j.molcel.2016.04.003

Sanders, S. S., Parsons, M. P., Mui, K. K., Southwell, A. L., Franciosi, S., Cheung, D., et al. (2016). Sudden death due to paralysis and synaptic and behavioral deficits when Hip14/Zdhhc17 is deleted in adult mice. *BMC Biol.* 14:108. doi: 10.1186/s12915-016-0333-7

Shah, B. S., Shimell, J. J., and Bamji, S. X. (2019). Regulation of dendrite morphology and excitatory synapse formation by zDHHC15. *J. Cell Sci.* 132:jcs230052. doi: 10.1242/jcs.230052

Shenoy-Scaria, A. M., Dietzen, D. J., Kwong, J., Link, D. C., and Lublin, D. M. (1994). Cysteine3 of Src family protein tyrosine kinase determines palmitoylation and localization in caveolae. *J. Cell Biol.* 126, 353–363. doi: 10.1083/jcb.126.2.353

Shibata, R., Misonou, H., Campomanes, C. R., Anderson, A. E., Schrader, L. A., Doliveira, L. C., et al. (2003). A fundamental role for KChIPs in determining the molecular properties and trafficking of Kv4.2 potassium channels. *J. Biol. Chem.* 278, 36445–36454. doi: 10.1074/jbc.m306142200

Shipston, M. J. (2014). Ion channel regulation by protein S-acylation. *J. Gen. Physiol.* 143, 659–678. doi: 10.1085/jgp.201411176

Takeshima, H., Hoshijima, M., and Song, L. S. (2015). Ca(2)(+) microdomains organized by junctophilins. *Cell Calcium.* 58, 349–356. doi: 10.1016/j.ceca.2015.01.007

Takimoto, K., Yang, E. K., and Conforti, L. (2002). Palmitoylation of KChIP splicing variants is required for efficient cell surface expression of Kv4.3 channels. *J. Biol. Chem.* 277, 26904–26911. doi: 10.1074/jbc.m203651200

Tomatis, V. M., Trenchi, A., Gomez, G. A., and Daniotti, J. L. (2010). Acyl-Protein thioesterase 2 catalizes the deacylation of peripheral membrane-associated GAP-43. *Plos One* 5:e15045. doi: 10.1371/journal.pone.0015045

Tsutsumi, R., Fukata, Y., and Fukata, M. (2008). Discovery of protein-palmitoylating enzymes. *Pflugers Arch.* 456, 1199–1206. doi: 10.1007/s00424-008-0465-x

Tsutsumi, R., Fukata, Y., Noritake, J., Iwanaga, T., Perez, F., and Fukata, M. (2009). Identification of G protein alpha subunit-palmitoylating enzyme. *Mol. Cell Biol.* 29, 435–447. doi: 10.1128/MCB.01144-08

Tulloch, L. B., Howie, J., Wypijewski, K. J., Wilson, C. R., Bernard, W. G., Shattock, M. J., et al. (2011). The inhibitory effect of phospholemman on the sodium pump requires its palmitoylation. *J. Biol. Chem.* 286, 36020–36031. doi: 10.1074/jbc.M111.282145

Van Oort, R. J., Garbino, A., Wang, W., Dixit, S. S., Landstrom, A. P., Gaur, N., et al. (2011). Disrupted junctional membrane complexes and hyperactive ryanodine receptors after acute junctophilin knockdown in mice. *Circulation* 123, 979–988. doi: 10.1161/CIRCULATIONAHA.110.006437

Vanninen, S. U. M., Leivo, K., Seppala, E. H., Aalto-Setala, K., Pitkanen, O., Suursalmi, P., et al. (2018). Heterozygous junctophilin-2 (JPH2) p.(Thr161Lys) is a monogenic cause for HCM with heart failure. *PLoS One* 13:e0203422. doi: 10.1371/journal.pone.0203422

Voigt, N., Li, N., Wang, Q., Wang, W., Trafford, A. W., Abu-Taha, I., et al. (2012). Enhanced sarcoplasmic reticulum Ca2+ leak and increased Na+-Ca2+ exchanger function underlie delayed afterdepolarizations in patients with chronic atrial fibrillation. *Circulation* 125, 2059–2070. doi: 10.1161/CIRCULATIONAHA.111.067306

Won, S. J., and Martin, B. R. (2018). Temporal profiling establishes a dynamic s-palmitoylation cycle. *ACS Chem. Biol.* 13, 1560–1568. doi: 10.1021/acschembio.8b00157

Woon, M. T., Long, P. A., Reilly, L., Evans, J. M., Keefe, A. M., Lea, M. R., et al. (2018).). Pediatric dilated cardiomyopathy-associated LRRC10 (Leucine-Rich Repeat-Containing 10) variant reveals lrrc10 as an auxiliary subunit of cardiac L-Type Ca(2+) channels. *J. Am. Heart Assoc.* 7:e006428. doi: 10.1161/JAHA.117.006428

Yokoi, N., Fukata, Y., Sekiya, A., Murakami, T., Kobayashi, K., and Fukata, M. (2016). Identification of PSD-95 depalmitoylating enzymes. *J. Neurosci.* 36, 6431–6444. doi: 10.1523/JNEUROSCI.0419-16.2016

Zaballa, M. E., and Van Der Goot, F. G. (2018). The molecular era of protein S-acylation: spotlight on structure, mechanisms, and dynamics. *Crit. Rev. Biochem. Mol. Biol.* 53, 420–451. doi: 10.1080/10409238.2018.1488804

Zhang, C., Chen, B., Guo, A., Zhu, Y., Miller, J. D., Gao, S., et al. (2014). Microtubule-mediated defects in junctophilin-2 trafficking contribute to myocyte transverse-tubule remodeling and Ca2+ handling dysfunction in heart failure. *Circulation* 129, 1742–1750. doi: 10.1161/CIRCULATIONAHA.113.008452

Zhang, P., and Mende, U. (2011). Regulators of G-protein signaling in the heart and their potential as therapeutic targets. *Circ. Res.* 109, 320–333. doi: 10.1161/CIRCRESAHA.110.231423

Zhao, H., Yu, Y., Wu, X., Liu, S., Liu, B., Du, J., et al. (2017). A Role of BK channel in regulation of Ca(2+) channel in ventricular myocytes by substrate stiffness. *Biophys. J.* 112, 1406–1416. doi: 10.1016/j.bpj.2017.01.036

Zhou, P., and Pu, W. T. (2016). Recounting cardiac cellular composition. *Circ. Res.* 118, 368–370. doi: 10.1161/circresaha.116.308139

Zhou, Q., Li, J., Yu, H., Zhai, Y., Gao, Z., Liu, Y., et al. (2014). Molecular insights into the membrane-associated phosphatidylinositol 4-kinase IIalpha. *Nat. Commun.* 5, 3552. doi: 10.1038/ncomms4552

Zhou, T., Li, J., Zhao, P., Liu, H., Jia, D., Jia, H., et al. (2015). Palmitoyl acyltransferase Aph2 in cardiac function and the development of cardiomyopathy. *Proc. Natl. Acad. Sci. U.S.A.* 112, 15666–15671. doi: 10.1073/pnas.1518368112

Conflict of Interest: The authors declare that the research was conducted in the absence of any commercial or financial relationships that could be construed as a potential conflict of interest.

frontiers in Physiology

CONCEPTUAL ANALYSIS
published: 28 February 2020
doi: 10.3389/fphys.2020.00164

Cardiomyocyte Calcium Ion Oscillations—Lessons From Physics

*Ohad Cohen and Samuel A. Safran**

Department of Chemical and Biological Physics, Weizmann Institute of Science, Rehovot, Israel

We review a theoretical, coarse-grained description for cardiomyocytes calcium dynamics that is motivated by experiments on RyR channel dynamics and provides an analogy to other spontaneously oscillating systems. We show how a minimal model, that focuses on calcium channel and pump dynamics and kinetics, results in a single, easily understood equation for spontaneous calcium oscillations (the Van-der-Pol equation). We analyze experiments on isolated RyR channels to quantify how the channel dynamics depends both on the local calcium concentration, as well as its temporal behavior ("adaptation"). Our oscillator model analytically predicts the conditions for spontaneous oscillations, their frequency and amplitude, and how each of those scale with the small number of relevant parameters related to calcium channel and pump activity. The minimal model is easily extended to include the effects of noise and external pacing (electrical or mechanical). We show how our simple oscillator predicts and explains the experimental observations of synchronization, "bursting" and reduction of apparent noise in the beating dynamics of paced cells. Thus, our analogy and theoretical approach provides robust predictions for the beating dynamics, and their biochemical and mechanical modulation.

Keywords: cardiomyocyte, calcium, biological physics, oscillations, coarse-grained theory

OPEN ACCESS

Edited by:
Shin'Ichi Ishiwata,
Waseda University, Japan

Reviewed by:
Robin Lewis Cooper,
University of Kentucky, United States
D. George Stephenson,
La Trobe University, Australia

****Correspondence:***
Samuel A. Safran
sam.safran@weizmann.ac.il

Specialty section:
This article was submitted to Striated Muscle Physiology, a section of the journal Frontiers in Physiology

Received: *20 December 2019*
Accepted: *12 February 2020*
Published: *28 February 2020*

Citation:
Cohen O and Safran SA (2020) Cardiomyocyte Calcium Ion Oscillations—Lessons From Physics. Front. Physiol. 11:164. doi: 10.3389/fphys.2020.00164

1. INTRODUCTION

The heart is an extraordinary organ. From several weeks after conception, and throughout its entire life, the heart constantly beats, generating considerable stresses and strains on its tissues and cells (Hill and Olson, 2012). The individual muscle cells (called cardiomyocytes) that comprise the heart generate contractile forces (Engler et al., 2008; Hersch et al., 2013; Dasbiswas et al., 2015; Nitsan et al., 2016) that translate to relatively large periodic deformations of the heart, i.e., beating. Contraction of adult cardiac cells in tissue is highly regulated by pacemaker cells (Huxley, 1974; Hill and Olson, 2012), which produce electrical impulses that are transmitted to cardiomyocytes, signaling them to contract (Hill and Olson, 2012). The pacemaker cells, unlike adult cardiomyocyte cells, show spontaneous contraction-relaxation cycles even in the absence of an external electrical signal (Vinogradova et al., 2004, 2006; Maltsev and Lakatta, 2007). These cells beat at a relatively fixed frequency, between 0.5 and 3 Hz depending on the species (Kehat et al., 2001; Yang et al., 2002; Majkut et al., 2013). We note that embryonic and neonatal cardiomyocytes also show spontaneous beating, even when cultured as isolated cells (Engler et al., 2006; Tang et al., 2011; Nitsan et al., 2016).

Cardiac contraction is driven by a rise in cytoplasmic calcium ion concentration ($[Ca^{2+}]$) that is coupled to the mechanical contractions of the heart cell (Bers, 2001, 2002). In muscle cells, $[Ca^{2+}]$ in the cytoplasm is usually maintained at a relatively low concentration compared with $[Ca^{2+}]$ outside the cell and the $[Ca^{2+}]$ in a membrane-enclosed organelle called the sarcoplasmic

reticulum (SR) (Ibrahim et al., 2011). Oscillations in cytoplasmic $[Ca^{2+}]$ are driven by the exchange of calcium ions between the cytoplasm, the extracellular environment and the SR, which is achieved by numerous types of ionic channels and pumps embedded in the extracellular membrane and the SR (Eisner et al., 2000; Bers, 2002; Reed et al., 2014). Activation of a cardiac muscle cell is usually induced by fluctuations or changes in ion channel and pump activity, which cause an influx of calcium ions into the cytoplasm from either the extracellular environment or the SR (Maltsev and Lakatta, 2007). Calcium RyR channels embedded in the SR membrane (Bers, 2002) usually open and close stochastically (with a probability heavily biased toward the closed conformation), but when the calcium in the vicinity of the SR binds to their cytoplasmic side, it forces a conformational change that increases the opening probability (Bers, 2002; Fill and Copello, 2002). Opened RyR channels release calcium stored in the SR into the cytoplasm in a process known as calcium-induced-calcium-release (CICR) (Bers, 2002). After a certain amount of calcium is released, RyR channels revert to their pre-bound dynamics, and ionic pumps restore the cytoplasmic $[Ca^{2+}]$ to its baseline value (Huxley, 1974; Bers, 2002).

We focus here on the unique role of RyR channels in the cytoplasmic $[Ca^{2+}]$ cycle, since recent studies have shown that calcium ion oscillations in pacemaker cells can occur independently of calcium entry across the surface membrane (Vinogradova et al., 2004, 2006; Maltsev and Lakatta, 2007). An important observation is that RyR channels show a time dependent response to changes in Ca^{2+} concentration (see **Figure 1**) (Valdivia et al., 1995). In these experiments, isolated RyR channels were incorporated in a synthetic membrane, and the Ca^{2+} on the "cytoplasmic" side was dynamically controlled externally with high precision. When $[Ca^{2+}]$ was varied slowly (with a time scale of ∼10 s), the opening probability of the channel followed the instantaneous $[Ca^{2+}]$, in what is referred to in the physics literature as an "adiabatic process" (Risken, 1984) (see **Figure 1A**). However, when Ca^{2+} was rapidly increased and held constant (a "step function" increase), the opening probability showed an "adaptive" response, an initial sharp increase (overshoot) followed by an exponential relaxation to a steady-state value, with a typical time-scale of ∼ 100 ms (Valdivia et al., 1995) (see **Figure 1B**). This response suggests that the channel dynamics depends not only on the instantaneous calcium concentration, but also on the rate at which it changes. The adaptive response (along with calcium pump activity) turns out to be a crucial component in the generation of spontaneous calcium oscillations (Cohen and Safran, 2019).

2. MINIMAL MODEL OF CALCIUM DYNAMICS

Previous models of calcium dynamics (Dupont et al., 1991; Wilders et al., 1991; Atri et al., 1993; Tang and Othmer, 1994; Keizer and Levine, 1996; Jafri et al., 1998; Höfer, 1999; Sneyd et al., 2017) focus on the short time, molecular details of the coupled, multi-component kinetic processes that underlie $[Ca^{2+}]$ oscillations. A key feature of many of those models are slow regulatory processes (Atri et al., 1993; Keizer and Levine, 1996; Jafri et al., 1998; Sneyd et al., 2017). As we show below, these effectively cause a time delay in the response of RyR-calcium channels to changes in cytoplasmic $[Ca^{2+}]$. While these models can numerically reproduce many of the features of calcium oscillations, it is difficult to obtain intuition as to *why* myocytes can spontaneously beat in the first place, and how the onset and frequency of beating scale with the characteristic biophysical rates of the system. In contrast, we have recently shown that a minimal model that accounts only for the adaptive RyR dynamics coupled to calcium pump activity (Cohen and Safran, 2019) predicts, in a simple manner, spontaneous calcium oscillations (see **Figure 2** for schematic representation). As we review below, these dynamics can be mapped onto a single oscillator equation, with coarse-grained parameters that effectively encapsulate the microscopic dynamics.

The model focuses on the two most relevant degrees of freedom, the opening probability of the RyR channel [denoted by $P(t)$, with an average value $\bar{P}$], and the cytoplasmic $[Ca^{2+}]$ concentration [denoted by $C(t)$ with an average value $\bar{C}$]. The average $[Ca^{2+}]$ concentration reflects a kinetic balance of channels that increase cytoplasmic $[Ca^{2+}]$, and active pumps that remove calcium from the cytoplasm (to the SR and or elsewhere). Note that the average $[Ca^{2+}]$ concentration can include contributions from an influx of calcium from outside of the cell (via channel activity, or thermal fluctuations), but these are not necessary to generate spontaneous oscillations [as also shown by experimental studies (Vinogradova et al., 2004, 2006; Maltsev and Lakatta, 2007)]. The dynamics of the RyR channels are written in the most general form as:

$$\dot{P} = R^{+}[C]\,(1-P) - R^{-}[C]\,P \tag{1}$$

where $R^{\pm}[C]$ are opening and closing rate of the channel that depend on $[Ca^{2+}]$ in a general manner. These rates are much faster [∼100 Hz (Jafri et al., 1998; Fill and Gillespie, 2018)] than the typical timescale of $[Ca^{2+}]$ oscillations (∼1 Hz). This allows us to expand Equation (1) around steady-state, and to integrate it over time. The result is an expression for the deviations of P from its average $p = (P - \bar{P})$, as a function of the deviation of $[Ca^{2+}]$ from its average value $c = (C - \bar{C})$:

$$p(t) \approx \alpha \bar{C}\, c(t) + \beta \int_{-\infty}^{t} \dot{c}(t'') e^{-H(t-t'')} dt'' \tag{2}$$

The first term in the right-hand-side of Equation (2) accounts for the response of the RyR channel to changes in $[Ca^{2+}]$ concentration relative to steady-state, with a proportionality constant α that reflects the changes of the rates $R^{\pm}$ with $[Ca^{2+}]$ around steady-state. The second term accounts for the "adaptive" response of the channel to changes in the $[Ca^{2+}]$ concentration, with a magnitude proportional to β that quantifies the overshoot in the channel response to fast changes in the $[Ca^{2+}]$ concentration. Equation (2) encapsulates the "adaptive" response observed in experiments (Valdivia et al., 1995). When $[Ca^{2+}]$ is slowly varied on the cytoplasmic side of the channel ($\dot{c} \ll 1$), the first term dominates, and the opening probability

follows the instantaneous $[Ca^{2+}]$ concentration (an "adiabatic" change—see **Figure 1A**). However, if $[Ca^{2+}]$ is varied quickly ($\dot{c} \gg 1$), the opening probability overshoots by a factor β, and then slowly relaxes to its "adiabatic" value with a typical rate $H \sim 10$ Hz (Valdivia et al., 1995) (see **Figure 1B**). The "adaptive" RyR response to calcium than enters into the kinetic equation for cytoplasmic $[Ca^{2+}]$:

$$\dot{C} = J_p[C]\, P(t) - K\, C(t) \tag{3}$$

The first term on the right-hand-side accounts for the calcium released from the SR into the cytoplasm, where $J_p[C]$ is the calcium current through the open RyR channels which is in general also a function of cytoplasmic $[Ca^{2+}]$ (Bers, 2002). The second term accounts for the various process [SERCA pumps, membrane bound Na^+–Ca^{2+} pumps and mitochondrial Ca^{2+} uniports activity (Bers, 2002)] that work to return $[Ca^{2+}]$ to its steady-state concentration, with K the coarse-grained, effective pump-rate at which calcium is restored. Note that since calcium is pumped to the cellular environment, or back into the SR, K represents an active process that works against the concentration gradient and as such, requires energy in the form of ATP hydrolysis (Eisner et al., 2000; Bers, 2002). Expanding Equation (3) again, around steady-state, inserting Equation (2) for the RyR dynamics and utilizing again the separation of time scales between the adaptive response ($H \sim 10$ Hz) and the timescale of $[Ca^{2+}]$ variation ($\sim$1 Hz), allows us to derive a single equation for the $[Ca^{2+}]$ dynamics (Cohen and Safran, 2019):

$$m^*\ddot{c} + \eta^*\,\dot{c} + \Gamma\, c^2\dot{c} + \kappa c = 0 \tag{4}$$

with the coarse-grained parameters derived from the microscopic dynamics:

$$m^* = \frac{\beta\bar{J}}{H^2}, \quad \eta^* = \left(1 - \frac{\beta\bar{J}}{H}\right), \quad \kappa = K(1-\alpha),$$
$$\Gamma = \gamma m^* H \tag{5}$$

where $\bar{J}$ is the average current through the channel at steady-state ($\bar{C}$) and the non-linear effect characterized by

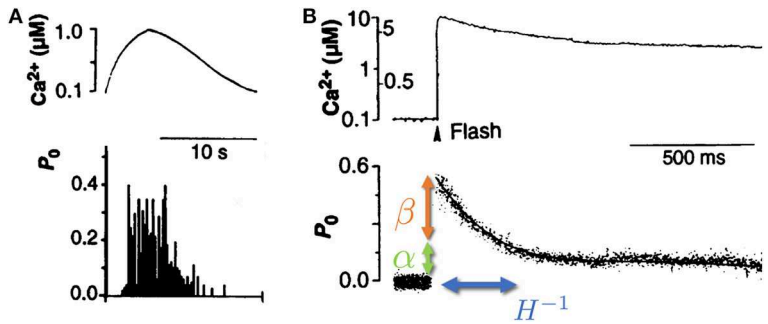

FIGURE 1 | Isolated RyR channel opening probability P_0 as a function of cytoplasmic calcium concentration Ca^{2+}. **(A)** When the cytoplasmic calcium concentration (top) was varied slowly (on a scale of $\sim$10 s), the RyR opening probability (bottom) was shown to follow the instantaneous $[Ca^{2+}]$. **(B)** When the calcium concentration (top) was increased rapidly ($\sim$1 μs) and kept roughly constant afterwards, the RyR opening probability (bottom) displayed a rapid increase (overshoot, denoted by β—orange arrow), followed by a slow relaxation (with typical rate of $\sim$10 Hz, denoted by H—blue arrow) to a new steady-state determined by the long time calcium concentration (denoted by α—green arrow). Adapted from Valdivia et al. (1995). Reprinted with permission from AAAS.

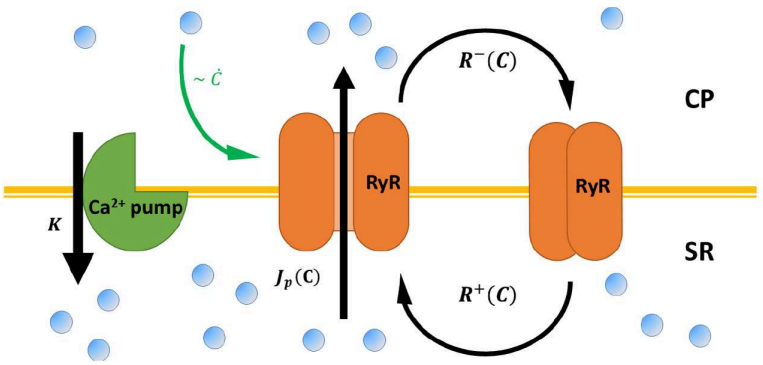

FIGURE 2 | A schematic representation of calcium cycling between the cytoplasm (CP) and the sarcoplasmic reticulum (SR), according to the model presented in Cohen and Safran (2019) and the main text. RyR channels (orange) embedded in the SR membrane stochastically switch between closed (right) and opened (middle) conformation—with rates $R^{\pm}[C]$ that depend on cytoplasmic calcium C. Opened RyR release calcium to the cytoplasm with a current that, in principle, also depends on cytoplasmic calcium $J_p[C]$. Calcium is restored to baseline concentrations via calcium pumps embedded in the SR (green, left), the mitochondria, and the cellular membrane (not shown) with a "lumped" rate K. RyR "adaptive" response to calcium (see Equation 1) is marked by a green arrow.

$\gamma > 0$, enters from the expansion of $J_p[C]$ around steady-state. This represents (Bers, 2002) the tendency of the current to decrease with increasing $[Ca^{2+}]$ concentration (for more details see Cohen and Safran, 2019).

Equation (4) is the famous Van-der Pol equation for a non-linear, spontaneous oscillator (Guckenheimer, 1980), with a characteristic frequency $\Omega_c \approx \sqrt{\kappa/m^*}$. To understand the underlying physics, it is useful to draw an analogy to a classical "spring and mass" system. Consider an object tethered to a wall via a horizontal spring, placed on a frictionless surface, and released from an initial position where the spring is stretched beyond its equilibrium length. The force exerted by the spring causes the object to accelerate toward the equilibrium distance. When it passes that point, the object decelerates till it stops, reverses direction, and continues in the opposite direction, letting the cycle begin again. In short, the object overshoots the equilibrium length of the spring in both the left and right directions.

In a classical system, the first term in Equation (4) would represent inertia—which is the tendency of an object to maintain its velocity. Classical inertia is proportional to the mass of the object, the larger the mass, the larger the overshoot of the equilibrium point. In the chemical system of Equation (4) the "effective mass" m^* arises from the overshoot of the steady-state concentration $\bar{C}$ due to the delayed "adaptive" response of RyR channels to $[Ca^{2+}]$. Our model (Cohen and Safran, 2019) based on Equations (1) and (3) predicts that the overshot is proportional to the observed overshoot of the opening probability, β and the channel current $\bar{J}$. The expression for the effective mass in Equation (5), predicts that m^* decreases as the rate of adaptation H increases. This is because large H means that the $[Ca^{2+}]$ response quickly returns to its "adiabatic" value so that the overshooting has little effect.

The second term in Equation (4), proportional to η^*, represents an effective, linear friction. In the classical system friction is proportional to the velocity of the object, and always oppose the motion of the object. Thus, in the presence of friction, the oscillations of the mass decrease in amplitude as time increases and the object asymptotically comes to rest at the equilibrium length of the spring. Similarly, in the chemical system the "effective friction" is proportional to the rate of change of $[Ca^{2+}]$. However, the "effective friction" can switch from regular dissipation ($\eta^* > 0$) to "negative dissipation" ($\eta^* < 0$). When the "effective friction" is positive ($\eta^* > 0$), any oscillations decay over time and the system effectively goes to its steady state concentration at long times. On the other hand, if the "effective friction" is negative ($\eta^* < 0$), any change in the $[Ca^{2+}]$ concentration is amplified by the friction, which would cause a divergence in the $[Ca^{2+}]$ concentration as time increases. The origin of the "negative friction" (as one can see from Equation 5) is the same feedback effect that gives rise to the "effective mass." The increase is eventually saturated by higher order terms in the friction (third term in Equation 4, $\sim \Gamma$, see Appendix B of Cohen and Safran, 2019 for one possible derivation), which can be a combination of several microscopic effects (reduction of $[Ca^{2+}]$ current with increasing cytoplasmic $[Ca^{2+}]$, inactivation of RyR, variation of the adaptation rate etc.). Thus, given the right conditions ($\beta\bar{J} > H$), the activation of RyR by $[Ca^{2+}]$ is enough to destabilize the system.

Finally, in the classical system, the fourth term of Equation (4) would represent the restoring force applied by the spring which pulls the object toward the equilibrium distance. This restoring force in our calcium system is proportional to the activity of calcium pumps (K), with a correction due to the "adiabatic" response of RyR to $[Ca^{2+}]$ ($\alpha < 1$). It is important to note that, unlike the classical system, the steady-state around which the chemical system oscillates is far from equilibrium (since there is still a large concentration difference between the SR and the cytoplasm). Moreover, the calcium pumps that work to restore cytoplasmic $[Ca^{2+}]$ concentrations work against this concentration gradient, and thus require constant input of energy (in the form of ATP). Therefore, in contrast to the classical "passive" oscillator, the chemical oscillator of Equation (4) is inherently active. In the absence of pump activity, thermodynamics predicts the system will equilibrate with the $[Ca^{2+}]$ concentration in the SR and the cytoplasm becoming equal.

While further experiments are required to evaluate the parameters of the model, we can estimate those based on previous models for cardiomyocyte oscillations. As discussed above, the adaptation time of an RyR channel was measured as ~100 ms, which translates to $H \sim 10$ Hz (Valdivia et al., 1995). The average current through an RyR channel used in previous models (Dupont et al., 1991; Tang and Othmer, 1994) is on the order of $\bar{J} \sim 20\ \mu M \cdot s^{-1}$. The fact that isolated cells can switch between relaxation and spontaneous oscillations dynamics suggests that those are close to the critical transition of $\eta^* = 0$. Thus, for oscillating cells sufficiently close to this transition (we take here as an example $|\eta^*| = 0.1$), we estimate $\beta \approx 0.55\ \mu M^{-1}$. We thus approximate the effective mass as $m^* \approx 0.1\ s^{-2}$, which along with a pumping rate $K \sim 1\ s^{-1}$ (Dupont et al., 1991; Tang and Othmer, 1994), and $\alpha \approx 0.2$ (estimated from Valdivia et al., 1995) yields an oscillation frequency $\Omega_c \sim 2.5$ Hz, similar to the frequencies observed in experiments (Tang et al., 2011; Nitsan et al., 2016). Note that even further away from the transition to spontaneous oscillations ($\beta\bar{J}/H \gg 1$), the frequency of oscillations is even lower.

The amplitude of oscillations in our model scales as $\sim \sqrt{\eta^*/\Gamma}$ (Cohen and Safran, 2019), which represents the combined effects of both the linear and non-linear friction terms. For the observed amplitudes of ~5 μM around the steady-state (Dupont et al., 1991; Tang and Othmer, 1994), (and for the case of $|\eta^*| \sim 0.1$, close to the transition), one can estimate the non-linear saturation parameter as $\Gamma \sim 0.25\ \mu M^{-2}$. Note that the microscopic origin of the non-linearity can arise from several different effects (such as saturation of current, direct inactivation of the adaptation, calcium dependence of the adaptation time etc.), and more experiments are required to distinguish between these mechanisms.

3. ANALYTICAL PREDICTIONS OF THE MODEL

3.1. Response to Periodic Perturbations

Our model which derives Equation (4) from the biophysics of the system, provides an intuitive understanding of the physics of spontaneous [Ca^{2+}] oscillations, and how it relates to the kinetics and dynamics of the currents to and from the SR. Moreover, it predicts how the effective parameters (Equation 5) depend on the channel and pump properties and thus, the conditions for the transition from decaying to spontaneous oscillations ($\eta^* = 0$), and the frequency close to this transition ($\Omega_c \approx \sqrt{\kappa/m^*}$) (Cohen and Safran, 2019). If we add to Equation (4) an external driving force, we can predicts the response of the system to external perturbations. In the adult heart, [Ca^{2+}] oscillations in pacemaker cells effectively determine the heart's beating rate (Hill and Olson, 2012). These oscillations are externally paced by an electrical signal from the brain, which can speed-up or slow down the heart rate in response to oxygen and nutrient demand throughout the body. Pacing spontaneous oscillations is therefore physiologically important in healthy individuals, and any dysfunction may lead to pathological disease (Brodde et al., 1995; Eisner et al., 2000).

It was shown in several experiments that cardiomyocyte beating can be paced electrically (Xia et al., 2000; Radisic et al., 2004; Serena et al., 2009) or mechanically (Tang et al., 2011; Nitsan et al., 2016; Viner et al., 2019). For electrical pacing, the cell is subject to an external electrical field which causes voltage-sensitive ion channels on the cell membrane (or the SR) to open, allowing an influx of ions to the cytoplasm (Berger et al., 1994). For mechanical stimulation, the cell is subject to an oscillating mechanical force (Tang et al., 2011; Nitsan et al., 2016; Viner et al., 2019), which can couple to the cell membrane (or the SR), through integrin adhesions (Peter et al., 2011), or directly affect actomyosin contractility. Effectively, the mechanical deformation translates into a flux of Ca^{2+} ions into the cytoplasm (either from the environment, or from the SR).

Recent experiments have shown that purely mechanical signals, can control the beating of cardiomyocytes (Tang et al., 2011; Nitsan et al., 2016). In these measurements, nearby neonatal cardiac cells, seeded $\sim$100 μm apart on an elastic gel, synchronize their beating phase and frequency even without direct contact (Tang et al., 2011; Nitsan et al., 2016). By introducing (at similar distances) an inert probe that induced periodic elastic deformations in the substrate, the beating cells were entrained (i.e., synchronized their beating with the deformation of the substrate). All this despite that the cell and probe are not in direct physical contact, or coupled electrically in any way (Nitsan et al., 2016) (see **Figure 3**). Complete synchronization was observed for a range of frequency differences between the spontaneous and probe frequency. When the difference in frequencies becomes large enough, the cells displays "bursting" behavior, where intermittent periods of synchronized contraction and quiescence are observed. Interestingly, the bursting regime is characterized by several beats at the frequency of the probe, followed by a quiescent interval. The overall duration of the combined beating and quiescence is comparable to the inverse of the spontaneous beating frequency of the cell.

To account for the effects of external electrical or mechanical perturbations (e.g., the mechanical probe in Nitsan et al., 2016), we supplement Equation (4) on the right-hand-side with external periodic perturbations $f_c(t)$. We consider here the simple cosine-like perturbation applied in the experiments (Nitsan et al., 2016)—and add to the right-hand-side of Equation (4) a term $f_c(t) = a_p * \kappa \cos(\Omega_p t)$, where a_p and Ω_p are the amplitude and frequency of the perturbations, respectively, and κ is a constant scale factor so that $f_c(t)$ has the correct dimensions. The periodic external perturbation can entrain (synchronize) the spontaneous beating dynamics of the cell. This can be seen by deriving from the "forced" version of Equation (4), an equation for the dynamics of the beating phase $\phi_c(t)$, defined as difference between the observed beating frequency and the frequency of the perturbation Ω_p (Cohen and Safran, 2018):

$$\dot{\phi}_c = \Delta\Omega\left(1 - Q\cos(\phi_c)\right), \quad Q = \frac{1}{2}\frac{a_p\Omega_c^2}{a_c\,\Delta\Omega\,\Omega_p} \tag{6}$$

where we define the detuning $\Delta\Omega = (\Omega_c - \Omega_p)$, the spontaneous beating amplitude (in the absence of external pacing) $a_c = 2\sqrt{\eta^*/\Gamma}$ (Cohen and Safran, 2018), and the tuning parameter Q. Equation (6) is the well-known result by Adler (1946) for the synchronization of coupled electrical oscillators. Spontaneous oscillations occur when the phase changes linearly in time with the detuning $\Delta\Omega$ (i.e., $\dot{\phi}_c = \Delta\Omega$), which can only be achieved in the limit of $Q \to 0$ (very weak perturbations $a_p \ll a_c$, or very large detuning $\Delta\Omega \gg 1$, see the top panel of **Figure 4A**). On the other hand, complete synchronization is achieved when the phase becomes constant at long times (i.e., $\dot{\phi}_c \to 0$), which means that the cell beats with the frequency of the probe Ω_p. This occurs whenever the tuning parameter Q becomes larger than unity (i.e., $Q > 1$), which is the case for large enough probe amplitudes ($a_p \gg a_c$), or relatively small detuning ($\Delta\Omega \approx 0$) (see **Figure 4C**). Interestingly, when the tuning parameter is close to its critical value of unity, but is still below the threshold of entrainment (i.e., $Q \approx 1$), the phase dynamics consist of step-like increases in the beating phase, which translates to "bursting" beating behavior where the cell intermittently switches between beating with the pacing frequency and its spontaneous beating frequencies. This results in a pattern of several beats with the frequency of the probe, followed by short quiescence period, consistent with the experimental observations (see **Figure 4B**). Thus, the simple dynamics of the paced version of Equation (4) can qualitatively account for the spontaneous, "bursting" and paced dynamics observed in experiments.

3.2. Response to Noise

Equations (4) and (6) predict the onset of spontaneous oscillations, and their dynamics when subjected to external pacing in a deterministic manner. However, the beating dynamics of cardiac tissue is not completely deterministic. Irregularities in the beating of the heart have been linked to cardiovascular disease by numerous studies (Kjekshus, 1990; Gage et al., 2001;

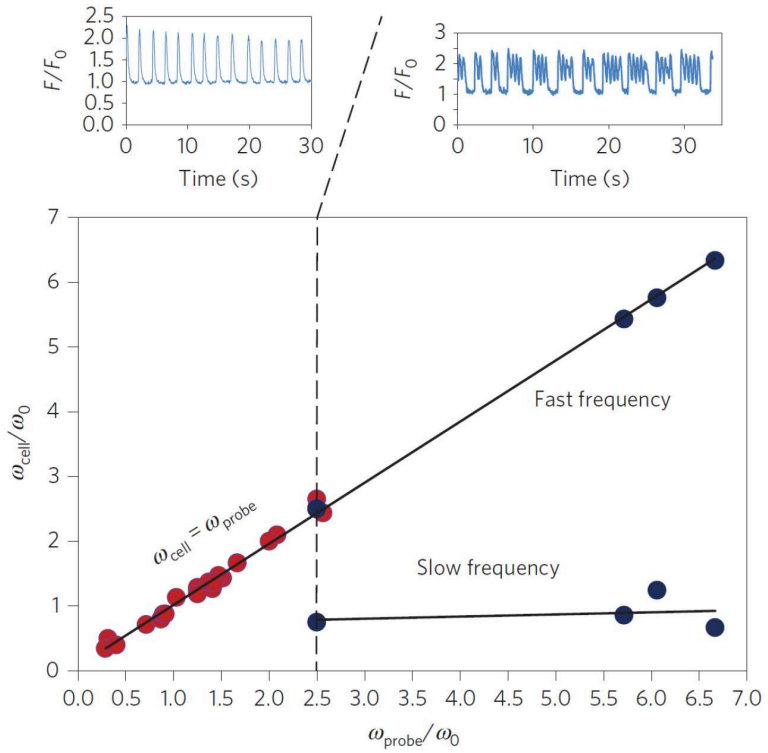

FIGURE 3 | Experimental entrainment of cardiomyocyte beating by a mechanical probe. Isolated cardiomyocytes (n = 30) seeded on an elastic substrate were subject to mechanical pacing by an oscillating inert probe located ∼100 μm away from the paced cell. The probe introduced periodic deformations of the underlying substrate with a frequency ω_{probe}. The cell beating frequency was measured before (ω_0) and ∼15 min after (ω_{cell}) the pacing probe was activated. The scaled cellular beating frequency (ω_{cell}/ω_0) was plotted vs. the scaled probe frequency (ω_{probe}/ω_0) since ω_0 varies between cells. Red dots represent full entrainment by the probe, i.e., synchronization to the probe frequency (see top left figure, plotting the scaled fluorescent [Ca^{2+}] signal F/F_0 of a representative cell). Blue dots represent "bursting" behavior, where the cell alternates between beating with the frequency of the probe ω_{probe} and quiescence (see top right figure). The time between consecutive intervals of quiescence was comparable to ω_0^{-1}. Reprinted by permission from Springer: Springer Nature (Nitsan et al., 2016).

Benjamin et al., 2018). Arrhythmia (a broad term describing different pathologies associated with increased, decreased, and chaotic heart rate) has been shown to increase the risk of stroke and heart failure (Kjekshus, 1990; Gage et al., 2001). It is therefore crucial that the heart maintain a regular beating pattern to ensure the health of an individual.

While it is reasonable to begin our understanding of the regularity of beating by focusing on an isolated, spontaneously beating cardiomyocyte, we note that single-cell beating dynamics are observed to be more stochastic than those of the entire heart organ (Zaniboni et al., 2000; Nitsan et al., 2016). The stochasticity is manifested in temporal variability of the mechanical stresses exerted by the cell (the amplitude of beating) and of the time between consecutive beats (or the frequency of beating). This variability represent the cumulative contribution of many processes that affect the beating, such as ATP availability, sarcomere structure and alignment, the activity of calcium channels and pumps and many other possible effects (Severs, 2000; Bers, 2002; Kobayashi and Solaro, 2005; Kobirumaki-Shimozawa et al., 2016). Thus, at long times, both the beating amplitude and frequency fluctuate around average values that represents the deterministic, "spontaneous" amplitude and frequency of each cell.

While fluctuations in amplitude affect the maximal stress exerted by an individual cardiomyocyte, these are usually small (∼5%) compared to the average amplitude of contraction (Domke et al., 1999; Nitsan et al., 2016). At the organ level, this translates to a roughly constant volume of blood pumped with each beating cycle. Thus, these fluctuations are less important from a physiological point of view. However, fluctuations in the beating frequency (or the time interval between consecutive beats) can range from a few, to tens of percents over time (Domke et al., 1999; Zaniboni et al., 2000; Nitsan et al., 2016). Unlike the fluctuations in amplitude, these deviation can accumulate over time, which translates to the heart cell "skipping" or "adding" beats. These deviations may therefore help understand organ level irregularities, such as arrhythmia.

Recent experiments on isolated, spontaneously beating cardiomyocytes quantify the noise in beating, and its response to external mechanical pacing (Viner et al., 2019). It was shown that cells mechanically paced with amplitudes a_p much lower than those that cause the onset of entrainment ($Q = 1$, in Equation 6) displayed an exponential reduction in the variance

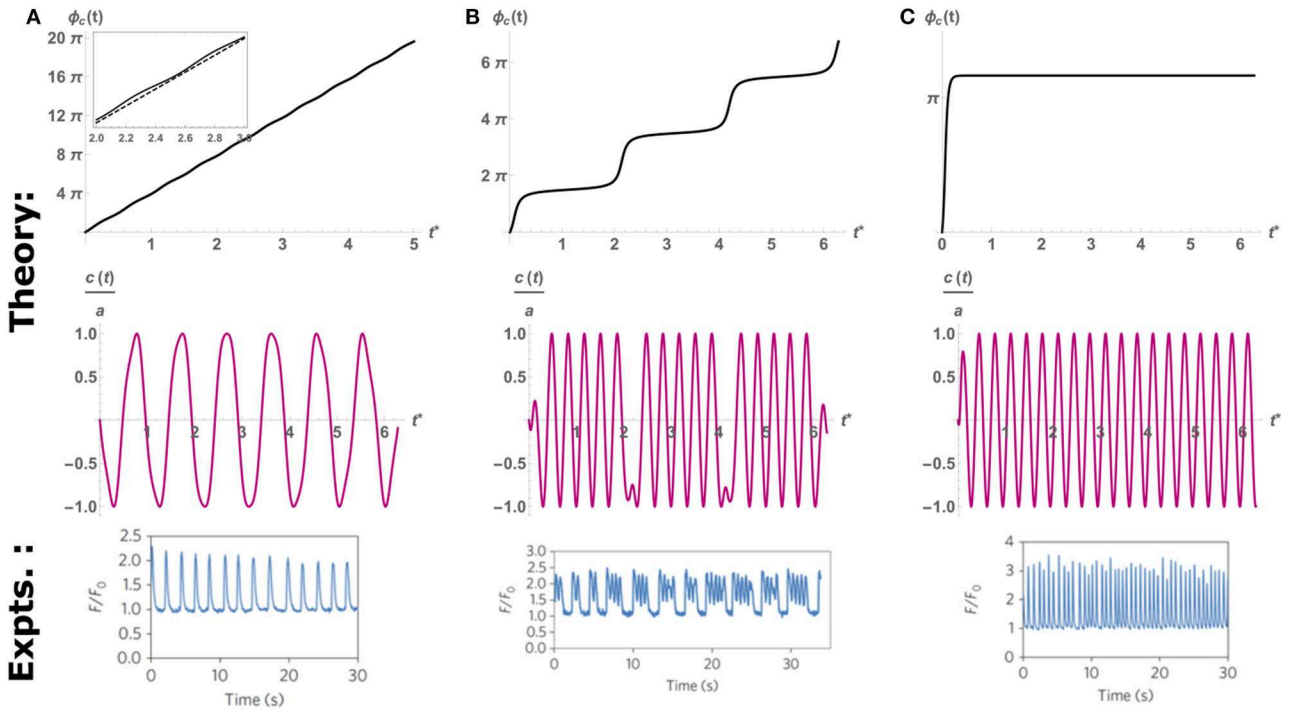

FIGURE 4 | An example of the time evolution of the phase predicted by the theoretical Equation (6) (top row), the resulting scaled oscillation in $c(t)$ (middle row), and the oscillations observed in experiments (bottom row). Here we fix the cell and probe frequency at $\Omega_c = 2\pi$, $\Omega_p = 6\pi$, respectively, and vary the amplitude of pacing to control the value of Q. **(A)** $Q = 0.2$, below threshold of entrainment ($Q = 1$), the cell beats with its spontaneous frequency Ω_c as indicated by the quasi-linear increase in phase. **Inset**: comparison to linear slope (dashed) that shows large regions of slips and much smaller intervals of plateaus. **(B)** $Q = 0.97$ Intermittent periods of entrainment (plateaus) followed by fast "phase-slip" events. This corresponds to the "bursting" behavior observed in experiments (bottom row). **(C)** $Q = 2$, above the threshold of entrainment. The cell beats with the probe frequency Ω_p. Top and middle rows adapted from Cohen and Safran (2018). Top and middle rows reprinted by permission from Springer: Springer Nature (Cohen and Safran, 2018). Bottom row reprinted by permission from Springer: Springer Nature (Nitsan et al., 2016).

of their beating frequency distribution with the pacing amplitude (Viner et al., 2019). This result demonstrates that even when the pacing force is not strong enough to entrain the cell, the introduction of even a weak, oscillating perturbation is enough to increase coherence in the beating of cells (the cells still beat with the spontaneous frequency Ω_c, but with considerably smaller fluctuations).

We have recently shown theoretically and analytically that the reduction in apparent noise can be predicted from the simple model of Equation (4), supplemented by the sum of both an external pacing force [$f_c(t)$ defined above] and a stochastic noise $\eta(t)$. The noise term is taken to be Gaussian, with average $\langle\eta(t)\rangle = 0$ and temporal correlations $\langle\eta(t)\eta(t) = 2D\delta(t - t')$ (Cohen and Safran, 2018). The presence of stochastic noise means that there is no deterministic solution and that one must consider the probability distribution of the time dependent [Ca^{2+}] concentration. This effectively translated (Hanggi and Riseborough, 1983; Cohen and Safran, 2018) into the probability distribution of the beating phase $\mathcal{P}[\phi_c]$:

$$\dot{\mathcal{P}} = -\frac{\partial}{\partial\phi_c}(\alpha^* \cos(\phi_c - \beta)\mathcal{P}) + D^*\frac{\partial^2\mathcal{P}}{\partial\phi_c^2} \qquad (7)$$

with $\alpha^* \sim a_p/a_c$ a measure of the relative strength of pacing, $\beta \sim \Delta\Omega$ a measure of the phase shift due to the detuning (not to be confused with the adaptation rate β of the previous section), and $D^* \sim D/(a_c^2\Omega_c^4)$ a measure of the magnitude of the noise-induced fluctuations of the spontaneously beating amplitude and frequency (i.e., the effective diffusion constant for the phase). Note that in this treatment, we consider the pacing to be below the threshold of entrainment ($Q \ll 1$). Thus, the beating phase in this case is defined with respect to the spontaneous frequency Ω_c (and not that of the pacing force Ω_p), and as such is confined to the range $0 \leq \phi_c \leq 2\pi$.

Equation (7) describes a diffusion-like process of the phase ϕ_c, but with a drift due to a periodic potential (Risken, 1984). While Equation (7) seems intimidating at first, it can actually be easily understood by examining the ratio α^*/D^*, which represents the relative strength of the pacing force compared to the inherent amplitude of the fluctuations. At long times (and given any initial phase ϕ_0) Equation (7) is expected to go to steady-state ($\dot{\mathcal{P}} \to 0$, $\mathcal{P} \to \mathcal{P}_s$). In the absence of any external pacing ($\alpha^*/D^* \to 0$), the inherent noise in the system will cause the phase ϕ_c to randomly diffuse over time, which means that at very long times the steady-state probability density is flat. This means that in steady-state the phase can take any value between $0 < \phi_c < 2\pi$ with equal probability. However, when the amplitude of the pacing force is increased (i.e., α^*/D^* increases), the probability density narrows, with an average around $\langle\phi_c\rangle = \beta + \pi/2$ (see **Figure 5**). Note that a narrowing of the phase does

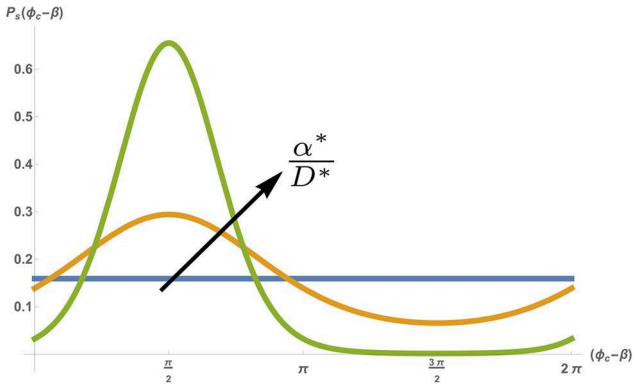

FIGURE 5 | Stationary probability density $P_s(\phi_c)$ as a function of the shifted phase $(\phi_c - \beta)$, for a fixed noise amplitude $D^* = 0.5$ $[s^{-1}]$, spontaneous frequency $\Omega_c = 1$ $[rad \cdot s^{-1}]$ and pacing frequency $\Omega_p = 1.5$ $[rad \cdot s^{-1}]$. Different colors show different pacing amplitudes with $\alpha^* = 0$ (blue) $\alpha^* = 0.5$ $[s^{-1}]$ (orange) and $\alpha^* = 2[s^{-1}]$ (green). Figure adapted by permission from Springer: Springer Nature (Cohen and Safran, 2018).

not mean that the cell becomes entrained (i.e., that it beats with the pacing frequency Ω_p). The average beating frequency is still fixed at Ω_c, but the fluctuations around this frequency becomes smaller as α^*/D^* increases. Indeed, in the limit of strong pacing $\alpha^*/D^* \gg 1$ (but still below the threshold of entrainment, i.e., $Q \ll 1$), the probability density approaches an infinitely sharp delta function ($\sim \delta(\phi_c - \beta - \pi/2)$), and we regain the deterministic beating behavior of Equation (4) (with a small effect of the weak pacing force).

4. CONCLUSION

We have demonstrated here the rich set of behaviors observed in the dynamics of spontaneously beating, and paced isolated cardiomyocytes can be captured by a minimal model derived from calcium pumps and channels dynamics. This approach allows for an intuitive understanding of spontaneous beating, and how it reacts to external perturbations. Fundamental understanding of the physics behind cardiomyocyte beating can facilitate the design of better medical treatment in the future. Drawing analogies to well-known physical systems, and understanding how the coarse-grained observables (amplitude, frequency, entrainment, fluctuations in beating) scale with changes introduced to the underlying kinetics, are essential to bridge the gap between the microscopic and the macroscopic view of cardiac beating. The resulting theory is useful in explaining why and how large-scale phenomena (spontaneous beating, entrainment etc.) emerge in a robust manner from the microscopic details. Future analysis should focus upon inter channel coupling within a single cell, and the coupling of calcium oscillations in neighboring cells (using our model as a basis) as a first step to predicting tissue level behavior (Grosberg et al., 2011). Extracting the essence of, and providing simple and testable predictions to the phenomenon of cardiomyocyte beating is an important step in deciphering the riddle of the beating heart.

AUTHOR CONTRIBUTIONS

All authors listed have made a substantial, direct and intellectual contribution to the work, and approved it for publication.

FUNDING

This work was funded by the U.S.-Israel Binational Science Foundation, the Israel Science Foundation, the Villalon Family Foundation, and the Perlman Family Foundation.

ACKNOWLEDGMENTS

We would like to thank K. Dasbiswas, D. Deviri, B. M. Friedrich, A. Grosberg, A. Y. Grosberg, S. Ishiwata, E. Lakatta, M. Lenz, S. K. Nandi, I. Nitsan, S. Tzlil, H. Valdivia, H. Viner, and X. Xu for useful discussions.

REFERENCES

Adler, R. (1946). A study of locking phenomena in oscillators. *Proc. IRE* 34, 351–357.

Atri, A., Amundson, J., Clapham, D., and Sneyd, J. (1993). A single-pool model for intracellular calcium oscillations and waves in the xenopus laevis oocyte. *Biophys. J.* 65, 1727–1739.

Benjamin, E. J., Virani, S. S., Callaway, C. W., Chamberlain, A. M., Chang, A. R., Cheng, S., et al. (2018). Heart disease and stroke statistics-2018 update: a report from the american heart association. *Circulation* 137, e67–e492. doi: 10.1161/CIR.0000000000000573

Berger, H.-J., Prasad, S. K., Davidoff, A., Pimental, D., Ellingsen, O., Marsh, J., et al. (1994). Continual electric field stimulation preserves contractile function of adult ventricular myocytes in primary culture. *Am. J. Physiol. Heart Circ. Physiol.* 266, H341–H349.

Bers, D. (2001). *Excitation-Contraction Coupling and Cardiac Contractile Force*, Vol. 237. Dordrecht: Springer Science & Business Media.

Bers, D. M. (2002). Cardiac excitation–contraction coupling. *Nature* 415, 198–205. doi: 10.1038/415198a

Brodde, O.-E., Michel, M. C., and Zerkowski, H.-R. (1995). Signal transduction mechanisms controlling cardiac contractility and their alterations in chronic heart failure. *Cardiovasc. Res.* 30, 570–584.

Cohen, O., and Safran, S. A. (2018). Theory of frequency response of mechanically driven cardiomyocytes. *Sci. Rep.* 8:2237. doi: 10.1038/s41598-018-20307-2

Cohen, O., and Safran, S. A. (2019). Physics of spontaneous calcium oscillations in cardiac cells and their entrainment. *Phys. Rev. Lett.* 122:198101. doi: 10.1103/PhysRevLett.122.198101

Dasbiswas, K., Majkut, S., Discher, D., and Safran, S. A. (2015). Substrate stiffness-modulated registry phase correlations in cardiomyocytes map structural order to coherent beating. *Nat. Commun.* 6:6085. doi: 10.1038/ncomms7085

Domke, J., Parak, W. J., George, M., Gaub, H. E., and Radmacher, M. (1999). Mapping the mechanical pulse of single cardiomyocytes with the atomic force microscope. *Eur. Biophys. J.* 28, 179–186.

Dupont, G., Berridge, M., and Goldbeter, A. (1991). Signal-induced Ca^{2+} oscillations: properties of a model based on Ca^{2+}-induced Ca^{2+} release. *Cell Calcium* 12, 73–85.

Eisner, D., Choi, H., Diaz, M., Oneill, S., and Trafford, A. (2000). Integrative analysis of calcium cycling in cardiac muscle. *Circ. Res.* 87, 1087–1094. doi: 10.1161/01.RES.87.12.1087

Engler, A. J., Carag-Krieger, C., Johnson, C. P., Raab, M., Tang, H.-Y., Speicher, D. W., et al. (2008). Embryonic cardiomyocytes beat best on a matrix with heart-like elasticity: scar-like rigidity inhibits beating. *J. Cell Sci.* 121, 3794–3802. doi: 10.1242/jcs.029678

Engler, A. J., Sen, S., Sweeney, H. L., and Discher, D. E. (2006). Matrix elasticity directs stem cell lineage specification. *Cell* 126, 677–689. doi: 10.1016/j.cell.2006.06.044

Fill, M., and Copello, J. A. (2002). Ryanodine receptor calcium release channels. *Physiol. Rev.* 82, 893–922. doi: 10.1152/physrev.00013.2002

Fill, M., and Gillespie, D. (2018). Ryanodine receptor open times are determined in the closed state. *Biophys. J.* 115, 1160–1165. doi: 10.1016/j.bpj.2018.08.025

Gage, B. F., Waterman, A. D., Shannon, W., Boechler, M., Rich, M. W., and Radford, M. J. (2001). Validation of clinical classification schemes for predicting stroke: results from the national registry of atrial fibrillation. *JAMA* 285, 2864–2870. doi: 10.1001/jama.285.22.2864

Grosberg, A., Alford, P. W., McCain, M. L., and Parker, K. K. (2011). Ensembles of engineered cardiac tissues for physiological and pharmacological study: heart on a chip. *Lab Chip* 11, 4165–4173. doi: 10.1039/c1lc20557a

Guckenheimer, J. (1980). Dynamics of the Van der Pol equation. *IEEE Trans. Circuits Syst.* 27, 983–989.

Hanggi, P., and Riseborough, P. (1983). Dynamics of nonlinear dissipative oscillators. *Am. J. Phys.* 51, 347–352.

Hersch, N., Wolters, B., Dreissen, G., Springer, R., Kirchgeßner, N., Merkel, R., et al. (2013). The constant beat: cardiomyocytes adapt their forces by equal contraction upon environmental stiffening. *Biol. Open* 2, 351–361. doi: 10.1242/bio.20133830

Hill, J., and Olson, E. (2012). *Muscle 2-Volume Set: Fundamental Biology and Mechanisms of Disease*. Cambridge: Academic Press.

Höfer, T. (1999). Model of intercellular calcium oscillations in hepatocytes: synchronization of heterogeneous cells. *Biophys. J.* 77, 1244–1256.

Huxley, A. (1974). Muscular contraction. *J. Physiol.* 243, 1–43.

Ibrahim, M., Gorelik, J., Yacoub, M. H., and Terracciano, C. M. (2011). The structure and function of cardiac t-tubules in health and disease. *Proc. R. Soc. Lond. B Biol. Sci.* 278, 2714–2723. doi: 10.1098/rspb.2011.0624

Jafri, M. S., Rice, J. J., and Winslow, R. L. (1998). Cardiac Ca^{2+} dynamics: the roles of ryanodine receptor adaptation and sarcoplasmic reticulum load. *Biophys. J.* 74, 1149–1168.

Kehat, I., Kenyagin-Karsenti, D., Snir, M., Segev, H., Amit, M., Gepstein, A., et al. (2001). Human embryonic stem cells can differentiate into myocytes with structural and functional properties of cardiomyocytes. *J. Clin. Invest.* 108, 407–414. doi: 10.1172/JCI200112131

Keizer, J., and Levine, L. (1996). Ryanodine receptor adaptation and Ca^{2+} (-) induced Ca^{2+} release-dependent Ca^{2+} oscillations. *Biophys. J.* 71, 3477–3487.

Kjekshus, J. (1990). Arrhythmias and mortality in congestive heart failure. *Am. J. Cardiol.* 65, 42–48.

Kobayashi, T., and Solaro, R. J. (2005). Calcium, thin filaments, and the integrative biology of cardiac contractility. *Annu. Rev. Physiol.* 67, 39–67. doi: 10.1146/annurev.physiol.67.040403.114025

Kobirumaki-Shimozawa, F., Oyama, K., Shimozawa, T., Mizuno, A., Ohki, T., Terui, T., et al. (2016). Nano-imaging of the beating mouse heart *in vivo*: importance of sarcomere dynamics, as opposed to sarcomere length *per se*, in the regulation of cardiac function. *J. Gen. Physiol.* 147, 53–62. doi: 10.1085/jgp.201511484

Majkut, S., Idema, T., Swift, J., Krieger, C., Liu, A., and Discher, D. E. (2013). Heart-specific stiffening in early embryos parallels matrix and myosin expression to optimize beating. *Curr. Biol.* 23, 2434–2439. doi: 10.1016/j.cub.2013.10.057

Maltsev, V. A., and Lakatta, E. G. (2007). Normal heart rhythm is initiated and regulated by an intracellular calcium clock within pacemaker cells. *Heart Lung Circ.* 16, 335–348. doi: 10.1016/j.hlc.2007.07.005

Nitsan, I., Drori, S., Lewis, Y. E., Cohen, S., and Tzlil, S. (2016). Mechanical communication in cardiac cell synchronized beating. *Nat. Phys.* 12, 472–477. doi: 10.1038/nphys3619

Peter, A. K., Cheng, H., Ross, R. S., Knowlton, K. U., and Chen, J. (2011). The costamere bridges sarcomeres to the sarcolemma in striated muscle. *Prog. Pediatr. Cardiol.* 31, 83–88. doi: 10.1016/j.ppedcard.2011.02.003

Radisic, M., Park, H., Shing, H., Consi, T., Schoen, F. J., Langer, R., et al. (2004). Functional assembly of engineered myocardium by electrical stimulation of cardiac myocytes cultured on scaffolds. *Proc. Natl. Acad. Sci. U.S.A.* 101, 18129–18134. doi: 10.1073/pnas.0407817101

Reed, A., Kohl, P., and Peyronnet, R. (2014). Molecular candidates for cardiac stretch-activated ion channels. *Glob. Cardiol. Sci. Pract.* 2014, 9–25. doi: 10.5339/gcsp.2014.19

Risken, H. (1984). *Fokker-Planck Equation*. Berlin; Heidelberg: Springer.

Serena, E., Figallo, E., Tandon, N., Cannizzaro, C., Gerecht, S., Elvassore, N., et al. (2009). Electrical stimulation of human embryonic stem cells: cardiac differentiation and the generation of reactive oxygen species. *Exp. Cell Res.* 315, 3611–3619. doi: 10.1016/j.yexcr.2009.08.015

Severs, N. J. (2000). The cardiac muscle cell. *Bioessays* 22, 188–199. doi: 10.1002/(SICI)1521-1878(200002)22:2<188::AID-BIES10>3.0.CO;2-T

Sneyd, J., Han, J. M., Wang, L., Chen, J., Yang, X., Tanimura, A., et al. (2017). On the dynamical structure of calcium oscillations. *Proc. Natl. Acad. Sci. U.S.A.* 114, 1456–1461. doi: 10.1073/pnas.1614613114

Tang, X., Bajaj, P., Bashir, R., and Saif, T. A. (2011). How far cardiac cells can see each other mechanically. *Soft Matter* 7, 6151–6158. doi: 10.1039/c0sm01453b

Tang, Y., and Othmer, H. G. (1994). A model of calcium dynamics in cardiac myocytes based on the kinetics of ryanodine-sensitive calcium channels. *Biophys. J.* 67, 2223–2235.

Valdivia, H. H., Kaplan, J. H., Ellis-Davies, G., and Lederer, W. J. (1995). Rapid adaptation of cardiac ryanodine receptors: modulation by Mg^{2+} and phosphorylation. *Science* 267, 1997–2000.

Viner, H., Nitsan, I., Sapir, L., Drori, S., and Tzlil, S. (2019). Mechanical communication acts as a noise filter. *iScience* 14, 58–68. doi: 10.1016/j.isci.2019.02.030

Vinogradova, T. M., Lyashkov, A. E., Zhu, W., Ruknudin, A. M., Sirenko, S., Yang, D., et al. (2006). High basal protein kinase a–dependent phosphorylation drives rhythmic internal Ca^{2+} store oscillations and spontaneous beating of cardiac pacemaker cells. *Circ. Res.* 98, 505–514. doi: 10.1161/01.RES.0000204575.94040.d1

Vinogradova, T. M., Zhou, Y.-Y., Maltsev, V., Lyashkov, A., Stern, M., and Lakatta, E. G. (2004). Rhythmic ryanodine receptor Ca^{2+} releases during diastolic depolarization of sinoatrial pacemaker cells do not require membrane depolarization. *Circ. Res.* 94, 802–809. doi: 10.1161/01.RES.0000122045.55331.0F

Wilders, R., Jongsma, H., and Van Ginneken, A. (1991). Pacemaker activity of the rabbit sinoatrial node. A comparison of mathematical models. *Biophys. J.* 60, 1202–1216.

Xia, Y., McMillin, J. B., Lewis, A., Moore, M., Zhu, W. G., Williams, R. S., et al. (2000). Electrical stimulation of neonatal cardiac myocytes activates the nfat3 and gata4 pathways and up-regulates the adenylosuccinate synthetase 1 gene. *J. Biol. Chem.* 275, 1855–1863. doi: 10.1074/jbc.275.3.1855

Yang, H.-T., Tweedie, D., Wang, S., Guia, A., Vinogradova, T., Bogdanov, K., et al. (2002). The ryanodine receptor modulates the spontaneous beating rate of cardiomyocytes during development. *Proc. Natl. Acad. Sci. U.S.A.* 99, 9225–9230. doi: 10.1073/pnas.142651999

Zaniboni, M., Pollard, A. E., Yang, L., and Spitzer, K. W. (2000). Beat-to-beat repolarization variability in ventricular myocytes and its suppression by electrical coupling. *Am. J. Physiol. Heart Circ. Physiol.* 278, H677–H687. doi: 10.1152/ajpheart.2000.278.3.H677

Conflict of Interest: The authors declare that the research was conducted in the absence of any commercial or financial relationships that could be construed as a potential conflict of interest.

frontiers in Physiology

ORIGINAL RESEARCH
published: 10 March 2020
doi: 10.3389/fphys.2020.00107

Modifications of Sarcoplasmic Reticulum Function Prevent Progression of Sarcomere-Linked Hypertrophic Cardiomyopathy Despite a Persistent Increase in Myofilament Calcium Response

*Shamim A. K. Chowdhury[1], Chad M. Warren[1], Jillian N. Simon[1], David M. Ryba[1], Ashley Batra[1], Peter Varga[2], Evangelia G. Kranias[3], Jil C. Tardiff[4], R. John Solaro[1] and Beata M. Wolska[1,5]**

[1] Department of Physiology and Biophysics and the Center for Cardiovascular Research, College of Medicine, University of Illinois at Chicago, Chicago, IL, United States, [2] Department of Pediatrics, Section of Cardiology, University of Illinois at Chicago, Chicago, IL, United States, [3] Department of Pharmacology and Systems Physiology, University of Cincinnati, Cincinnati, OH, United States, [4] Department of Medicine, Division of Cardiology, The University of Arizona, Tucson, AZ, United States, [5] Department of Medicine, Division of Cardiology, University of Illinois at Chicago, Chicago, IL, United States

OPEN ACCESS

Edited by:
Sachio Morimoto,
International University of Health and Welfare (IUHW), Japan

Reviewed by:
Steven Baxter Marston,
Imperial College London, United Kingdom
P. Bryant Chase,
Florida State University, United States

***Correspondence:**
Beata M. Wolska
bwolska@uic.edu

Specialty section:
This article was submitted to Striated Muscle Physiology, a section of the journal Frontiers in Physiology

Received: 20 December 2019
Accepted: 30 January 2020
Published: 10 March 2020

Citation:
Chowdhury SAK, Warren CM, Simon JN, Ryba DM, Batra A, Varga P, Kranias EG, Tardiff JC, Solaro RJ and Wolska BM (2020) Modifications of Sarcoplasmic Reticulum Function Prevent Progression of Sarcomere-Linked Hypertrophic Cardiomyopathy Despite a Persistent Increase in Myofilament Calcium Response. Front. Physiol. 11:107. doi: 10.3389/fphys.2020.00107

Hypertrophic cardiomyopathy (HCM) is a genetic disorder caused by mutations in different genes mainly encoding myofilament proteins and therefore called a "disease of the sarcomere." Despite the discovery of sarcomere protein mutations linked to HCM almost 30 years ago, the cellular mechanisms responsible for the development of this disease are not completely understood and likely vary among different mutations. Moreover, despite many efforts to develop effective treatments for HCM, these have largely been unsuccessful, and more studies are needed to better understand the cellular mechanisms of the disease. In experiments reported here, we investigated a mouse model expressing the mutant cTnT-R92Q, which is linked to HCM and induces an increase in myofilament Ca^{2+} sensitivity and diastolic dysfunction. We found that early correction of the diastolic dysfunction by phospholamban knockout (PLNKO) was able to prevent the development of the HCM phenotype in troponin T (TnT)-R92Q transgenic (TG) mice. Four groups of mice in FVB/N background were generated and used for the experiments: (1) non-transgenic (NTG)/PLN mice, which express wild-type TnT and normal level of PLN; (2) NTG/PLNKO mice, which express wild-type TnT and no PLN; (3) TG/PLN mice, which express TnT-R92Q and normal level of PLN; (4) TG/PLNKO mice, which express TnT-R92Q and no PLN. Cardiac function was determined using both standard echocardiographic parameters and speckle tracking strain measurements. We found that both atrial morphology and diastolic function were altered in TG/PLN mice but normal in TG/PLNKO mice. Histological analysis showed a disarray of myocytes and increased collagen deposition only in TG/PLN hearts. We also observed increased Ca^{2+}/calmodulin-dependent protein kinase II (CaMKII) phosphorylation only in TG/PLN hearts but not in TG/PLNKO hearts. The rescue of the

HCM phenotype was not associated with differences in myofilament Ca^{2+} sensitivity between TG/PLN and TG/PLNKO mice. Moreover, compared to standard systolic echo parameters, such as ejection fraction (EF), speckle strain measurements provided a more sensitive approach to detect early systolic dysfunction in TG/PLN mice. In summary, our results indicate that targeting diastolic dysfunction through altering Ca^{2+} fluxes with no change in myofilament response to Ca^{2+} was able to prevent the development of the HCM phenotype and should be considered as a potential additional treatment for HCM patients.

Keywords: hypertrophic cardiomyopathy, Ca^{2+}/calmodulin-dependent protein kinase II (CaMKII), myofilament Ca^{2+} sensitivity, phospholamban, troponin T (TnT), speckle strain, treatment

INTRODUCTION

Hypertrophic cardiomyopathy (HCM) is a genetic disorder caused by mutations in different genes mainly encoding myofilament proteins and therefore called a "disease of the sarcomere" (Ashrafian et al., 2011; Towbin, 2014; Marian and Braunwald, 2017). It is characterized by early onset of diastolic dysfunction, myocyte disarray, and a variable degree of fibrosis and progressive hypertrophy and later onset of systolic dysfunction. Symmetrical left ventricular or asymmetrical septal hypertrophy typifies the disorder, but some mutations do not result in thickening of left ventricle (LV) walls. HCM is the leading cause of sudden cardiac death (SCD) in young people typically associated with exercise (Maron and Maron, 2016). Despite the discovery of sarcomere protein mutations linked to HCM almost 30 years ago (Geisterfer-Lowrance et al., 1990), the cellular mechanisms responsible for the development of this disease are not completely understood and likely vary among different mutations. Moreover, despite multiple studies to discover specific treatments (Marian, 2009; Alves et al., 2010; Ashrafian et al., 2011; Tardiff et al., 2015), there are no specific treatments for HCM patients. Patients are treated for symptoms of left ventricular outflow tract (LVOT) obstruction or decreased cardiac output with negative inotropic medications, and the common complication of arrhythmias is treated both pharmacologically and with implanted defibrillators. Septal reduction by surgery and ethanol (EtOH) ablation procedures are often performed to alleviate LVOT obstruction (Gersh et al., 2011; Marian and Braunwald, 2017).

Initial diastolic dysfunction in HCM patients is triggered by altered myofilament properties induced by protein mutations. However, the overall HCM phenotype depends not only on the mutation *per se* but also on additional contributing factors during progression of the disease (Arad et al., 2002; Deranek et al., 2019). These factors include both the response of myofilament force and kinetics to Ca^{2+} as well as membrane-controlled Ca^{2+} fluxes to and from the myofilaments. In experiments reported here, we investigated a mouse model expressing mutant cTnT-R92Q, which induces an increase in myofilament Ca^{2+} sensitivity and results in diastolic dysfunction. We tested whether prevention of the diastolic dysfunction is able to delay or stop the development of HCM phenotype in troponin T (TnT)-R92Q mice. Our approach was to promote sarcoplasmic reticulum (SR) Ca^{2+} uptake in the TnT-R92Q HCM mouse model by phospholamban knockout (PLNKO). We determined cardiac function (using both standard echocardiographic parameters and speckle strain measurements), histology, and myofilament function. We also established levels of Ca^{2+}/calmodulin-dependent protein kinase II (CaMKII) phosphorylation, which has been reported to be a key signaling pathway in human HCM (Helms et al., 2016) and in mouse HCM models (Lehman et al., 2019). We observed that KO of PLN in hearts of cTnT-R92Q mice resulted in decreased CaMKII phosphorylation and a prevention of the development of the HCM phenotype, although the increase in myofilament Ca^{2+} sensitivity was preserved.

MATERIALS AND METHODS

Generation of New Transgenic Mice

Transgenic (TG) TnT-R92Q heterozygous mice with Myc-tag at NH_2-termini were originally generated and characterized in C57BL/6 genetic background (Tardiff et al., 1999). PLNKO mice used in this project were in FVB/N genetic background (Gaffin et al., 2011). Since it is well-documented that genetic background may have a significant effect on the HCM phenotype (Prabhakar et al., 2001; Michele et al., 2002; Rowlands et al., 2017), we first rederived and characterized TnT-R92Q mice in FVB/N background. We crossed TnT-R92Q heterozygous male with FVB/N female and created F1 generation of mice. Next, we bred TnT-R92Q-positive male from F1 generation with FVB/N female to obtain F2 generation of mice. We repeated this process up to F10 generation. To generate PLNKO mice expressing mutated TnT-R92Q, we bred positive male from F10 generation with PLNKO female. All mice from this breeding were heterozygous for PLN and express either normal wild-type TnT or mutated TnT (TnT-R92Q). Next, we bred heterozygous PLN male mouse that was positive for TnT-R92Q transgene with PLNKO female. This breeding allowed us to generate PLNKO mice that also expressed TnT-R92Q. These mice were used for further breeding with PLNKO females. The following abbreviations for the four groups of mice in FVB/N background were used: (1) non-transgenic (NTG)/PLN mice, which express wild-type TnT and normal level of PLN; (2) NTG/PLNKO mice, which express wild-type TnT and no PLN; (3) TG/PLN mice, which express TnT-R92Q and

normal level of PLN; (4) TG/PLNKO mice, which express TnT-R92Q and no PLN. All measurements in our studies were done at 16 weeks of age.

High-Resolution Echocardiography

Mice were initially anesthetized in a plexiglass chamber connected to a vaporizer providing isoflurane at 3% in 100% O_2 (Alves et al., 2014). Once induced, the mouse was secured in the supine position on a warming plate, and the isoflurane concentration was reduced to 1.5–2%, and hair was removed from the chest using a depilating agent. Body temperature was monitored and kept close to 37°C throughout the procedure. Transthoracic echocardiography was performed using a Vevo 770 High-Resolution *In Vivo* Imaging System and scan head with a center frequency of 40 MHz (VisualSonics, Toronto, ON, Canada). Anatomical M-Mode images of the left ventricle (LV) aortic root and left atrium (LA) were taken from the parasternal long axis view. The parasternal short axis view at the level of the papillary muscles was used to measure the LV internal dimension, anterior and posterior wall thicknesses. Pulsed-wave Doppler was performed in the apical four-chamber view. The mitral inflow was recorded with the Doppler sample volume at the tips of the mitral valve leaflets to obtain the peak velocities of flow in the early phase of diastole (E) and after LA contraction (A). The Doppler sample volume was moved toward the left ventricular outflow tract (LVOT), and both the mitral inflow and LV outflow were simultaneously recorded to measure the isovolumic relaxation time. Additional information about diastolic function was obtained with tissue Doppler imaging. Peak diastolic myocardial velocities in the early phase of diastole (e′) and after LA contraction (a′) and systolic velocity (s′) were obtained with the sample volume at the septal side of the mitral annulus in the four-chamber view. All measurements and calculations were averaged from three consecutive cycles and performed according to the American Society of Echocardiography guidelines. Data analysis was performed off-line with the Vevo 770 Analytic Software (VisualSonics, Toronto, ON, Canada). In addition, to generate data used for strain measurements, one cohort of mice was scanned using a Vevo 2100 High-Resolution *In Vivo* Imaging System and RMVTM MS-550D scan head with a center frequency of 40 MHz (VisualSonics, Toronto, ON, Canada), and images in short and long axes were obtained as described above. VevoStrain software was used to analyze the data (Bauer et al., 2011). Four to five consecutive cardiac cycles were selected for the analysis, and semiautomated tracing of the endocardial and epicardial borders was used. The tracing was corrected as needed, and longitudinal (LS), circumferential (CS), and radial strain (RS) and strain rates were calculated.

Force-Ca^{2+} Relations of Detergent-Extracted Myofiber Bundles

Force-Ca^{2+} relation measurements were performed as previously described (Ryba et al., 2019). Mice were heparinized (1,000 IU/kg) and anesthetized using 200 mg ketamine/20 mg xylazine/kg body weight. All mice were euthanized by cardiectomy under surgical anesthesia in accordance with the American Veterinary Medical Association Panel on Euthanasia Guidelines (American Veterinary Medical Association, 2013). Left ventricular papillary muscles were then isolated, dissected into fiber bundles approximately 200 μm in width and 3–4 mm in length, and detergent-extracted in a high relaxing (HR) solution (10 mmol/L EGTA, 41.89 mmol/L κ-Propinate, 100 mmol/L BES, 6.75 mmol/L $MgCl_2$, 6.22 mmol/L Na_2ATP, 10 mM Na_2CrP, 5 mmol/L NaN_3, pH 7.0) with 1% v/v Triton X-100 for 3–4 h at 4°C. The HR solution was then replaced with HR solution without Triton X-100. Free Ca^{2+} concentrations were calculated using WEBMAXC STANDARD and ranged from pCa ($-\log [Ca^{2+}]$) values of 8.0 to 4.5. Free Ca^{2+} concentrations were generated by mixing varying ratios of HR solution with solution containing 10 mmol/L $CaCl_2$. Fiber bundles were mounted between a micromanipulator and a force transducer and bathed in HR solution. We measured sarcomere length, which was kept constant throughout the experiment at 2.2 μm, using a He-Ne laser diffraction pattern to make adjustments with a micromanipulator. The fibers were initially stimulated to generate force at pCa 4.5 and placed back into the HR solution, and the width and diameter were measured along three points. Fibers were then subjected to sequential increases in Ca^{2+} concentration; their developed force was recorded on a chart recorder. All experiments were carried out at 23°C.

Histology

Histology was performed as previously described (Gaffin et al., 2011) with some slight modifications. Mice were anesthetized using 200 mg ketamine/20 mg xylazine per kg body weight. The hearts were quickly removed and retrogradely perfused through the aorta with ice-cold saline followed by 10% formalin. The heart was then transversely sliced into four pieces, and each piece was placed into a cassette. Cassettes were kept in formalin and shipped to the Veterinary Diagnostic Laboratory at the University of Illinois at Urbana-Champaign (UIUC) College of Veterinary Medicine for paraffin embedding and sectioning. Sections (5 μm) were placed on slides and stained using hematoxylin and eosin (H&E) and Masson's trichrome by conventional methods. Sections were imaged with a microscope coupled to a camera and viewed using Leica Aperio ImageScope software.

Wheat Germ Agglutinin Staining

Hearts of the mice used for WGA staining were mounted on a Langendorff apparatus with gravity-driven flow (70–80 mmHg). The excised hearts were retrogradely perfused on the Langendorff apparatus with phosphate-buffered saline (PBS) until the perfusate flowed clear, and then the perfusion solution was switched to 10% neutral buffered formalin (NBF) containing 100 mmol/L KCl for approximately 10 min. After perfusion, the hearts were transferred to a conical tube containing approximately 20 ml of NBF and allowed to sit at room temperature for 1 h. The heart was then put into cassettes, cut transversely into four sections, and allowed to fix for 24 h in approximately 20 ml of fresh NBF. After 24 h, the hearts were transferred to 70% EtOH solution and allowed to sit at room temperature for 24 h and sent to the Veterinary Diagnostic Laboratory at the UIUC College of Veterinary Medicine for

paraffin embedding and sectioning. To determine cell areas, the paraffin-embedded 3-μm-thick heart sections were taken, at 30-μm deep steps into the heart, for wheat germ agglutinin (WGA) staining. The sections were deparaffinized and rehydrated by placing the slides in 100% xylene twice for 3 min each, 1:1 xylene:EtOH once for 3 min, 100% EtOH twice for 3 min, 95% EtOH once for 3 min, 70% EtOH once for 3 min, 50% EtOH once for 3 min, and then placed in a bath of cool water. Antigen retrieval was performed by allowing the sections to sit in preheated antigen retrieval buffer (10 mmol/L sodium citrate, 0.05% tween-20, pH 6.0) at 95°C for 1 h. The slides were then removed from the antigen retrieval buffer, allowed to cool down and washed three times in PBS for 5 min. The slides were then incubated in FITC-conjugated WGA (Sigma L4895) at 10 μg/ml in PBS at room temp for 4 h. Next, the sections were washed three times for 5 min in PBS and mounted using ProLong Diamond antifade mountant (Invitrogen) and imaged the next day at the UIC Research Histology and Tissue Imaging core at the University of Illinois at Chicago using a Vectra multispectral microscope at 40 × magnification for quantification. A minimum of 10 different fields of view per biological replicate were used for the analysis. The cell areas were determined with Halo v2.3.2089.18 software at the Research Histology and Tissue Imaging core at the University of Illinois at Chicago.

Hydroxyproline Assay

Hydroxyproline (HOP) content was determined as previously described (Flesch et al., 1997; Heydemann et al., 2005; Pena et al., 2010). Liquid nitrogen frozen mouse cardiac tissue was minced into a tared Pyrex 9826 screw cap vial to determine the wet weight of the tissue (15–22 mg). A standard curve of *trans*-4-hydroxy-L-proline (0–500 μM) was included in each assay to determine the μM HOP/mg of tissue.

Assessment of Myofilament Phosphorylation by Pro-Q Diamond Stain

Mouse hearts were excised and immediately frozen in liquid nitrogen and stored at −80°C. Skinned myofibrils were prepared for phosphorylation analysis *via* Pro-Q Diamond and Coomassie staining as previously described with minor modifications (Layland et al., 2005). Briefly, 20 mg of left ventricular tissue was homogenized twice in 75 mM KCl, 10 mM imidazole pH 7.2, 2 mM $MgCl_2$, 2 mM EGTA, 1% (v/v) Triton X-100 (Solaro et al., 1971), 1 mM NaN_3 with protease and phosphatase inhibitors (Calbiochem #524624 1:100, Sigma #P-8340 1:100, and 500 nM Calyculin A) with a Dounce homogenizer. The homogenate was centrifuged at 16,000 × *g* for 1 min, and the pellets were washed once with the above buffer without Triton X-100 and centrifuged again. The pellets were solubilized in 8M urea, 2M thiourea, 0.05M Tris-HCl pH 6.8, 75 mM dithiothreitol (DTT) 3% sodium dodecyl sulfate (SDS), and 0.005% bromophenol blue (ISB buffer), and the protein concentration was determined with Pierce 660nm Protein Assay (Thermo Scientific) with the addition of the Ionic Detergent Compatibility Reagent (IDCR) following the manufacturer's recommendations. Twelve percent sodium dodecyl sulfate-polyacrylamide gel electrophoresis (SDS-PAGE) gels (Fritz et al., 1989) were run to separate 5 μg of myofilament proteins per lane. The gels were stained with a phosphorylation-specific stain Pro-Q Diamond following the manufacturer's recommendations (Invitrogen) and then subsequently stained with Coomassie G-250 following the manufacturer's recommendations (BioRad). Gel images were captured with a Chemidoc MP (BioRad) and analyzed with Image Lab v6.0 and Microsoft Excel.

Sodium Dodecyl Sulfate-Polyacrylamide Gel Electrophoresis for Myosin Heavy Chain Isoform Content

Myofilament protein samples prepared for the Pro-Q Diamond-stained gels were also used for the determination of myosin heavy chain isoform distribution. Myofilament protein (2.5 μg) was separated in 6% SDS-PAGE as previously described (Warren and Greaser, 2003). The gels were run in a Hoefer SE600 gel box and stained with Coomassie G-250 (BioRad) following manufacturer's recommendations. Gel images were captured with a Chemidoc MP (BioRad) and analyzed with Image Lab v6.0 and Microsoft Excel.

Immunoblot Analysis

Myofilament protein samples were also used for the determination of TnT-R92Q percent replacement. The TnT-R92Q has a myc-tag, which allows for a molecular weight separation versus the NTG-TnT isoforms 2 and 3. Myofilament protein (3 μg) was separated in 8% SDS-PAGE gels run in a Hoefer SE600 gel box at 22 mA with constant cooling (8°C) until the dye front was at the very bottom of the gel as previously described (Anderson et al., 1991). The gel was then trimmed to fit into a Criterion Transfer box (BioRad) and transferred onto 0.2 μm polyvinylidene fluoride (PVDF) membrane in 10 mM CAPS pH 11.0 (Matsudaira, 1987) buffer for 90 min at 20 V. The PDVF membrane was then probed with a TnT mouse monoclonal antibody 13-11 (Thermo Scientific #MS-295-P0) at 1:500 in 1% bovine serum albumin (BSA)-Tris-buffered saline with 0.1% Tween-20 (TBST).

Whole ventricular homogenates and skinned myofibrillar samples were prepared *via* an Omni International Bead Ruptor 24 Elite. The ventricular homogenates were ultimately solubilized in ISB buffer (see above), and the myofibrillar samples were prepared as previously (Hill et al., 2010; Patel et al., 2013; Utter et al., 2015) described for glutathione analysis and solubilized in 8M urea, 4% SDS, 0.05M Tris-HCl pH 6.8, and 0.005% bromophenol blue. A non-reducing 12% SDS-PAGE gel was run and transferred to 0.2 μm PVDF as above for the detection of glutathionylation (GSH) of MyBP-C and as previously described (Patel et al., 2013). To detect GSH, the membrane was first blocked in 5% non-fat dry milk-TBST with 2.5 mM NEM added. The membrane was then incubated with a mouse primary anti-GSH antibody (Virogen #101-A-250) 1:1,000 diluted in 5% non-fat dry milk-TBST. The membrane was then washed in TBST and incubated with a horseradish peroxidase (HRP)-conjugated mouse secondary antibody (Cell Signaling #7076S) 1:25,000 in 5%

non-fat dry milk-TBST. The membrane was exposed with Clarity ECL reagent (BioRad).

All other Western blots were reducing 12 or 15% SDS-PAGE and transferred onto 0.2 μm PVDF membrane as described above. The membranes were incubated with various primary antibodies diluted in either 5% non-fat dry milk-TBST or 1% BSA-TBST: mouse sarco(endo)plasmic reticulum Ca^{2+} ATPase (SERCA)2a 1:1,000 (Abcam #2861), rabbit glyceraldehyde 3-phosphate dehydrogenase (GAPDH) 1:4,000 (Santa Cruz #sc-25778), rabbit phosphoSer16-phospholamban 1:1,000 (Millipore 07-052), mouse phospholamban clone A1 1:2,000 (Badrilla #A010-14), rabbit phosphoThr17-phospholamban 1:2,500 (Badrilla #A010-13AP), rabbit delta, beta, gamma-phosphoT287-CaMKII 1:1,000 (Invitrogen #PA5-37833), and rabbit delta CaMKII 1:5,000 (Badrilla #A010-56AP). After washing in TBST, the membranes were then detected with an HRP-conjugated mouse or rabbit secondary antibody (Cell Signaling #7076S or #7074S) 1:20,000–1:25,000 in 5% non-fat dry milk-TBST. Membranes were exposed to either Clarity ECL reagent (BioRad) or Pierce SuperSignal West Femto (Thermo Scientific #34094) and imaged with a Chemidoc MP (BioRad) and analyzed with Image Lab v6.0 and Microsoft Excel.

Statistical Analysis

Gaussian distribution was assessed using the Shapiro–Wilk test and equal variance using Brown–Forsythe test. Data that show normal distribution and equal variance were analyzed using a one-way ANOVA followed by Tukey's *post hoc* test for multiple comparisons. Data that show normal distribution and unequal variance were analyzed using Brown–Forsythe and Welch ANOVA tests followed by Tamahane T2 test or unpaired *t*-test with Welch's correction for multiple comparisons. Otherwise, non-parametric Kruskal–Wallis test followed by Dunn's test for multiple comparisons were used. When two groups were compared, unpaired *t*-test was used. All data are presented as mean ± SE. Significance was set at $P < 0.05$ and marked as * for $P < 0.05$, ** for $P < 0.01$, and *** for $P < 0.001$. All statistical analyses were performed using GraphPad Prism 8.0 Software (GraphPad, Inc., La Jolla, CA, United States).

RESULTS

Baseline Cardiac Function and Morphology of Transgenic/Phospholamban Mice in FVB/N Background

To determine the influence of the genetic background on the HCM-linked phenotype, we crossed TnT-R92Q C57/Bl mice (Tardiff et al., 1999) into the FVB/N background for 10 generations as described in Section "Materials and Methods." Baseline cardiac function and morphology of the TG/PLN mouse model in the FVB/N background was examined using high-resolution echocardiography. Echocardiography revealed that at 16 weeks of age, mice display severe atrial remodeling and diastolic dysfunction, but no left ventricular hypertrophy (**Figure 1** and **Table 1**). **Figure 1** shows representative B-mode images of parasternal long (panel A, top) and short axis (panel A, bottom), M-mode images in long axis at the level of the aortic root and atria (panel B), and average LA size (panel C) in NTG/PLN and TG/PLN mice. The representative images of pulsed-wave Doppler of mitral flow and tissue Doppler images of mitral annulus in NTG/PLN and TG/PLN mice are shown in panel D. The LA size was significantly enlarged in TG/PLN mice compared to NTG/PLN mice (**Figure 1C**), but no changes were found in left ventricular internal diastolic dimension (LVIDd), LV mass, or relative wall thickness (RWT) between the NTG/PLN and TG/PLN groups (**Table 1**). However, TG/PLN hearts showed significant diastolic dysfunction as assessed by an increase in E/A ratio (the ratio of early to late diastolic mitral flow), an increase in the E/e′ ratio (ratio of early diastolic mitral flow to early diastolic mitral annulus velocity), and e′ (**Figures 1E,F** and **Table 1**). The global systolic function was preserved as no significant changes were observed between the ejection fraction (EF) and the velocity of circumferential shortening (V_{cf}). However, we found depressed peak systolic annular velocity (S′) in the TG/PLN mice compared to the NTG/PLN mice (**Table 1**).

Cardiac Function and Morphology Are Normal in Transgenic/Phospholamban Knockout Mice

To test the hypothesis that increased SR Ca^{2+} uptake can prevent the HCM phenotype in TG TnT-R92Q mice, we crossed the TnT-R92 with PLNKO mice to generate mutant mice that do not express PLN (TG/PLNKO). Echocardiography showed that at 16 weeks of age, TG/PLNKO mice show normal morphology (LA size, LV mass, LVIDd, and RWT) and diastolic (E/A ratio, E/e′, IVRT, and DT) and systolic function (EF, S′, and V_{cf}) (**Table 1**). TG/PLNKO mice also showed no changes in the HW/BW and HW/TL ratios compared to the NTG/PLN and NTG/PLNKO groups (**Figures 2A,B**). In addition to our finding of no changes in LV mass among all four groups (**Table 1**), the sizes (cross-section areas) of ventricle cardiac myocytes were not different between all four groups (**Figures 2C,D**).

In order to further investigate potential regional changes in systolic function among the mouse groups, we performed speckle tracking-based strain analysis using the Vevo2100 system. **Figure 3A** shows original recordings of strain and strain rate obtained in NTG/PLN, TG/PLN, and TG/PLNKO mice. We calculated longitudinal (LS), radial (RS), and circumferential strain (CS) and strain rate (LSR, RSR, and CSR, respectively) (**Figure 3B**). Analysis did not reveal significant changes between the TG/PLN and NTG/PLN groups in global LS (GLS), LS in endocardium, LS in epicardium, LS rate in endocardium (LSR), or LSR in epicardium (**Figures 3C–G**). However, TG/PLNKO hearts showed increased LSR in the endocardium and epicardium when compared to TG/PLN hearts (**Figures 3F,G**). Although LS measurements (**Figure 3**) did not show any changes between the NTG/PLN and TG/PLN groups, CS measurements (**Figure 4**) revealed reduced global CS (GCS) (panel A), CS in endocardium (CS Endo, panel B), and CSR in the endocardium (CSR Endo, panel C) in the TG/PLN group, but no changes in CS and

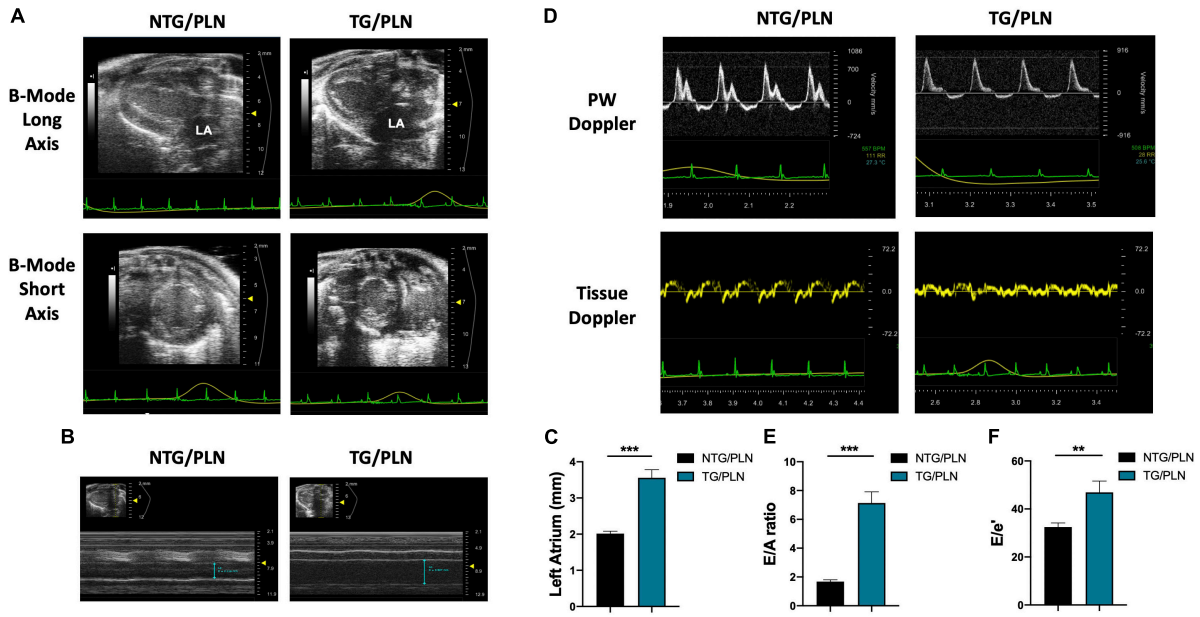

FIGURE 1 | Echocardiographic measurements show atrial enlargement and diastolic dysfunction in transgenic (TG)/phospholamban (PLN) mice. **(A)** Representative B mode images of parasternal long axis (top) and short axis (bottom). **(B)** Long axis M-mode images of aorta and left atrium (LA). **(C)** Summary data of LA size in non-transgenic (NTG)/PLN and TG/PLN mice. **(D)** Pulsed-wave Doppler of mitral flow (top) and tissue Doppler images (bottom) of the mitral annulus obtained from echocardiography. Summary data of peak velocity blood flow in early diastole (the E wave) to peak velocity flow in late diastole (A wave) (E/A) ratio **(E)** and peak velocity blood flow in early diastole (E wave) to peak mitral annular velocity during early filling (e′) (E/e′) ratio **(F)** in NTG/PLN and TG/PLN mice. Summary data are presented as means ± SEM. Differences among groups were analyzed by Mann–Whitney test. *N* = 13 (NTG/PLN) and 11 (TG/PLN) per group. $^{*}P < 0.05$, $^{**}P < 0.01$, $^{***}P < 0.001$.

TABLE 1 | Echocardiographic assessment of cardiac function.

Parameter/group	NTG/PLN	TG/PLN	NTG/PLNKO	TG/PLNKO
Sample size (n)	13	12	13	14
LA (mm)	2.01 ± 0.06	3.56 ± 0.22***	1.90 ± 0.10‡‡‡	2.06 ± 0.05‡‡‡
LVIDd (mm)	3.76 ± 0.10	3.84 ± 0.15	3.82 ± 0.07	3.80 ± 0.12
LV mass (mg)	74.52 ± 2.99	89.08 ± 5.08	84.20 ± 4.92	75.72 ± 3.39
RWT	0.39 ± 0.03	0.43 ± 0.03	0.40 ± 0.01	0.40 ± 0.03
E/A ratio	1.68 ± 0.12	7.13 ± 0.78***	1.76 ± 0.10‡‡‡	1.95 ± 0.10‡‡
E/e′ ratio	−32.48 ± 1.68	−46.92 ± 4.71*	−30.11 ± 1.10‡‡	−32.30 ± 1.38‡
E (mm/s)	797.7 ± 37.61	716.1 ± 36.79	842.0 ± 36.10	836.6 ± 30.00
e′ (mm/s)	22.97 ± 1.01	15.56 ± 1.58*	27.08 ± 1.02‡‡‡	26.29 ± 1.16‡‡‡
IVRT (ms)	13.09 ± 0.88	14.21 ± 0.85	10.94 ± 0.46‡	12.57 ± 0.43
DT (ms)	21.70 ± 0.88	23.20 ± 1.47	21.80 ± 1.08	20.60 ± 0.69
HR (beats/min)	437.2 ± 14.63	445.8 ± 26.01	484.2 ± 12.87	458.2 ± 15.90
SV (μl)	41.33 ± 1.63	45.69 ± 3.50	40.75 ± 1.72	45.78 ± 3.04
EF (%)	67.51 ± 2.08	67.95 ± 2.23	63.85 ± 1.58	70.07 ± 1.70
S′ (mm/s)	21.41 ± 1.11	13.99 ± 1.53***	24.50 ± 0.88‡‡‡	24.17 ± 0.94‡‡‡
V_{cf} (circ/s)	6.77 ± 0.30	6.43 ± 0.28	7.65 ± 0.27‡	7.48 ± 0.33

*Non-transgenic (NTG)/phospholamban (PLN), mice express wild-type troponin T (TnT) and normal level of PLN; NTG/phospholamban knockout (PLNKO), mice express wild-type TnT and no PLN; transgenic (TG)/PLN, mice express TnT-R92Q and normal level of PLN; TG/PLNKO, mice express TnT-R92Q and no PLN. LA, left atrial dimension; LV mass, left ventricular mass; LVIDd, left ventricular internal diastolic dimension; RWT, relative wall thickness; E/A, peak velocity blood flow in early diastole (the E wave) to peak velocity flow in late diastole (A wave); E/e′, peak velocity blood flow in early diastole (E wave) to peak mitral annular velocity during early filling (e′); IVRT, isovolumetric relaxation time; DT, E wave deceleration time; HR, heart rate; SV, stoke volume; EF, ejection fraction; S′, peak systolic annular velocity; V_{cf}, velocity of circumferential shortening. Data are presented as mean ± SEM (n, number of animals). Differences between groups in LVIDd, LV mass, E, EF, V_{cf}, S′, and DT were analyzed by one-way ANOVA followed by Tukey's multiple comparison test. Differences between groups in HR, LA, RWT, E/A, E/e′, e′, and IVRT were analyzed using non-parametric Kruskal–Wallis test followed by Dunn's test for multiple comparisons. For SV, data were analyzed by Brown–Forsythe and Welch ANOVA test followed by Dunnett's multiple comparison test. *Significantly different vs. NTG/PLN, ‡significantly different vs. TG/PLN. *** or ‡‡‡$P < 0.001$, ** or ‡‡$P < 0.01$, * or ‡$P < 0.05$.*

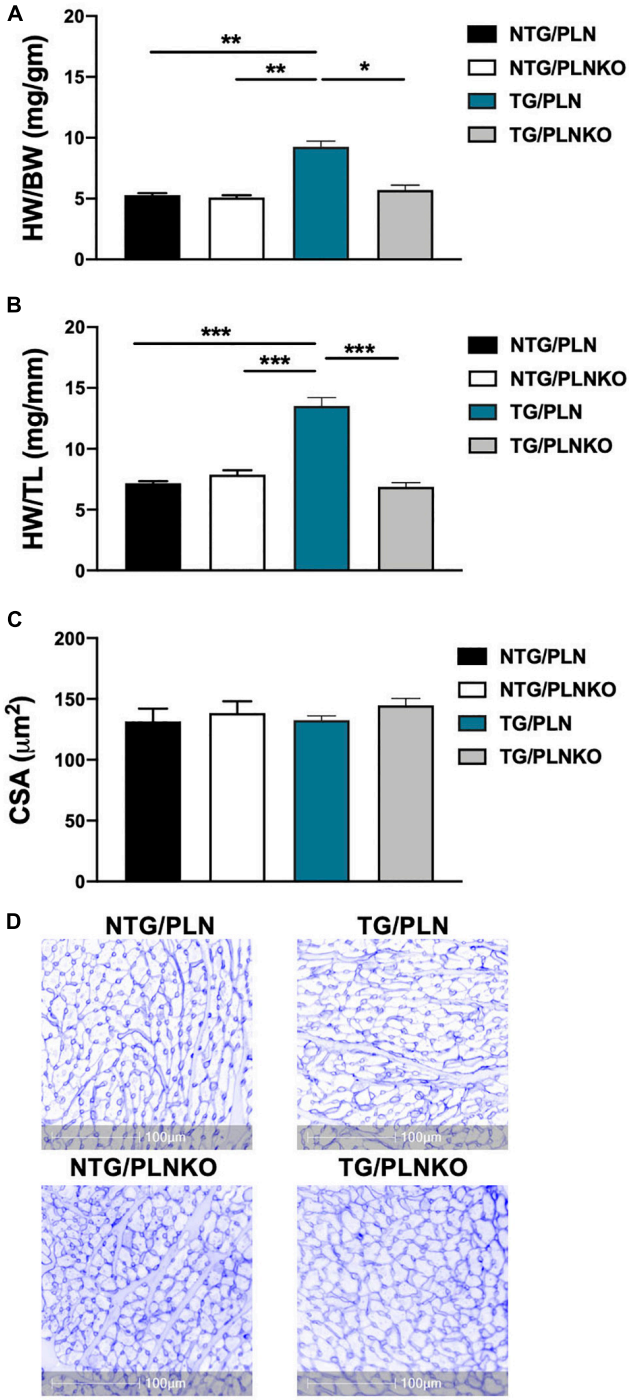

FIGURE 2 | Evaluation of cardiac hypertrophy. Summary data of **(A)** heart weight to body weight (HW/BW) ratio, **(B)** heart weight to tibia length (HW/TL) ratio, and **(C)** cross-sectional area (CSA) of cardiac myocytes calculated from cardiac cross section stained with wheat germ agglutinin (WGA). **(D)** Representative images of cardiac cross section stained with WGA. Data are presented as means ± SEM. Differences among HW/TL and CSA groups by one-way ANOVA followed by Tukey's multiple comparison test. Differences among HW/BW groups were determined using Kruskal–Wallis test followed by Dunn's multiple comparison test. N = 6–11 per group. $^{*}P < 0.05$, $^{**}P < 0.01$, $^{***}P < 0.001$.

CSR in the epicardium (panels D, E). RS in the long axis was not significantly reduced in the TG/PLN group compared to the NTG/PLN group (**Figure 5A**). Nonetheless, RS in the short axis (**Figure 5B**) and RSR in both the long and short axes (**Figures 5C,D**) were depressed in the TG/PLN group. Importantly, PLN ablation was able to restore all the parameters to normal levels in TG mice (**Figures 5B–D**).

Fibrosis Is Upregulated in Troponin T-R92Q Mice but Not Altered in Transgenic-Phospholamban Knockout Mice

Since both atrial morphology and diastolic function were altered in TG/PLN mice but remained normal in TG/PLNKO mice, we tested whether there is a difference in the degree of fibrosis between the groups. Histological analysis showed myocyte disarray and increased collagen deposition in TG/PLN hearts compared to other groups (**Figures 6A,B**). Increased collagen content seen in histological sections in TG/PLN mice quantified with the HOP assay showed increased HOP content only in TG/PLN hearts (**Figure 6C**). Taken together, these data indicate an increase in fibrosis only in TG/PLN mice.

Phospholamban Knockout Does Not Alter Myofilament Response to Ca^{2+}

To test whether altered myofilament sensitivity contributes to the functional and morphological improvement in TG/PLNKO mice, we measured the force–Ca^{2+} relationship in detergent-extracted fiber bundles from papillary muscles in NTG/PLN, NTG/PLNKO, TG/PLN, and TG/PLNKO mice (**Figure 7**). Consistent with previous reports on the TnT-R92Q mouse model in the C57BL/6 genetic background (Chandra et al., 2001), myofilaments from TG/PLN hearts showed a significantly increased Ca^{2+} sensitivity compared to myofilaments from NTG/PLN mice [pCa_{50} = 6.04 ± 0.02 (n = 5) vs. 5.79 ± 0.02 (n = 5)]. PLNKO did not result in altered myofilament Ca^{2+} sensitivity in either group (pCa_{50} = 5.75 ± 0.02, n = 6 in NTG/PLNKO mice and 6.03 ± 0.04, n = 5 in TG/PLNKO mice). Increased myofilament Ca^{2+} sensitivity observed in the TG groups was associated with a reduction in cooperativity, as measured by the Hill coefficient (**Figure 7C**) and decreased max tension only in the TG/PLNKO group (**Figure 7D**).

Phosphorylation of Cardiac Myofilament Proteins Is Not Altered, but Expression of β-MHC Isoform Is Increased in Transgenic/Phospholamban Mice

The expression of different myofilament isoforms and their post-translational modifications are known to affect myofilament properties (Kobayashi and Solaro, 2005; van der Velden and Stienen, 2019) and could contribute to the recovered cardiac function. We therefore investigated the phosphorylation status of myofilament proteins (**Figure 8A**). There were no changes in titin, tropomyosin, MyBP-C, or desmin phosphorylation among all groups. However, there was an increase in TnT

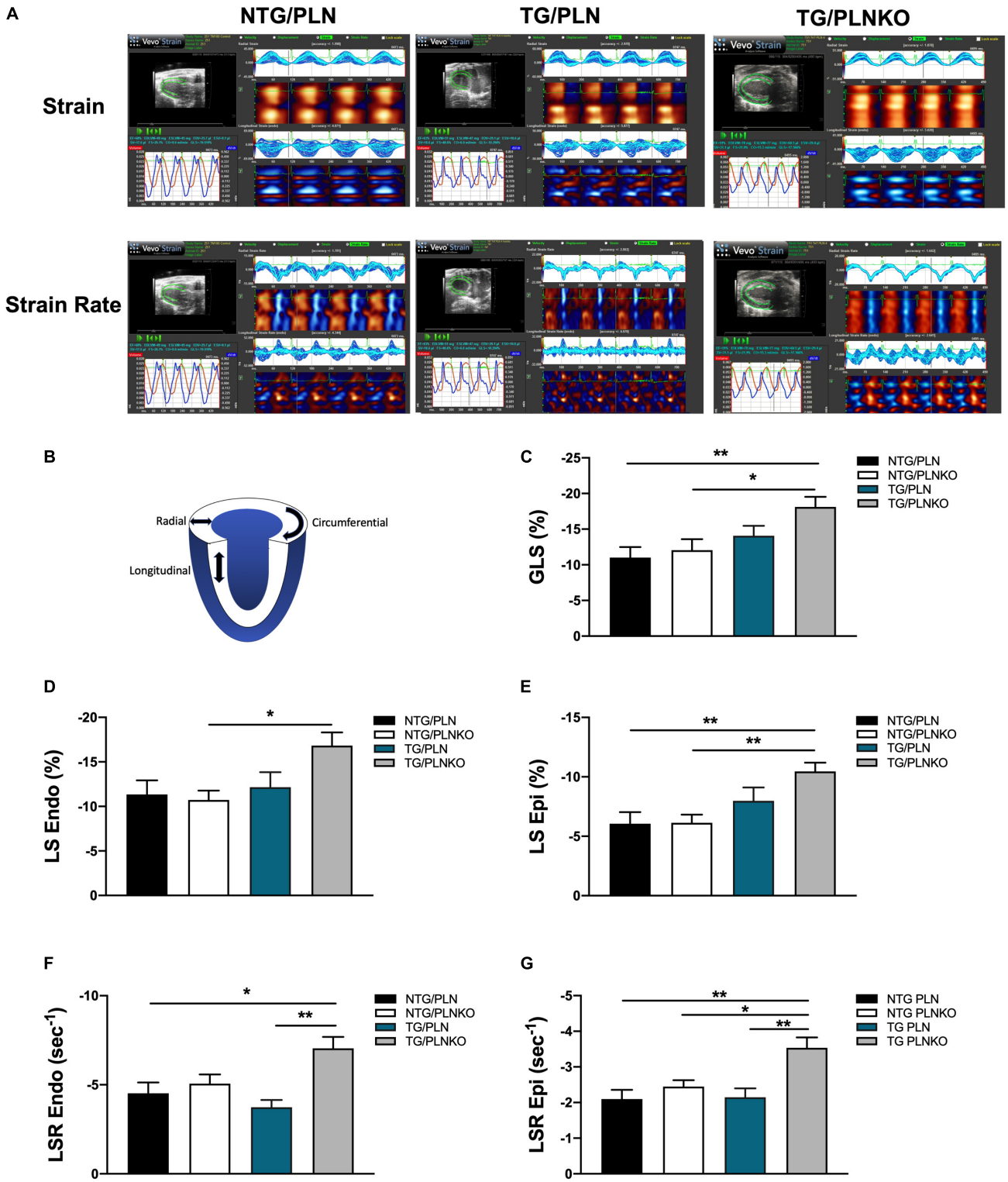

FIGURE 3 | Longitudinal strain (LS) measurements by echocardiography. **(A)** Representative images of speckle-tracking echocardiography in non-transgenic (NTG)/phospholamban (PLN), transgenic (TG)/PLN, and TG/phospholamban knockout (PLNKO) mice. **(B)** Schematic drawing of left ventricle with indication of longitudinal (LS), radial, and circumferential strain measurements. Summary of **(C)** global LS (GLS), **(D)** LS in endocardium (LS Endo), **(E)** LS in epicardium (LS Epi), **(F)** LS rate (LSR) in endocardium (LSR Endo), and **(G)** LSR in epicardium (LSR Epi) in the NTG/PLN, NTG/PLNKO, TG/PLN, and TG/PLNKO groups. Data are presented as means ± SEM. N = 7–12. Differences among groups were analyzed by one-way ANOVA followed by Tukey's multiple comparison test. $^{*}P < 0.05$, $^{**}P < 0.01$, $^{***}P < 0.001$.

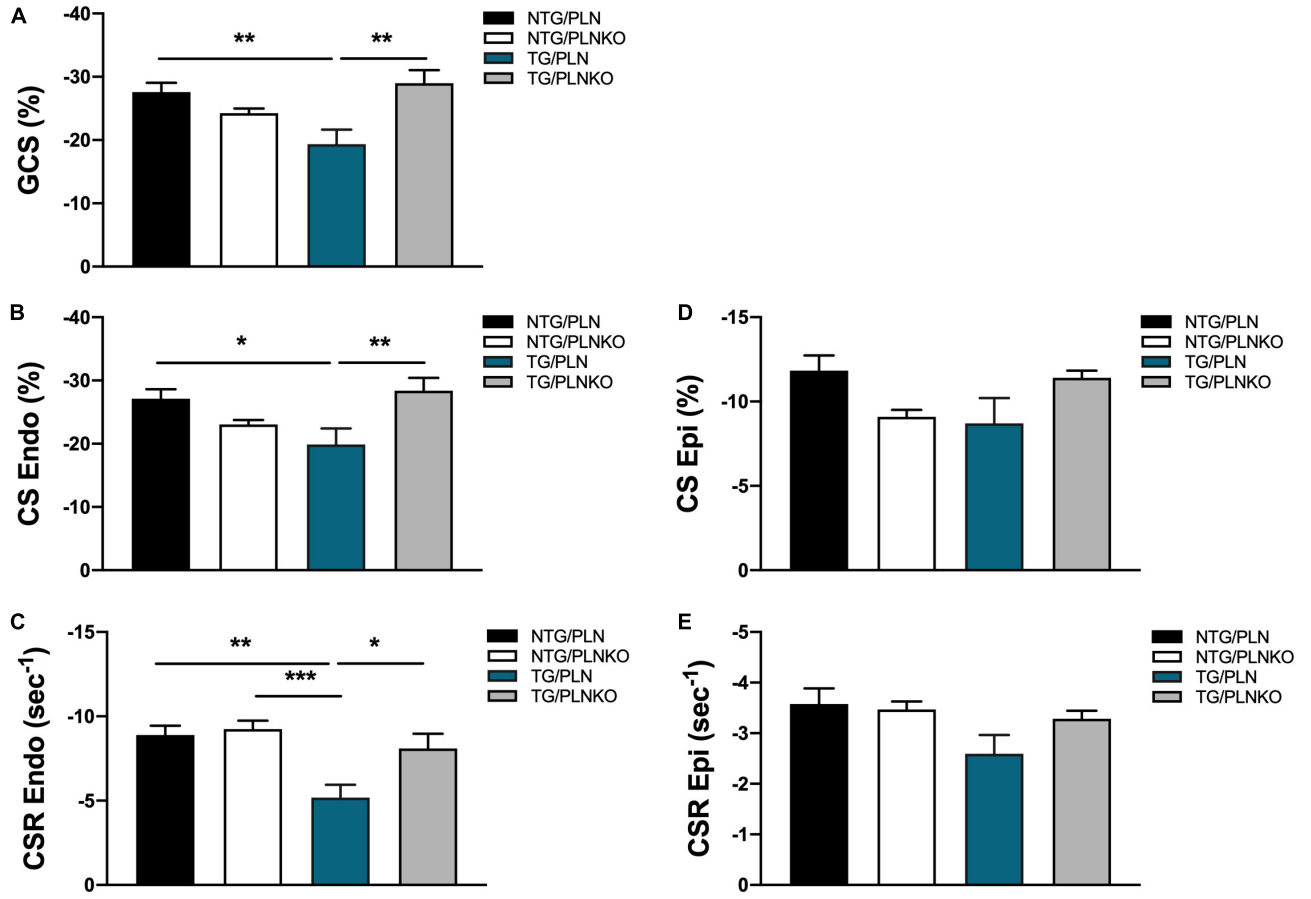

FIGURE 4 | Circumferential strain (CS) measurements by echocardiography. Summary of **(A)** global CS (GCS), **(B)** CS in endocardium (CS Endo), **(C)** CS rate in endocardium (CSR Endo), **(D)** CS in epicardium (CS Epi) and **(E)** CSR in epicardium (CSR Epi) in non-transgenic (NTG)/phospholamban (PLN), NTG/phospholamban knockout (PLNKO), transgenic (TG)/PLN and TG/PLNKO groups. Data are presented as means ± SEM. Differences among GCS, CS Endo, CSR Endo and CSR Epi groups were analyzed by one-way ANOVA followed by Tukey's multiple comparisons test. Differences among CS Ep groups were analyzed using Kruskal-Wallis test followed by Dunn's multiple comparison test. $N = 7–12$ $^{*}p < 0.05$, $^{**}P < 0.01$, $^{***}P < 0.001$.

phosphorylation and a decrease in phosphorylation of MLC2 in the TG/PLNKO group compared to the NTG/PLN group (**Figures 8B–H**), indicating the presence of some compensatory mechanisms. Since the expression of TnT-R92Q may alter myofilament Ca^{2+} sensitivity, we assessed the levels of abundance of TnT-R92Q in TG/PLN and TG/PLNKO hearts but found that both groups had similar levels of TnT-R92Q (**Figures 8I,J**). In previous studies with another model of HCM (Tm-E180G) (Ryba et al., 2019), we showed an increased expression of the fetal β-MHC isoform. We, therefore, tested MHC isoform population in all four groups of mice. We found a significant expression of the fetal β-MHC isoform in TnT/PLN mice, which was reduced in the TnT/PLNKO group, but did not reach levels seen in NTG groups (**Figures 8K,L**). We have also previously reported that S-glutathionylation of cMyBP-C is increased in Tm-E180G mice and contributes to the increased myofilament Ca^{2+} sensitivity. Thus, we tested the level of S-glutathionylation of cMyBP-C in the NTG and TG groups but found no changes between groups (**Figures 8M–O**).

Expression of Sarco(endo)plasmic Reticulum Ca^{2+} ATPase (SERCA)2a, Phospholamban, and Ca^{2+}/Calmodulin-Dependent Protein Kinase II

Modification or expression of the Ca^{2+}-regulatory proteins PLN and SERCA has been implicated in the regulation of inotropy and lusitropy in the heart. We investigated the level of SERCA expression in NTG/PLN, NTG/PLNKO, TG/PLN, and TG/PLNKO hearts (**Figures 9A,B**) and found a significant reduction in SERCA2 expression in the TG/PLN group only compared to the NTG/PLNKO group. No differences in the expression of PLN or phosphorylation at Ser16 and Thr17 were found between the NTG/PLN and TG/PLN groups (**Figures 9C–H**).

Changes in CaMKII signaling have been previously reported in human and mouse models of HCM (Helms et al., 2016; Lehman et al., 2019). We, therefore, also assessed the levels of expression and phosphorylation of CaMKII in our mice. The total

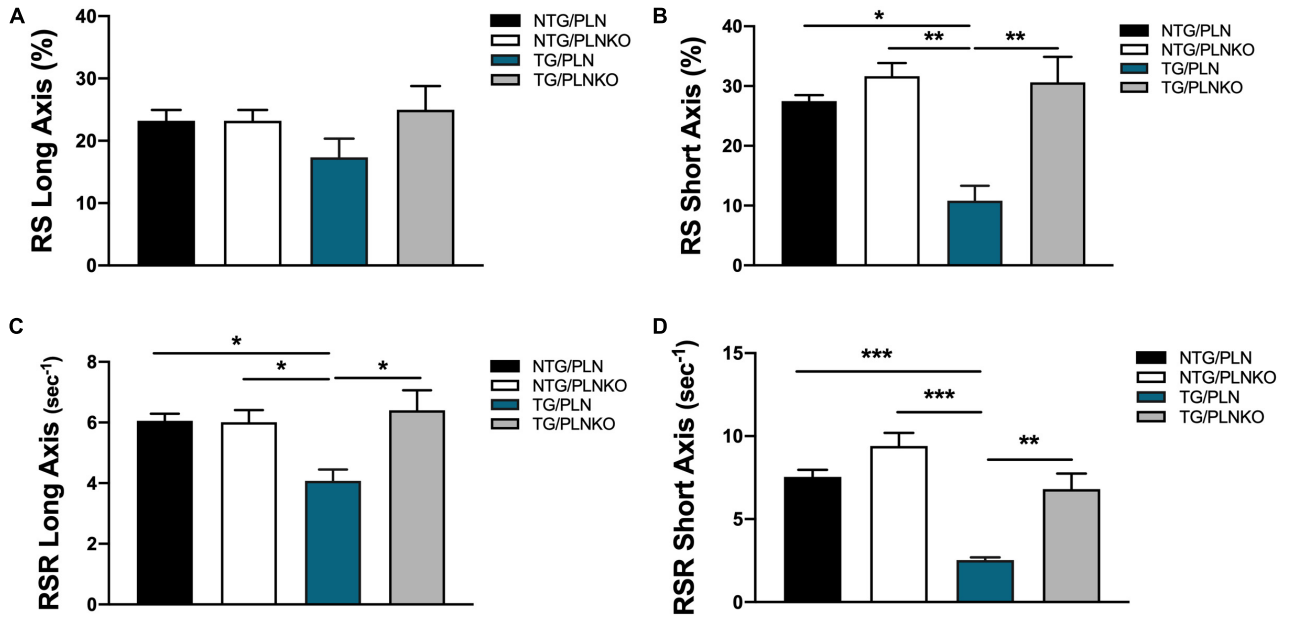

FIGURE 5 | Radial strain measurements by echocardiography. Summary of **(A)** radial strain (RS) in long axis, **(B)** RS in short axis, **(C)** radial strain rate (RSR) in long axis, and **(D)** radial strain rate (RSR) in short axis. Data are presented as means ± SEM. Differences among RS, RS in short axis, and RSR in long axis groups were analyzed by one-way ANOVA followed by Tukey's multiple comparison test. Differences among RSR in short axis were analyzed using Brown–Forsythe and Welch ANOVA tests followed by Dunnett's T3 test for multiple comparisons. $N = 7–12$. $^{*}P < 0.05$, $^{**}P < 0.01$, $^{***}P < 0.001$.

abundance of CaMKII was not different among these groups. However, phosphorylation of CaMKII was significantly increased in the TG/PLN group compared to the other NTG groups but was normalized by PLN ablation in the TG/PLNKO group (**Figures 9I–K**).

DISCUSSION

A major novel finding from experiments reported here is the demonstration that PLNKO was able to prevent the development of the HCM disorder in the TG mouse model without altering the increases in myofilament Ca^{2+} sensitivity or their phosphorylation. Our results strongly suggest that the rescue of the HCM phenotype involved an increased activity of SERCA2 that resulted in normal relaxation, prevention of an increased phosphorylation of CaMKII, development of fibrosis, and diminished activation of the "fetal/hypertrophic gene program." We also found that compared to standard systolic echo parameters such as EF, speckle strain measurements provide a more sensitive approach to detect systolic dysfunction in our model of HCM.

An important aspect of our findings is that mice expressing mutated TnT-R92Q in FVB/N genetic background develop profound atrial dilation without LV hypertrophy compared to smaller LV size (Tardiff et al., 1999) or septal hypertrophy (Coppini et al., 2017) previously reported in C57BL/6 genetic background most likely due to differential presence of modifying genes in these two genetic backgrounds. Moreover, more severe diastolic dysfunction and systolic dysfunction, observed by speckle-tracking echocardiography, were observed compared to the originally reported about 20% decrease in diastolic function and 18% improvement in systolic function measured in working heart preparation (Tardiff et al., 1999). Recently, Ferrantini et al. (2017) using echocardiography reported a small (about 5%) increase in EF and reduced E/A ratio from about 1.4 to 1.0 in mice with TnT-R92Q mutation. Interestingly, independent of the genetic background, hearts with the TnT-R92Q mutation show increased fibrosis (Tardiff et al., 1999; Ferrantini et al., 2017) and myofilament Ca^{2+} sensitivity (delta $pCa_{50} = 0.28$) (Chandra et al., 2001), which are all characteristics of HCM in both human and mouse models (Ashrafian et al., 2011; Frey et al., 2012). Our findings demonstrate that the genetic background of the mice influences the HCM phenotype caused by TnT-R92Q mutation. Moreover, it has been previously presented in two HCM mouse models that mice expressing tropomyosin (Tm-E180G) developed a more pronounced hypertrophic phenotype in FVB/N than in C57BL/6 genetic background (Prabhakar et al., 2001; Michele et al., 2002), and in mice with a mutation in actin (ACTZ E99K), the probability of sudden cardiac death was almost completely eliminated in mice bred on C57/BL6 background (Rowlands et al., 2017). The importance of the mouse genetic background on the basal cardiac function, adaptations to exercise, or stress is also well-documented (Barnabei et al., 2010; Peng et al., 2011; Gibb et al., 2016).

Increased myofilament Ca^{2+} sensitivity observed in HCM can be directly targeted or counterbalanced by alteration of Ca^{2+} fluxes (Alves et al., 2010). We (Alves et al., 2014; Warren et al., 2015) and others (Tadano et al., 2010) have previously reported the beneficial effects of targeting directly the myofilament Ca^{2+} sensitivity in HCM. Since on the cellular level, diastolic function is regulated by both myofilament Ca^{2+} responsiveness and

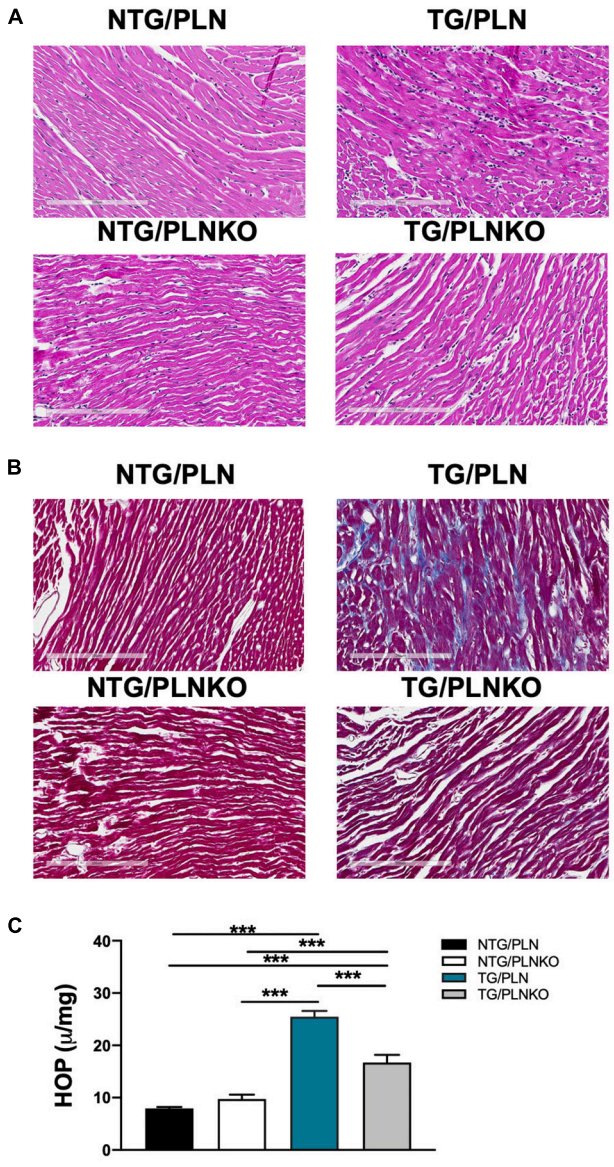

FIGURE 6 | Histology and hydroxyproline (HOP) assay of non-transgenic (NTG)/phospholamban (PLN), NTG/phospholamban knockout (PLNKO), transgenic (TG)/PLN, and TG/PLNKO mouse hearts. Representative left ventricular (LV) heart sections stained with **(A)** hematoxylin and eosin and **(B)** Masson's trichrome (MT). The intense myocyte disarray is depicted in H&E-stained sections, and extensive fibrosis is observed in MT-stained sections (blue stain) in TG/PLN hearts. TG/PLNKO hearts show less disarray and fibrosis than TG/PLN hearts. **(C)** Hydroxyproline content. Data are presented as means ± SEM. $N = 6$ per group. Differences among groups were analyzed by one-way ANOVA followed by Tukey's multiple comparison test. $^{*}P < 0.05$, $^{**}P < 0.01$, $^{***}P < 0.001$.

Ca^{2+} fluxes, several studies targeted mechanisms involved in E-C coupling. It has been shown that L-type Ca^{2+} channel blocker, diltiazem, has a favorable effect in HCM with mutation in alpha MHC (Arg403Gln) (Semsarian et al., 2002), and buffering of Ca^{2+} with parvalbumin corrected slower relaxation in adult cardiac myocytes expressing mutated Tm (Tm-E180G, Tm-A63V) (Coutu et al., 2004). We have previously shown that HCM Tm-E180G mice can be rescued either by partially restoring myofilament Ca^{2+} sensitivity (Alves et al., 2014) or by increased SERCA2 activity by PLNKO or increased expression of SERCA2 (Pena et al., 2010; Gaffin et al., 2011). Data from these experiments indicated that SERCA2 activity may be a good target for HCM linked to mutations associated with increased myofilament Ca^{2+} sensitivity, but PLNKO failed to rescue hypertrophy caused by a truncation in thick filament, MYBP-C (Song et al., 2003). Moreover, the potential benefits of PLN ablation have not been directly tested in any other model with mutations in thin filament proteins besides the Tm-E180G HCM mouse. TG TnT-R92Q C57BL/6 mice were reported to show decreased SERCA2 and increased CaMKII activity that resulted in an increased level of diastolic Ca^{2+} (Ferrantini et al., 2017). In our current studies, differences in the expression levels of SERCA2 between the NTG/PLN and TG/PLN groups did not reach significance, although we saw a clear trend toward lower levels in the TG/PLN group with a significant difference between the TG/PLN and NTG/PLNKO groups. These results indicate potential dysregulation of E-C coupling and successful rescue of the TnT-R92Q model of HCM in the FVB/N background.

In addition, consistent with the previous report in mice expressing the same mutation (Ferrantini et al., 2017), we found a significantly increased phosphorylation level of CaMKII, which was completely normalized in mice rescued by PLNKO (TG/PLNKO). Chronic activation of CaMKII was recently reported in human samples from mutation-positive HCM (Helms et al., 2016) and in other HCM mouse models with TnT-R92L and TnT-R92W mutations (Lehman et al., 2019). These data suggest that CaMKII activation plays a role in progression of the disease in HCM and may serve as a therapeutic target, but only for a particular cohort of patients with specific mutations, since inhibition of CaMKII resulted in recovery of diastolic function only in the R92W but not in R92L mice (Lehman et al., 2019). Why inhibition of CaMKII only works for some mutations is not completely understood. Another intriguing finding is that in TG/PLN mice, activation of CaMKII did not result in altered phosphorylation of PLN at Thr17, that was previously reported in ketoconazole-treated TnT-R92Q C57BL/6 mice (Coppini et al., 2017) and in human samples from mutation-positive HCM patients (Helms et al., 2016). Phosphorylation level of CaMKII was normal in hearts of mice rescued by PLNKO. We think that the most likely mechanism for the normalization is an increased SR Ca^{2+} uptake and improved relaxation that led to a reduction in local mechanical strain caused by R92Q mutation. Along these lines, it has been proposed that increased mechanical strain observed in TnT-R92Q mice results in activation of CaMKII (Jian et al., 2014). It is also possible that initially, there is an increase in PLN Thr17 associated with improved systolic function, but during progression of the disease, the level of PLN phosphorylation decreases as the heart remodels and systolic function starts to decline as we observed in this study.

Our data support the hypothesis that speckle-tracking strain measurements especially circumferential and radial parameters, which indicate impairment in systolic function, may be

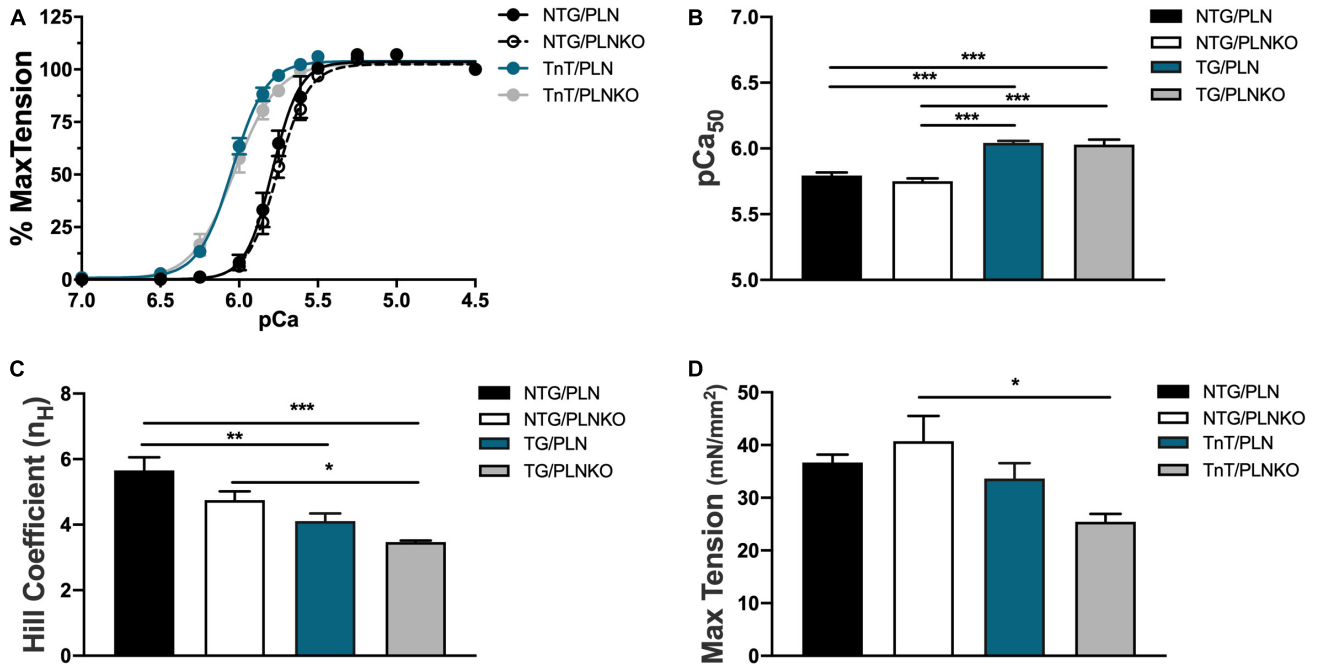

FIGURE 7 | The myofilament Ca^{2+} response is increased in transgenic (TG) mice. **(A)** Force–Ca^{2+} relationship of fibers isolated from non-transgenic (NTG)/phospholamban (PLN), NTG/phospholamban knockout (PLNKO), TG/PLN, and TG/PLNKO mice. Summary data of **(B)** myofilament Ca^{2+} sensitivity [Ca^{2+} concentration of half-maximal activation (pCa_{50})], **(C)** cooperativity measured by the Hill coefficient (n_H), and **(D)** maximal tension generation. Data are presented as means ± SEM. N = 5–6. Differences among groups were analyzed by one-way ANOVA followed by Tukey's multiple comparison test. $^*P < 0.05$, $^{**}P < 0.01$, $^{***}P < 0.001$.

a more sensitive early marker for systolic dysfunction in HCM. We show that at 16 weeks of age, systolic function based on EF is not altered in TG/PLN mice compared to other groups, whereas there is a significant change in strain parameters. Use of the speckle-tracking technique to detect mechanical dyssynchrony before organ failure in a K_{ATP} channel-knockout mouse model of dilated cardiomyopathy has been previously reported by Yamada et al. (2013). The authors showed evidence that speckle-tracking echocardiography was able to detect myocardial changes at a time point when standard echocardiographic parameters did not detect any changes. RS, LS, and reverse LS compared to conventional echocardiographic measurements were also reported to be more sensitive to detect early changes in LV diastolic and systolic function in aging (de Lucia et al., 2019). On the other hand, Peng et al. (2009) have previously reported that TAC-induced heart failure and fibrotic changes were better tracked by CS measurements rather than RS measurements. These conflicting data may suggest that a full range of strain-derived measurements should be included in addition to conventional echo parameters in early detection of cardiac dysfunction. Moreover, recent human data showed that strain measurements permit detection of abnormalities in myocardial mechanics before the development of clinical hypertrophy (Williams et al., 2018). Data also indicate that abnormal GLS is an independent factor associated with poor cardiac outcomes (Reant et al., 2016; Liu et al., 2017).

Improvement in diastolic function in TG/PLNKO mice was not associated with significant changes in myofilament Ca^{2+} sensitivity. This lack of change in myofilament Ca^{2+} sensitivity correlates well with the lack of changes in myofilament phosphorylation and in no increase in S-glutathionylation of MyBP-C. Interestingly, in contrast to our findings with the TnT-R92Q mice, the Tm-E180G HCM mouse model demonstrated increased oxidative stress and expression of NOX2 that resulted in S-glutathionylation of MyBP-C. The result was a further increase in myofilament Ca^{2+} sensitivity that was rescued by treatment with FTY720 (fingolimod) (Ryba et al., 2019) or NAC treatment (Wilder et al., 2015). FTY720 treatment improved diastolic function mainly through reversal of S-glutathionylation of MyBP-C without affecting fibrosis. Here, we did not find changes in myofilament Ca^{2+} sensitivity, but prevention of fibrosis. These data suggest that several mechanisms contribute to diastolic dysfunction in HCM, and their contribution and therefore treatment may be mutation dependent.

In summary, our results indicate that targeting diastolic dysfunction through altering Ca^{2+} fluxes was able to prevent the development of the HCM phenotype and should be considered as a potential new therapeutic target for HCM patients. Current therapies involve a focus on sarcomere myosin de-activators such as mavacamten, developed largely based on mutations and truncations in the thick filament proteins (Green et al., 2016). However, as emphasized by Maron et al. (2019), the heterogeneity

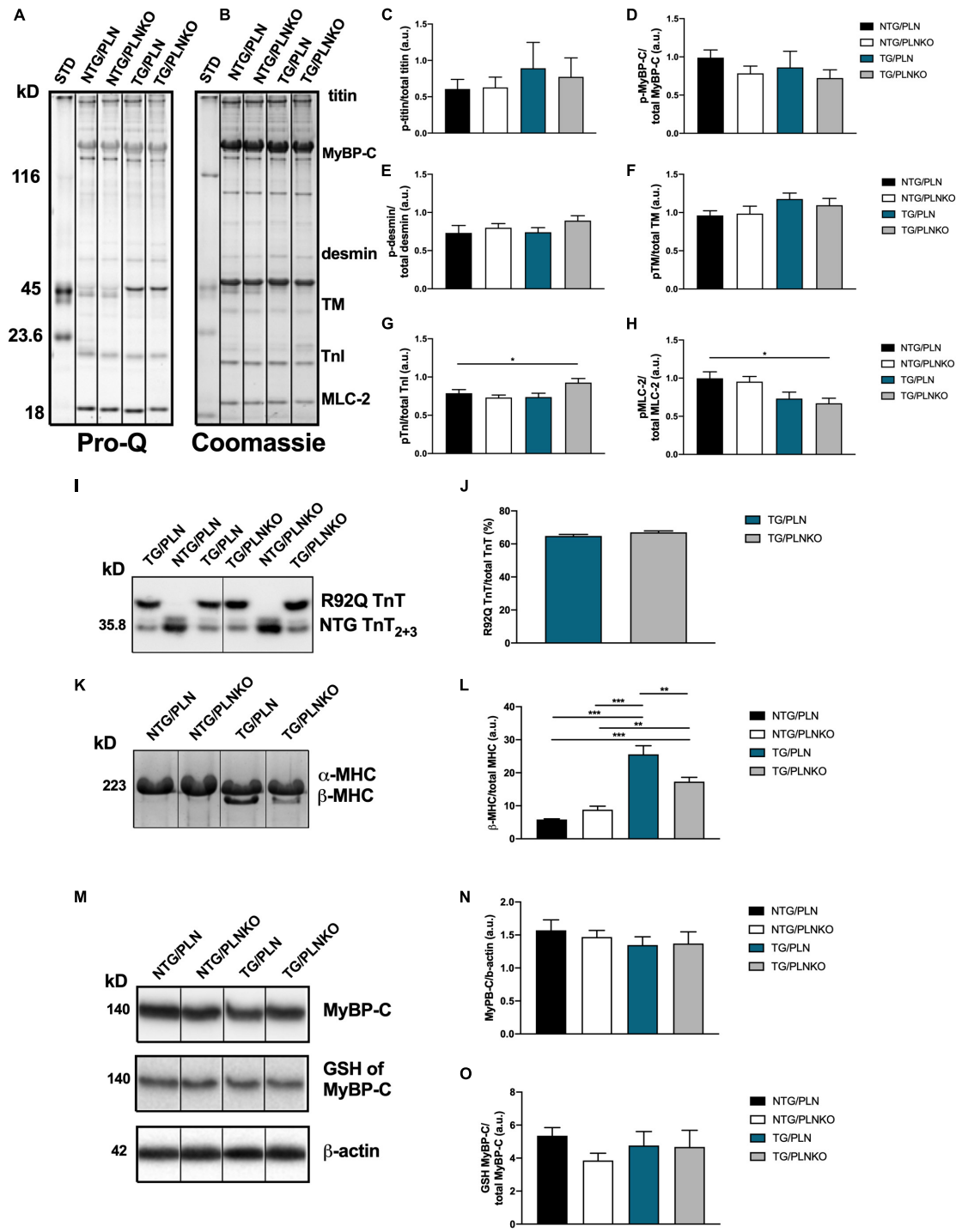

FIGURE 8 | Myofilament isoform abundance and modifications in non-transgenic (NTG)/phospholamban (PLN), NTG/phospholamban knockout (PLNKO), transgenic (TG)/PLN, and TG/PLNKO mice. **(A)** Representative Pro-Q gel image. **(B)** Representative Coomassie blue gel image. Summary of phosphorylation data of **(C)** titin, **(D)** myosin binding protein C (p-MyBP-C), **(E)** desmin, **(F)** tropomyosin (TM), **(G)** troponin I (TnI), and **(H)** myosin light chain 2 (MLC-2). Phosphorylation of each myofilament protein was calculated from Pro-Q image **(A)** and normalized to total abundance of these proteins from Coomassie gel **(B)**. **(I,J)** Abundance of mutated TnT-R92Q protein in TG/PLN and TG/PLNKO hearts. TnT_{2+3} refers to isoforms of TnT, and the R92Q TnT has a myc-tag that allows for a molecular weight distinction with the NTG TnT. **(K)** Sodium dodecyl sulfate–polyacrylamide gel electrophoresis (SDS-PAGE) Coomassie blue gel image of myosin heavy chain (MHC) isoforms. **(L)** Summary data of MHC isoforms. **(M)** Western blot analysis of myosin binding protein C (MyBP-C), S-glutathionylation (GSH) of MyBP-C and β-actin. **(N)** Summary abundance of MyBP-C. **(O)** Summary data of GSH of MyBP-C. Data are presented as means ± SEM. $N = 4–6$. Differences among four groups were analyzed by one-way ANOVA followed by Tukey's multiple comparison test. If only two groups were compared, unpaired *t*-test was used. $^{*}P < 0.05$, $^{**}P < 0.01$, $^{***}P < 0.001$.

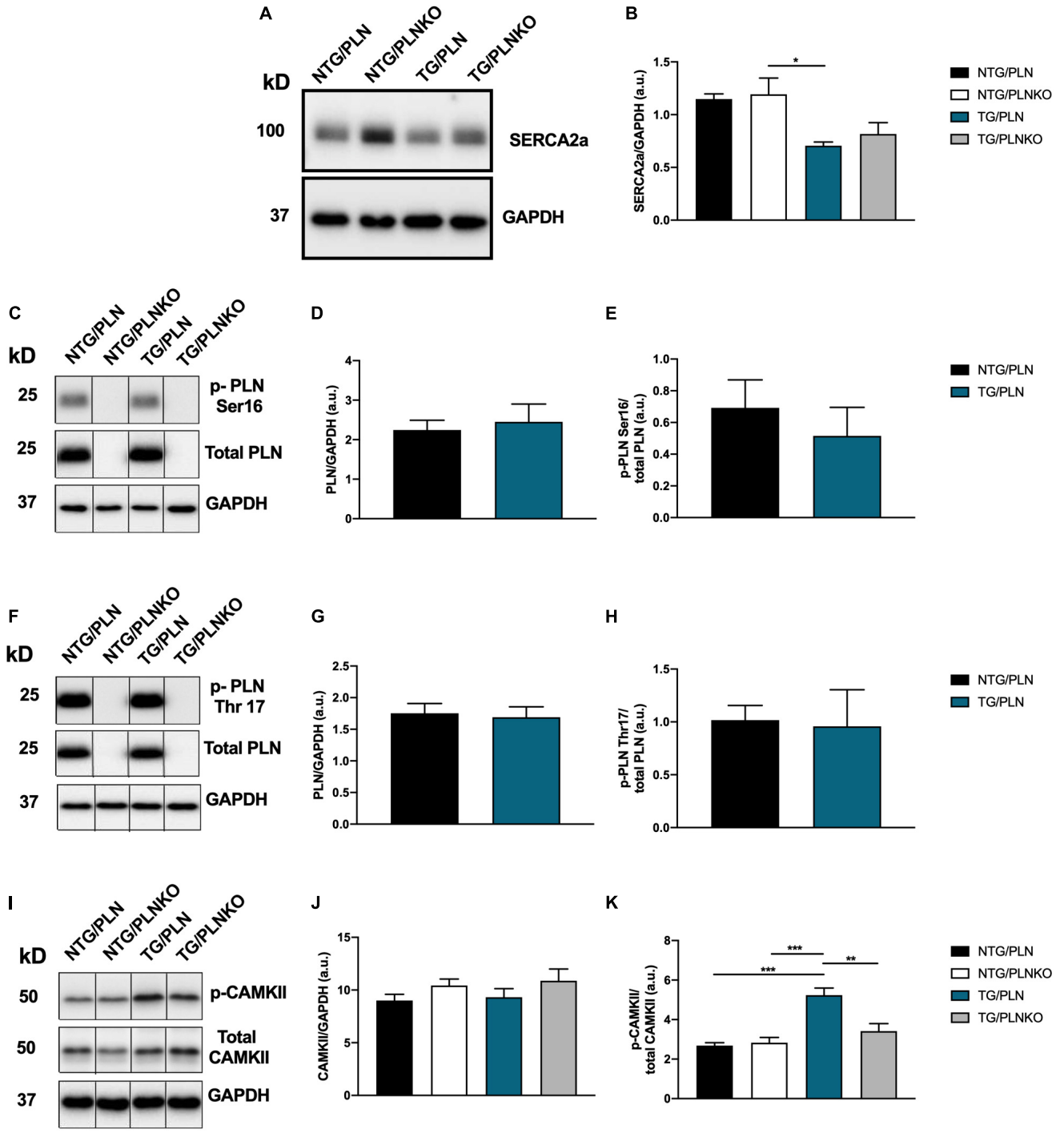

FIGURE 9 | Expression of Ca^{2+} regulatory proteins. **(A)** Representative Western blot of sarco(endo)plasmic reticulum Ca^{2+} ATPase (SERCA)2 and glyceraldehyde 3-phosphate dehydrogenase (GAPDH), and **(B)** summary data of SERCA2a show no significant changes between transgenic (TG)/phospholamban (PLN) and TG/phospholamban knockout (PLNKO) groups. **(C)** Representative Western blot of phosphorylation PLN expression and phosphorylation at Ser16 (p-PLN Ser16) and GAPDH. Summary data show no significant changes in PLN abundance **(D)** and p-PLN Ser16 **(E)** between the non-transgenic (NTG)/PLN and TG/PLN groups. **(F)** Representative Western blot of PLN expression and phosphorylation at Thr17 (p-PLN Thr17) and GAPDH. Summary data show no significant changes in PLN expression **(G)** and p-PLN Thr17 **(H)** between the NTG/PLN and TG/PLN groups. **(I)** Representative Western blot of CaMKII abundance, phosphorylation (T287), and GAPDH. Summary data show no significant changes in CaMKII expression **(J)** but increased phosphorylation of CaMKII **(K)** in TG/PLN group. Data are presented as means ± SEM. $N = 4–6$. Differences among groups were analyzed by one-way ANOVA followed by Tukey's multiple comparison test. If only two groups were compared, unpaired *t*-test was used. $^{*}P < 0.05$, $^{**}P < 0.01$, $^{***}P < 0.001$.

of the pathobiology and genetics in HCM may require approaches in precision medicine. These approaches permit formulation of a network medicine analysis with aspects of personalized medicine in which it is likely that therapies may include both sarcomere tension-directed therapies and therapies altering Ca^{2+} fluxes.

DATA AVAILABILITY STATEMENT

The datasets generated for this study are available on request to the corresponding author.

ETHICS STATEMENT

The animal study was reviewed and approved by Office of Animal Care and Institutional Biosafety Committee at UIC.

AUTHOR CONTRIBUTIONS

SC performed and calculated the echocardiographic, histology, and HOP experiments. CW, DR, and AB performed and analyzed the biochemical experiments. JS performed and analyzed the skinned fiber experiments. EK provided the PLNKO mouse model and edited the manuscript. JT provided the TnT-R92Q mouse model. BW and RS were involved in designing the experiments, writing the manuscript, and financial support. CW contributed also to the financial support. PV was involved in the preparation and review of the manuscript.

FUNDING

Our work was supported by NIH grants R01 HL128468 (to BW and RS) and P01 HL062426 Project 1 and Core C (to RS and CW) and by a grant from the Leducq Foundation (EK).

ACKNOWLEDGMENTS

Part of the work presented in this manuscript was used to partially fulfill the Ph.D. requirement for Shamim Ara Khan Chowdhury at Bangabandhu Sheikh Mujib Medical University (BSMMU), Dhaka, Bangladesh. We thank Professor Dr. Noorzahan Begum for supervision of Dr. Chowdhury's work at the Department of Physiology, BSMMU.

REFERENCES

Alves, M. L., Dias, F. A. L., Gaffin, R. D., Simon, J. N., Montminy, E. M., Biesiadecki, B. J., et al. (2014). Desensitization of myofilaments to Ca2+ as a therapeutic target for hypertrophic cardiomyopathy with mutations in thin filament proteins. *Circ. Cardiovasc. Genet.* 7, 132–143. doi: 10.1161/CIRCGENETICS.113.000324

Alves, M. L., Gaffin, R. D., and Wolska, B. M. (2010). Rescue of familial cardiomyopathies by modifications at the level of sarcomere and Ca2+ fluxes. *J. Mol. Cell. Cardiol.* 48, 834–842. doi: 10.1016/j.yjmcc.2010.01.003

Anderson, P. A., Malouf, N. N., Oakeley, A. E., Pagani, E. D., and Allen, P. D. (1991). Troponin T isoform expression in humans. A comparison among normal and failing adult heart, fetal heart, and adult and fetal skeletal muscle. *Circ. Res.* 69, 1226–1233. doi: 10.1161/01.res.69.5.1226

Arad, M., Seidman, J. G., and Seidman, C. E. (2002). Phenotypic diversity in hypertrophic cardiomyopathy. *Hum. Mol. Genet.* 11, 2499–2506. doi: 10.1093/hmg/11.20.2499

Ashrafian, H., McKenna, W. J., and Watkins, H. (2011). Disease pathways and novel therapeutic targets in hypertrophic cardiomyopathy. *Circ. Res.* 109, 86–96. doi: 10.1161/CIRCRESAHA.111.242974

American Veterinary Medical Association (2013). *AVMA Guidelines for the Euthanasia of Animals: 2013 Edition*. Schamburg, IL.

Barnabei, M. S., Palpant, N. J., and Metzger, J. M. (2010). Influence of genetic background on ex vivo and in vivo cardiac function in several commonly used inbred mouse strains. *Physiol. Genomics* 42A, 103–113. doi: 10.1152/physiolgenomics.00071.2010

Bauer, M., Cheng, S., Jain, M., Ngoy, S., Theodoropoulos, C., Trujillo, A., et al. (2011). Echocardiographic speckle-tracking based strain imaging for rapid cardiovascular phenotyping in mice. *Circ. Res.* 108, 908–916. doi: 10.1161/CIRCRESAHA.110.239574

Chandra, M., Rundell, V. L., Tardiff, J. C., Leinwand, L. A., De Tombe, P. P., and Solaro, R. J. (2001). Ca(2+) activation of myofilaments from transgenic mouse hearts expressing R92Q mutant cardiac troponin T. *Am. J. Physiol. Heart Circ. Physiol.* 280, H705–H713.

Coppini, R., Mazzoni, L., Ferrantini, C., Gentile, F., Pioner, J. M., Laurino, A., et al. (2017). Ranolazine prevents phenotype development in a mouse model of hypertrophic cardiomyopathy. *Circ. Heart Fail.* 10:e003565. doi: 10.1161/CIRCHEARTFAILURE.116.003565

Coutu, P., Bennett, C. N., Favre, E. G., Day, S. M., and Metzger, J. M. (2004). Parvalbumin corrects slowed relaxation in adult cardiac myocytes expressing hypertrophic cardiomyopathy-linked alpha-tropomyosin mutations. *Circ. Res.* 94, 1235–1241. doi: 10.1161/01.res.0000126923.46786.fd

de Lucia, C., Wallner, M., Eaton, D. M., Zhao, H., Houser, S. R., and Koch, W. J. (2019). Echocardiographic strain analysis for the early detection of left ventricular systolic/diastolic dysfunction and dyssynchrony in a mouse model of physiological aging. *J. Gerontol. A Biol. Sci. Med. Sci.* 74, 455–461. doi: 10.1093/gerona/gly139

Deranek, A. E., Klass, M. M., and Tardiff, J. C. (2019). Moving beyond simple answers to complex disorders in sarcomeric cardiomyopathies: the role of integrated systems. *Pflugers Arch.* 471, 661–671. doi: 10.1007/s00424-019-02269-0

Ferrantini, C., Coppini, R., Pioner, J. M., Gentile, F., Tosi, B., Mazzoni, L., et al. (2017). Pathogenesis of hypertrophic cardiomyopathy is mutation rather than disease specific: a comparison of the cardiac troponin T E163R and R92Q mouse models. *J. Am. Heart Assoc.* 6:e005407. doi: 10.1161/JAHA.116.005407

Flesch, M., Schiffer, F., Zolk, O., Pinto, Y., Rosenkranz, S., Hirth-Dietrich, C., et al. (1997). Contractile systolic and diastolic dysfunction in renin-induced hypertensive cardiomyopathy. *Hypertension* 30, 383–391. doi: 10.1161/01.hyp.30.3.383

Frey, N., Luedde, M., and Katus, H. A. (2012). Mechanisms of disease: hypertrophic cardiomyopathy. *Nat. Rev. Cardiol.* 9, 91–100. doi: 10.1038/nrcardio.2011.159

Fritz, J. D., Swartz, D. R., and Greaser, M. L. (1989). Factors affecting polyacrylamide gel electrophoresis and electroblotting of high-molecular-weight myofibrillar proteins. *Anal. Biochem.* 180, 205–210. doi: 10.1016/0003-2697(89)90116-4

Gaffin, R. D., Pena, J. R., Alves, M. S., Dias, F. A., Chowdhury, S. A., Heinrich, L. S., et al. (2011). Long-term rescue of a familial hypertrophic cardiomyopathy caused by a mutation in the thin filament protein, tropomyosin, via modulation of a calcium cycling protein. *J. Mol. Cell. Cardiol.* 51, 812–820. doi: 10.1016/j.yjmcc.2011.07.026

Geisterfer-Lowrance, A. A., Kass, S., Tanigawa, G., Vosberg, H. P., McKenna, W., Seidman, C. E., et al. (1990). A molecular basis for familial hypertrophic cardiomyopathy: a beta cardiac myosin heavy chain gene missense mutation. *Cell* 62, 999–1006. doi: 10.1016/0092-8674(90)90274-i

Gersh, B. J., Maron, B. J., Bonow, R. O., Dearani, J. A., Fifer, M. A., Link, M. S., et al. (2011). 2011 ACCF/AHA guideline for the diagnosis and treatment of

hypertrophic cardiomyopathy: a report of the American College of Cardiology Foundation/American Heart Association task force on practice guidelines. *Circulation* 124, e783–e831.

Gibb, A. A., McNally, L. A., Riggs, D. W., Conklin, D. J., Bhatnagar, A., and Hill, B. G. (2016). FVB/NJ mice are a useful model for examining cardiac adaptations to treadmill exercise. *Front. Physiol.* 7:636. doi: 10.3389/fphys.2016.00636

Green, E. M., Wakimoto, H., Anderson, R. L., Evanchik, M. J., Gorham, J. M., Harrison, B. C., et al. (2016). A small-molecule inhibitor of sarcomere contractility suppresses hypertrophic cardiomyopathy in mice. *Science* 351, 617–621. doi: 10.1126/science.aad3456

Helms, A. S., Alvarado, F. J., Yob, J., Tang, V. T., Pagani, F., Russell, M. W., et al. (2016). Genotype-dependent and -independent calcium signaling dysregulation in human hypertrophic cardiomyopathy. *Circulation* 134, 1738–1748. doi: 10.1161/circulationaha.115.020086

Heydemann, A., Huber, J. M., Demonbreun, A., Hadhazy, M., and McNally, E. M. (2005). Genetic background influences muscular dystrophy. *Neuromuscul. Disord.* 15, 601–609. doi: 10.1016/j.nmd.2005.05.004

Hill, B. G., Ramana, K. V., Cai, J., Bhatnagar, A., and Srivastava, S. K. (2010). Measurement and identification of S-glutathiolated proteins. *Methods Enzymol.* 473, 179–197. doi: 10.1016/S0076-6879(10)73009-3

Jian, Z., Han, H., Zhang, T., Puglisi, J., Izu, L. T., Shaw, J. A., et al. (2014). Mechanochemotransduction during cardiomyocyte contraction is mediated by localized nitric oxide signaling. *Sci. Signal.* 7:ra27. doi: 10.1126/scisignal.2005046

Kobayashi, T., and Solaro, R. J. (2005). Calcium, thin filaments, and the integrative biology of cardiac contractility. *Annu. Rev. Physiol.* 67, 39–67. doi: 10.1146/annurev.physiol.67.040403.114025

Layland, J., Cave, A. C., Warren, C., Grieve, D. J., Sparks, E., Kentish, J. C., et al. (2005). Protection against endotoxemia-induced contractile dysfunction in mice with cardiac-specific expression of slow skeletal troponin I. *FASEB J.* 19, 1137–1139. doi: 10.1096/fj.04-2519fje

Lehman, S. J., Tal-Grinspan, L., Lynn, M. L., Strom, J., Benitez, G. E., Anderson, M. E., et al. (2019). Chronic calmodulin-kinase II activation drives disease progression in mutation-specific hypertrophic cardiomyopathy. *Circulation* 139, 1517–1529. doi: 10.1161/CIRCULATIONAHA.118.034549

Liu, H., Pozios, I., Haileselassie, B., Nowbar, A., Sorensen, L. L., Phillip, S., et al. (2017). Role of global longitudinal strain in predicting outcomes in hypertrophic cardiomyopathy. *Am. J. Cardiol.* 120, 670–675. doi: 10.1016/j.amjcard.2017.05.039

Marian, A. J. (2009). Experimental therapies in hypertrophic cardiomyopathy. *J. Cardiovasc. Transl. Res.* 2, 483–492. doi: 10.1007/s12265-009-9132-7

Marian, A. J., and Braunwald, E. (2017). Hypertrophic cardiomyopathy: genetics, pathogenesis, clinical manifestations, diagnosis, and therapy. *Circ. Res.* 121, 749–770. doi: 10.1161/CIRCRESAHA.117.311059

Maron, B. J., and Maron, M. S. (2016). Contemporary strategies for risk stratification and prevention of sudden death with the implantable defibrillator in hypertrophic cardiomyopathy. *Heart Rhythm* 13, 1155–1165. doi: 10.1016/j.hrthm.2015.12.048

Maron, B. J., Maron, M. S., Maron, B. A., and Loscalzo, J. (2019). Moving beyond the sarcomere to explain heterogeneity in hypertrophic cardiomyopathy: JACC review topic of the week. *J. Am. Coll. Cardiol.* 73, 1978–1986. doi: 10.1016/j.jacc.2019.01.061

Matsudaira, P. (1987). Sequence from picomole quantities of proteins electroblotted onto polyvinylidene difluoride membranes. *J. Biol. Chem.* 262, 10035–10038.

Michele, D. E., Gomez, C. A., Hong, K. E., Westfall, M. V., and Metzger, J. M. (2002). Cardiac dysfunction in hypertrophic cardiomyopathy mutant tropomyosin mice is transgene-dependent, hypertrophy-independent, and improved by beta-blockade. *Circ. Res.* 91, 255–262. doi: 10.1161/01.res.0000027530.58419.82

Patel, B. G., Wilder, T., and Solaro, R. J. (2013). Novel control of cardiac myofilament response to calcium by S-glutathionylation at specific sites of myosin binding protein C. *Front. Physiol.* 4:336. doi: 10.3389/fphys.2013.00336

Pena, J. R., Szkudlarek, A. C., Warren, C. M., Heinrich, L. S., Gaffin, R. D., Jagatheesan, G., et al. (2010). Neonatal gene transfer of Serca2a delays onset of hypertrophic remodeling and improves function in familial hypertrophic cardiomyopathy. *J. Mol. Cell. Cardiol.* 49, 993–1002. doi: 10.1016/j.yjmcc.2010.09.010

Peng, H., Yang, X. P., Carretero, O. A., Nakagawa, P., D'Ambrosio, M., Leung, P., et al. (2011). Angiotensin II-induced dilated cardiomyopathy in Balb/c but not C57BL/6J mice. *Exp. Physiol.* 96, 756–764. doi: 10.1113/expphysiol.2011.057612

Peng, Y., Popovic, Z. B., Sopko, N., Drinko, J., Zhang, Z., Thomas, J. D., et al. (2009). Speckle tracking echocardiography in the assessment of mouse models of cardiac dysfunction. *Am. J. Physiol. Heart Circ. Physiol.* 297, H811–H820. doi: 10.1152/ajpheart.00385.2009

Prabhakar, R., Boivin, G. P., Grupp, I. L., Hoit, B., Arteaga, G., Solaro, R. J., et al. (2001). A familial hypertrophic cardiomyopathy alpha-tropomyosin mutation causes severe cardiac hypertrophy and death in mice. *J. Mol. Cell. Cardiol.* 33, 1815–1828. doi: 10.1006/jmcc.2001.1445

Reant, P., Mirabel, M., Lloyd, G., Peyrou, J., Lopez Ayala, J. M., Dickie, S., et al. (2016). Global longitudinal strain is associated with heart failure outcomes in hypertrophic cardiomyopathy. *Heart* 102, 741–747. doi: 10.1136/heartjnl-2015-308576

Rowlands, C. T., Owen, T., Lawal, S., Cao, S., Pandey, S. S., Yang, H. Y., et al. (2017). Age- and strain-related aberrant Ca(2+) release is associated with sudden cardiac death in the ACTC E99K mouse model of hypertrophic cardiomyopathy. *Am. J. Physiol. Heart Circ. Physiol.* 313, H1213–H1226. doi: 10.1152/ajpheart.00244.2017

Ryba, D. M., Warren, C. M., Karam, C. N., Davis, R. T. III, Chowdhury, S. A. K., Alvarez, M. G., et al. (2019). Sphingosine-1-phosphate receptor modulator, FTY720, improves diastolic dysfunction and partially reverses atrial remodeling in a Tm-E180G mouse model linked to hypertrophic cardiomyopathy. *Circ. Heart Fail.* 12:e005835. doi: 10.1161/CIRCHEARTFAILURE.118.005835

Semsarian, C., Ahmad, I., Giewat, M., Georgakopoulos, D., Schmitt, J. P., McConnell, B. K., et al. (2002). The L-type calcium channel inhibitor diltiazem prevents cardiomyopathy in a mouse model. *J. Clin. Invest.* 109, 1013–1020. doi: 10.1172/jci200214677

Solaro, R. J., Pang, D. C., and Briggs, F. N. (1971). The purification of cardiac myofibrils with Triton X-100. *Biochim. Biophys. Acta* 245, 259–262. doi: 10.1016/0005-2728(71)90033-8

Song, Q., Schmidt, A. G., Hahn, H. S., Carr, A. N., Frank, B., Pater, L., et al. (2003). Rescue of cardiomyocyte dysfunction by phospholamban ablation does not prevent ventricular failure in genetic hypertrophy. *J. Clin. Invest.* 111, 859–867. doi: 10.1172/jci200316738

Tadano, N., Du, C. K., Yumoto, F., Morimoto, S., Ohta, M., Xie, M. F., et al. (2010). Biological actions of green tea catechins on cardiac troponin C. *Br. J. Pharmacol.* 161, 1034–1043. doi: 10.1111/j.1476-5381.2010.00942.x

Tardiff, J. C., Carrier, L., Bers, D. M., Poggesi, C., Ferrantini, C., Coppini, R., et al. (2015). Targets for therapy in sarcomeric cardiomyopathies. *Cardiovasc. Res.* 105, 457–470. doi: 10.1093/cvr/cvv023

Tardiff, J. C., Hewett, T. E., Palmer, B. M., Olsson, C., Factor, S. M., Moore, R. L., et al. (1999). Cardiac troponin T mutations result in allele-specific phenotypes in a mouse model for hypertrophic cardiomyopathy. *J. Clin. Invest.* 104, 469–481. doi: 10.1172/jci6067

Towbin, J. A. (2014). Inherited cardiomyopathies. *Circ. J.* 78, 2347–2356.

Utter, M. S., Warren, C. M., and Solaro, R. J. (2015). Impact of anesthesia and storage on posttranslational modifications of cardiac myofilament proteins. *Physiol. Rep.* 3:e12393. doi: 10.14814/phy2.12393

van der Velden, J., and Stienen, G. J. M. (2019). Cardiac disorders and pathophysiology of sarcomeric proteins. *Physiol. Rev.* 99, 381–426. doi: 10.1152/physrev.00040.2017

Warren, C. M., and Greaser, M. L. (2003). Method for cardiac myosin heavy chain separation by sodium dodecyl sulfate gel electrophoresis. *Anal. Biochem.* 320, 149–151. doi: 10.1016/s0003-2697(03)00350-6

Warren, C. M., Karam, C. N., Wolska, B. M., Kobayashi, T., de Tombe, P. P., Arteaga, G. M., et al. (2015). Green tea catechin normalizes the enhanced Ca2+ sensitivity of myofilaments regulated by a hypertrophic cardiomyopathy-associated mutation in human cardiac troponin I (K206I). *Circ. Cardiovasc. Genet.* 8, 765–773. doi: 10.1161/CIRCGENETICS.115.001234

Wilder, T., Ryba, D. M., Wieczorek, D. F., Wolska, B. M., and Solaro, R. J. (2015). N-acetylcysteine reverses diastolic dysfunction and hypertrophy in

familial hypertrophic cardiomyopathy. *Am. J. Physiol. Heart Circ. Physiol.* 309, H1720–H1730. doi: 10.1152/ajpheart.00339.2015

Williams, L. K., Misurka, J., Ho, C. Y., Chan, W. X., Agmon, Y., Seidman, C., et al. (2018). Multilayer myocardial mechanics in genotype-positive left ventricular hypertrophy-negative patients with hypertrophic cardiomyopathy. *Am. J. Cardiol.* 122, 1754–1760. doi: 10.1016/j.amjcard.2018.08.008

Yamada, S., Arrell, D. K., Kane, G. C., Nelson, T. J., Perez-Terzic, C. M., Behfar, A., et al. (2013). Mechanical dyssynchrony precedes QRS widening in ATP-sensitive K(+) channel-deficient dilated cardiomyopathy. *J. Am. Heart Assoc.* 2:e000410. doi: 10.1161/JAHA.113.000410

Conflict of Interest: The authors declare that the research was conducted in the absence of any commercial or financial relationships that could be construed as a potential conflict of interest.

frontiers in Physiology

ORIGINAL RESEARCH
published: 18 March 2020
doi: 10.3389/fphys.2020.00173

Single-Molecule Force Spectroscopy on the N2A Element of Titin: Effects of Phosphorylation and CARP

*Thomas Lanzicher[1,2], Tiankun Zhou[3], Chandra Saripalli[1], Vic Keschrumrus[1], John E. Smith III[1], Olga Mayans[3], Orfeo Sbaizero[2] and Henk Granzier[1]**

[1] Department of Cellular & Molecular Medicine, The University of Arizona, Tucson, AZ, United States, [2] Department of Engineering and Architecture, University of Trieste, Trieste, Italy, [3] Department of Biology, University of Konstanz, Konstanz, Germany

OPEN ACCESS

Edited by:
Jose Renato Pinto,
Florida State University, United States

Reviewed by:
Ranganath Mamidi,
Case Western Reserve University, United States
Wen-Ji Dong,
Washington State University, United States
Han-Zhong Feng,
Wayne State University School of Medicine, United States

***Correspondence:**
Henk Granzier
granzier@email.arizoma.edu;
granzier@email.arizona.edu

Specialty section:
This article was submitted to Striated Muscle Physiology, a section of the journal Frontiers in Physiology

Received: 21 December 2019
Accepted: 13 February 2020
Published: 18 March 2020

Citation:
Lanzicher T, Zhou T, Saripalli C, Keschrumrus V, Smith JE III, Mayans O, Sbaizero O and Granzier H (2020) Single-Molecule Force Spectroscopy on the N2A Element of Titin: Effects of Phosphorylation and CARP. Front. Physiol. 11:173. doi: 10.3389/fphys.2020.00173

Titin is a large filamentous protein that forms a sarcomeric myofilament with a molecular spring region that develops force in stretched sarcomeres. The molecular spring has a complex make-up that includes the N2A element. This element largely consists of a 104-residue unique sequence (N2A-Us) flanked by immunoglobulin domains (I80 and I81). The N2A element is of interest because it assembles a signalosome with CARP (Cardiac Ankyrin Repeat Protein) as an important component; CARP both interacts with the N2A-Us and I81 and is highly upregulated in response to mechanical stress. The mechanical properties of the N2A element were studied using single-molecule force spectroscopy, including how these properties are affected by CARP and phosphorylation. Three protein constructs were made that consisted of 0, 1, or 2 N2A-Us elements with flanking I80 and I81 domains and with specific handles at their ends for study by atomic force microscopy (AFM). The N2A-Us behaved as an entropic spring with a persistence length (Lp) of ∼0.35 nm and contour length (Lc) of ∼39 nm. CARP increased the Lp of the N2A-Us and the unfolding force of the Ig domains; force clamp experiments showed that CARP reduced the Ig domain unfolding kinetics. These findings suggest that CARP might function as a molecular chaperone that protects I81 from unfolding when mechanical stress is high. The N2A-Us was found to be a PKA substrate, and phosphorylation was blocked by CARP. Mass spectrometry revealed a PKA phosphosite (Ser-9895 in NP_001254479.2) located at the border between the N2A-Us and I81. AFM studies showed that phosphorylation affected neither the Lp of the N2A-Us nor the Ig domain unfolding force (F_{unfold}). Simulating the force-sarcomere length relation of a single titin molecule containing all spring elements showed that the compliance of the N2A-Us only slightly reduces passive force (1.4%) with an additional small reduction by CARP (0.3%). Thus, it is improbable that the compliance of the N2A element has a mechanical function *per se*. Instead, it is likely that this compliance has local effects on binding of signaling molecules and that it contributes thereby to strain- and phosphorylation- dependent mechano-signaling.

Keywords: titin, passive stiffness, spring elements, post-translational modification, mechano-signaling

INTRODUCTION

Titin is a giant protein located in the sarcomere of striated muscle, where it plays critical roles in muscle health and disease (Granzier and Labeit, 2005; LeWinter and Granzier, 2014; Linke, 2018). The spring segment of titin, located in the I-band region of the molecule, has been extensively studied (Trombitas et al., 1995; Granzier et al., 1996). In response to sarcomere stretch, titin's molecular spring generates passive force, which is important for maintaining the structural integrity of the contracting sarcomere, limiting sarcomere length inhomogeneity along myofibrils, and tuning the level of active force during contraction (Horowits et al., 1989; Labeit and Kolmerer, 1995; Fukuda et al., 2008; Anderson and Granzier, 2012). The molecular spring segment of titin consists of multiple extensible elements that each behave as entropic wormlike chains (WLCs) but with distinct contour length (Lc) and persistence length (Lp) (Linke and Granzier, 1998; Li et al., 2002; Watanabe et al., 2002a,b). Two of these spring elements are found in all muscle types: the tandem Ig segments (serially linked immunoglobulin domains organized in proximal, middle, and distal segments) and the PEVK segment (Freiburg et al., 2000). A third spring element is the cardiac-specific N2B element that contains a large unique sequence (∼550 amino acids) that provides ∼200 nm extensibility to cardiac titin (Helmes et al., 1999). A fourth element, located between the middle tandem Ig segment and the PEVK segment, is the N2A element, found in skeletal muscle titin, fetal cardiac titin, and adult cardiac N2BA titin (Cazorla et al., 2000; Bang et al., 2001). The N2A element is the least well-studied portion of titin's molecular spring. It contains four Ig domains and unique sequences, of which the 104-residue unique sequence (N2A-Us) with flanking Ig domains (I80 and I81) is a major component (Labeit and Kolmerer, 1995). The importance of the N2A element to muscle health is supported by a mouse model with a spontaneous mutation resulting in an in-frame deletion of part of the N2A element (the MDM model) that develops severe myopathy with early death (Garvey et al., 2002). Additionally, missense mutations in the N2A-Us have been linked to cardiomyopathy (Arimura et al., 2009).

N2A-Us had been assumed to be largely unstructured, but recent evidence suggests that it contains α-helical secondary structure (Zhou et al., 2016; Tiffany et al., 2017). It is often assumed that the N2A-Us contributes significantly to the extensibility of titin, but this remains to be established. Here we studied the mechanical properties of the N2A-Us and its flanking Ig domains using single-molecule force spectroscopy. Protein constructs were engineered consisting of 0, 1, or 2 N2A-Us domains, flanked by I80 and I81, and with specific handles at the ends (a halo-tag at the C-terminus and a double cysteine at the N-terminus) for attachment in an atomic force microscope (AFM). We measured the biophysical characteristics of the N2A-Us and used these in a serially linked WLC model that incorporates all spring elements to simulate the role of the N2A-Us in the passive force-sarcomere length relation of the whole titin molecule.

The N2A element is also a protein-binding hub, as it interacts with calpains (calcium-dependent cysteine proteases) (Ojima et al., 2007; Hayashi et al., 2008; Lostal et al., 2019), smyd2 (Donlin et al., 2012; Voelkel et al., 2013; Munkanatta Godage et al., 2018), F-actin (Dutta et al., 2018), and a family of muscle-specific ankyrin repeat proteins, the MARPs (Miller et al., 2003). The MARP family member CARP (Cardiac Ankyrin Repeat Protein) is particularity interesting considering, for example, the importance of CARP-regulated Nkx-2.5-dependent signaling pathways (Witt et al., 2004), that CARP interacts with the signaling molecule myopalladin (Bang et al., 2001), and that mutations in CARP that increase its binding affinity to titin have been linked to cardiomyopathy (Arimura et al., 2009). Furthermore, in response to mechanical stress imposed on the heart, CARP is up-regulated and localizes to titin's I-band region, where it co-localizes with the N2A element (Witt et al., 2004). In skeletal muscle, CARP is normally present at very low levels, but also, in this muscle type, CARP has been found to be highly upregulated under conditions of mechanical stress (Barash et al., 2004). A prime example is the unilateral diaphragm denervation model, where CARP protein levels are increased ∼400-fold in the denervated hemi-diaphragm (van der Pijl et al., 2018, 2019). It was recently shown that CARP interacts with both the N2A-Us and I81 (Zhou et al., 2016), and since this might affect the extensibility of the N2A-Us, we studied the effect of CARP on the mechanical properties of the N2A-Us and its flanking Ig domains.

It has been well-established that the mechanical properties of titin's N2B and PEVK spring elements can be tuned via phosphorylation by kinases important in multiple cell signaling processes in striated muscle (e.g., ERK2, PKA, and PKG) (Fukuda et al., 2005; Kruger et al., 2009; Hidalgo and Granzier, 2013; Perkin et al., 2015). However, whether the N2A element can be phosphorylated and how this affects extensibility are less clear. Recent studies showed that PKA phosphorylates the N2A-Us (Lun et al., 2014; Adams et al., 2019), and earlier studies showed that the N2A-Us can be phosphorylated by PKG but not PKA (Kruger et al., 2009; Hisman et al., 2011). Hence, we also focused on N2A phosphorylation and how it affects the extensibility of N2A-Us and Ig domain unfolding.

MATERIALS AND METHODS

Protein Engineering

Three different N2A recombinant protein constructs were made. The first consisted of the four Ig domains (I80, I81, I80, and I81), the second contained a single N2A-Us embedded between the first I80-I81 pair, and the third contained two N2A-Us elements, each embedded between a I80-I81 pair; these are referred to as the 0, 1, and 2 N2A-Us constructs, respectively (**Figure 1**). All constructs also contained a HaloTag at the C-terminus (for covalent attachment to a glass surface, via an ester bond with a chloroalkane ligand; see below) and a double cysteine at the N-terminus for attachment to a gold-coated AFM cantilever. The bacterial codon-optimized expression construct (and its derivatives) were synthesized by DNA2.0 (now Atum) and cloned into the pJ404 expression vector with ampicillin resistance, a lacO-flanked T5 promoter, and a strong ribosome binding site. The full-length expressed protein consists

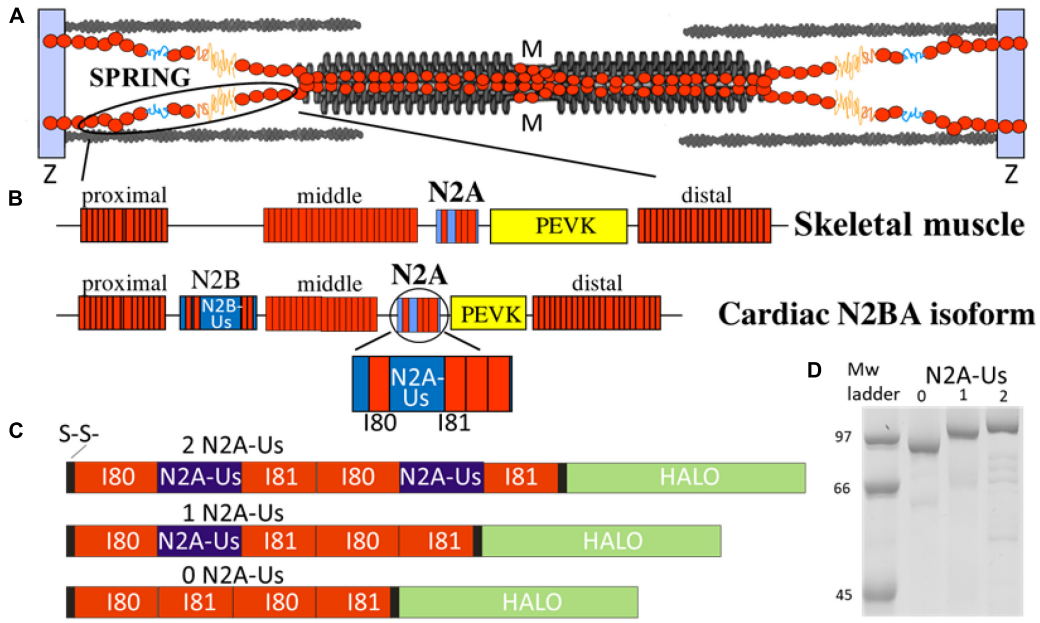

FIGURE 1 | The N2A element is part of titin's molecular spring. **(A)** Titin spans from the Z-disk to the M-band of the sarcomere; the I-band region of the molecule functions as a molecular spring. **(B)** Domain composition of the molecular spring region of skeletal muscle titin (top) and adult cardiac N2BA isoform (bottom) with expanded N2A element shown at bottom. Red rectangle: immuno-globulin domains making up a proximal, middle, and distal tandem Ig segment; blue: unique sequence; yellow: PEVK. **(C)** Domain composition of the three N2A constructs used in this study: all contain two I80 and two I81 immunoglobulin domains (red) and either 0, 1, or 2 N2A-Us elements (blue). **(D)** Expressed constructs are of the expected molecular weight with minimal signs of protein degradation.

of Cys(x2)-His(x6)-[amino acids 9689-9988 of human Titin (NP_001254479.2)](x2)-TEV cleavage site-[amino acids 3-296 of HALO7 (AQS79242.1)]; see **Supplementary Figures S1A,B**. The derivative expression constructs have internal deletions of either the second or both unique sequence regions between Ig domains I80 and I81 (amino acids 9792-9895 of human Titin). Protein was expressed in BLR(DE3)pLysS cells (Novagen) by induction with 1 mM IPTG in LB overnight at 15C. Lysate was prepared from bacterial pellet using Lysis Buffer [20 mM Tris, 10 mM imidazole, 150 mM NaCl, 10% glycerol, 0.2% NP-40, 2 mM β-mercaptoethanol, complete protease inhibitor (Roche), pH 8] to disrupt bacterial cells with sonication pulses (using a Branson Sonifier). Proteins were purified using the His tag with batch Ni^{2+}-NTA (Qiagen) affinity chromatography. Proteins were eluted with 330 mM imidazole in Lysis Buffer without detergent and exchanged into 10 mM HEPES, 150 mM NaCl, 1 mM EDTA, 10% glycerol, pH 7.2. Aliquots of the protein were frozen in liquid nitrogen and stored at −80°C until used.

The CARP experiments used a recombinant N-terminally truncated CARP construct corresponding to the titin-binding region of CARP, $CARP^{106-319}$. This CARP construct contains all Ankyrin Repeat (AR) domains and has been shown to bind to the N2A-Us and I81 (Zhou et al., 2016). Binding of CARP to the N2A-Us and N2A-Us-I81 titin segments occurs upon mixing of the samples, as shown previously by size exclusion chromatography (SEC) and SEC-coupled to multi-angle laser light scattering (SEC-MALLS) (Zhou et al., 2016). Binding in this work was achieved similarly. The production of CARP has been described previously (Zhou et al., 2016). Briefly, human $CARP^{106-319}$ (UniProtKB Q15327) was cloned into the pET-Trx1a vector. Proteins were expressed in Rosetta(DE3) *E. coli* (Novagen), and cells were harvested and lyzed in 25 mM HEPES pH7.5, 300 mm NaCl. The purification from supernatants followed Ni^{2+}-NTA affinity chromatography, tag removal by TEV protease digestion, reverse affinity chromatography, and size exclusion chromatography [for additional details, see (Zhou et al., 2016)].

Protein Phosphorylation

The purified recombinant proteins (containing 0, 1, or 2 N2A unique sequence regions) were used in phosphorylation assays along with no-kinase and kinase-plus-inhibitor controls by incubation in kinase buffer [final concentration in mM: NaATP 2.36, HEPES 6, imidazole 16, NaCl 90, $K(C_2H_5COO)$ 28, $Mg(CH_3COO)_2$ 2.56, creatine phosphate 4, EGTA 4, EDTA 0.6, NaN_3 2, DTT 0.4, E-64 0.04, leupeptin 0.16, NaF 20, Na_3VO_4 4] for 4 hr at 30°C along with the following. PKA phosphorylation: Incubated with 1.0 U/ul PKA catalytic subunit (Sigma-Aldrich P2645), ± 0.04 mM PKA inhibitor fragment 6-22 amide (Sigma-Aldrich P6062). PKG phosphorylation: Incubated with 1.2 mM cGMP (Sigma-Aldrich C5438), 25 U/ul PKG (Promega V5171), and 0.04 mM PKA inhibitor, ± inhibitor KT-5823 (Sigma-Aldrich K1388). ERK2 phosphorylation: Incubated with 1.3 U/ul activated recombinant human MAPK2 (Calbiochem 454854), ± ERK Inhibitor II/FR180204 (EMD Millipore 328007). Reactions were at 30°C for 4 h. Reactions were stopped by the addition of an equal volume of 2X reducing sample buffer (5% 2-mercaptoethanol, 60 mM Tris, 10% glycerol, 2% SDS, 0.005% bromophenol blue) and incubated at 95°C 10 min.

Proteins were separated by 10% SDS-PAGE and visualized sequentially with Pro-Q Diamond phospho-stain (Invitrogen P33300) and either SYPRO Ruby Protein Stain (Invitrogen S12000) or Coomassie Blue stain for normalization of Pro-Q diamond signal. Scanned images were analyzed using One-D San (Scanalytics). Incubation with CARP: A 2:1 ratio (w/w) of CARP:N2A-Us recombinant protein was incubated for PKA phosphorylation as described above. Mass Spectrometry: PKA-phosphorylated recombinant protein (with two N2A-Us) and the matching no-kinase control were gel-purified to remove the kinase and other bacterial contaminants. TiO_2 phosphopeptide enrichment (High-Select kit, Thermo Fisher Scientific A32993) was performed following the manufacturer's recommendations, and samples were submitted to the University of Arizona Analytical and Biological Mass Spectrometry Core Facility. Tandem mass spectrometry (LC-MS/MS) of trypsin-digested samples used the LTQ Orbitrap Velos (Fisher Scientific), and MS spectra of peptides were analyzed with TurboSEQUEST. The Mass Spectrometry data for this study can be found at the Harvard Dataverse[1]. All other datasets for this study are included in the article/**Supplementary Material**.

Attachment of Single-Molecules

The attachment chemistry was conducted according to Taniguchi and Kawakami (2010) and Popa et al. (2013). Briefly, glass slides were cleaned using piranha solution and silanized with (3-Aminopropyl)triethoxysilane. These amine-terminated surfaces were then reacted for 1 h with 10 mM NHS-PEG-Maleimide Cross-linker [SM(PEG), Thermo Fisher Scientific] dissolved in 50 mM Borax buffer, pH 8.5. After washing with double-distilled water, the surfaces were further reacted overnight with a 7.5 mM Thiol-PEG4-Chloroalkane ligand (HaloTag Thiol O4 ligand, Promega) dissolved in 50 mM Borax buffer pH 8.5. The reaction was quenched with 50 mM 2-mercaptoethanol. Just prior to an experiment, a protein aliquot was thawed, and the protein solution was added to the chloroalkane-containing glass surface for ∼60 min. For the CARP experiments, ∼6.5 μ CARP was then added to the slide, followed by incubation for 60 min. The surface was then washed with AFM buffer (10 mM HEPES pH 7.2, 150 mM NaCl, 1 mM EDTA), and AFM measurements were performed in the AFM buffer.

Single-Molecule Force Spectroscopy

An MFP-3D AFM (Asylum Research, Santa Barbara, CA, United States) was used for force spectroscopy. Cantilevers were gold-coated, and their spring constant was determined at the beginning and end of each experiment through a thermal calibration procedure (typically ∼20 pN/nm) (Florin et al., 1995). The piezo motor moved the cantilever up and down and was set to operate at a pulling velocity of 400 nm/s. This speed makes comparisons to previous work possible, is a speed that falls within the physiological speed range (it corresponds to 2 × 400 nm/s per sarcomere or 1/3 lengths per second, assuming a sarcomere length of ∼2.4 μm), and, finally, it is a speed that allows single-molecule experiments to have a relatively high throughput. The cantilever tip was used to probe the glass surface and, by regularly moving the slide laterally by a short distance, different surface locations (and different molecules) were probed. The cantilever tip approached and retracted from the surface of the slide, and when an extension/retraction force curve was obtained, it was evaluated whether it displayed multiple regularly spaced (∼30 nm) saw-tooth force peaks (one for each Ig domain present), a larger force peak due to unfolding of the HaloTag, and a final peak due to detachment of the molecule from one of its attachment points. The obtained force-extension curves were analyzed with the wormlike chain (WLC) equation (Marko and Siggia, 1994):

$$F = \frac{k_B T}{L_p}\left(\frac{1}{4(1-\frac{z}{L_c})^2} - \frac{1}{4} + \frac{z}{L_c}\right) \quad (1)$$

F is the force, k_BT is the thermal energy (k_B is Boltzmann's constant, and T is the absolute temperature), Lp is the persistence length of the molecule, Lc the contour length, and z is the end-to-end length of the molecule. The persistence length, Lp, is the minimal distance along the backbone of the molecule over which tangent lines are correlated. As Lp increases, the molecule is less flexible, and lower force values are required to stretch the molecule to a given fractional extension.

Although the protein constructs have two sets of identical domains (two I80 and two I81 domains), the identical domains are expected to unfold sequentially and not simultaneously. Unfolding is a force-dependent and stochastic process where identical domains will rarely unfold at the same time. Instead, unfolding occurs one by one, with each unfolding event triggering a similar length gain. The classical AFM studies by Fernandez and colleagues on polyproteins that contain a large number of identical Ig domains (up to 12) show this clearly. See, for example (Carrion-Vazquez et al., 1999). Hence, identical domains in our protein constructs are expected to unfold sequentially.

Force clamp protocols were also performed to measure force-dependent unfolding. The cantilever was initially held onto the surface for 2 s to allow attachment to occur, and the cantilever was then moved away from the surface until the measured force matched a pre-determined set point, which initiated the force-clamp phase of the protocol. To control force, the proportional-integral-derivative feedback (PID feedback) with a 2-ms time resolution was used. Each time an unfolding event takes place, a sudden increase in the extension of the molecule is registered. The resulting length-versus-time traces (Oberhauser et al., 2001) exhibit staircases in which the height of each step serves as a fingerprint for the unfolding of a module, and time marks the unfolding dwell time, t, from the moment the force is applied. The force-dependence of the rate of unfolding has been shown to follow the Bell model (Bell, 2008).

$$\alpha(F) = \alpha_0 \exp\left(\frac{F\Delta x}{k_B T}\right) \quad (2)$$

where F is the pulling force, α_0s the rate constant in the absence of external applied force, Δx is the distance to the transition state,

[1]https://doi.org/10.7910/DVN/OZQD7G

and $k_B$at the experimental room temperature is 4.114 pN·nm. This expression can be rearranged into:

$$\ln \alpha (F) = \alpha_0 + \frac{F\Delta x}{k_B T} \quad (3)$$

The model implies probabilistic behavior of the process with a single rate constant, which can be obtained from the single exponential fit to the average Ig domain failure trajectory, normalized by the length of the clamp events. The probability of unfolding over time, P(t), is given by:

$$P(t) = 1 - e^{-\alpha t} \quad (4)$$

Simulated Force-Sarcomere Length Relation of Single-Molecules

To determine how the compliance of N2A-Us affects the force-sarcomere length behavior of a single titin molecule in the sarcomere, the spring region of titin was simulated as four WLCs in series: (1) the tandem Ig segment (combined proximal, middle, and distal segments), (2) the PEVK segment, (3) the N2B-Uc, and (4) the N2A-Us. For a WLC, the external force is given by equation 1 (see above). Based on previous work (Trombitas et al., 1998a; Kellermayer et al., 2000, 2001, 2003; Trombitas et al., 2000; Li et al., 2001; Anderson and Granzier, 2012; Anderson et al., 2013; Chung et al., 2013), the contour lengths of tandem Ig segments, the N2B-Uc, and the PEVK were assumed to be 325 nm, 200 nm, and 350 nm, respectively, and their respective Lp values to be 10, 0.65, and 1.0 nm. Based on the present study (see below) the Lc of the N2A-Us was taken as 40 nm and the Lp as either zero (i.e., inextensible N2A-Us), 0.34 nm (no CARP), or 0.44 nm (CARP). Because spring elements are in series, they bear equivalent forces, and the fractional extension (z/L) at each force can be calculated. From the fractional extensions and the Lc value (above) the corresponding SLs were determined assuming that the inextensible Z-disk and A-band segments of titin are 700 nm long (per half sarcomere) (Trombitas et al., 1998b).

Statistical Analysis

Statistical analysis was performed in GraphPad Prism (GraphPad Software, Inc.). A one-way ANOVA with a Bonferroni *post hoc* analysis was used to calculate adjusted *p*-values corrected for multiple comparisons. When non-normally distributed data were analyzed, a Kruskal–Wallis test was used. Normality was tested with the D'Agostino and Pearson test. A value of $p < 0.05$ was taken as significant. Values were also plotted in histograms that were fit with Gaussian curves. Results are shown as mean ± SEM.

RESULTS

The location of titin in the sarcomere and the domain composition of titin's spring region are shown in **Figures 1A,B**. The best-characterized spring elements are the serially linked immunoglobulin domains, organized in proximal, middle, and distal segments, the N2B element (cardiac-specific) and the PEVK. The N2A element is found in both N2BA cardiac titin and skeletal muscle titin and contains a large unique sequence (N2A-Us, 104 residues), flanked at one end by I80 and at the other by I81 (Bang et al., 2001). We studied titin's N2A element using single-molecule force spectroscopy. Three distinct constructs were used, all with two I80 and two I81 domains but with either 0, 1, or 2 N2A-Us elements (see **Figures 1C,D**). Additionally, all constructs contained a Halo-tag at one end and a double cysteine at the other (**Figure 1C** and **Supplementary Figure S1**) for specific attachment to a functionalized slide and gold-coated cantilever tip, respectively.

Examples of force-extension curves for each of the constructs are depicted in **Figure 2**. There is an initial low-force phase, likely dominated by extension of the N2A-Us, followed by four force peaks at similar height, likely due to Ig domain unfolding. The fifth peak occurs at a higher force and is likely due to unfolding of the HaloTag. The final force peak represents the breaking loose of the molecule from one of its attachment points.

The contour length (Lc) of the force-trace leading up to each of the force peaks was determined by fitting the data to the wormlike chain (WLC) force equation (Methods). Lc increased linearly with peak number with slopes that were similar in the three constructs (∼30 nm, **Figure 3**), as expected since the different constructs contain identical Ig domains. This ∼30 nm value is consistent with the notion that each force peak is derived from the length of an unfolded Ig domain (∼35 nm) minus the length of a folded domain (∼5 nm). The offset of the lines reflects the Lc of the N2A-Us (**Figure 3**), with the Lc of a single N2A-Us at ∼39 nm. The N2A-Us contains 104 residues, and the Lc value indicates an average residue spacing of 0.38 nm.

The fifth unfolding peak had a mean value of 306 ± 12 pN, significantly higher ($p < 0.0001$) than the 163 ± 3 pN of the preceding force peak ($n = 293$). This is consistent with the fifth peak being derived from the unfolding of the Halo tag and preceding peaks from unfolding of Ig domains. Thus, the available constructs make it possible to study the unfolding forces of the Ig domains (force peaks 1–4) and the characteristics of N2A-Us (low-force phase preceding the 1st unfolding peak). Furthermore, we used the constructs to study the effects of CARP on Ig domain unfolding and extension of the N2A-Us.

The persistence length (Lp) of the N2A-Us was determined from the WLC fit to the low-force phase preceding the first unfolding peak. Both without and with CARP, the Lp distribution ranged from ∼0.1 to 1.0 nm (**Figures 4A,B**). CARP did not affect Lc (39 nm) but increased Lp from 0.34 ± 0.01 nm ($n = 190$) to 0.44 ± 0.03 nm ($n = 56$) (p: 0.002).

The Ig domain unfolding force (F_{unfold}) increased with peak number, which is a common feature of multi-domain proteins (see section "Discussion"). The F_{unfold} varied from ∼125 to ∼165 pN, which indicates that these domains are amongst the least stable of the studied titin Ig domains (Watanabe et al., 2002a). The presence of CARP had no effect on Lc (determined from the slope of Lc vs. peak number), but CARP significantly increased unfolding force by an average of ∼20 pN (see **Figure 4C**).

The increased F_{unfold} in the presence of CARP suggests that the mechanical stability of the constructs is increased by CARP.

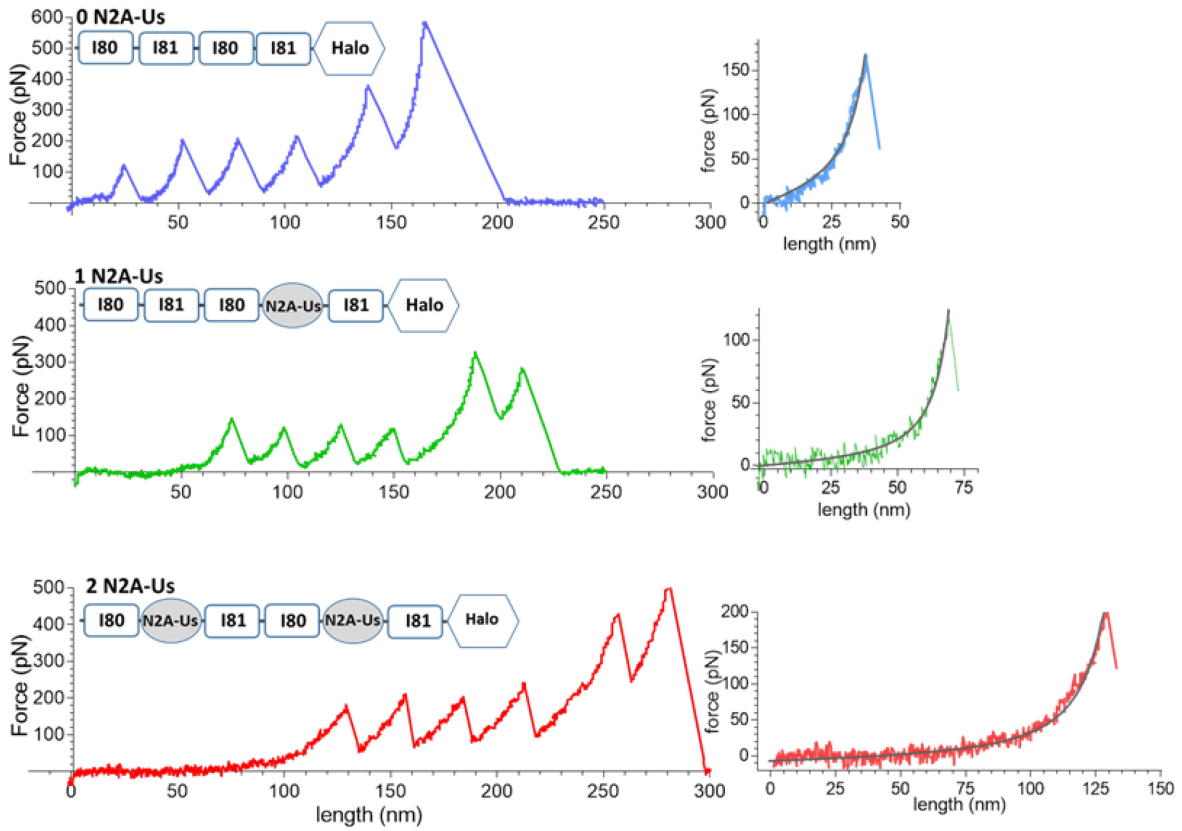

FIGURE 2 | Example force-extension curves. Constructs that were pulled had 0, 1, and 2 N2A-Us; the domain composition of the constructs is shown at the top of each trace. **(Left)** Full traces. Each trace has a low-force extension phase that is followed by six force peaks, the first five of which are likely due to Ig domain and Halo-tag unfolding and the sixth due to the molecule breaking loose from one of its anchors. **(Right)** Initial force traces leading up to the first force peak shown on expanded scales with superimposed black WLC fits. The length of the initial low force varies with the number of N2A-Us elements.

To determine the effect of CARP on the unfolding kinetics, we performed force clamp experiments in which the molecule was held at a constant force and the resulting staircase-like increase in the length of the tethered molecule was determined. We performed load clamps in the 100–150 pN range, with mean clamp values in all experiments of 135.1 ± 0.9 pN and 132.7 ± 0.8 pN for the construct with and without CARP, and with mean step-size of 27.0 ± 0.1 nm without CARP (n = 630) and 26.8 ± 0.1 nm with CARP (n = 627). The rate of unfolding α was determined at different clamp forces from the probability of unfolding over time $P(t) = 1 - e^{-\alpha t}$. The unfolding rate at each force level was higher without CARP than with CARP, e.g., at 100 pN, α was 3.2 s^{-1} and 2.4 s^{-1}, respectively. Plotting ln(α) at a range of clamp forces results in a linear relationship of the form $\ln a = a_0 + F\Delta x/(K_BT)$; α_0 is the unfolding rate constant in the absence of external applied force, Δx is the distance to the transition state, k_Bs the Boltzmann constant, and T is absolute temperature k_B(T 4.11 pN·nm). The line fit to the results obtained without CARP was distinct from the one with CARP (**Figure 4D**), and the slopes and Y-intercepts of the linear regression fits revealed $\alpha_0$0.55 s^{-1} without CARP and 0.43 s^{-1} with CARP. These results indicate that CARP slowed the unfolding kinetics of the Ig domains that flank the N2A-Us, likely explaining the higher average unfolding force in the presence of CARP.

Effect of Protein Kinase a (PKA) Phosphorylation

Various kinases are known to phosphorylate the N2B and PEVK spring elements and modulate titin's stiffness (Hidalgo and Granzier, 2013). However, whether the N2A element can be phosphorylated and the resultant effect on stiffness are less clear. Using the 3 N2A-Us constructs, we studied PKA, PKG, and ERK2 phosphorylation. This established that PKG and ERK2 do not clearly phosphorylate the N2A-Us (**Supplementary Figure S2**). In contrast, PKA did phosphorylate the N2A element, and its phosphorylation level was found to vary with the number of N2A-Us elements (**Figures 5A,C**). Consistent with this finding, mass-spectrometry analysis revealed a PKA phospho-site [Ser-9895 (NP_001254479.2), the same site as reported by Adams et al. (2019)], located at the C-terminal end of the N2A-Us and start of I81; see **Figure 1D** and **Supplementary Figure S1**. This site is identical in a wide range of species but in mouse, rat, and rabbit is a threonine (**Supplementary Figure S3**).

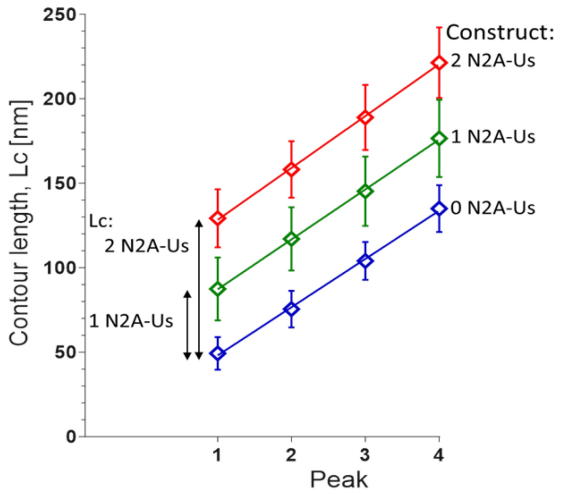

FIGURE 3 | Contour length (Lc) of N2A constructs. Lc was measured by fitting the force-extension traces leading up to each of the first four unfolding peaks with the WLC equation. The slopes of the linear fits are 28.6 ± 0.8 nm, 29.6 ± 0.4 nm, and 30.7 ± 0.6 nm for 0, 1, and 2 N2A-Us-containing constructs, respectively. These values reflect the Lc gain due to Ig domain unfolding. The differences in the offsets of the linear regression fits reflect the Lc of 1 and 2 N2A-Us element, 38.1 and 78.2 nm, respectively.

We also studied the effect of CARP on N2A phosphorylation by incubating the 2 N2A-Us protein with only PKA or PKA and CARP. This revealed that phosphorylation on the 2 N2A-Us protein was effectively blocked by CARP (**Figures 5B,C**, right 3 bars). Because CARP itself is not phosphorylated (**Figure 5B**), it is unlikely that CARP competes with N2A-Us, but, instead, CARP is likely to physically block PKA from interacting with the N2A-Us.

The effects of PKA phosphorylation of S9895 on the Lp of N2A-Us and Ig unfolding forces were also studied. No significant effects were detected on the Lp of the N2A-Us (**Figure 5D**, left two bars) nor on the Ig unfolding force (**Figure 5D**, right four bar pairs). This is not surprising considering that the location of the phosphorylation site is in/near the linker sequence between N2A-Us and I81 (see also section "Discussion"). In summary, PKA phosphorylates the N2A element, but this does not affect the mechanical properties of either the N2A-Us or the Ig unfolding forces.

Finally, the single-molecule force-sarcomere length relation of N2BA cardiac titin was simulated, in which the extensibility of the N2A-Us was taken into account (previously, only the tandem segments, the N2B element, and the PEVK were considered). Results show that inclusion of the N2A-Us modestly lowers passive force (within the shown sarcomere length range by 1.4%) and that including the effect of CARP (which increased Lp of N2A-Us from 0.34 to 0.44 nm) slightly increased this value (from 1.4 to 1.7%); see **Figure 6**.

DISCUSSION

It is well-established that in the I-band region of the sarcomere, titin functions as a molecular spring composed of distinct spring elements: the tandem Ig segments, the N2B element (N2B-Us), and the PEVK. The N2A element is located near the middle of the molecular spring, and the unique sequence that it contains (N2A-Us) is typically also viewed as a spring element. Additionally, CARP binds to both the N2A-Us and the flanking Ig domain I81, and CARP had been proposed to function analogously to a "clamp" between the N2A-Us and I81 and to reduce thereby the extensibility of the N2A-Us. The present study reveals that the N2A-Us behaves as a WLC with an Lc of 39 nm and an Lp of ∼0.35 nm and that CARP increases both the Lp of the N2A-Us and the unfolding force of I81. Furthermore, the N2A element is phosphorylated by PKA, phosphorylation is blocked by CARP, and phosphorylation does not alter the mechanical properties of the N2A element. Below we discuss these findings in detail.

Protein Constructs

In order to obtain AFM results that can be easily interpreted, different protein constructs were used that all consist of four immunoglobulin (Ig) domains but a variable number of N2A-Us domains. This design allowed us to better identify the molecular origin of features in the force-extension curve. The power of this can be clearly seen in **Figure 3**, where the displacement of the curves obtained with the different protein constructs provides high confidence that the extension of the N2A-Us is 39 nm. If only the 1 N2A-Us molecule had been studied, this would not have been possible. Sequential unfolding of the Ig domains during extension of the constructs provided a characteristic single-molecule fingerprint, ensuring that the results were from single-molecules. To achieve specific attachment at the ends of the constructs, thiol chemistry was used to attach the N-terminal double cysteine residues to a gold-coated cantilever, and this was combined with a Halo-tag at the C-terminus to form an ester bond with a chloroalkane-functionalized glass side. Covalent tethering was confirmed by five force peaks in the force-extension curve, reflecting the unfolding of five protein domains contained in the constructs (four Ig domains and the Halo tag). The constructs were engineered such that the direction of force was applied through the Halo-tag N-terminus, since it is known that this results in a higher Halo-tag unfolding force (F_{unfold}) than when force is applied through its C-terminus (Popa et al., 2013). As a result, the Halo-tag unfolds at a much higher force than the Ig domains (∼310 pN vs. ∼160 pN) and will therefore typically unfold last during full extension of the molecule. In conclusion, the constructs that were made ensured that single-molecules were studied and that force-extension curves were obtained from the full-length molecule. Importantly, by comparing results from constructs with 0, 1, and 2 N2A-Us domains, the properties of N2A-Us and Ig domain unfolding could be "dissected."

I80 and I81 Unfolding Force (F_{unfold})

The I80 and I81 F_{unfold} levels ranged from ∼125 pN (first force peak) to ∼165 pN (fourth force peak). The increase in F_{unfold} with peak number is a common feature of polyproteins (Carrion-Vazquez et al., 1999; Zhu et al., 2009) and can be explained by the stochastic nature of unfolding and the reduced

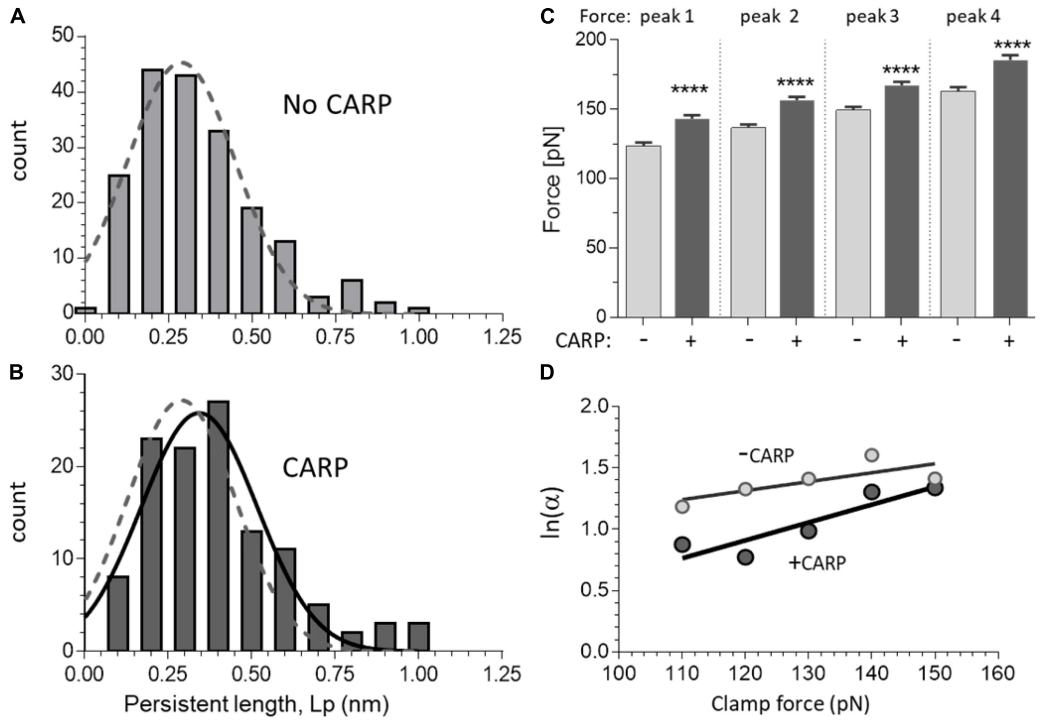

FIGURE 4 | Effect of CARP on the force-extension curves of N2A constructs. A and B) Persistence length (Lp) distribution of N2A-Us in the absence of CARP **(A)** and in the presence of CARP **(B)**. Data obtained from constructs with 1 and with 2 N2A-Us elements were not statically different, which is expected, and were pooled. Gaussian fits are shown. The fit of the without-CARP data was overlaid in panel **(B)** as a dashed line. Note that the Lp graph is slightly right-shifted by CARP. **(C)** Peak force of peaks 1–4 measured with and without CARP. Force levels of all force peaks are higher in the presence of CARP. **(D)** Logarithm of unfolding rate α as a function of force, measured in force-clamp experiments. The two lines represent the fitting of the Bell expression (see section "Materials and Methods") and give values of α_o = 1.55 s^{-1}, Δx = 0.30 Å for the without-CARP data and α_o = 0.43 s^{-1}, Δx = 0.60 Å for the CARP data. ****$p < 0.0001$.

likelihood of unfolding of a single domain in a chain with a lower number of remaining folded domains (Anderson et al., 2013). The F_{unfold} – peak number relation might also, in part, be due to a difference in the F_{unfold} between I80 and I81, although the difference is unlikely to be large, considering the gradual and linear increase of F_{unfold} with peak number (**Figure 4C**). Distinct F_{unfold} levels are seen when domains of different mechanical stability are linked (Li and Fernandez, 2003). The present study was conducted at a pulling speed of 400 nm/s, and comparing the results to earlier studies in which Ig domains were stretched at the same or a similar speed shows that I80 and I81 unfold at lower force levels than domains from the distal and middle tandem Ig segments (Carrion-Vazquez et al., 1999; Li et al., 2002; Watanabe et al., 2002a; Zhu et al., 2009) but at levels similar or slightly higher than domains from the proximal tandem Ig segment (Li and Fernandez, 2003; Anderson et al., 2013). For example, the proximal tandem Ig segment domain I1 unfolds at ∼110 pN (pulling speed 400 nm/sec) (Li and Fernandez, 2003), and I10 unfolds at ∼120 pN (pulling speed 1000 nm/s) (Anderson et al., 2013). Interestingly, the flanking Ig domains of the N2B-Us (I24 and I25) unfold at 125–165 pN (pulling speed 500 nm/s) (Zhu et al., 2009), which is nearly identical to the I80 and I81 F_{unfold}. Although it is uncertain to what extent unfolding of Ig domains occurs under physiological conditions (Trombitas et al., 1998b; Chen et al., 2015), if it does occur, this might involve Ig domains from the proximal tandem Ig segment and domains that flank the unique sequences of both the N2B and N2A elements.

N2A-Us Extension

The low-force phase of the extension curve prior to the first unfolding peak can be fit well with the WLC force equation, and comparing the thus-obtained contour length (Lc) of the constructs with 0,1, and 2 N2A-Us domains convincingly shows that a single N2A-Us domain has an Lc of ∼39 nm. Considering that the N2A-Us contains 104 residues, this Lc value indicates an average residue spacing of 3.75 Å. This value is close to the 3.8 Å maximal residue spacing of an unfolded polypeptide chain (Cantor, 1980), suggesting that no secondary structures exist in the N2A-Us when the first Ig domain unfolds. However, a recent structural study revealed that N2A-Us has α-helical-rich secondary structures (∼60–70% helical content), with helices arranged into a 3D-fold, similar to the MyBP-C tri-helix bundle (Howarth et al., 2012; Bezold et al., 2013; Zhou et al., 2016). The axial residue spacing along the α-helix axis is 1.47 Å (Pauling et al., 1951), and assuming that 70% of the N2A-Us is α-helical results in an Lc of 10.7 nm (the α-helical region will be more compact than this if the α-helices adopt 3-D folds). Considering the much longer Lc value that was obtained in this study, α-helices must have largely unfolded

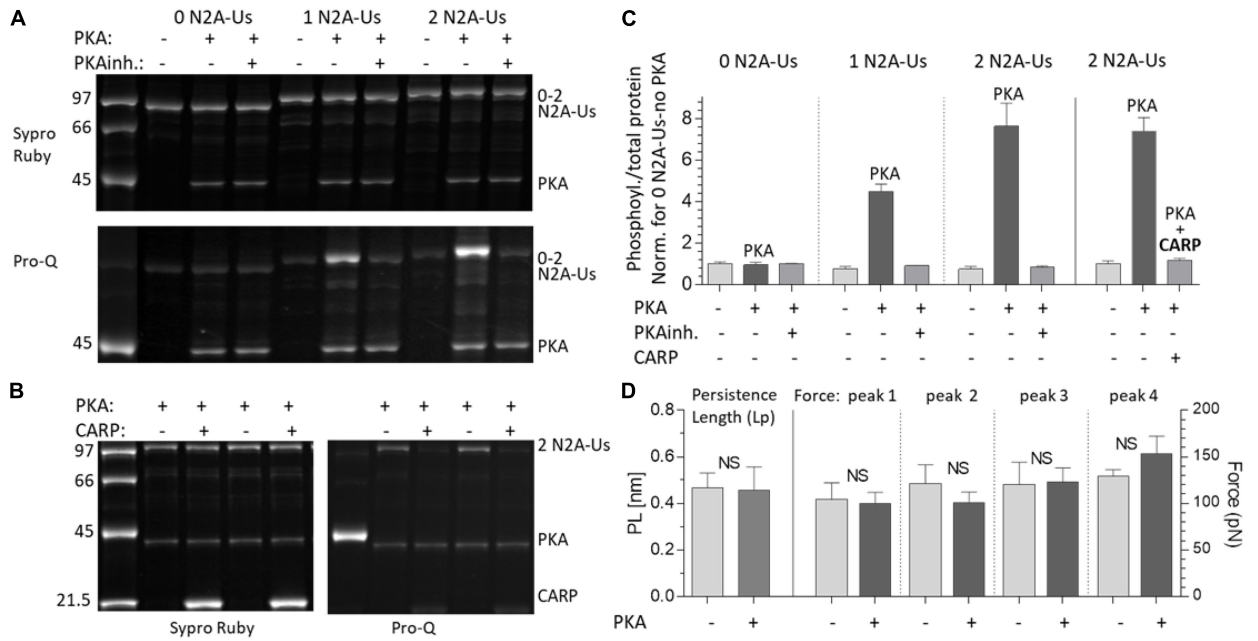

FIGURE 5 | PKA phosphorylates the N2A-Us; phosphorylation is blocked by CARP and does not affect the molecular mechanics of the N2A element. **(A)** The N2A constructs with 0, 1, and 2 N2A-Us elements were incubated with PKA with and without PKA inhibitor (PKAinh.). Top: protein-stained gel (Sypro-ruby stain); bottom: Pro-Q Diamond phosphoprotein-stained gel (same gel). Constructs are phosphorylated by PKA but only when N2A-Us is present and in a manner that scales with the number of N2A-Us elements contained in the construct. This is visually apparent **(A)** and is clear from the gel analysis (**C**, left three triplicate sets of bars). **(B)** PKA phosphorylation of the N2A construct (2 N2BA-Uc elements) with and without CARP. Left: protein-stained gel (Sypro-Ruby stain). Right: Pro-Q Diamond phosphoprotein-stained gel. It is visually apparent **(B)** and is clear from the analysis (**C**, right three bars) that CARP blocks N2A-Us phosphorylation. Note on the pro-Q Diamond-stained gel that PKA is auto-phosphorylated and that this is unaffected by CARP. **(D)** Lp of the N2A-Us (left pair of bars and left *Y*-axis) and Ig F_{unfold} (right four bar pairs and right *Y*-axis) with and without PKA phosphorylation. Phosphorylation does not affect the Lp of the N2A-Us or the Ig domain F_{unfold}.

well before the first Ig domain unfolding peak was registered. No force peaks were observed in the traces leading up to the first Ig domain unfolding peak, either in the 1 N2A-Us or 2 N2A-Us construct. In a previous AFM study, we showed that when pulling the α-helical protein spectrin, clear unfolding peaks are detectable in the 15–25 pN force regime (Watanabe et al., 2002a), and we are confident that if similar force peaks had occurred while pulling N2A-Uc, they would also have been detected.

The lack of unfolding peaks during N2A-Us extension suggests either that the unfolding force of the α-helical secondary structures is below the resolution limit of our AFM (∼10 pN) or that unfolding occurs non-cooperatively and does not produce a distinct force peak. The lack of force peaks due to N2A-Us unfolding is consistent with AFM measurements on α-helical domains from myosin-10 in which unfolding peaks were also absent (Wolny et al., 2014). This myosin-10 study included molecular dynamics (MD) simulations that showed gradual unfolding of α-helical domains at an approximately constant force. This force varied with pulling speed and was ∼50 pN at the slowest pulling speed used in the MD simulation, 1 m/s. Considering that the present AFM study pulled N2A-Us 2.5×10^4 slower than the MD simulation (400 nm/s) and the well-known speed-dependence of unfolding, the force level at which α-helical domains unfold might be quite low at our experimental pulling speed and thus might be undetectable. Future studies with higher force resolution techniques (e.g., laser tweezers) will be required to establish how the N2A-Us extends at low force levels. Based on the present AFM study, the N2A-Us can be modeled as a WLC with Lc 39 nm and Lp 0.34 nm.

Role of N2A-Us in the Passive Force-Sarcomere Length Relation of Titin

To evaluate the role that the N2A-Us plays in passive force generation, the molecular spring region of cardiac N2BA titin was simulated as a serially linked WLC comprised of tandem Ig segments, the N2B-Uc, the PEVK, and the N2A-Us. The Lp and Lc values for the first three spring elements were based on previous work (see section "Materials and Methods") and for the N2A-Us on the present study. The simulated force-sarcomere length relation (**Figure 6**) shows that, within the evaluated sarcomere length range, the compliance provided by the N2A-Us only slightly lowers passive force, on average by 1.4%. This effect is expected to be even smaller in fetal cardiac titin and skeletal muscle titin because their PEVK and tandem Ig segments are longer than in adult cardiac N2BA titin (Freiburg et al., 2000; Lahmers et al., 2004), and the small effect of N2A-Us compliance on passive force will be further "diluted."

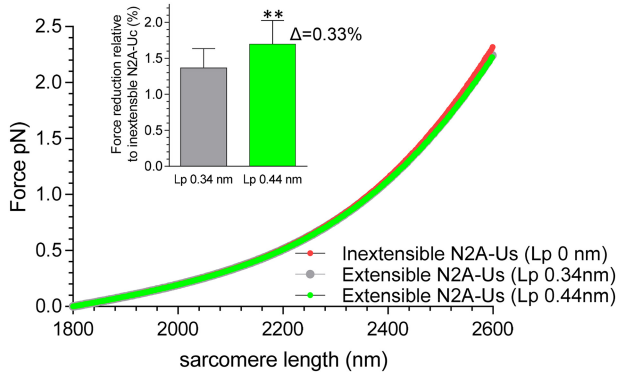

FIGURE 6 | Effect of extensible N2A-Us on simulated single-molecule force-sarcomere length relation. A serially linked wormlike chain entropic spring model was used (see section "Materials and Methods"). The Lc of the N2A-Us was assumed to be 39 nm and the Lp either zero (i.e., inextensible, red symbols), 0.34 nm (no CARP, gray symbol), or 0.44 nm (CARP, green). The symbols largely overlap. The extensible N2A-Us lowers passive force slightly, on average within the shown sarcomere length range 1.7 ± 0.3% (Lp 0.44 nm) and 1.4 ± 0.3% (Lp 0.34 nm). Thus, increasing Lp from 0.34 to 0.44 (CARP effect) lowers force by an additional 0.33%. $^{**}p < 0.01$.

The effect is also expected to be less if α-helical structures exist in the N2A-Us that gradually unfold (see above). Thus, the extensibility of the N2A-Us has a negligible effect on the level of passive force that titin generates, and, in contrast to the tandem Ig segments, the N2B-Us, and the PEVK, the N2A-Us is unlikely to function primarily as a molecular spring element.

CARP

The presence of CARP slightly increased both the Lp of the N2A-Us and the unfolding force (F_{unfold}) of its flanking Ig domains (**Figure 4**), findings consistent with earlier biochemical studies that showed that CARP interacts with both the N2A-Us and I81 (Zhou et al., 2016). Based on this dual interaction, it has been proposed that CARP regulates the stretch response of the N2A element (Zhou et al., 2016). However, the predicted effect of the increase in Lp on passive force is, at 0.4%, miniscule (**Figure 6**), and it seems unlikely that this is an important biological function of CARP binding to titin. The increased F_{unfold} could be relevant if I81 is at risk of unfolding, which might be the case considering that the measured F_{unfold} is comparatively low (see above) and CARP is upregulated under conditions of mechanical stress where unfolding is more likely to occur (Barash et al., 2004; van der Pijl et al., 2019). At present, it cannot be excluded that, *in vivo*, CARP does affect passive force, since multiple complexities occur in the sarcomere that are absent in single-molecule assays (if the sarcomere thin filaments are present, CARP might dimerize and crosslink different filaments, etc.) The increased F_{unfold} that our single-molecule study revealed (**Figure 4C**) suggests that it is possible that CARP functions as a chaperone. This would be similar to αB-crystallin, which acts as a chaperone for the N2B element by increasing the F_{unfold} of the Ig domains that flank the N2B-Us (Zhu et al., 2009), and αB-crystallin is also upregulated under conditions of stress (Bullard et al., 2004). Thus, CARP might function as a molecular chaperone that protects I81 from unfolding when mechanical stress is high.

Phosphorylation and Signaling

The N2A-Us was found to contain a PKA site (S9895 in NP_001254479.2) at the border between the N2A-Us and I81, outside the α-helical N2A-Us region that was discussed above. This site is the same as the PKA site reported by Adams et al. (2019) and presumably also the same site that was phosphorylated by PKA in the study Lun et al. (2014) (the authors did not locate the amino acid(s) that was(were) phosphorylated by PKA). Interestingly the N2A element has been reported to be a PKG substrate and not a PKA substrate by Kruger et al. (2009). The same laboratory showed later that the PKG phosphosite is S9895 (Hisman et al., 2011), i.e., the same site as the PKA site that we and Adams et al. (2019) found (note that the reported PKG site S8651 used NP_596869.4 as the reference sequence and that this site is the same as S9895 in NP_001254479.2 that we used). The reason for the discrepancy is not clear. All phosphorylation studies used the human N2A sequence, and a species difference is therefore ruled out. Considering the convincing phosphorylation of N2A-Us by PKA that we found (**Figure 5A**) and the clear correspondence between our study and the studies from two other laboratories (Lun et al., 2014; Adams et al., 2019) the case for N2A-Us as a PKA substrate with as phospho-site SS9895 is strong.

No effect of phosphorylation was found on the persistence length of the N2A-Us nor on the unfolding force of I81. This is consistent with the location of the PKA site in what is likely an unstructured region that links the N2A-Us to I81. Thus unlike PKA phosphorylation of the N2B-Us, which increases the compliance of the N2B-Us (Yamasaki et al., 2002; Kruger et al., 2009), phosphorylation of Ser-9895 does not affect the mechanical properties of N2A-Us. Considering that the N2A-Us PKA site is well conserved (**Supplementary Figure S3**), it is likely that PKA phosphorylation does have a biological function. This might be regulating the binding affinity between the N2A-Us and other proteins. For example, CARP binding could be sensitive to PKA phosphorylation. However, despite CARP binding precluding N2A-Us phosphorylation (**Figures 5B,C**), N2A phosphorylation does not abolish the binding of CARP (results not shown). CARP is a member of a conserved gene family referred to as MARPs (muscle ankyrin repeat proteins) that also includes ankrd-2/Arpp/MARP2 and DARP/MARP3. All MARP family members contain within their ankyrin repeat region a binding site for the N2A element of titin (Miller et al., 2003), and thus it is possible that unlike CARP, other MARP family members do bind to titin in a manner that depends on S9895 phosphorylation. Another N2A-Us-binding protein with an affinity that might be controlled through S9895 phosphorylation is the lysine methyltransferase Smyd2. Smyd2

has been shown to bind to N2A-Us and to play an important role in the structural stabilization of sarcomeric proteins, including protecting the N2A element from degradation (Voelkel et al., 2013). A final possible candidate with titin-binding affinity that might be controlled by PKA phosphorylation of S9895 is calpain3. Calpain3 has multiple binding sites to titin, including the I80-N2A-Us region (Hayashi et al., 2008), and binding suppresses the activity of this protease (Ono et al., 2006). *In vitro* cell culture experiments have shown that the binding of calpain3 is stretch-dependent and that increasing sarcomere length increases calpain3 accumulation at the N2A site (Ojima et al., 2010). Clearly, additional studies are required to establish the functional role of PKA phosphorylation of S9895 and whether this includes regulating the binding affinity and function of titin-binding proteins.

CONCLUSION

In AFM experiments, the N2A-Us behaves as an entropic spring with an Lp of ∼0.35 nm and an Lc of 39 nm. CARP increases the unfolding force of I81 and might thereby act as a molecular chaperone that protects I81 from unfolding when mechanical stress is high. The N2A-Us is a PKA substrate, and phosphorylation can be blocked by CARP. Simulating the force–sarcomere length relation of a single titin molecule containing all spring elements shows that the compliance of the N2A-Us only slightly reduces passive force, suggesting that it is unlikely that the N2A element has a mechanical function *per se*. Considering that the N2A element is an anchoring hub for signaling proteins, it is likely that the compliance of the N2A-Us has local effects on binding of signaling molecules and that it contributes thereby to strain- and phosphorylation-dependent mechano-signaling.

DATA AVAILABILITY STATEMENT

The datasets generated for this study can be found in the Mass Spectrometry data for this study can be found at the Harvard Dataverse (https://doi.org/10.7910/DVN/OZQD7G).

AUTHOR CONTRIBUTIONS

All authors listed have made a substantial, direct and intellectual contribution to the work, and approved it for publication. VK made contributions to the acquisition and analysis of data for this work and drafting of the revised manuscript, provided final approval of the version to be published, and agreed to be accountable for all aspects of the work in ensuring that questions related to the accuracy or integrity of any part of the work are appropriately investigated and resolved.

ACKNOWLEDGMENTS

We thank all lab members involved in supporting this work. We also thank the funders: Leducq Foundation (13CVD04 and 14-CVD03), NIAMS (National Institute of Arthritis and Musculoskeletal and Skin Disease) R01AR073179, and NHLBI (National Heart, Lung, and Blood Institute) R35HL144998.

SUPPLEMENTARY MATERIAL

The Supplementary Material for this article can be found online at: https://www.frontiersin.org/articles/10.3389/fphys.2020.00173/full#supplementary-material

REFERENCES

Adams, M., Fleming, J. R., Riehle, E., Zhou, T., Zacharchenko, T., and Markovic, M. (2019). Scalable, non-denaturing purification of phosphoproteins using Ga(3+)-IMAC: N2A and M1M2 titin components as study case. *Protein J.* 38, 181–189. doi: 10.1007/s10930-019-09815-w

Anderson, B. R., Bogomolovas, J., Labeit, S., and Granzier, H. (2013). Single molecule force spectroscopy on titin implicates immunoglobulin domain stability as a cardiac disease mechanism. *J. Biol. Chem.* 288, 5303–5315. doi: 10.1074/jbc.M112.401372

Anderson, B. R., and Granzier, H. L. (2012). Titin-based tension in the cardiac sarcomere: molecular origin and physiological adaptations. *Prog. Biophys. Mol. Biol.* 110, 204–217. doi: 10.1016/j.pbiomolbio.2012.08.003

Arimura, T., Bos, J. M., Sato, A., Kubo, T., Okamoto, H., and Nishi, H. (2009). Cardiac ankyrin repeat protein gene (ANKRD1) mutations in hypertrophic cardiomyopathy. *J. Am. Coll. Cardiol.* 54, 334–342. doi: 10.1016/j.jacc.2008.12.082

Bang, M. L., Centner, T., Fornoff, F., Geach, A. J., Gotthardt, M., and McNabb, M. (2001). The complete gene sequence of titin, expression of an unusual approximately 700-kDa titin isoform, and its interaction with obscurin identify a novel Z-line to I-band linking system. *Circ. Res.* 89, 1065–1072. doi: 10.1161/hh2301.100981

Barash, I. A., Mathew, L., Ryan, A. F., Chen, J., and Lieber, R. L. (2004). Rapid muscle-specific gene expression changes after a single bout of eccentric contractions in the mouse. *Am. J. Physiol. Cell Physiol.* 286, C355–C364.

Bell, G. (2008). Models for the specific adhesion of cells to cells. A theoretical framework for adhesion mediated by reversible bonds between cell surface molecules. *Cell Proteom.* 200, 618–627.

Bezold, K. L., Shaffer, J. F., Khosa, J. K., Hoye, E. R., and Harris, S. P. (2013). A gain-of-function mutation in the M-domain of cardiac myosin-binding protein-C increases binding to actin. *J. Biol. Chem.* 288, 21496–21505. doi: 10.1074/jbc.M113.474346

Bullard, B., Ferguson, C., Minajeva, A., Leake, M. C., Gautel, M., and Labeit, D. (2004). Association of the chaperone alphaB-crystallin with titin in heart muscle. *J. Biol. Chem.* 279, 7917–7924. doi: 10.1074/jbc.m307473200

Cantor, C. (1980). *The Behavior of Biological Macromolecules*. San Francisco: Freeman and Company, 849–1371.

Carrion-Vazquez, M., Marszalek, P. E., Oberhauser, A. F., and Fernandez, J. M. (1999). Atomic force microscopy captures length phenotypes in single proteins. *Proc. Natl. Acad. Sci. U.S.A.* 96, 11288–11292. doi: 10.1073/pnas.96.20.11288

Cazorla, O., Freiburg, A., Helmes, M., Centner, T., McNabb, M., and Wu, Y. (2000). Differential expression of cardiac titin isoforms and modulation of cellular stiffness. *Circ. Res.* 86, 59–67. doi: 10.1161/01.res.86.1.59

Chen, H., Yuan, G., Winardhi, R. S., Yao, M., Popa, I., and Fernandez, J. M. (2015). Dynamics of equilibrium folding and unfolding transitions of titin immunoglobulin domain under constant forces. *J. Am. Chem. Soc.* 137, 3540–3546. doi: 10.1021/ja5119368

Chung, C. S., Hutchinson, K. R., Methawasin, M., Saripalli, C., Smith, J. E., and Hidalgo, C. G. (2013). Shortening of the elastic tandem immunoglobulin

segment of titin leads to diastolic dysfunction. *Circulation* 128, 19–28. doi: 10.1161/CIRCULATIONAHA.112.001268

Donlin, L. T., Andresen, C., Just, S., Rudensky, E., Pappas, C. T., and Kruger, M. (2012). Smyd2 controls cytoplasmic lysine methylation of Hsp90 and myofilament organization. *Genes Dev.* 26, 114–119. doi: 10.1101/gad.177758.111

Dutta, S., Tsiros, C., Sundar, S. L., Athar, H., Moore, J., Nelson, B., et al. (2018). Calcium increases titin N2A binding to F-actin and regulated thin filaments. *Sci. Rep.* 8:14575. doi: 10.1038/s41598-018-32952-8

Florin, E. L., Lehmann, H., Ludwig, M., Dornmair, C., Moy, V. T., and Gaub, H. E. (1995). Sensing specific molecular interactions with the atomic force microscope. *Biosens. Bioelectron.* 10, 895–901. doi: 10.1016/0956-5663(95)99227-c

Freiburg, A., Trombitas, K., Hell, W., Cazorla, O., Fougerousse, F., Centner, T., et al. (2000). Series of exon-skipping events in the elastic spring region of titin as the structural basis for myofibrillar elastic diversity. *Circ. Res.* 86, 1114–1121. doi: 10.1161/01.res.86.11.1114

Fukuda, N., Granzier, H. L., Ishiwata, S., and Kurihara, S. (2008). Physiological functions of the giant elastic protein titin in mammalian striated muscle. *J. Physiol. Sci.* 58, 151–159. doi: 10.2170/physiolsci.RV005408

Fukuda, N., Wu, Y., Nair, P., and Granzier, H. L. (2005). Phosphorylation of titin modulates passive stiffness of cardiac muscle in a titin isoform-dependent manner. *J. Gen. Physiol.* 125, 257–271. doi: 10.1085/jgp.200409177

Garvey, S. M., Rajan, C., Lerner, A. P., Frankel, W. N., and Cox, G. A. (2002). The muscular dystrophy with myositis (mdm) mouse mutation disrupts a skeletal muscle-specific domain of titin. *Genomics* 79, 146–149. doi: 10.1006/geno.2002.6685

Granzier, H., Helmes, M., and Trombitas, K. (1996). Nonuniform elasticity of titin in cardiac myocytes: a study using immunoelectron microscopy and cellular mechanics. *Biophys. J.* 70, 430–442. doi: 10.1016/s0006-3495(96)79586-3

Granzier, H. L., and Labeit, S. (2005). Titin and its associated proteins: the third myofilament system of the sarcomere. *Adv. Protein Chem.* 71, 89–119. doi: 10.1016/s0065-3233(04)71003-7

Hayashi, C., Ono, Y., Doi, N., Kitamura, F., Tagami, M., and Mineki, R. (2008). Multiple molecular interactions implicate the connectin/titin N2A region as a modulating scaffold for p94/calpain 3 activity in skeletal muscle. *J. Biol. Chem.* 283, 14801–14814. doi: 10.1074/jbc.M708262200

Helmes, M., Trombitas, K., Centner, T., Kellermayer, M., Labeit, S., Linke, W. A., et al. (1999). Mechanically driven contour-length adjustment in rat cardiac titin's unique N2B sequence: titin is an adjustable spring. *Circ. Res.* 84, 1339–1352. doi: 10.1161/01.res.84.11.1339

Hidalgo, C., and Granzier, H. (2013). Tuning the molecular giant titin through phosphorylation: role in health and disease. *Trends Cardiovasc. Med.* 23, 165–171. doi: 10.1016/j.tcm.2012.10.005

Hisman, K. S., Schiffer, K., and Linke, W. A. (2011). Protein Kinase G mnediated phosphoryation of the elastic N2A titin domains. *Acta Physiol.* 201:9.

Horowits, R., Maruyama, K., and Podolsky, R. J. (1989). Elastic behavior of connectin filaments during thick filament movement in activated skeletal muscle. *J. Cell Biol.* 109, 2169–2176. doi: 10.1083/jcb.109.5.2169

Howarth, J. W., Ramisetti, S., Nolan, K., Sadayappan, S., and Rosevear, P. R. (2012). Structural insight into unique cardiac myosin-binding protein-C motif: a partially folded domain. *J. Biol. Chem.* 287, 8254–8262. doi: 10.1074/jbc.M111.309591

Kellermayer, M. S., Bustamante, C., and Granzier, H. L. (2003). Mechanics and structure of titin oligomers explored with atomic force microscopy. *Biochim. Biophys. Acta* 1604, 105–114. doi: 10.1016/s0005-2728(03)00029-x

Kellermayer, M. S., Smith, S., Bustamante, C., and Granzier, H. L. (2000). Mechanical manipulation of single titin molecules with laser tweezers. *Adv. Exp. Med. Biol.* 481, 127–128.

Kellermayer, M. S., Smith, S. B., Bustamante, C., and Granzier, H. L. (2001). Mechanical fatigue in repetitively stretched single molecules of titin. *Biophys. J.* 80, 852–863. doi: 10.1016/s0006-3495(01)76064-x

Kruger, M., Kotter, S., Grutzner, A., Lang, P., Andresen, C., and Redfield, M. M. (2009). Protein kinase G modulates human myocardial passive stiffness by phosphorylation of the titin springs. *Circ. Res.* 104, 87–94. doi: 10.1161/CIRCRESAHA.108.184408

Labeit, S., and Kolmerer, B. (1995). Titins: giant proteins in charge of muscle ultrastructure and elasticity. *Science* 270, 293–296. doi: 10.1126/science.270.5234.293

Lahmers, S., Wu, Y., Call, D. R., Labeit, S., and Granzier, H. (2004). Developmental control of titin isoform expression and passive stiffness in fetal and neonatal myocardium. *Circ. Res.* 94, 505–513. doi: 10.1161/01.res.0000115522.52554.86

LeWinter, M. M., and Granzier, H. L. (2014). Cardiac titin and heart disease. *J. Cardiovasc. Pharmacol.* 63, 207–212. doi: 10.1097/fjc.0000000000000007

Li, H., and Fernandez, J. M. (2003). Mechanical design of the first proximal Ig domain of human cardiac titin revealed by single molecule force spectroscopy. *J. Mol. Biol.* 334, 75–86. doi: 10.1016/j.jmb.2003.09.036

Li, H., Linke, W. A., Oberhauser, A. F., Carrion-Vazquez, M., Kerkvliet, J. G., and Lu, H. (2002). Reverse engineering of the giant muscle protein titin. *Nature* 418, 998–1002.

Li, H., Oberhauser, A. F., Redick, S. D., Carrion-Vazquez, M., Erickson, H. P., and Fernandez, J. M. (2001). Multiple conformations of PEVK proteins detected by single-molecule techniques. *Proc. Natl. Acad. Sci. U.S.A.* 98, 10682–10686. doi: 10.1073/pnas.191189098

Linke, W. A. (2018). Titin gene and protein functions in passive and active muscle. *Annu. Rev. Physiol.* 80, 389–411. doi: 10.1146/annurev-physiol-021317-121234

Linke, W. A., and Granzier, H. (1998). A spring tale: new facts on titin elasticity. *Biophys. J.* 75, 2613–2614. doi: 10.1016/s0006-3495(98)77706-9

Lostal, W., Roudaut, C., Faivre, M., Charton, K., Suel, L., and Bourg, N. (2019). Titin splicing regulates cardiotoxicity associated with calpain 3 gene therapy for limb-girdle muscular dystrophy type 2A. *Sci. Transl. Med.* 11:eaat6072. doi: 10.1126/scitranslmed.aat6072

Lun, A. S., Chen, J., and Lange, S. (2014). Probing muscle ankyrin-repeat protein (MARP) structure and function. *Anat. Rec.* 297, 1615–1629. doi: 10.1002/ar.22968

Marko, J. F., and Siggia, E. D. (1994). Fluctuations and supercoiling of DNA. *Science* 265, 506–508. doi: 10.1126/science.8036491

Miller, M. K., Bang, M. L., Witt, C. C., Labeit, D., Trombitas, C., and Watanabe, K. (2003). The muscle ankyrin repeat proteins: CARP, ankrd2/Arpp and DARP as a family of titin filament-based stress response molecules. *J. Mol. Biol.* 333, 951–964. doi: 10.1016/j.jmb.2003.09.012

Munkanatta Godage, D. N. P., VanHecke, G. C., Samarasinghe, K. T. G., Feng, H. Z., Hiske, M., and Holcomb, J. (2018). SMYD2 glutathionylation contributes to degradation of sarcomeric proteins. *Nat. Commun.* 9:4341. doi: 10.1038/s41467-018-06786-x

Oberhauser, A. F., Hansma, P. K., Carrion-Vazquez, M., and Fernandez, J. M. (2001). Stepwise unfolding of titin under force-clamp atomic force microscopy. *Proc. Natl. Acad. Sci. U.S.A.* 98, 468–472. doi: 10.1073/pnas.98.2.468

Ojima, K., Kawabata, Y., Nakao, H., Nakao, K., Doi, N., and Kitamura, F. (2010). Dynamic distribution of muscle-specific calpain in mice has a key role in physical-stress adaptation and is impaired in muscular dystrophy. *J. Clin. Invest.* 120, 2672–2683. doi: 10.1172/JCI40658

Ojima, K., Ono, Y., Doi, N., Yoshioka, K., Kawabata, Y., Labeit, S., et al. (2007). Myogenic stage, sarcomere length, and protease activity modulate localization of muscle-specific calpain. *J. Biol. Chem.* 282, 14493–14504. doi: 10.1074/jbc.m610806200

Ono, Y., Torii, F., Ojima, K., Doi, N., Yoshioka, K., and Kawabata, Y. (2006). Suppressed disassembly of autolyzing p94/CAPN3 by N2A connectin/titin in a genetic reporter system. *J. Biol. Chem.* 281, 18519–18531. doi: 10.1074/jbc.m601029200

Pauling, L., Corey, R. B., and Branson, H. R. (1951). The structure of proteins; two hydrogen-bonded helical configurations of the polypeptide chain. *Proc. Natl. Acad. Sci. U.S.A.* 37, 205–211.

Perkin, J., Slater, R., Del Favero, G., Lanzicher, T., Hidalgo, C., and Anderson, B. (2015). Phosphorylating Titin's cardiac N2B element by ERK2 or CaMKIIdelta lowers the single molecule and cardiac muscle force. *Biophys. J.* 109, 2592–2601. doi: 10.1016/j.bpj.2015.11.002

Popa, I., Berkovich, R., Alegre-Cebollada, J., Badilla, C. L., Rivas-Pardo, J. A., and Taniguchi, Y. (2013). Nanomechanics of HaloTag tethers. *J. Am. Chem. Soc.* 135, 12762–12771. doi: 10.1021/ja4056382

Taniguchi, Y., and Kawakami, M. (2010). Application of HaloTag protein to covalent immobilization of recombinant proteins for single molecule force spectroscopy. *Langmuir* 26, 10433–10436. doi: 10.1021/la101658a

Tiffany, H., Sonkar, K., and Gage, M. J. (2017). The insertion sequence of the N2A region of titin exists in an extended structure with helical characteristics. *Biochim. Biophys. Acta Proteins Proteom.* 1865, 1–10. doi: 10.1016/j.bbapap.2016.10.003

Trombitas, K., Greaser, M., French, G., and Granzier, H. (1998a). PEVK extension of human soleus muscle titin revealed by immunolabeling with the anti-titin antibody 9D10. *J. Struct. Biol.* 122, 188–196. doi: 10.1006/jsbi.1998.3984

Trombitas, K., Greaser, M., Labeit, S., Jin, J. P., Kellermayer, M., Helmes, M., et al. (1998b). Titin extensibility in situ: entropic elasticity of permanently folded and permanently unfolded molecular segments. *J. Cell Biol.* 140, 853–859. doi: 10.1083/jcb.140.4.853

Trombitas, K., Jin, J. P., and Granzier, H. (1995). The mechanically active domain of titin in cardiac muscle. *Circ. Res.* 77, 856–861. doi: 10.1161/01.res.77.4.856

Trombitas, K., Redkar, A., Centner, T., Wu, Y., Labeit, S., and Granzier, H. (2000). Extensibility of isoforms of cardiac titin: variation in contour length of molecular subsegments provides a basis for cellular passive stiffness diversity. *Biophys. J.* 79, 3226–3234. doi: 10.1016/s0006-3495(00)76555-6

van der Pijl, R., Strom, J., Conijn, S., Lindqvist, J., Labeit, S., Granzier, H., et al. (2018). Titin-based mechanosensing modulates muscle hypertrophy. *J. Cachexia. Sarcopenia. Muscle* 9, 947–961. doi: 10.1002/jcsm.12319

van der Pijl, R. J., Granzier, H. L., and Ottenheijm, C. A. C. (2019). Diaphragm contractile weakness due to reduced mechanical loading: role of titin. *Am. J. Physiol. Cell Physiol.* 317, C167–C176. doi: 10.1152/ajpcell.00509.2018

Voelkel, T., Andresen, C., Unger, A., Just, S., Rottbauer, W., and Linke, W. A. (2013). Lysine methyltransferase Smyd2 regulates Hsp90-mediated protection of the sarcomeric titin springs and cardiac function. *Biochim. Biophys. Acta* 1833, 812–822. doi: 10.1016/j.bbamcr.2012.09.012

Watanabe, K., Muhle-Goll, C., Kellermayer, M. S., Labeit, S., and Granzier, H. (2002a). Different molecular mechanics displayed by titin's constitutively and differentially expressed tandem Ig segments. *J. Struct. Biol.* 137, 248–258. doi: 10.1006/jsbi.2002.4458

Watanabe, K., Nair, P., Labeit, D., Kellermayer, M. S., Greaser, M., Labeit, S., et al. (2002b). Molecular mechanics of cardiac titin's PEVK and N2B spring elements. *J. Biol. Chem.* 277, 11549–11558. doi: 10.1074/jbc.m200356200

Witt, C. C., Ono, Y., Puschmann, E., McNabb, M., Wu, Y., and Gotthardt, M. (2004). Induction and myofibrillar targeting of CARP, and suppression of the Nkx2.5 pathway in the MDM mouse with impaired titin-based signaling. *J. Mol. Biol.* 336, 145–154. doi: 10.1016/j.jmb.2003.12.021

Wolny, M., Batchelor, M., Knight, P. J., Paci, E., Dougan, L., and Peckham, M. (2014). Stable single alpha-helices are constant force springs in proteins. *J. Biol. Chem.* 289, 27825–27835. doi: 10.1074/jbc.M114.585679

Yamasaki, R., Wu, Y., McNabb, M., Greaser, M., Labeit, S., and Granzier, H. (2002). Protein kinase A phosphorylates titin's cardiac-specific N2B domain and reduces passive tension in rat cardiac myocytes. *Circ. Res.* 90, 1181–1188. doi: 10.1161/01.res.0000021115.24712.99

Zhou, T., Fleming, J. R., Franke, B., Bogomolovas, J., Barsukov, I., and Rigden, D. J. (2016). CARP interacts with titin at a unique helical N2A sequence and at the domain Ig81 to form a structured complex. *FEBS Lett.* 590, 3098–3110. doi: 10.1002/1873-3468.12362

Zhu, Y., Bogomolovas, J., Labeit, S., and Granzier, H. (2009). Single molecule force spectroscopy of the cardiac titin N2B element: effects of the molecular chaperone alphaB-crystallin with disease-causing mutations. *J. Biol. Chem.* 284, 13914–13923. doi: 10.1074/jbc.M809743200

Conflict of Interest: The authors declare that the research was conducted in the absence of any commercial or financial relationships that could be construed as a potential conflict of interest.

frontiers in Physiology

BRIEF RESEARCH REPORT
published: 19 March 2020
doi: 10.3389/fphys.2020.00241

Pressure Overload Is Associated With Low Levels of Troponin I and Myosin Binding Protein C Phosphorylation in the Hearts of Patients With Aortic Stenosis

*O'neal Copeland[1], Andrew Messer[1], Andrew Jabbour[2], Corrado Poggesi[3], Sanjay Prasad[2] and Steven Marston[1]**

[1] Imperial College London, London, United Kingdom, [2] Royal Brompton Hospital, and Imperial College London, London, United Kingdom, [3] University of Florence, Florence, Italy

In previous studies of septal heart muscle from HCM patients with hypertrophic obstructive cardiomyopathy (HOCM, LVOT gradient 50–120 mmHg) we found that the level of phosphorylation of troponin I (TnI) and myosin binding protein C (MyBP-C) was extremely low yet samples from hearts with HCM or DCM mutations that did not have pressure overload were similar to donor heart controls. We therefore investigated heart muscle samples taken from patients undergoing valve replacement for aortic stenosis, since they have pressure overload that is unrelated to inherited cardiomyopathy. Thirteen muscle samples from septum and from free wall were analyzed (LVOT gradients 30–100 mmHg) The levels of TnI and MyBP-C phosphorylation were determined in muscle myofibrils by separating phosphospecies using phosphate affinity SDS-PAGE and detecting with TnI and MyBP-C specific antibodies. TnI was predominantly monophosphorylated and total phosphorylation was 0.85 ± 0.03 molsPi/mol TnI. This phosphorylation level was significantly different ($p < 0.0001$) from both donor heart TnI (1.6 ± 0.06 molsPi/mol TnI) and HOCM heart TnI (0.19 ± 0.04 molsPi/mol TnI). MyBP-C is phosphorylated at up to four sites. In donor heart the 4P and 3P species predominate but in the pressure overload samples the 4P species was much reduced and 3P and 1P species predominated. Total phosphorylation was 2.0 ± 0.2 molsPi/mol MyBP-C ($n = 8$) compared with 3.4 ± 0.07 ($n = 21$) in donor heart and 1.1 ± 0.1 ($n = 10$) in HOCM heart. We conclude that pressure overload may be associated with substantial dephosphorylation of troponin I and MyBP-C.

Keywords: troponin I, phosphorylation, aortic stenosis, pressure overload, cardiomyopathy, protein kinase A, myosin binding protein C

OPEN ACCESS

Edited by:
Sachio Morimoto, International University of Health and Welfare (IUHW), Japan

Reviewed by:
Lori A. Walker, University of Colorado Denver, United States
R. John Solaro, The University of Illinois at Chicago, United States

****Correspondence:***
Steven Marston
s.marston@imperial.ac.uk

Specialty section:
This article was submitted to Striated Muscle Physiology, a section of the journal Frontiers in Physiology

Received: *19 December 2019*
Accepted: *02 March 2020*
Published: *19 March 2020*

Citation:
Copeland O, Messer A, Jabbour A, Poggesi C, Prasad S and Marston S (2020) Pressure Overload Is Associated With Low Levels of Troponin I and Myosin Binding Protein C Phosphorylation in the Hearts of Patients With Aortic Stenosis. Front. Physiol. 11:241. doi: 10.3389/fphys.2020.00241

INTRODUCTION

Cardiac muscle contractility is modulated by the β-adrenergic system that primarily acts via activation of protein kinase A (PKA). In the cardiac muscle sarcomere the main targets of PKA are myosin binding protein C (MyBP-C) and Troponin I (TnI) and phosphorylation of these proteins plays a vital role in the enhanced contraction and relaxation kinetics induced by adrenergic stimulation (Layland et al., 2005b; Barefield and Sadayappan, 2010; Messer and Marston, 2014). In

non-diseased heart muscle from donor human hearts or from mice, the level of phosphorylation of TnI and MyBP-C are both relatively high (Messer et al., 2009; Copeland et al., 2010). TnI has a total level of phosphorylation of 1.6 molsPi/mol in human and 1.2 in mouse with the majority of TnI being bis-phosphorylated. MyBP-C has a total level of phosphorylation of 3.4 molsPi/mol MyBP-C with 4P and 3P species predominating.

In heart disease the phosphorylation level is often low. For instance in idiopathic (non-ischaemic) end stage heart failure explants, phosphorylation levels are 0.26 molsPi/mol TnI and 0.62 molsPi/mol MyBP-C (van der Velden et al., 2003; Messer et al., 2007; Zaremba et al., 2007; Messer et al., 2009). In genetic heart disease the situation appears to be more complex. Explanted heart samples with inherited DCM can be associated with high or low levels of phosphorylation in the range 0.3–1.5 molsPi/mol TnI (Memo et al., 2013). However, myectomy samples taken from patients with inherited hypertrophic obstructive cardiomyopathy (HOCM) always have a low level of phosphorylation (Messer et al., 2009; Copeland et al., 2010; Bayliss et al., 2012). Thus, there appears to be no direct relationship between mutations causing heart disease and the TnI and MyBP-C phosphorylation level.

The HCM-associated mutations often cause a hypertrophied interventricular septum that can lead to left ventricular outflow tract obstruction (LVOTO). The septal myectomy operation for patients with HCM is usually indicated to reduce the obstruction when there is a high Aorta/LV pressure difference, typically 100 mmHg (Firoozi et al., 2002; Elliott and McKenna, 2004). We hypothesized that the pressure gradient may be a major factor in inducing the secondary phenotype of HOCM heart. To test this we have studied TnI and MyBP-C phosphorylation levels in heart muscle from patients with HCM but without pressure overload and heart muscle from patients without HCM but with pressure overload due to aortic stenosis (Bates, 2011).

METHODS

Tissue Sources

Donor hearts and the K280N HCM sample were supplied by the Sydney Heart Bank (Li et al., 2013; Messer et al., 2016). Donor sample (NH) had no history of cardiac disease and normal ECG and ventricular function and were obtained when no suitable transplant recipient was found. HOCM sample (MV) was obtained from a patient undergoing septal myectomy operation at The Heart Hospital (UCL), London (Jacques et al., 2008). Clinical data for NH and MV has been previously reported in Messer et al. (2007), Bayliss et al. (2012) and in **Supplementary Table 1**. Measurements of TnI and MyBP-C phosphorylation were described in Messer et al. (2009) and Copeland et al. (2010).

Biopsies were taken from septum and free wall of patients undergoing valve replacement surgery to relieve aortic stenosis at the Royal Brompton Hospital, London and Careggi University Hospital, Florence. The ACTC E99K patient sample was kindly supplied by Dr. Lorenzo Monserrat, La Coruña, Spain (Monserrat et al., 2007; Song et al., 2011). Available clinical data on these samples is given in the **Supplementary Material**.

Patients gave written consent with PIS approved by the relevant ethical committee. All samples are anonymised. The investigations conform to the principles of the Declaration of Helsinki.

Ethical approval for collection and distribution of the human heart samples was granted by the Research Integrity, Human Research Ethics Committee, University of Sydney (Protocol No. 15401); the Joint UCL/UCLH Ethics Committee Rec No: 04/0035; Outer North East London Research Ethics Committee REC ref: 10/H0701/8; Careggi University Hospital Ref: 2006/0024713 and Comite Ético de Investigatio ń Clìnica de Galicia. Permission for study of the samples was granted by the NHS National Research Ethics Service, South West London REC3 (10/H0803/147).

Measurement of TnI and MyBP-C Phosphorylation Level

Twenty milligrams of heart muscle sample, stored in liquid nitrogen were crushed in a liquid nitrogen cooled percussion mortar and then homogenized in 200 μl buffer (5 mmol/l NaH_2PO_4, 5 mmol/l Na_2HPO_4 pH 7.0, 0.1 mol/l NaCl, 5 mmol/l $MgCl_2$, 0.5 mmol/l EGTA, 0.1% Triton X-100, 20 mmol/l NaF and 5 mmol/l DTT with 2 μg/ml each of the protease inhibitors E64, chymostatin, leupeptin and pepstatin A). The homogenate was then centrifuged at 16,500 × *g* for 5 min and the supernatant discarded. The wash process was repeated and then the pellet was dissolved in sample buffer containing 8 M urea, 2 M thiourea, 0.05 M Tris-HCl, pH 6.8, 75 mM DTT, 3% SDS and 0.05% bromophenol blue as decribed (Layland et al., 2005a; Messer et al., 2007).

TnI phosphorylation levels in heart muscle myofirils was measured by Phosphate affinity SDS-PAGE as described by Messer et al. (2009). Discontinuous SDS-PAGE gels were hand-cast and run using the Mini-PROTEAN system (Bio-Rad). Gel compositions are as follows: stacking gel: 4% acrylamide (29:1 acrylamide:bis-acrylamide), resolving gel: 10% acrylamide (29:1 acrylamide:bis-acrylamide, 100 μM $MnCl_2$ (from 10 mM stock) and 50 μM Phos-TagTM acrylamide [from 5 mM stock solution of Phos-TagTM acylamide AAL-107 (NARD Institute, Hyogo, Japan)] prepared according to suppliers instructions (Kinoshita et al., 2006).

Gels were probed with the phosphorylation-independent anti-human-cardiac troponin I (hcTnI) clone 14G5 mouse mAb (Abcam plc antibodies), 1/2,000 dilution on Western blots. Secondary antibody was HRP- conjugated anti-rabbit IgG (1:1,000) and the blots were visualized using ECL (GE Biosciences). Chemiluminescence was detected by a cooled CCD camera-based gel imager (G:BOX Chemi HR16, Syngene).

To resolve MyBP-C phosphospecies the myofibril samples were run on the gels for 165 min. The current was initially 25 mA, raised to 35 mA once the samples had entered the resolving gel. The gels were Western blotted and probed with a rabbit polyclonal antibody against cMyBP-C residues 2–14 which recognizes total cMyBP-C or with phosphorylation site-specific antibodies (Bardswell et al., 2009; Sadayappan et al., 2009; Copeland et al., 2010).

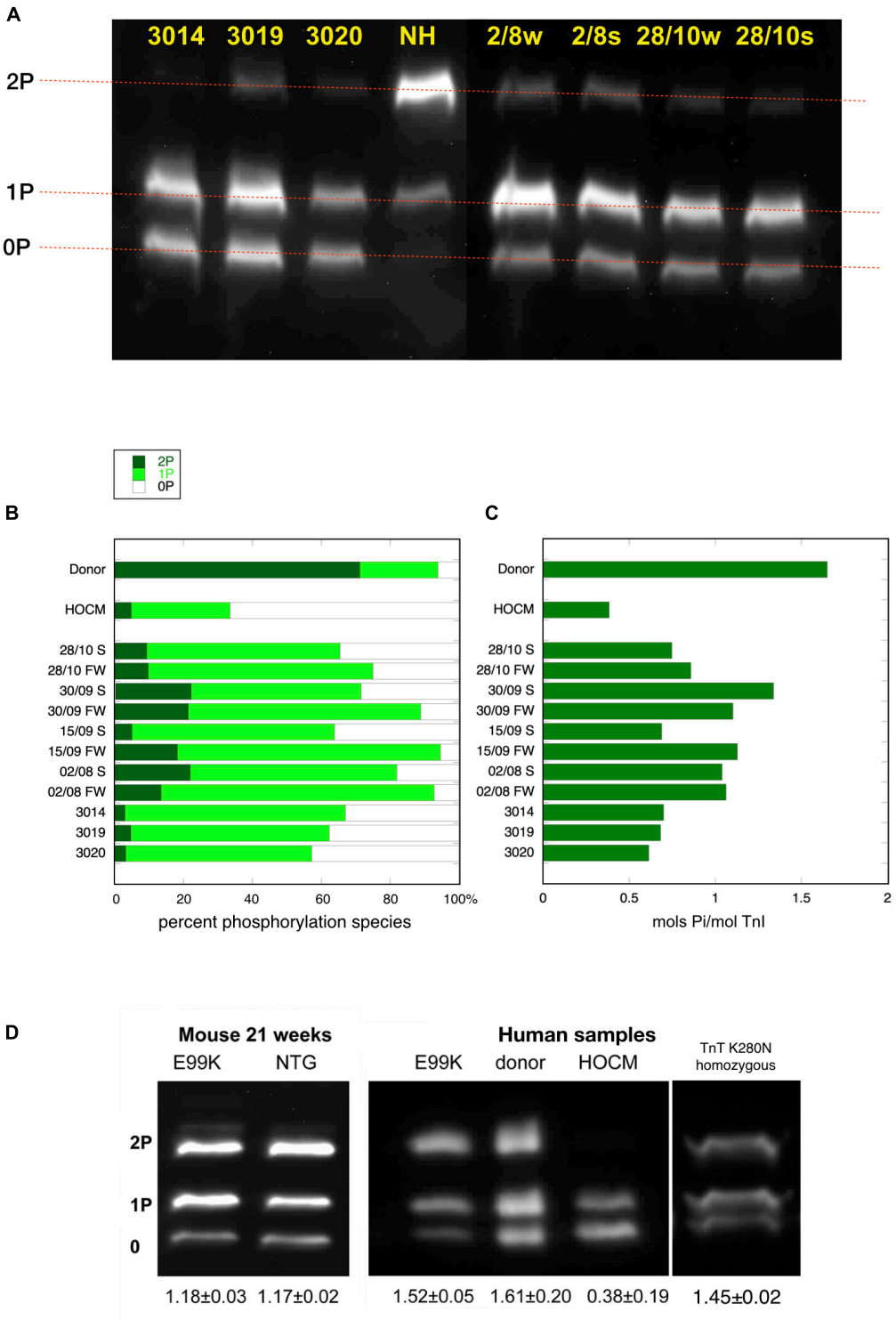

FIGURE 1 | Phosphate affinity SDS-PAGE separation of myofibrils, probed with antibody 14G5 to troponin I. **(A)** Example of separation of phosphospecies. Phosphorylated protein is retarded in proportion to level of phosphorylation yielding discrete bands for bis- mono- and unphosphorylated troponin I. NH is a donor heart sample showing a high level of 2P species. The other lanes are aortic stenosis samples which show high level of 1P and 0P species. **(B)** Distribution of 2P, 1P, and 0P species in heart muscle samples. The results for each sample are the means of 2–4 replicate assays. S, septum; FW, free wall. Donor heart NH and HOCM heart MV control results are the mean of replicates included in the same gels as the pressure overload samples. Full data is shown in **Supplementary Table 2**. **(C)** Calculated total phosphorylation level for these samples. **(D)** Phosphate affinity SDS-PAGE of ACTC E99K mouse, ACTC E99K human heart and TNNT2 K280N human heart samples with donor and HOCM controls. Total phosphorylation is shown below underneath each lane.

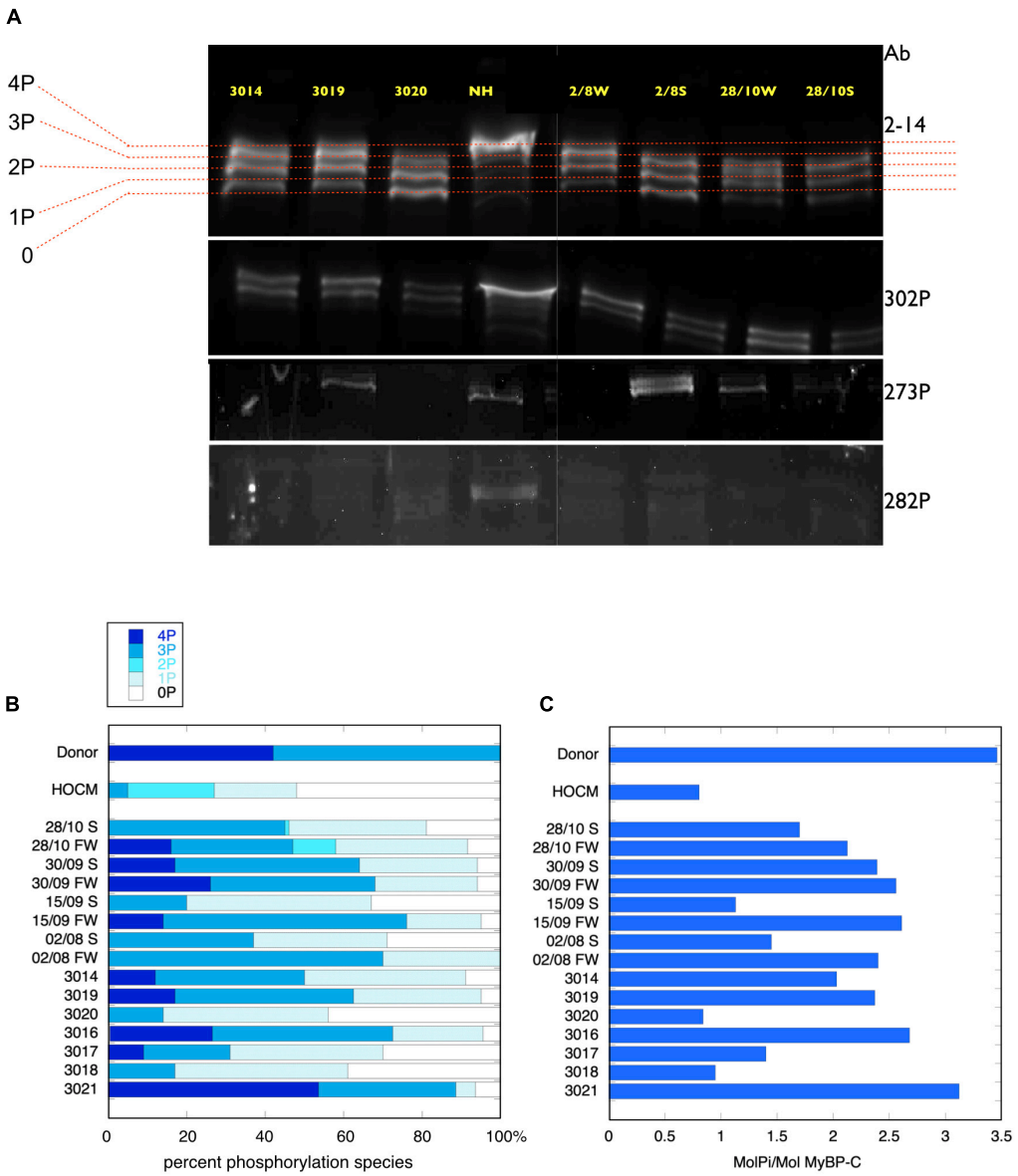

FIGURE 2 | Phosphate affinity SDS-PAGE separation of myofibrils, probed with antibodies to MyBP-C. (**A**, top) Example of separation of MyBP-C phosphospecies probed with 2–14 pan MyBP-C antibody. NH is a donor heart sample showing a high level of 3P and 4P species. The other lanes are aortic stenosis samples which show less 4P and more 1P and 0P species. (**A**, lower panels) the same samples probed with antibody specific to phosphorylated ser 302, ser 273 and ser 282. **(B)** Distribution of 4P, 3P, 2P, 1P, and 0P species of MyBP-C in heart muscle samples. The results for each sample are the means of 2–4 replicate assays. Donor heart NM and HOCM heart MV control results are the mean of replicates included in the same gels as the pressure overload samples. Full data is shown in **Supplementary Table 3**. S, septum; FW, free wall. **(C)** Calculated total phosphorylation level for these samples.

RESULTS AND DISCUSSION

Reduced Level of Phosphorylation in Pressure Overloaded Heart

We studied 13 heart muscle biopsies from intraventricular septum and free wall taken from patients undergoing valve surgery to relieve pressure overload and compared them with previously studied donor heart samples and myectomy samples from patients with HOCM (Messer et al., 2009; Copeland et al., 2010). LVOT gradients ranged from 30 to 100 mmHg in the pressure overload patients compared with 90–120 mmHg in the HOCM patients' hearts and close to zero in the donor hearts (see **Supplementary Tables 1** and **2**).

The levels of TnI and MyBP-C phosphorylation were determined in muscle myofibrils by separating phosphospecies using phosphate affinity SDS-PAGE and detecting with TnI and MyBP-C specific, but phosphorylation-independent antibodies previously characterized. This technique measures the proportions of bis-phosphorylated, monophosphorylated

and unphosphorylated species of TnI. We previously showed that in donor hearts, 70% of the troponin I is bis-phosphorylated and 21% is monophosphorylated with a calculated total phosphorylation of 1.6 ± 0.06 molsPi/mol TnI. The HOCM samples were just 5% bis-phosphorylated and 30% monophosphorylated with a calculated total phosphorylation level of 0.18 ± 0.02 molsPi/mol TnI (Messer et al., 2009; **Figure 1**).

In the pressure overload samples, we found that TnI was predominantly monophosphorylated (0P = 24 ± 2%, 1P = 67 ± 2%, 2P = 9 ± 1%, $n = 21$) and total phosphorylation was 0.85 ± 0.03 molsPi/mol TnI and was not significantly different in septum and free wall samples (see **Supplementary Figure 1**). Thus in pressure overload samples, the phosphorylation level was significantly less than donor heart and significantly more than in HOCM heart Troponin I ($p \leq 0.0001$). Western blotting using antibodies to bis-phosphorylated troponin I confirmed that phosphorylation at serines 22 and 23 was low relative to donor heart samples. Mass spectrometry measurements showed that only Ser22 or Ser23 were phosphorylated with no evidence for phosphorylation at other sites in Troponin I.

MyBP-C is phosphorylated at up to four sites. In donor heart samples we showed that the 4P and 3P species predominate (4P = 43%, 3P = 57%, 2P = 0%, 1P = 0%, 0P = 0%) (Copeland et al., 2010). In the pressure overload samples the 4P species was much reduced and 3P and 1P species predominated (4P = 9 ± 3%, 3P = 41 ± 5%, 2P = 1 ± 1%, 1P = 33 ± 2%, 0P 15 ± 4%, $n = 15$) (**Figure 2**). Total phosphorylation was 2.0 ± 0.2 molsPi/mol MyBP-C ($n = 15$) compared with 3.4 ± 0.07 ($n = 21$) in donor heart and 1.1 ± 0.1 ($n = 10$) in HOCM heart (Copeland et al., 2010). Comparison of free wall and septal samples indicated higher phosphorylation levels in the free wall that was barely statistically significant (see **Supplementary Figure 2**). We used antibodies specific to the main targets of PKA in MYBP-C: phosphorylation sites at Ser 302, 273 and 283 but found no consistent pattern of phosphorylation in the pressure overload samples that was different from the pan-MyBP-C antibody, 2–14.

Normal Level of Phosphorylation in HCM Samples Without Pressure Overload

To test whether the low level of phosphorylation in HOCM myectomy samples is due to the mutation or the pressure overload, we investigated samples from HCM patients that did not have pressure overload. The ACTC E99K mutation is associated with HCM, with the hypertrophy often confined to the apex of the heart and does not develop HOCM (Monserrat et al., 2007). We have previously studied a biopsy from a 33 year old patient with the ACTC E99K mutation who showed no signs of LVOTO and was not on any medication (Song et al., 2011). The tissue sample was obtained from an operation to repair an atrial septal defect. Troponin I, troponin T, and MyBP-C phosphorylation levels in myofibrils were the same as donor heart samples (see **Figure 1D**). Likewise, *The ACTC* E99K mouse model of HCM develops apical hypertrophy without LVOTO or symptoms of heart failure at 21 weeks (Song et al., 2011). The HCM mouse myofibrils have the same level of troponin I, troponin T, and MyBP-C phosphorylation as NTG littermates (**Figure 1D**).

We have also studied a heart muscle sample from a patient with an HCM-causing mutation [homozygous TNNT2 K280N (Sequeira et al., 2013; Messer et al., 2016; Piroddi et al., 2019)]. The patient had a myectomy operation that relieved LVOTO permanently but later developed heart failure requiring a heart transplant. This sample is from the explanted heart. The troponin I phosphorylation level was comparable to donor heart (**Figure 1D**). These two examples suggest that reduced levels of phosphorylation are related primarily to the pressure overload.

CONCLUSION

In these limited studies on human heart muscle samples we have found that a reduced level of phosphorylation of TnI and MyBP-C, the sarcomeric targets of PKA, is associated with pressure overload, i.e., a mean transvalvular pressure gradient >40 mmHg, but is not associated with hypertrophic cardiomyopathy in the absence of pressure overload.

Since we are using human samples obtained during surgery our results could be confounded by a number of uncontrolled variables such as the time between excision of the sample and freezing and the medication, particularly beta-blockers, taken by the patients. On the other hand we have more than 12 years experience making measurements with human heart samples and have not yet been able to detect a correlation between these variables and any measurements we made (Messer et al., 2007, 2009; Jacques et al., 2008; Copeland et al., 2010; Song et al., 2011; Bayliss et al., 2012; Memo et al., 2013).

We do not know the underlying cause of the reduced phosphorylation levels but in HCM and heart failure there is evidence for both the reduction in PKA activity and the increase in phosphatase activity in pathological heart muscle that could account for this observation. In the diseased myocardium β adrenoceptors are often downregulated via receptor phosphorylation and β-arrestin binding (Mangmool et al., 2018) whilst protein phosphatase activity is enhanced via inactivation of phosphatase inhibitor-1 (El-Armouche et al., 2004; Champion, 2005).

DATA AVAILABILITY STATEMENT

All datasets generated for this study are included in the article/**Supplementary Material**.

ETHICS STATEMENT

Ethical approval for collection and distribution of the human heart samples was granted by the Research Integrity, Human Research Ethics Committee, University of Sydney (Protocol No. 15401); the Joint UCL/UCLH Ethics Committee Rec No: 04/0035; Outer North East London Research Ethics

Committee REC ref: 10/H0701/8; Careggi University Hospital Ref: 2006/0024713 and Comite É tico de Investigatio ń Clínica de Galicia. Permission for study of the samples was granted by the NHS National Research Ethics Service, South West London REC3 (10/H0803/147). The patients/participants provided their written informed consent to participate in this study.

AUTHOR CONTRIBUTIONS

OC, AM, and SM performed the experimental work. AJ, CP, and SP supplied the tissue samples. All the authors contributed to and approved the final manuscript that was edited by SM.

FUNDING

This work was supported by a grant from the British Heart Foundation (BHF RG/08/010/25918) and the Seventh Framework Program of the European Union "BIG-HEART," (grant agreement 241577). AJ was supported by a grant from the National Health and Medical Research Council of Australia.

ACKNOWLEDGMENTS

We thank Douglas Ward, Birmingham University for the mass spectrometry measurements and Sakthivel Sadayappan, University of Cincinatti for the MyBP-C – specific antibodies.

SUPPLEMENTARY MATERIAL

The Supplementary Material for this article can be found online at: https://www.frontiersin.org/articles/10.3389/fphys.2020.00241/full#supplementary-material

REFERENCES

Bardswell, S. C., Cuello, F., Rowland, A. J., Sadayappan, S., Robbins, J., Gautel, M., et al. (2009). Distinct sarcomeric substrates are responsible for protein kinase D-mediated regulation of cardiac myofilament Ca2+ sensitivity and crossbridge cycling. *J. Biol. Chem.* 285, 5674–5682. doi: 10.1074/jbc.m109.066456

Barefield, D., and Sadayappan, S. (2010). Phosphorylation and function of cardiac myosin binding protein-C in health and disease. *J. Mol. Cell Cardiol.* 48, 866–875. doi: 10.1016/j.yjmcc.2009.11.014

Bates, E. R. (2011). Treatment options in severe aortic stenosis. *Circulation* 124, 355–359. doi: 10.1161/circulationaha.110.974204

Bayliss, C. R., Jacques, A. M., Leung, M.-C., Ward, D. G., Redwood, C. S., Gallon, C. E., et al. (2012). Myofibrillar Ca2+-sensitivity is uncoupled from troponin I Phosphorylation In Hypertrophic obstructive cardiomyopathy due to abnormal troponin T. *Cardiovasc. Res.* 97, 500–508. doi: 10.1093/cvr/cvs322

Champion, H. C. (2005). Targeting protein phosphatase 1 in heart failure. *Circ. Res.* 96, 708–710. doi: 10.1161/01.res.0000164359.95588.25

Copeland, O., Sadayappan, S., Messer, A. E., Stienen, G. J., Velden, J., and Marston, S. B. (2010). Analysis of cardiac myosin binding protein-C phosphorylation in human heart muscle. *J. Mol. Cell Cardiol.* 49, 1003–1011. doi: 10.1016/j.yjmcc.2010.09.007

El-Armouche, A., Pamminger, T., Ditz, D., Zolk, O., and Eschenhagen, T. (2004). Decreased protein and phosphorylation level of the protein phosphatase inhibitor-1 in failing human hearts. *Cardiovasc. Res.* 61, 87–93. doi: 10.1016/j.cardiores.2003.11.005

Elliott, P., and McKenna, W. J. (2004). Hypertrophic cardiomyopathy. *Lancet* 363, 1881–1891.

Firoozi, S., Elliott, P. M., Sharma, S., Murday, A., Brecker, S. J., Hamid, M. S., et al. (2002). Septal myotomy-myectomy and transcoronary septal alcohol ablation in hypertrophic obstructive cardiomyopathy. A comparison of clinical, haemodynamic and exercise outcomes. *Eur. Heart J.* 23, 1617–1624. doi: 10.1053/euhj.2002.3285

Jacques, A., Briceno, N., Messer, A., Gallon, C., Jalizadeh, S., Garcia, E., et al. (2008). The molecular phenotype of human cardiac myosin associated with hypertrophic obstructive cardiomyopathy. *Cardiovasc. Res.* 79, 481–491. doi: 10.1093/cvr/cvn094

Kinoshita, E., Kinoshita-Kikuta, E., Takiyama, K., and Koike, T. (2006). Phosphate-binding tag, a new tool to visualize phosphorylated proteins. *Mol. Cell Proteom.* 5, 749–757. doi: 10.1074/mcp.t500024-mcp200

Layland, J., Cave, A. C., Warren, C., Grieve, D. J., Sparks, E., Kentish, J. C., et al. (2005a). Protection against endotoxemia-induced contractile dysfunction in mice with cardiac-specific expression of slow skeletal troponin I. *FASEB J.* 19, 1137–1139. doi: 10.1096/fj.04-2519fje

Layland, J., Solaro, R. J., and Shah, A. M. (2005b). Regulation of cardiac contractile function by troponin I phosphorylation. *Cardiovasc. Res.* 66, 12–21. doi: 10.1016/j.cardiores.2004.12.022

Li, A., Estigoy, C., Raftery, M., Cameron, D., Odeberg, J., Pontén, F., et al. (2013). Heart research advances using database search engines, human protein atlas and the sydney heart bank. *Heart Lung Circ.* 22, 819–826. doi: 10.1016/j.hlc.2013.06.006

Mangmool, S., Parichatikanond, W., and Kurose, H. (2018). Therapeutic targets for treatment of heart failure: focus on GRKs and β-Arrestins affecting βAR signaling. *Front. Pharmacol.* 9:1336.

Memo, M., Leung, M.-C., Ward, D. G., dos Remedios, C., Morimoto, S., Zhang, L., et al. (2013). Mutations in thin filament proteins that cause familial dilated cardiomyopathy uncouple troponin i phosphorylation from changes in Myofibrillar Ca2+-sensitivity. *Cardiovasc. Res.* 99, 65–73. doi: 10.1093/cvr/cvt071

Messer, A., Bayliss, C., El-Mezgueldi, M., Redwood, C., Ward, D. G., Leung, M.-C., et al. (2016). Mutations in troponin T associated with hypertrophic cardiomyopathy increase Ca2+-sensitivity and suppress the modulation of Ca2+-sensitivity by troponin I phosphorylation. *Arch. Biochem. Biophys.* 601, 113–120. doi: 10.1016/j.abb.2016.03.027

Messer, A., Gallon, C., McKenna, W., Elliott, P., Dos Remedios, C., and Marston, S. (2009). The use of phosphate-affinity SDS-PAGE to measure the troponin I phosphorylation site distribution in human heart muscle. *Proteom. Clin. Appl.* 3, 1371–1382. doi: 10.1002/prca.200900071

Messer, A., and Marston, S. (2014). Investigating the role of uncoupling of Troponin I phosphorylation from changes in myofibrillar Ca2+-sensitivity in the pathogenesis of Cardiomyopathy. *Front. Physiol.* 5:315. doi: 10.3389/fphys.2014.00315

Messer, A. E., Jacques, A. M., and Marston, S. B. (2007). Troponin phosphorylation and regulatory function in human heart muscle: dephosphorylation of Ser23/24 on troponin I could account for the contractile defect in end-stage heart failure. *J. Mol. Cell Cardiol.* 42, 247–259. doi: 10.1016/j.yjmcc.2006.08.017

Monserrat, L., Hermida-Prieto, M., Fernandez, X., Rodriguez, I., Dumont, C., Cazon, L., et al. (2007). Mutation in the alpha-cardiac actin gene associated with apical hypertrophic cardiomyopathy, left ventricular non-compaction, and septal defects. *Eur. Heart J.* 28, 1953–1961. doi: 10.1093/eurheartj/ehm239

Piroddi, N., Witjas-Paalberends, E. R., Ferrara, C., Ferrantini, C., Vitale, G., Scellini, B., et al. (2019). The homozygous K280N troponin T mutation alters cross-bridge kinetics and energetics in human HCM. *J. Gen. Physiol.* 151, 18–29. doi: 10.1085/jgp.201812160

Sadayappan, S., Gulick, J., Klevitsky, R., Lorenz, J. N., Sargent, M., Molkentin, J. D., et al. (2009). Cardiac myosin binding protein-C phosphorylation in a

{beta}-myosin heavy chain background. *Circulation* 119, 1253–1262. doi: 10.1161/CIRCULATIONAHA.108.798983

Sequeira, V., Wijnker, P. J. M., Nijenkamp, L. L. A. M., Kuster, D. W. D., Najafi, A., Witjas-Paalberends, E. R., et al. (2013). Perturbed length-dependent activation in human hypertrophic cardiomyopathy with missense sarcomeric gene mutations. *Circ. Res.* 112, 1491–1505. doi: 10.1161/CIRCRESAHA.111.300436

Song, W., Dyer, E., Stuckey, D., Copeland, O., Leung, M., Bayliss, C., et al. (2011). Molecular mechanism of the Glu99lys mutation in cardiac actin (ACTC gene) that causes apical hypertrophy in man and mouse. *J. Biol. Chem.* 286, 27582–27593. doi: 10.1074/jbc.M111.252320

van der Velden, J., Papp, Z., Zaremba, R., Boontje, N. M., de Jong, J. W., Owen, V. J., et al. (2003). Increased Ca2+-sensitivity of the contractile apparatus in end-stage human heart failure results from altered phosphorylation of contractile proteins. *Cardiovasc. Res.* 57, 37–47. doi: 10.1016/s0008-6363(02)00606-5

Zaremba, R., Merkus, D., Hamdani, N., Lamers, J., Paulus, W., Dos Remedios, C., et al. (2007). Quantitative analysis of myofilament protein phosphorylation in small cardiac biopsies. *Proteom. Clin. Appl.* 1, 1285–1290. doi: 10.1002/prca.200600891

Conflict of Interest: The authors declare that the research was conducted in the absence of any commercial or financial relationships that could be construed as a potential conflict of interest.

frontiers in Physiology

ORIGINAL RESEARCH
published: 15 April 2020
doi: 10.3389/fphys.2020.00240

Modulation of Titin-Based Stiffness in Hypertrophic Cardiomyopathy via Protein Kinase D

Melissa Herwig[1,2,3,4†], Detmar Kolijn[1,2,3,4†], Mária Lódi[1,2,3,5,6], Soraya Hölper[7], Árpád Kovács[1,2,3], Zoltán Papp[5], Kornelia Jaquet[1,2,3], Peter Haldenwang[8], Cris Dos Remedios[9], Peter H. Reusch[3], Andreas Mügge[1,2], Marcus Krüger[10,11], Jens Fielitz[12,13], Wolfgang A. Linke[14] and Nazha Hamdani[1,2,3,4]*

[1] Department of Molecular and Experimental Cardiology, Ruhr University Bochum, Bochum, Germany, [2] Department of Cardiology, St. Josef-Hospital, Ruhr University Bochum, Bochums, Germany, [3] Department of Clinical Pharmacology, Ruhr University Bochum, Bochum, Germany, [4] Institute of Physiology, Ruhr University Bochum, Bochum, Germany, [5] Division of Clinical Physiology, Department of Cardiology, Faculty of Medicine, University of Debrecen, Debrecen, Hungary, [6] Kálmán Laki Doctoral School, University of Debrecen, Debrecen, Hungary, [7] Sanofi-Aventis Deutschland GmbH Industriepark Höchst, Frankfurt, Germany, [8] Department of Cardiothoracic Surgery, University Hospital Bergmannsheil Bochum, Bochum, Germany, [9] School of Medical Sciences, Bosch Institute, University of Sydney, Camperdown, NSW, Australia, [10] Institute for Genetics, Cologne Excellence Cluster on Cellular Stress Responses in Aging-Associated Diseases, Cologne, Germany, [11] Center for Molecular Medicine (CMMC), University of Cologne, Cologne, Germany, [12] Department of Internal Medicine B, Cardiology, University Medicine Greifswald, Greifswald, Germany, [13] DZHK (German Center for Cardiovascular Research), Partner Site Greifswald, Greifswald, Germany, [14] Institute of Physiology II, University Hospital Münster, University of Münster, Münster, Germany

OPEN ACCESS

Edited by:
Sachio Morimoto, International University of Health and Welfare (IUHW), Japan

Reviewed by:
Miklos Kellermayer, Semmelweis University, Hungary
Joseph D. Powers, University of California, San Diego, United States

***Correspondence:**
Nazha Hamdani
nazha.hamdani@rub.de

[†]These authors have contributed equally to this work

Specialty section:
This article was submitted to Striated Muscle Physiology, a section of the journal Frontiers in Physiology

Received: *19 December 2019*
Accepted: *02 March 2020*
Published: *15 April 2020*

Citation:
Herwig M, Kolijn D, Lódi M, Hölper S, Kovács Á, Papp Z, Jaquet K, Haldenwang P, Dos Remedios C, Reusch PH, Mügge A, Krüger M, Fielitz J, Linke WA and Hamdani N (2020) Modulation of Titin-Based Stiffness in Hypertrophic Cardiomyopathy via Protein Kinase D. Front. Physiol. 11:240. doi: 10.3389/fphys.2020.00240

The giant protein titin performs structure-preserving functions in the sarcomere and is important for the passive stiffness ($F_{passive}$) of cardiomyocytes. Protein kinase D (PKD) enzymes play crucial roles in regulating myocardial contraction, hypertrophy, and remodeling. PKD phosphorylates myofilament proteins, but it is not known whether the giant protein titin is also a PKD substrate. Here, we aimed to determine whether PKD phosphorylates titin and thereby modulates cardiomyocyte $F_{passive}$ in normal and failing myocardium. The phosphorylation of titin was assessed in cardiomyocyte-specific PKD knock-out mice (cKO) and human hearts using immunoblotting with a phosphoserine/threonine and a phosphosite-specific titin antibody. PKD-dependent site-specific titin phosphorylation *in vivo* was quantified by mass spectrometry using stable isotope labeling by amino acids in cell culture (SILAC) of SILAC-labeled mouse heart protein lysates that were mixed with lysates isolated from hearts of either wild-type control (WT) or cKO mice. $F_{passive}$ of single permeabilized cardiomyocytes was recorded before and after PKD and HSP27 administration. All-titin phosphorylation was reduced in cKO compared to WT hearts. Multiple conserved PKD-dependent phosphosites were identified within the Z-disk, A-band and M-band regions of titin by quantitative mass spectrometry, and many PKD-dependent phosphosites detected in the elastic titin I-band region were significantly decreased in cKO. Analysis of titin site-specific phosphorylation showed unaltered or upregulated phosphorylation in cKO compared to matched WT hearts. $F_{passive}$ was elevated in cKO compared to WT cardiomyocytes and PKD administration lowered $F_{passive}$ of WT and cKO cardiomyocytes. Cardiomyocytes from hypertrophic cardiomyopathy (HCM) patients showed higher $F_{passive}$ compared to control hearts and significantly lower $F_{passive}$ after PKD treatment. In addition, we found higher phosphorylation at CaMKII-dependent titin sites in HCM compared to control hearts. Expression and phosphorylation of HSP27,

a substrate of PKD, were elevated in HCM hearts, which was associated with increased PKD expression and phosphorylation. The relocalization of HSP27 in HCM away from the sarcomeric Z-disk and I-band suggested that HSP27 failed to exert its protective action on titin extensibility. This protection could, however, be restored by administration of HSP27, which significantly reduced $F_{passive}$ in HCM cardiomyocytes. These findings establish a previously unknown role for PKDin regulating diastolic passive properties of healthy and diseased hearts.

Keywords: titin, HCM, PKD, Hsp27, stiffness

INTRODUCTION

Protein kinase (PK)D is a serine/threonine kinase that belongs to the family of calcium/calmodulin-dependent kinases (CaMKII) due to its catalytic domain structure and substrate specificity. The PKD kinase family consists of three members: PKD1 (formerly known as PKCμ) (Valverde et al., 1994) and the predominant isoforms in the heart (Sin and Baillie, 2012), PKD2 (Sturany et al., 2001), and PKD3 (also known as PKCν) (Hayashi et al., 1999). The isoforms differ in structural and enzymatic properties from members of the PKC family. Some substrates that are targets of PKC are not phosphorylated by PKD (Johannes et al., 1994; Valverde et al., 1994; Van Lint et al., 1995), and unlike CaMKII, PKD is not directly activated by Ca^{2+} or calmodulin (Avkiran et al., 2008).

PKD can be activated by other stimuli including reactive oxygen species (ROS), growth factors (i.e., platelet-derived growth factor), and triggering of immune cell receptors. The PKD kinase is involved in the regulation of myocardial contraction by phosphorylating cardiac myosin binding protein C (cMyBP-C), cardiac troponin I (cTnI) and the L-type, voltage gated Ca^{2+} channel (Haworth et al., 2004; Cuello et al., 2007; Aita et al., 2011; Dirkx et al., 2012). Phosphorylation of TnI by PKD resulted in a significant rightward shift of the tension–pCa relationship, indicating reduced myofilament Ca^{2+} sensitivity (Haworth et al., 2004; Cuello et al., 2007; Aita et al., 2011; Dirkx et al., 2012). At submaximal Ca^{2+} activation, PKD-mediated phosphorylation also accelerated isometric cross-bridge cycling kinetics (Haworth et al., 2004; Cuello et al., 2007), suggesting a beneficial effect of PKD activation on cardiac function. PKD also alters gene expression leading to hypertrophy and influencing cardiac remodeling processes (Vega et al., 2004; Harrison et al., 2006).

With a molecular mass ranging from 3,000 to 3,700 kDa, titin is the largest known protein and its function as a molecular spring is important for the elasticity of striated muscle. Spanning the half-sarcomere from the Z-disk to the M-band, titin is expressed in various isoforms that confer different elastic properties to the sarcomere. Two main isoform classes of titin are expressed in the human heart: a shorter, stiffer N2B (3,000 kDa) isoform and several longer, more compliant, N2BA isoforms (>3,200 kDa). These variants differ in their elastic I-band region due to alternative splicing, whereas the Z-disk, A-band, and M-band regions of titin are essentially constitutively expressed. The titin spring region has a complex sequence comprising two types of extensible segments: (1) regions composed of immunoglobulin-like (Ig-) domains (proximal; middle; distal) arranged in tandem; and (2) intrinsically disordered structures, including a unique sequence of the cardiac specific "N2-B" element ("N2-Bus") and the "PEVK" segment rich in proline, glutamate, valine, and lysine.

The titin filaments in cardiomyocytes are considered to be a main determinant of myocardial "passive" stiffness, along with the collagen fibers of the extracellular matrix and additional factors such as diastolic Ca^{2+} levels. We have previously demonstrated that the stiffness of cardiac titin is highly variable and depends on titin isoform switching and/or post-translational modifications such as phosphorylation and oxidation (Linke and Hamdani, 2014).

In our previous study, using a CaMKII knockout mouse model together with the stable isotope labeling of amino acids in cell culture (SILAC) mouse model, we found ∼20 CaMKII-dependent phosphosites along the titin molecule (Hamdani et al., 2013b). Some phosphosites were located within the extensible region of titin, e.g., at the N2-Bus and PEVK spring elements, while others were within the A-band, M-band, and Z-disk regions of titin. Using this approach, we also detected >50 additional titin phosphosites that appeared to be not regulated by CaMKII. As regards to other kinases, protein kinase A and G and ERK2 were shown to phosphorylate the titin springs at specific sites within the cardiac-specific N2-Bus element (Kruger et al., 2009; Kotter et al., 2013). This modification alters the molecular stiffness of N2-Bus. Yet another kinase, PKCα, was shown to phosphorylate titin's PEVK element (Hidalgo et al., 2009).

A well-known substrate of PKD, among others, is heat shock protein 27 (HSP27) (Doppler et al., 2005). HSPs are molecular chaperones comprising a large family of proteins involved in protection against various forms of cellular stress (Mymrikov et al., 2011). HSPs generally facilitate protein refolding, target misfolded proteins to the proteasome and stabilize and transport partially folded proteins to different cellular compartments. Under various environmental insults such as heat, oxidative stress or acidosis, protein denaturation occurs and leads to unfolding and undesirable protein aggregates (Mymrikov et al., 2011). HSP27 is a small (ATP-independent) HSP whose function is regulated, in part, by posttranslational modifications, including phosphorylation at Ser-18, Ser-78, Ser-82, and Thr-143 (Kostenko and Moens, 2009; Mymrikov et al., 2011). Previous work showed that the unfolded Ig regions of I-band titin, but not the intrinsically disordered segments, can aggregate, causing high titin-dependent myocyte stiffness,

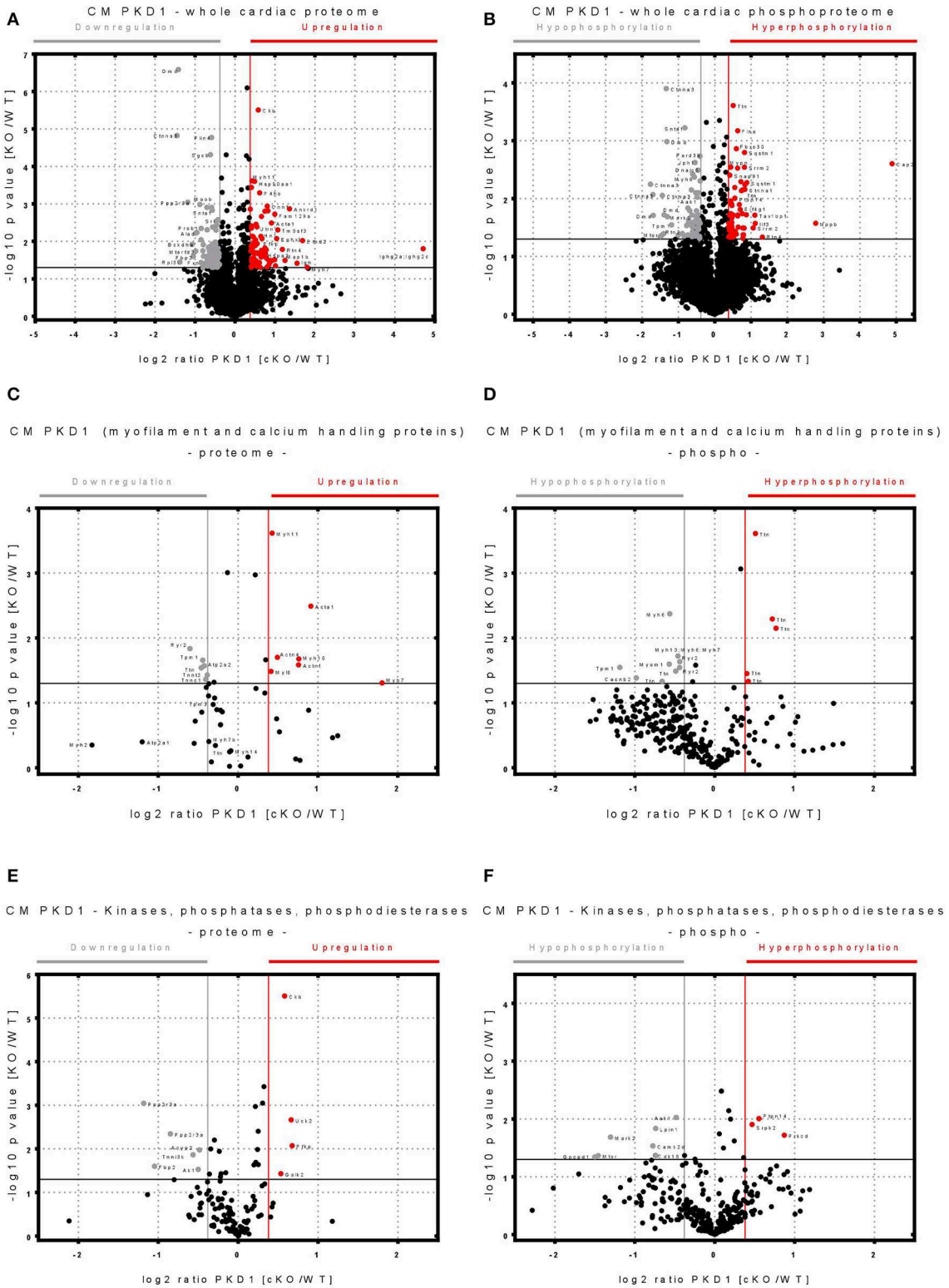

FIGURE 1 | Volcano plots showing changes in the cardiac proteome and phosphoproteome in protein kinase D 1 (PKD1)-cKO and matched wild-type (WT) mouse hearts. **(A)** Volcano plot of whole cardiac proteome with identified significantly up- or down-regulated peptides in wild type (WT) vs. cardiomyocyte specific Protein Kinase D1 (PKD1) knock-out (KO) animals. **(B)** Volcano plot of whole cardiac phosphoproteome with identified significantly hyper- or hypo-phosphorylated peptides in WT vs. PKD1 cKO mice.

(Continued)

FIGURE 1 | (C) Volcano plot of myofilament and calcium handling proteins with significantly up- or down-regulated peptides in WT vs. PKD1 cKO mice. **(D)** Volcano plot of myofilament and calcium handling proteins with significantly hyper- or hypo-phosphorylated peptides in WT vs. PKD1 cKO mice. **(E)** Volcano plot of kinases, phosphatases, phosphodiesterases identified with significantly up- or down-regulated peptides in WT vs. PKD1 cKO mice. **(F)** Volcano plot of kinases, phosphatases, phosphodiesterases identified with significantly hyper- or hypo-phosphorylated peptides in WT vs. PKD1 cKO mice. Protein content or phosphorylation considered as significantly changed (-log10 $p \geq 1.3$, log2 ratio $\geq \pm 0.37$) over the WT are color-coded. Only values with a $-\log10\, p > 0$ are shown. Experiments were performed in triplicates.

and that HSP27 prevented this aggregation and suppressed the stiffening (Kotter et al., 2014). We speculated that cardiomyocyte elastic function could be protected under stress, at least in part, by HSP27 being regulated via PKD-mediated phosphorylation. The main aim of the present study was to investigate the effects of PKD on titin phosphorylation *in vivo* and resulting functional changes using cardiomyocyte specific *Prkd1*, which encodes for PKD1, knockout mice, SILAC mouse hearts, and human hypertrophic cardiomyopathy (HCM) heart tissues. We identified various PKD1-dependent phosphosites within titin using quantitative mass spectrometry (MS) and showed that PKD1-mediated titin-phosphorylation reduces cardiomyocyte $F_{passive}$. Additionally, we found increased oxidative stress in human HCM tissues along with increased HSP27 expression and phosphorylation. HCM tissues also showed increased CaMKII-dependent phosphorylation at the PEVK and N2Bus titin regions. High cardiomyocyte stiffness was corrected by incubation with HSP27 and PKD, probably through relief of titin aggregation. Taken together, our results highlight the important roles of PKD and HSP27, in the presence of oxidative stress, in modulating diastolic function via titin-based stiffness regulation.

METHODS

Detailed methods descriptions are provided in the online **Supplementary Methods**.

Human Heart Tissues

The investigation conforms to the principles outlined in the Declaration of Helsinki and samples were obtained after informed consent and with approval of the local Ethics Committee. LV tissue was obtained from end-stage heart failure patients (NYHA III or IV; $n = 10$), hypertrophic cardiomyopathy (male, mean age 45 years). LV tissue from non-failing donor hearts ($N = 10$; +- 40 years of age) served as reference and was obtained from donor hearts ($n = 5$).

Cardiomyocyte Specific *Prkd1* Knock-Out Mice

All animal procedures were performed in accordance with the guidelines of Charité Universitätsmedizin Berlin as well as Max-Delbrück Center for Molecular Medicine and were approved by the Landesamt für Gesundheit und Soziales (LaGeSo, Berlin, Germany) for the use of laboratory animals (permit number: G 0229/11) and followed the 'Principles of Laboratory Animal Care' (NIH publication no. 86–23, revised 1985) as well as the current version of German Law on the Protection of Animals. The generation and usage of the conditional *Prkd1* allele was published elsewhere (Fielitz et al., 2008; Kim et al., 2008). The Cre-loxP recombination system was used for the generation of a conditional *Prkd1* allele. *Prkd1*loxP/loxP mice were crossed with Cre carrying mice controlled by cardiomyocyte-specific alpha-myosin-heavy-chain promotor (αMHC-Cre) (Agah et al., 1997) (cKO, *Prkd1*loxP/loxP; αMHC-Cre). αMHC-Cre-negative littermates were used as controls (WT, *Prkd1*loxP/loxP). Cardiac tissue was obtained when mice were 8–10 weeks of age. $N = 7$ for both KO and WT.

SILAC-Based Quantitative Mass Spectrometry

We mixed equal amounts of protein lysates from heart tissue (7.5 mg) from the 13Lys6 heavy-labeled SILAC mouse and a non-labeled WT or non-labeled *Prkd1* cKO mouse. After protein digestion and phosphopeptide enrichment, the ratio of labeled:unlabeled peptides was determined by liquid chromatography and tandem MS and used to identify the cKO:WT ratio of titin phosphopeptides (Kruger et al., 2008).

Titin Isoform Separation

Homogenized myocardial samples were analyzed by 1.8% SDS-PAGE. Protein bands were visualized by Coomassie staining and analyzed densitometrically.

All-Titin Phosphorylation Assays

Titin bands were stained with anti-phospho-antibody directed against phospho-serine/threonine. Phospho-protein signals were indexed to total-protein signals and normalized to the intensity of coomassie staining to correct for differences in sample loading. Alternatively, all-titin phosphorylation was measured by PKD-mediated back-phosphorylation (Hamdani et al., 2013b).

Titin and Phosphotitin Western Blots

Western blots were performed using custom-made, affinity-purified, anti-phosphoserine-specific antibodies directed against phospho-Ser-4010, -Ser-4062, -Ser-4099 (all N2Bus), -Ser-11878, and –Ser-12022 (both PEVK), of human titin (UniProtKB identifyer, Q8WZ42), and antibodies recognizing the corresponding nonphosphorylated sequence at these sites (Hamdani et al., 2013b). We also used phosphosite-specific antibodies against phospho-Ser-3991, -Ser-4043, -Ser-4080 (all N2Bus), -Ser-12742, and –Ser-12884 (both PEVK), of mouse titin (UniProtKB identifyer, A2ASS6) (Hamdani et al., 2013b).

Force Measurements on Isolated Cardiomyocytes

Cardiomyocytes were skinned and single isolated cells ($n = 12$–42/5–6 heart/group) attached between a force transducer and

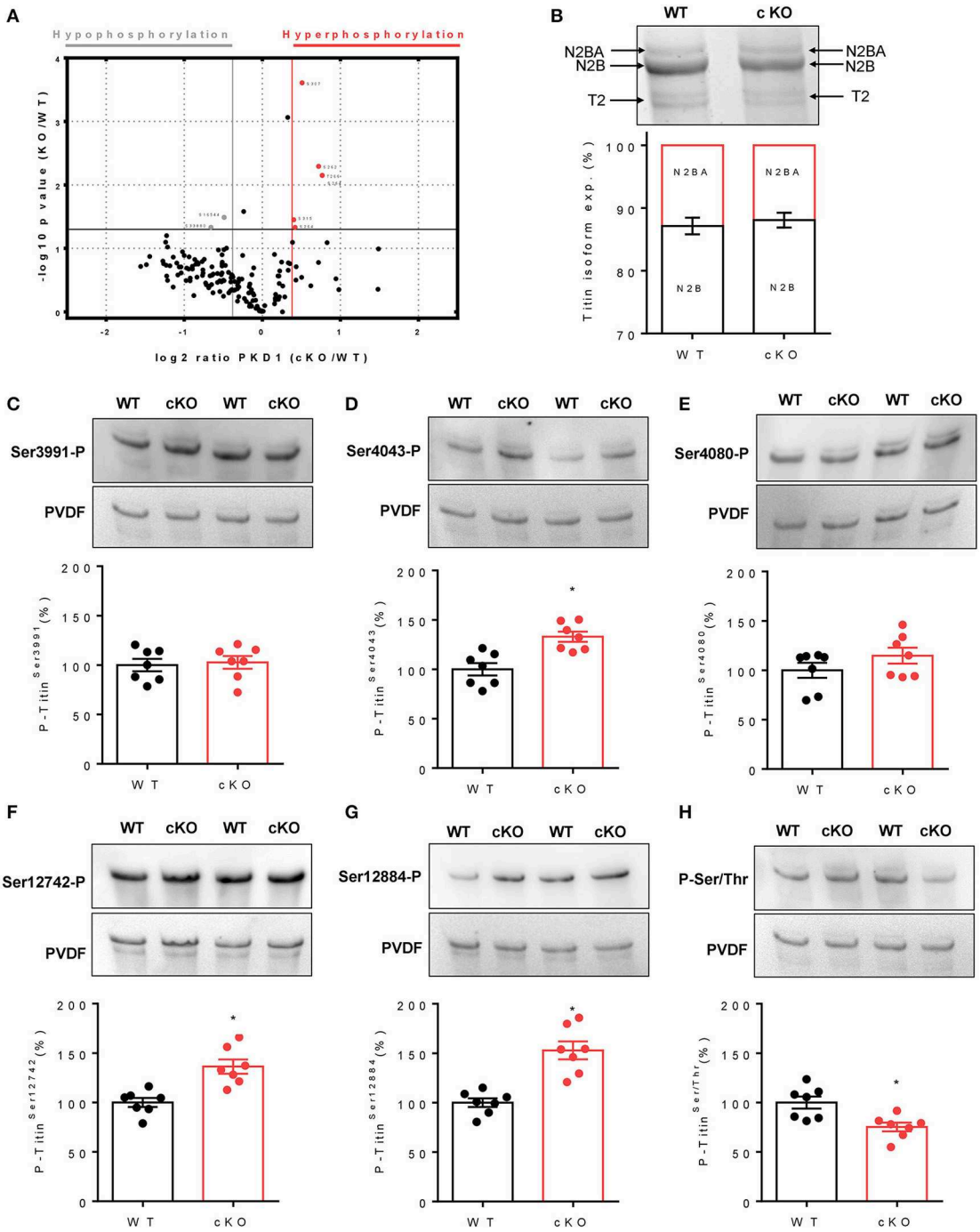

FIGURE 2 | Titin phosphorylation and titin isoform composition in protein kinase D1 knockout (PKD1 cKO) and matched wild-type (WT) mouse hearts. **(A)** Volcano plot of SILAC-quantified titin phosphosites in heart tissue of PKD1 cKO vs. WT mice ($n = 3$ hearts/group). **(B)** Titin isoform composition. **(C)** Site-specific phosphorylation (P) of titin-N2B isoform at Ser3991 within N2Bus. **(D)** Site-specific P of titin-N2B isoform at Ser4043 within N2Bus. **(E)** Site-specific P of titin-N2B isoform at Ser4080 within N2Bus. **(F)** Site-specific P of titin-N2B isoform at Ser12742 within PEVK segment. **(G)** Site-specific P of titin-N2B isoform at Ser12884 within PEVK segment. **(H)** Total N2B-titin phosphorylation in PKD1 cKO/WT hearts. Western blot data are means ± SEM; $n = 7$ hearts/group; each heart analyzed in duplicate. *$P < 0.05$ in Students unpaired t-test.

motor (Hamdani et al., 2013a,b). $F_{passive}$ was recorded over the sarcomere length (SL) range, 1.8–2.4 μm, and was measured before/after PKD and/or HSP27 incubation.

Quantification of Tissue Oxidative Stress

Myocardial levels ($n = 7$ LV sample/group) of oxidative stress markers were tested with enzyme-linked immunosorbent assay

TABLE 1 | Significantly changed titin phosphosites (–log 10 *p*-value KO/WT > 1.3).

Position within titin	UniProt identifyer	Log2 ratio (KO/WT)	–Log 10 *p*-value KO/WT	Charge	Multiplicity	Localization probability	Classification of phosphosite	Sequence window
S33880	A2ASS6	−0.659036	1.33033	3	1	1	Class 1	DLYYYRRRRRSLGDMSDEELLLPIDDYLAMK
S264	A2ASS6	0.419615	1.33152	2	2	1	Class 1	PHKTPPRIPPKPKSRSPTPPSIAAKAQLARQ
S315	A2ASS6	0.40279	1.45166	2	1	0.997856	Class 1	PSPVRSVSPAGRISTSPIRSVKSPLLIRKTQ
S16544	A2ASS6	−0.489219	1.48858	3	1	0.993809	Class 1	AEEEEPFSLPLTERLSINNSKQGESQLRIRD
S20332	A2ASS6	−0.239112	1.58029	2	1	1	Class 1	IIGYVVEMRPKIADASPDEGWKRCNAAAQLI
S264	A2ASS6	0.767076	2.14935	2	3	1	Class 1	PHKTPPRIPPKPKSRSPTPPSIAAKAQLARQ
T266	A2ASS6	0.767076	2.14935	2	3	1	Class 1	KTPPRIPPKPKSRSPTPPSIAAKAQLARQQS
S262	A2ASS6	0.720452	2.29218	2	3	1	Class 1	QLPHKTPPRIPPKPKSRSPTPPSIAAKAQLA
S322	A2ASS6	0.325277	3.06343	2	1	1	Class 1	SPAGRISTSPIRSVKSPLLIRKTQTTTMATG
S307	A2ASS6	0.509144	3.60898	2	2	1	Class 1	VRHVRAPTPSPVRSVSPAGRISTSPIRSVKS

Z-disk.
A-band.
M-band.
Multiplicity contains information about the phosphorylation of the peptides (single. double. triply phosphorylated).

TABLE 2 | Detected phosphosites in the elastic I band titin spring (–log 10 *p*-value KO/WT >0).

Position within titin	UniProt identifyer	Log2 ratio (KO/WT)	–Log 10 *p*-value KO/WT	Charge	Multiplicity	Localization probability	Classification of phosphosite	Sequence window
T9146	A2ASS6	−0.650309	0.429695	3	1	0.616703	Class 2	KERLIPPSFTKKLSETVEETEGNSFKLEGRV
S3286	A2ASS6	−0.938293	0.866542	2	1	0.851679	Class 1	RPQPKISWYKEEQLLSTGFKCKFLHDGQEYT
S3977	A2ASS6	−0.319098	0.36361	2	1	0.840288	Class 1	CTEGKILMASADTLKSTGQDVALRTEEGKSL
T13665	A2ASS6	−0.316873	0.41921	2	1	1	Class 1	CEVSREPKTFRWLKGTQEITGDDRFELIKDG
S13228	A2ASS6	−0.273069	0	2	1	0.993076	Class 1	DIPGEWKLKGELLRPSPTCEIKAEGGKRFLT
S9201	A2ASS6	−0.230981	0	2	1	1	Class 1	IMFKNNALLLQVKRASMADAGLYTCKATNDA
S9144	A2ASS6	−0.203903	0.163212	2	1	1	Class 1	NIKERLIPPSFTKKLSETVEETEGNSFKLEG
S4175	A2ASS6	−0.168399	0.396358	3	1	1	Class 1	HEEDKIDVQGGRDHLSDAQKVETVIEAEADS
T14268	A2ASS6	−0.16409	0.087451	2	1	0.99985	Class 1	VFTKNLANLEVSEGDTIKLVCEVSKPGAEVI
S9459	A2ASS6	−0.158813	0.124587	3	1	1	Class 1	DLRAMLKKTPALKKGSGEEEEIDIMELLKNV
S13204	A2ASS6	−0.0662166	0.089154	2	1	0.880947	Class 1	LKPIEDVTIYEKESASFDAEISEEDIPGEWK
S4018	A2ASS6	−0.018641	0	2	1	0.675564	Class 2	VLLKEEQSEVVAVPTSQTSKSEKEPEAIKGV
S3991	A2ASS6	−0.0149712	0.0107483	2	1	0.999502	Class 1	KSTGQDVALRTEEGKSLSFPLALEEKQVLLK
S3870	A2ASS6	−0.00516502	0.0056415	3	1	0.991661	Class 1	EPEGVFPGASSAAQVSPVTIKPLITLTAEPK
S14664	A2ASS6	0.0113125	0.0110327	2	1	1	Class 1	REIKEGKKYKFEKDGSIHRLIIKDCRLEDEC
S13764	A2ASS6	0.200173	0	2	1	1	Class 1	SWFKNDQRLHTSKRVSMHDEGKTHSITFKDL
S3676	A2ASS6	0.258327	0	4	1	0.878152	Class 1	EDMPLYTSVCYTIIHSPDGSGTFIVNDPQRG
S12678	A2ASS6	0.331543	0.65471	3	1	1	Class 1	IEKPKLKPRPPARPPSPPKEDVKEKMFQLKA
T10276	A2ASS6	0.395205	0	3	1	0.637793	Class 2	EVQKKVVTEEKIAIITQREESPPPAVPEIPK
S10281	A2ASS6	0.719508	0.777963	3	1	0.999995	Class 1	VVTEEKIAIITQREESPPPAVPEIPKKKVPE
S12871	A2ASS6	0.829341	1.09019	3	1	1	Class 1	AKPKGPIKGVAKKTPSPIEAERKKLRPGSGG
S12884	A2ASS6	0.94305	0.52056	3	1	1	Class 1	TPSPIEAERKKLRPGSGGEKPPDEAPFTYQL
S12871	A2ASS6	0.981417	0.3495	3	2	1	Class 1	AKPKGPIKGVAKKTPSPIEAERKKLRPGSGG
T12869	A2ASS6	0.981417	0.3495	3	2	1	Class 1	EAAKPKGPIKGVAKKTPSPIEAERKKLRPGS

Proximal Ig region.
N2B-element.
Middle Ig region.
PEVK.
Distal Ig domains.

TABLE 3 | Downregulated titin phosphosites (log2 ratio KO/WT <−0.37).

Position within titin	UniProt identifyer	Log2 ratio (KO/WT)	–Log 10 *p*-value KO/WT	Charge	Multiplicity	Localization probability	Classification of phosphosite	Sequence window
S23560	A2ASS6	−0.372779	0	3	1	0.692852	Class 2	PGPPGNPRVLDTSRSSISIAWNKPIYDGGSE
S18225	A2ASS6	−0.376743	0.548646	2	1	0.5	Class 2	PPGPPFPKVTDWTKSSVDLEWSPPLKDGGSK
S30484	A2ASS6	−0.380153	0	2	1	0.999969	Class 1	TWKLEEMRLKETDRMSIATTKDRTTLTVKDS
S34451	A2ASS6	−0.384564	0.573934	2	1	0.999956	Class 1	TLTVQKARVIEKAVTSPPRVKSPEPRVKSPE
S33933	A2ASS6	−0.390718	0.578927	2	1	0.999999	Class 1	SRSPPRFELSSLRYSSPPAHVKVEDRRRDFR
S34808	A2ASS6	−0.390976	0.349281	2	1	1	Class 1	IAEEVKRSAAASLEKSIVHEEVTKTSQASEE
S26062	A2ASS6	−0.391391	0	3	1	0.992938	Class 1	KWSVVAESKVCNAVVSGLSSGQEYQFRVKAY
S21726	A2ASS6	−0.391912	0.585051	2	1	0.999998	Class 1	FLTEENKWQRVMKSLSLQYSTKDLKEGKEYT
T27227	A2ASS6	−0.392365	0	3	1	0.598045	Class 2	QATVAWKKDGQVLRETTRVNVASSKTVTTLS
S34476	A2ASS6	−0.399261	0.538309	2	1	1	Class 1	RVKSPETVKSPKRVKSPEPVTSHPKAVSPTE
S28859	A2ASS6	−0.403171	0.471662	2	1	0.990318	Class 1	EPVVAKNAFVTPGPPSIPEVTKITKNSMTVV
T4070	A2ASS6-3	−0.408659	0.331878	3	1	0.998519	Class 1	RELLSFPVEIQITAATPTPEQNKECRELFEL
S22271	A2ASS6	−0.42308	0	3	1	0.944504	Class 1	VSVLDVPGPPGPIEISNVSAEKATLTWTPPL
S1196	A2ASS6	−0.429651	0.300969	3	1	0.887311	Class 1	ALVKTQQEMLYQTQMSTFIQEPKVGEIAPGF
S29764	A2ASS6	−0.433024	0.621301	2	1	0.999999	Class 1	FGPEYFDGLVIKSGDSLRIKALVQGRPVPRV
S26804	A2ASS6	−0.433475	0	3	1	0.524536	Class 2	LYPPGPPSNPKVTDTSRSSVSLAWNKPIYDG
S22184	A2ASS6	−0.435231	0	2	1	0.999983	Class 1	LDPTIKDGLTVKAGDSIVLSAISILGKPLPK
S28389	A2ASS6	−0.440064	0	2	1	0.999873	Class 1	ESVTLKWEPPKYDGGSHVTNYIVLKRETSTA
S19152	A2ASS6	−0.442809	0	2	1	0.686958	Class 2	RKDVATAQWSPLSTTSKKKSHMAKHLTEGNQ
S34292	A2ASS6	−0.458658	1.00349	2	1	0.997471	Class 1	LTKTEAYAVSSFKRTSELEAASSVREVKSQM
S848	A2ASS6	−0.472572	0.731925	2	1	0.999987	Class 1	ASIAGSAIATLQKELSATSSTQKITKSVKAP
S19518	A2ASS6	−0.479462	0	3	1	0.999999	Class 1	DITENAATVSWTLPKSDGGSPITGYYVERRE
T4827	A2ASS6-3	−0.480703	0	3	2	0.682593	Class 2	VRDTKHKAQLVQSDSTTSMEVEEVTFNTVYE
S16544	A2ASS6	−0.489219	1.48858	3	1	0.993809	Class 1	AEEEEPFSLPLTERLSINNSKQGESQLRIRD
S29489	A2ASS6	−0.490109	0.49045	2	1	0.999929	Class 1	GGGEITCYSIEKREASQTNWKMVCSSVARTT
S35097	A2ASS6	−0.491363	0.979128	3	1	0.972789	Class 1	ESFVEMSSSSFMGKSSMTQLESSTSRMLKAG
S29997	A2ASS6	−0.496859	0.246525	3	1	0.999978	Class 1	KKSTRWVKVISKRPISETRFKVTGLVEGNEY
S23358	A2ASS6	−0.498498	0.499119	3	1	0.855607	Class 1	RPGPPEGPLAVSDVTSEKCVLSWLPPLDDGG
S262	A2ASS6	−0.501588	0	2	1	1	Class 1	QLPHKTPPRIPPKPKSRSPTPPSIAAKAQLA
S30452	A2ASS6	−0.513035	0.782215	2	1	0.968235	Class 1	DLTGITNQLITCKAGSTFTIDVPISGRPAPK
S16548	A2ASS6	−0.515562	0.899345	3	1	0.999832	Class 1	EPFSLPLTERLSINNSKQGESQLRIRDSLRP
S24061	A2ASS6	−0.515855	0.613502	2	1	0.97456	Class 1	SVTLSWEPPKYDGGSSINNYIVEKRDTSTTA
T23053	A2ASS6	−0.515985	0.758139	2	1	0.999999	Class 1	SVVANYPFKVPGPPGTPQVTAVTKDSMTISW
S1120	A2ASS6	−0.516292	0.722335	2	1	1	Class 1	CQIGGNPKPHVYWKKSGVPLTTGYRYKVSYN
S21895	A2ASS6	−0.522994	0.473161	2	1	1	Class 1	EAMTLKWGPPKDDGGSEITNYVLEKRDSVNN
S34756	A2ASS6	−0.525721	0.586585	2	1	1	Class 1	VSTQKTSEVTSQKKASAQEEISQKALTSEEI
S21162	A2ASS6	−0.54349	0.319895	2	1	0.836052	Class 1	VNRKDSGDYTITAENSSGSKSATIKLKVLDK
S34778	A2ASS6	−0.543969	0.489795	2	1	0.999964	Class 1	QKALTSEEIKMSEVKSHETLAIKEEASKVLI
T22513	A2ASS6	−0.551522	0	3	1	0.958776	Class 1	VEHQKVGDDAWIKDTTGTALRITQFVVPDLQ
T24135	A2ASS6	−0.561529	0.975063	2	1	1	Class 1	PVVAQYPFKVPGPPGTPFVTLASKDSMEVQW
T23980	A2ASS6	−0.573932	0.604136	3	1	0.631224	Class 2	PPAVTWHKDDIPLKQTTRVNAESTENNSLLT
S21730	A2ASS6	−0.574432	0.464884	2	1	0.798102	Class 1	ENKWQRVMKSLSLQYSTKDLKEGKEYTFRVS
S23609	A2ASS6	−0.587423	0	2	1	0.995346	Class 1	VTPPAGLKATSYTITSLIENQEYKIRIYAMN
S4650	A2ASS6-3	−0.606701	0	3	1	0.981316	Class 1	ALFQTPSADVEEANVSETGASVENGDKTFIS
T25062	A2ASS6	−0.625343	0	3	1	0.499999	Class 2	KPSISWTKDGMPLKQTTRINVTDSLDLTTLS
T25063	A2ASS6	−0.625343	0	3	1	0.499999	Class 2	PSISWTKDGMPLKQTTRINVTDSLDLTTLSI
S16620	A2ASS6	−0.62959	0.594816	3	1	0.999999	Class 1	DSVLCKWEPPLDDGGSEIINYTLEKKDKTKP
S25817	A2ASS6	−0.632049	0.301091	2	1	1	Class 1	VKPEDKLEAPELDLDSELRKGIVVRAGGSAR
S34207	A2ASS6	−0.63678	0	2	1	0.992242	Class 1	AEVKWYHNGVELQESSKIHYTNTSGVLTLEI
S20215	A2ASS6	−0.644393	0.578427	2	1	0.989323	Class 1	EMTVVWNAPEYDGGKSITGYYLEKKEKHAVR

(Continued)

TABLE 3 | Continued

Position within titin	UniProt identifyer	Log2 ratio (KO/WT)	–Log 10 *p*-value KO/WT	Charge	Multiplicity	Localization probability	Classification of phosphosite	Sequence window
T30560	A2ASS6	−0.645399	0.70904	2	1	1	Class 1	ESCVLSWTEPKDDGGTEITNYIVEKRESGTT
T9146	A2ASS6	−0.650309	0.429695	3	1	0.616703	Class 2	KERLIPPSFTKKLSETVEETEGNSFKLEGRV
S33880	A2ASS6	−0.659036	1.33033	3	1	1	Class 1	DLYYYRRRRRSLGDMSDEELLLPIDDYLAMK
S21163	A2ASS6	−0.662774	0	2	1	0.555375	Class 2	NRKDSGDYTITAENSSGSKSATIKLKVLDKP
S32940	A2ASS6	−0.669661	0.567747	3	1	0.991067	Class 1	DSVNLTWTEPASDGGSKVTNYIVEKCATTAE
T27381	A2ASS6	−0.676248	0.40741	2	1	0.987482	Class 1	AVVAEYPFSPPGPPGTPKVVHATKSTMVVSW
S22466	A2ASS6	−0.68697	0.37929	3	1	0.971535	Class 1	NPVLMKDVAYPPGPPSNAHVTDTTKKSASLA
S15406	A2ASS6	−0.717398	0.426932	2	1	1	Class 1	NSIFLTWDPPKNDGGSRIKGYIVEKCPRGSD
S24060	A2ASS6	−0.726107	0.454637	2	1	0.965865	Class 1	DSVTLSWEPPKYDGGSSINNYIVEKRDTSTT
S17508	A2ASS6	−0.743691	0.827831	3	1	0.854636	Class 1	PPGPPSCPEVKDKTKSSISLAWKPPAKDGGS
S22646	A2ASS6	−0.746741	0	3	1	0.999997	Class 1	TGKFVMTIENPAGKKSGFVNVRVLDTPGPVL
Y21461	A2ASS6	−0.750766	0	2	1	0.997236	Class 1	NTEYQFRVYAVNKIGYSDPSDVPDKHCPKDI
S34464	A2ASS6	−0.758656	0.611225	2	1	1	Class 1	VTSPPRVKSPEPRVKSPETVKSPKRVKSPEP
S19128	A2ASS6	−0.761375	0.661405	3	1	1	Class 1	DSCYLTWKEPLDDGGSVVTNYVVERKDVATA
S17509	A2ASS6	−0.765849	0.574468	2	1	0.499998	Class 2	PGPPSCPEVKDKTKSSISLAWKPPAKDGGSP
S34009	A2ASS6	−0.77042	0.791858	2	1	1	Class 1	LLRPVTTTQRLSEYKSELDYMSKEEKSKKKS
S30820	A2ASS6	−0.787034	0	3	1	0.779125	Class 1	VLAKNAAGVISKGSESTGPVTCRDEYAPPKA
S34653	A2ASS6	−0.82199	0.752192	2	1	0.95726	Class 1	SSKPVIVTGLRDTTVSSDSVAKFTIKVTGEP
S32936	A2ASS6	−0.824822	0	3	1	0.909829	Class 1	DVSRDSVNLTWTEPASDGGSKVTNYIVEKCA
T16910	A2ASS6	−0.831267	0.77835	3	1	1	Class 1	LDVSVKGGIQIMAGKTLRIPAEVTGRPVPTK
S15236	A2ASS6	−0.836399	0.546251	3	1	0.997816	Class 1	DQVLEEGDRVKMKTISAYAELVISPSERTDK
S21637	A2ASS6	−0.851016	0.751694	2	1	0.999673	Class 1	WSTVTTECSKTSFRVSNLEEGKSYFFRVFAE
T30103	A2ASS6	−0.851493	0	3	1	0.499919	Class 2	DWHKVNTEPCVKTRYTVTDLQAGEEYKFRVS
S32230	A2ASS6	−0.864269	0.82444	2	1	0.991873	Class 1	DPFDKPSQPGELEILSISKDSVTLQWEKPEC
S34005	A2ASS6	−0.876525	0	3	1	0.999798	Class 1	EEEELLRPVTTTQRLSEYKSELDYMSKEEKS
S18731	A2ASS6	−0.87685	0.25695	3	1	0.995523	Class 1	EYMVISWKPPLDDGGSEITNYIIEKKELGKD
S4248	A2ASS6-3	−0.893375	0	4	1	0.967119	Class 1	VQGEPVRTHFYDHTVSPFAAQSNIKEYTIRE
T30453	A2ASS6	−0.895531	0.674399	3	1	0.861201	Class 1	LTGITNQLITCKAGSTFTIDVPISGRPAPKV
S1805	A2ASS6	−0.895653	0.717555	2	1	1	Class 1	GTDHTSATLIVKDEKSLVEESQLPDGKKGLQ
S15266	A2ASS6	−0.907094	0	2	1	0.977731	Class 1	KGIYTLTLENPVKSISGEINVNVIAPPSAPK
S25399	A2ASS6	−0.923229	0.531448	2	1	0.967678	Class 1	VIAKNAAGAISKPSDSTGPITAKDEVELPRI
S27960	A2ASS6	−0.925189	0.489628	2	1	0.834475	Class 1	RVRSLNKMGASDPSDSSDPQVAKEREEEPVF
S3286	A2ASS6	−0.938293	0.866542	2	1	0.851679	Class 1	RPQPKISWYKEEQLLSTGFKCKFLHDGQEYT
T22529	A2ASS6	−0.943427	0.67514	2	1	1	Class 1	GTALRITQFVVPDLQTKEKYNFRISAINDAG
S4720	A2ASS6-3	−0.959846	0	3	1	0.9499	Class 1	PRGAVHGAEVPHRRLSLSQDLPFLMTGEQQD
S35060	A2ASS6	−0.967557	0	2	1	0.845469	Class 1	SASKQEASFSSFSSSSASSMTEMKFASMSAQ
Y20757	A2ASS6	−0.96841	0.688841	2	1	0.999745	Class 1	SSVLIIKDVTRKDSGYYSLTAENSSGSDTQK
S25797	A2ASS6	−0.975471	0.492227	2	1	0.999986	Class 1	IRVCALNKVGLGEAASVPGTVKPEDKLEAPE
S23925	A2ASS6	−1.00025	0.887458	3	1	0.999906	Class 1	VSAQNEKGISDPRQLSVPVIAKDLVIPPAFK
S25613	A2ASS6	−1.02282	0.946511	2	1	1	Class 1	PVLMKNPFVLPGPPKSLEVTNIAKDSMTVCW
S29299	A2ASS6	−1.03903	0.614927	2	1	0.999999	Class 1	TDYLVERKGKGEQAWSHAGISKTCEIEIGQL
Y20182	A2ASS6	−1.04142	0.707871	3	1	1	Class 1	TGPPTESKPVIAKTKYDRPGRPDPPEVTKVS
S35104	A2ASS6	−1.0585	0	2	1	0.746582	Class 2	SSSFMGKSSMTQLESSTSRMLKAGGRGIPPK
S15616	A2ASS6	−1.06363	0.707178	2	1	0.999998	Class 1	GSKITNYVVERKATDSDVWHKLSSTVKDTNF
S20732	A2ASS6	−1.08258	0.581344	2	1	0.997277	Class 1	PICKWKKGDDEVVTSSHLAIHKADGSSVLII
T16946	A2ASS6	−1.0848	0	2	1	1	Class 1	EGELDKERVIIENVGTKSELIIKNALRKDHG
S24436	A2ASS6	−1.0957	0.769352	3	1	0.997797	Class 1	KVLDRPGPPEGPVAISGVTAEKCTLAWKPPL
S19776	A2ASS6	−1.13133	0	4	1	0.570984	Class 2	VRADHGKYIISAKNSSGHAQGSAIVNVLDRP
T30100	A2ASS6	−1.14081	0.86237	2	1	0.999845	Class 1	DLGDWHKVNTEPCVKTRYTVTDLQAGEEYKF

(Continued)

TABLE 3 | Continued

Position within titin	UniProt identifyer	Log2 ratio (KO/WT)	–Log 10 *p*-value KO/WT	Charge	Multiplicity	Localization probability	Classification of phosphosite	Sequence window
S28970	A2ASS6	−1.14229	0.390143	2	1	0.848484	Class 1	PPGPPAKIRIADSTKSSITLGWSKPVYDGGS
S23728	A2ASS6	−1.15678	0	2	1	0.680757	Class 2	FDSGKYILTVENSSGSKSAFVNVRVLDTPGP
S23604	A2ASS6	−1.18392	0	2	1	0.760984	Class 1	DEWQVVTPPAGLKATSYTITSLIENQEYKIR
T22805	A2ASS6	−1.18392	0.725798	2	1	0.948992	Class 1	IEAQRKGSDQWTHISTVKGLECVVRNLTEGE
S25730	A2ASS6	−1.2141	1.02176	2	1	0.999999	Class 1	AHVVDTTKNSITLAWSKPIYDGGSEILGYVV
S24155	A2ASS6	−1.21435	0.495954	3	1	0.938049	Class 1	LASKDSMEVQWHEPVSDGGSKVIGYHLERKE
T23603	A2ASS6	−1.22489	0.565233	2	1	0.891141	Class 1	EDEWQVVTPPAGLKATSYTITSLIENQEYKI
S29402	A2ASS6	−1.22605	1.20053	2	1	1	Class 1	LKDGLPLKESEYVRFSKTENKITLSIKNSKK
T25518	A2ASS6	−1.23095	0.735191	3	1	0.981598	Class 1	KVLDRPGPPEGPVQVTGVTAEKCTLAWSPPL
T19879	A2ASS6	−1.23865	1.098	3	1	1	Class 1	CAENKVGVGPTIETKTPILAINPIDRPGEPE
Y29398	A2ASS6	−1.26528	0.758789	2	1	1	Class 1	SISWLKDGLPLKESEYVRFSKTENKITLSIK
S32140	A2ASS6	−1.27419	0.799964	2	1	0.998818	Class 1	PEVLDVTKSSVSLSWSRPKDDGGSRVTGYYI
S28985	A2ASS6	−1.28346	0	2	1	0.999999	Class 1	SSITLGWSKPVYDGGSDVTGYVVEMKQGDEE
S35029	A2ASS6	−1.33441	0	3	1	0.960754	Class 1	PLVEEPPREVVLKTSSDVSLHGSVSSQSVQM
S34457	A2ASS6	−1.40297	0	2	2	1	Class 1	ARVIEKAVTSPPRVKSPEPRVKSPETVKSPK
S35096	A2ASS6	−1.44254	0.872837	2	1	0.869587	Class 1	QESFVEMSSSSFMGKSSMTQLESSTSRMLKA
T22515	A2ASS6	−1.45339	0	3	1	0.998937	Class 1	HQKVGDDAWIKDTTGTALRITQFVVPDLQTK
S25026	A2ASS6	−1.48484	0.743171	3	1	0.949735	Class 1	IAKDLVIEPDVRPAFSSYSVQVGQDLKIEVP
S21724	A2ASS6	−1.49957	0	2	1	0.965611	Class 1	VDFLTEENKWQRVMKSLSLQYSTKDLKEGKE
S27185	A2ASS6	−1.55785	0.714422	2	1	1	Class 1	QLGVPVIAKDIEIKPSVELPFNTFNVKANDQ
S34009	A2ASS6	−2.60171	0	2	2	1	Class 1	LLRPVTTTQRLSEYKSELDYMSKEEKSKKKS

Novex-3 (A2ASS6-3).
Z-disk.
Proximal Ig region.
Middle Ig region.
A-band.
M-band.

(ELISA). Hydrogen peroxide (H_2O_2) was assessed in LV tissue homogenates (n = 4–10/group). Samples containing equal amounts of total protein were analyzed for H_2O_2 formation. Total reduced glutathione in heart samples was determined in duplicate with a colorimetric glutathione assay kit (CS0260, Sigma Aldrich).

Amount and Phosphorylation of PKD and HSP27

The content of PKD and HSP27, as well as their phosphorylation were measured by 15% SDS–PAGE and western blot.

CaMKII Content and Activity

The content of CaMKII was determined using 15% SDS–PAGE and western blot and its activity by using non-radioactive kinase activity-assay kit (CycLex).

Immunofluorescence Imaging

Frozen histological LV sections (n = 3/group) were fixed, blocked and dual-stained with anti-PKD (Sigma-Aldrich; dilution 1:200) or anti-phospho-HSP27 (Ser 82) (Cell Signaling Technology; 1:50) and anti-α-actinin (sarcomere; Sigma-Aldrich; dilution 1:400) antibody, and were incubated with the appropriate secondary antibodies: (FITC) anti-mouse (Rockland Immunochemicals Inc, Limerick, PA, USA; dilution 1:300) and Cy3 anti-rabbit (Jackson ImmunoResearch Laboratories Inc, West Grove, PA, USA; dilution 1:100). Immunostained samples were analyzed by confocal laser scanning microscopy (Nikon Eclipse Ti-E Inverted Microscope System; Nikon Instruments, Nikon Corp, Shinagawa, Tokyo, Japan). Immunofluorescence imaging was processed equally among groups, for 2D intensity histogram analysis the Coloc2 plugin in FIJI was used.

Electron Microscopy (EM)

Frozen LV samples were cut, fixed and blocked. Samples were then immunolabeled against primary antibodies of PKD (Abcam; 1:200) and HSP27 (Abcam; 1:200), then with nanogold conjugated secondary antibodies. After counterstaining with osmium-tetroxide, and dehydration, blocks were embedded into resin. 50 nm thin sections were cut.

Statistics

Values are given as mean ± SEM. Statistically significant differences were tested using Bonferroni adjusted unpaired or paired Student's t-test, with $P < 0.05$ considered significant.

TABLE 4 | Upregulated titin phosphosites (log2 ratio KO/WT > 0.37).

Position within titin	UniProt identifyer	Log2 ratio (KO/WT)	–Log 10 *p*-value KO/WT	Charge	Multiplicity	Localization probability	Classification of phosphosite	Sequence window
T314	A2ASS6	0.386936	1.09573	2	1	0.982868	Class 1	TPSPVRSVSPAGRISTSPIRSVKSPLLIRKT
T10276	A2ASS6	0.395205	0	3	1	0.637793	Class 2	EVQKKVVTEEKIAIITQREESPPPAVPEIPK
S315	A2ASS6	0.40279	1.45166	2	1	0.997856	Class 1	PSPVRSVSPAGRISTSPIRSVKSPLLIRKTQ
S264	A2ASS6	0.419615	1.33152	2	2	1	Class 1	PHKTPPRIPPKPKSRSPTPPSIAAKAQLARQ
S35038	A2ASS6	0.429709	0.499475	2	1	0.987556	Class 1	VVLKTSSDVSLHGSVSSQSVQMSASKQEASF
S262	A2ASS6	0.433659	0.711028	2	2	1	Class 1	QLPHKTPPRIPPKPKSRSPTPPSIAAKAQLA
S23788	A2ASS6	0.438542	0	2	1	0.993369	Class 1	KNYIVEKRESTRKAYSTVATNCHKTSWKVDQ
S1527	A2ASS6	0.44247	0	3	1	0.86319	Class 1	VIKEDGTQSLIIVPASPSDSGEWTVVAQNRA
S31025	A2ASS6	0.474799	0	3	1	0.838063	Class 1	GLGVPVESEPIVARNSFTIPSQPGIPEEVGA
S834	A2ASS6	0.503759	0.543576	2	1	0.99992	Class 1	VSKISVPKTEHGYEASIAGSAIATLQKELSA
S307	A2ASS6	0.509144	3.60898	2	2	1	Class 1	VRHVRAPTPSPVRSVSPAGRISTSPIRSVKS
T314	A2ASS6	0.608677	0	2	2	0.982868	Class 1	TPSPVRSVSPAGRISTSPIRSVKSPLLIRKT
S774	A2ASS6	0.620881	0.40983	2	1	0.98142	Class 1	HVVPQAVKPAVIQAPSETHIKTTDQMGMHIS
S879	A2ASS6	0.704194	0	3	2	0.998042	Class 1	TVKPGETRVRAEPTPSPQFPFADMPPPDTYK
S10281	A2ASS6	0.719508	0.777963	3	1	0.999995	Class 1	VVTEEKIAIITQREESPPPAVPEIPKKKVPE
S262	A2ASS6	0.720452	2.29218	2	3	1	Class 1	QLPHKTPPRIPPKPKSRSPTPPSIAAKAQLA
S264	A2ASS6	0.767076	2.14935	2	3	1	Class 1	PHKTPPRIPPKPKSRSPTPPSIAAKAQLARQ
T266	A2ASS6	0.767076	2.14935	2	3	1	Class 1	KTPPRIPPKPKSRSPTPPSIAAKAQLARQQS
S799	A2ASS6	0.787488	0	3	1	0.834492	Class 1	MGMHISSQVKKTTDISTERLVHVDKRPRTAS
S12871	A2ASS6	0.829341	1.09019	3	1	1	Class 1	AKPKGPIKGVAKKTPSPIEAERKKLRPGSGG
S12884	A2ASS6	0.94305	0.52056	3	1	1	Class 1	TPSPIEAERKKLRPGSGGEKPPDEAPFTYQL
S12871	A2ASS6	0.981417	0.3495	3	2	1	Class 1	AKPKGPIKGVAKKTPSPIEAERKKLRPGSGG
T12869	A2ASS6	0.981417	0.3495	3	2	1	Class 1	EAAKPKGPIKGVAKKTPSPIEAERKKLRPGS
S838	A2ASS6	1.20302	0	3	1	0.999952	Class 1	SVPKTEHGYEASIAGSAIATLQKELSATSST
S32133	A2ASS6	1.4809	0.355789	2	1	0.791719	Class 1	PEPPSNPPEVLDVTKSSVSLSWSRPKDDGGS

Z-disk.
PEVK.
A-band.
M-band.

RESULTS

We hypothesized that *Prkd1* cKO mouse hearts would show altered titin phosphorylation compared to matched WT hearts.

Quantitative Mass Spectrometry Detects Disturbed Regulation in *Prkd1* cKO Mice

Using the SILAC technique, we detected a wide range of cardiac proteins that were either significantly upregulated (>80 proteins), downregulated (>105 proteins) or unchanged (remainder) in cKOs (**Figure 1A**). In total we detected 9,833 phosphosites (4,859 of them with $-\log10\ p > 0$) from 3,652 different proteins (2,507 of them with $\log10\ p > 0$) (**Figure 1B**). In total, 505 proteins were downregulated in cKO (log2 ratio KO/WT <−0.37) with a significant downregulation of 105 proteins. In addition to 422 proteins found to be upregulated (log2 ratio KO/WT >0.37), 80 proteins showed a significant upregulation, while the rest remained either unchanged or with no relevant pvalue (**Figure 1A**). Among the significantly up- or downregulated proteins were numerous myofilament and calcium handling proteins, in addition to several phosphatases and kinases (**Figures 1C–F**). We also detected many cardiac peptides that were either hypophosphorylated (70 phosphopeptides), hyperphosphorylated (63 phosphopeptides), or unchanged in cKOs (**Figure 1B**).

Quantitative Mass Spectrometry Detects Conserved PKD Phosphosites in Titin

Quantitative MS was combined with a modified SILAC technique to facilitate identification of PKD-dependent phosphorylation sites in titin. Titin was among the proteins that showed the largest alterations in phosphorylation in cKO compared to WT hearts. We identified 332 titin phosphopeptide (including 77.7% serines, 19.3% threonines, and 3.0% tyrosines), including 258 phosphosites with a ratio of cKO to WT phosphorylation levels (ratio WT/cKO) for titin. Among them, 164 phosphosites were with $-\log10\ p > 0$ (**Figure 2A**). Most of the identified phosphopeptides were class 1 (localization probability 0.75–1.00), although 27 phosphopeptides showed a localization probability <0.75 and were therefore class 2 phosphopeptides (see **Tables 1–5**). The majority of the phosphopeptides showed single phosphorylation, although some showed double phosphorylation. According to the conservative estimate that a cKO/WT ratio should be ≤ -0.37 or $\geq +0.37$ in order to

TABLE 5 | Unchanged titin phosphosites (−0.37 < log2 ratio KO/WT < 0.37).

Position within titin	UniProt identifyer	Log2 ratio (KO/WT)	–Log 10 *p*-value KO/WT	Charge	Multiplicity	Localization probability	Classification of phosphosite	Sequence window
T26299	A2ASS6	−0.367305	0.338896	2	1	0.999988	Class 1	PVVVQYPFKEPGPPGTPFVTSISKDQMLVQW
S23354	A2ASS6	−0.359797	0	3	1	0.990613	Class 1	KVLDRPGPPEGPLAVSDVTSEKCVLSWLPPL
S34298	A2ASS6	−0.356955	0	3	1	0.609727	Class 2	YAVSSFKRTSELEAASSVREVKSQMTETRES
S34470	A2ASS6	−0.355278	0	2	1	1	Class 1	VKSPEPRVKSPETVKSPKRVKSPEPVTSHPK
S33875	A2ASS6	−0.353589	0.477593	3	2	1	Class 1	PSPDYDLYYYRRRRRSLGDMSDEELLLPIDD
S33880	A2ASS6	−0.353589	0.477593	3	2	1	Class 1	DLYYYRRRRRSLGDMSDEELLLPIDDYLAMK
S18562	A2ASS6	−0.350673	0.345871	2	1	1	Class 1	IGTEKFHKVTNDNLLSRKYTVKGLKEGDTYE
T22520	A2ASS6	−0.329784	0	3	1	0.995336	Class 1	DDAWIKDTTGTALRITQFVVPDLQTKEKYNF
S3977	A2ASS6	−0.319098	0.36361	2	1	0.840288	Class 1	CTEGKILMASADTLKSTGQDVALRTEEGKSL
S19146	A2ASS6	−0.318534	0.168528	2	1	0.995484	Class 1	TNYVVERKDVATAQWSPLSTTSKKKSHMAKH
T13665	A2ASS6	−0.316873	0.41921	2	1	1	Class 1	CEVSREPKTFRWLKGTQEITGDDRFELIKDG
S17098	A2ASS6	−0.305806	0.472482	2	1	0.933227	Class 1	PPTSPERLTYTERTKSTITLDWKEPRSDGGS
S24868	A2ASS6	−0.302999	0	2	1	0.998408	Class 1	KIKNYIVEKREATRKSYAAVVTNCHKNSWKI
S34470	A2ASS6	−0.302672	0.238728	2	2	1	Class 1	VKSPEPRVKSPETVKSPKRVKSPEPVTSHPK
S26806	A2ASS6	−0.301597	0	2	1	0.655766	Class 2	PPGPPSNPKVTDTSRSSVSLAWNKPIYDGGA
S18224	A2ASS6	−0.300622	0.391952	2	1	0.832005	Class 1	APPGPPFPKVTDWTKSSVDLEWSPPLKDGGS
S34464	A2ASS6	−0.2992	0.235518	2	2	1	Class 1	VTSPPRVKSPEPRVKSPETVKSPKRVKSPEP
S2080	A2ASS6	−0.298846	0.520376	2	1	1	Class 1	ITIPTFKPERIELSPSMEAPKIFERIQSQTV
S19448	A2ASS6	−0.273899	0	2	1	0.805061	Class 1	QDTRKGTWGVVSAGSSKLKLKVPHLQKGCEY
S13228	A2ASS6	−0.273069	0	2	1	0.993076	Class 1	DIPGEWKLKGELLRPSPTCEIKAEGGKRFLT
S27374	A2ASS6	−0.266139	0	3	1	0.820467	Class 1	SSYSESSAVVAEYPFSPPGPPGTPKVVHATK
S20517	A2ASS6	−0.265893	0	3	1	0.748614	Class 2	TSCHVSWAPPENDGGSQVTHYIVEKREAERK
S28343	A2ASS6	−0.263658	0	3	1	0.780076	Class 1	SVTTDAGRYEITAANSSGTTKTFINIIVLDR
S32318	A2ASS6	−0.262435	0.516907	2	1	0.999971	Class 1	SRPRRTAMSVKTKLTSGEAPGVRKEMADVTT
S3622	A2ASS6-3	−0.260512	0	3	1	0.962608	Class 1	VEEKGMVRTIHFRSASPVRRADYVYNDEWSE
Y21274	A2ASS6	−0.257528	0	3	1	1	Class 1	VGDPILTEPAIAKNPYDPPGRCDPPVISNIT
T22220	A2ASS6	−0.252516	0.8886	3	1	0.940036	Class 1	AGKDIRPSDIAQITSTPTSSMLTVKYATRKD
S22152	A2ASS6	−0.241103	0	2	1	0.761358	Class 1	IRAKNTAGAISAPSESTGTIICKDEYEAPTI
S20332	A2ASS6	−0.239112	1.58029	2	1	1	Class 1	IIGYVVEMRPKIADASPDEGWKRCNAAAQLI
S9201	A2ASS6	−0.230981	0	2	1	1	Class 1	IMFKNNALLLQVKRASMADAGLYTCKATNDA
S4098	A2ASS6-3	−0.229673	0	3	1	1	Class 1	FELEPEVTPRDQAIQSPKHKFIFSSDITNEP
S27782	A2ASS6	−0.229019	0	3	1	0.547507	Class 2	DPFTTPSPPTSLEITSVTKDSMTLCWSRPET
T27228	A2ASS6	−0.228542	0.209869	3	1	0.955571	Class 1	ATVAWKKDGQVLRETTRVNVASSKTVTTLSI
S20036	A2ASS6	−0.211545	0	2	1	0.999133	Class 1	EVAWTKDKDATDLTRSPRVKIDTSAESSKFS
S9144	A2ASS6	−0.203903	0.163212	2	1	1	Class 1	NIKERLIPPSFTKKLSETVEETEGNSFKLEG
S22416	A2ASS6	−0.192457	0	2	1	0.999998	Class 1	EKKGLRWVRATKTPVSDLRCKVTGLQEGNTY
S30939	A2ASS6	−0.186488	0	2	1	0.998923	Class 1	VKVLDSPGPCGKLTVSRVTEEKCTLAWSLPQ
S18535	A2ASS6	−0.184072	0	3	1	1	Class 1	NTVSLTWNPPKYDGGSEIINYVLESRLIGTE
T266	A2ASS6	−0.174257	0.297613	2	1	1	Class 1	KTPPRIPPKPKSRSPTPPSIAAKAQLARQQS
S4175	A2ASS6	−0.168399	0.396358	3	1	1	Class 1	HEEDKIDVQGGRDHLSDAQKVETVIEAEADS
T23981	A2ASS6	−0.166376	0	3	1	0.5	Class 2	PAVTWHKDDIPLKQTTRVNAESTENNSLLTI
T14268	A2ASS6	−0.16409	0.087451	2	1	0.99985	Class 1	VFTKNLANLEVSEGDTIKLVCEVSKPGAEVI
S1529	A2ASS6	−0.159512	0.439196	3	1	0.943823	Class 1	KEDGTQSLIIVPASPSDSGEWTVVAQNRAGK
S9459	A2ASS6	−0.158813	0.124587	3	1	1	Class 1	DLRAMLKKTPALKKGSGEEEEIDIMELLKNV
T30575	A2ASS6	−0.154592	0	3	1	0.788648	Class 1	TEITNYIVEKRESGTTAWQLINSSVKRTQIK
S28281	A2ASS6	−0.146693	0.305079	3	1	0.999999	Class 1	DMKNFPSHTVYVRAGSNLKVDIPISGKPLPK
S26695	A2ASS6	−0.140014	0.346765	3	1	0.797368	Class 1	EPVIACNPYKRPGPPSTPEASAITKDSMVLT
S24391	A2ASS6	−0.137242	0.088548	2	1	0.993652	Class 1	TARLEIKSTDFATSLSVKDAVRVDSGNYILK
T29649	A2ASS6	−0.134127	0.58377	3	1	0.997724	Class 1	PSKFTLAVSPVDPPGTPDYIDVTRETITLKW

(Continued)

TABLE 5 | Continued

Position within titin	UniProt identifyer	Log2 ratio (KO/WT)	–Log 10 *p*-value KO/WT	Charge	Multiplicity	Localization probability	Classification of phosphosite	Sequence window
T21731	A2ASS6	−0.127027	0	2	1	0.718367	Class 2	NKWQRVMKSLSLQYSTKDLKEGKEYTFRVSA
T33772	A2ASS6	−0.120166	0.177658	2	1	1	Class 1	RMPYEVPEPRRFKQATVEEDQRIKQFVPMSD
S16477	A2ASS6	−0.120059	0.290657	2	1	0.960016	Class 1	KAVDPIDAPKVILRTSLEVKRGDEIALDATI
T25842	A2ASS6	−0.117083	0	2	1	0.999999	Class 1	AGGSARIHIPFKGRPTPEITWSKEEGEFTDK
S17015	A2ASS6	−0.116476	0	3	1	0.999637	Class 1	KMCLLNWSDPADDGGSDITGFIIERKDAKMH
S3827	A2ASS6-3	−0.110284	0.69199	2	1	1	Class 1	SNEEVHGYKSRGICESPDKVSQVLTPYPSES
S34488	A2ASS6	−0.108085	0.264442	2	1	0.999994	Class 1	RVKSPEPVTSHPKAVSPTETKPTEKGQHLPV
S790	A2ASS6	−0.10482	0	3	1	0.790373	Class 1	ETHIKTTDQMGMHISSQVKKTTDISTERLVH
T26696	A2ASS6	−0.0857946	0.182593	3	1	0.989467	Class 1	PVIACNPYKRPGPPSTPEASAITKDSMVLTW
S1977	A2ASS6	−0.081692	0.055874	2	1	0.990373	Class 1	KLQFEVQKVDRPVDTSETKEVVKLKRAERIT
S19447	A2ASS6	−0.0663668	0	2	1	0.591546	Class 2	KQDTRKGTWGVVSAGSSKLKLKVPHLQKGCE
S13204	A2ASS6	−0.0662166	0.089154	2	1	0.880947	Class 1	LKPIEDVTIYEKESASFDAEISEEDIPGEWK
S25920	A2ASS6	−0.0488367	0.044418	3	1	1	Class 1	PGPPQNLAVKEVRKDSVLLVWEPPIIDGGAK
S22804	A2ASS6	−0.0380723	0.014722	2	1	0.805129	Class 1	VIEAQRKGSDQWTHISTVKGLECVVRNLTEG
S34611	A2ASS6	−0.0345249	0	2	1	0.68296	Class2	TGQSFKSIHEQVSSISETTKSVQKTAESAEA
S30572	A2ASS6	−0.0335397	0	2	1	0.832922	Class 1	DGGTEITNYIVEKRESGTTAWQLINSSVKRT
S35063	A2ASS6	−0.0245479	0	2	1	0.632417	Class2	KQEASFSSFSSSSASSMTEMKFASMSAQSMS
S4018	A2ASS6	−0.018641	0	2	1	0.675564	Class 2	VLLKEEQSEVVAVPTSQTSKSEKEPEAIKGV
S35036	A2ASS6	−0.0161605	0	2	1	0.952755	Class 1	REVVLKTSSDVSLHGSVSSQSVQMSASKQEA
S3991	A2ASS6	−0.0149712	0.0107483	2	1	0.999502	Class 1	KSTGQDVALRTEEGKSLSFPLALEEKQVLLK
S17113	A2ASS6	−0.01187	0.0154739	3	1	0.985972	Class 1	STITLDWKEPRSDGGSPIQGYIIEKRRHDKP
S814	A2ASS6	−0.0108688	0.0162498	2	1	0.999999	Class 1	STERLVHVDKRPRTASPHFTVSKISVPKTEH
S20755	A2ASS6	−0.0093163	0.0181907	2	1	1	Class 1	DGSSVLIIKDVTRKDSGYYSLTAENSSGSDT
S27556	A2ASS6	−0.0092088	0.0073245	2	1	0.999755	Class 1	DQRYEFRVFARNAADSVSEPSESTGPITVKD
S3870	A2ASS6	−0.0051650	0.0056415	3	1	0.991661	Class 1	EPEGVFPGASSAAQVSPVTIKPLITLTAEPK
S4672	A2ASS6-3	−0.0048496	0.0087214	3	1	1	Class 1	ENGDKTFISQLKRAASEEECLEDHEMEDGPT
S28731	A2ASS6	−0.0040724	0.0043022	2	1	0.974739	Class 1	LASILIKDANRLNSGSYELKLRNAMGSASAT
S17109	A2ASS6	0.00032406	0	3	1	0.836525	Class 1	ERTKSTITLDWKEPRSDGGSPIQGYIIEKRR
S14664	A2ASS6	0.0113125	0.0110327	2	1	1	Class 1	REIKEGKKYKFEKDGSIHRLIIKDCRLEDEC
T21632	A2ASS6	0.0207359	0	2	1	0.819558	Class 1	AERKSWSTVTTECSKTSFRVSNLEEGKSYFF
S17316	A2ASS6	0.02154	0	3	1	0.980872	Class 1	ESCYLTWDAPLDNGGSEITHYIIDKRDASRK
S34623	A2ASS6	0.0307702	0.0977465	2	1	1	Class 1	SSISETTKSVQKTAESPEAKKQEPIAPESIS
S756	A2ASS6	0.0341452	0.0943439	3	1	1	Class 1	HISTTKVPEQPRRPASEPHVVPQAVKPAVIQ
S34573	A2ASS6	0.0437442	0	3	1	0.978092	Class 1	SADGTYELKIHNLSESDCGEYVCEVSGEGGT
S34571	A2ASS6	0.120101	0	2	1	0.99376	Class 1	HYSADGTYELKIHNLSESDCGEYVCEVSGEG
T32113	A2ASS6	0.130455	0	3	1	0.999962	Class 1	GISKPLKSEEPVIPKTPLNPPEPPSNPPEVL
T25315	A2ASS6	0.134102	0	3	1	1	Class 1	NSECYVARDPCDPPGTPEAIIVKRNEITLQW
S2078	A2ASS6	0.155502	0.903734	2	1	1	Class 1	GKITIPTFKPERIELSPSMEAPKIFERIQSQ
T21345	A2ASS6	0.156475	0.125556	3	1	0.999996	Class 1	PVIERTLKATGLQEGTEYEFRVTAINKAGPG
S31438	A2ASS6	0.158509	0	2	1	0.78457	Class 1	VPLVPTKLEVVDVTKSTVTLAWEKPLYDGGS
S34488	A2ASS6	0.158631	0	2	2	0.999994	Class 1	RVKSPEPVTSHPKAVSPTETKPTEKGQHLPV
S34476	A2ASS6	0.159999	0	2	2	1	Class 1	RVKSPETVKSPKRVKSPEPVTSHPKAVSPTE
S35128	A2ASS6	0.165174	0.213397	2	1	0.999984	Class 1	GRGIPPKIEALPSDISIDEGKVLTVACAFTG
S315	A2ASS6	0.166903	0.183848	2	2	0.997856	Class 1	PSPVRSVSPAGRISTSPIRSVKSPLLIRKTQ
S22797	A2ASS6	0.170233	0.274145	2	1	1	Class 1	GSKITGYVIEAQRKGSDQWTHISTVKGLECV
S25870	A2ASS6	0.199285	0	2	1	1	Class 1	TDKVQIEKGINFTQLSIDNCDRNDAGKYILK
S13764	A2ASS6	0.200173	0	2	1	1	Class 1	SWFKNDQRLHTSKRVSMHDEGKTHSITFKDL
S814	A2ASS6	0.200474	0.566341	2	2	0.999999	Class 1	STERLVHVDKRPRTASPHFTVSKISVPKTEH

(Continued)

TABLE 5 | Continued

Position within titin	UniProt identifyer	Log2 ratio (KO/WT)	–Log 10 *p*-value KO/WT	Charge	Multiplicity	Localization probability	Classification of phosphosite	Sequence window
S21152	A2ASS6	0.207222	0.196717	2	1	1	Class 1	RNLCTLELFSVNRKDSGDYTITAENSSGSKS
S307	A2ASS6	0.21303	0.565178	2	1	1	Class 1	VRHVRAPTPSPVRSVSPAGRISTSPIRSVKS
S2078	A2ASS6	0.216232	0.446394	2	2	1	Class 1	GKITIPTFKPERIELSPSMEAPKIFERIQSQ
S2080	A2ASS6	0.216232	0.446394	2	2	1	Class 1	ITIPTFKPERIELSPSMEAPKIFERIQSQTV
S33353	A2ASS6	0.219718	0.237812	3	1	1	Class 1	IRSQRGVSVAKVKVASIEIGPVSGQIMHAIG
T812	A2ASS6	0.223205	0.643762	4	2	0.999999	Class 1	DISTERLVHVDKRPRTASPHFTVSKISVPKT
Y33436	A2ASS6	0.229236	0	2	1	0.996224	Class 1	TKFDDGTYRCKVVNDYGEDSSYAELFVKGVR
S264	A2ASS6	0.246749	0.784633	2	1	1	Class 1	PHKTPPRIPPKPKSRSPTPPSIAAKAQLARQ
S3676	A2ASS6	0.258327	0	4	1	0.878152	Class 1	EDMPLYTSVCYTIIHSPDGSGTFIVNDPQRG
S879	A2ASS6	0.26138	0.407205	3	1	0.998042	Class 1	TVKPGETRVRAEPTPSPQFPFADMPPPDTYK
S1214	A2ASS6	0.287447	0.235319	2	1	1	Class 1	IQEPKVGEIAPGFAYSEYEKEYEKEQALIRK
S322	A2ASS6	0.325277	3.06343	2	1	1	Class 1	SPAGRISTSPIRSVKSPLLIRKTQTTTMATG
S12678	A2ASS6	0.331543	0.65471	3	1	1	Class 1	IEKPKLKPRPPARPPSPPKEDVKEKMFQLKA
T266	A2ASS6	0.332311	0.771702	2	2	1	Class 1	KTPPRIPPKPKSRSPTPPSIAAKAQLARQQS
S2032	A2ASS6	0.353204	0.75905	2	1	1	Class 1	EAITAVELKSRKKDESYEELLKKTKDELLHW

Novex-3 (A2ASS6-3).
Z-disk.
Proximal Ig region.
N2B-element.
Middle Ig region.
PEVK.
Distal Ig domains.
A-band.
M-band.

represent a significant change in cKO vs. WT, ten significantly altered titin phosphorylation sites could be identified in cKO hearts (**Table 1**). We identified 24 phosphosites in the elastic spring region of titin (see **Table 2**). Most of them were located in the N2B-element, PEVK region and distal Ig region. In total, hypophosphorylation (log2 ratio cKO/WT<-0.37) was seen in 133 titin phosphopeptides, the majority of which originated from A- and M-band titin (see **Table 3**). Furthermore, 25 titin phosphosites were hyperphosphorylated (log2 ratio cKO/WT >0.37; **Table 4**). One hundred and twelve titin phosphopeptides showed no significant differences in phosphorylation in cKO compared to WT ($-0.37>$ cKO/ WT ratio$<+0.37$; see **Table 5**).

Titin Isoform Composition in PKD1 cKO Mice

To study whether PKD has an influence on titin isoform composition, homogenized myocardial samples of cKO and matched WT mice were separated using SDS-PAGE, the protein bands visualized by Coomassie staining and the two cardiac titin isoforms N2BA and N2B analyzed using densitometry; a representative titin gel showing these two isoforms in WT and cKO is shown in **Figure 2C**. On average, titin isoform composition remained unchanged in cKO vs. WT mouse hearts. For both groups, the ratio of N2B to N2BA was ∼85:15% (**Figure 2B**). A "T2" titin degradation band was also detectable in hearts of both cKO and WT, but showed no significant change.

Site-Specific Phosphorylation at Titin-N2Bus and Titin-PEVK

To confirm titin phosphorylation sites identified by quantitative MS and to analyse site-specific titin phosphorylation, affinity-purified anti-phosphosite-specific antibodies were generated against conserved serines of human/mouse N2Bus at Ser4010/Ser3991, Ser4062/Ser4043, and Ser4099/Ser4080, as well as human/mouse PEVK at Ser11878/Ser12742 and Ser12022/Ser12884. The PVDF staining served as a protein loading control.

Using the titin anti-phospho-antibodies we found unaltered phosphorylation at the positions Ser3991 (**Figure 2C**) and Ser4080 (**Figure 2E**) but significantly increased phosphorylation at the positions Ser4043 (**Figure 2D**), Ser12742 (**Figure 2F**), and Ser12884 (**Figure 2G**) in cKO compared to WT hearts. Using an anti-phosphor-Ser/Thr antibody, overall-titin phosphorylation was found to be greatly decreased, by ≈25% on average, in cKO compared to WT hearts (**Figure 2H**).

Cardiomyocyte $F_{Passive}$ Is Elevated in cKO Hearts

The passive length–tension relationship of single skinned cardiomyocytes in relaxing solution was steeper in cKO than in WT hearts (**Figures 3A,B**). Significantly increased $F_{passive}$ levels in cKO vs. WT cells were found at sarcomere lengths (SL) of 2.1 μm or higher. Administering

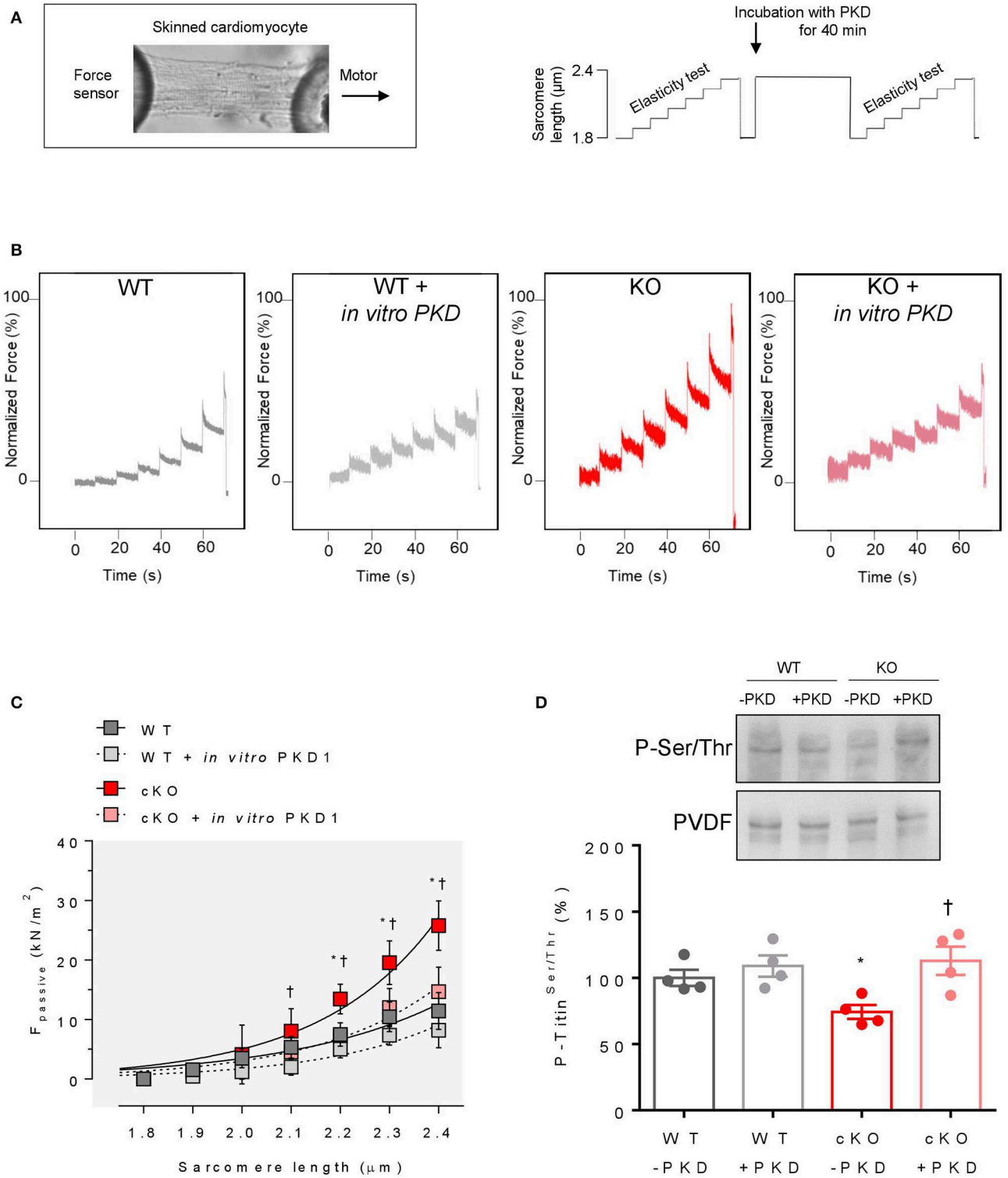

FIGURE 3 | Cardiomyocyte passive stiffness and overall-titin phosphorylation in WT and PKD1 cKO mice by back-phosphorylation. **(A)** Representative image (left) and stretch protocol (right) used in the experiments **(B)** Original recordings of the force response to stepwise cell stretching of isolated skinned cardiomyocytes. **(C)** WT and PKD1 cKO $F_{passive}$ at sarcomere length 1.8–2.4 µm in the presence or absence of *in vitro* PKD1 (16–20 cardiomyocytes/group). Curves are second-order polynomial fits to the means (± SEM; $n = 4$ cardiomyocytes/heart). For B; $^{*}P < 0.05$ WT vs. cKO, $^{\dagger}P < 0.05$ cKO vs. cKO after PKD treatment in Student *t*-test. **(D)** Representative immunoblot and graph before (–PKD1) and after incubation with protein kinase D1 (+PKD1). Data are means ± SEM; $n = 4$ hearts/group. Each heart was analyzed in duplicate. $^{*}P < 0.05$ in Students unpaired and paired *t*-test.

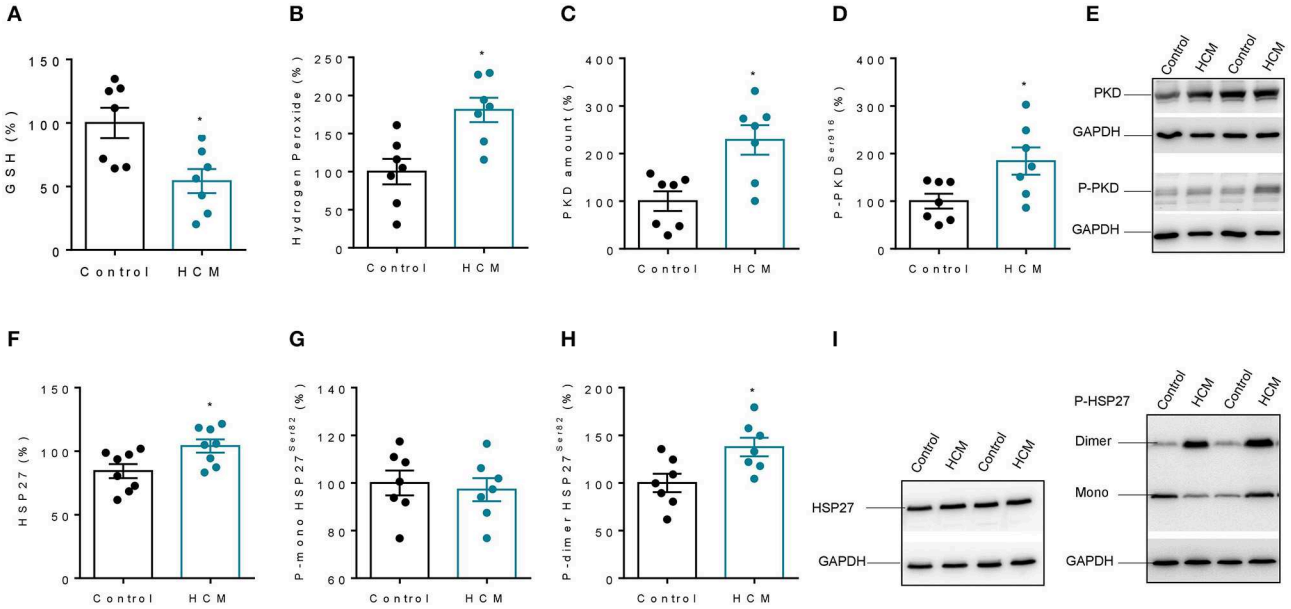

FIGURE 4 | Myocardial oxidative stress parameters, PKD-content and phosphorylation, and HSP27-content and phosphorylation in HCM patients. **(A)** Reduced Glutathione (GSH). **(B)** Hydrogen Peroxide (H_2O_2). **(C)** Protein Kinase D (PKD). **(D)** Phospho-Ser916 PKD. **(E)** Representative blots of (Phospho)PKD and GAPDH. **(F)** Heat Shock Protein 27 (HSP27). **(G)** Phospho-monomer HSP27. **(H)** Phospho-dimer HSP27. **(I)** Representative blots of HSP27 and monomer and dimer of HSP27. Data are means ± SEM; $n = 7$–8 hearts/group.

PKD to non-activated skinned cardiomyocytes from cKO hearts in relaxing solution significantly reduced $F_{passive}$ at SL 2.2 μm or higher, returning it to levels found in matched WT cells (**Figure 3C**), whereas administration of PKD to WT cardiomyocytes did not affect $F_{passive}$.

In an alternative approach, demembranated cardiac fiber bundles from hearts of these mice were phosphorylated *ex vivo* by PKD and then titin SDS-PAGE was performed followed by Western blot analysis. Titin phosphorylation was significantly increased after PKD treatment in cKO hearts, while in WT it remained unaltered (**Figure 3D**).

Increased PKD and HSP27 Activity Is Associated With Increased Oxidative Stress

In HCM hearts, we found less reduced glutathione (GSH) and increased hydrogen peroxide (H_2O_2), both of which indicate that oxidative stress was increased in HCM hearts compared to control non-failing hearts (**Figures 4A,B**). Myocardial PKD content and PKD phosphorylation at phosphosite Ser916 were both significantly higher in HCM hearts compared to controls, indicating total myocardial PKD activity in HCM (**Figures 4C–E**). In addition, the amount of HSP27 was higher in hearts of HCM patients compared to controls (**Figure 4F**) and the phosphorylation of HSP27 resulted in an altered dimer phosphorylation of HSP27 in HCM compared to controls, while HSP27 monomers remained unchanged (**Figures 4G–I**).

Cardiomyocyte $F_{Passive}$ Is Elevated in HCM Hearts

Cardiomyocytes from human end-stage failing hearts (only from patients with hypertrophic cardiomyopathy) showed a higher cardiomyocyte $F_{passive}$ at sarcomere length 2.1 μm or higher compared to non-failing human heart samples. Administering human recombinant PKD to non-activated skinned cardiomyocytes from human HCM hearts in relaxing solution significantly reduced $F_{passive}$ at sarcomere length 2.1 μm or higher, lowering it to levels found in cells from control hearts (**Figures 5A–C**). In addition, upon treatment with human recombinant HSP27, $F_{passive}$ was significantly reduced at all sarcomere lengths, whereas control cardiomyocytes remained unaltered (**Figures 5D,E**).

Titin Phosphorylation in Hearts of Human HCM Patients

We found increased CaMKII phosphosites at titin positions Ser4062 and Ser12022 in HCM compared to control hearts (**Figures 6A,B**), which went along with increased myocardial CaMKII content and activity (**Figures 6C,D**). Total titin phosphorylation was significantly lower in HCM compared to non-failing hearts (**Figure 6E**). Using an alternative approach, we measured total titin phosphorylation in demembranated cardiac fiber bundles obtained from HCM and non-failing human hearts before and after *ex vivo* phosphorylation by human recombinant PKD (**Figure 6E**). Strong signals were seen for both isoforms N2BA and N2B after kinase treatment, and the total phosphorylation of titin was significantly

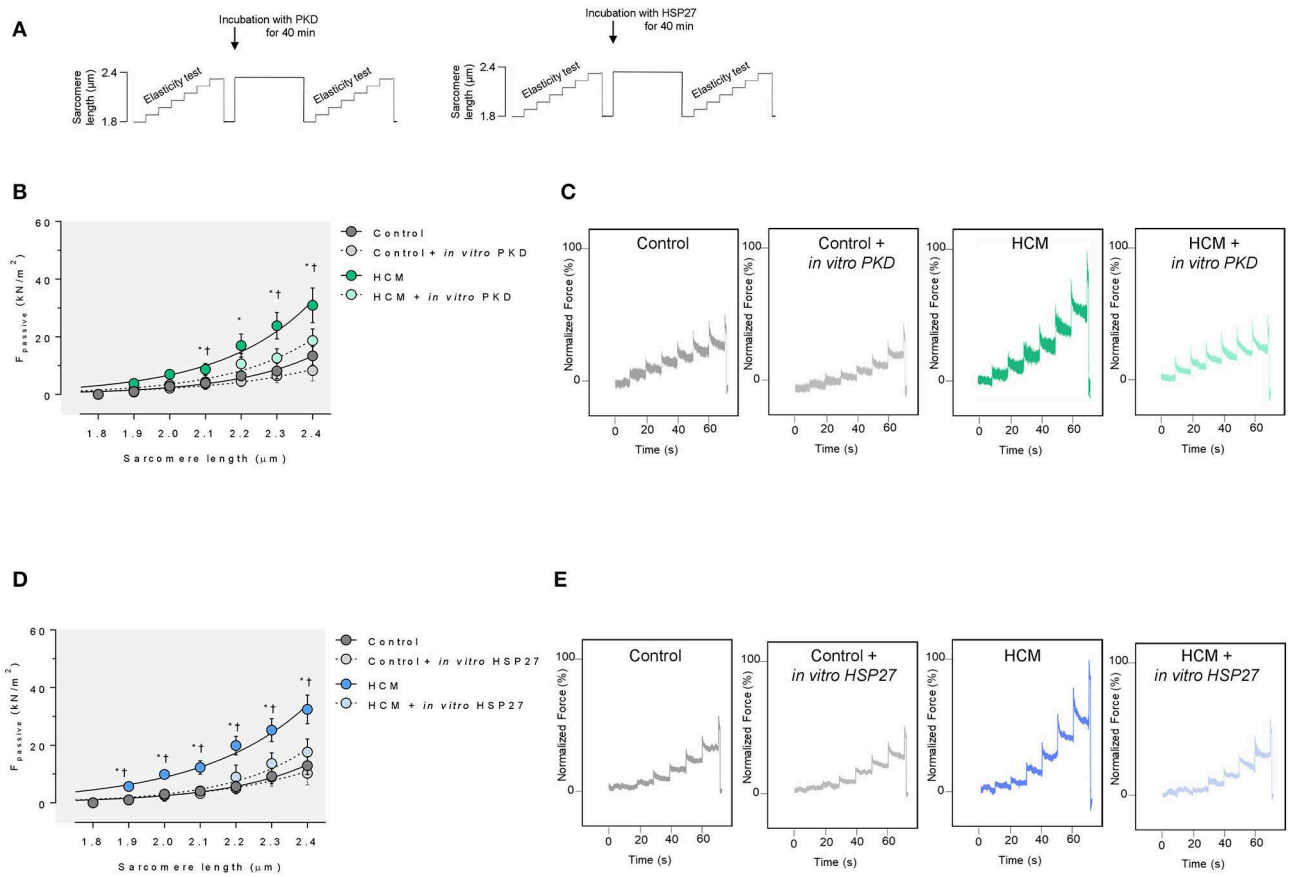

FIGURE 5 | Cardiomyocyte passive stiffness in human non-failing and failing HCM hearts. **(A)** Stretch protocol used in experiments. **(B)** $F_{passive}$ at sarcomere length 1.8–2.4 μm in the presence or absence of *in vitro* human recombinant PKD of human non-failing control and failing HCM. **(C)** Original recordings of the force response to stepwise cell stretching of isolated skinned cardiomyocytes. Curves are second-order polynomial fits to the means (± SEM; $n = 4$ cardiomyocytes/heart). For **(B)**; $^{*}P < 0.05$ Control vs. HCM, $^{\dagger}P < 0.05$ HCM vs. HCM after PKD or HSP27 treatment in Student *t*-test. **(D)** Human non-failing control and failing HCM $F_{passive}$ at sarcomere length 1.8–2.4 μm in the presence or absence of *in vitro* human recombinant HSP27. **(E)** Original recordings of the force response to stepwise cell stretching of isolated skinned cardiomyocytes.

increased by more than 20% in non-failing and failing HCM hearts.

Subcellular Localization and Overlay of PKD and HSP27 in HCM and Control Hearts

As we found a relatively high level of PKD expression in failing HCM hearts using western blot, we wished to determine the cellular distribution of PKD using confocal laser scanning and electron microscopy. The confocal images showed a clear overlay of PKD signals with sarcomeres in control and HCM hearts (**Figure 7A**). Phospho-HSP27 was clearly present at the periphery of the cardiomyocytes in HCM compared to control hearts, whereas in control hearts, phospho-HSP27 was distributed throughout the cardiomyocyte (**Figure 7B**). 2D intensity histograms show two channels and the level of overlapping. For a high overlapping level, the histogram pixels tend to concentrate more along the y = x line. 2D intensity histogram analysis showed a more intense presence of PKD in HCM but distribution was not significantly different, while phospho-HSP27 in HCM hearts compared to controls showed less correlation with α-actinin as more pixels concentrate at the axis of the histogram, the less correlation can be expected (**Figures 7C,D**). In keeping with these findings, electron microscopy confirmed the higher level of PKD in myocardium HCM compared to control hearts (**Figures 8A,B**). Using electron microscopy, HSP27 showed a strongly altered localization away from the Z-disk and A-band in HCM, whereas HSP27 was located preferentially at the Z-disk and A-band in controls (**Figures 8C,D**).

DISCUSSION

PKD has emerged as a key regulator of excitation-contraction coupling and cardiac hypertrophic signaling. Cardiac-specific PKD1-cKO mice show resistance to cardiac hypertrophy and fibrosis in response to pressure overload and angiotensin II treatment (Fielitz et al., 2008). Overexpression of constitutively active PKD1 in mouse hearts leads to dilated cardiomyopathy,

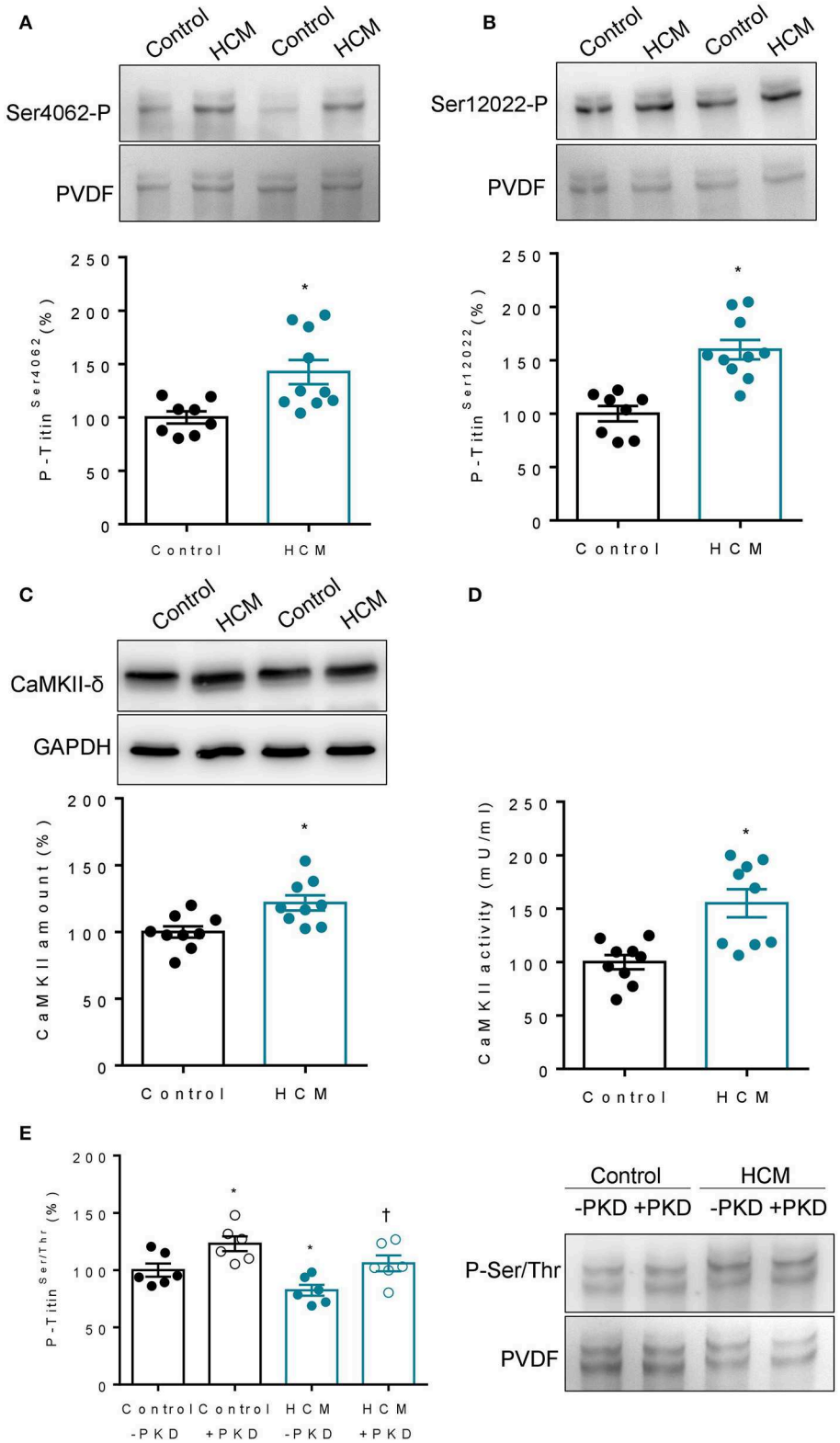

FIGURE 6 | Titin phosphorylation and CaMKII content and activity in hearts of failing HCM and non-failing control patients. **(A)** Site-specific phosphorylation at position Ser4062 in N2Bus ($n = 8 - 10$ hearts/group; each heart analysed in duplicate). **(B)** Site specific phosphorylation at position Ser12022 in PEVK region ($n = 8 - 10$ hearts/group; each heart analysed in duplicate). **(C)** CaMKII content in HCM vs. control hearts ($n = 9$ hearts/group). or absence of *in vitro* PKD. **(D)** CaMKII

(Continued)

FIGURE 6 | activity in HCM vs. control hearts ($n = 9$ hearts/group). **(E)** Total N2B-titin phosphorylation in HCM vs. control hearts ($n = 8 - 10$ hearts/group; each heart analysed in duplicate). Representative immunoblot right panel and graph left panel before (–PKD) and after incubation with protein kinase D1 (+PKD). Data are means ± SEM; $n = 6$ hearts/group. Each heart was analyzed in duplicate. $^{*}P < 0.05$ vs. Control untreated; $^{\dagger}P < 0.05$ vs. HCM untreated.

and an increase in PKD1 expression and activity is seen in failing hearts of rats (Harrison et al., 2006), rabbits and humans (Bossuyt et al., 2008). These findings indicate the importance of PKD1 in regulating cardiac pathophysiology and the potential of the kinase as a therapeutic target in cardiovascular disease (Nichols et al., 2014). As PKD1 showed some beneficial effects on cardiomyocyte function (Haworth et al., 2004; Cuello et al., 2007), we wanted to know if PKD is also involved in the phosphorylation of titin. We demonstrated that titin is an important substrate of PKD. In a quantitative MS screen using PKD1-cKO hearts and the SILAC mouse heart, we found that titin was among the cardiac proteins most highly affected by PKD1 deletion. Overall, titin phosphorylation was significantly reduced in cKO compared to WT hearts. Many of the phosphosites found in titin are located within the Z-disk, A-band, or M-band sections of the molecule, where they could be involved in regulating protein–protein interactions or mechanical signaling (**Figure 9**). In addition, we identified many phosphosites within the I-band titin region (proximal Ig region, N2-Bus and PEVK region) present in the N2BA and N2B cardiac titin isoforms (**Figure 9**). Furthermore, we showed that PKD reduces cardiomyocyte stiffness in PKD1 cKO mice and in failing hearts of human HCM patients. As PKD1 activation and increased PKD1 phosphorylation is observed in the hypertrophic heart from mice that have undergone tac surgery and as PKD plays an important role in the development of cardiac hypertrophy as shown via inhibition of hypertrophy in isolated neonatal cardiomyocytes from Wistar rats with PKD deletion (Zhao et al., 2017, 2019), we used human HCM tissues to validate how important is PKD in human heart failure with hypertrophy. We found disturbed titin phosphorylation in human HCM hearts, possibly contributing to the mechanical dysfunction. This was associated with increased PKD and CaMKII content and activity in these hearts. Moreover, we detected an increased amount and phosphorylation of HSP27, a substrate of PKD, in human HCM hearts. Changes in PKD, CaMKII and HSP27 were associated with increased oxidative stress parameters. Our work reveals a previously unknown role of PKD in regulating diastolic passive properties of healthy and diseased hearts, and its association with oxidative stress and changes affecting HSP27.

Titin Is a Substrate of PKD

Changes in titin stiffness due to isoform switching or post-translational modifications such as phosphorylation and oxidation have been reported in a variety of species. Previous studies showed that heart failure is associated with a chronic deficit in global titin phosphorylation (Bishu et al., 2011; Falcao-Pires et al., 2011; Hamdani et al., 2013a,b). Titin is phosphorylated by PKA at the N2B spring element, which results in a reduction of cardiomyocyte $F_{passive}$ (Yamasaki et al., 2002; Kruger and Linke, 2006). In addition, titin is phosphorylated by PKG at the N2Bus (Kruger et al., 2009; Kotter et al., 2013), a modification that also reduces cardiomyocyte $F_{passive}$ (Borbely et al., 2009; Hamdani et al., 2013a, 2014). Following short-term cGMP-enhancing treatment with sildenafil and B-type natriuretic peptide (BNP) in an animal model of heart failure with preserved ejection fraction (HFpEF) (elderly hypertensive dogs) (Bishu et al., 2011), PKG-mediated phosphorylation of titin resulted in acutely increased cardiac extensibility and may also positively regulate hypertrophic signaling. Our study provides the first evidence that PKD also phosphorylates titin. Notably, altered phosphorylation of titin sites was seen within the PEVK-domain, especially at the phosphosites that are also CaMKII-dependent. Perhaps this hints at a compensatory mechanism due to the loss of PKD in these mice.

Cardiomyocyte Stiffness and PKD

Cardiomyocyte $F_{passive}$ was elevated in cKO compared to WT, and incubating skinned cardiomyocytes with PKD lowered $F_{passive}$ in cKO, but did not affect WTs. Furthermore, cardiomyocyte isolated from failing HCM hearts showed increased $F_{passive}$, which could be reduced upon treatment with PKD enzyme. Thus, PKD alters $F_{passive}$ in the same direction as PKA, PKG, ERK2, and CaMKIIδ, an effect that may depend mainly on the phosphorylation of N2Bus. The latter increases the persistence length of N2Bus and thereby reduces $F_{passive}$ (Kruger et al., 2009). Another possible mechanism is via phosphorylation of titin Ig domains, although this is not yet proven. To date, PKCα is the only kinase that increases cardiomyocyte stiffness via phosphorylation of the PEVK region. The mechanical effect of PKCα-mediated PEVK phosphorylation includes increased persistence length of PEVK causing increased stretch-dependent force of the titin spring, thus elevating cardiomyocyte passive tension (Hidalgo et al., 2009). Reduced all-titin phosphorylation contribute to the development of heart failure, against the reduced phosphorylation, increased phosphorylation has been demonstrated in heart failure, the PKCα-dependent phosphosite at S11878 within the PEVK-titin segment was hyperphosphorylated in HFpEF animal models (Hamdani et al., 2013a, 2014; Linke and Hamdani, 2014; Franssen et al., 2016). PKCα was shown to be increased in heart failure (Belin et al., 2007) and in the HFpEF dog hearts. We believe what might determine the spatial arrangement phosphorylation along the titin molecule is the distinct micro-environment of phospho-sites either surrounded by negatively charged micro-environment and phospho-sites located at hydrophobic environment and close to cysteines sites. This may induce distinct biological and mechanical responses that may have differential effects on heart muscle exposed to oxidative stress and inflammation.

In failing human hearts, the activities of PKA and PKG are typically reduced (Hamdani et al., 2013a, 2014; Linke and Hamdani, 2014; Franssen et al., 2016), whereas the activity

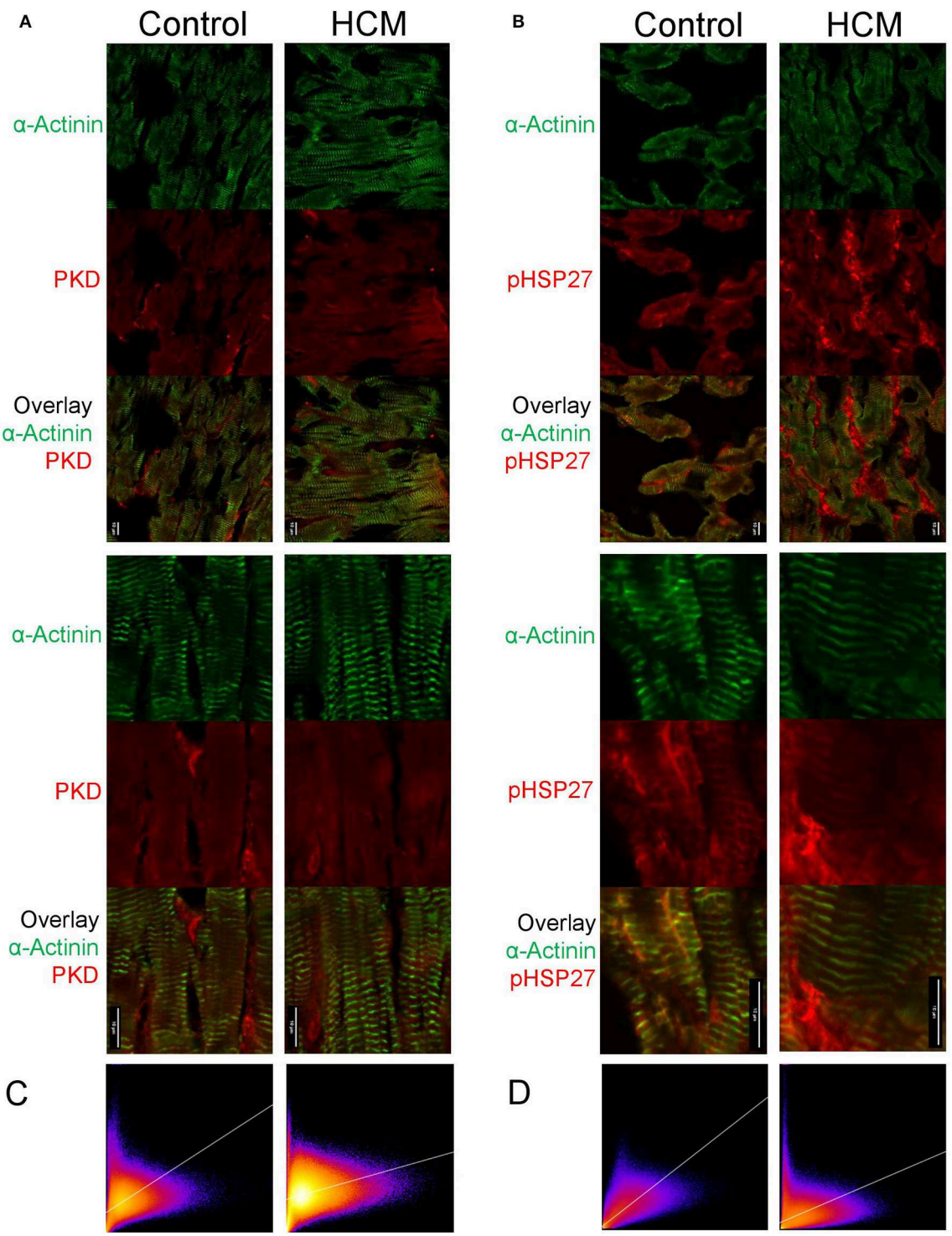

FIGURE 7 | Images of confocal laser scanning microscopy of PKD or HSP27 in human cardiomyocytes from failing HCM and control hearts. **(A)** Representative immunohistochemistry of PKD labeling in non-failing control human biopsy specimens along with a volume view. **(B)** Representative immunohistochemistry of PKD labeling in HCM human biopsy specimens along with a volume view. **(C)** 2D intensity histograms showing the relationship of intensities at the exact position between two channels representing alpha-actinin and PKD. **(D)** 2D intensity histograms showing the relationship of intensities at the exact position between two channels representing HSP-27 and alpha-actinin.

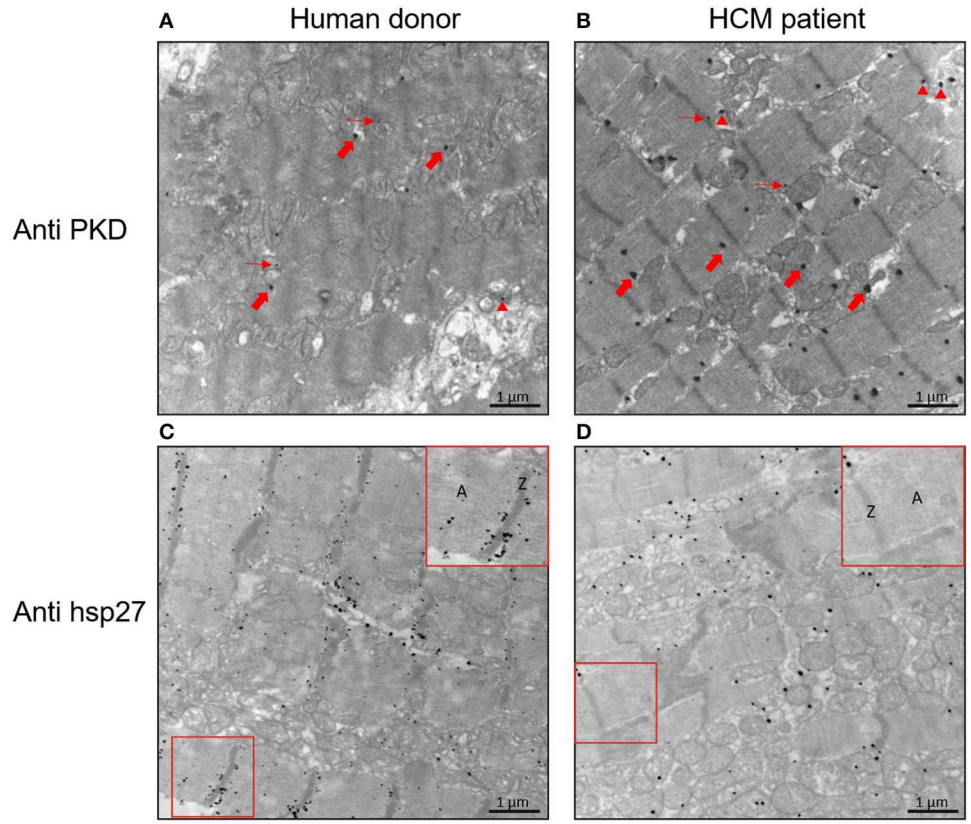

FIGURE 8 | Electron microscopy images to illustrate sarcomeric localization of PKD and HSP27 in human cardiomyocytes of failing HCM and non-failing control hearts. **(A)** Representative electron microscopy images with PKD labeling in non-failing control human. **(B)** Representative electron microscopy images with PKD labeling in HCM. **(C)** Representative electron microscopy images with HSP27 labeling in non-failing control human. **(D)** Representative electron microscopy images with HSP27 labeling in HCM. Small red arrow is for monomer; arrowhead red is for dimer; and big red arrow is for polymer.

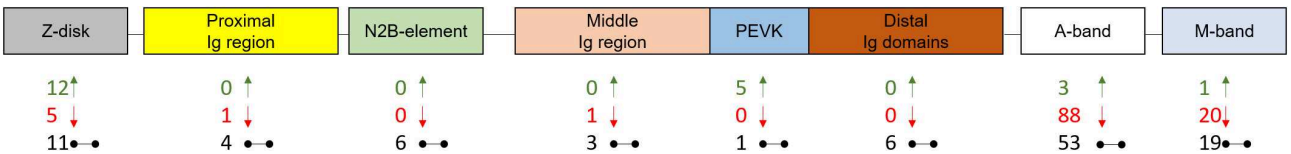

FIGURE 9 | Overview of identified phosphosites on the entire titin molecule Figure shows all detected phosphosites on the Z-disk, Proximal Ig region, N2B-element, Middle Ig region, PEVK, Distal Ig domains, A-band, and M-band. ↑Upregulated, ↓downregulated, and ●—● unchanged.

and the expression of PKCα, ERK2, and CaMKIIδ are usually increased, perhaps because of the presence of hypertrophy. In human failing HCM hearts, cardiomyocyte $F_{passive}$ was increased compared to non-failing hearts, an effect that was related to increased CaMKII activity and consequently, increased phosphorylation of titin within the PEVK region at CaMKIIδ-dependent phosphosites (Bishu et al., 2011; Falcao-Pires et al., 2011; Hamdani et al., 2013a,b). Cardiomyocyte $F_{passive}$ has been found to be pathologically elevated in human HFpEF and heart failure with reduced ejection fraction (HFrEF), due to disturbed activity of PKA and PKG. While inhibition of PKCα activity has been suggested as a potential therapeutic target for hypertrophied hearts, boosting PKD enzyme activity in failing, overly stiff, hearts could be beneficial for cardiomyocyte stiffness, similar to PKA, PKG, and ERK2 (Borbely et al., 2009; Raskin et al., 2012; van Heerebeek et al., 2012; Hamdani et al., 2013a, 2014; Kotter et al., 2013; Linke and Hamdani, 2014). A reduction in PKD-mediated titin phosphorylation, in turn, would increase $F_{passive}$ and be detrimental to diastolic filling. However, a stiffer titin spring could speed up diastolic recoil and amplify some of the mechanosensory functions of titin.

The PKD Substrate HSP27

The current study also showed that HSP27 content and phosphorylation is increased in human HCM hearts, a mechanism that might work to protect cardiomyocytes from

damage, as an established function of HSP27 is to prevent stress-induced protein aggregation and myocardial damage (Linke and Hamdani, 2014). The observed increase in HSP27 was associated with increased oxidative stress and increased content and activity of PKD, which also phosphorylates HSP27. PKD showed a polymer formation on EM, which indicates that PKD is oxidized. This may thus explain the beneficial *ex-vivo* effect of PKD on cardiomyocyte $F_{passive}$ and indicates that perhaps increased PKD activity observed in HCM hearts is partially due to PKD oxidation as well-suggesting that by lowering oxidation we may improve cardiomyocyte function in a manner similar to administration of endogenous PKD *ex vivo*. PKD is an important downstream regulator of the oxidative stress response, and increased oxidative stress leads to the activation of different PKD isoforms and subsequent phosphorylation of HSP27 (Doppler et al., 2005; Stetler et al., 2012). In our study, phosphorylation of HSP27 was increased in HCM hearts, which is in line with previous findings showing that HSP27 phosphorylation prevents apoptosis by protecting cells against heat shock, apoptosis effectors, oxidative stress, and ischemia (Martin et al., 1997; Benjamin and McMillan, 1998; Knowlton et al., 1998; Yoshida et al., 1999; Dohke et al., 2006; Li et al., 2012). HSP27 is abundant in cardiac muscle cells, commonly localized to the Z-disk and I-band regions of the sarcomere, and involved in the protection of titin and intermediate filaments (Kotter et al., 2014; Linke and Hamdani, 2014). In HCM hearts, HSP27 showed a strongly altered localization away from the Z-disk and I-band, whereas in non-failing hearts, HSP27 was preferentially localized to the Z-disk and I-band. Whether the translocation of HSP27 depends on the altered phosphorylation status of HSP27 is still controversial (Mymrikov et al., 2011); altered phosphorylation of HSP27 at least did not alter the binding to titin domains (Kotter et al., 2014; Linke and Hamdani, 2014). HSP27 can function as an inhibitor of cell death upon its phosphorylation and dissociation to lower-molecular-weight oligomers, while the presence of the high-molecular-weight, non-phosphorylated form of HSP27 appears to be necessary for cellular protection against cardiac ischemia/reperfusion (Golenhofen et al., 2002, 2006; Kadono et al., 2006; Pinz et al., 2008). PKD specifically phosphorylates HSP27 in pancreatic cancer cells (Yuan and Rozengurt, 2008) and endothelial cells (Evans et al., 2008). Phosphorylation of Ser82 is considered to be the main "effector" step for the shift from large molecular weight multimers to differentially functional oligomers. As regards titin, HSP27 specifically protects the unfolded Ig regions, but not the intrinsically disordered segments (N2Bus and PEVK), from aggregating under acidic stress (Kotter et al., 2014). The protective role of small HSPs on titin extensibilitywas also evident in earlier studies in which α-B crystallin lowered the persistence length of the N2Bus segment and reduced the unfolding probability of the immunoglobulin domains flanking the N2Bus segment (Bullard et al., 2004). Isolated hearts lacking sHSPs (DKO) showed severe contractile dysfunction (Pinz et al., 2008), increased myocardial injury and resting tension (Golenhofen et al., 2006), accompanied by diastolic dysfunction in response to ischemia/reperfusion *ex vivo* (Pinz et al., 2008). This accords with our previous findings in isolated human cardiomyocytes in which under conditions promoting titin aggregation (pre-stretch and acidic pH), passive stiffness was high in the absence of sHSPs but normal in the presence of sHSPs (Kotter et al., 2014). In our present work on human HCM cardiomyocytes, HSP27 lowered $F_{passive}$ to the levels previously reported after administration of PKA and/or PKG (Borbely et al., 2005; Fukuda et al., 2005; Kruger et al., 2009; Falcao-Pires et al., 2011). In addition, $F_{passive}$ fell to the level observed after PKD administration.

CONCLUSION

Our findings have important therapeutic implications as they imply that drugs that balance PKD activity and restore HSP27 localization to the Z-disk and I band may show efficacy as a treatment for diastolic LV dysfunction related to high cardiomyocyte stiffness.

DATA AVAILABILITY STATEMENT

All datasets generated for this study are included in the article/**Supplementary Material**.

ETHICS STATEMENT

All animal procedures were performed in accordance with the guidelines of Charité Universitätsmedizin Berlin as well as Max-Delbrück Center for Molecular Medicine and were approved by the Landesamt für Gesundheit und Soziales (LaGeSo, Berlin, Germany) for the use of laboratory animals (permit number: G 0229/11) and followed the Principles of Laboratory Animal Care (NIH publication no. 86-23, revised 1985) as well as the current version of German Law on the Protection of Animals. The studies involving human participants were reviewed and approved by (St Vincent's Hospital of Sydney, Australia, Human Research Ethics Committee; File number: H03/118; Title: Molecular Analysis of Human Heart Failure. The patients/participants provided their written informed consent to participate in this study.

AUTHOR CONTRIBUTIONS

MH has generated all mass spectrometry and biochemistry data, analyzed all data, and has written the manuscript. DK has generated the confocal images and written the manuscript. ML has made the electron microscopy. SH and MK helped and supervised the mass spectrometry. ÁK performed mechanic experiments. ZP contributed to mechanics and rewrote the manuscript. KJ helped with re-analyzing the biochemistry data and rewrote the manuscript. PH provided the tissues. CD provided the human HCM biopsies. PR re-analyzed some data. AM re-analyzed the data and rewrote the manuscript. JF provided the Prkd1 mice and rewrote the manuscript. WL supervised and rewrote the manuscript. NH supervised, re-analyzed all data, performed mechanics, and wrote the manuscript.

FUNDING

This work was supported by DFG (HA 7512/2-1) and FoRUM-Projekt (F765-13, F808N-14, and F882R-2017).

ACKNOWLEDGMENTS

We gratefully acknowledge the technical assistance of Anja Vöge and Frauke De Pasquale. Also we acknowledge support by the DFG Open Access Publication Funds of the Ruhr-Universität Bochum.

SUPPLEMENTARY MATERIAL

The Supplementary Material for this article can be found online at: https://www.frontiersin.org/articles/10.3389/fphys.2020.00240/full#supplementary-material

REFERENCES

Agah, R., Frenkel, P. A., French, B. A., Michael, L. H., Overbeek, P. A., and Schneider, M. D. (1997). Gene recombination in postmitotic cells. targeted expression of cre recombinase provokes cardiac-restricted, site-specific rearrangement in adult ventricular muscle *in vivo*. *J. Clin. Invest.* 100, 169–179.

Aita, Y., Kurebayashi, N., Hirose, S., and Maturana, A. D. (2011). Protein kinase D regulates the human cardiac L-type voltage-gated calcium channel through serine 1884. *FEBS Lett.* 585, 3903–6. doi: 10.1016/j.febslet.2011.11.011

Avkiran, M., Rowland, A. J., Cuello, F., and Haworth, R. S. (2008). Protein kinase d in the cardiovascular system: emerging roles in health and disease. *Circ. Res.* 102, 157–63. doi: 10.1161/CIRCRESAHA.107.168211

Belin, R. J., Sumandea, M. P., Allen, E. J., Schoenfelt, K., Wang, H., Solaro, R. J., et al. (2007). Augmented protein kinase C-α-induced myofilament protein phosphorylation contributes to myofilament dysfunction in experimental congestive heart failure. *Circ. Res.* 101, 195–204. doi: 10.1161/CIRCRESAHA.107.148288

Benjamin, I. J., and McMillan, D. R. (1998). Stress (heat shock) proteins: molecular chaperones in cardiovascular biology and disease. *Circ. Res.* 83, 117–132. doi: 10.1161/01.res.83.2.117

Bishu, K., Hamdani, N., Mohammed, S. F., Kruger, M., Ohtani, T., Ogut, O., et al. (2011). Sildenafil and B-type natriuretic peptide acutely phosphorylate titin and improve diastolic distensibility *in vivo*. *Circulation* 124, 2882–2891. doi: 10.1161/CIRCULATIONAHA.111.048520

Borbely, A., Falcao-Pires, I., van Heerebeek, L., Hamdani, N., Edes, I., Gavina, C., et al. (2009). Hypophosphorylation of the stiff N2B titin isoform raises cardiomyocyte resting tension in failing human myocardium. *Circ. Res.* 104, 780–786. doi: 10.1161/CIRCRESAHA.108.193326

Borbely, A., van der Velden, J., Papp, Z., Bronzwaer, J. G., Edes, I., Stienen, G. J., et al. (2005). Cardiomyocyte stiffness in diastolic heart failure. *Circulation* 111, 774–781. doi: 10.1161/01.CIR.0000155257.33485.6D

Bossuyt, J., Helmstadter, K., Wu, X., Clements-Jewery, H., Haworth, R. S., Avkiran, M., et al. (2008). Ca2+/calmodulin-dependent protein kinase IIdelta and protein kinase D overexpression reinforce the histone deacetylase 5 redistribution in heart failure. *Circ. Res.* 102, 695–702. doi: 10.1161/CIRCRESAHA.107.169755

Bullard, B., Ferguson, C., Minajeva, A., Leake, M. C., Gautel, M., Labeit, D., et al. (2004). Association of the chaperone alphaB-crystallin with titin in heart muscle. *J. Biol. Chem.* 279, 7917–7924. doi: 10.1074/jbc.M307473200

Cuello, F., Bardswell, S. C., Haworth, R. S., Yin, X., Lutz, S., Wieland, T., et al. (2007). Protein kinase D selectively targets cardiac troponin i and regulates myofilament Ca2+ sensitivity in ventricular myocytes. *Circ. Res.* 100, 864–873. doi: 10.1161/01.RES.0000260809.15393.fa

Dirkx, E., Cazorla, O., Schwenk, R. W., Lorenzen-Schmidt, I., Sadayappan, S., Van Lint, J., et al. (2012). Protein kinase D increases maximal Ca2+-activated tension of cardiomyocyte contraction by phosphorylation of cMyBP-C-Ser315. *Am. J. Physiol. Heart Circ. Physiol.* 303, H323–H331. doi: 10.1152/ajpheart.00749.2011

Dohke, T., Wada, A., Isono, T., Fujii, M., Yamamoto, T., Tsutamoto, T., et al. (2006). Proteomic analysis reveals significant alternations of cardiac small heat shock protein expression in congestive heart failure. *J. Card. Fail.* 12, 77–84. doi: 10.1016/j.cardfail.2005.07.006

Doppler, H., Storz, P., Li, J., Comb, M. J., and Toker, A. (2005). A phosphorylation state-specific antibody recognizes Hsp27, a novel substrate of protein kinase D. *J. Biol. Chem.* 280, 15013–15019. doi: 10.1074/jbc.C400575200

Evans, I. M., Britton, G., and Zachary, I. C. (2008). Vascular endothelial growth factor induces heat shock protein (HSP) 27 serine 82 phosphorylation and endothelial tubulogenesis via protein kinase D and independent of p38 kinase. *Cell. Signal.* 20, 1375–1384. doi: 10.1016/j.cellsig.2008.03.002

Falcao-Pires, I., Hamdani, N., Borbely, A., Gavina, C., Schalkwijk, C. G., van der Velden, J., et al. (2011). Diabetes mellitus worsens diastolic left ventricular dysfunction in aortic stenosis through altered myocardial structure and cardiomyocyte stiffness. *Circulation* 124, 1151–1159. doi: 10.1161/CIRCULATIONAHA.111.025270

Fielitz, J., Kim, M. S., Shelton, J. M., Qi, X., Hill, J. A., Richardson, J. A., et al. (2008). Requirement of protein kinase D1 for pathological cardiac remodeling. *Proc. Natl. Acad. Sci. U.S.A.* 105, 3059–3063. doi: 10.1073/pnas.0712265105.

Franssen, C., Chen, S., Unger, A., Korkmaz, H. I., De Keulenaer, G. W., Tschope, C., et al. (2016). Myocardial microvascular inflammatory endothelial activation in heart failure with preserved ejection fraction. *JACC Heart Fail.* 4, 312–324. doi: 10.1016/j.jchf.2015.10.007

Fukuda, N., Wu, Y., Nair, P., and Granzier, H. L. (2005). Phosphorylation of titin modulates passive stiffness of cardiac muscle in a titin isoform-dependent manner. *J. Gen. Physiol.* 125, 257–271. doi: 10.1085/jgp.200409177

Golenhofen, N., Arbeiter, A., Koob, R., and Drenckhahn, D. (2002). Ischemia-induced association of the stress protein alpha B-crystallin with I-band portion of cardiac titin. *J. Mol. Cell. Cardiol.* 34, 309–319. doi: 10.1006/jmcc.2001.1513

Golenhofen, N., Redel, A., Wawrousek, E. F., and Drenckhahn, D. (2006). Ischemia-induced increase of stiffness of alphaB-crystallin/HSPB2-deficient myocardium. *Pflugers Arch.* 451, 518–525. doi: 10.1007/s00424-005-1488-1

Hamdani, N., Bishu, K. G., von Frieling-Salewsky, M., Redfield, M. M., and Linke, W. A. (2013a). Deranged myofilament phosphorylation and function in experimental heart failure with preserved ejection fraction. *Cardiovasc. Res.* 97, 464–471. doi: 10.1093/cvr/cvs353

Hamdani, N., Hervent, A.-S., Vandekerckhove, L., Matheeussen, V., Demolder, M., Baerts, L., et al. (2014). Left ventricular diastolic dysfunction and myocardial stiffness in diabetic mice is attenuated by inhibition of dipeptidyl peptidase 4. *Cardiovasc. Res.* 104, 423–431. doi: 10.1093/cvr/cvu223

Hamdani, N., Krysiak, J., Kreusser, M. M., Neef, S., Dos Remedios, C. G., Maier, L. S., et al. (2013b). Crucial role for Ca2(+)/calmodulin-dependent protein kinase-II in regulating diastolic stress of normal and failing hearts via titin phosphorylation. *Circ. Res.* 112, 664–674. doi: 10.1161/CIRCRESAHA.111.300105

Harrison, B. C., Kim, M. S., van Rooij, E., Plato, C. F., Papst, P. J., Vega, R. B., et al. (2006). Regulation of cardiac stress signaling by protein kinase d1. *Mol. Cell. Biol.* 26, 3875–3888. doi: 10.1128/MCB.26.10.3875-3888.2006

Haworth, R. S., Cuello, F., Herron, T. J., Franzen, G., Kentish, J. C., Gautel, M., et al. (2004). Protein kinase D is a novel mediator of cardiac troponin i phosphorylation and regulates myofilament function. *Circ. Res.* 95, 1091–1099. doi: 10.1161/01.RES.0000149299.34793.3c

Hayashi, A., Seki, N., Hattori, A., Kozuma, S., and Saito, T. (1999). PKCnu, a new member of the protein kinase C family, composes a fourth subfamily with PKCmu. *Biochim. Biophys. Acta* 1450, 99–106. doi: 10.1016/s0167-4889(99)00040-3

Hidalgo, C., Hudson, B., Bogomolovas, J., Zhu, Y., Anderson, B., Greaser, M., et al. (2009). PKC phosphorylation of titin's PEVK element: a novel and conserved pathway for modulating myocardial stiffness. *Circ. Res.* 105, 631–638. doi: 10.1161/CIRCRESAHA.109.198465

Johannes, F. J., Prestle, J., Eis, S., Oberhagemann, P., and Pfizenmaier, K. (1994). PKCu is a novel, atypical member of the protein kinase C family. *J. Biol. Chem.* 269, 6140–6148

Kadono, T., Zhang, X. Q., Srinivasan, S., Ishida, H., Barry, W. H., and Benjamin, I. J. (2006). CRYAB and HSPB2 deficiency increases myocyte mitochondrial permeability transition and mitochondrial calcium uptake. *J. Mol. Cell. Cardiol.* 40, 783–789. doi: 10.1016/j.yjmcc.2006.03.003

Kim, M. S., Fielitz, J., McAnally, J., Shelton, J. M., Lemon, D. D., McKinsey, T. A., et al. (2008). Protein kinase D1 stimulates MEF2 activity in skeletal muscle and enhances muscle performance. *Mol. Cell. Biol.* 28, 3600–3609. doi: 10.1128/MCB.00189-08

Knowlton, A. A., Kapadia, S., Torre-Amione, G., Durand, J. B., Bies, R., Young, J., et al. (1998). Differential expression of heat shock proteins in normal and failing human hearts. *J. Mol. Cell. Cardiol.* 30, 811–818. doi: 10.1006/jmcc.1998.0646

Kostenko, S., and Moens, U. (2009). Heat shock protein 27 phosphorylation: kinases, phosphatases, functions and pathology. *Cell. Mol. Life Sci.* 66, 3289–3307. doi: 10.1007/s00018-009-0086-3

Kotter, S., Gout, L., Von Frieling-Salewsky, M., Muller, A. E., Helling, S., Marcus, K., et al. (2013). Differential changes in titin domain phosphorylation increase myofilament stiffness in failing human hearts. *Cardiovasc. Res.* 99, 648–656. doi: 10.1093/cvr/cvt144

Kotter, S., Unger, A., Hamdani, N., Lang, P., Vorgerd, M., Nagel-Steger, L., et al. (2014). Human myocytes are protected from titin aggregation-induced stiffening by small heat shock proteins. *J. Cell. Biol.* 204, 187–202. doi: 10.1083/jcb.201306077

Kruger, M., Kotter, S., Grutzner, A., Lang, P., Andresen, C., Redfield, M. M., et al. (2009). Protein kinase G modulates human myocardial passive stiffness by phosphorylation of the titin springs. *Circ. Res.* 104, 87–94. doi: 10.1161/CIRCRESAHA.108.184408

Kruger, M., and Linke, W. A. (2006). Protein kinase-A phosphorylates titin in human heart muscle and reduces myofibrillar passive tension. *J. Muscle Res. Cell Motil.* 27, 435–444. doi: 10.1007/s10974-006-9090-5

Kruger, M., Moser, M., Ussar, S., Thievessen, I., Luber, C. A., Forner, F., et al. (2008). SILAC mouse for quantitative proteomics uncovers kindlin-3 as an essential factor for red blood cell function. *Cell* 134, 353–364. doi: 10.1016/j.cell.2008.05.033

Li, Z., Liu, X., Zhao, Z., and Liu, W. (2012). [Heat shock protein 27 enhances the inhibitory effect of influenza A virus NS1 on the expression of interferon-beta]. *Sheng Wu Gong Cheng Xue Bao* 28, 1205–1215.

Linke, W. A., and Hamdani, N. (2014). Gigantic business: titin properties and function through thick and thin. *Circ. Res.* 114, 1052–1068. doi: 10.1161/CIRCRESAHA.114.301286

Martin, J. L., Mestril, R., Hilal-Dandan, R., Brunton, L. L., and Dillmann, W. H. (1997). Small heat shock proteins and protection against ischemic injury in cardiac myocytes. *Circulation* 96, 4343–4348. doi: 10.1161/01.cir.96.12.4343

Mymrikov, E. V., Seit-Nebi, A. S., and Gusev, N. B. (2011). Large potentials of small heat shock proteins. *Physiol. Rev.* 91, 1123–1159. doi: 10.1152/physrev.00023.2010

Nichols, C. B., Chang, C. W., Ferrero, M., Wood, B. M., Stein, M. L., Ferguson, A. J., et al. (2014). beta-adrenergic signaling inhibits Gq-dependent protein kinase D activation by preventing protein kinase D translocation. *Circ. Res.* 114, 1398–1409. doi: 10.1161/CIRCRESAHA.114.303870

Pinz, I., Robbins, J., Rajasekaran, N. S., Benjamin, I. J., and Ingwall, J. S. (2008). Unmasking different mechanical and energetic roles for the small heat shock proteins CryAB and HSPB2 using genetically modified mouse hearts. *FASEB J.* 22, 84–92. doi: 10.1096/fj.07-8130com

Raskin, A., Lange, S., Banares, K., Lyon, R. C., Zieseniss, A., Lee, L. K., et al. (2012). A novel mechanism involving four-and-a-half LIM domain protein-1 and extracellular signal-regulated kinase-2 regulates titin phosphorylation and mechanics. *J. Biol. Chem.* 287, 29273–29284. doi: 10.1074/jbc.M112.372839

Sin, Y. Y., and Baillie, G. S. (2012). Protein kinase D in the hypertrophy pathway. *Biochem. Soc. Trans.* 40, 287–289. doi: 10.1042/BST20110626

Stetler, R. A., Gao, Y., Zhang, L., Weng, Z., Zhang, F., Hu, X., et al. (2012). Phosphorylation of HSP27 by protein kinase D is essential for mediating neuroprotection against ischemic neuronal injury. *J. Neurosci.* 32, 2667–2682. doi: 10.1523/JNEUROSCI.5169-11.2012

Sturany, S., van Lint, J., Muller, F., Wilda, M., Hameister, H., Hocker, M., et al. (2001). Molecular cloning and characterization of the human protein kinase D2. a novel member of the protein kinase D family of serine threonine kinases. *J. Biol. Chem.* 276, 3310–3318. doi: 10.1074/jbc.M008719200

Valverde, A. M., Sinnett-Smith, J., Van Lint, J., and Rozengurt, E. (1994). Molecular cloning and characterization of protein kinase D: a target for diacylglycerol and phorbol esters with a distinctive catalytic domain. *Proc. Natl. Acad. Sci. U.S.A.* 91, 8572–8576. doi: 10.1073/pnas.91.18.8572

van Heerebeek, L., Hamdani, N., Falcao-Pires, I., Leite-Moreira, A. F., Begieneman, M. P., Bronzwaer, J. G., et al. (2012). Low myocardial protein kinase G activity in heart failure with preserved ejection fraction. *Circulation* 126, 830–839. doi: 10.1161/CIRCULATIONAHA.111.076075

Van Lint, J. V., Sinnett-Smith, J., and Rozengurt, E. (1995). Expression and characterization of PKD, a phorbol ester and diacylglycerol-stimulated serine protein kinase. *J. Biol. Chem.* 270, 1455–1461. doi: 10.1074/jbc.270.3.1455

Vega, R. B., Harrison, B. C., Meadows, E., Roberts, C. R., Papst, P. J., Olson, E. N., et al. (2004). Protein kinases C and D mediate agonist-dependent cardiac hypertrophy through nuclear export of histone deacetylase 5. *Mol. Cell. Biol.* 24, 8374–8385. doi: 10.1128/MCB.24.19.8374-8385.2004

Yamasaki, R., Wu, Y., McNabb, M., Greaser, M., Labeit, S., and Granzier, H. (2002). Protein kinase A phosphorylates titin's cardiac-specific N2B domain and reduces passive tension in rat cardiac myocytes. *Circ. Res.* 90, 1181–1188. doi: 10.1161/01.res.0000021115.24712.99

Yoshida, N., Kristiansen, A., and Liberman, M. C. (1999). Heat stress and protection from permanent acoustic injury in mice. *J. Neurosci.* 19, 10116–10124.

Yuan, J., and Rozengurt, E. (2008). PKD, PKD2, and p38 MAPK mediate Hsp27 serine-82 phosphorylation induced by neurotensin in pancreatic cancer PANC-1 cells. *J. Cell. Biochem.* 103, 648–662. doi: 10.1002/jcb.21439

Zhao, D., Gao, Y., Wang, W., Pei, H., Xu, C., Zhao, Z. (2019). PKD deletion promotes autophagy and inhibits hypertrophy in cardiomyocyte. *Exp. Cell Res.* 386:111742. doi: 10.1016/j.yexcr.2019.111742

Zhao, D., Wang, W., Wang, H., Peng, H., Liu, X., Guo, W., et al. (2017). PKD knockdown inhibits pressure overload-induced cardiac hypertrophy by promoting autophagy via AKT/mTOR pathway. *Int. J. Biol. Sci.* 13, 276–285. doi: 10.7150/ijbs.17617

Conflict of Interest: SH was employed by the company Sanofi-Aventis Deutschland GmbH Industriepark Höchst.

The remaining authors declare that the research was conducted in the absence of any commercial or financial relationships that could be construed as a potential conflict of interest.

frontiers in Physiology

MINI REVIEW
published: 16 April 2020
doi: 10.3389/fphys.2020.00278

Thermal Activation of Thin Filaments in Striated Muscle

Shuya Ishii[1,2†], Kotaro Oyama[2,3†], Seine A. Shintani[4], Fuyu Kobirumaki-Shimozawa[1], Shin'ichi Ishiwata[5] and Norio Fukuda[1*]*

[1] Department of Cell Physiology, The Jikei University School of Medicine, Tokyo, Japan, [2] Quantum Beam Science Research Directorate, National Institutes for Quantum and Radiological Science and Technology, Gunma, Japan, [3] PRESTO, Japan Science and Technology Agency, Saitama, Japan, [4] Department of Biomedical Sciences, College of Life and Health Sciences, Chubu University, Kasugai, Japan, [5] Department of Physics, Faculty of Science and Engineering, Waseda University, Tokyo, Japan

In skeletal and cardiac muscles, contraction is triggered by an increase in the intracellular Ca^{2+} concentration. During Ca^{2+} transients, Ca^{2+}-binding to troponin C shifts the "*on–off*" equilibrium of the thin filament state toward the "*on*" sate, promoting actomyosin interaction. Likewise, recent studies have revealed that the thin filament state is under the influence of temperature; *viz.*, an increase in temperature increases active force production. In this short review, we discuss the effects of temperature on the contractile performance of mammalian striated muscle at/around body temperature, focusing especially on the temperature-dependent shift of the "*on–off*" equilibrium of the thin filament state.

Keywords: actomyosin, Ca^{2+} sensitivity, cardiac muscle, skeletal muscle, temperature, tropomyosin, troponin

OPEN ACCESS

Edited by:
Jose Renato Pinto, Florida State University, United States

Reviewed by:
Henry G. Zot, University of West Georgia, United States
Kristina Bezold Kooiker, University of Washington, United States
Maria Papadaki, Loyola University Chicago, United States

****Correspondence:***
Kotaro Oyama
oyama.kotaro@qst.go.jp
Norio Fukuda
noriof@jikei.ac.jp

† These authors have contributed equally to this work

Specialty section:
This article was submitted to Striated Muscle Physiology, a section of the journal Frontiers in Physiology

Received: *16 January 2020*
Accepted: *12 March 2020*
Published: *16 April 2020*

Citation:
Ishii S, Oyama K, Shintani SA, Kobirumaki-Shimozawa F, Ishiwata S and Fukuda N (2020) Thermal Activation of Thin Filaments in Striated Muscle. Front. Physiol. 11:278. doi: 10.3389/fphys.2020.00278

INTRODUCTION

Under physiological conditions, striated muscle generates force and heat. Skeletal muscle plays a critical role in maintaining body temperature which increases during exercise. Human body temperature is maintained at ∼37 ± 1°C throughout the day (Refinetti, 2010; Geneva et al., 2019). In humans, body temperature rises to ∼39°C during exercise (Saltin et al., 1968) and exceeds ∼40°C during heat-related illnesses (e.g., heat stroke and malignant hyperthermia) (Glazer, 2005; Rosenberg et al., 2015). Physiologists have long perceived that a change in body temperature affects the mechanical properties of skeletal and cardiac muscles, such as active force generation and shortening velocity. However, the molecular mechanisms are yet to be fully understood, due, primarily, to the fact that sarcomere proteins have varying degrees of temperature sensitivity. Here, we briefly review the effects of temperature on the mechanical properties of skeletal and cardiac muscles in the range between ∼36 and ∼40°C, and discuss how striated muscle works efficiently at/around body temperature.

EXCITATION–CONTRACTION COUPLING

Contraction of skeletal and cardiac muscles is initiated by depolarization of the sarcolemmal membrane. In skeletal muscle, sarcolemmal depolarization directly triggers the release of Ca^{2+} from the sarcoplasmic reticulum (SR) via ryanodine receptors; however, in cardiac muscle, it is

Abbreviations: $[Ca^{2+}]_i$, intracellular Ca^{2+} concentration; RCC, rapid cooling contracture; SPOC, spontaneous sarcomeric auto-oscillations; SR, sarcoplasmic reticulum; Tm, tropomyosin; Tn, troponin.

the Ca^{2+} entry from the extracellular fluid through voltage-dependent L-type Ca^{2+} channels that triggers the Ca^{2+} release, a mechanism known as Ca^{2+}-induced Ca^{2+} release (Bers, 2002; Endo, 2009). In both skeletal and cardiac muscles, an increase in the intracellular Ca^{2+}concentration ($[Ca^{2+}]_i$) promotes Ca^{2+} binding to troponin C (TnC) on thin filaments (Fukuda et al., 2009; Kobirumaki-Shimozawa et al., 2014). Unlike in skeletal muscle, cardiac myofilaments are not fully activated under physiological conditions because $[Ca^{2+}]_i$ is maintained relatively low ($\sim 10^{-6}$ M), even at the peak of systole (Bers, 2002). Because of this partial activation nature, cardiac myofilaments exhibit non-linear properties, such as length-dependent activation (Kobirumaki-Shimozawa et al., 2014) and spontaneous sarcomeric auto-oscillations (SPOC) (see Ishiwata et al., 2011; Kagemoto et al., 2018). In both skeletal and cardiac muscles, lowering $[Ca^{2+}]_i$ dissociates Ca^{2+} from TnC, resulting in dissociation of myosin from thin filaments, i.e., relaxation.

Ca^{2+}-DEPENDENT ACTIVATION OF THIN FILAMENTS

Ca^{2+}-activated muscle contraction is mediated by regulatory proteins, i.e., troponin (Tn) and tropomyosin (Tm), which form a complex on actin filaments. At rest, the Tn–Tm complex prevents/weakens actomyosin interaction. At this "*off*" state, the carboxyl-terminal domain of TnI strongly binds to actin, and Tm blocks myosin binding to actin and/or force production of bound myosin. When $[Ca^{2+}]_i$ is increased, Ca^{2+}-bound TnC interacts with TnI, and the carboxyl-terminal domain of TnI is dissociated from actin. The Tn conformational changes result in displacement of Tm on actin, which subsequently induces myosin binding to actin and force generation (e.g., Haselgrove, 1973; Huxley, 1973; Lehman et al., 1994; Vibert et al., 1997; Xu et al., 1999; Fukuda et al., 2009; Risi et al., 2017; Matusovsky et al., 2019). It has been reported that during the shift of the thin filament state from "*off*" to "*on*," strongly bound myosin cooperatively enhances binding of neighboring myosin molecules that have ATP and thereby potentially produce force (Greene and Eisenberg, 1980; Trybus and Taylor, 1980).

MODULATION OF MYOFIBRILLAR Ca^{2+} SENSITIVITY

The "*on–off*" equilibrium of the thin filament state is most typically reflected as Ca^{2+} sensitivity of active force development in skinned fibers. The parameter pCa_{50} ($= -\log[Ca^{2+}]$) (required for half-maximal Ca^{2+}-activated force) is widely used to express Ca^{2+} sensitivity; an increase in the pCa_{50} value indicates an increase in Ca^{2+} sensitivity and *vice versa*. Ca^{2+} sensitivity is influenced by various factors, such as the intracellular concentrations of Mg^{2+} (Fabiato and Fabiato, 1975; Best et al., 1977; Donaldson et al., 1978), MgATP (Fabiato and Fabiato, 1975; Best et al., 1977), MgADP (Fukuda et al., 1998, 2000) and inorganic phosphate (Kentish, 1986; Millar and Homsher, 1990; Fukuda et al., 1998, 2001), and ionic strength (Kentish, 1984; Fink et al., 1986) and pH (Fabiato and Fabiato, 1978; Orchard and Kentish, 1990; Fukuda and Ishiwata, 1999; Fukuda et al., 2001). Ca^{2+} sensitivity is likewise under the influence of phosphorylation/dephosphorylation of thick or thin filament proteins. Most importantly, protein kinase A, activated upon β-adrenergic stimulation in cardiac muscle, phosphorylates TnI, resulting in a decrease in Ca^{2+} sensitivity via weakening of the TnI–TnC interaction (see Solaro and Rarick, 1998 for details). Likewise, other translational modifications such as glycation (Papadaki et al., 2018) and acetylation (Gupta et al., 2008) may affect Ca^{2+} sensitivity.

EFFECTS OF TEMPERATURE ON THE MECHANICAL PROPERTIES OF CARDIAC MUSCLE

A rapid decrease in solution temperature generates contraction in intact cardiac muscle [rapid cooling contracture (RCC): see Kurihara and Sakai, 1985; Bridge, 1986]. The mechanism of RCC can be explained as follows: upon lowering of the solution temperature, Ca^{2+} is released from the SR via ryanodine receptors (Protasi et al., 2004), causing contraction in a Ca^{2+}-dependent manner. Chronic cooling also enhances contraction in intact cardiac muscle under varying experimental conditions (hypothermic inotropy) (Shattock and Bers, 1987; Puglisi et al., 1996; Mikane et al., 1999; Janssen et al., 2002; Hiranandani et al., 2006; Shutt and Howlett, 2008; Obata et al., 2018) (see **Figure 1A** and **Table 1** for effects of alteration of temperature on striated muscle properties). For instance, Shattock and Bers (1987) reported that cooling from 37 to 25°C increases twitch force greater than approximately ∼fivefold in "intact" rabbit and rat ventricular muscle. However, cooling from 36 to 29°C *decreases* maximal Ca^{2+}-activated force in "skinned" rabbit ventricular muscle, coupled presumably with depressed actomyosin ATPase activity, with no significant change in Ca^{2+} sensitivity (Harrison and Bers, 1989) (cooling to 22°C decreases both force production and Ca^{2+} sensitivity, see **Table 1**). We, therefore, consider that hypothermic inotropy is caused by the positive effect of cooling on $[Ca^{2+}]_i$ minus its negative effect on myofibrils: *viz.*, cooling increases the amplitude of the intracellular Ca^{2+} transients and prolongs the duration of the amplitude (i.e., longer time to peak $[Ca^{2+}]_i$ and slower $[Ca^{2+}]_i$ decline) (Puglisi et al., 1996; Janssen et al., 2002; Shutt and Howlett, 2008), hence, augmenting contractility in a Ca^{2+}-dependent manner, by a magnitude greater than the decrease at the myofibrillar level.

In contrast, an increase in temperature to ∼40–42°C has been reported to decrease end-systolic pressure in canine (Mikane et al., 1999; Saeki et al., 2000) and rat (Obata et al., 2018) hearts. The findings of these studies were confirmed by a study using rat ventricular trabeculae where twitch force was decreased by ∼30% accompanied by an increase in temperature from 37 to 42°C (Hiranandani et al., 2006). The mechanisms of hyperthermic negative inotropy are yet to be clarified; however, a decrease in the peak or duration time of Ca^{2+} transients is likely to underlie the inhibited active force production.

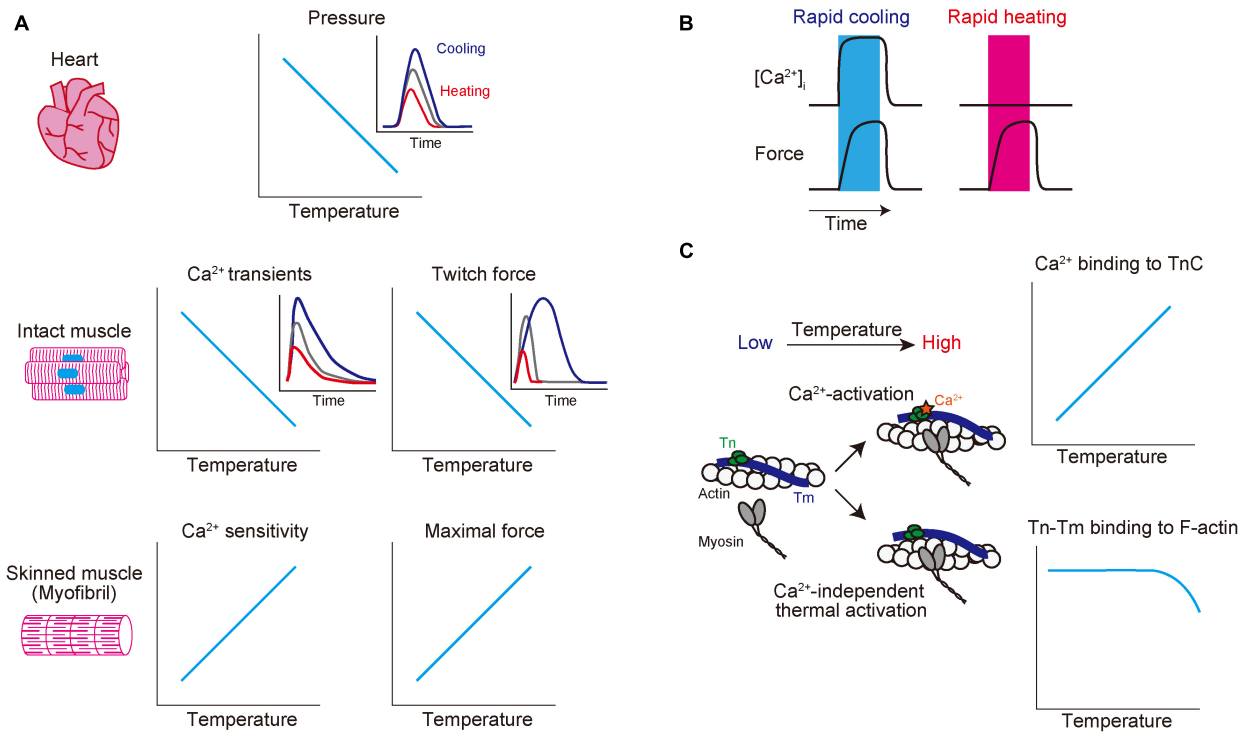

FIGURE 1 | Schematic showing the effects of altered temperature on functional properties of mammalian striated muscle. **(A)** Top: relationship of temperature vs. endo-systolic pressure in mammalian hearts. Inset: time-course of ventricular pressure at different temperatures. Blue, gray, and red lines indicate hypothermic, physiological, and hyperthermic conditions, respectively. Middle: relationship of temperature vs. Ca^{2+} transients (left) and twitch force (right) in intact muscles. Blue, gray, and red lines indicate hypothermic, physiological, and hyperthermic conditions, respectively. Bottom: relationship of temperature vs. Ca^{2+} sensitivity (left) and maximal force (right) in skinned muscles. **(B)** Effects of rapid cooling (left; shown in blue bar) or rapid heating (right; shown in red bar) on $[Ca^{2+}]_i$ (top) and force (bottom) in intact cardiomyocytes. Rapid cooling increases both $[Ca^{2+}]_i$ and force, while rapid heating increases force with little or no influence on $[Ca^{2+}]_i$. **(C)** Effects of a change in temperature on thin filaments. Increasing temperature 1) enhances Ca^{2+} binding to TnC (see top graph) and 2) induces Ca^{2+}-independent thermal activation of thin filaments via partial dissociation of the Tn–Tm complex from actin (see bottom graph), thereby coordinately acting to increase the fraction of the "*on*" state of thin filaments. See text for details.

HEATING-INDUCED CONTRACTION IN RESTING MUSCLE

Physiologists have realized for nearly a century that despite being under resting conditions, the warming of muscles increases active force, known as "heat contraction" or "heat rigor". For instance, Vernon (1899) investigated heat contraction in cardiac and skeletal muscles that had been obtained from 18 species of cold-blooded animals. Likewise, Hill (1970) reported in frog sartorius muscle that resting tension is increased in a linear fashion with increasing temperature from 0 to 23°C and more steeply in the higher temperature range. Later, using intact and skinned rabbit skeletal muscle fibers, Ranatunga (1994) confirmed Hill's finding that resting force is increased in a linear fashion in the low temperature range, i.e., <∼25°C and more sharply increased in the higher temperature range (30–40°C).

Recently, we demonstrated that rapid and repetitive heating via infrared laser irradiation (0.2 s at 2.5 Hz) induces transient and reversible shortening in isolated intact rat ventricular myocytes (Oyama et al., 2012). In this previous study, at the baseline temperature of 36°C, the magnitude of the rise in temperature to induce myocyte shortening was ∼5°C. It is important that this temperature-dependent contraction occurs in a Ca^{2+}-independent manner, and instead, it is regulated at the sarcomere level. Indeed, intracellular Ca^{2+} imaging with fluo-4 revealed little or no increase in $[Ca^{2+}]_i$ upon infrared laser irradiation, and heating-induced contraction was blocked by the myosin II inhibitor blebbistatin. A similar phenomenon was observed in C2C12 myotubes (from mouse) when temperature was increased from 36.5 to 41.5°C using gold nanoshells in combination with near-infrared laser irradiation (Marino et al., 2017). These studies using differing preparations indicate that a rise in temperature from physiological ∼37 to ∼40°C directly activates sarcomeres in a Ca^{2+}-independent fashion (**Figures 1B,C**).

THERMAL ACTIVATION OF THIN FILAMENTS

The characteristics of heating-induced contraction are consistent with the notion that Ca^{2+} sensitivity is increased with increasing temperature above 37°C (e.g., Ranatunga, 1994; Oyama et al., 2012). Mühlrad and Hegyi (1965) reported that increasing

TABLE 1 | Effects of alteration of temperature on functional properties of mammalian striated muscles.

Preparation	Parameter	Temperature change (°C)	Change in parameter value	Direction, change in parameter value	References
Canine heart (isolated)	Systolic pressure (mmHg)	35.9→30.7 35.9→39.8	69.4→102.0* 69.4→44.8*	Increase Decrease	Mikane et al., 1999
Canine heart (isolated)	Systolic pressure (mmHg)	36.3→41	125.1→80.5***	Decrease	Saeki et al., 2000
Rat heart (isolated)	Systolic pressure (mmHg)	37→32 37→42	103.4→134.6* 103.4→76.0*	Increase Decrease	Obata et al., 2018
Guinea pig cardiac muscle	Force	36.5→17	–	Increase	Kurihara and Sakai, 1985
Rabbit cardiac muscle	Force	30→1	–	Increase	Bridge, 1986
Rabbit cardiac muscle	Twitch force	37→25	–	Increase	Shattock and Bers, 1987
Rat cardiac muscle	Twitch force	37→25	–	Increase	Shattock and Bers, 1987
Rat cardiac muscle	Twitch force (mN/mm^2)	37.5→30	30→86	Increase	Janssen et al., 2002
Rat cardiac muscle	Twitch force (%, normalized at 37°C)	37→32 37→42	– 100→67.2	Increase Decrease	Hiranandani et al., 2006
Rabbit cardiac muscle	Twitch shortening (%)	35→25	7.6→13.1**	Increase	Puglisi et al., 1996
Ferret cardiac muscle	Twitch shortening (%)	35→25	2.9→4.9*	Increase	Puglisi et al., 1996
Cat cardiac muscle	Twitch shortening (%)	35→25	10.8→6.0*	Decrease	Puglisi et al., 1996
Guinea pig cardiac muscle	Twitch shortening (%)	37→22	2.6→8.3*	Increase	Shutt and Howlett, 2008
Rabbit cardiac muscle (skinned)	Maximal force (%, normalized at 22°C)	36→29 36→22	118.5→108* 118.5→100**	Decrease Decrease	Harrison and Bers, 1989
Rat skeletal fiber	Resting force (intact) Resting force (skinned)	30→40 30→40	– –	Increase Increase	Ranatunga, 1994
Rat cardiac muscle	Shortening	36→41	–	Increase	Oyama et al., 2012
C2C12 myotube	Shortening (%)	36.5→41.5	0→2.4*	Increase	Marino et al., 2017
Rabbit cardiac muscle	Ca^{2+} transient amplitude (nM)	35→25	248→454**	Increase	Puglisi et al., 1996
Rat cardiac muscle	Ca^{2+} transient amplitude (μM)	37.5→30	0.73→1.33	Increase	Janssen et al., 2002
Guinea pig cardiac muscle	Ca^{2+} transient amplitude (nM)	37→22	35→157*	Increase	Shutt and Howlett, 2008
Actin (RS) + Tm (HC) + Tn (HC) + HMM (RS)	Sliding velocity at pCa 5 Sliding velocity at pCa 9 Sliding velocity at pCa 9	∼20→∼60 ∼20→∼43 ∼43→∼60	– – –	Increase No change Increase	Brunet et al., 2012
Actin (RS) + Tm (HC) + Tn (BC) + HMM (RS)	Sliding velocity at pCa 5 (μm/s) Sliding velocity at pCa 9 (μm/s)	25→41.0 25→40.8	6.4→17.9 0→14.5	Increase Increase	Ishii et al., 2019
Actin (RS) + Tm (HC) + Tn (BC) + HMM (BC)	Sliding velocity at pCa 5 (μm/s) Sliding velocity at pCa 9 (μm/s)	24→40.0 24→39.9	1.19→8.89 0→3.37	Increase Increase	Ishii et al., 2019
Rabbit cardiac muscle (skinned)	pCa_{50} (active force)	36→29 36→22	5.473→5.494 (NS) 5.473→5.340**	No change Decrease	Harrison and Bers, 1989
Rabbit skeletal myofibril	pCa_{50} (ATPase)	30→37	7.05→7.52	Increase	Mühlrad and Hegyi, 1965
Rabbit skeletal myofibril	pCa_{50} (ATPase)	30→40	–	Increase	Murphy and Hasselbach, 1968
TnC (BC)	pCa_{50} (Ca^{2+} binding)	21→37	5.29→5.42*	Increase	Gillis et al., 2000
TnC (HC)	pCa_{50} (Ca^{2+} binding)	30→45	5.04→5.17	Increase	Veltri et al., 2017

*Data obtained under various experimental conditions are summarized. Sliding velocity was obtained in the in vitro motility assay with reconstituted thin filaments (actin plus Tn–Tm). BC, bovine cardiac; HC, human cardiac; HMM, heavy meromyosin; RS, rabbit skeletal. *P < 0.05; **P < 0.01; ***P < 0.001. NS, not significant.*

temperature in the range of 0–37°C reduces [Ca^{2+}] for half-maximal and maximal ATPase activity in rabbit skeletal myofibrils. Warming to ∼40°C further reduces [Ca^{2+}] for half-maximal ATPase activity in rabbit skeletal myofibrils (i.e., increased Ca^{2+} sensitivity) (see Murphy and Hasselbach, 1968), and interestingly, the Ca^{2+} sensitivity is lost at ∼50°C (Hartshorne et al., 1972).

By taking advantage of the *in vitro* motility assay, recent studies confirmed heating-induced activation of thin filaments by measuring the sliding velocity of reconstituted thin filaments. Brunet et al. (2012) analyzed sliding movements of thin filaments that had been reconstituted with human cTn and Tm at temperatures above ∼43°C under relaxing conditions in the absence of Ca^{2+} (+EGTA). We performed a rapid-heating experiment using infrared laser irradiation and found that thin filaments that had been reconstituted with bovine cTn and human Tm exhibited sliding movements at >∼35°C in the absence of Ca^{2+} (Ishii et al., 2019). Because the sliding velocity was ∼30% at 37°C compared to the maximum, this previous finding suggests that thin filaments are partially activated in diastole at physiological body temperature, enabling rapid and efficient myocardial dynamics in systole (see Ishii et al., 2019 for details).

The molecular mechanisms of thermal activation of thin filaments are yet to be fully understood. One possible mechanism is "partial dissociation" of Tn–Tm from F-actin upon increasing

temperature (as discussed in Oyama et al., 2012; Ishii et al., 2019); *viz.*, Tanaka and Oosawa (1971) demonstrated that Tm dissociates from F-actin at >∼40°C. Later experiments by Ishiwata (1978) on reconstituted thin filaments (F-actin plus Tn–Tm) showed that Tn–Tm starts to partially dissociate from F-actin at ∼41°C, with dissociation temperatures of 48.8 and 47.0°C in the absence and presence of Ca^{2+}, respectively.

While in older studies the structural changes in thin filaments were unable to be detected, newer studies suggest that heating-induced Ca^{2+}-independent contraction may result not only from partial dissociation of Tm or Tn–Tm from F-actin but also from structural changes in Tn, Tm, or both. Consistent with this view, Kremneva et al. (2003) reported that thermal unfolding occurs in Tm in reconstituted thin filaments comprised of F-actin and Tn–Tm. They found that a low-temperature transition reflecting the denaturation of the C-terminus of Tm started to occur at ∼40°C in the presence of 1 mM EGTA (hence under the relaxing condition). Likewise, it has previously been reported that instability of the coiled-coil structure of Tm is essential for optimal interaction with actin (Singh and Hitchcock-DeGregori, 2009). It is therefore likely that the unfolding of Tm may promote the shift of the thin filament state from the "*off*" state to the "*on*" state and thereby gives rise to, at least in part, heating-induced contraction.

It is likewise known that the Ca^{2+}-binding affinity of TnC is increased with temperature. For instance, Gillis et al. (2000) reported that the Ca^{2+}-binding affinity of bovine cardiac TnC is increased with temperature within the range between 7 and 37°C. The affinity of human cardiac TnC for Ca^{2+} also increases with temperature within the range between 21 and 45°C (Veltri et al., 2017). It should be noted that the temperature sensitivity of TnC for Ca^{2+} is isoform dependent. For instance, Harrison and Bers (1990) reported that the cooling-induced decrease in Ca^{2+} sensitivity is attenuated after reconstitution with skeletal TnC in skinned rat ventricular muscle.

POSSIBLE USE OF LOCAL HEATING FOR THE TREATMENT OF DILATED CARDIOMYOPATHY

Accumulating evidence shows that mutations in sarcomere proteins, including Tn subunits (TnT, TnI, and TnC) and Tm, modulate Ca^{2+} sensitivity and thereby promote the pathogenesis of DCM or HCM (Ohtsuki and Morimoto, 2008). A general consensus has been achieved in that myofibril Ca^{2+} sensitivity is decreased by DCM mutations and increased by HCM mutations (Ohtsuki and Morimoto, 2008; Kobirumaki-Shimozawa et al., 2014). Because an increase in temperature enables sarcomeric contraction in a Ca^{2+}-independent manner (Oyama et al., 2012), local heating, such as via infrared laser irradiation, may have a potential to augment contractility in patients with DCM without causing the intracellular Ca^{2+}overload that can cause fatal arrhythmias. In order to avoid hyperthermal negative inotropy, local heating targeting myofibrils, but not global heating, is essential to augment contractility of myocardium in the heart. For instance, Marino et al. (2017) demonstrated gold nanoshell-mediated remote activation of myotubes via near-infrared laser irradiation, which does not cause a change in $[Ca^{2+}]_i$. Likewise, heating of nanoparticles by the magnetic field may be useful to increase temperature of the myocardium in various layers from the epicardium to the endocardium of the heart *in vivo* (as demonstrated by Chen et al., 2015 for deep brain stimulation).

It is worthwhile noting that in previous studies discussed, thus far, different mammals were used that have different body temperatures (cf. **Table 1**), thus, future studies using human samples need to be conducted under various experimental conditions to systematically investigate how alteration of temperature affects the function of the heart in humans.

CONCLUSION

In striated muscle, sarcolemmal depolarization causes an increase in $[Ca^{2+}]_i$. The Ca^{2+}-dependent structural changes of thin filaments allow for myosin binding to actin and thereby facilitate active force production. Cooling increases the contractility of striated muscle via Ca^{2+}-dependent activation: first, a rapid decrease in temperature triggers a release of Ca^{2+} from the SR, and second, long-term cooling increases the amplitude as well as the period of intracellular Ca^{2+} transients. Contrary to these cooling effects, heating increases myofibrillar active force (and ATPase activity) and Ca^{2+} sensitivity; the latter is coupled with an increase in the affinity of TnC for Ca^{2+}. Moreover, heating induces structural changes of thin filaments (i.e., partial dissociation of the Tn–Tm complex from F-actin), thereby shifting the "*on–off*" equilibrium of the thin filament state toward the "*on*" state at a given $[Ca^{2+}]_i$ (Ca^{2+}-independent activation). The characteristics of heating-induced, Ca^{2+}-independent activation may be useful to augment the heart's contractility in patients with DCM in future clinical settings.

AUTHOR CONTRIBUTIONS

SIs, KO, and NF wrote the first version of the manuscript. SS, FK-S, and S'Is contributed comments and suggestions. All authors approved the final version of the manuscript.

FUNDING

This study was supported by PRESTO, Japan Science and Technology Agency (to KO: JPMJPR17P3), Ministry of Education, Culture, Sports, Science and Technology of Japan Grant-in-Aid for Scientific Research (C) (to FK-S: JP18K06878), Grant-in-Aid for Young Scientists (B) (to SS: 17K15102), Quantum Leap Flagship Program (Q-LEAP; to SIs: JPMXS 0118067395), the Naito Foundation (to FK-S), and Japan Heart Foundation Dr. Hiroshi Irisawa and Dr. Aya Irisawa Memorial Research Grant (to FK-S).

REFERENCES

Bers, D. M. (2002). Cardiac excitation-contraction coupling. *Nature* 415, 198–205. doi: 10.1038/415198a

Best, P. M., Donaldson, S. K., and Kerrick, W. G. L. (1977). Tension in mechanically disrupted mammalian cardiac cells: effects of magnesium adenosine triphosphate. *J. Physiol.* 256, 1–17. doi: 10.1113/jphysiol.1977.sp011702

Bridge, J. H. B. (1986). Relationships between the sarcoplasmic reticulum and sarcolemmal calcium transport revealed by rapidly cooling rabbit ventricular muscle. *J. Gen. Physiol.* 88, 437–473. doi: 10.1085/jgp.88.4.437

Brunet, N. M., Mihajloviæ, G., Aledealat, K., Wang, F., Xiong, P., von Molnár, S., et al. (2012). Micromechanical thermal assays of Ca^{2+}-regulated thin-filament function and modulation by hypertrophic cardiomyopathy mutants of human cardiac troponin. *J. Biomed. Biotechnol.* 2012:657523. doi: 10.1155/2012/657523

Chen, R., Romero, G., Christiansen, M. G., Mohr, A., and Anikeeva, P. (2015). Wireless magnetothermal deep brain stimulation. *Science* 347, 1477–1480. doi: 10.1126/science.1261821

Donaldson, S. K., Best, P. M., and Kerrick, G. L. (1978). Characterization of the effects of Mg^{2+} on Ca^{2+}- and Sr^{2+}-activated tension generation of skinned rat cardiac fibers. *J. Gen. Physiol.* 71, 645–655. doi: 10.1085/jgp.71.6.645

Endo, M. (2009). Calcium-induced calcium release in skeletal muscle. *Physiol. Rev.* 89, 1153–1176. doi: 10.1152/physrev.00040.2008

Fabiato, A., and Fabiato, F. (1975). Contractions induced by a calcium-triggered release of calcium from the sarcoplasmic reticulum of single skinned cardiac cells. *J. Physiol.* 249, 469–495. doi: 10.1113/jphysiol.1975.sp011026

Fabiato, A., and Fabiato, F. (1978). Effects of pH on the myofilaments and the sarcoplasmic reticulum of skinned cells from cardiace and skeletal muscles. *J. Physiol.* 276, 233–255. doi: 10.1113/jphysiol.1978.sp012231

Fink, R. H. A., Stephenson, D. G., and Williams, D. A. (1986). Potassium and ionic strength effects on the isometric force of skinned twitch muscle fibres of the rat and toad. *J. Physiol.* 370, 317–337. doi: 10.1113/jphysiol.1986.sp015937

Fukuda, N., Fujita, H., Fujita, T., and Ishiwata, S. (1998). Regulatory roles of MgADP and calcium in tension development of skinned cardiac muscle.J. *Muscle Res. Cell.Motil.* 19, 909–921. doi: 10.1023/a:1005437517287

Fukuda, N., and Ishiwata, S. (1999). Effects of pH on spontaneous tension oscillation in skinned bovine cardiac muscle. *Pflügers Arch.* 438, 125–132. doi: 10.1007/s004240050889

Fukuda, N., Kajiwara, H., Ishiwata, S., and Kurihara, S. (2000). Effects of MgADP on length dependence of tension generation in skinned rat cardiac muscle. *Circ. Res.* 86, E1–E6. doi: 10.1161/01.res.86.1.e1

Fukuda, N., O-Uchi, J., Sasaki, D., Kajiwara, H., Ishiwata, S., and Kurihara, S. (2001). Acidosis or inorganic phosphate enhances the length dependence of tension in rat skinned cardiac muscle. *J. Physiol.* 536, 153–160. doi: 10.1111/j.1469-7793.2001.00153.x

Fukuda, N., Terui, T., Ohtsuki, I., Ishiwata, S., and Kurihara, S. (2009). Titin and troponin: central players in the frank-starling mechanism of the heart. *Curr. Cardiol. Rev.* 5, 119–124. doi: 10.2174/157340309788166714

Geneva, I. I., Cuzzo, B., Fazili, T., and Javaid, W. (2019). Normal body temperature: A systematic review. *Open Forum Infect. Dis.* 6, 1–7. doi: 10.1093/ofid/ofz032

Gillis, T. E., Marshall, C. R., Xue, X. H., Borgford, T. J., and Tibbits, G. F. (2000). Ca^{2+} binding to cardiac troponin C: effects of temperature and pH on mammalian and salmonid isoforms. *Am. J. Physiol. Regul. Integr. Comp. Physiol.* 279, R1707–R1715. doi: 10.1152/ajpregu.2000.279.5.R1707

Glazer, J. L. (2005). Management of heatstroke and heat exhaustion. *Am. Fam. Physician* 71, 2133–2142.

Greene, L. E., and Eisenberg, E. (1980). Cooperative binding of myosin subfragment-1 to the actin-troponin-tropomyosin complex. *Proc. Natl. Acad. Sci. U.S.A.* 77, 2616–2620. doi: 10.1073/pnas.77.5.2616

Gupta, M. P., Samant, S. A., Smith, S. H., and Shroff, S. G. (2008). HDAC4 and PCAF bind to cardiac sarcomeres and play a role in regulating myofilament contractile activity. *J. Biol. Chem.* 283, 10135–10146. doi: 10.1074/jbc.M710277200

Harrison, S. M., and Bers, D. M. (1989). Influence of temperature on the calcium sensitivity of the myofilaments of skinned ventricular muscle from the rabbit. *J. Gen. Physiol.* 93, 411–428. doi: 10.1085/jgp.93.3.411

Harrison, S. M., and Bers, D. M. (1990). Modification of temperature dependence of myofilament Ca sensitivity by troponin C replacement. *Am. J. Physiol.* 258, C282–C288. doi: 10.1152/ajpcell.1990.258.2.C282

Hartshorne, D. J., Barns, E. M., Parker, L., and Fuchs, F. (1972). The effect of temperature on actomyosin. *Biochim. Biophys. Acta* 267, 190–202. doi: 10.1016/0005-2728(72)90150-8

Haselgrove, J. C. (1973). X-ray evidence for conformational changes in the myosin filaments of vertebrate striated muscle. *Cold Spring Harb. Symp. Quant. Biol.* 37, 341–352. doi: 10.1016/0022-2836(75)90094-7

Hill, D. K. (1970). The effect of temperature on the resting tension of frog's muscle in hypertonic solutions. *J. Physiol.* 208, 741–756. doi: 10.1113/jphysiol.1970.sp009146

Hiranandani, N., Varian, K. D., Monasky, M. M., and Janssen, P. M. L. (2006). Frequency-dependent contractile response of isolated cardiac trabeculae under hypo-, normo-, and hyperthermic conditions. *J. Appl. Physiol.* 100, 1727–1732. doi: 10.1152/japplphysiol.01244.2005

Huxley, H. E. (1973). Structural changes in the actin- and myosin-containing filaments during contraction. *Cold Spring Harb. Symp. Quant. Biol.* 37, 361–376. doi: 10.1101/sqb.1973.037.01.046

Ishii, S., Oyama, K., Arai, T., Itoh, H., Shintani, S. A., Suzuki, M., et al. (2019). Microscopic heat pulses activate cardiac thin filaments. *J. Gen. Physiol.* 151, 860–869. doi: 10.1085/jgp.201812243

Ishiwata, S. (1978). Studies on the F-actin.tropomyosin.troponin complex. III. Effects of troponin components and calcium ion on the binding affinity between tropomyosin and F-actin. *Biochim. Biophys. Acta* 534, 350–357. doi: 10.1016/0005-2795(78)90018-1

Ishiwata, S., Shimamoto, Y., and Fukuda, N. (2011). Contractile system of muscle as an auto-oscillator. *Prog. Biophys. Mol. Biol.* 105, 187–198. doi: 10.1016/j.pbiomolbio.2010.11.009

Janssen, P. M. L., Stull, L. B., and Marbán, E. (2002). Myofilament properties comprise the rate-limiting step for cardiac relaxation at body temperature in the rat. *Am. J. Physiol. Heart Circ. Physiol.* 282, H499–H507. doi: 10.1152/ajpheart.00595.2001

Kagemoto, T., Oyama, K., Yamane, M., Tsukamoto, S., Kobirumaki-Shimozawa, F., Li, A., et al. (2018). Sarcomeric auto-oscillations in single myofibrils from the heart of patients with dilated cardiomyopathy. *Circ. Hear. Fail.* 11:e004333. doi: 10.1161/CIRCHEARTFAILURE.117.004333

Kentish, J. C. (1984). The inhibitory effects of monovalent ions on force development in detergent-skinned ventricular muscle from guinea-pig. *J. Physiol.* 352, 353–374. doi: 10.1113/jphysiol.1984.sp015296

Kentish, J. C. (1986). The effects of inorganic phosphate and creatine phosphate on force production in skinned muscles from rat ventricle. *J. Physiol.* 370, 585–604. doi: 10.1113/jphysiol.1986.sp015952

Kobirumaki-Shimozawa, F., Inoue, T., Shintani, S. A., Oyama, K., Terui, T., Minamisawa, S., et al. (2014). Cardiac thin filament regulation and the Frank-Starling mechanism. *J. Physiol. Sci.* 64, 221–232. doi: 10.1007/s12576-014-0314-y

Kremneva, E. V., Nikolaeva, O. P., Gusev, N. B., Levitskij, D. I., and Levitsky, D. I. (2003). Effects of troponin on thermal unfolding of actin-bound tropomyosin. *Biokhimiya* 68, 976–984. doi: 10.1023/A:1025043202615

Kurihara, S., and Sakai, T. (1985). Effects of rapid cooling on mechanical and electrical responses in ventricular muscle of guinea-pig. *J. Physiol.* 361, 361–378. doi: 10.1113/jphysiol.1985.sp015650

Lehman, W., Craig, R., and Vibert, P. (1994). Ca^{2+}-induced tropomyosin movement in Limulus thin filaments revealed by three-dimensional reconstruction. *Nature* 368, 65–67. doi: 10.1038/368065a0

Marino, A., Arai, S., Hou, Y., Degl'Innocenti, A., Cappello, V., Mazzolai, B., et al. (2017). Gold nanoshell-mediated remote myotube activation. *ACS Nano* 11, 2494–2508. doi: 10.1021/acsnano.6b08202

Matusovsky, O. S., Mansson, A., Persson, M., Cheng, Y. S., and Rassier, D. E. (2019). High-speed AFM reveals subsecond dynamics of cardiac thin filaments upon Ca2+ activation and heavy meromyosin binding. *Proc. Natl. Acad. Sci. U.S.A.* 116, 16384–16393. doi: 10.1073/pnas.1903228116

Mikane, T., Araki, J., Suzuki, S., Mizuno, J., Shimizu, J., Mohri, S., et al. (1999). O2 cost of contractility but not of mechanical energy increases with temperature in canine left ventricle. *Am. J. Physiol. Hear. Circ. Physiol.* 277, 65–73. doi: 10.1152/ajpheart.1999.277.1.h65

Millar, N. C., and Homsher, E. (1990). The effect of phosphate and calcium on force generation in glycerinated rabbit skeletal muscle fibers. *J. Biol. Chem.* 265, 20234–20240.

Mühlrad, A., and Hegyi, G. (1965). The role of Ca^{2+} in the adenosine triphosphatase activity of myofibrils. *Biochim. Biophys. Acta* 105, 341–351. doi: 10.1016/s0926-6593(65)80158-8

Murphy, R. A., and Hasselbach, W. (1968). Calcium ion-dependent myofibrillar adenosine triphosphatase activity correlated with the contractile response. Temperature-induced loss of calcium ion sensitivity. *J. Biol. Chem.* 243, 5656–5662.

Obata, K., Takeshita, D., Morita, H., and Takaki, M. (2018). Left ventricular mechanoenergetics in excised, cross-circulated rat hearts under hypo-, normo-, and hyperthermic conditions. *Sci. Rep.* 8:16246. doi: 10.1038/s41598-018-34666-3

Ohtsuki, I., and Morimoto, S. (2008). Troponin: Regulatory function and disorders. *Biochem. Biophys. Res. Commun.* 369, 62–73. doi: 10.1016/j.bbrc.2007.11.187

Orchard, C. H., and Kentish, J. C. (1990). Effects of changes of pH on the contractile function of cardiac muscle. *Am. J. Physiol.* 258, C967–C981. doi: 10.1152/ajpcell.1990.258.6.C967

Oyama, K., Mizuno, A., Shintani, S. A., Itoh, H., Serizawa, T., Fukuda, N., et al. (2012). Microscopic heat pulses induce contraction of cardiomyocytes without calcium transients. *Biochem. Biophys. Res. Commun.* 417, 607–612. doi: 10.1016/j.bbrc.2011.12.015

Papadaki, M., Holewinski, R. J., Previs, S. B., Martin, T. G., Stachowski, M. J., Li, A., et al. (2018). Diabetes with heart failure increases methylglyoxal modifications in the sarcomere, which inhibit function. *JCI Insight* 3:e121264. doi: 10.1172/jci.insight.121264

Protasi, F., Shtifman, A., Julian, F. J., and Allen, P. D. (2004). All three ryanodine receptor isoforms generate rapid cooling responses in muscle cells. *Am. J. of Physiol. Cell Physiol.* 286, C662–C670. doi: 10.1152/ajpcell.00081.2003

Puglisi, J. L., Bassani, R. A., Bassani, J. W., Amin, J. N., and Bers, D. M. (1996). Temperature and relative contributions of Ca transport systems in cardiac myocyte relaxation. *Am. J. Physiol.* 270, H1772–H1778. doi: 10.1152/ajpheart.1996.270.5.H1772

Ranatunga, K. W. (1994). Thermal stress and Ca-independent contractile activation in mammalian skeletal muscle fibers at high temperatures. *Biophys. J.* 66, 1531–1541. doi: 10.1016/S0006-3495(94)80944-0

Refinetti, R. (2010). The circadian rhythm of body temperature. *Front. Biosci.* 15:564–594. doi: 10.2741/3634

Risi, C., Eisner, J., Belknap, B., Heeley, D. H., White, H. D., Schröder, G. F., et al. (2017). Ca^{2+}-induced movement of tropomyosin on native cardiac thin filaments revealed by cryoelectron microscopy. *Proc. Natl. Acad. Sci. U.S.A.* 114, 6782–6787. doi: 10.1073/pnas.1700868114

Rosenberg, H., Pollock, N., Schiemann, A., Bulger, T., and Stowell, K. (2015). Malignant hyperthermia: a review. *Orphanet J. Rare Dis.* 10:93. doi: 10.1186/s13023-015-0310-1

Saeki, A., Goto, Y., Hata, K., Takasago, T., Nishioka, T., and Suga, H. (2000). Negative inotropism of hyperthermia increases oxygen cost of contractility in canine hearts. *Am. J. Physiol. Hear. Circ. Physiol.* 279, 11–18. doi: 10.1152/ajpheart.2000.279.6.h2855

Saltin, B., Gagge, A. P., and Stolwijk, J. A. (1968). Muscle temperature during submaximal exercise in man. *J. Appl. Physiol.* 25, 679–688. doi: 10.1152/jappl.1968.25.6.679

Shattock, M. J., and Bers, D. M. (1987). Inotropic response to hypothermia and the temperature-dependence of ryanodine action in isolated rabbit and rat ventricular muscle: implications for excitation-contraction coupling. *Circ. Res.* 61, 761–771. doi: 10.1161/01.res.61.6.761

Shutt, R. H., and Howlett, S. E. (2008). Hypothermia increases the gain of excitation-contraction coupling in guinea pig ventricular myocytes. *Am. J. Physiol. Cell Physiol.* 295, 692–700. doi: 10.1152/ajpcell.00287.2008

Singh, A., and Hitchcock-DeGregori, S. E. (2009). A peek into tropomyosin binding and unfolding on the actin filament. *PLoS One* 4:e6336. doi: 10.1371/journal.pone.0006336

Solaro, R. J., and Rarick, H. M. (1998). Troponin and tropomyosin: proteins that switch on and tune in the activity of cardiac myofilaments. *Circ. Res.* 83, 471–480. doi: 10.1161/01.RES.83.5.471

Tanaka, H., and Oosawa, F. (1971). The effect of temperature on the interaction between F-actin and tropomyosin. *Biochim. Biophys. Acta* 253, 274–283. doi: 10.1016/0005-2728(71)90253-2

Trybus, K. M., and Taylor, E. W. (1980). Kinetic studies of the cooperative binding of subfragment 1 to regulated actin. *Proc. Natl. Acad. Sci. U.S.A.* 77, 7209–7213. doi: 10.1073/pnas.77.12.7209

Veltri, T., de Oliveira, G. A. P., Bienkiewicz, E. A., Palhano, F. L., Marques, M., de, A., et al. (2017). Amide hydrogens reveal a temperature-dependent structural transition that enhances site-II Ca^{2+}-binding affinity in a C-domain mutant of cardiac troponin C. *Sci. Rep.* 7:691. doi: 10.1038/s41598-017-00777-6

Vernon, H. M. (1899). Heat rigor in cold-blooded animals. *J. Physiol.* 24, 239–287. doi: 10.1113/jphysiol.1899.sp000757

Vibert, P., Craig, R., and Lehman, W. (1997). Steric-model for activation of muscle thin filaments. *J. Mol. Biol.* 266, 8–14. doi: 10.1006/jmbi.1996.0800

Xu, C., Craig, R., Tobacman, L., Horowitz, R., and Lehman, W. (1999). Tropomyosin positions in regulated thin filaments revealed by cryo-electron microscopy. *Biophys. J.* 77, 985–992. doi: 10.1016/S0006-3495(99)76949-3

Conflict of Interest: The authors declare that the research was conducted in the absence of any commercial or financial relationships that could be construed as a potential conflict of interest.

frontiers in Physiology

REVIEW
published: 12 May 2020
doi: 10.3389/fphys.2020.00368

Advances in Stem Cell Modeling of Dystrophin-Associated Disease: Implications for the Wider World of Dilated Cardiomyopathy

Josè Manuel Pioner[1], Alessandra Fornaro[2], Raffaele Coppini[3], Nicole Ceschia[2], Leonardo Sacconi[4], Maria Alice Donati[5], Silvia Favilli[6], Corrado Poggesi[1], Iacopo Olivotto[2] and Cecilia Ferrantini[1]*

[1] Division of Physiology, Department of Experimental and Clinical Medicine, Università degli Studi di Firenze, Florence, Italy, [2] Cardiomyopathy Unit, Careggi University Hospital, Florence, Italy, [3] Department of NeuroFarBa, Università degli Studi di Firenze, Florence, Italy, [4] LENS, Università degli Studi di Firenze and National Institute of Optics (INO-CNR), Florence, Italy, [5] Metabolic Unit, A. Meyer Children's Hospital, Florence, Italy, [6] Pediatric Cardiology, Meyer Children's Hospital, Florence, Italy

Familial dilated cardiomyopathy (DCM) is mostly caused by mutations in genes encoding cytoskeletal and sarcomeric proteins. In the pediatric population, DCM is the predominant type of primitive myocardial disease. A severe form of DCM is associated with mutations in the *DMD* gene encoding dystrophin, which are the cause of Duchenne Muscular Dystrophy (DMD). DMD-associated cardiomyopathy is still poorly understood and orphan of a specific therapy. In the last 5 years, a rise of interest in disease models using human induced pluripotent stem cells (hiPSCs) has led to more than 50 original studies on DCM models. In this review paper, we provide a comprehensive overview on the advances in DMD cardiomyopathy disease modeling and highlight the most remarkable findings obtained from cardiomyocytes differentiated from hiPSCs of DMD patients. We will also describe how hiPSCs based studies have contributed to the identification of specific myocardial disease mechanisms that may be relevant in the pathogenesis of DCM, representing novel potential therapeutic targets.

Keywords: dilated cardiomyopathy (DCM), duchenne muscular dystrophy (DMD), dystrophin (DMD), hiPSC-cardiomyocyte, stem cell models

OPEN ACCESS

Edited by:
Henk Granzier,
University of Arizona, United States

Reviewed by:
Beata M. Wolska,
University of Illinois at Chicago, United States
Michelle S. Parvatiyar,
Florida State University, United States

****Correspondence:***
Josè Manuel Pioner
josemanuel.pioner@unifi.it

Specialty section:
This article was submitted to Frontiers in Physiology Striated Muscle Physiology, a section of the journal Frontiers in Physiology

Received: *20 January 2020*
Accepted: *30 March 2020*
Published: *12 May 2020*

Citation:
Pioner JM, Fornaro A, Coppini R, Ceschia N, Sacconi L, Donati MA, Favilli S, Poggesi C, Olivotto I and Ferrantini C (2020) Advances in Stem Cell Modeling of Dystrophin-Associated Disease: Implications for the Wider World of Dilated Cardiomyopathy. Front. Physiol. 11:368. doi: 10.3389/fphys.2020.00368

Abbreviations: AAV, Adeno-associated virus; *ABCC9,* Sulfonylurea receptor 2A, component of ATP-sensitive potassium channel; ABD1, actin-binding domain; *ACTC1,* α-cardiac actin; ACTN2, α-actinin 2; AF, atrial fibrillation; *ANKRD1,* Cardiac ankyrin repeat protein; *ARVC,* arrhythmogenic right ventricular cardiomyopathy; *BAG3,* BCL2-associated athanogene 3; BMD, Becker Muscular Dystrophy; CM, Cardiomyocytes; CMR, cardiac magnetic resonance; CRISPR-Cas9, Clustered Regularly Interspaced Short Palindromic Repeats; *CRYAB,* α-B-crystallin; *CSRP3,* Muscle LIM protein; DCM, Dilated cardiomyopathy; *DES,* Desmin; DGC, dystrophin glycoproteic complex; DMD, Duchenne Muscular Dystrophy; *DMD,* dystrophin gene; *DNAJC19,* HSP40 homolog, C19; Dp427, Full-length dystrophin isoform (427 kDa); Dp71, Dystrophin isoform (71 kDa); *DSP,* Desmoplakin; ECG, electrocardiogram; EHT, engineered heart tissue; *EMD,* Emerin; fast k_{REL}, fast phase of myofibril relaxation; *FLNC,* Filamin C; HCM, hypertrophic cardiomyopathy; HF, Heart failure; hiPSC, Human induced pluripotent stem cell; HT, heart transplantation; ICD, implantable cardioverter defibrillators; k_{ACT}, myofibril kinetic of force development; *KCNQ1,* Potassium channel; *LDB3,* Cipher/ZASP; *LMNA,* Lamin A/C; *LQT,* long QT syndrome; LV, left ventricle; LVEF, left ventricular ejection fraction; LVNC, left ventricular non-compaction; MF, myocardial fibrosis; *MYH7,* β-Myosin heavy chain; *NEBL,* Nebulette; nNOS, nitric oxide synthase; OMT, optimal medical therapy; PAM, protospacer adjacent motif; PLN, Phospholamban; PMO, phosphorodiamidate morpholino oligomer; *RBM20,* RNA-binding protein 20; RCM, restrictive cardiomyopathy; RCT, randomized control trial; SCD, sudden cardiac death; *SCN5A,* Type V voltage-gatedcardiac Na channel; SGCA, SGCB, SGCD, α-/β-/δ-Sarcoglycan; slow k_{REL}, slow linear phase of myofibril relaxation; TALEN, transcription activator-like effector nucleases; *TAZ/G4.5,* Tafazzin; *TCAP,* Titin-cap/telethonin; *TNNC1,* Cardiac troponin C; *TNNI3,* Cardiac troponin I; *TNNI3K,* Troponin I–interactingkinase; *TNNT2,* Cardiac troponin T; *TPM1,* α-Tropomyosin; *TTN,* Titin; *VCL,* Metavinculin; VF, ventricular fibrillation; VT, ventricular tachycardia.

HIGHLIGHTS

- Mutations in the *DMD* gene (encoding dystrophin) account for 2% of inherited dilated cardiomyopathy (DCM). Advances in *in vitro* disease modeling using induced pluripotent stem cell-derived cardiomyocytes (hiPSC-CMs) may help develop specific therapies aimed at restoring or blunting myocardial damage and dysfunction in Duchenne and Becker Muscular Dystrophy.
- This review focuses on the physiological role of dystrophin in cardiomyocyte function during cardiac development and disease progression. The pathological mechanisms caused by the absence of dystrophin or the presence of truncated dystrophin isoforms are discussed. We provide an overview of the most recent and remarkable results obtained using hiPSC-CM lines with DMD mutations.
- Many studies employed hiPSC-CMs for pilot tests of gene therapy strategies. *In vitro* models such as DMD patient-cardiomyocytes offers a limitless source of human tissue to explore novel disease mechanisms that may represent targets for pharmacological intervention, tested and validated using novel high-throughput cell-screening techniques. Dystrophin-associated cardiomyopathy is an example of a rare cardiac disease where stem cell-based disease-modeling may help developing truly "patient-specific" therapeutic strategies.

Mutations in the dystrophin gene at the Xp21.1 locus are associated with devastating X-linked skeletal muscle disorders, such as Duchenne or Becker muscular dystrophies (DMD/BMD), and account for <2% of dilated cardiomyopathy (DCM) cases. The incidence of DMD is 1/5,000 male births (Mendell et al., 2012). Despite its low prevalence (<3/10,000), dystrophin-associated cardiomyopathy is the form of DCM that has been modeled *in vitro* more extensively using induced pluripotent stem cell-derived cardiomyocytes (iPSC-CMs) from patients. As a case in point, twenty original studies based on the use of DMD/BMD iPS-derived cell lines are present in the recent literature (2015–2019), as opposed to only few isolated examples for other genetically determined DCMs (**Table 1**). Why is dystrophin-associated cardiomyopathy more widely studied *in vitro* compared to other forms of DCM? And are DMD/BMD *in vitro* models specific in recapitulating dystrophin-related pathophysiology, or can lessons be learned regarding the wider spectrum of DCM?

The first answer is simple: an intense and growing interest in DMD/BMD models derives from its potential for gene therapy. Given the severity of skeletal muscle damage associated with dystrophin depletion, a number of gene-targeted therapies aimed at inducing dystrophin expression have been developed. These promising gene-editing approaches have been developed for DMD to a level far beyond what has been achieved for any other cardiac or skeletal muscle diseases. Gene-editing strategies are being thoroughly evaluated *in vitro* in hopes of improving/delaying cardiac as well as muscular involvement in DMD patients.

The second issue is far more challenging and largely unresolved. Lack of dystrophin and of its stabilizing effects on the cytoskeleton causes a variety of downstream pathogenic mechanisms, ultimately leading to calcium dysregulation and sarcomere dysfunction. Whether and how all or part of these pathways are relevant to other forms of genetically-driven or acquired DCM, remains to be studied. In light of the advancements introduced by iPSC-derived cardiomyocyte modeling, the present review aims to describe the principal pathophysiological mechanisms associated with DMD, with the purpose of defining to what extent these mechanisms are specific to dystrophin depletion or rather, they are part of the wider spectrum of DCM-related cardiac abnormalities. Finally, we will discuss their implications for therapeutic discovery and tailored patient management.

THE EMERGING SPECTRUM OF GENETIC DCM

DCM is a disease of the myocardium characterized by left ventricular (LV) dilatation and dysfunction with an estimated prevalence of 1:2,500, an incidence of 7:100,000 and a male to female ratio of 3:1, in adults (Rakar et al., 1997). Recent estimates suggest a considerably higher prevalence of $\geq$1 in 250 individuals (Hershberger et al., 2013). In the pediatric population, DCM is the predominant type of cardiomyopathy and its incidence is higher in the first year of life (Lipshultz et al., 2003). DCM is one of the leading causes of heart failure (HF) and the most frequent indication for heart transplantation (Japp et al., 2016).

In almost 40% of cases, DCM is genetically determined and associated with mutations in genes coding for titin (19–25%), lamin (5–6%), and sarcomeric thin (1–3%) or thick (3–4%) filament proteins. A variety of pathways and cellular structures are affected by these mutations with negative effects on mechanisms like calcium homeostasis, generation–transmission of mechanic force in the myocardium, muscle contraction and ion channel function. The prevailing pattern of inheritance is autosomal dominant, with incomplete, penetrance, and variable age-related expression. The complex interaction between common and rare variants, the presence of additional modifier gene mutations or polymorphisms, as well as a number of environmental factors, may be responsible for the clinical heterogeneity of DCM even in families carrying the same pathogenic gene variant (Bondue et al., 2018). While the etiology of a wide proportion of cases remains unknown after genetic testing (the so-called "idiopathic" DCM), these apparently "non-genetic" forms, even when clearly acquired (e.g., alcohol- or chemotherapy-related or post-partum cardiomyopathies), are often influenced by the individual genetic profile (McNally and Mestroni, 2017). On the other hand, the pathogenicity of a gene mutation is modulated by interfering factors like age, the hormonal milieu, the status if the innate immune system, the presence of comorbidities such as chronic inflammatory diseases or hypertension, inherited mitochondrial alterations or the exposure to specific environmental triggers (such as cardio-toxic substances or drugs); all these can profoundly alter the clinical phenotype as well as the outcome. In this complex scenario, understanding genotype–phenotype correlations represents the

TABLE 1 | Principal pathogenic gene mutations described in genetic DCM along with their clinical and cellular phenotype.

Gene	Prevalence	Clinical phenotype	#hiPSC studies (References)	Functional output
Titin (*TTN*)	19–25% of familial forms 11–18% of sporadic forms	Usually milder forms of DCM, with LV reverse remodeling described after OMT. Can be associated with tibial muscle dystrophy and HCM (McNally and Mestroni, 2017). Truncating variants are related to alterations in mitochondrial function, increased interstitial fibrosis and reduced hypertrophy, along with increased ventricular arrhythmias at long-term follow-up, with a similar survival and overall cardiac function with respect to idiopathic DCM (Verdonschot et al., 2018).	5 (Hinson et al., 2015; Streckfuss-Bomeke et al., 2017; Chopra et al., 2018; Schick et al., 2018; Zaunbrecher et al., 2019)	Contractile deficit
Lamin A/C (*LMNA*)	5–6% of genetic DCM	Malignant DCM characterized by young onset, high penetrance, dysrhythmias (sinus node dysfunction, AF, atrioventricular node dysfunction, VT, VF, SCD), LV dysfunction and HF with reduced survival and frequent need for HT. Cardiac conduction system disease usually precedes the development of LV dilation and dysfunction (Hasselberg et al., 2018).	6 (Siu et al., 2012; Wyles et al., 2016a; Lee et al., 2017; Bertero et al., 2019; Salvarani et al., 2019; Shah et al., 2019)	LMNA haploinsufficieny; conduction defects; contractile defects
β-Myosin heavy chain (*MYH7*)	3–4% of DCM	Sarcomeric rare variant carriers show a more rapid progression toward death or HT compared to non-carriers, particularly after 50 years of age (Merlo et al., 2013).	?	
Cardiac troponin T (*TNNT2*)	3% of DCM	Clinical and prognostic profiles depend on type of mutation: carriers of Arg92Gln mutation have a worse prognosis than those with other mutations in *TNNT2* or other sarcomeric genes (Ripoll-Vera et al., 2016).	6 (Sun et al., 2012; Wu et al., 2015; Broughton et al., 2016; Burridge et al., 2016; Wang L. et al., 2018; Shafaattalab et al., 2019)	Calcium handling abnormalities; contractile defects
Type V voltage-gated cardiac Na channel (*SCN5A*)	2–3% of DCM	Arrhythmias (commonly AF) and myocyte dysfunction leading to progressive deterioration of LV systolic function (Bondue et al., 2018). Overlapping phenotypes: LQT, Brugada.	1 (Moreau et al., 2018)	Electrophysiological defects; Arrhythmias
RNA-binding protein 20 (*RBM20*)	1–5% of DCM	Malignant arrhythmic phenotype with high frequency of AF and progressive HF (Ripoll-Vera et al., 2016).	3 (Wyles et al., 2016a,b; Streckfuss-Bomeke et al., 2017)	Calcium handling abnormalities; contractile defects
Desmoplakin (*DSP*)	2% of DCM	Associated with Carvajal syndrome (autosomal recessive genetic disorder characterized by woolly hair, striate palmoplantar keratoderma and DCM). Additional phenotypic signs: dental abnormalities and leukonychia. LV dilatation usually asymptomatic at an early age. DCM progresses rapidly, leading to HF or SCD in adolescence (Yermakovich et al., 2018).	1 (Ng et al., 2019)	ACM
Dystrophin (*DMD*, Xp21.1 locus 16)	<2% of genetic DCM	Associated with Duchenne and Becker muscular dystrophy. Severe cardiac involvement in Duchenne (milder and later onset in Becker muscular dystrophy) with supraventricular arrhythmias, atrio-ventricular blocks and right bundle branch block, progressive LV dysfunction and HF (Mestroni et al., 2014).	20 (Dick et al., 2013; Guan et al., 2014; Zatti et al., 2014; Lin et al., 2015; Macadangdang et al., 2015; Japp et al., 2016; Nanni et al., 2016; Young et al., 2016; Kyrychenko et al., 2017; Zhang et al., 2017; Long et al., 2018; Caluori et al., 2019; Eisen et al., 2019; Farini et al., 2019; Jelinkova et al., 2019; Min et al., 2019; Pioner et al., 2019a; Sato et al., 2019; Tsurumi et al., 2019; Moretti et al., 2020)	Calcium handling abnormalities; contractile defects
α-Tropomyosin (*TPM1*)	1–2% of DCM	Overlapping phenotypes: LVNC, HCM (McNally and Mestroni, 2017)	1 (Takasaki et al., 2018)	Sarcomere defects

(Continued)

TABLE 1 | Continued

Gene	Prevalence	Clinical phenotype	#hiPSC studies (References)	Functional output
Desmin (*DES*)	1–2% of DCM (Taylor et al., 2007)	Malignant phenotype associated with desminopathies and myofibrillar myopathy. Can cause a spectrum of phenotypes from skeletal myopathy, mixed skeletal–cardiac disease ("desmin-related myopathy"), and cardiomyopathy (DCM as well as HCM or RCM). DCM is typically preceded by skeletal myopathy and can be associated with conduction defects (Mestroni et al., 2014).	1 (Tse et al., 2013)	DES protein aggregates
Filamin C (*FLNC*)	1% of DCM	Cardiomyopathy associated with myofibrillar myopathy and LVNC; high rate of ventricular arrhythmias and SCD (particularly in truncating variants) (Ader et al., 2019).	?	
Metavinculin (*VCL*)	1% of DCM	Can cause either DCM or HCM phenotype (Vasile et al., 2006)	?	
Phospholamban (PLN)	Rare (except for Netherlands where prevalence reaches 15% of DCM due to R14del mutation with founder effect) (van der Zwaag et al., 2012)	Early onset DCM with lethal ventricular arrhythmias. Low QRS complex potentials and decreased R wave amplitude, negative T waves in left precordial leads (Hof et al., 2019). PLN R14del mutation associated with high risk for malignant arrhythmias and end-stage HF from late adolescence, can cause either a DCM phenotype or ARVC (Mestroni et al., 2014). A milder phenotype is also reported (DeWitt et al., 2006).	4 (Karakikes et al., 2015; Stillitano et al., 2016; Ceholski et al., 2018; Stroik et al., 2019)	Electrophysiological defects
α-/β-/δ-Sarcoglycan (SGCA, SGCB, SGCD)	Rare	Recessive mutations in δ-sarcoglycan linked to limb girdle muscular dystrophy 2F, dominant mutations in δ-sarcoglycan linked to DCM (Campbell et al., 2016).	?	Ca handling abnormalities; Contractile defects
α-cardiac actin (*ACTC1*)	Rare	Familial atrial septal defect combined with a late-onset DCM (Frank et al., 2019). Can be associated with HCM and LVNC	?	
Cardiac troponin I (*TNNI3*)	Rare	Overlapping phenotype: HCM (McNally and Mestroni, 2017).	1 (Chang et al., 2018)	Telomere shortening
Cardiac troponin C (*TNNC1*)	Rare	Overlapping phenotypes: LVNC, HCM (McNally and Mestroni, 2017).	?	
Troponin I–interacting kinase (*TNNI3K*)	Rare	Conduction defect, AF (McNally and Mestroni, 2017).	?	
α-actinin 2 (ACTN2)	Rare	Overlapping phenotype: LVNC (McNally and Mestroni, 2017).	?	
BCL2-associated athanogene 3 (*BAG3*)	Rare	Associated with myofibrillar myopathy (McNally and Mestroni, 2017).	1 (Judge et al., 2017)	Disrupted myofibril; Contractile deficit
α-B-crystallin (*CRYAB*)	Rare	Associated with protein aggregation myopathy (McNally and Mestroni, 2017).	1 (Mitzelfelt et al., 2016)	Protein Aggregates; cellular stress
Titin-cap/telethonin (*TCAP*)	Rare	Associated with limb-girdle muscular dystrophy (McNally and Mestroni, 2017).	?	
Muscle LIM protein (*CSRP3*)	Rare	Overlapping phenotype: HCM (McNally and Mestroni, 2017).	1 (Li et al., 2019)	Calcium handling abnormalities
Cardiac ankyrin repeat protein (*ANKRD1*)	Rare	Associated with congenital heart disease (McNally and Mestroni, 2017).	?	
Cipher/ZASP (*LDB3*)	Rare	Overlapping phenotype: LVNC (McNally and Mestroni, 2017).	?	
Nebulette (*NEBL*)	Rare	Overlapping phenotypes: LVNC, HCM (McNally and Mestroni, 2017).	?	
Emerin (*EMD*)	Rare	Associated with Emery–Dreifuss muscular dystrophy (McNally and Mestroni, 2017).	1 (Shimojima et al., 2017)	Calcium handling abnormalities

(Continued)

TABLE 1 | Continued

Gene	Prevalence	Clinical phenotype	#hiPSC studies (References)	Functional output
Sulfonylurea receptor 2A, component of ATP-sensitive potassium channel (*ABCC9*)	Rare	Associated with AF, Osteochondrodysplasia (McNally and Mestroni, 2017).	?	
Potassium channel (*KCNQ1*)	Rare	Associated with AF, LQT1, short QT1, Jervell and Lange-Nielsen syndrome (McNally and Mestroni, 2017).	?	
HSP40 homolog, C19 (*DNAJC19*)	Rare	Associated with 3-methylglutaconic aciduria, type V (McNally and Mestroni, 2017).	1 (Rohani et al., 2020)	Mitochondrial abnormalities
Tafazzin (*TAZ/G4.5*)	Rare	Associated with LVNC, Barth syndrome, endocardial fibroelastosis 2 (McNally and Mestroni, 2017).	1 (Wang et al., 2014)	Mitochondrial defects; contractile defects

ultimate challenge for translational research in the field of cardiomyopathies.

Mutations in the *TTN* gene coding for titin, a giant protein that works as a nano-spring, account for most known genetic forms of DCM (19–25% of familial forms and 11–18% of sporadic forms), with incomplete penetrance and variable expression, frequently (but not always) presenting with relatively mild phenotypes and slow progression (Bondue et al., 2018). Conversely, mutations in the *LMNA* gene (lamin A/C, representing 5–6% of genetic DCM) (Hasselberg et al., 2018), *FLNC* (filamin C) (Ortiz-Genga et al., 2016), *DES* (desmin) (Capetanaki et al., 2015), *PLN* (phospholamban) (Schmitt et al., 2003), *SCN5A* (McNair et al., 2011), and mutations of *RBM20*, the regulator of *TTN* splicing (Refaat et al., 2012), have been identified as malignant causes of DCM, featuring a marked arrhythmic propensity in patients. The electrical instability characterizing these forms gives rise to a clinical overlap between DCM, arrhythmogenic cardiomyopathy and channelopathies (**Table 1**), as these different disease may share a similar cellular and molecular basis of arrhythmogenesis, ultimately leading to an increased risk of sudden cardiac death (Gigli et al., 2019). Currently, lamin A/C gene mutations represent the only instance where the presence of a specific genetic background *per se* modifies clinical management, warranting consideration for the implantation of cardioverter defibrillators (ICDs), regardless of the severity of LV dysfunction (Priori et al., 2015).

CLINICAL PROFILE OF DYSTROPHIN-ASSOCIATED DCM

DMD is a severe disorder diagnosed in childhood: without supportive care, young men with DMD typically die in their late teens or early 20 s. Historically, the most common cause of death has been respiratory failure. However, with improved respiratory support and the introduction of steroid therapy, DMD cardiomyopathy is becoming an increasingly important cause of morbidity and mortality, due to HF and ventricular arrhythmias leading to sudden death (Eagle et al., 2002; McNally, 2007). From the clinical perspective, dystrophin-associated cardiomyopathy is characterized by a consistently severe phenotype (**Table 1**), and progresses relentlessly. Regional progression of contractile impairment (from the inferolateral wall to the rest of the LV) and diffuse/transmural replacement fibrosis of the inferolateral LV wall are common features of this form of DCM, relatively specific instrumental markers that help distinguish DMD-cardiomyopathy from other forms of DCM (Frankel and Rosser, 1976). LV dimensions and myocardial stiffness increase progressively as the extension of myocardial fibrosis (MF) increases (**Figure 1**). This, in turn, leads to an increased cardiac workload and to the activation of the renin angiotensin and the sympathetic nervous systems, thus leading to worse cardiac function and more severe HF-related symptoms and signs (Perloff, 1984). DMD patients are usually extremely limited in their mobility since the first decade, so that HF-related symptoms are often blunted by the relative lack of physical activity: overt cardiac symptoms have been reported in less than 30% of patients aged <18 (Nigro et al., 1990), underestimating the true extent and prevalence of HF in DMD subjects. Patients may complain about palpitations, dizziness or fainting, the latter commonly associated with the presence of conduction abnormalities at ECG (Fayssoil et al., 2017). Dyspnea is controlled by the mechanical ventilation used for neuromuscular respiratory failure: in this setting, peripheral edema and ascites are common findings and are related to the ventilator-driven positive intrathoracic pressures that reduce venous return (Nigro et al., 1990). Pleural effusion is frequently seen in end-stage disease (Fayssoil et al., 2014). Once HF appears the prognosis is poor, despite the extensive use of the complete therapeutic armamentarium including neuro-hormonal blockade. This is in contrast with other genetic forms of DCM where therapy can alter the progression of LV dysfunction and reverse remodeling is common (Japp et al., 2016; Ader et al., 2019). So far, no clear association between specific dystrophin genotypes and the severity of the cardiac phenotype has been established.

ECG abnormalities are often seen in DMD patients: the most frequently reported changes are sinus tachycardia, short PR intervals, deep and narrow "pseudo-necrosis" Q waves in

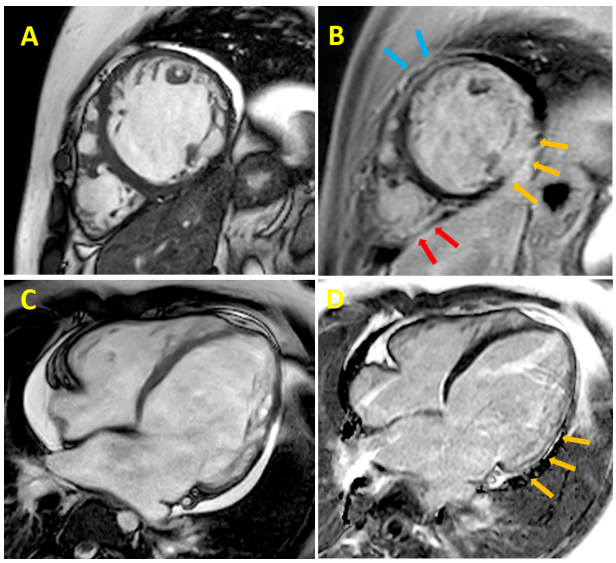

FIGURE 1 | Cardiac magnetic resonance (CMR) cine imaging of a 24 years old DMD patient. The collection of representative images from patients was approved by the Ethical Committee of the Meyer Pediatric Hospital of Florence in the context of a project funded by Telethon Italy (grant GGP16191). Informed consent to patients was performed conform the declaration of Helsinki. This data does not contribute to any novel finding. **(A)** Late gadolinium-enhancement **(B)** left ventricular (LV) short-axis section images of a patient with Duchenne muscular dystrophy (DMD). Yellow arrows indicate the inferolateral subepicardial and midwall contiguous fibrosis; light blue arrows indicate the anterior segment and the red arrows the posterolateral right ventricle wall, both showing midwall fibrosis; CMR cine imaging **(C)** and late gadolinium-enhancement **(D)** LV long-axis section images of the same patient with DMD; yellow arrows indicate midwall fibrosis of the inferolateral segment.

inferolateral leads, tall R wave in the right precordial leads, right bundle branch block and flat/inverted T waves (Manning and Cropp, 1958; Takami et al., 2008). Arrhythmias such as atrial flutter (Perloff, 1984), non-sustained or sustained ventricular tachycardia (Corrado et al., 2002), complete atrioventricular blocks and sick sinus syndrome (Fayssoil et al., 2008, 2010) are seen mainly in patients with severe LV dysfunction (Gigli et al., 2019). Doppler echocardiography typically shows early LV dilatation and dysfunction, beginning in the pediatric age range (McNally et al., 2015). Abnormal indices of diastolic function have been proposed as early indicators of myocardial abnormalities, preceding the development of chamber enlargement and systolic dysfunction in the early stages of DMD-related DCM (Markham et al., 2006). Likewise, regional myocardial abnormalities have been reported in early stages, affecting mainly the inferolateral region of the LV (Giatrakos et al., 2006). Mitral functional regurgitation may also be present, as a consequence of LV and mitral annulus dilation. In the recent years, cardiac magnetic resonance (CMR) has been demonstrated to be a valuable tool for detection of early cardiac involvement and prediction of ventricular arrhythmias, cardiac remodeling and long-term outcome (Mertens et al., 2008; McNally, 2017; Silva et al., 2017).

Management of DMD cardiomyopathy is challenging, due to the interplay of respiratory and cardiac manifestations, poor response to standard treatment and severe systemic manifestations of DMD. Moreover, large-scale randomized clinical trials (RCTs) are rare in this field. Therefore, the latest guidelines for the management of DMD cardiomyopathy are mostly based on the consensus of experts from a wide range of disciplines (Rakar et al., 1997; McNally et al., 2015). Specifically, in the absence of dystrophin-specific targeted cardiac therapies, the 2014 NHLBI working group recommended the introduction of angiotensin-converting enzyme inhibitors (ACEi) or angiotensin receptor blockers (ARBs) in boys with DMD by 10 years of age, in addition to traditional HF treatments (i.e., beta-blockers, mineralocorticoid receptor antagonists, diuretics), as LV dysfunction progresses (Silva et al., 2017). Steroid therapy primarily used to prolong ambulation, also showed a cardioprotective effect in DMD patients (Markham et al., 2008). Early initiation of noninvasive nocturnal ventilation increases long-term survival (McNally and Mestroni, 2017). The surveillance and management of arrhythmias in DMD patients is currently based on general adult HF recommendations. However, aggressive options such as an implantable cardioverter defibrillator (ICD) or the use of cardiac resynchronization therapy (CRT) is controversial in these patients, due to the limited life expectancy and the increased procedural risk (Wang M. et al., 2018). The same considerations apply to mechanical circulatory support (Iodice et al., 2015) and left ventricular assist devices (LVAD), rarely appropriate in this setting. Cardiac transplant is generally contraindicated in DMD (Rakar et al., 1997).

DYSTROPHIN AND DYSTROPHIN-GLYCOGEN COMPLEX

Dystrophin (DMD gene), the largest known gene in the human genome (2.5 million base pairs) (Mandel, 1989), was also the first found to be associated with DCM (Towbin et al., 1993). Ninety-nine percent of the mRNA transcribed from DMD gene is made by introns (non-coding sequences) and the coding sequence accounts for 86 exons. The full-length mRNA (14,000 bp) has a low tissue specificity and is detectable almost ubiquitously. Conversely, protein expression is confined to striated muscle and the neuropil (areas of the nervous system composed of mostly unmyelinated axons, dendrites and glial cell processes that forms a synaptically dense region containing a relatively low number of cell bodies). The obvious discrepancy between mRNA and protein distribution remains unresolved (Vogel and Marcotte, 2012). High levels of full-length dystrophin protein are present in both cardiac and skeletal myocytes, while the protein has a lower expression in unmyelinated axons, dendrites and glial cell processes forming synapsis-dense regions of the brain ("neuropil"). Notably, the DMD gene produces many protein isoforms for different tissue-specific functions (Muntoni et al., 2003), owing to alternative splicing events. Splice variants are formed by *exon skipping*, i.e., exclusion of exons from primary transcripts, or by *exon scrambling*, i.e., subversion of the reciprocal order of exons in the transcript (Muntoni, 2003).

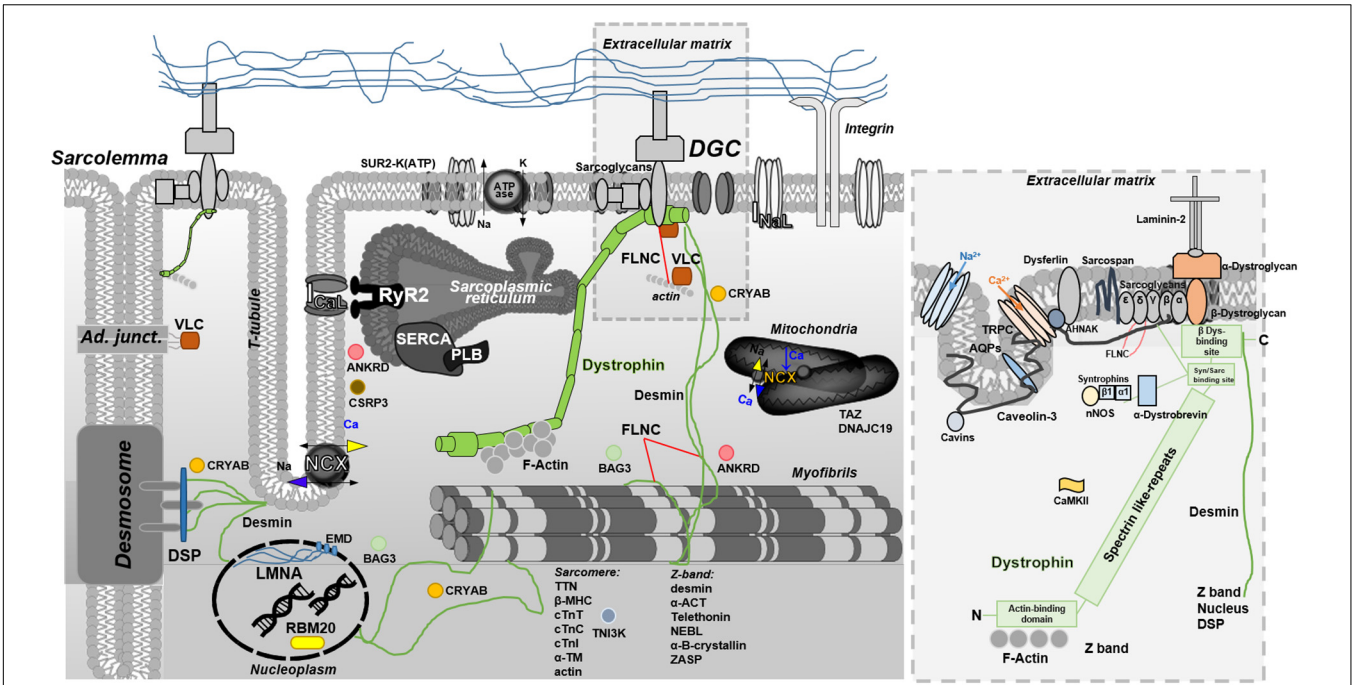

FIGURE 2 | Overview of full-length dystrophin in the context of other DCM-related proteins. The blow-up box, is a focus on full-length dystrophin structure and interactions. Full-length dystrophin is a large rod-shaped protein with a molecular weight of 427 kDa composed by 4 structural domains. The amino (N)-terminal domain has homology with α-actinin and binds, in particular, the F-actin; the central rod-domain contains 24–25 spectrin-like repeats the cysteine-rich domain intereacting with syntrophin and sarcoglycans; the last carboxy (C)-terminal domain associates at the C-terminal with β-dystroglican and several other proteins to form a major protein complex referred to as the dystrophin glycoproteic complex (DGC) (Hoffman et al., 1987; Ervasti and Campbell, 1993). The DGC consists of α- and β-dystroglycan subunits, α-, β-, δ-, γ-, and ε-sarcoglycans, sarcospan, α- and β-syntrophins, α-dystrobrevin, and neuronal nitric oxide synthase (nNOS) (Mosqueira et al., 2013). DGC related-pathways include Ca^{2+} homeostasis and E-C coupling, mitochondrial function, motor protein interaction (sarcomere/Z-band), and gene expression. For instance, the acetylcholine receptor, the skeletal and cardiac isoforms of the voltage-gated sodium channels (Nav1.4 and Nav1.5, respectively), the L-type Ca^{2+} channel, aquaporin, and stretch-activated channel or transient receptor potential (TRP) cation channels (Shirokova and Niggli, 2013) are closely associated with the DGC via syntrophins. In the cardiac tissue, dystrophin is also associated to: Cavin-1 and Caveolin-3 (responsible for caveolae/T tubule formation), Ahnak1 (modulates L-type Ca^{2+} channel), CryAB (involved in cytoprotection and antiapoptosis), and Cipher (plays a role in muscle contraction maintaining the Z-line integrity and signaling). Dystrophin can be also target of phosphorylation by Calmodulin-dependent kinase II (CaMKII) that modulates the affinity for F-actin and syntrophin (Madhavan and Jarrett, 1994). Other short isoforms of dystrophin come from spliced variants and are expressed in several other tissues. In particular, the Dp71 is expressed in cardiac muscle and likely present in T-tubular membranes (Kaprielian and Severs, 2000; Kaprielian et al., 2000).

Full-length dystrophin (depicted in **Figure 2**, in the context of other proteins associated with DCM) is a large rod-shaped protein with a molecular weight of 427 kDa, composed by 4 structural domains. The amino (N)-terminal domain has homology with α-actinin and binds, among other proteins, F-actin. The central rod-domain contains 24–25 spectrin-like repeats. The third one is a cysteine-rich domain. The last carboxy (C)-terminal domain associates at the C-terminal with several other proteins to form a major protein complex referred to as the dystrophin-glycoproteic complex (DGC) (Hoffman et al., 1987; Ervasti and Campbell, 1993). The DGC consists of α- and β-dystroglycan subunits, α-, β-, δ-, γ -, and ε-sarcoglycans, sarcospan, α- and β-syntrophins, α-dystrobrevin, and neuronal nitric oxide synthase (nNOS) (Mosqueira et al., 2013). A central role of dystrophin within this network is evidenced by the collapse of the entire DGC in the absence of dystrophin (Leyva-Leyva et al., 2018). Dystrophin is localized at the cytoplasmic face of the muscle cell plasma membrane, or sarcolemma, particularly within a cytoskeletal lattice termed costameres. Through an extensive network of interacting proteins (Ervasti, 2003) costameres physically couple the sarcolemma with the Z disk of force-generating myofibrils (Rahimov and Kunkel, 2013). In the striated muscle, the dystrophin network covers almost the entire cytoplasmic surface of the plasma membrane. It is strategically placed to serve in as a shock absorber, promoting membrane stability and transduction of mechanical force from the extracellular matrix during muscle contraction/stretch. A single-molecule analysis by atomic force microscopy revealed that dystrophin, by stretching with stochastic unfolding and refolding of its central domain, is able to keep elastic forces around 25 pN over a significant length change up to ∼800 nm (90% of fully unfolded central domain length), an extension range that is close to the change of sarcomere length during myofilament contraction in striated muscle (Le et al., 2018). In addition, the DGC serves a variety of signaling pathways that regulate several myocyte functions including Ca^{2+} homeostasis and excitation-contraction coupling, mitochondrial function, motor protein interaction, and gene expression. For instance, the acetylcholine receptor, the skeletal and cardiac isoforms of the voltage-gated

sodium channels (Nav1.4 and Nav1.5, respectively), the L-type Ca^{2+} channel, aquaporin, stretch-activated channels and other transient receptor potential (TRP) cation channels (Shirokova and Niggli, 2013) are closely associated with the DGC via syntrophins and are likely modulated by changes of dystrophin conformation. Moreover, in the myocardium dystrophin appears to serve as a signaling scaffold and membrane protein organizer, targeted by numerous signaling molecules that participate in a diverse set of pathways. For instance, it is also associated with Cavin-1 and Caveolin-3 (responsible for caveolae/T tubule formation), Ahnak1 (modulator of L-type Ca^{2+} channel), CryAB (involved in cytoprotection and antiapoptosis), and Cipher (involved in maintaining Z-line integrity and signaling). Dystrophin can be a target of phosphorylation by Calmodulin-dependent kinase II (CaMKII), modulating the affinity for F-actin and syntrophin (Madhavan and Jarrett, 1994). Other short isoforms of dystrophin originate from spliced variants and are expressed elsewhere. Specifically, Dp71 is expressed in cardiac muscle and is likely present in the T-tubular membrane (Kaprielian and Severs, 2000; Kaprielian et al., 2000). Another important protein is utrophin, a large (376 kDa) cytoskeletal protein, autosomal paralog of dystrophin with similar binding partners and structure that have been used to replace dystrophin in striated muscle, as a therapeutic strategy for DMD (Blake et al., 1996). Dystrophin and utrophin exhibit marked differences in amino acid sequence, particularly within the large rod domain. Thus, it is possible that proteins with unique specificity for dystrophin or utrophin exist, though specific binding properties remain to be identified.

Mutations in DMD that shift the reading frame generate a truncated protein, which cannot anchor itself to the glycoprotein complex. The protein is, therefore, unstable and present at undetectable levels in muscle tissue. It is widely accepted that the predominant functional consequence of the lack of dystrophin is cellular vulnerability to mechanical stress associated with muscle contraction. Membrane fragility and altered Ca^{2+} homeostasis stem from the loss of dystrophin in both skeletal muscle fibers and cardiomyocytes, as demonstrated by studies in DMD animal models. These studies are consistent in showing that the absence of dystrophin leads to altered myogenesis and myofiber commitment in skeletal muscle, originally observed in X Chromosome-Linked Muscular Dystrophy (*mdx*, genetic mouse model of DMD that completely lacks full-length dystrophin) mouse embryos (Merrick et al., 2009) and skeletal muscle biopsies from human fetuses affected by DMD (Farini et al., 2016). Myogenesis was severely disrupted in mdx embryos, which displayed developmental delays including altered myotube size and shape, lower number of myotubes, displacement defects and aberrant Pax7-positive skeletal muscle stem cell behavior (Merrick et al., 2009). Moreover, Dumont and collaborators demonstrated that dystrophin is highly expressed in satellite cells (skeletal muscle stem cells) and regulates their polarity and asymmetric division. Hence, loss of dystrophin results not only in myofiber fragility but also – due to strikingly reduced asymmetric divisions – in the lack of regenerating myofibers (Dumont et al., 2015). Farini and collaborators proposed that PLC/IP3/IP3R/RyR1/Ca^{2+} signaling pathway may be activated differently in fetal compared to adult DMD skeletal muscle fibers, and proposed that this mechanism was directly linked to defects in myofiber formation and to a rearrangement in the expression of fast/slow-muscle specific genes (Farini et al., 2016).

A Developmental Role for Dystrophin in the Heart

The role of dystrophin during human cardiac development is still not completely deciphered. The absence of a shock absorber that may preserve membrane homeostasis and may be involved in several intracellular pathways is supposed to negatively affect physiological human myocardium formation. Previous studies reported that dystrophin is already expressed on the surface of cardiomyocytes in 8-week-old fetuses (Chevron et al., 1994) and, while no studies have investigated earlier phases of gestation, some authors hypothesize that specific fetal dystrophin isoforms may be present during early embryo development (Mora et al., 1994). Of note, a greater quantity of dystrophin was found in cardiac than skeletal muscle in fetuses, likely related to the earlier development of the myocardium. In the same study, Mora and colleagues reported that DGC proteins were expressed variably in period between 8 and 12 weeks of gestation. The expression of spectrin, a DGC-protein involved in the maintenance of plasma membrane integrity and cytoskeletal structure, was detected earlier than vinculin and talin (cytoskeletal proteins connecting integrins), suggesting that dystrophin is probably required on the sarcolemma before these two proteins. At 8 weeks, β-dystroglycan were found patchily on cardiac cells and immunostaining intensity did not appear to change with heart maturation. Adhalin (α-Sarcoglycan) did not appear in the cardiac tissue at 8 weeks and showed limited expression at 12 and at 16 weeks. The dystrophin-like protein utrophin was found at 8 weeks and faintly increased from 8 to 16 weeks (Mora et al., 1996). Finally, other authors identified a distinct pool of dystrophin molecules associated with myofibrils and localized within the Z-disks of the sarcomeres in association with α-actinin and desmin, in cardiac but not in skeletal muscle (Meng et al., 1996). Whether contractile function and dystrophin distribution influence each other in the early stages of development is still unknown.

HUMAN INDUCED PLURIPOTENT STEM CELL DERIVED CARDIOMYOCYTES AS A MODEL OF DYSTROPHIN-ASSOCIATED CARDIOMYOPATHY

The advent of human induced pluripotent stem cells (hiPSCs) has opened the door to the exploration of core biomedical questions using personalized, renewable patient-specific human cell models instead of animal models. Cardiomyocytes derived from hiPSCs represent a unique platform to penetrate the pathophysiological processes related to early-stage defects underlying the onset and progression of DMD cardiomyopathy and delineate the so-called "cellular" phenotypes. Recent validation of these cellular

models compared to native myocardial tissue (Ronaldson-Bouchard et al., 2018), and the possibility to increase the level of maturation of hiPSCs using long-term cultures combined with nanostructured surfaces that mimic the extracellular matrix (Pioner et al., 2019a), will allow future research to comprehensively perform complex biophysical studies to simultaneously monitor membrane fragility, intracellular calcium handling and myofilament function. This represents a unique opportunity in the context of DCM, a disease rarely requiring surgical strategies and therefore difficult to study *in vitro* on human myocardial samples.

Notably, studies using patient-derived tissues often represent the final stages of disease, therefore separating primary mechanisms (i.e., those induced by the lack of full-length dystrophin) from the secondary mechanisms (i.e., those induced by chronic neurohormonal stimulation, adverse remodeling and effects of medications) is nearly impossible. On the other hand, small rodent models recapitulate facets of the human cardiomyopathy phenotype at the early stages of disease development. However, rat and mice cardiomyocytes differ from human cells in the expression of key contractile proteins, heart rate, electrical properties and ion channel function, often making it difficult to translate findings to humans. Cardiomyocytes obtained from the differentiation of iPSCs are the most prominent model to date for modeling human heart *in vitro*. Since the first report of Yamanaka and Takahashi in 2006, the reprogramming of somatic cells into embryonic-like induced pluripotent stem cells (iPSC) has becoming a widely used strategy for disease-in-a-dish modeling (Takahashi and Yamanaka, 2006). Generation of iPSCs bypass ethical concerns regarding disruption of embryos and, differently from embryonic stem cells (ESCs), can be derived directly from patients or healthy donors. Patient-derived iPSCs (hiPSCs) today provide the opportunity to characterize specific disease phenotypes in different tissues, thanks to tissue-specific differentiation protocols. Furthermore, targeting specific genes by CRISPR-Cas9 gene editing technology is a major resource allowing phenotyping of any cardiomyopathy-associated mutation, as well as a direct testing of the pathogenicity of variants of uncertain significance (**Figure 3A**).

It must be emphasized that, even after differentiation into cardiomyocytes, hiPSC-CMs retain immature features resembling developmental cardiomyocytes. In the very early phases (day 20–30 post differentiation), hiPSC-CMs exhibit fetal-type proteomic patterns (van den Berg et al., 2015), automaticity (spontaneous contraction), fetal-like ion channel expression (Davis et al., 2011), contractile properties (Pioner et al., 2016), and metabolism (Ulmer and Eschenhagen, 2019). A developmental-like behavior underlies the changes in hiPSC-CM structure and function. Using conventional culture conditions, cell growth, the organization of subcellular structures and the improvement of cardiomyocyte function are all time-dependent events. For instance, increase of repolarizing ion currents (I_{k1} in particular) and reduction of the funny current (I_f) decrease automaticity, together with a prolongation of cardiomyocyte action potential (Sartiani et al., 2007). Furthermore, sarcoplasmic reticulum calcium content becomes more prominent in the regulation of calcium handling (Itzhaki et al., 2006). Limited information is still available for the contractile apparatus. Sarcomere protein composition and isoform expression can be extremely variable in hiPSC-CMs. In a time window of 100 days after differentiation, hiPSC-CMs undergo sarcomere formation and isoform switch. This is similar to the process of fetal cardiac development (Sasse et al., 1993; Reiser et al., 2001; Racca et al., 2016), which occurs *in vitro* in a time- dependent manner. Furthermore, our current knowledge of sarcomere protein isoforms in hiPSC-CMs is limited by the lack of any truly effective chamber-specific differentiation protocol: for this reason, observations refer to the general cardiomyocyte population. At thick filament level, the cardiac fast alpha myosin heavy chain isoform (α-MHC, MHY6) and the atrial myosin regulatory light chain (MLC-2a, MYL7) are overall prevalent in hiPSC-CMs but long-term culture and stiff substrates (Weber et al., 2016) drive the isoform switch toward a predominant expression of the slow beta myosin heavy chain isoform (β-MHC, *MHY7*) and of the ventricular regulatory light chain (MLC-2v, *MYL2*) (Cai et al., 2019), and increase myosin binding protein C (cMyBP-C) expression (Cai et al., 2019). Titin (TTN) isoforms N2B and N2BA are co-expressed with a pattern similar to that found in the heart tissue of healthy individuals (Streckfuss-Bomeke et al., 2017). Sarcomeric protein composition is of extreme importance when modeling hiPSC-CM for the impact on contraction kinetics. In addition, some studies that used CRISPR-mediated genomic deletion in WT-hiPSC-CM lines for studying *de novo* sarcomere assembly reported that β-MHC, its connection with titin (Chopra et al., 2018) and the expression of the newly discovered Cronos titin (Zaunbrecher et al., 2019) are necessary for sarcomere assembly and function; non-muscle myosin II (NMM II) or α-MHC, instead, are not required. Another fundamental sarcomeric property is the Ca^{2+} buffering capacity of troponin C, which contributes to determine the Ca^{2+} sensitivity (pCa50) of myofibril tension development. Differences in thin filament protein isoform expression or phosphorylation patterns may account for changes in myofilament Ca^{2+} buffering. In hiPSC-CMs, prevalence of slow skeletal troponin I (ssTnI, TNNI1) may recapitulate properties typical of the embryonic age characterized by higher myofilament Ca^{2+} sensitivity and lower pH sensitivity, which may be particularly important for fetal hearts, which have modest amounts of Ca^{2+} delivered to the sarcomeres and are exposed to hypoxic conditions. As previously reported, the mechanisms responsible for the inhibition of myofilament force generation by acidosis include: (1) reduction in the affinity of troponin C (TnC) for Ca^{2+}, (2) alterations in thin filament activation, especially the TnI-TnC interaction, and (3) inhibition of the actin-myosin interaction (Wolska et al., 2001). Long-term culture (>90 days after differentiation) have shown co-expression (almost 1:1) of ssTnI with the adult cardiac troponin I isoform (cTnI) (Bedada et al., 2014; Pioner et al., 2016). Similarly, co-expression of slow skeletal Troponin T (ssTnT) and cardiac troponin T (cTnT) has been reported (Iorga et al., 2017). Of note, using the current differentiation protocols, we and other groups have found myofibril force comparable to fetal myofibrils and kinetic properties that more closely reflect those of adult ventricular

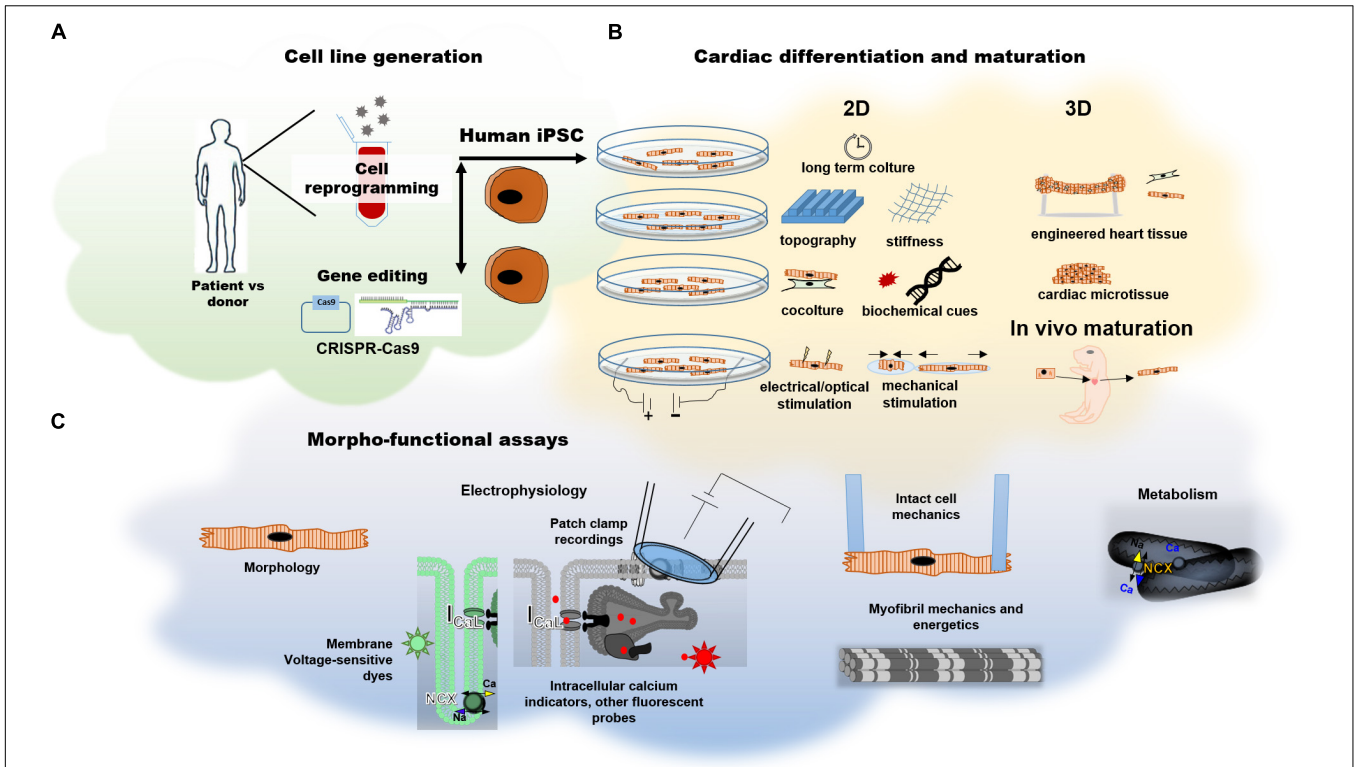

FIGURE 3 | Human induced pluripotent stem cell derived cardiomyocytes. **(A)** Generation of hiPSCs by cell reprogramming of somatic cells from patients or healthy donors or via CRISPR-Cas9 gene editing for the generation of isogenic pairs. **(B)** Current maturation strategies for hiPSC-CMs at cell level (2D strategies) or in multicellular model (3D strategies). **(C)** Possible methods for the assessment of electrophysiological and contractile properties.

myofibrils expressing β MHC (Pioner et al., 2016; Racca et al., 2016; Iorga et al., 2017).

For this reason, maturation strategies applied to hiPSC-CMs are a primary challenge in the field. In the last few years, many researchers have explored ways to induce greater structure and function development of hiPSC-CMs, using a wide range of methods such as long-term culture (Lundy et al., 2013), biomimetic substrates (Macadangdang et al., 2014, 2015; Ribeiro et al., 2015), electrical or mechanical stimulation (Nunes et al., 2013), co-culture with other cell types (Tulloch et al., 2011), alteration of growth media (Birket et al., 2015) and 3D culture system such as engineered heart tissue (EHTs), heart on a chip or even *in vivo* neonatal rat heart system (Cho et al., 2017; **Figure 3B**). Since hiPSC-CMs possess features of developing cardiomyocytes, they can serve as human models for investigating the developmental time-course of early-stage cardiac diseases at cardiac cell level (**Figure 3C**).

Modeling Early-Stages of DMD-Associated DCM Using hiPSC-CMs

Cardiomyocytes derived from patient-hiPSCs can be considered a unique platform to address early-stage defects underlying DMD cardiomyopathy in a developing human heart. Models for inherited DCM have been obtained for mutated genes involving sarcomere and sarcomere Z-band stability, E-C coupling proteins, cytoskeleton, mitochondria and desmosomes (**Table 1**). Models for relatively common (arrhytmogenic right ventricular cardiomyopathies, laminopathies) as well as rare genetic syndromes associated with DCM (Friedreich's ataxia, Barth syndrome, carnitine palmitoyltransferase II deficiency, LEOPARD syndrome, Pompe disease) have been reported (Burridge et al., 2016). Many studies using hiPSCs sought to mirror the pathomechanisms found in end-stage human samples or animal models, although none addressed in-depth the potential for novel therapeutic targets. Patient-derived hiPSC-cardiomyocytes and genome editing of DMD via CRISPR-Cas9 or TALEN can provide direct evidence that the lack of dystrophin directly impacts cardiomyocyte function. In normal hiPSC-CMs, full-length dystrophin (Dp427) is expressed early after differentiation. Recently, mass spectroscopy analysis has suggested that dystrophin is upregulated in a period of time from days 30 to 60 post differentiation. This is also supported by similar results in the developmental expression pattern of embryonic and postnatal mouse hearts (Cai et al., 2019). A lack of information limits the comprehension of the physiological role and expression levels of the Dp71 isoform and of utrophin. However, a novel transient dystrophin isoform (Dp412 kDa) was identified in hiPSCs during mesodermal differentiation induced by a 72 h exposure to bone morphogenetic protein 4 (BMP4), suggesting a role of shorter isoforms during development (Massourides et al., 2015). Furthermore, Jelinkova et al. (2019)

tested a WT hiPSC and two WT hESC lines and reported that Dp427 is already expressed before differentiation and that the absence of dystrophin leads to increased ROS production, NOS activity and DNA damage in DMD-hiPSCs (2 independent patients). These results further support the value of the hiPSC platform for modeling early-stages of DMD.

In such perspective, we have summarized the major findings and limitations of published DMD-hiPSC-CMs models in **Table 2**.

Excitation Contraction Coupling of DMD-hiPSC Cardiomyocyte Models

Calcium handling abnormalities have been described as a major consequence of dystrophin and other DCM-related mutations but the mechanistic progression remains unclear. A study from the Wu laboratory explored DCM-patient derived cell lines carrying the R173W-cTnT mutation, reporting reduced sarcoplasmic reticulum calcium content and higher rate of spontaneous arrhythmic electrical activity compared to normal cardiomyocytes (Sun et al., 2012). In this mutant cell line, decreased cell contractility was determined by atomic force microscopy and compared with lines obtained from the non-affected members of the same family. Overexpression of the sarcoplasmic reticulum Ca^{2+} adenosine triphosphatase (Serca2a) enhanced the intracellular Ca^{2+} transient and restored force production (Sun et al., 2012). These and other works have provided reports of stem cell lines with DCM-associated mutations including RBM20 (Wyles et al., 2016a), PLB (Karakikes et al., 2015), EMD (Shimojima et al., 2017), or CSRP3 (Li et al., 2019), showing marked calcium handling abnormalities that may recapitulate the early myocardial alterations occurring in human DCM hearts. However, the underlying molecular mechanisms of myocardial dysfunction and damage in the presence of DCM-related mutations in various genes can be completely different despite the common final phenotype.

For DMD, two main hypotheses have been advanced: (1) membrane fragility or damage leading to membrane tear or rupture that facilitates abnormal calcium influx, as indirectly demonstrated by treating DMD cells with membrane sealants (i.e., Polaxamer 188) (Yasuda et al., 2005); (2) altered ion channel function and dysregulation of calcium homeostasis as a direct consequence of the altered dystrophin complex (Zhan et al., 2014). Guan and collaborators generated cardiomyocytes derived from the urine of a dystrophin-mutant DMD patient with a deletion of exon 50 (DMD-Δ exon 50), resulting in a dystrophin-deficient phenotype. DMD-Δexon50 displayed unique features such as increased membrane susceptibility to hypotonic stress, slower Ca^{2+} transients in the early phases after differentiation and increased probability of mitochondrial permeability pore opening (Guan et al., 2014). Similarly, DMD cell lines with deletion of exons 49–50 (DMD-Δ exons 49–50) overexpressed the immunoproteasome subunits, while their inhibition by ONX-0914 (proteasome inhibitor) reduced the sarcolemmal damage, as indicated by decreased release of cTnI and TNF-α after treatment (Farini et al., 2019). Lin and collaborators described hiPSC-CM cell lines from two patients carrying out-of-frame deletion in DMD exons 45–52 (DMD-Δ exons 45–52). They reported DMD-CMs with profound reduction of the L-type calcium current and increased cytosolic Ca^{2+} levels, and identified a downstream activation DIABLO-CASP3 that was related to mitochondrial apoptosis (Hinson et al., 2015). This mechanism is in keeping with the increased reactive oxygen species (ROS) levels found in DMD-CM models (Gartz et al., 2018; Jelinkova et al., 2019). The membrane sealant P188 (Polaxamer 188) was able to normalize the increased diastolic calcium levels and to revert the increase in the rate of apoptosis, supporting the hypothesis that membrane damage/fragility leads to intracellular calcium overload even in the early stages of myocardial differentiation (Lin et al., 2015). A unifying hypothesis may involve mechanosensitive channels, e.g., the transient receptor potential canonical channel 1 (TRPC1), which transduce membrane stretch into a cationic (Na^+, K^+, Ca^{2+}, and Mg^{2+}) flux across the sarcolemma, and may be gated by an excessive tension developed within the lipid bilayer, as previously reviewed (Maroto et al., 2005). In support of this idea, a recent test exposed DMD (DMD-Δ exons 43–45) and control hiPSC-CMs, plated on a fibronectin-coated silicon chamber, to a periodical mechanical stretching (120% elongation) at a frequency of 60 cycles per min and measured the response of intracellular calcium levels after 3 h (Tsurumi et al., 2019). A short-term mechanical stretch protocol was sufficient to increase diastolic calcium levels and calcium transient amplitude in DMD cells while it did not cause such effects in controls. However, these studies are limited by the small number of cell lines and by the use of immature cardiomyocytes in the early-phases of cardiac differentiation and maturation. We recently reported the analysis of calcium transients in hiPSC-CMs at day 100 of differentiation, comparing the DMD-Δ Exon 50 line to a healthy control and its CRISPR-Cas9 genome edited isogenic control (Exon 1 deletion in the DMD gene, DMD-c.263delG) (Pioner et al., 2019a; **Figure 4**). At this advanced stage of differentiation and maturation, hiPSC-CMs paced by field stimulation showed adaptation to frequency changes. DMD-Δ Exon 50 showed slower calcium transient rise and decay compared to controls, and these changes were comparable to those observed in our CRISPR-Cas9 generated cell line (DMD-c.263delG) expressing a shorter synthetic dystrophin. Slower duration of calcium transients is an alteration found in other DMD cell lines (**Figure 4C**). Both cell lines were associated with prolonged cardiomyocyte relaxation at low loading conditions (**Figure 4D**). This directly demonstrated that the lack of the full-length dystrophin is sufficient to perturb normal contractility of cardiomyocytes, with abnormal calcium homeostasis as a leading consequence. Moreover, another recent study generated a cell line from a male patient (DMD- c.5899C > T) and from a DMD female carrier (Δ Exons 8–12). Interestingly, both DMD cell lines showed prolonged action potential (AP) duration compared to control lines, and those measured in cells from the female carrier were even larger (APD90, 600 vs. 400 ms in the male patient). The prolongation of APs was attributed to an increase of L-type calcium (I_{Ca-L}) peak current amplitude and CACNA1C expression (I_{Ca-L} main channel subunit), which were even more evident in the iPSC-CMs obtained from the female carrier. Regulation or expression of ion channels might be dependent

TABLE 2 | DMD-cardiomyopathy studies based on hiPSC-CMs: individual mutations vs. functional parameter and therapeutic attempts *in vitro*.

Mutation/ parameter	Membrane	Electrophysiology	Calcium handling	Sarcomere	Metabolism and oxidative stress	Therapeutic approach	References
Δ Exon 50	Fragility/damage		Slower calcium transients	↓ myofibril force, slower myofibril relaxation, ↑ myofibril calcium sensitivity	↑ mPTP opening; unaffected mitochondrial respiration		Guan et al., 2014; Macadangdang et al., 2015; Pioner et al., 2019a
Δ Exons 49–50	Fragility/damage	↑Spontaneous electrical activity	↑Intracellular diastolic calcium level	↑cTnI release (marker of cell damage)		ONX-0914 reduced ROS level	Farini et al., 2019
DMD; nonspecified mut.					Reduced Nup153 factor (regulates cardiac remodeling)		Nanni et al., 2016
Δ Exons 45–52	Fragility/damage		↑Intracellular diastolic calcium level	↓Sarcomere transcriptome	Mitochondrial damage, CASP3 activation, apoptosis	Poloxamer 188, reduced resting cytosolic Ca^{2+} level, CASP3 activation and apoptosis	Lin et al., 2015
c.263ΔG	Fragility/damage		Slower calcium transients	↓Alignment; ↓acto-myosin turnover; cellular hypertrophy			Macadangdang et al., 2015; Pioner et al., 2019a
Δ Exons 52–54					NOS-induced ROS release		Jelinkova et al., 2019
Δ Exons 43–45			↑Stretch-induced intracellular calcium entry				Tsurumi et al., 2019
Δ Exons 8–12		↑I_{Ca-L} density; prolonged APD					Eisen et al., 2019
c.5899C > T		↑I_{Ca-L} density; prolonged APD					Eisen et al., 2019
Δ Exon 8-9		↑Spontaneous electrical activity	Slower calcium transients	↓Force production		Rescue by CRISPR-Cas9-deletion of 3–9, 6–9, 7–11	Kyrychenko et al., 2017
Δ Exon 3–6					Mitochondrial damage; ↑ROS level ↑exosome protection	Exosome protection	Gartz et al., 2018

(Continued)

TABLE 2 | Continued

Mutation/ parameter	Membrane	Electrophysiology	Calcium handling	Sarcomere	Metabolism and oxidative stress	Therapeutic approach	References
Δ Exons 45–50		↑Spontaneous electrical activity					Caluori et al., 2019
Δ Exons 48–50						CRISPR-Cas9 deletion of exons 45–55 restored DGC	Young et al., 2016
Δ Exons 46–55	Fragility/damage		Cellular arrhythmias			Exon 45 skipping with PMO improved arrhythmias	Sato et al., 2019
Δ Exon 44						CRISPR-Cas9 restoration	Min et al., 2019
Exon 45, 51, 45, 53, 44, 46, 52, 50, 43, 6, 7, 8, 55						CRISPR-Cas9 restoration	Long et al., 2018
Δ Exons 48–50				↓Force production		CRISPR-Cpf1 reframing of Exon 51 or exon skipping: restored dystrophin; enhanced contractile function.	Zhang et al., 2017
Δ Exons 4–43				↓Force production		Restoration by HAC carrying the full-length genomic dystrophin sequence	Zatti et al., 2014
Δ Exons 48–50, 47–50, Δ TG from exon 35, c.3217G > T						Antisense oligonucleotide-mediated skipping of exon 51 and delivery of dystrophin minigene	Dick et al., 2013
Δ Exon 52			Slower calcium transients; arrhythmic events			AAV6-Cas9-g51-mediated excision of exon 51 restored dystrophin expression and ameliorate skeletal myotube formation as well as abnormal cardiomyocyte Ca^{2+} handling and arrhythmogenic susceptibility	Moretti et al., 2020

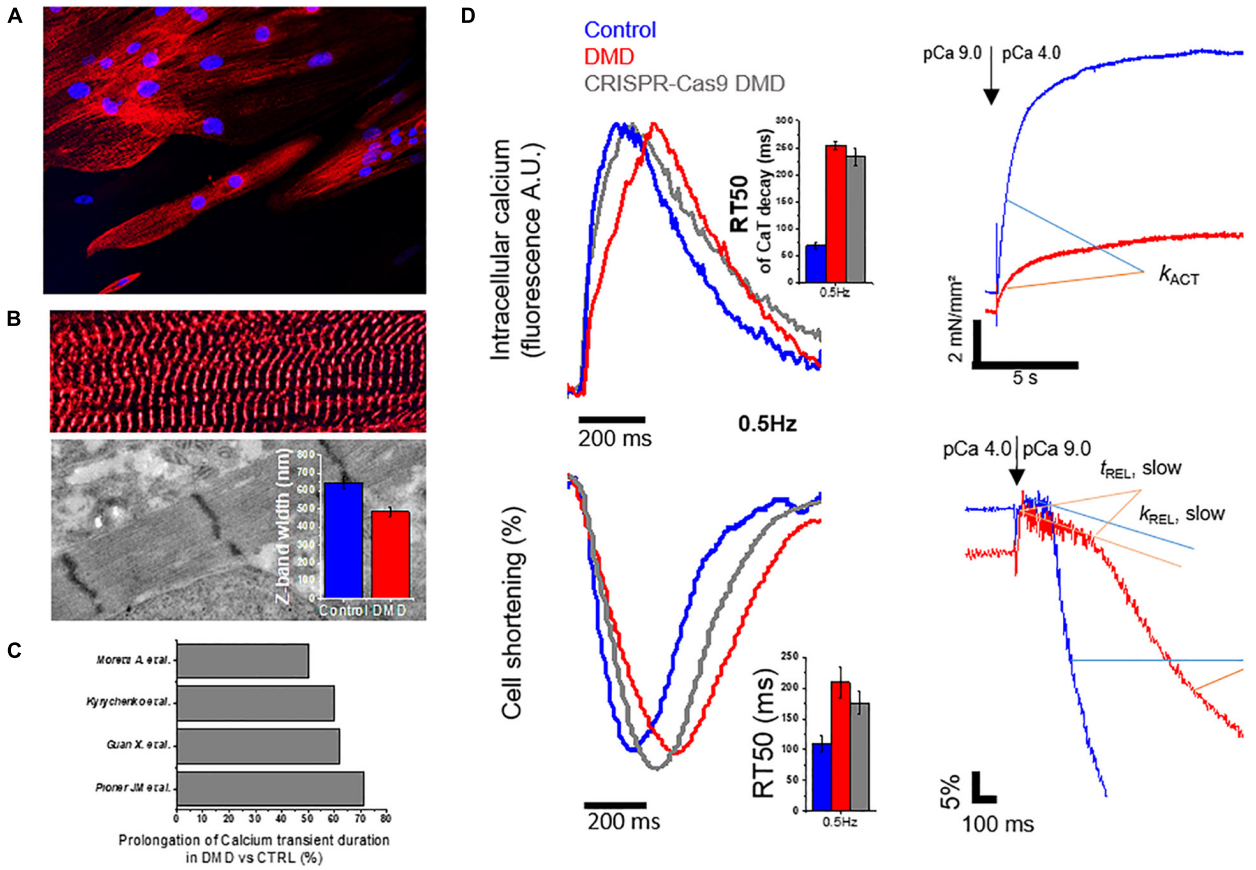

FIGURE 4 | Morphology and function altered in DMD-hiPSC-CMs from patient confirmed in a CRISPR-Cas9 gene edited cell line. Original data are modified from Pioner et al. (2019b) with the correct permission from the owner (Pioner et al., 2019a). A DMD-hiPSC-cell line from a patient (with Δ Exon 50 in DMD gene) and a CRISPR-Cas9 gene edited cell line (c.263 ΔG) targeting Exon 1 in healthy control cell line (Control) were generated and the cardiomyocytes were matured onto nanotopographic cues for 3 months. **(A)** DMD-hiPSC-CMs displayed aspect ratio similar to adult cardiomyocytes and Z-bands were observed across the entire cell width (diameter), suggesting DMD-CMs experienced hypertrophy and a greater number of myofibrils in parallel. **(B)** Despite similar myofibril alignment to control-hiPSC-CMs, sarcomere diameters (estimated from the length of Z-bands by transmitted electron microscopy) were significantly smaller, suggesting a possible reduction in the parallel assembly of myofilaments within individual myofibrils. **(C)** Meta-analysis on Calcium transient duration. **(D)** Representative traces of calcium transients (CaT), cell shortening and myofibril mechanics of DMD-hiPSC-CMs compared to controls. Simultaneous recordings at single cell level revealed slower CaT decay (estimated from time to peak to 50% of CaT decay, RT50, ms), slower cell relaxation (RT50, ms) at 37°C and external pacing (0.5 Hz reported). Compared to other studies reporting similar analysis of calcium transients, slower CaT duration might be a peculiarity of DMD-hiPSC-CMs. Single myofibrils showed lower isometric-tension generating capacity and slower myofibril relaxation (slow t_{REL} and fast k_{REL}). This study concluded that both calcium handling and myofibril abnormalities may contribute to prolong cell relaxation.

on the specific protein defects rather than on the common downstream pathways related to cell degeneration toward a DCM phenotype. For instance, another DCM-hiPSC model was obtained from patients harboring a fukutin-related protein gene mutation (826C > A; Leu276Ile, transmembrane protein) associated to Limb-Girdle muscular dystrophy (LGMD) and was studied at comparable levels of maturation. In this case, the authors reported DCM-hiPSC-CMs with reduced AP amplitude and shorter AP duration compared to healthy controls, with reduced peak and late Na currents (I_{Na}), as well as lower peak L-type calcium channel current; these changes were likely related to the reduced expression of their related genes, SCN5A and CACNA1C. In addition, the rapidly activating delayed rectifier potassium current (I_{Kr}) was reduced, whereas the transient outward current (I_{to}) and slowly activating delayed-rectifier potassium current (I_{Ks}) were similar in DCM and control cardiomyocytes (El-Battrawy et al., 2018).

Force and Contractile Properties of DMD-hiPSC Cardiomyocyte Models

The N-terminal domain of dystrophin has homology for cytoskeletal F-actin and interacts in the context of costamere domains that couple sarcolemma to sarcomeric Z-bands. As cardiac cells rapidly shorten during contraction, electrostatic interaction between the basic spectrin repeats and actin filaments serve to dampen elastic extension during stretch (Ervasti, 2007). In this context, a complex network involves multiple DCM-related proteins including the sarcomere proteins titin (TTN), β-myosin heavy chain (β-MHC), cTnT, cTnI, cTnC, tropomyosin

cardiac troponin I (cTnI)–interacting kinase (TNNI3K) and other Z-band interacting proteins such as α-actinin, desmin, telethonin, cardiac ankyrin repeat protein, nebulette, α-B-crystallin and cipher. The Z-band complex seems to be involved in the mechanosensory mechanisms that convert mechanical stimuli into biochemical signals, and dystrophin has connections with several Z-band proteins. Consequently, DMD-with Δexon50 displayed less adaptiveness to variations of the topographical cues (cell and sarcomere alignment), which was related to reduced actin turnover, as studied by fluorescence recovery after photobleaching (FRAP). This behavior was reproduced in a DMD CRISPR-Cas9 gene-edited cell line (Macadangdang et al., 2015). By comparison, hiPSC-CMs with a mutation in the RBM20 gene exhibited heterogeneous sarcomeric organization patterns. RBM20-engineered heart tissues (EHTs) showed impaired force of contraction and increased passive tension that was associated to a lower degree of the switch from the N2BA to the N2B isoform of titin, as a consequence of the S635A RBM20 mutation impacting on RNA splicing and transcription (Streckfuss-Bomeke et al., 2017). In a different way, loss of dystrophin may impact both cytoskeletal F-actin and sarcomeric actin in cardiomyocytes.

Myofibrils are the most abundant organelles of adult cardiomyocytes, occupying approximately 50–60% of the cytoplasmic volume. However, myofibrils are less represented in the contractile machinery of hiPSC-CMs, in which the sarcomere bands and lines gradually form in the advanced stages of maturation (Gherghiceanu et al., 2011). In this context, we investigated whether loss of dystrophin may affect the contractile properties at single myofibril level by applying a cell skinning protocol followed by tissue homogenizationto obtain single myofibrils, which were studied using a custom-made force-recording apparatus with fast solution switching, as previously described (Pioner et al., 2016). We found reduced tension production upon Ca-mediated activation in DMD myofibrils, as compared to controls. However, the kinetics of force development (k_{ACT}) and relaxation (slow k_{REL}) after calcium removal were not different, suggesting no changes in the rate of crossbridge cycling during tension development and detachment. Also, we found a slower fast phase of relaxation (fast k_{REL}), which is mainly regulated by inter-sarcomere dynamics (Pioner et al., 2019a; **Figure 4D**), paralleled by a slower contraction (shortening) of intact cells (**Figure 4B**). Altered myofibril contractile function could be related to developmental alterations, although the mechanism is not clear (**Figure 4A**). This should encourage future studies to better define the fundamental role of sarcomere protein composition for the definition of contractile properties. Another group investigated mutations in the dystrophin actin-binding domain (ABD1) causing truncated forms of dystrophin (DMD- Δ Exon 3–9, 6–9, or 7–11). Force measurements using multicellular preparations (engineered heart muscle, EHM) displayed lower force in DMD-mutant cell lines and the *de novo* insertion of the missing exon using CRISPR-Cas9 technology only partially restored the contractile performance. Among other DCM models, the hiPSC-CMs with absence/reduction of full-length dystrophin may contribute to evaluate the functional consequences of dystrophin loss and elucidate the role of a variety of proteins interacting around the N-terminal of full-length dystrophin, which are still elusive.

OVERCOMING THE LIMITATIONS OF HIPSC-CMS: PATIENT-SPECIFIC VALIDATION AND HIGH-THROUGHPUT STUDIES

To date, the possibility of using hiPSC-CMs to predict individual prognosis or response to therapies is limited by lack of direct validations, that is, patient-specific hiPSC-CMs have never been tested against actual adult cardiomyocytes from the same patient or from patients with a similar condition. This is due to the poor availability of human samples from patients with cardiomyopathies or other arrhythmogenic conditions, and the limited experience of many research centers in investigating fresh human myocardium and cardiomyocytes (Tardiff et al., 2015). We have recently developed a technique (Coppini et al., 2014) to isolate single ventricular cardiomyocytes and trabecule from the surgical samples of obstructive HCM patients. We were therefore able to study adult CMs in order to characterize the functional abnormalities of action potentials, ion currents, Ca^{2+} handling, myocardial contraction and relaxation, and test the effectiveness of different ion channel blockers such as ranolazine or disopyramide (Coppini et al., 2013; Coppini et al., 2018; Ferrantini et al., 2018). In Pioner et al. (2019b), we compared the physiological properties of iPSC-CMs from an healthy donor, differentiated using nanopatterned surfaces and long-term cultures, with those of adult cardiomyocytes from non-failing non-hypertrophic surgical patients (Pioner et al., 2019b). In terms of action potential shape and duration, calcium transient properties and response to β-adrenergic agonists, hiPSC-CMs at an advanced degree of maturation closely approximated the features of freshly isolated human adult cardiomyocytes (Pioner et al., 2019b). While obtaining fresh cardiac samples from DMD patients is hardly feasible, our technique can be developed to allow the isolation of cardiomyocytes from intramyocardial biopsies, to be used for functional studies in selected patients, allowing a direct comparison with individual hiPSC-CMs. Moreover, in order to improve hiPSC-CM maturation, single cardiomyocytes or 3D cultures (engineered heart tissues; Gupta et al., 2018) could be challenged during maturation using electrical stimulation at different pacing rates and periodic stretch-release protocols, simulating the contraction-relaxation cycle of the native heart (Sun and Nunes, 2017; Ronaldson-Bouchard et al., 2019). Such approach to cardiomyocyte differentiation might be easily achieved using smart contractile materials as culture substrates, such as liquid-crystal elastomer, which we recently developed and characterized (Martella et al., 2017; Ferrantini et al., 2019).

The possibility offered by hiPSC-CMs to identify patient- or mutation-specific mechanisms of disease and test novel therapies in a personalized manner is hampered by the fact that current approaches are extremely costly and time consuming. The development of rapid high-throughput assays to study the pathophysiological features of different hiPSC-CM lines and

TABLE 3 | Gene therapy strategies and application to hiPSC-CM models to restore dystrophin function.

Approach	Target mutation type	Dystrophin product	Strengths	Challenges	hiPSC-CM
Stop codon readthrough	Nonsense point mutations	Complete	• Well-tolerated (PTC124 or ataluren)	• *Low efficiency in the heart* • Low prevalence of amenable mutations • Frequent re-dosing	?
AON-mediated exon skipping	Frameshift mutations	Lacking existing deletion and additional exon(s)	• Well-tolerated • *Effective at cell level*	• Poor cardiac uptake of PMO • Frequent re-dosing • Low number of amenable mutations for each AON drug	• Efficacy • Reduced arrhythmias (Liang et al., 2019)
AAV micro-dystrophin	not interacting with endogenous gene)	Extensively truncated but functional	• *High efficacy in heart* • High efficacy in skeletal muscle • Lasting (multiple years)	• Potentially immunogenic • Potential for null effect with pre-existing immunity	?
CRISPR-Cas9	Frameshift, insertion, and nonsense mutations	Depends on editing strategy [ranging from complete to lacking deletion and additional exon(s)]	• *High efficacy in heart and skeletal muscle* • Versatile • Genomic correction is life-long (theoretically)	• Potentially immunogenic • *Risk of off-target editing* • Low number of amenable mutations for each CRISPR drug	• Efficacy • Restored contractile force of EHTs (Kyrychenko et al., 2017; Long et al., 2018; Min et al., 2019; Zhang et al., 2017)

test novel therapeutic approaches is therefore warranted. We recently developed a system to simultaneously record action potentials and intracellular Ca^{2+} from multiple iPSC-CMs using a fast camera, paralleled by a streamlined data analysis system to rapidly extract the main functional biomarkers from each recording (Pioner et al., 2019b). In an attempt to further improve the throughput of cell-line analysis, a possible approach would be an all-optical semi-automatic platform combining the parallel detection of multiple functional properties with electrode-free optogenetic control of electrical function in the sample. This approach would be feasible using genetically encoded voltage indicators (GEVIs) or calcium indicators (GECIs) (Kaestner et al., 2014; Huebsch et al., 2015; Shaheen et al., 2018) and gene-encoded actuators (channelrhodopsin) (Klimas et al., 2016). Such comprehensive platform, when combined with a semi-automated experimental-control and analysis system (Klimas et al., 2016), will allow repeatable longitudinal prolonged evaluations of iPSC-CMs at different time points and facilitate the evaluation of their response to different treatments. In addition to these technologies, CRISPR-Cas9 gene repair was recently improved by the newly discovered CRISPR-Cpf1 nuclease (Zhang et al., 2017). CRISPR-Cpf1 is driven by a single RNA guide (gRNA) and prefers T-rich protospacer adjacent motif (PAM) sequences: this feature is important for the potential correction of other disease-related mutations, because not all mutation sites contain G-rich PAM sequences for SpCas9 or PAMs for other Cas9 orthologs. Importantly, Cpf1 is about 140 amminoacids smaller than the most widely used SpCas9, which can potentially enhance the packaging and delivery by adenovirus, adeno-associated (AAV) or other viral constructs. Finally, Cpf1 can be used to permanently correct *DMD* mutations, restoring dystrophin expression and efficiently preventing the progression of the disease, as reported in DMD patient-derived iPSCs and *mdx* mice. The combination of biophysical approaches with the breakthrough of increasingly precise genome editing techniques may pave the way to a truly personalized medicine for DMD patients.

TRANSLATING STEM CELL MODELING FROM BENCH TO BED SIDE

Four groups of molecules are currently in use in the clinical management of patients with DMD cardiomyopathy: renin-angiotensin-inhibiting agents, beta-adrenergic receptor blockers, mineralocorticoid receptor antagonists and corticosteroids. Although useful for symptom management, none of these molecules is capable of modifying the natural history of the disease. Currently, none of the stem cell-based studies have reported or suggested novel pharmacological approaches for dystrophin-associated cardiomyopathies. Few pilot tests on animal models were attempted, using a membrane sealant

(Lin et al., 2015) or an immunoproteasome inhibitor (Farini et al., 2019), but these agents are not currently under development for use in patients. In other DCM models, a limited number of disease modifying therapeutic approaches were attempted, including the overexpression of Serca2a by viral-vector gene-therapy (Sun et al., 2012), and the modulation of SERCA/PLN through the mechanoreceptor protein integrin-linked kinase (ILK) (Traister et al., 2014). Indeed, most of the DCM hiPSC studies sought to identify novel mechanistic targets and were only labeled as a promising platform for a pharmacological therapy, but never used for an actual pharmacological validation. This is undoubtedly related to the immaturity of hiPSC-CM models and the fact that findings obtained using *in vitro* models cannot be so easily translated into trials *in vivo*.

In recent years, potentially curative approaches for DMD have begun to take shape. Unlike small molecule treatments, CRISPR-Cas9 or TALEN gene-targeted therapies are designed with the goal to induce expression of a functional gene product that will reestablish normal myocyte physiology. Since these therapies aim to repair the original defect in the cell by restoring functional dystrophin expression, their success is less dependent upon identifying the exact molecular consequences of the lack of dystrophin. As shown in **Table 3**, major efforts involved the use CRISPR-Cas9 in the design of mutation-specific therapies, which include exon skipping, reframe or deletion of portions in the DMD gene. Notably, successful restoration of contractile function was observed in a large group of hiPSC models carrying mutations in the ABD domain (mostly linked to BMD) or in the central domains (mostly associated to DMD) (Kyrychenko et al., 2017; Zhang et al., 2017; Long et al., 2018; Min et al., 2019). For this purpose, more effort should be moved toward the generation of BMD-patient cell lines (Gowran et al., 2018), as this patient group frequently diagnosed mid-life and is definitely an understudied group. In addition, BMD patients appear to be the most promising candidates for autologous cell transplantation as well as for *in vitro* studies aimed at identifying specific, novel targets that emerge in the presence of semi-functional truncated dystrophin proteins. Current strategies still lack the ability to obtain a lasting and efficient correction of the primary defect. In addition, DMD and BMD are associated with a variety of different mutations in the DMD gene. Therefore, a host of different therapeutic approaches are required for different patient subgroups, depending on the site and nature of their mutation. For instance, PTC124 (Ataluren) has been used in Europe to treat DMD patients carrying nonsense mutations (10% of total variants; Bladen et al., 2015). PTC124 renders ribosomes less sensitive to premature stop codons by promoting insertion of near-cognate tRNA at the site of nonsense codons with no apparent effects on downstream transcription, mRNA processing, or stability of the resulting protein, thereby allowing the production of functional dystrophin proteins. Ataluren works particularly well for the stop codon "UGA" (Welch et al., 2007). For this reason, the drug could be eligible for preclinical personalized tests on patient-specific stem cell-based models, which have been rarely attempted so far (Koopmann et al., 2012; Lee et al., 2017). Finally, innovative therapeutic approaches may consider repositioning drugs in use for other conditions or strategies acting on molecular factors that induce or downregulate common molecular pathways involved in genetic cardiomyopathies. Although such "universal" approaches will not restore dystrophin expression in the heart, they could still delay disease progression, be well tolerated, and be appropriate for a broader range of patients with DMD.

CONCLUSION

In this review, we analyzed the current insights of DMD-associated cardiomyopathy, from the clinical aspects to innovative disease modeling based on human iPSC derived cardiomyocytes, in the attempt to decipher specific mechanisms underlying DCM pathogenesis in DMD patients. Human models of iPSC-cardiomyocytes are a viable cell-based platform for investigating the human cardiac phenotype resulting from specific gene mutations. These models can recapitulate the facets of the physiology and pathophysiology of native cardiomyocytes, opening new opportunities for research. hiPSC-cardiomyocytes allow the study of unique individual patients without reliance on isogenic strains of animals and avoiding invasive biopsies of human cardiac tissue samples. Their progressive maturation of their cardiac phenotype, obtained with advanced differentiation techniques, is a powerful tool for investigating the early-stage consequences of dystrophin mutations that DMD, and their effects on cardiac development. Existing studies suggest that the pathogenic mechanisms appear early in the disease progression as a combination of the developmental consequences of the absence of full-length dystrophin (Dp427) in cardiomyocytes. Gene therapy with micro dystrophin, up-regulation of utrophin or exon skipping approaches are currently the most promising ways to rescue or at least mitigate the DMD phenotype. For this reason, despite the obvious limitations related mostly to their immature phenotype, the advent of hiPSC-cardiomyocytes presents a unique opportunity to improve our approach to the understanding of the pathophysiology of DMD cardiomyopathy.

AUTHOR CONTRIBUTIONS

JP, AF, and CF contributed to the design and wrote the manuscript in consultation with RC, LS, MD, SF, CP, and IO. JP and NC performed the meta-analysis and prepared figures and tables. All authors critically reviewed the manuscript and declared that the research was conducted in the absence of any commercial or financial relationships that could be construed as a potential conflict of interest.

FUNDING

This work was supported by Fondazione Telethon Italy (GGP16191), Fondazione Telethon-UILDM (GUP19012), 777204/Horizon 2020 (SILICO-FCM project).

REFERENCES

Ader, F., De Groote, P., Réant, P., Rooryck-Thambo, C., Dupin-Deguine, D., Rambaud, C., et al. (2019). FLNC pathogenic variants in patients with cardiomyopathies: prevalence and genotype-phenotype correlations. *Clin. Genet.* 96, 317–329. doi: 10.1111/cge.13594

Bedada, F. B., Chan, S. S., Metzger, S. K., Zhang, L., Zhang, J., Garry, D. J., et al. (2014). Acquisition of a quantitative, stoichiometrically conserved ratiometric marker of maturation status in stem cell-derived cardiac myocytes. *Stem Cell Rep.* 3, 594–605. doi: 10.1016/j.stemcr.2014.07.012

Bertero A, Fields PA, Smith AST, Leonard A, Beussman K, Sniadecki NJ, et al. (2019). Chromatin compartment dynamics in a haploinsufficient model of cardiac laminopathy. *J. Cell Biol.* 218, 2919–2944. doi: 10.1083/jcb.201902117

Birket MJ, Ribeiro MC, Kosmidis G, Ward D, Leitoguinho AR, van de Pol V, et al. (2015). Contractile defect caused by mutation in MYBPC3 revealed under conditions optimized for human PSC-Cardiomyocyte function. *Cell Rep.* 13, 733–745. doi: 10.1016/j.celrep.2015.09.025

Bladen, C. L., Salgado, D., Monges, S., Foncuberta, M. E., Kekou, K., and Kosma, K. (2015). The TREAT-NMD DMD global database: analysis of more than 7,000 duchenne muscular dystrophy mutations. *Hum Mutat.* 36, 395–402. doi: 10.1002/humu.22758

Blake, D. J., Tinsley, J. M., and Davies, K. E. (1996). Utrophin: a structural and functional comparison to dystrophin. *Brain Pathol.* 6, 37–47.

Bondue, A., Arbustini, E., Bianco, A., Ciccarelli, M., Dawson, D., De Rosa M., et al. (2018). Complex roads from genotype to phenotype in dilated cardiomyopathy: scientific update from the working group of myocardial function Of The European Society Of cardiology. *Cardiovascu. Rese* 114, 1287–1303.

Broughton, K. M., Li, J., Sarmah, E., Warren, C. M., Lin, Y. H., Henze, M. P., et al. (2016). A myosin activator improves actin assembly and sarcomere function of human-induced pluripotent stem cell-derived cardiomyocytes with a troponin T point mutation. *Am. J Physiol Heart Circ. Physiol.* 311, H107–H117. doi: 10.1152/ajpheart.00162.2016

Burridge, P. W., Diecke, S., Matsa, E., Sharma, A., Wu, H., and Wu, J. C. (2016). Modeling cardiovascular diseases with patient-specific human pluripotent stem cell-derived cardiomyocytes. *Methods Mol. Biol.* 1353, 119–130.

Cai W, Zhang J, de Lange WJ, Gregorich ZR, Karp H, Farrell ET, et al. (2019). an unbiased proteomics method to assess the maturation of human pluripotent stem cell-derived cardiomyocytes. *Circ. Res.* 125, 936–953. doi: 10.1161/CIRCRESAHA.119.315305

Caluori, G., Pribyl, J., Pesl, M., Jelinkova, S., Rotrekl, V., Skladal, P., et al. (2019). Non-invasive electromechanical cell-based biosensors for improved investigation of 3D cardiac models. *Biosens. Bioelectr.* 125, 129–135. doi: 10.1016/j.bios.2018.10.021

Campbell, M. D., Witcher, M., Gopal, A., and Michele, D. E. (2016). Dilated cardiomyopathy mutations in delta-sarcoglycan exert a dominant-negative effect on cardiac myocyte mechanical stability. *Am. J. Physiol Heart Circ. Physiol.* 310, H1140–H1150. doi: 10.1152/ajpheart.00521.2015

Capetanaki, Y., Papathanasiou, S., Diokmetzidou, A., Vatsellas, G., and Tsikitis, M., (2015). Desmin related disease: a matter of cell survival failure. *Curr. Opin. Cell Biol.* 32, 113–120. doi: 10.1016/j.ceb.2015.01.004

Ceholski, D. K., Turnbull, I. C., Kong, C. W., Koplev, S., Mayourian, J., Gorski, P. A., et al. (2018). Functional and transcriptomic insights into pathogenesis of R9C phospholamban mutation using human induced pluripotent stem cell-derived cardiomyocytes. *J. Mol. Cell. Cardiol.* 119, 147–154. doi: 10.1016/j.yjmcc.2018.05.007

Chang, A. C. Y., Chang, A. C. H., Kirillova, A., Sasagawa, K., Su, W., Weber, G., et al. (2018). Telomere shortening is a hallmark of genetic cardiomyopathies. *Proc. Nat;l. Acad. Sci. U.S.A* 115, 9276–9281.

Chevron, M. P., Girard, F., Claustres, M., and Demaille, J. (1994). Expression and subcellular localization of dystrophin in skeletal, cardiac and smooth muscles during the human development. *Neuromusc. Disord.* 4, 419–432.

Cho, G. S., Tampakakis, E., Andersen, P., and Kwon, C., (2017). Use of a neonatal rat system as a bioincubator to generate adult-like mature cardiomyocytes from human and mouse pluripotent stem cells. *Nat. Protoc.* 12, 2097–2109. doi: 10.1038/nprot.2017.089

Chopra, A., Kutys, M. L., Zhang, K., Polacheck, W. J., Sheng, C. C., Luu, R. J., et al. (2018). Force generation via beta-cardiac myosin, titin, and alpha-actinin drives cardiac sarcomere assembly from cell-matrix adhesions. *Dev. Cell* 44, 87.e5–96 e5. doi: 10.1016/j.devcel.2017.12.012

Coppini, R., Ferrantin, C., Aiazzi, A., Mazzoni, L., Sartianiet, L., Mugelli, A., et al. (2014). Isolation and functional characterization of human ventricular cardiomyocytes from fresh surgical samples. *J. Visual. Exp.* 86:e51116. doi: 10.3791/51116

Coppini, R., Ferrantini, C., Mugelli, A., Poggesi, C., and Cerbai, E. (2018). Altered Ca(2+) and Na(+) homeostasis in human hypertrophic cardiomyopathy: implications for arrhythmogenesis. *Front. Physiol.* 9:1391. doi: 10.3389/fphys.2018.01391

Coppini, R., Ferrantini, C., Yao, L., Fan, P., Del Lungo, M., and Stillitano, F. (2013). Late sodium current inhibition reverses electromechanical dysfunction in human hypertrophic cardiomyopathy. *Circulation* 127, 575–584. doi: 10.1161/CIRCULATIONAHA.112.134932

Corrado, G., Lissoni, A., Beretta, S., Terenghi, L., Tadeo, G., and Foglia-Manzillo, G. (2002). Prognostic value of electrocardiograms, ventricular late potentials, ventricular arrhythmias, and left ventricular systolic dysfunction in patients with duchenne muscular dystrophy. *Am. J. Cardiol.* 89, 838–841.

Davis, RP, van den Berg, CW, Casini S, Braam, S. R, Mummery, C. L. et al. (2011). Pluripotent stem cell models of cardiac disease and their implication for drug discovery and development. *Trends Mol. Med.* 17, 475–484. doi: 10.1016/j.molmed.2011.05.001

DeWitt, M. M., MacLeod, H. M., Soliven, B., and McNally, E. M. (2006). Phospholamban R14 deletion results in late-onset, mild, hereditary dilated cardiomyopathy. *J. Am. Col. Cardiol.* 48, 1396–1398.

Dick, E., Kalra, S., Anderson, D., George, V., Ritso, M., and Laval, S. H. (2013). Exon skipping and gene transfer restore dystrophin expression in human induced pluripotent stem cells-cardiomyocytes harboring DMD mutations. *Stem Cells Dev.* 22, 2714–2724. doi: 10.1089/scd.2013.0135

Dumont, N. A., Wang, Y. X., von Maltzahn, J., Pasut, A., Bentzinger, C. F., Brun, C. E., et al. (2015). Dystrophin expression in muscle stem cells regulates their polarity and asymmetric division. *Nat. Med.* 21, 1455–1463. doi: 10.1038/nm.3990

Eagle, M., Baudouin, S. V., Chandler, C., Giddings, D. R., Bullock, R., and Bushby, K. (2002). Survival in Duchenne muscular dystrophy: improvements in life expectancy since 1967 and the impact of home nocturnal ventilation. *Neuromusc. Disord.* 12, 926–929.

Eisen, B., Ben Jehuda, R., Cuttitta, A. J., Mekies, L. N., Shemer, Y., and Baskin, P. (2019). Electrophysiological abnormalities in induced pluripotent stem cell-derived cardiomyocytes generated from duchenne muscular dystrophy patients. *J. Cell. Mol. Med.* 23, 2125–2135. doi: 10.1111/jcmm.14124

El-Battrawy, I., Zhao, Z., Lan, H., Li, X., Yücel, G., Lang, S., et al. (2018). Ion channel dysfunctions in dilated cardiomyopathy in limb-girdle muscular dystrophy. *Circ.. Genomic Precis. Med.* 11:e001893. doi: 10.1161/CIRCGEN.117.001893

Ervasti, J. M. (2003). Costameres: the achillesl heel of herculean muscle. *J. Biol. Chem.* 278, 13591–13594.

Ervasti, J. M. (2007). Dystrophin, its interactions with other proteins, and implications for muscular dystrophy. *Biochim. Biophys. Acta* 1772, 108–117.

Ervasti, J. M., and Campbell, K. P. (1993). A role for the dystrophin-glycoprotein complex as a transmembrane linker between laminin and actin. *J. Cell Biol.* 122, 809–823.

Farini, A., Gowran, A., Bella, P., Sitzia, C., Scopece, A., Castiglioni, E., et al. (2019). Fibrosis rescue improves cardiac function in dystrophin-deficient mice and duchenne patient-specific cardiomyocytes by immunoproteasome modulation. *Am. J. Pathol.* 189, 339–353. doi: 10.1016/j.ajpath.2018.10.010

Farini, A., Sitzia, C., Cassinelli, L., Colleoni, F., Parolini, D., and Giovanella, U. (2016). Inositol 1,4,5-trisphosphate (IP3)-dependent Ca2+ signaling mediates delayed myogenesis in Duchenne muscular dystrophy fetal muscle. *Development* 143, 658–669. doi: 10.1242/dev.126193

Fayssoil, A., Abasse, S., and Silverston, K. (2017). Cardiac Involvement classification and therapeutic management in patients with duchenne muscular dystrophy. *J. Neuromusc. Dis.* 4, 17–23. doi: 10.3233/JND-160194

Fayssoil, A., Orlikowski, D., Nardi, O., and Annane, D. (2008). Complete atrioventricular block in duchenne muscular dystrophy. *Eur. Eur. Pacing, ArrhythmiasCardiac Electrophysiol.* 10, 1351–1352.

Fayssoil, A., Orlikowski, D., Nardi, O., and Annane, D. (2010). Pacemaker implantation for sinus node dysfunction in a young patient with duchenne muscular dystrophy. *Congest. Heart Fail.* 16, 127–128.

Fayssoil, A., Ritzenthaler, T., Luis, D., Hullin, T., Clair, B., Annane, D., et al. (2014). Be careful about abdominal discomfort in adult patients with muscular dystrophy. *Res. Neurol.* 170, 548–550. doi: 10.1016/j.neurol.2014.06.003

Ferrantini, C., Pioner, J. M., Martella, D., Coppini, R., Piroddi, N., Paoli, P., et al. (2019). Development of light-responsive liquid crystalline elastomers to assist cardiac contraction. *Circ. Res.* 124, e44–e54. doi: 10.1161/CIRCRESAHA.118.313889

Ferrantini, C., Pioner, J. M., Mazzoni, L., Gentile, F., Tosi, B., Rossi, A., et al. (2018). Late sodium current inhibitors to treat exercise-induced obstruction in hypertrophic cardiomyopathy: an in vitro study in human myocardium. *Br. J. Pharmacol.* 175, 2635–2652. doi: 10.1111/bph.14223

Frank, D., Yusuf Rangrez, A., Friedrich, C., Dittmann, S., Stallmeyer, B., Yadav, P., et al. (2019). Cardiac alpha-Actin (ACTC1) gene mutation causes atrial-septal defects associated with late-onset dilated cardiomyopathy. *Circ. Genomic Preci. Med.* 12, e002491. doi: 10.1161/CIRCGEN.119.002491

Frankel, K. A., and Rosser, R. J. (1976). The pathology of the heart in progressive muscular dystrophy: epimyocardial fibrosis. *Hum. Pathol.* 7, 375–386.

Gartz, M., Darlington, A., Afzal, M. Z., and Strande, J. L. (2018). Exosomes exert cardioprotection in dystrophin-deficient cardiomyocytes via ERK1/2-p38/MAPK signaling. *Sci. Rep.* 8, 16519. doi: 10.1038/s41598-018-34879-6

Gherghiceanu, M., Barad, L., Novak, A., Reiter, I., Itskovitz-Eldor, J., Binah, O., et al. (2011). Cardiomyocytes derived from human embryonic and induced pluripotent stem cells: comparative ultrastructure. *J. Cell. Mol. Med.* 15, 2539–2551. doi: 10.1111/j.1582-4934.2011.01417.x

Giatrakos, N., Kinali, M., Stephens, D., Dawson, D., Muntoni, F., and Nihoyannopoulos, P. (2006). Cardiac tissue velocities and strain rate in the early detection of myocardial dysfunction of asymptomatic boys with duchenne's muscular dystrophy: relationship to clinical outcome. *Heart* 92, 840–842.

Gigli, M., Merlo, M., Graw, S. L., Barbati, G., Rowland, T. J., Slavov, D. B., et al. (2019). Genetic risk of arrhythmic phenotypes in patients with dilated cardiomyopathy. *J. Am. Coll. Cardiol.* 74, 1480–1490. doi: 10.1016/j.jacc.2019.06.072

Gowran, A., Spaltro, G., Casalnuovo, F., Vigorelli, V., Spinelli, P., and Castiglioni, E. (2018). Generation of induced pluripotent stem cells from a Becker muscular dystrophy patient carrying a deletion of exons 45-55 of the dystrophin gene (CCMi002BMD-A-9 45-55). *Stem Cell Res.* 28, 21–24. doi: 10.1016/j.scr.2018.01.025

Guan, X., Mack, D. L., Moreno, C. M., Strande, J. L., Mathieu, J., and Shi, Y. (2014). Dystrophin-deficient cardiomyocytes derived from human urine: new biologic reagents for drug discovery. *Stem Cell Res.* 12, 467–480. doi: 10.1016/j.scr.2013.12.004

Gupta, N., Susa, K., Yoda, Y., Bonventre, J. V., Valerius, M. T., and Morizane, R. (2018). CRISPR/Cas9-based targeted genome editing for the development of monogenic diseases models with human pluripotent stem cells. *Curr. Protoc. Stem Cell Biol.* 45:e50. doi: 10.1002/cpsc.50

Hasselberg, N. E., Haland, T. F., Saberniak, J., Brekke, P. H., Berge, K. E., Leren, T. P., et al. (2018). Lamin A/C cardiomyopathy: young onset, high penetrance, and frequent need for heart transplantation. *Eur. Heart J.* 39, 853–860. doi: 10.1093/eurheartj/ehx596

Hershberger, R. E., Hedges, D. J., and Morales, A., (2013). Dilated cardiomyopathy: the complexity of a diverse genetic architecture. *Na. Rev. Cardiol.* 10, 531–547. doi: 10.1038/nrcardio.2013.105

Hinson, J. T., Chopra, A., Nafissi, N., Polacheck, W. J., Benson, C. C., Swist, S., et al. (2015). HEART DISEASE. Titin mutations in iPS cells define sarcomere insufficiency as a cause of dilated cardiomyopathy. *Science* 349, 982–986. doi: 10.1126/science.aaa5458

Hof, I. E., van der Heijden, J. F., Kranias, E. G., Sanoudou, D., de Boer, R. A., van Tintelen, J. P., et al. (2019). Prevalence and cardiac phenotype of patients with a phospholamban mutation. *Netherlands Heart J.* 27, 64–69.

Hoffman, E. P., Brown, R. H. Jr., and Kunkel, L. M. (1987). Dystrophin: the protein product of the Duchenne muscular dystrophy locus. *Cell* 51, 919–928.

Huebsch, N., Loskill, P., Mandegar, M. A., Marks, N. C., Sheehan, A. S., Ma, Z., et al. (2015). Automated video-based analysis of contractility and calcium flux in human-induced pluripotent stem cell-derived cardiomyocytes cultured over different spatial scales. *Tissue Eng Part C* 21, 467–479. doi: 10.1089/ten.TEC.2014.0283

Iodice, F., Testa, G., Averardi, M., Brancaccio, G., Amodeo, A., and Cogo, P. (2015). Implantation of a left ventricular assist device as a destination therapy in Duchenne muscular dystrophy patients with end stage cardiac failure: management and lessons learned. *Neuromusc. Disord.*25, 19–23. doi: 10.1016/j.nmd.2014.08.008

Iorga, B., Schwanke, K., Weber, N., Wendland, M., Greten, S., Piep, B., et al. (2017). Differences in contractile function of myofibrils within human embryonic stem cell-derived cardiomyocytes vs. adult ventricular myofibrils are related to distinct sarcomeric protein isoforms. *Front. Physiol.* 8:1111. doi: 10.3389/fphys.2017.01111

Itzhaki, I., Schiller, J., Beyar, R., Satin, J., and Gepstein, L., (2006). Calcium handling in embryonic stem cell-derived cardiac myocytes: of mice and men. *Ann. N. Y. Acad. Sci.* 1080, 207–215.

Japp, A. G., Gulati, A., Cook, S. A., Cowie, M. R., and Prasad, S. K., (2016). The diagnosis and evaluation of dilated cardiomyopathy. *J. Am. Coll. Cardiol.* 67, 2996–3010. doi: 10.1016/j.jacc.2016.03.590

Jelinkova, S., Fojtik, P., Kohutova, A., Vilotic, A., Markova, L., Pesl, M., et al. (2019). Dystrophin deficiency leads to genomic instability in human pluripotent stem cells via no synthase-induced oxidative stress. *Cells* 8:53. doi: 10.3390/cells8010053

Judge, L. M., Perez-Bermejo, J. A., Truong, A., Ribeiro, A. J., Yoo, J. C., and Jensen, C. L. (2017). A BAG3 chaperone complex maintains cardiomyocyte function during proteotoxic stress. *JCI Insight* 2:e94623. doi: 10.1172/jci.insight.94623

Kaestner, L., Scholz, A., Tian, Q. H., Ruppenthal, S., Tabellion, W., and Wiesen, K. (2014). Genetically Encoded Ca2+ indicators in cardiac myocytes. *Circ. Res.* 114, 1623–1639. doi: 10.1161/CIRCRESAHA.114.303475

Kaprielian, R. R., and Severs, N. J. (2000). Dystrophin and the cardiomyocyte membrane cytoskeleton in the healthy and failing heart. *Heart Fail Rev.* 5, 221–238.

Kaprielian, R. R., Stevenson, S., Rothery, S. M., Cullen, M. J., and Severs, N. J. (2000). Distinct patterns of dystrophin organization in myocyte sarcolemma and transverse tubules of normal and diseased human myocardium. *Circulation* 101, 2586–2594.

Karakikes, I., Stillitano, F., Nonnenmacher, M., Tzimas, C., Sanoudou, D., and Termglinchan, V. (2015). Correction of human phospholamban R14del mutation associated with cardiomyopathy using targeted nucleases and combination therapy. *Nat. Commun.* 6:6955. doi: 10.1038/ncomms7955

Klimas, A., Ambrosi, C. M., Yu, J. Z., Williams, J. C., Bien, H., and Entcheva, E. (2016). OptoDyCE as an automated system for high-throughput all-optical dynamic cardiac electrophysiology. *Nat. Commun.* 7:11542. doi: 10.1038/ncomms11542

Koopmann, T. T., Verkerk, A. O., Bezzina, C. R., de Bakker, J. M., and Wilde, A. A. (2012). The chemical compound PTC124 does not affect cellular electrophysiology of cardiac ventricular myocytes. *Cardiovascu. Drugs Ther.* 26, 41–45.

Kyrychenko, V., Kyrychenko, S., Tiburcy, M., Shelton, J. M., Long, C., and Schneider, J. W. (2017). Functional correction of dystrophin actin binding domain mutations by genome editing. *JCI Insight* 2:e95918. doi: 10.1172/jci.insight.95918

Le, S., Yu, M., Hovan, L., Zhao, Z., Ervasti, J., and Yan, J. (2018). Dystrophin As a Molecular Shock Absorber. *ACS Nano* 12, 12140–12148. doi: 10.1021/acsnano.8b05721

Lee, Y. K., Lau, Y. M., Cai, Z. J., Lai, W. H., Wong, L. Y., Tse, H. F., et al. (2017). Modeling treatment response for lamin A/C related dilated cardiomyopathy in human induced pluripotent stem cells. *J. Am. Heart Assoc.* 6:e005677. doi: 10.1161/JAHA.117.005677

Leyva-Leyva, M., Sandoval, A., Felix, R., and Gonzalez-Ramirez, R. (2018). Biochemical and functional interplay between ion channels and the components of the dystrophin-associated glycoprotein complex. *J. Memb. Biol.* 251, 535–550. doi: 10.1007/s00232-018-0036-9

Li, X., Lu, W. J., Li, Y., Wu, F., Bai, R., Ma, S., et al. (2019). MLP-deficient human pluripotent stem cell derived cardiomyocytes develop hypertrophic cardiomyopathy and heart failure phenotypes due to abnormal calcium handling. *Cell Death Dis.* 10:610. doi: 10.1038/s41419-019-1826-4

Liang, W., Duan, Y. P., Shang, B. R., Wang, Y. P., Hu, C., and Lippke, S. (2019). A web-based lifestyle intervention program for Chinese college students: study

protocol and baseline characteristics of a randomized placebo-controlled trial. *BMC Public Health* 19:1097. doi: 10.1186/s12889-019-7438-1

Lin, B., Li, Y., Han, L., Kaplan, A. D., Ao, Y., Kalra, S., et al. (2015). Modeling and study of the mechanism of dilated cardiomyopathy using induced pluripotent stem cells derived from individuals with duchenne muscular dystrophy. *Dis. Models Mech.* 8, 457–466. doi: 10.1242/dmm.019505

Lipshultz, S. E., Sleeper, L. A., Towbin, J. A., Lowe, A. M., Orav, E. J., Cox, G. F., et al. et al. (2003). The incidence of pediatric cardiomyopathy in two regions of the United States. *N. Eng. J. Med.* 348, 1647–1655.

Long, C., Li, H., Tiburcy, M., Rodriguez-Caycedo, C., Kyrychenko, V., and Zhou, H. (2018). Correction of diverse muscular dystrophy mutations in human engineered heart muscle by single-site genome editing. *Sci. Adv.* 4:eaa9004. doi: 10.1126/sciadv.aap9004

Lundy, S. D., Zhu, W. Z., Regnier, M., and Laflamme, M. A., (2013). Structural and functional maturation of cardiomyocytes derived from human pluripotent stem cells. *Stem Cells Dev.* 22, 1991–2002. doi: 10.1089/scd.2012.0490

Macadangdang, J., Guan, X., Smith, A. S., Lucero, R., Czerniecki, S., Childers, M. K., et al. (2015). Nanopatterned Human iPSC-based model of a dystrophin-null cardiomyopathic phenotype. *Cell. Mol. Bioeng.* 8, 320–332.

Macadangdang, J., Lee, H. J., Carson, D., Jiao, A., Fugate, J., Pabon, L., et al. (2014). Capillary force lithography for cardiac tissue engineering. *J. Visual. Exp.* 88:e50039. doi: 10.3791/50039

Madhavan, R., and Jarrett, H. W. (1994). Calmodulin-activated phosphorylation of dystrophin. *Biochemistry* 33:5797–5804.

Mandel, J. L. (1989). Dystrophin. The gene and its product. *Nature* 339, 584–586.

Manning, G. W., and Cropp, G. J. (1958). The electrocardiogram in progressive muscular dystrophy. *Br. Heart J.* 20, 416–420.

Markham, L. W., Kinnett, K., Wong, B. L., Woodrow Benson, D., and Cripe, L. H. (2008). Corticosteroid treatment retards development of ventricular dysfunction in Duchenne muscular dystrophy. *Neuromusc. Disord.* 18, 365–370.

Markham, L. W., Michelfelder, E. C., Border, W. L., Khoury, P. R., Spicer, R. L., and Wong, B. L. (2006). Abnormalities of diastolic function precede dilated cardiomyopathy associated with Duchenne muscular dystrophy. *J. Am. Soc. Echocardiogr.* 19, 865–871.

Maroto, R., Raso, A., Wood, T. G., Kurosky, A., Martinac, B., and Hamill, O. P. (2005). TRPC1 forms the stretch-activated cation channel in vertebrate cells. *Nat. Cell Biol.* 7, 179–185.

Martella, D., Paoli, P., Pioner, J. M., Sacconi, L., Coppini, R., Santini, L., et al. (2017). Liquid crystalline networks toward regenerative medicine and tissue repair. *Small* 13:46. doi: 10.1002/smll.201702677

Massourides, E., Polentes, J., Mangeot, P. E., Mournetas, V., Nectoux, J., Deburgrave, N., et al. (2015). Dp412e: a novel human embryonic dystrophin isoform induced by BMP4 in early differentiated cells. *Skeletal Muscle* 5:40. doi: 10.1186/s13395-015-0062-6

McNair, W. P., Sinagra, G., Taylor, M. R., Di Lenarda, A., Ferguson, D. A., et al. (2011). SCN5A mutations associate with arrhythmic dilated cardiomyopathy and commonly localize to the voltage-sensing mechanism. *J. Am. Coll. Cardiol.* 57, 2160–2168. doi: 10.1016/j.jacc.2010.09.084

McNally, E. M. (2007). New approaches in the therapy of cardiomyopathy in muscular dystrophy. *Ann. Rev. Med.* 58, 75–88.

McNally, E. M. (2017). Cardiomyopathy in muscular dystrophy: when to treat? *JAMA Cardiol.* 2:199.

McNally, E. M., Kaltman, J. R., Benson, D. W., Canter, C. E., Cripe, L. H., Duan, D., et al. (2015). Parent project muscular, contemporary cardiac issues in duchenne muscular dystrophy. working group of the national heart, lung, and blood institute in collaboration with parent project muscular dystrophy. *Circulation* 131, 1590–1598.

McNally, E. M., and Mestroni, L., (2017). Dilated cardiomyopathy: genetic determinants and mechanisms. *Circ. Res.* 121, 731–748.

Mendell, J. R., Shilling, C., Leslie, N. D., Flanigan, K. M., R. al-Dahhak, J. Gastier-Foster, et al. (2012). Evidence-based path to newborn screening for duchenne muscular dystrophy. *Ann. Neurol.* 71 304–313. doi: 10.1002/ana.23528

Meng, H., Leddy, J. J., Frank, J., Holland, P., and Tuana, B. S. (1996). The association of cardiac dystrophin with myofibrils/Z-disc regions in cardiac muscle suggests a novel role in the contractile apparatus. *T J. Bio. Chem.* 271, 12364–12371.

Merlo, M., Sinagra, G., Carniel, E., Slavov, D., Zhu, X., Barbati, G., et al. (2013). Poor prognosis of rare sarcomeric gene variants in patients with dilated cardiomyopathy. *Clin. Trans. Sci.* 6, 424–428. doi: 10.1111/cts.12116

Merrick, D., Stadler, L. K., Larner, D., and Smith, J. (2009). Muscular dystrophy begins early in embryonic development deriving from stem cell loss and disrupted skeletal muscle formation. *Dis. Models Mech.* 2, 374–388. doi: 10.1242/dmm.001008

Mertens, L., Ganame, J., Claus, P., Goemans, N., Thijs, D., and Eyskens, B. (2008). Early regional myocardial dysfunction in young patients with duchenne muscular dystrophy. *J. Am. Soc. Echocardiogr.* 21, 1049–1054.

Mestroni, L., Brun, F., Spezzacatene, A., Sinagra, G., and Taylor, M. R. (2014). Genetic causes of dilated cardiomyopathy. *Prog. Pediatr. Cardiol.* 37, 13–18.

Min, Y. L., Li, H., Rodriguez-Caycedo, C., Mireault, A. A., Huang, J., and Shelton, J. M. (2019). CRISPR-Cas9 corrects duchenne muscular dystrophy exon 44 deletion mutations in mice and human cells. *Sci. Adv.* 5:eaav4324. doi: 10.1126/sciadv.aav4324

Mitzelfelt, K. A., Limphong, P., Choi, M. J., Kondrat, F. D., Lai, S., and Kolander, K. D. (2016). The Human 343delT HSPB5 chaperone associated with early-onset skeletal myopathy causes defects in protein solubility. *J. Biol Chem.* 291, 14939–14953. doi: 10.1074/jbc.M116.730481

Mora, M., Di Blasi, C., Barresi, R., Morandi, L., Brambati, B., Jarre, L., et al. (1996). Developmental expression of dystrophin, dystrophin-associated glycoproteins and other membrane cytoskeletal proteins in human skeletal and heart muscle. *Brain Res.. Dev. Brain Res.* 91, 70–82.

Mora, M., Morandi, L., Merlini, L., Vita, G., Baradello, A., and Barresi, R. (1994). Fetus-like dystrophin expression and other cytoskeletal protein abnormalities in centronuclear myopathies. *Muscle Nerve* 17, 1176–1184.

Moreau, A., Gosselin-Badaroudine, P., Mercier, A., Burger, B., Keller, D. I., and Chahine, M. (2018). A leaky voltage sensor domain of cardiac sodium channels causes arrhythmias associated with dilated cardiomyopathy. *Sci. Rep.* 8:13804. doi: 10.1038/s41598-018-31772-0

Moretti, A., Fonteyne, L., Giesert, F., Hoppmann, P., Meier, A. B., Bozoglu, T., et al. (2020). Somatic gene editing ameliorates skeletal and cardiac muscle failure in pig and human models of duchenne muscular dystrophy. *Nat. Med.* 26, 207–214. doi: 10.1038/s41591-019-0738-2

Mosqueira, M., Zeiger, U., Forderer, M., Brinkmeier, H., and Fink, R. H. (2013). Cardiac and respiratory dysfunction in duchenne muscular dystrophy and the role of second messengers. *Med. Res. Rev.* 33, 1174–1213. doi: 10.1002/med.21279

Muntoni, F. (2003). Cardiomyopathy in muscular dystrophies. *Curr,. Opin. Neurol.* 16, 577–583.

Muntoni, F., Torelli, S., and Ferlini, A. (2003). Dystrophin and mutations: one gene, several proteins, multiple phenotypes. *Lancet. Neurol.* 2, 731–740.

Nanni, S., Re, A., Ripoli, C., Gowran, A., Nigro, P., D'Amario, D., et al. (2016). The nuclear pore protein Nup153 associates with chromatin and regulates cardiac gene expression in dystrophic mdx hearts. *Cardiovasc. Res.* 112, 555–567. doi: 10.1093/cvr/cvw204

Ng, R., Manring, H., Papoutsidakis, N., Albertelli, T., Tsai, N., and See, C. J. (2019). Patient mutations linked to arrhythmogenic cardiomyopathy enhance calpain-mediated desmoplakin degradation. *JCI Insight* 5:e128643. doi: 10.1172/jci.insight.128643

Nigro, G., Comi, L. I., Politano, L., and Bain, R. J. (1990). The incidence and evolution of cardiomyopathy in duchenne muscular dystrophy. *Int. J. Cardiol.* 26, 271–277.

Nunes, S. S., Miklas, J. W., Liu, J., R. Aschar-Sobbi, Xiao, Y., Zhang, B., et al. (2013). Biowire: a platform for maturation of human pluripotent stem cell-derived cardiomyocytes. *Nat. Methods* 10, 781–787. doi: 10.1038/nmeth.2524

Ortiz-Genga, MF, Cuenca, S, Dal Ferro, M, Zorio, E, Salgado-Aranda, R, Climent, V, (2016). Truncating FLNC mutations are associated with high-risk dilated and arrhythmogenic cardiomyopathies. *J. Am. Coll. Cardiol.* 68, 2440–2451.

Perloff, J. K. (1984). Cardiac rhythm and conduction in duchenne's muscular dystrophy: a prospective study of 20 patients. *J. Am. Coll. Cardiol.* 3, 1263–1268.

Pioner, J. M., Guan, X., Klaiman, J. M., Racca, A. W., Pabon, L., and Muskheli, V. (2019a). Absence of full-length dystrophin impairs normal maturation and contraction of cardiomyocytes derived from human induced pluripotent stem cells. *Cardiovas. Res.* 116, 368–382. doi: 10.1093/cvr/cvz109

Pioner, J. M., Santini, L., Palandri, C., Martella, D., Lupi, F., Langione, M., et al. (2019b). Optical investigation of action potential and calcium handling

maturation of hiPSC-Cardiomyocytes on biomimetic substrates. *Int. J. Mol. Sci.* 20:3799. doi: 10.3390/ijms20153799

Pioner, J. M., Racca, A. W., Klaiman, J. M., Yang, K. C., Guan, X., Pabon, L., et al. (2016). Isolation and mechanical measurements of myofibrils from human induced pluripotent stem cell-derived cardiomyocytes. *Stem Cell Rep.* 6, 885–896. doi: 10.1016/j.stemcr.2016.04.006

Priori, S. G., Blomstrom-Lundqvist, C., Mazzanti, A., Blom, N., Borggrefe, M., Camm, J., et al. (2015). 2015 ESC guidelines for the management of patients with ventricular arrhythmias and the prevention of sudden cardiac death: the task force for the management of patients with ventricular arrhythmias and the prevention of sudden cardiac death of the European Society of Cardiology (ESC). Endorsed by: association for European Paediatric and Congenital Cardiology (AEPC). *Eur. Heart J.* 36, 2793–2867.

Racca, A. W., Klaiman, J. M., Pioner, J. M., Cheng, Y., Beck, A. E., Moussavi-Harami, F., et al. (2016). Contractile properties of developing human fetal cardiac muscle. *J. Physiol* 594, 437–452. doi: 10.1113/JP271290

Rahimov, F., and Kunkel, L. M. (2013). The cell biology of disease: cellular and molecular mechanisms underlying muscular dystrophy. *J. Cell Biol.* 201, 499–510. doi: 10.1083/jcb.201212142

Rakar, S., Sinagra, G., Di Lenarda, A., Poletti, A., Bussani, R., Silvestri, F., et al. (1997). Epidemiology of dilated cardiomyopathy. a prospective post-mortem study of 5252 necropsies. the heart muscle disease study group. *Eur. Heart J.* 18, 117–123.

Refaat, M. M., Lubitz, S. A., Makino, S., Islam, Z., Frangiskakis, J. M., Mehdi, H., et al. (2012). Genetic variation in the alternative splicing regulator RBM20 is associated with dilated cardiomyopathy. *Heart Rhythm* 9, 390–396. doi: 10.1016/j.hrthm.2011.10.016

Reiser, P. J., Portman, M. A., Ning, X. H., and C. Schomisch Moravec, (2001). Human cardiac myosin heavy chain isoforms in fetal and failing adult atria and ventricles. American journal of physiology. *Heart Circ. Physiol.* 280, H1814–H1820.

Ribeiro, M. C., Tertoolen, L. G., Guadix, J. A., Bellin, M., Kosmidis, G., C. D'Aniello, J et al. (2015).Functional maturation of human pluripotent stem cell derived cardiomyocytes in vitro–correlation between contraction force and electrophysiology. *Biomaterials* 51, 138–150. doi: 10.1016/j.biomaterials.2015.01.067

Ripoll-Vera, T., Gámez, J. M., Govea, N., Gómez, Y., Núñez, J., Socías, L., et al. (2016). Clinical and prognostic profiles of cardiomyopathies caused by mutations in the troponin T Gene. *Rev. Espanola Cardiol.* 69, 149–158. doi: 10.1016/j.rec.2015.06.025

Rohani, L., Machiraju, P., Sabouny, R., Meng, G., Liu, S., Zhao, T., et al. (2020). Reversible mitochondrial fragmentation in iPSC-derived cardiomyocytes from children with DCMA, a mitochondrial cardiomyopathy. *Can. J. Cardiol.* 36, 554–563. doi: 10.1016/j.cjca.2019.09.021

Ronaldson-Bouchard, K., Ma, S. P., Yeager, K., Chen, T., Song, L., Sirabella, D., et al. (2018). Advanced maturation of human cardiac tissue grown from pluripotent stem cells. *Nature* 556, 239–243. doi: 10.1038/s41586-018-0016-3

Ronaldson-Bouchard, K., Yeager, K., Teles, D., Chen, T., Ma, S., Song, L., et al. (2019). Engineering of human cardiac muscle electromechanically matured to an adult-like phenotype. *Nat. Protoc.* 14, 2781–2817. doi: 10.1038/s41596-019-0189-8

Salvarani, N., Crasto, S., Miragoli, M., Bertero, A., Paulis, M., Kunderfranco, P., et al. (2019). The K219T-Lamin mutation induces conduction defects through epigenetic inhibition of SCN5A in human cardiac laminopathy. *Nat. Commun.* 10:2267. doi: 10.1038/s41467-019-09929-w

Sartiani, L., Bettiol, E., Stillitano, F., Mugelli, A., Cerbai, E., Jaconi, M. E., et al. (2007). Developmental changes in cardiomyocytes differentiated from human embryonic stem cells: a molecular and electrophysiological approach. *Stem Cells* 25, 1136–1144.

Sasse, S., Brand, N. J., Kyprianou, P., Dhoot, G. K., Wade, R., Arai, M., et al. (1993). Troponin I gene expression during human cardiac development and in end-stage heart failure. *Circ. Res.* 72, 932–938.

Sato, M., Shiba, N., Miyazaki, D., Shiba, Y., Echigoya, Y., and Yokota, T. (2019). Amelioration of intracellular Ca(2+) regulation by exon-45 skipping in Duchenne muscular dystrophy-induced pluripotent stem cell-derived cardiomyocytes. *Biochem Biophys. Res. Commun.* 520, 179–185. doi: 10.1016/j.bbrc.2019.09.095

Schick, R., Mekies, L. N., Shemer, Y., Eisen, B., Hallas, T., Ben Jehuda R., et al. (2018). Functional abnormalities in induced pluripotent Stem Cell-derived cardiomyocytes generated from titin-mutated patients With dilated cardiomyopathy. *PloS One* 13:e0205719.

Schmitt, J. P., Kamisago, M., Asahi, M., Li, G. H., Ahmad, F., Mende, U., et al. (2003). Dilated cardiomyopathy and heart failure caused by a mutation in phospholamban. *Science* 299, 1410–1413.

Shafaattalab, S., Li, A. Y., Lin, E., Stevens, C. M., Dewar, L. J., and Lynn, F. C. (2019). In vitro analyses of suspected arrhythmogenic thin filament variants as a cause of sudden cardiac death in infants. *Proc. Natl. Acad. Sci. U.S.A.* 116, 6969–6974. doi: 10.1073/pnas.1819023116

Shah, D., Virtanen, L., Prajapati, C., Kiamehr, M., Gullmets, J., West, G., et al. (2019). Modeling of LMNA-related dilated cardiomyopathy using human induced pluripotent stem cells. *Cells* 8:594.

Shaheen, N., Shiti, A., Huber, I., Shinnawi, R., Arbel, G., and Gepstein, A. (2018). Human induced pluripotent stem cell-derived cardiac cell sheets expressing genetically encoded voltage indicator for pharmacological and arrhythmia studies. *Stem cell Rep.* 10, 1879–1894. doi: 10.1016/j.stemcr.2018.04.006

Shimojima, M., Yuasa, S., Motoda, C., Yozu, G., Nagai, T., Ito, S., et al. (2017). Emerin plays a crucial role in nuclear invagination and in the nuclear calcium transient. *Sci. Rep.* 7, 44312. doi: 10.1038/srep44312

Shirokova, N., and Niggli, E. (2013). Cardiac phenotype of duchenne muscular dystrophy: insights from cellular studies. *J. Mol. Cell. Cardiol.* 58, 217–224. doi: 10.1016/j.yjmcc.2012.12.009

Silva, M. C., Magalhaes, T. A., Meira, Z. M., Rassi, C. H., Andrade, A. C., Gutierrez, P. S., et al. (2017). Myocardial fibrosis progression in duchenne and becker muscular dystrophy: a randomized clinical trial. *JAMA Cardiol.* 2, 190–199.

Siu, C. W., Lee, Y. K., Ho, J. C., Lai, W. H., Chan, Y. C., Ng, K. M., et al. (2012). Modeling of lamin A/C mutation premature cardiac aging using patient-specific induced pluripotent stem cells. *Aging* 4, 803–822.

Stillitano, F., Turnbull, I. C., Karakikes, I., Nonnenmacher, M., Backeris, P., and Hulot, J. S. (2016). Genomic correction of familial cardiomyopathy in human engineered cardiac tissues. *Eur. Heart J.* 37, 3282–3284.

Streckfuss-Bomeke, K, Tiburcy, M., Fomin, A., Luo, X., Li, W., Fischer, C., et al. (2017). Severe DCM phenotype of patient harboring RBM20 mutation S635A can be modeled by patient-specific induced pluripotent stem cell-derived cardiomyocytes. *J. Mol. Cell Cardiol.* 113, 9–21. doi: 10.1016/j.yjmcc.2017.09.008

Stroik, D. R., Ceholski, D. K., Bidwell, P. A., Mleczko, J., Thanel, P. F., and Kamdar, F. (2019). Viral expression of a SERCA2a-activating PLB mutant improves calcium cycling and synchronicity in dilated cardiomyopathic hiPSC-CMs. *J. Mol. Cell. Cardiol.* 138, 59–65. doi: 10.1016/j.yjmcc.2019.11.147

Sun, N., Yazawa, M., Liu, J., Han, L., Sanchez-Freire, V., and Abilez, O. J. (2012). Patient-specific induced pluripotent stem cells as a model for familial dilated cardiomyopathy. *Sci. Transl. Med.* 4, 130ra47. doi: 10.1126/scitranslmed.3003552

Sun, X., and Nunes, S. S. (2017). Bioengineering approaches to mature human pluripotent stem Cell-Derived cardiomyocytes. *Front. Cell Dev. Biol.* 5:19. doi: 10.3389/fcell.2017.00019

Takahashi, K., and Yamanaka, S. (2006). Induction of pluripotent stem cells from mouse embryonic and adult fibroblast cultures by defined factors. *Cell* 126, 663–676.

Takami, Y., Takeshima, Y., Awano, H., Okizuka, Y., Yagi, M., and Matsuo, M. (2008). High incidence of electrocardiogram abnormalities in young patients with duchenne muscular dystrophy. *Pediatr. Neurol* 39, 399–403. doi: 10.1016/j.pediatrneurol.2008.08.006

Takasaki, A., Hirono, K., Hata, Y., Wang, C., Takeda, M., Yamashita, J. K., et al. (2018). Sarcomere gene variants act as a genetic trigger underlying the development of left ventricular noncompaction. *Pediatr. Res.* 84, 733–742. doi: 10.1038/s41390-018-0162-1

Tardiff, J. C., Carrier, L., Bers, D. M., Poggesi, C., Ferrantini, C., and Coppini, R. (2015). Targets for therapy in sarcomeric cardiomyopathies. *Cardiovasc Res.* 105, 457–470. doi: 10.1093/cvr/cvv023

Taylor, M. R., Slavov, D., Ku, L., Lenarda, A. Di, Sinagra, G., Carniel, E., et al. (2007). Prevalence of desmin mutations in dilated cardiomyopathy. *Circulation* 115, 1244–1251.

Towbin, J. A., Hejtmancik, J. F., Brink, P., Gelb, B., Zhu, X. M., Chamberlain, J. S., et al. (1993). X-linked dilated cardiomyopathy. Molecular genetic evidence of linkage to the Duchenne muscular dystrophy (dystrophin) gene at the Xp21 locus. *Circulation* 87, 1854–1865.

Traister, A., Li, M., Aafaqi, S., Lu, M., Arab, S., Radisic, M., et al. (2014). Integrin-linked kinase mediates force transduction in cardiomyocytes by modulating SERCA2a/PLN function. *Nat. Commun.* 5, 4533. doi: 10.1038/ncomms5533

Tse, H. F., Ho, J. C., Choi, S. W., Lee, Y. K., Butler, A. W., Ng, K. M., et al. (2013). Patient-specific induced-pluripotent stem cells-derived cardiomyocytes recapitulate the pathogenic phenotypes of dilated cardiomyopathy due to a novel DES mutation identified by whole exome sequencing. *Hum. Mol. Genet.* 22, 1395–1403. doi: 10.1093/hmg/dds556

Tsurumi, F., Baba, S., Yoshinaga, D., Umeda, K., Hirata, T., Takita, J., et al. (2019). The intracellular Ca2+ concentration is elevated in cardiomyocytes differentiated from hiPSCs derived from a Duchenne muscular dystrophy patient. *PloS One* 14:e0213768. doi: 10.1371/journal.pone.0213768

Tulloch, N. L., Muskheli, V., Razumova, M. V., Korte, F. S., Regnier, M., Hauch, K. D., et al. (2011). Growth of engineered human myocardium with mechanical loading and vascular coculture. *Circ. Res.* 109, 47–59. doi: 10.1161/CIRCRESAHA.110.237206

Ulmer, B. M., and Eschenhagen, T., (2019). Human pluripotent stem cell-derived cardiomyocytes for studying energy metabolism. *Biochim. Biophys. Acta. Mol. Cell Res.* 1867: 118471 doi: 10.1016/j.bbamcr.2019.04.001

van den Berg, C. W., Okawa, S., Chuva de Sousa Lopes , S. M., van Iperen, L., Passier, R., Braam, S. R., et al. (2015). Transcriptome of human foetal heart compared with cardiomyocytes from pluripotent stem cells. *Development* 142, 3231–3238. doi: 10.1242/dev.123810

van der Zwaag, P. A., van Rijsingen , I. A., Asimaki, A., Jongbloed, J. D., van Veldhuisen , D. J., Wiesfeld, A. C., et al. (2012). Phospholamban R14del mutation in patients diagnosed with dilated cardiomyopathy or arrhythmogenic right ventricular cardiomyopathy: evidence supporting the concept of arrhythmogenic cardiomyopathy. *Eur. J. Heart Fail.* 14, 1199–1207. doi: 10.1093/eurjhf/hfs119

Vasile, V. C., Will, M. L., Ommen, S. R., Edwards, W. D., Olson, T. M., and Ackerman, M. J. (2006). Identification of a metavinculin missense mutation, R975W, associated with both hypertrophic and dilated cardiomyopathy. *Mol. Genet. Metab.* 87, 169–174.

Verdonschot JAJ, Hazebroek MR, Derks KWJ, Barandiarán Aizpurua A, Merken JJ, Wang P, et al. (2018). Titin cardiomyopathy leads to altered mitochondrial energetics, increased fibrosis and long-term life-threatening arrhythmias. *Eur. Heart J.* 39, 864–873. doi: 10.1093/eurheartj/ehx808

Vogel, C., and Marcotte, E. M. (2012). Insights into the regulation of protein abundance from proteomic and transcriptomic analyses. *Nat. Rev. Genet.* 13, 227–232. doi: 10.1038/nrg3185

Wang, G., McCain, M. L., Yang, L., He, A., Pasqualini, F. S., and Agarwal, A. (2014). Modeling the mitochondrial cardiomyopathy of Barth syndrome with induced pluripotent stem cell and heart-on-chip technologies. *Nat. Med.* 20, 616–623. doi: 10.1038/nm.3545

Wang, L., Kim, K., Parikh, S., Cadar, A. G., Bersell, K. R., He, H., et al. (2018). Hypertrophic cardiomyopathy-linked mutation in troponin T causes myofibrillar disarray and pro-arrhythmic action potential changes in human iPSC cardiomyocytes. *J. Mol. Cell. Cardiol.* 114, 320–327. doi: 10.1016/j.yjmcc.2017.12.002

Wang, M., Birnkrant, D. J., Super, D. M., Jacobs, I. B., and Bahler, R. C. (2018). Progressive left ventricular dysfunction and long-term outcomes in patients with Duchenne muscular dystrophy receiving cardiopulmonary therapies. *Open Heart* 5:e000783. doi: 10.1136/openhrt-2018-000783

Weber, N., Schwanke, K., Greten, S., Wendland, M., Iorga, B., Fischer, M., et al. (2016). Stiff matrix induces switch to pure beta-cardiac myosin heavy chain expression in human ESC-derived cardiomyocytes. *Basic Res. Cardiol.* 111:68.

Welch, E. M., Barton, E. R., Zhuo, J., Tomizawa, Y., Friesen, W. J., and Trifillis, P. (2007). targets genetic disorders caused by nonsense mutations. *Nature* 447, 87–91.

Wolska, B. M., Vijayan, K., Arteaga, G. M., Konhilas, J. P., Phillips, R. M., Kim, R., et al. (2001). Expression of slow skeletal troponin I in adult transgenic mouse heart muscle reduces the force decline observed during acidic conditions. *J. Physiol.* 536, 863–870.

Wu, H., Lee, J., Vincent, L. G., Wang, Q., Gu, M., and Lan, F. (2015). Epigenetic regulation of phosphodiesterases 2A and 3A underlies compromised beta-adrenergic signaling in an iPSC Model of dilated cardiomyopathy. *Cell Stem Cell* 17, 89–100.

Wyles, S. P., Hrstka, S. C., Reyes, S., Terzic, A., Olson, T. M., and Nelson, T. J. (2016a). Pharmacological modulation of calcium homeostasis in familial dilated cardiomyopathy: an in vitro analysis from an RBM20 patient-derived iPSC model. *Clin. Transl. Sci.* 9, 158–167. doi: 10.1111/cts.12393

Wyles, S. P., Li, X., Hrstka, S. C., Reyes, S., Oommen, S., Beraldi, R., et al. (2016b). Modeling structural and functional deficiencies of RBM20 familial dilated cardiomyopathy using human induced pluripotent stem cells. *Hum. Mol. Genet.* 25, 254–265. doi: 10.1093/hmg/ddv468

Yasuda, S., Townsend, D., Michele, D. E., Favre, E. G., Day, S. M., and Metzger, J. M. (2005). Dystrophic heart failure blocked by membrane sealant poloxamer. *Nature* 436, 1025–1029.

Yermakovich, D., Sivitskaya, L., Vaikhanskaya, T., Danilenko, N., and Motuk, I. (2018). Novel desmoplakin mutations in familial carvajal syndrome. *Acta Myol.* 7, 263–266.

Young, C. S., Hicks, M. R., Ermolova, N. V., Nakano, H., Jan, M., Younesi, S., et al. (2016). A single CRISPR-Cas9 deletion strategy that targets the majority of DMD patients restores dystrophin function in hiPSC-derived muscle cells. *Cell Stem Cell* 18, 533–540. doi: 10.1016/j.stem.2016.01.021

Zatti, S., Martewicz, S., Serena, E., Uno, N., Giobbe, G., Kazuki, Y., et al. (2014). Complete restoration of multiple dystrophin isoforms in genetically corrected Duchenne muscular dystrophy patient-derived cardiomyocytes. *Mol. Ther. Methods Clin. Dev.* 1:1. doi: 10.1038/mtm.2013.1

Zaunbrecher, R. J., Abel, A. N., Beussman, K., Leonard, A., von Frieling-Salewsky, M., Fields, P. A., et al. (2019). Cronos titin is expressed in human cardiomyocytes and necessary for normal sarcomere function. *Circulation* 140, 1647–1660.

Zhan, H., Stanciauskas, R., Stigloher, C., Dizon, K. K., Jospin, M., Bessereau, J. L., et al. (2014). In vivo single-molecule imaging identifies altered dynamics of calcium channels in dystrophin-mutant C. elegans. *Nat. Commun.* 5:4974. doi: 10.1038/ncomms5974

Zhang, Y., Long, C., Li, H., McAnally, J. R., Baskin, K. K., and Shelton, J. M. (2017). CRISPR-Cpf1 correction of muscular dystrophy mutations in human cardiomyocytes and mice. *Sci. Adva.* 3:e1602814. doi: 10.1126/sciadv.1602814

Conflict of Interest: The authors declare that the research was conducted in the absence of any commercial or financial relationships that could be construed as a potential conflict of interest.

frontiers in Physiology

ORIGINAL RESEARCH
published: 25 May 2020
doi: 10.3389/fphys.2020.00468

Regulation of Myofilament Contractile Function in Human Donor and Failing Hearts

Kerry S. McDonald[1], Laurin M. Hanft[1], Joel C. Robinett[1], Maya Guglin[2] and Kenneth S. Campbell[2,3]*

[1] Department of Medical Pharmacology and Physiology, University of Missouri, Columbia, MO, United States, [2] Division of Cardiovascular Medicine, University of Kentucky, Lexington, KY, United States, [3] Department of Physiology, University of Kentucky, Lexington, KY, United States

OPEN ACCESS

Edited by:
Norio Fukuda, Jikei University School of Medicine, Japan

Reviewed by:
Martina Krüger, Heinrich Heine University of Düsseldorf, Germany
Margaret Westfall, University of Michigan, United States
John Peter Konhilas, University of Arizona, United States

****Correspondence:***
Kerry S. McDonald
mcdonaldks@missouri.edu

Specialty section:
This article was submitted to Striated Muscle Physiology, a section of the journal Frontiers in Physiology

Received: *20 January 2020*
Accepted: *16 April 2020*
Published: *25 May 2020*

Citation:
McDonald KS, Hanft LM, Robinett JC, Guglin M and Campbell KS (2020) Regulation of Myofilament Contractile Function in Human Donor and Failing Hearts. Front. Physiol. 11:468. doi: 10.3389/fphys.2020.00468

Heart failure (HF) often includes changes in myocardial contractile function. This study addressed the myofibrillar basis for contractile dysfunction in failing human myocardium. Regulation of contractile properties was measured in cardiac myocyte preparations isolated from frozen, left ventricular mid-wall biopsies of donor (n = 7) and failing human hearts (n = 8). Permeabilized cardiac myocyte preparations were attached between a force transducer and a position motor, and both the Ca^{2+} dependence and sarcomere length (SL) dependence of force, rate of force, loaded shortening, and power output were measured at 15 ± 1°C. The myocyte preparation size was similar between groups (donor: length 148 ± 10 μm, width 21 ± 2 μm, n = 13; HF: length 131 ± 9 μm, width 23 ± 1 μm, n = 16). The maximal Ca^{2+}-activated isometric force was also similar between groups (donor: 47 ± 4 $kN \cdot m^{-2}$; HF: 44 ± 5 $kN \cdot m^{-2}$), which implicates that previously reported force declines in multi-cellular preparations reflect, at least in part, tissue remodeling. Maximal force development rates were also similar between groups (donor: k_{tr} = 0.60 ± 0.05 s^{-1}; HF: k_{tr} = 0.55 ± 0.04 s^{-1}), and both groups exhibited similar Ca^{2+} activation dependence of k_{tr} values. Human cardiac myocyte preparations exhibited a Ca^{2+} activation dependence of loaded shortening and power output. The peak power output normalized to isometric force (PNPO) decreased by ∼12% from maximal Ca^{2+} to half-maximal Ca^{2+} activations in both groups. Interestingly, the SL dependence of PNPO was diminished in failing myocyte preparations. During sub-maximal Ca^{2+} activation, a reduction in SL from ∼2.25 to ∼1.95 μm caused a ∼26% decline in PNPO in donor myocytes but only an ∼11% change in failing myocytes. These results suggest that altered length-dependent regulation of myofilament function impairs ventricular performance in failing human hearts.

Keywords: heart failure, human cardiac myocytes, contractile properties, rate of force development, loaded shortening, power output, sarcomere length

INTRODUCTION

Human heart failure is defined as the inability of the cardiac pump function to meet peripheral demands. Heart failure afflicts ∼6 million patients in the US and is associated with 1 in 9 deaths (Benjamin et al., 2018). Most current medication strategies for heart failure are designed to alleviate symptoms by decreasing the hemodynamic load (arterial blood pressure). Thus, new precision-based approaches that focus on the disease mechanisms intrinsic to the myocardium could have a significant impact.

The etiology of human heart failure is complex and encompasses ventricular remodeling and alterations to cardiac myocyte biology, which include energetic deficiencies and alterations in calcium handling and myofilament function. The purpose of this study was to address the myofibrillar basis for contractile dysfunction in failing human myocardium. Regulation of steady-state and dynamic contractile properties was measured in single permeabilized cardiac myocyte preparations isolated from frozen, left ventricular mid-wall biopsies of donor and failing human hearts.

MATERIALS AND METHODS

Samples were obtained from patients undergoing heart transplants at the University of Kentucky and from organ donors who did not have heart failure. Hearts were handed to a researcher as soon as these were excised from the body. Mid-wall myocardial samples of distal anterior left ventricular free wall were dissected and snap frozen in liquid nitrogen and stored at -150°C before shipping to the University of Missouri. All procedures were approved by the University of Kentucky Institutional Review Board, and written informed consent was obtained from each patient who had heart failure and from a legally authorized representative of each organ donor. Samples were obtained from seven organ donors (mean age of 39 ± 6, 3 female, 6 white, 1 African-American), four patients with ischemic heart failure (mean age of 48 ± 10, 1 female, 3 white, 1 African American), and four patients with non-ischemic heart failure (mean age of 51 ± 4, 3 female, 3 white, 1 African American). Data are presented as two groups, donor and heart failure (HF).

Single Permeabilized Myocardial Samples and Functional Measurements

A total of 29 permeabilized single cardiac myocyte preparations from eight hearts from patients who had heart failure and seven hearts from organ donors were analyzed for this work (**Table 1**). Single permeabilized cardiac myocyte preparations (see **Figure 1**) were mounted between a force transducer and a motor, and contractile properties were measured during maximal and sub-maximal Ca^{2+} activations at long (∼2.25 μm) and short sarcomere lengths (∼1.95 μm), which are thought to span the sarcomere working range (Pollack and Huntsman, 1974; Grimm et al., 1980; Guccione et al., 1997; Chung et al., 2018). In brief, cardiac myocyte preparations were attached by placing the ends of the myocyte into stainless steel troughs (25 gauge) and ends were secured by overlaying a 0.5-mm length of 4–0 monofilament nylon suture (Ethicon, Inc.) and tying the suture into the troughs with loops of 10–0 monofilament (Ethicon, Inc.). The attachment procedure was performed under a stereomicroscope (∼100× magnification) using finely shaped forceps (McDonald, 2000). Prior to the mechanical measurements, the experimental apparatus was mounted on the stage of an inverted microscope (model IX-70, Olympus Instrument Co., Japan). Mechanical measurements were performed using a capacitance-gauge transducer plus a 10× amplifier (Aurora Scientific, Inc., Aurora, ON, Canada). Length changes were introduced using a DC torque motor (model 308, Aurora Scientific, Inc.) driven by voltage commands from a personal computer via a 16-bit D/A converter (AT-MIO-16E-1, National Instruments Corp., Austin, TX, United States). Force and length signals were digitized at 1 kHz and stored on a personal computer using LabVIEW for Windows (National Instruments Corp.). Sarcomere length was monitored using an IonOptix SarcLen system (IonOptix, Milton, MA, United States), which used a fast Fourier transform algorithm of the video image of the myocyte. Following attachment, the relaxed, permeabilized cardiac myocyte preparation was adjusted to a sarcomere length of ∼2.25 μm and passive tension was measured by slacking the preparation in pCa 9.0 solution (McDonald and Moss, 1995; McDonald, 2000). Cardiac myocyte preparation force, rates of force development, and force-velocity and power-load measurements were made at 15 ± 1°C as previously described (McDonald, 2000; Hinken and McDonald, 2004; Hanft et al., 2017).

Data and Statistical Analysis

Force redevelopment kinetics (k_{tr}) following a slack-restretch maneuver were determined by fitting a single exponential function to the force recovery profile using the equation

$$F = F_{max}(1 - e^{-ktr^t})$$

where F is tension at time t, F_{max} is maximal tension, and k_{tr} is the rate constant of force development.

Myocyte length traces, force-velocity curves, and power-load curves were analyzed as previously described (McDonald, 2000). Myocyte length and sarcomere length traces during loaded shortening were fit to a single decaying exponential equation:

$$L = Ae^{-kt} + C$$

where L is cell length at time t, A and C are constants with dimensions of length, and k is the rate constant of shortening ($k_{shortening}$). Velocity of shortening at any given time, t, was determined as the slope of the tangent to the fitted curve at that time point. In this study, loaded shortening velocities were calculated at time equal to 100 ms after the onset of the force clamp.

Hyperbolic force-velocity curves were fit to the relative force-velocity data using the Hill equation (Hill, 1938)

$$(P + a)(V + b) = (P_o + a)b$$

where P is force during shortening at velocity V, P_o is the maximal isometric force, and a and b are constants with

TABLE 1 | Human permeabilized cardiac myocyte preparations.

	Cardiac myocyte preparations	Length (μm)	Width (μm)	Sarcomere length (μm)	Passive force (kN · m^{-2})	Peak power (pW)	pCa for half-max. force	Relative force half-max. pCa
Donor	13	148 ± 10	21 ± 2	2.26 ± 0.01	1.91 ± 0.40	54 ± 12	5.77 ± 0.01	0.53 ± 0.03
HF	16	131 ± 9	23 ± 5	2.27 ± 0.01	1.67 ± 0.26	43 ± 25	5.85 ± 0.01	0.56 ± 0.02

Values are means ± S.E.M.

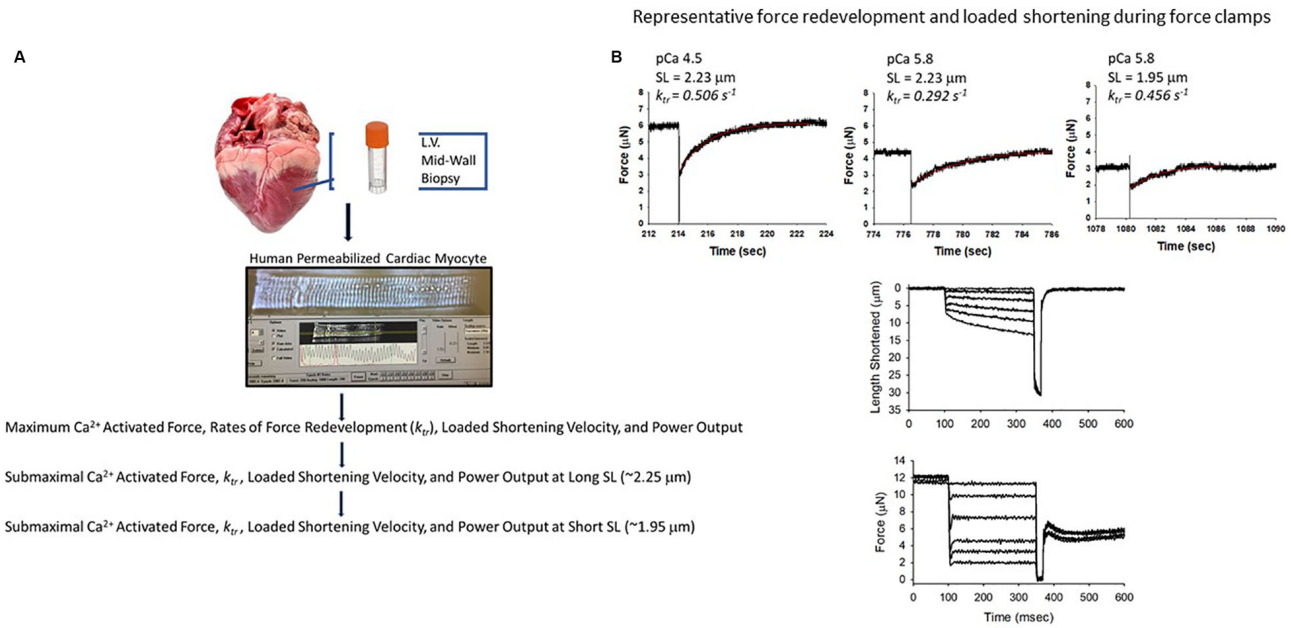

FIGURE 1 | Experimental design. **(A)** Tissue was procured as part of the University of Kentucky Heart Transplant program and Biobank program. Mid-wall myocardial samples of distal anterior left ventricular free wall were dissected and snap frozen in liquid nitrogen and stored at -150°C before shipping to the University of Missouri. Single human permeabilized cardiac myocyte preparations were mounted between a force transducer and a motor, and contractile properties were measured during maximal and sub-maximal Ca^{2+} activations at long (~2.25 μm) and short sarcomere lengths (~1.95 μm). **(B)** Representative force redevelopment and loaded shortening traces from a human permeabilized cardiac myocyte preparation.

dimensions of force and velocity, respectively. Force-velocity data were normalized to isometric force to illustrate condition effects on loaded shortening velocity. Power-load curves were obtained by multiplying force x velocity at each relative load on the force-velocity curve, and statistical analysis compared peak normalized power output (PNPO) values, which were obtained by multiplying relative force at optimum power x velocity at optimum power. Curve fitting was performed using a customized program written in QBasic, as well as commercial software (SigmaPlot).

The experimental data were analyzed in SAS 9.1.3 (SAS Institute, Cary, NC, United States) using linear mixed effects. As previously described (Haynes et al., 2014), this statistical approach accounts for the hierarchical structure of the data (values obtained from different numbers of myocyte preparations from hearts procured from organ donors and patients who had heart failure) and has greater statistical power than standard ANOVA for this type of design. Compound symmetry was assumed for the covariance structure, and *post-hoc* analyses were performed using Tukey-Kramer corrections. $P < 0.05$ was accepted as a statistically significant difference. N = number of hearts. n = number of cardiac myocyte preparations. Values are expressed as means ± SEM.

RESULTS

Contractile Properties of Human Single Permeabilized Cardiac Myocyte Preparations

Permeabilized human cardiac myocyte preparations were similar in size between donor and heart failure groups (**Table 1**). At sarcomere length (SL) ~2.25 μm, passive tension was similar between groups (donor: 1.91 ± 0.40 vs. HF: 1.67 ± 0.26 kN · m^{-2}) (**Table 1**).

Maximal Ca^{2+}-activated tension was similar between donor and heart failure cardiac myocyte preparations (donor: 47 ± 4 kN · m^{-2}; HF: 44 ± 5 kN · m^{-2}) (**Figure 2**). For all figures, the different symbols indicate data points from each heart sample to indicate variability among tissues. After the entire experimental protocol (see **Figure 1**), the final maximal

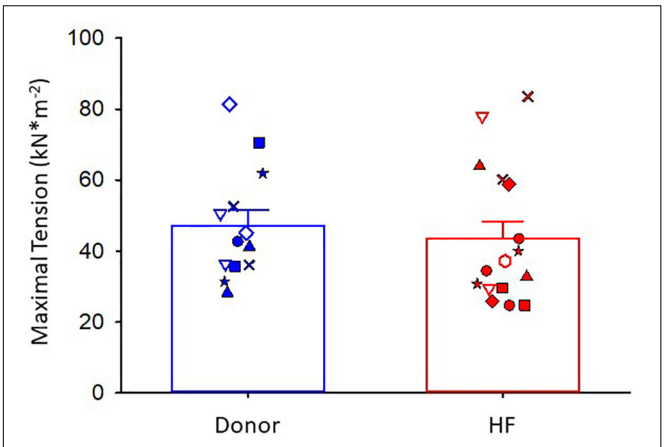

FIGURE 2 | Maximal Ca^{2+}-activated tension. Donor group, N = 7 hearts, n = 13 cardiac myocyte preparations. HF group, N = 8 hearts, n = 16 cardiac myocyte preparations. Different symbols indicate data points from each heart sample. Linear mixed model, p = 0.715.

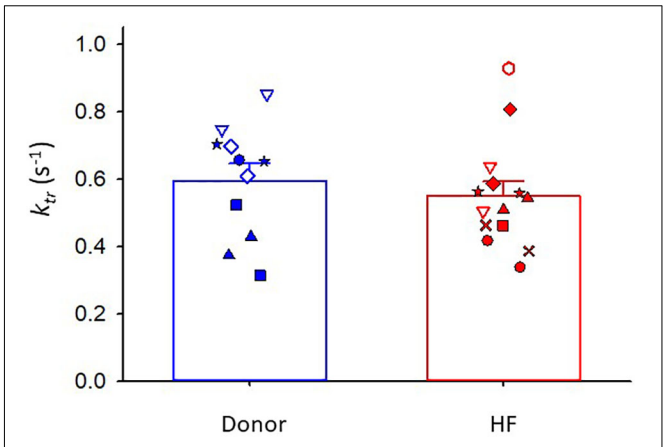

FIGURE 3 | Rate of force development (k_{tr}) during maximal Ca^{2+} activation. Donor group, N = 6 hearts, n = 11 cardiac myocyte preparations. HF group, N = 8 hearts, n = 14 cardiac myocyte preparations. Different symbols indicate data points from each heart sample. Linear mixed model, p = 0.663.

Ca^{2+}-activated tension was 0.902 ± 0.037 of the initial pCa 4.5 force in donor preparations and 0.806 ± 0.032 in heart failure preparations (p = 0.064).

Maximal rates of force development (as indexed by the rate constant, k_{tr}) were also similar between donor and heart failure groups Donor: k_{tr} = 0.60 ± 0.05 s^{-1}; HF: k_{tr} = 0.55 ± 0.04 s^{-1}) (**Figure 3**). All human cardiac myocyte preparations exhibited a robust Ca^{2+} activation dependence of k_{tr}, i.e., lower k_{tr} values at half-maximal Ca^{2+} activation ($p < 0.001$) (**Figure 4**). In addition, k_{tr} values increased at short sarcomere length (SL) compared with those at long SL during sub-maximal Ca^{2+} activations ($p < 0.001$).

The maximal absolute power generating capacity was similar between donor and heart failure groups (donor: 1.23 ± 0.15 μW · mg^{-1}; HF: 1.07 ± 0.14 μW · mg^{-1}) (**Figure 5**). Statistical analysis showed that the peak normalized power output (PNPO) fell as Ca^{2+} activation was reduced in cells from organ donors and patients who had heart failure (**Figures 6A,B**). At sub-maximal Ca^{2+} activations, PNPO also decreased at short sarcomere length in both groups. Interestingly, **Figure 6C** shows that cells from failing hearts exhibited a markedly reduced sarcomere length dependence of PNPO (p = 0.004). This indicates that normalized power falls further as sarcomere length is reduced in cells from organ donors than it does in cells from patients who had heart failure.

No differences were observed in either maximal Ca^{2+}-activated tension or k_{tr} values between sexes in cardiac myocyte preparations from donor or heart failure samples (**Supplementary Figures S1, S2**).

DISCUSSION

Brief Summary

Steady-state and dynamic contractile properties were measured in human single permeabilized cardiac myocyte preparations. Human cardiac myocytes exhibited both Ca^{2+} activation and sarcomere length dependence of force development and power output. Maximal Ca^{2+}-activated contractile force, rates of force development, and power were similar between human donor and failing samples. Conversely, the sarcomere length dependence of power was diminished in myofilaments from failing hearts, which provides a sub-cellular, biophysical mechanism for the depressed Frank-Starling relationship in failing human hearts.

Human Permeabilized Cardiac Myocyte Preparations

For both donor and heart failure samples, human single permeabilized cardiac myocyte preparations displayed Ca^{2+} activation dependence of force, k_{tr} values, loaded shortening, and power output, which has previously been reported in rodent and porcine permeabilized cardiac myocyte preparations (McDonald, 2000; McDonald et al., 2012). Previous studies have reported the Ca^{2+} sensitivity of both force (Wolff et al., 1996; van der Velden et al., 2000, van Der Velden et al., 2001; van der Velden et al., 2003, 2006; Kooij et al., 2010; Wijnker et al., 2013; Haynes et al., 2014; Swenson et al., 2017) and rates of force development (Edes et al., 2007) in human permeabilized cardiac myocyte preparations. Our study is the first, to our knowledge, to show the Ca^{2+} activation dependence of loaded shortening and power output in human permeabilized cardiac myocyte preparations. Compared with those during maximal Ca^{2+} activations, the velocity at optimal power, peak normalized power output, and absolute power output were all lower during half-maximal Ca^{2+} activations, which signifies that changes in both force and loaded shortening velocity account for the regulation of human myofilament power output generating capacity by activator [Ca^{2+}]. Also, human cardiac myocyte preparations exhibited a sarcomere length dependence of force, k_{tr} values, loaded shortening, and power output,

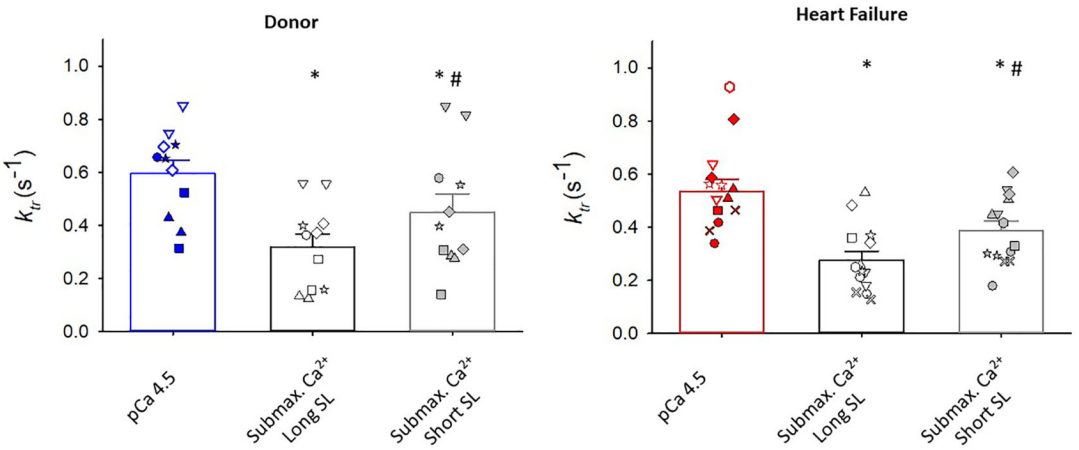

FIGURE 4 | Regulation of rate of force development (k_{tr}). In myocytes from organ donors (N = 6 hearts, n = 11 cardiac myocyte preparations) and patients with heart failure (N = 8 hearts, n = 14 cardiac myocyte preparations), k_{tr} values were lower during half maximal than maximal Ca^{2+} activations ($^{*}p < 0.001$). At half-maximal Ca^{2+} activations, k_{tr} values were lower at long sarcomere length ($^{\#}p < 0.001$). Different symbols indicate data points from each heart sample. Linear mixed model testing for main effects of heart failure status, k_{tr} experimental condition, and their statistical interaction.

similar to reports on rodent (Fabiato and Fabiato, 1975; Adhikari et al., 2004; Stelzer and Moss, 2006; Korte and McDonald, 2007; Hanft and McDonald, 2009, 2010; Hanft et al., 2016) and porcine (McDonald et al., 2012) permeabilized cardiac myocyte preparations.

Donor vs. Heart Failure Human Permeabilized Cardiac Myocyte Preparations

Maximal Ca^{2+}-activated tension, k_{tr} values, and absolute power output were similar between donor and heart failure cardiac myocyte preparations. Other studies have reported similar maximal Ca^{2+}-activated tensions in human single permeabilized cardiac myocytes obtained from donor and end-stage heart failure samples stored in liquid nitrogen (Wolff et al., 1996; van der Velden et al., 2000, van Der Velden et al., 2001; van der Velden et al., 2003, 2006). In contrast, maximal Ca^{2+}-activated tension has been reported to be reduced in single permeabilized cardiac myocytes from small-animal mixed models of heart failure (Belin et al., 2006; de Waard et al., 2007; Edes et al., 2008; Hanft et al., 2017). In addition, k_{tr} values, loaded shortening, and power output have been reported to be decreased in single permeabilized myocytes from late-stage heart failure in rodent models (Edes et al., 2008; Hanft et al., 2017). The exact reasons for the differences between human and rodent heart failure studies are uncertain but likely arise, at least in part, from confounding variables associated with human patients (e.g., age, sex, medications, disease etiology, genetic variability, fresh vs. frozen samples). Consistent with this, contractile properties showed more variability in human cardiac myocyte preparation in this study compared with those in previous reports on rodent permeabilized cardiac myocyte preparations (Edes et al., 2008; Hanft et al., 2017).

Length-Dependent Activation of Power in Human Permeabilized Cardiac Myocyte Preparations From Donor vs. Heart Failure Samples

The relationship between ventricular filling and ventricular output was described in the early twentieth century and is known as the Frank-Starling relationship (Frank, 1895; Patterson and Starling, 1914). The functional importance of the Frank-Starling relationship is to dynamically match left and right ventricular outputs and adapt hemodynamics to peripheral demands. The molecular mechanism underlying the Frank-Starling relationship involve sarcomere physical factors, including alterations in inter-filament lattice spacing (Fuchs and Martyn, 2005) and myosin cross-bridge orientation (Ait Mou et al., 2016), perhaps mediated by titin (Cazorla et al., 2001; Fukuda et al., 2003). The Frank-Starling relationship often is markedly depressed in late-stage cardiac failure (Braunwald and Ross, 1964; Ross and Braunwald, 1964; Holubarsch et al., 1996). Depressed Frank-Starling relationships result, at least in part, from the reduced length dependence of the activation of cardiac myofilaments from failing hearts. For instance, studies have reported reduced the length dependence of the Ca^{2+} sensitivity of force in single permeabilized cardiac myocyte preparations from failing human hearts (Schwinger et al., 1994; Holubarsch et al., 1996; Sequiera et al., 2013; Wijnker et al., 2014). Our study extended previous studies by examining the length dependence of cardiac myofilament loaded shortening and power output, which ultimately determines ventricular ejection. Interestingly, the length dependence of power was significantly depressed in failing human cardiac myocyte preparations, providing evidence of novel dynamic myofibrillar mechanisms (in addition to the length dependence of steady-state force) for depressed Frank-Starling relationships in failing human hearts. The exact molecular mechanisms for the depressed myofilament length

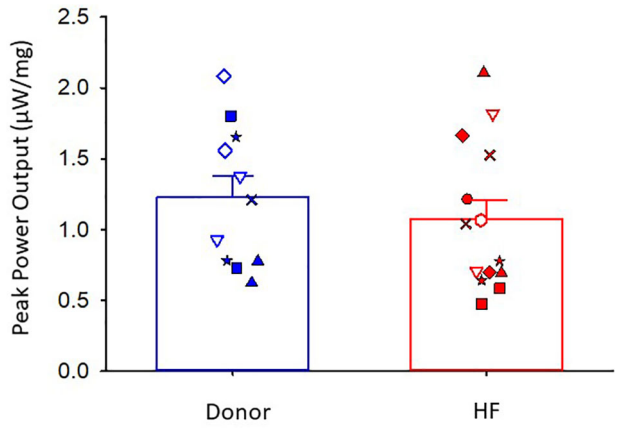

FIGURE 5 | Peak absolute power output. Donor group, N = 6 hearts, n = 11 cardiac myocyte preparations. HF group, N = 8 hearts, n = 14 cardiac myocyte preparations. Different symbols indicate data points from each heart sample. Linear mixed model, p = 0.542.

dependence of power remain to be determined. Certainly, lower levels of PKA-mediated phosphorylation of cardiac myofilament proteins with heart failure may contribute (Wolff et al., 1996; van der Velden et al., 2003; Messer et al., 2007; Copeland et al., 2010; Kooij et al., 2010; Haynes et al., 2014). For instance, PKA phosphorylation and troponin exchange with pseudo-phosphorylation affect the length dependence of force (Kooij et al., 2010; Wijnker et al., 2013, 2014) and have been shown to, in part, restore the length dependence of the Ca^{2+} sensitivity of force in failing cardiac myocyte preparations. Another plausible molecular regulator of the length dependence of power is cardiac myocyte binding protein-C (cMyBP-C), a protein that resides in the C-zone of thick filaments and the phosphorylation state is depressed in failing myocardium (Hamdani et al., 2008; Copeland et al., 2010; Kooij et al., 2010; Haynes et al., 2014; Stathopoulou et al., 2016). In addition, preliminary studies from our lab have shown that the sarcomere length dependence of power is regulated by PKA phosphorylation sites on cMyBP-C in a transgenic mouse (Hanft et al., 2019). This finding raises the intriguing possibility that thick filament ON state may contribute to the length dependence of power output, which could be addressed experimental by small molecules or peptides that regulate thick filament states (Green et al., 2016). There also may be many dynamic changes in sarcomere signals beyond PKA, and the dynamic signaling at the sarcomere may vary widely between "normal" and heart failure myocardia, which requires exploration of sarcomere functional proteomics in response to varied stimuli, e.g., neurohumoral factors, activation frequency (i.e., heart rate), and medications (Hamdani et al., 2008).

Integration of Findings in Failing Human Myocardium

Heart failure is postulated to arise from a variety of changes in cardiac myocyte biology, including loss of cells, morphological changes, transformed intracellular signaling, disrupted energetics, altered Ca^{2+} handling, and modifications of myofilament function. There is evidence of several contractility adaptations of intact myocardial preparations from failing human hearts, which include (*i*) decreased β-adrenergic responsiveness, (*ii*) depressed force-frequency relations, and (*iii*) slowed relaxation rates (Chung et al., 2018). From a myofilament standpoint, findings from failing permeabilized myocardial preparations include the (*i*) increased Ca^{2+} sensitivity of force, (*ii*) depressed length dependence of the Ca^{2+} sensitivity of force, and (*iii*) decreased PKA phosphorylation of myofilament proteins. One parameter that has yielded mixed results, especially between permeabilized multi-cellular and single-cell preparations, is maximal Ca^{2+}-activated tension. In this regard, a recent study showed depressed force and power in multi-cellular preparations obtained from the transmural region of the left ventricular free wall of human failing myocardium (Haynes et al., 2014). Our current study directly addressed the sub-cellular mechanistic underpinnings of this finding by measuring force and power in single permeabilized cardiac myocytes obtained from the same region of the left ventricles of donor and failing myocardia. Our finding that force and power in single cells does not depend on the heart failure status implies that the changes in multi-cellular myocardial preparations arise, at least in part, from tissue remodeling, perhaps due to the loss of myofilaments and consequent augmentation of myocardial fibrosis (Haynes et al., 2014).

Study Limitations

There are several limitations with human cardiac myocyte contractile property studies. First, there is the caveat of categorizing non-failing, donor myocardium as normal because of the possibility of high blood levels of catecholamines and inotropic support at the time of procurement. Second, the diversity of factors that contribute to non-ischemic disease likely augments experimental variability. Third, any assessment of cardiac myocyte size is precluded because ventricular biopsies are mechanically disrupted, which yields highly variable sized fragments. Fourth, permeabilized cardiac myocyte contractile property studies have an inherent bias due to the selection of rod-shaped cardiac myocyte-sized preparations. The selection of myocyte preparations (to only those that can withstand measurements) may exclude populations with, for instance, diminished maximum tension-generating capacity. The preparation selection process increases the possibility of a false-negative result about tension generation capacity. Fifth, the labor-intensive nature of single cardiac myocyte contractile property measurements limits the sample size, which in combination with regional variability (Kuro-o et al., 1986; Cazorla et al., 2000), disease etiology, and varied treatments also increases the likelihood of false-negative results. Sixth, the small size of single cardiac myocyte preparations (tens of nanograms) tests the limits of conventional techniques to assess myofilament protein isoforms and post-translational modifications in preparations that had their mechanics measured (Herron et al., 2001; Herron and McDonald, 2002; Korte et al., 2005; Hanft et al., 2013).

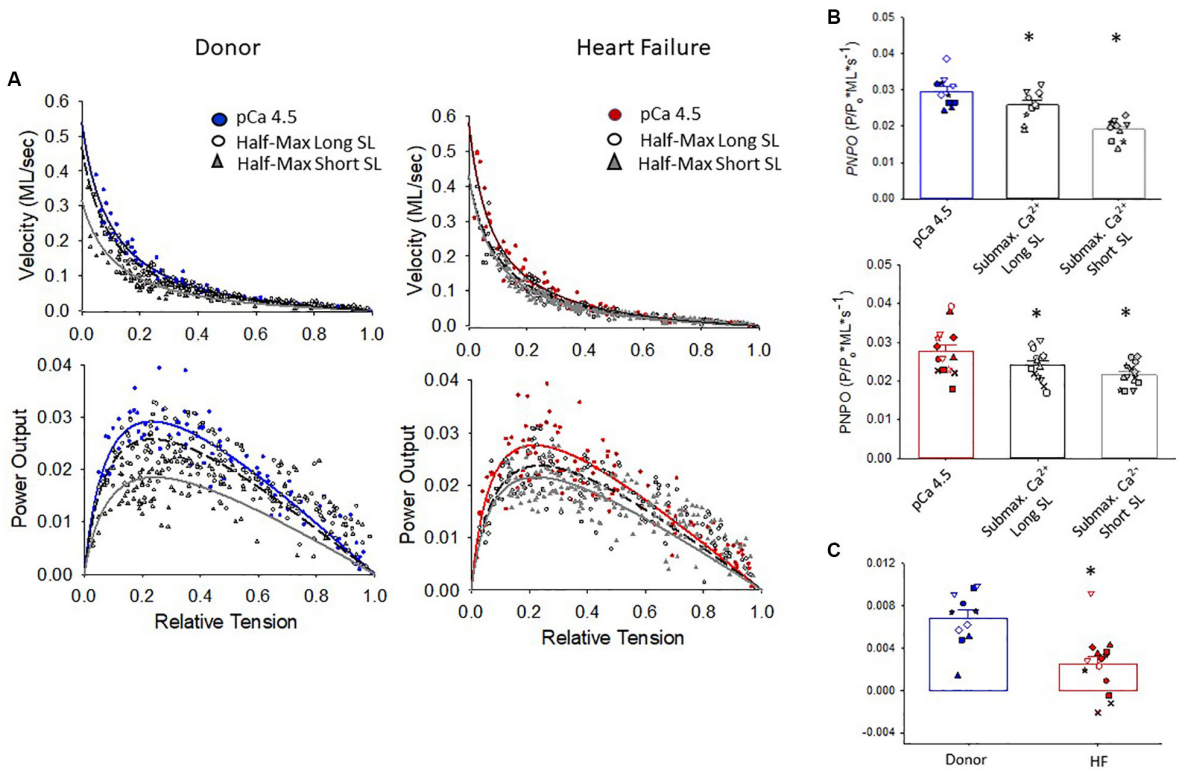

FIGURE 6 | Normalized force-velocity and power-load curves. **(A)** Cumulative force-velocity and power-load curves from donor and HF preparations. **(B)** In myocyte preparations from organ donors and patients with heart failure, the peak normalized power output (PNPO) was lower at half-maximal Ca^{2+} activation than at maximal Ca^{2+} activation (*p = 0.027 or lower depending on comparisons). **(C)** Sarcomere length dependence of PNPO (that is, PNPO at long SL half max – short SL half-max) was significantly reduced in failing samples, *p = 0.004. Different symbols indicate data points from each heart sample. All tests were performed using the linear mixed model.

Next Steps

This study provides a comprehensive assessment of contractile properties of human single permeabilized cardiac myocytes from donor and patients who have heart failure. The study implicates myocardial tissue remodeling to explain, at least in part, previous reports of depressed force and mechanics in human multi-cellular myocardial preparations. Additionally, since the sarcomere length dependence of power was diminished in myofilaments from failing hearts, it is likely that that altered length dependence of myofilament power contributes to the depressed Frank-Starling relationship in failing human hearts. Future exploration of unique molecular mechanisms will necessitate next-generation, unbiased, cellular functional proteomic approaches on preparations that had their mechanics measured. Additional work is needed to address other myofilament properties, including dynamic response to calcium transients, myofilament efficiency, thin and thick filament dynamics, and relaxation kinetics, and how these are affected during the progression to heart failure. Future investigations will also require systematic delineation of how confounders such as genetics, disease etiology, environment, age, sex, co-morbidities, and medications affect myofilament function studies. Both the expansion of dynamic myofilament studies and critical evaluation of individual patient scenarios are necessary for future, best-practice precision medicine to treat the underlying molecular mechanisms that cause human hearts to fail.

DATA AVAILABILITY STATEMENT

The datasets generated for this study are available on request to the corresponding author.

ETHICS STATEMENT

All procedures were approved by the University of Kentucky Institutional Review Board and written informed consent was obtained from each patient who had heart failure and from a legally authorized representative of each organ donor, subjects gave informed consent.

AUTHOR CONTRIBUTIONS

KM, LH, and JR performed human single cardiac myocyte preparation experiments. MG and KC procured human tissue. KM, LH, JR, MG, and KC contributed to data analysis and manuscript preparation.

FUNDING

This work was supported by (i) the National Institutes of Health (NIH) HL57852 and a University of Missouri, School of Medicine Bridge Grant to KM; (ii) NIH TR033173, HL133359, and HL146676 to KC; and (iii) SEC Visiting Faculty Grant Program to KM and KC.

ACKNOWLEDGMENTS

The content is solely the responsibility of the authors and does not necessarily represent the official views of the National Institutes of Health.

SUPPLEMENTARY MATERIAL

The Supplementary Material for this article can be found online at: https://www.frontiersin.org/articles/10.3389/fphys.2020.00468/full#supplementary-material

FIGURE S1 | Maximal Ca^{2+} activated tension- Effects of sex. Male, N = 8 hearts, n = 15 cardiac myocyte preparations. Female, N = 7 hearts, n = 14 cardiac myocyte preparations. Different symbols indicate data points from each heart sample. Linear mixed model, p = 0.549.

FIGURE S2 | Rate of force development (k_{tr}) during maximal Ca^{2+} activation- Effects of sex. Male, N = 7 hearts, n = 11 cardiac myocyte preparations. Female, N = 7 hearts, n = 12 cardiac myocyte preparations. Different symbols indicate data points from each heart sample. Linear mixed model, p = 0.993.

REFERENCES

Adhikari, B. B., Regnier, M., Rivera, A. J., Kreutziger, K. L., and Martyn, D. A. (2004). Cardiac length dependence of force and force redevelopment kinetics with altered cross-bridge cycling. *Biophys. J.* 87, 1784–1794. doi: 10.1529/biophysj.103.039131

Ait Mou, Y., Hsu, K., Farman, G. P., Kumar, M., Greaser, M. L., Irving, T. C., et al. (2016). Titin strain contributes to the Frank-Starling law of the heart by structural rearrangements of both thin- and thick-filament proteins. *Proc. Natl. Acad. Sci. U.S.A.* 113, 2306–2311. doi: 10.1073/pnas.1516732113

Belin, R. J., Sumandea, M. P., Kobayashi, T., Walker, L. A., Rundell, V. L., Urboniene, D., et al. (2006). Left ventricular myofilament dysfunction in rat experimental hypertrophy and congestive heart failure. *Am. J. Physiol. Heart Circ. Physiol.* 291, H2344–H2353. doi: 10.1152/ajpheart.00541.2006

Benjamin, E. J., Virani, S. S., Callaway, C. W., Chamberlain, A. M., Chang, A. R., Cheng, S., et al. (2018). Heart disease and stroke statistics-2018 update: a report from the american heart association. *Circulation* 137, e67–e492. doi: 10.1161/CIR.0000000000000573

Braunwald, E., and Ross, J. (1964). Applicability of Starling's law of the heart to man. *Circ. Res.* 2, 169–181.

Cazorla, O., Le Guennec, J.-Y., and White, E. (2000). Length-tension relationships of subepicardial and sub-endocardial single ventricular myocytes from rat and ferret hearts. *J. Mol. Cell. Cardiol.* 32, 735–744. doi: 10.1006/jmcc.2000.1115

Cazorla, O., Wu, Y., Irving, T. C., and Granzier, H. (2001). Titin-based modulation of calcium sensitivity of active tension in mouse skinned cardiac myocytes. *Circ. Res.* 88, 1028–1035. doi: 10.1161/hh1001.090876

Chung, J. H., Martin, B. L., Canan, B. D., Elnakish, M. T., Milani-Nejad, N., Saad, N. S., et al. (2018). Etiology-dependent impairment of relaxation kinetics in right ventricular end-stage failing human myocardium. *J. Mol. Cell. Cardiol.* 121, 81–93. doi: 10.1016/j.yjmcc.2018.07.005

Copeland, O., Sadayappan, S., Messer, A. E., Steinen, G. J., van der Velden, J., and Marston, S. B. (2010). Analysis of cardiac myosin binding protein-C phosphorylation in human heart muscle. *J. Mol. Cell. Cardiol.* 49, 1003–1011. doi: 10.1016/j.yjmcc.2010.09.007

de Waard, M. C., van der Velden, J., Bito, V., Ozdemir, S., Biesmans, L., Boontje, N. M., et al. (2007). Early exercise training normalizes myofilament function and attenuates left ventricular pump dysfunction in mice with a large myocardial infarction. *Circ. Res.* 100, 1079–1088. doi: 10.1161/01.RES.0000262655.16373.37

Edes, I. F., Czuriga, D., Csanyi, G., Chlopicki, S., Recchia, F. A., Borbely, A., et al. (2007). The rate of tension redevelopment is not modulated by sarcomere length in permeabilized human, murine and porcine cardiomyocytes. *Am. J. Physiol.* 293, R20–R29. doi: 10.1152/ajpregu.00537.2006

Edes, I. F., Toth, A., Csanyi, G., Lomnicka, M., Chlopicki, S., Edes, I., et al. (2008). Late-stage alterations in myofibrillar contractile function in a transgenic mouse model of dilated cardiomyopathy (Tgalphaq*44). *J. Mol. Cell. Cardiol.* 45, 363–372. doi: 10.1016/j.yjmcc.2008.07.001

Fabiato, A., and Fabiato, F. (1975). Dependence of the contractile activation of skinned cardiac cells on the sarcomere length. *Nature* 256, 54–56. doi: 10.1038/256054a0

Frank, O. (1895). Zur dynamik des herzmuskels. *Z. Biol.* 32, 370–447.

Fuchs, F., and Martyn, D. A. (2005). Length-dependent Ca2+ activation in cardiac muscle: some remaining questions. *J. Muscle Res. Cell Motil.* 26, 199–212. doi: 10.1007/s10974-005-9011-z

Fukuda, N., Wu, Y., Farman, G., Irving, T. C., and Granzier, H. (2003). Titin isoform variance and length dependence of activation in skinned bovine cardiac muscle. *J. Physiol.* 553, 147–154. doi: 10.1113/jphysiol.2003.049759

Green, E. M., Wakimoto, H., Anderson, R. L., Evanchik, M. J., Gorham, J. M., Harrison, B. C., et al. (2016). A small-molecule inhibitor of sarcomere contractility suppresses hypertrophic cardiomyopathy in mice. *Science* 351, 617–621. doi: 10.1126/science.aad3456

Grimm, A. F., Lin, H.-L., and Grimm, B. R. (1980). Left ventricular free wall and intraventricular pressure-sarcomere length distributions. *Am. J. Physiol.* 239, H101–H107. doi: 10.1152/ajpheart.1980.239.1.H101

Guccione, J. M., O'Dell, W. G., McCulloch, A. D., and Hunter, W. C. (1997). Anterior and posterior left ventricular sarcomere lengths behave similarly during ejection. *Am. J. Physiol.* 272, H469–H477. doi: 10.1152/ajpheart.1997.272.1.H469

Hamdani, N., de Waard, M., Messer, A. E., Boontje, N. M., Kooij, V., van Dijk, S., et al. (2008). Myofilament dysfunction in cardiac disease from mice to men. *J. Muscle Res. Cell. Motil.* 29, 189–201. doi: 10.1007/s10974-008-9160-y

Hanft, L. M., Biesiadecki, B. J., and McDonald, K. S. (2013). Length dependence of striated muscle force generation is controlled by phosphorylation of cTnI at serines 23/24. *J. Physiol.* 591, 4535–4547. doi: 10.1113/jphysiol.2013.258400

Hanft, L. M., Cornell, T. D., McDonald, C. A., Rovetto, M. J., Emter, C. A., and McDonald, K. S. (2016). Molecule specific effects of PKA-mediated phosphorylation on rat isolated heart and cardiac myofibrillar function. *Arch. Biochem. Biophys.* 601, 22–31. doi: 10.1016/j.abb.2016.01.019

Hanft, L. M., Emter, C. A., and McDonald, K. S. (2017). Cardiac myofibrillar contractile properties during the progression from hypertension to decompensated heart failure. *Am. J. Physiol. Heart Circ. Physiol.* 313, H103–H113. doi: 10.1152/ajpheart.00069.2017

Hanft, L. M., Fitzsimons, D. P., Hacker, T. A., Moss, R. L., and McDonald, K. S. (2019). The role of cardiac MyBP-C in regulating Frank-Starling relationships. *Biophys. J.* 116:166a.

Hanft, L. M., and McDonald, K. S. (2009). Sarcomere length dependence of power output is increased after PKA treatment in rat cardiac myocytes. *Am. J. Physiol. Heart Circ. Physiol.* 296, H1524–H1531. doi: 10.1152/ajpheart.00864.2008

Hanft, L. M., and McDonald, K. S. (2010). Length dependence of force generation exhibit similarities between rat cardiac myocytes and skeletal muscle fibres. *J. Physiol.* 588, 2891–2903. doi: 10.1113/jphysiol.2010.190504

Haynes, P., Nava, K. E., Lawson, B. A., Chung, C. S., Mitov, M. I., Campbell, S. G., et al. (2014). Transmural heterogeneity of cellular level power output is reduced in human heart failure. *J. Mol. Cell. Cardiol.* 72, 1–8. doi: 10.1016/j.yjmcc.2014.02.008

Herron, T. J., Korte, F. S., and McDonald, K. S. (2001). Loaded shortening and power output in cardiac myocytes are dependent on myosin heavy chain isoform expression. *Am. J. Physiol. Heart Circ. Physiol.* 281, H1217–H1222. doi: 10.1152/ajpheart.2001.281.3.H1217

Herron, T. J., and McDonald, K. S. (2002). Small amounts of alpha-myosin heavy chain isoform expression significantly increase power output of rat cardiac myocyte fragments. *Circ. Res.* 90, 1150–1152. doi: 10.1161/01.res.0000022879.57270.11

Hill, A. V. (1938). The heat of shortening and the dynamic constants of muscle. *Proc. R. Soc. Lond. Ser. B* 126, 136–195. doi: 10.1152/advan.00072.2005

Hinken, A. C., and McDonald, K. S. (2004). Inorganic phosphate speeds loaded shortening in rat skinned cardiac myocytes. *Am. J. Physiol. Cell Physiol.* 287, C500–C507. doi: 10.1152/ajpcell.00049.2004

Holubarsch, C., Ruf, T., Goldstein, D. J., Ashton, R. C., Nickl, W., Pieske, B., et al. (1996). Existence of the Frank-Starling mechanism in the failing human heart: investigations on the organ, tissue, and sarcomere levels. *Circulation* 94, 683–689. doi: 10.1161/01.cir.94.4.683

Kooij, V., Saes, M., Jaquet, K., Zaremba, R., Foster, D. B., Murphy, A. M., et al. (2010). Effect of troponin I ser23/24 phosphorylation on Ca2+-sensitivity in human myocardium depends on the phosphorylation background. *J. Mol. Cell. Cardiol.* 48, 954–963. doi: 10.1016/j.yjmcc.2010.01.002

Korte, F. S., Herron, T. J., Rovetto, M. J., and McDonald, K. S. (2005). Power output is linearly related to MyHC content in rat skinned myocytes and isolated working hearts. *Am. J. Physiol. Heart Circ. Physiol.* 289, H801–H812. doi: 10.1152/ajpheart.01227.2004

Korte, F. S., and McDonald, K. S. (2007). Sarcomere length dependence of rat skinned cardiac myocyte mechanical properties: dependence on myosin heavy chain. *J. Physiol.* 581, 725–739. doi: 10.1113/jphysiol.2007.128199

Kuro-o, M., Tsuchimochi, H., Ueda, S., Takaku, F., and Yazaki, Y. (1986). Distribution of cardiac myosin isozymes in human conduction system. Immunohistochemical study using monoclonal antibodies. *J. Clin. Invest.* 77, 340–347. doi: 10.1172/JCI112310

McDonald, K. S. (2000). Ca2+ dependence of loaded shortening in rat skinned cardiac myocytes and skeletal muscle fibers. *J. Physiol.* 525, 169–181. doi: 10.1111/j.1469-7793.2000.00169.x

McDonald, K. S., Hanft, L. M., Domeier, T. L., and Emter, C. A. (2012). Length and PKA dependence of force generation and loaded shortening in porcine cardiac myocytes. *Biochem. Res. Int.* 5:371415. doi: 10.1155/2012/371415

McDonald, K. S., and Moss, R. L. (1995). Osmotic compression of single cardiac myocytes reverses the reduction in Ca2+ sensitivity of tension observed at short sarcomere length. *Circ. Res.* 77, 199–205. doi: 10.1161/01.res.77.1.199

Messer, A. E., Jacques, A. M., and Marston, S. B. (2007). Troponin phosphorylation and regulatory function in human heart muscle: dephosphorylation of Ser 23/24 on troponin I could account for the contractile defect in end-stage heart failure. *J. Mol. Cell. Cardiol.* 42, 247–259. doi: 10.1016/j.yjmcc.2006.08.017

Patterson, S., and Starling, E. H. (1914). On the mechanical factors which determine the output of the ventricles. *J. Physiol.* 48, 357–379. doi: 10.1113/jphysiol.1914.sp001669

Pollack, G. H., and Huntsman, L. L. (1974). Sarcomere length-active force relations in living mammalian cardiac muscle. *Am. J. Physiol.* 227, 383–389. doi: 10.1152/ajplegacy.1974.227.2.383

Ross, J., and Braunwald, E. (1964). Studies on Starling's law of the heart: the effect of impeding venous return on performance of the normal and failing human left ventricle. *Circulation* 30, 719–727. doi: 10.1161/01.cir.30.5.719

Schwinger, R. H., Bohm, M., Koch, A., Schmidt, U., Morano, I., Eissner, H. J., et al. (1994). The failing human heart is unable to use the Frank-Starling mechanism. *Circ. Res.* 74, 959–969. doi: 10.1161/01.res.74.5.959

Sequiera, V., Wijnker, P. J., Nijenkamp, L. L., Kuster, D. W., Najafi, A., Witjas-Paalberends, R., et al. (2013). Perturbed length-dependent activation in human hypertrophic cardiomyopathy with missense sarcomeric gene mutations. *Circ. Res.* [Epub ahead of print]. doi: 10.1161/CIRCRESAHA.111.300436

Stathopoulou, K., Wittig, I., Heidler, J., Piasecki, A., Richter, F., Diering, S., et al. (2016). S-glutathiolation impairs phosphoregulation and function of cardiac myosin-binding protein C in human heart failure. *FASEB J.* 30, 1849–1864. doi: 10.1096/fj.201500048

Stelzer, J. E., and Moss, R. L. (2006). Contributions of stretch activation to length-dependent contraction in murine Myocardium. *J. Gen. Physiol.* 128, 461–471. doi: 10.1085/jgp.200609634

Swenson, A. M., Tang, W., Blair, C. A., Fetrow, C. M., Unrath, W. C., Previs, M. J., et al. (2017). Omecamtiv mecarbil enhances the duty ratio of human beta-cardiac myosin resulting in increased calcium sensitivity and slowed force development in cardiac muscle. *J. Biol. Chem.* 292, 3768–3778. doi: 10.1074/jbc.M116.748780

van der Velden, J., de Jong, J. W., Owen, V. J., Burton, P. B. J., and Stienen, G. J. M. (2000). Effect of protein kinase A on calcium sensitivity of force and its sarcomere length dependence in human cardiomyocytes. *Cardiovasc. Res.* 46, 487–495. doi: 10.1016/s0008-6363(00)00050-x

van Der Velden, J., Klein, L. J., Zaremba, R., Boontje, N. M., Huybregts, M. A., Stooker, W., et al. (2001). Effects of calcium, inorganic phosphate, and pH on isometric force in single skinned cardiomyocytes from donor and failing human hearts. *Circulation* 104, 1140–1146. doi: 10.1161/hc3501.095485

van der Velden, J., Narolska, N. A., Lamberts, R. R., Boontje, N. M., Borbely, A., Zaremba, R., et al. (2006). Functional effects of protein kinase C-mediated myofilament phosphorylation in human myocardium. *Cardiovasc. Res.* 69, 876–887. doi: 10.1016/j.cardiores.2005.11.021

van der Velden, J., Papp, Z., Zaremba, R., Boontje, N. M., de Jong, J. W., Owen, V. J., et al. (2003). Increased calcium sensitivity of the contractile apparatus in end-stage human heart failure results from altered phosphorylation of contractile proteins. *Cardiovasc. Res.* 57, 37–47. doi: 10.1016/s0008-6363(02)00606-5

Wijnker, P. J., Murphy, A. M., Stienen, G. J., and van der Velden, J. (2014). Troponin I phosphorylation in human myocardium in health and disease. *Netherlands Heart J.* 22, 463–469. doi: 10.1007/s12471-014-0590-4

Wijnker, P. J. M., Foster, D. B., Tsao, A. L., Frazier, A. H., dos Remedios, C. G., Murphy, A. M., et al. (2013). Impact of site-specific phophorylation of protein kinase A sites Ser23 and Ser24 of cardiac troponin I in human cardiomyocytes. *Am. J. Physiol.* 304, H260–H268. doi: 10.1152/ajpheart.00498.2012

Wolff, M. R., Buck, S. H., Stoker, S. W., Greaser, M. L., and Mentzer, R. M. (1996). Myofibrillar calcium sensitivities of isometric tension is increased in human dilated cardomyopathies. *J. Clin. Investig.* 98, 167–176.

Conflict of Interest: The authors declare that the research was conducted in the absence of any commercial or financial relationships that could be construed as a potential conflict of interest.

frontiers in Physiology

ORIGINAL RESEARCH
published: 25 May 2020
doi: 10.3389/fphys.2020.00345

Enhanced Cardiomyocyte Function in Hypertensive Rats With Diastolic Dysfunction and Human Heart Failure Patients After Acute Treatment With Soluble Guanylyl Cyclase (sGC) Activator

*Detmar Kolijn[1,2,3,4†], Árpád Kovács[1,2,3,4†], Melissa Herwig[1,2,3,4†], Mária Lódi[1,2,3,5,6], Marcel Sieme[1,2], Abdulatif Alhaj[1,2,3], Peter Sandner[7], Zoltán Papp[5], Peter H. Reusch[2], Peter Haldenwang[8], Ines Falcão-Pires[9], Wolfgang A. Linke[10], Kornelia Jaquet[1,2,3], Sophie Van Linthout[11], Andreas Mügge[1,3], Carsten Tschöpe[11] and Nazha Hamdani[1,2,3,4]**

[1] Department of Molecular and Experimental Cardiology, Ruhr University Bochum, Bochum, Germany, [2] Department of Clinical Pharmacology, Ruhr University Bochum, Bochum, Germany, [3] Department of Cardiology, St. Joseph Hospital, Ruhr University Bochum, Bochum, Germany, [4] Institute of Physiology, Ruhr University Bochum, Bochum, Germany, [5] Division of Clinical Physiology, Department of Cardiology, Faculty of Medicine, University of Debrecen, Debrecen, Hungary, [6] University of Debrecen, Kálmán Laki Doctoral School, Debrecen, Hungary, [7] Bayer AG, Drug Discovery Cardiology, Wuppertal, Germany, [8] Department of Cardiothoracic Surgery, University Hospital Bergmannsheil Bochum, Bochum, Germany, [9] Department of Surgery and Physiology and Cardiovascular Research Centre, Faculty of Medicine, University of Porto, Porto, Portugal, [10] Institute of Physiology II, University Hospital Münster, University of Münster, Münster, Germany, [11] Department of Medicine and Cardiology (CVK), Charité-Universitätsmedizin Berlin, Berlin, Germany

OPEN ACCESS

Edited by:
Sachio Morimoto, International University of Health and Welfare (IUHW), Japan

Reviewed by:
Viacheslav Nikolaev, University of Göttingen, Germany
Robert Lukowski, University of Tübingen, Germany

***Correspondence:**
Nazha Hamdani
nazha.hamdani@rub.de

† These authors have contributed equally to this work

Specialty section:
This article was submitted to Striated Muscle Physiology, a section of the journal Frontiers in Physiology

Received: *19 December 2019*
Accepted: *26 March 2020*
Published: *25 May 2020*

Citation:
Kolijn D, Kovács Á, Herwig M, Lódi M, Sieme M, Alhaj A, Sandner P, Papp Z, Reusch PH, Haldenwang P, Falcão-Pires I, Linke WA, Jaquet K, Van Linthout S, Mügge A, Tschöpe C and Hamdani N (2020) Enhanced Cardiomyocyte Function in Hypertensive Rats With Diastolic Dysfunction and Human Heart Failure Patients After Acute Treatment With Soluble Guanylyl Cyclase (sGC) Activator. Front. Physiol. 11:345. doi: 10.3389/fphys.2020.00345

Aims: Our aim was to investigate the effect of nitric oxide (NO)-independent activation of soluble guanylyl cyclase (sGC) on cardiomyocyte function in a hypertensive animal model with diastolic dysfunction and in biopsies from human heart failure with preserved ejection fraction (HFpEF).

Methods: Dahl salt-sensitive (DSS) rats and control rats were fed a high-salt diet for 10 weeks and then acutely treated *in vivo* with the sGC activator BAY 58-2667 (cinaciguat) for 30 min. Single skinned cardiomyocyte passive stiffness ($F_{passive}$) was determined in rats and human myocardium biopsies before and after acute treatment. Titin phosphorylation, activation of the NO/sGC/cyclic guanosine monophosphate (cGMP)/protein kinase G (PKG) cascade, as well as hypertrophic pathways including NO/sGC/cGMP/PKG, PKA, calcium–calmodulin kinase II (CaMKII), extracellular signal-regulated kinase 2 (ERK2), and PKC were assessed. In addition, we explored the contribution of pro-inflammatory cytokines and oxidative stress levels to the modulation of cardiomyocyte function. Immunohistochemistry and electron microscopy were used to assess the translocation of sGC and connexin 43 proteins in the rat model before and after treatment.

Results: High cardiomyocyte $F_{passive}$ was found in rats and human myocardial biopsies compared to control groups, which was attributed to hypophosphorylation of total

titin and to deranged site-specific phosphorylation of elastic titin regions. This was accompanied by lower levels of PKG and PKA activity, along with dysregulation of hypertrophic pathway markers such as CaMKII, PKC, and ERK2. Furthermore, DSS rats and human myocardium biopsies showed higher pro-inflammatory cytokines and oxidative stress compared to controls. DSS animals benefited from treatment with the sGC activator, as $F_{passive}$, titin phosphorylation, PKG and the hypertrophic pathway kinases, pro-inflammatory cytokines, and oxidative stress markers all significantly improved to the level observed in controls. Immunohistochemistry and electron microscopy revealed a translocation of sGC protein toward the intercalated disc and t-tubuli following treatment in both control and DSS samples. This translocation was confirmed by staining for the gap junction protein connexin 43 at the intercalated disk. DSS rats showed a disrupted connexin 43 pattern, and sGC activator was able to partially reduce disruption and increase expression of connexin 43. In human HFpEF biopsies, the high $F_{passive}$, reduced titin phosphorylation, dysregulation of the NO–sGC–cGMP–PKG pathway and PKA activity level, and activity of kinases involved in hypertrophic pathways CaMKII, PKC, and ERK2 were all significantly improved by sGC treatment and accompanied by a reduction in pro-inflammatory cytokines and oxidative stress markers.

Conclusion: Our data show that sGC activator improves cardiomyocyte function, reduces inflammation and oxidative stress, improves sGC–PKG signaling, and normalizes hypertrophic kinases, indicating that it is a potential treatment option for HFpEF patients and perhaps also for cases with increased hypertrophic signaling.

Keywords: oxidative stress, inflammation, HFPEF, sGC activator, titin

INTRODUCTION

Despite major therapeutic advances in the treatment of heart failure (HF) in general, the subtype HF with preserved ejection fraction (HFpEF) continues to take a significant clinical toll in terms of morbidity and mortality. Current treatment options for HFpEF patients are limited, and no drug has yet been shown to improve diastolic function in HFpEF patients. Many of the tested compounds were ineffective in reducing morbidity and mortality, and numerous clinical trials have failed to show that the drug under investigation delivered any positive effect. Patient management is presently limited to amelioration of symptoms and the treatment of common comorbidities such as hypertension, diabetes, obesity, and atrial fibrillation. The recent outcome of the PARAGON-HF trial showed evidence of a heterogeneous response to treatment, with potential benefit in certain subgroups such as women and patients with an EF below the median. These data strongly imply that "one size might not fit all" in HFpEF (ClinicalTrials.gov Identifier: NCT0192071). Many studies from our and other groups have suggested that boosting the cyclic guanosine monophosphate (cGMP)-dependent protein kinase or protein kinase G (cGMP–PKG) pathways is a promising target when aiming to improve diastolic function in HFpEF patients (Bishu et al., 2011; Hamdani et al., 2013a, 2014). Studies have shown that PKG is reduced in HFpEF patients and animal models probably due to inflammation and oxidative stress, thus suggesting that it is a possible treatment target in patients (Franssen et al., 2016). Unfortunately, the RELAX trial using a phosphodiesterase (PDE)5 inhibitor to increase cGMP failed to show any beneficial effect in HFpEF patients (van Heerebeek et al., 2012), as inhibition of PDE5 did not appear to improve the low cGMP content found in HFpEF (Redfield et al., 2013). In the >100 HFpEF patients studied, sildenafil failed to raise plasma cGMP or ameliorate diastolic left ventricular (LV) dysfunction. The authors suggested that these disappointing results were (partially) attributable to the relatively low right-sided heart pressures in their patient group compared with earlier studies in HF with reduced EF (HFrEF); moreover, PDE5 was undetectable in humans or experimental models of HF lysates, whereas it is present in the murine and bovine lung samples which were used as a positive control (Degen et al., 2015). These results indicate that if PDE5 is expressed in cardiac tissue, it is present in very low quantities. In addition, based on the elevated basal plasma levels of N-terminal pro-B type natriuretic peptide (NT-proBNP) and the high prevalence of atrial fibrillation, it seems that patients in the RELAX trial were at an advanced stage of HFpEF and therefore less likely to benefit from a limited strategy involving only inhibition of cGMP breakdown *via* PDE5. In particular, PDE9 was recently shown to be upregulated in hypertrophy and cardiac failure. PDE9 is expressed in the mammalian heart (including human) and regulates NP rather than NO-stimulated cGMP in cardiomyocytes (Lee et al., 2015), and its inhibition protects against pathological responses to

neurohormones *in vitro* and sustained pressure overload stress *in vivo*. PDE9 expression is increased in the LV of patients with hypertrophy due to aortic stenosis (pressure overload), and even more so in HFpEF patients. These data suggest that inhibition of PDE9 activated PKG and might blunt pathological stress responses. Both PDE5 and PDE9 regulate cGMP–PKG activity, and in combination, they could be beneficial in the treatment of HFpEF. Given the possibility that changes in cGMP may be an important underlying pathophysiologic mechanism in HFpEF, stimulation of cGMP production remains an interesting therapeutic strategy in HFpEF. However, boosting myocardial cGMP levels might be possible by alternative means, and many different strategies for cGMP enhancement are available. The soluble guanylyl cyclase (sGC) stimulators and activators may have a particular therapeutic potential in cardiovascular disease (Evgenov et al., 2006), and the effect of both depends on the oxidation state and heme content of sGC, and both have been shown to be effective in increasing the pool of cGMP (Evgenov et al., 2006). sGC stimulators, such as BAY 41–2272, BAY 41-8543, BAY 63-2521 (riociguat), and BAY 1021189 (vericiguat), increase sGC activity of the native non-oxidized and heme-containing sGC. Thus, sGC stimulators are NO-independent but heme-dependent. In contrast, sGC activators such as Bay 58-2667 (cinaciguat) increase enzyme activity when the heme iron is oxidized (Fe3+) or the heme group is missing (Stasch et al., 2001, 2011; Sandner et al., 2019), and they are termed NO-independent and heme-independent sGC activators. Under physiological conditions, sGC exists in equilibrium between its reduced and oxidized state, but oxidative stress shifts this equilibrium toward the NO-insensitive ferric/heme-free form (Stasch et al., 2006). In line with these findings, cinaciguat relaxed blood vessels in diseased animal models including hypertensive rats and hyperlipidemic rabbits, more efficacious compared to control, healthy animals. These effects are enhanced in the presence of oxidized sGC (Stasch et al., 2006).

Studies of sGC stimulators and activators in experimental models of hypertension have provided valuable insights into their therapeutic potential. These drugs induced vasodilation, attenuated cardiac fibrosis and hypertrophy, normalized blood pressure, protected against cardiac and renal damage, and improved survival in rat models of hypertension (Mittendorf et al., 2009; Stasch and Hobbs, 2009; Wilck et al., 2018). Beneficial effects were also observed in patients with pulmonary arterial hypertension (Stasch et al., 2011). In addition, other potential effects in HF may involve the prevention of myocardial dysfunction, dysregulation of the NO–sGC–cGMP pathway, and increased diastolic stiffness associated with endothelial dysfunction. Augmenting sGC activity might therefore decrease titin-based stiffness through increased cardiomyocyte cGMP and thus counteract myocardial stiffening in HF, particularly in HFpEF.

A clinical trial using the sGC stimulator, vericiguat, showed that the compound was well tolerated when given once a day to patients with HFrEF, leading to lower levels of N-terminal pro-B type natriuretic peptide (NT-proBNP) (trial SOCRATES-REDUCED) (Gheorghiade et al., 2016). Vericiguat was also tested in HFpEF patients in the SOCRATES-PRESERVED trial, a phase IIb study of NO–sGC stimulation with vericiguat for 12 weeks. The outcome was improved quality of life without changing NT-proBNP levels, thus encouraging further studies to boost the NO-sGC pathway in HFpEF patients (Pieske et al., 2017).

The present study investigated the effects of an sGC activator in Dahl salt-sensitive (DSS) rats exhibiting hypertension and diastolic dysfunction and was designed to examine the underlying mechanisms and pathways that contribute to cGMP decline in HFpEF. Since both NO and sGC levels are reduced in HFpEF, we hypothesized that treatment with the sGC activator BAY 58-2667 would improve the functioning of this pathway and thereby improve cardiomyocyte function *via* enhanced titin phosphorylation.

METHODS

Human Studies

All procedures were performed according to the Declaration of Helsinki and were approved by the local ethics committee. Biopsies were obtained for the primary purpose of diagnosis following ethics committee approval (EA2/140/16) and informed consent. Control samples were obtained from explanted donor hearts following ethics committee approval (OKAR/1066/2008/OKAR). Effects of *in vitro* incubation of sGC stimulation on cardiomyocyte passive mechanics and titin phosphorylation were studied on LV myocardial samples obtained from biopsies from HFpEF patients (n = 14/samples; for patient characteristics, see **Table 1**) as well as from healthy donors (n = 10/samples).

HFpEF patients were referred for cardiac catheterization and endomyocardial biopsy procurement because of clinical suspicion of a cardiomyopathy. They all had been admitted

TABLE 1 | HFpEF patient characteristics.

HFpEF patients	
n	**14**
Age, years (mean ± SD)	61.5 ± 14.5
EF, % (mean ± SD)	65.6 ± 11.6
NYHA class	II–III
LV EDP, mmHg (mean ± SD)	16.3 ± 6.3
NT-proBNP, ng/L (mean ± SD)	520 ± 440
E/E'	16.8 ± 4.6
ACE inhibitors (%)	76.0
Diuretics (%)	66.5
Digoxin (%)	12.5
AT_1 receptor antagonists (%)	30.1
Aldosterone antagonists (%)	13.5
Amiodarone (%)	19.5
Beta-blockers (%)	80.0

EDP, end-diastolic pressure; EF, ejection fraction; LV, left ventricular; NT-proBNP, N-terminal pro-B type natriuretic peptide; NYHA, New York Heart Association; E/E', mitral inflow E wave/tissue Doppler mitral annulus velocity; HFpEF, heart failure with preserved ejection fraction.

to hospital because of worsening HF. Subsequent histological examination ruled out a cardiomyopathy/infiltrative myocardial disease. Coronary angiography showed the absence of significant coronary artery stenosis or graft vasculopathy. All patients satisfied the criteria as proposed by the European study group on HFpEF, i.e., signs and symptoms of congestive HF, LV ejection fraction (EF) $\geq$ 50% and abnormal LV end-diastolic pressure at rest > 12 mmHg (van Heerebeek et al., 2006, 2008, 2012). All patients had one or more predisposing risk factors for diastolic LV dysfunction. Endomyocardial biopsies were obtained from the LV and were snap frozen in liquid nitrogen and stored at −80°C until processing.

Animal Model

Care and use of laboratory animals, as well as experimental procedures, were reviewed and approved by Ruhr University Bochum (Germany; ethical statement number: 84-02.04.2015.A449). Our study complied with the *Declaration of Helsinki* and with the *Directive 2010/63/EU of the European Parliament and of the Council "on the protection of animals used for scientific purposes."* Male DSS rat (SS/JrHsdMcwiCrl; n = 55) and SS-13^{BN} (SS-Chr 13^{BN}/McwiCrl; n = 55) consomic control strains were obtained from Charles River Laboratories (Wilmington, MA, United States). Eight-week-old DSS rats were fed a high-salt diet for 10 weeks to induce hypertension. Then, the rats were treated with BAY 58-2667 (obtained from Bayer AG, Wuppertal, Germany). Administration of sGC activator BAY 58-2667 was initiated at 18th week of age intravenously for 30 min. The animals (eight animals from each group) were housed on a 12/12 h light/dark cycle with constant temperature (22–23°C), with access to food and tap water *ad libitum*. Animals were anesthetized with either isoflurane (induction with 3%, maintenance with 1.5%), and the hearts were taken out and frozen in nitrogen.

Force Measurements on Isolated Cardiomyocytes

Force measurements were performed on single demembranated cardiomyocytes (n = 12–42/5–6 heart/group) as described before[17]. Briefly, LV samples were de-frozen in relaxing solution (containing in mM: 1.0 free Mg^{2+}; 100 KCl; 2.0 EGTA; 4.0 Mg-ATP; 10 imidazole; pH 7.0), mechanically disrupted and incubated for 5 min in relaxing solution supplemented with 0.5% Triton X-100 (all from Sigma-Aldrich). The cell suspension was washed five times in relaxing solution. Single cardiomyocytes were selected under an inverted microscope (Zeiss Axiovert 135, 40× objective; Carl Zeiss AG Corp., Obochen, Germany) and attached with a silicone adhesive between a force transducer and a high-speed length controller (piezoelectric motor) as part of a "Permeabilized Myocyte Test System" (1600A; with force transducer 403A; Aurora Scientific, Aurora, ON, Canada).

Cardiomyocyte Ca^{2+}-independent passive force ($F_{passive}$) was measured in relaxing buffer at room temperature within a sarcomere length (SL) range between 1.8 and 2.4 μm. Force values were normalized to myocyte cross-sectional area calculated from the diameter of the cells, assuming a circular shape. Subsequently, cardiomyocytes were incubated for 40 min in relaxing solution supplemented in one set with PKA and the other set with PKG1α (batch 034K1336, 0.1 U/ml; Sigma-Aldrich), cGMP (10 μM; Sigma-Aldrich), and dithiothreitol (DTT; 6 mM; Sigma-Aldrich). Thereafter $F_{passive}$ measurements were again performed in relaxing solution at SL 1.8–2.4 μm.

Human LV samples were thawed in relaxing solution and incubated *in vitro* with 0.3 μM/L sGC stimulator for 30 min. Demembranation was performed following incubation with sGC stimulator. Cardiomyocyte (n = 12/group) $F_{passive}$ was thereafter measured within an SL range between 1.8 and 2.4 μm as described above.

Titin and Phospho-Titin Analysis by Western Blot

Polyacrylamide gel electrophoresis (PAGE) was performed to separate titin as previously described (Hamdani et al., 2013b). Briefly, LV tissue samples (n = 8–10/group) were solubilized in 50 mM Tris-sodium dodecyl sulfate (SDS) buffer (pH 6.8) containing 8 μg/ml leupeptin (Peptide Institute Inc., Ibaraki, Osaka, Japan) and 10 μl/ml phosphatase inhibitor cocktail (P2850; Sigma-Aldrich). Samples were heated for 3 min at 96°C and centrifuged. Samples were applied in duplicates at concentrations that were within the linear range of the detection system (20 and 25 μg dry weight; checked by spectroscopic methods) and separated by agarose-strengthened 1.8% SDS-PAGE. Gels were run at 4 mA constant current for 16 h. Thereafter, Western blot (WB) was performed to measure site-specific and total phosphorylation of titin. Following SDS-PAGE, proteins were transferred to polyvinylidene difluoride (PVDF) membranes (Immobilon-P 0.45 μm; Merck Millipore, Burlington, MA, United States). Blots were pre-incubated with 3% bovine serum albumin in Tween Tris-buffered saline (TTBS; containing 10 mM Tris-HCl; pH 7.6; 75 mM NaCl; 0.1% Tween; all from Sigma-Aldrich) for 1 h at room temperature. Then, blots were incubated overnight at 4°C with the primary antibodies.

Anti-phospho serine (Ser)/threonine (Thr) antibody (dilution 1:500; ECM Biosciences LLC, Versailles, KY, United States) was used to assess total titin phosphorylation. Phosphosite-specific anti-titin antibodies were custom-made by Eurogentec (Seraing, Belgium) with positions in N2Bus (N2B unique sequence) and PEVK (rich in proline, glutamate, valine, and lysine amino acids) domains of mouse (*Mus musculus*) titin according to UniProtKB identifier A2ASS6 (Hamdani et al., 2013b). The following rabbit polyclonal affinity purified antibodies were used:

– anti-phospho-N2Bus (**SER3991**) against EEGKS(PO3H2)LSFPLA (dilution 1:500);
– anti-phospho-N2Bus (**SER4043**) against QELLS(PO3H2)KETLFP (dilution 1:100);
– anti-phospho-N2Bus (**SER4080**) against LFS(PO3H2)EWLRNI (dilution 1:500);
– anti-phospho-PEVK (**SER12742**) against EVVLKS(PO3H2)VLRK (dilution 1:100);
– anti-phospho-PEVK (**SER12884**) against KLRPGS(PO3H2)GGEKPP (dilution 1:500).

The amino acid sequences of rat titin at Ser3991, Ser4043, Ser4080, Ser12742, and Ser12884 are identical to the amino acid sequences of mouse and refer to human titin at Ser4010, Ser4062, Ser4099, Ser11878, and Ser12022, respectively.

After washing with TTBS, primary antibody binding was visualized using secondary horseradish peroxidase (HRP)-labeled, goat anti-rabbit antibody (dilution 1:10,000; DakoCytomation, Glostrup, Denmark) and enhanced chemiluminescence (ECL Western Blotting Detection; Amersham Biosciences). WB signals were visualized using the LAS-4000 Image Reader and analyzed with Multi Gauge V3.2 software (both from FUJIFILM Corp., Minato, Tokyo, Japan). Coomassie-based PVDF stains were saved for comparison of protein load, and titin phosphorylation levels were indexed to the signal intensities obtained from PVDF staining. Finally, signals obtained from phospho-specific antibodies were normalized to signals obtained from PVDF stains referring to the entire protein amount transferred.

Human LV samples from HFpEF patients and donor controls (n = 8–10/group) were incubated *in vitro* with 1.0 μM/L sGC activator for 30 min. Subsequently, total titin phosphorylation of the sum of N2BA and N2B titin as Ser/Thr phosphorylation and PKA and PKG site-specific titin phosphorylation as Ser4010 and Ser4099 phosphorylation were assessed as described above.

For human phosphosite-specific anti-titin antibodies were custom-made by Eurogentec (Seraing, Belgium) with positions in N2Bus (N2B unique sequence) domains of human titin according to UniProtKB identifier Q8WZ42 (Hamdani et al., 2013b). The following rabbit polyclonal affinity purified antibodies were used:

– anti-phospho-N2Bus (**Ser4010**) against EEGKS(PO3H2)LSFPLA (dilution 1:500);

– anti-phospho-N2Bus (**Ser4099**) against QELLS(PO3H2)KETLFP (dilution 1:100).

Myocardial Cyclic Guanosine Monophosphate Level

According to previous protocol (Franssen et al., 2016), myocardial cGMP was determined in LV homogenates (n = 8–10/group) by use of parameter cGMP assay immunoassay kit (R&D Systems, Minneapolis, MN, United States), in which cGMP present in the homogenate competes with a fixed amount of HRP-labeled cGMP for sites on a rabbit polyclonal antibody. The homogenates were diluted in cell lysis buffer, and 100 μl of 0.025-μg/μl protein aliquots were assayed according to manufacturer's instructions. Results of duplicate determinations were averaged and expressed as μg/μl.

Myocardial Protein Kinase G Activity

LV tissues samples (n = 8–10 samples) were homogenized in 25 mM Tris-HCl (pH 7.4), 1 mM EDTA, 2 mM EGTA, 5 mM DTT, 0.05% Triton X-100, and protease inhibitor cocktail (all from Sigma-Aldrich) and centrifuged for 5 min. Supernatants containing equal amounts of total protein were analyzed for PKG activity as described previously (Franssen et al., 2016). Briefly, reaction mixtures were incubated at 30°C for 10 min. Reaction mixtures contained 40 mM Tris-HCl (pH 7.4), 20 mM $Mg(CH_3COO)_2$, 0.2 mM [^{32}P] adenosine triphosphate (ATP) (500–1,000 cpm pM^{-1}; Amersham PLC, Little Chalfont, United Kingdom), 113 mg/ml heptapeptide (RKRSRAE), and 3 μM cGMP (both from Promega Corp., Madison, WI, United States), and a highly specific inhibitor of cyclic adenosine monophosphate-dependent protein kinase (5–24; Calbiochem, San Diego, CA, United States). The reaction was terminated by spotting 70 μl onto Whatman P-81 filters (MACHEREY-NAGEL). Samples were subsequently incubated and washed with 75 mM H_3PO_4 for 5 min to remove unbound ATP. Filters were then washed with 100% ethanol and air-dried before quantification. PKG activity was quantified using a Wallac 1409 Liquid Scintillation Counter (Hidex Oy, Turku, Finland). Specific activity of PKG was expressed as pM of ^{32}P incorporated into the substrate (pM/min/mg protein).

Myocardial Protein Kinase A and C Activity

PKA and PKC activity (n = 8–10 samples) was analyzed using non-radioactive PKA and PKC kinase activity assay kit (Enzo Life Science). Samples were homogenized in cell lysis buffer (20 mmol/L MOPS, 50 mmol/L β-glycerolphosphate, 50 mmol/L sodium fluoride, 1 mmol/L sodium vanadate, 5 mmol/L EGTA, 2 mmol/L EDTA, 1% NP40, 1 mmol/L DTT, 1 mmol/L benzamidine, 1 mmol/L phenylmethanesulphonylfluoride, and 10 μg/ml leupeptin and aprotinin, each). Supernatants were collected after centrifugation at 13,000 rpm for 30 min. Supernatants containing equal amounts of total protein (30 ng/μl protein aliquots were assayed according to manufacturer's instructions) were added into the appropriate wells of the PKA and PKC substrates microliter plate. PKA and PKC kinase reaction was initiated by addition of ATP, and samples were subsequently incubated at 30°C for 90 min. Phosphorylated peptide substrates were recognized by phospho-specific substrate antibody. The phospho-specific antibody was subsequently bound by a peroxidase-conjugated secondary antibody anti-rabbit IgG:HRP. The assay was developed with tetramethylbenzidine, and the intensity of the color was measured in a microplate reader at 450 nm. Results of triplicate determinations were averaged, and specific activity of PKA was expressed as ng/μl.

Myocardial Calcium–Calmodulin Kinase II Activity Testing

CaMKII activity (n = 8–10 samples) was determined using a CycLex® CaMKII assay kit (CY-1173; MBL Corporation, MA, United States) according to the manufacturer's guidelines. Briefly, frozen heart tissues were homogenized in sample buffer containing 15% glycerol, 62.5 mmol/L Tris; pH 6.8; 1% (w/v) SDS, protease inhibitor, and protein phosphatase inhibitor, all prepared in distilled H_2O. Homogenates were centrifuged at 10,000 × g for 15 min at 4°C. The supernatant was removed and stored at -80°C. Protein samples were loaded onto microtiter wells (concentration, ∼2.0 μg/well) coated with CaMKII specific substrate, syntide-2, along with kinase reaction buffer with or without Ca^{2+}/calmodulin. To quantify CaMKII activity, a

standard curve correlating the amount of active CaMKII and the level of phosphorylation of syntide-2 was constructed.

Myocardial Protein Kinase Extracellular Signal-Regulated Kinase 2

ERK2 activity (n = 8–10 samples) was analyzed using non-radioactive ERK2 kinase activity assay kit (CHEMICON). Homogenates were made in cell lysis buffer (50 mM Tris, pH 8.0, 150 mM NaCl, 0.5 mM EDTA, 1 mM DTT, 1% NP-40, 0.5% sodium deoxycholate, 0.1% SDS, 32 μM phenazine methosulphate (PMS), 200 nM aprotinin, 4 μM leupeptin, 100 μM sodium vanadate). Supernatants were collected after centrifugation at 12,000 rpm for 10 min at 4°C. Then, 20 μl of anti-MAP kinase antibody were added to 1 ml of cell lysate and incubated for 1–12 h at 4°C on a shaking or rocking platform. ERK2 kinase reactions were initiated by addition of 10 μl of 5× ATP/$MgCl_2$ solution, and samples were subsequently incubated at 30°C for 60 min. Phosphorylated peptide substrates were recognized by phosphospecific substrate antibody. The enzyme reaction was terminated by adding 100 μl of stop solution to each well, including the control wells. Color intensity was measured in a microplate reader at 450 nm. Results of triplicate determinations were averaged.

Immunofluorescence Imaging

Frozen LV unfixed slides (n = 3 samples/heart) were air-dried for 10 min and fixed in 4% paraformaldehyde in phosphate buffered saline (PBS; Sigma-Aldrich). After washing 3 times in PBS for 5 min, tissue was blocked in 5% bovine serum albumin (Sigma-Aldrich) in PBS for 1 h at room temperature. After further washing 3 times in PBS for 5 min, fixed slides were dual-stained with anti-guanylyl cyclase β1 ER-19 (Sigma-Aldrich; dilution 1:200) or Connexin 43 (Sigma-Aldrich; dilution 1:400/Thermofisher Scientific; dilution 1:200) antibodies and anti-α-actinin (sarcomere; Sigma-Aldrich; dilution 1:400) overnight at 4°C. After washing in PBS, slides were subsequently incubated overnight with secondary antibodies: fluorescein (FITC) anti-mouse (Rockland Immunochemicals Inc., Limerick, PA, USA; dilution 1:300) and Cy3 anti-rabbit (Jackson ImmunoResearch Laboratories Inc., West Grove, PA, USA; dilution 1:100). After multiple washings slides were covered and sealed by Mowiol mounting medium and ultrathin glass coverslips (Thermo Fisher Scientific). Immuno-stained samples were analyzed by confocal laser scanning microscopy (cLSM) (Nikon Eclipse Ti-E Inverted Microscope System; Nikon Instruments, Nikon Corp, Shinagawa, Tokyo, Japan). Immunofluorescence imaging parameters were identical among groups.

Electron Microscopy

A small piece from the flash-frozen rat LV was cut and fixed in a 0.1 M PBS buffered fixative containing 4% paraformaldehyde (Sigma Aldrich, St. Louis, MO, United States) and 15% picric acid (Sigma Aldrich, St. Louis, MO, United States) overnight 4°C on a shaker. After washing the tissues three times in 0.1 M PBS and blocking with 20% normal goat serum (NGS) in PBS for 1 h, the primary antibody against PKG (Enzo Life Sciences, Farmingdale, United States) (1:200) and sGC (Sigma Aldrich, St. Louis, MO, United States) was used in a blocking solution (2% NGS in 0.1 M PBS) overnight 4°C on a shaker. After three times washing in 0.1 M PBS, the tissues were exposed to 1.4 nm nanogold conjugated anti-rabbit secondary antibody (Nanoprobes, NY, United States) (1:100) in the blocking solution overnight 4°C on shaker. After washing, the tissues were fixed in 1% glutaraldehyde in PBS for 10 min at room temperature. Silver enhancement was performed with HQ silver kit (Nanoprobes, NY, United States) after washing the samples with 0.1 M PBS and distillated water. After the enhancement, tissues were washed again, then treated with 0.5% osmium-tetroxide for 45 min, dehydrated in a grading series of ethanol and in propylene oxide, and embedded in DURCUPAN™ ACM resin (Sigma Aldrich, St. Louis, MO, United States). Sections of 50 nm were cut, counterstained with UranyLess (Electron Microscopy Sciences, Hatfield, PA, United States) for 10 min, and investigated using a Zeiss LEO 910 electron microscope. Pictures were made using magnifications of 4,000× and 8,000×.

Quantification of Tissue Oxidative Stress and Inflammation

Myocardial levels (n = 8–10 samples) of oxidative stress and inflammatory markers were tested using enzyme-linked immunosorbent assay (ELISA) and colorimetric assay kits: 3-nitrotyrosine ELISA kit (ab116691; Abcam), lipid peroxidation (malondialdehyde) assay kit (ab118970; Abcam), interleukin-6 (IL6) ELISA kit (ab100772; Abcam), intercellular cell adhesion molecule-1 (ICAM1) ELISA kit (ERICAM1; Thermo Fisher Scientific), vascular cell adhesion molecule-1 (VCAM1) ELISA kit (KHT0601; Thermo Fisher Scientific), and tumor necrosis factor alpha (TNFα) ELISA kit (ab108913; Abcam). Hydrogen peroxide (H_2O_2) was assessed in LV tissue homogenates (n = 8–10/group). Samples containing equal amounts of total protein were analyzed for H_2O_2 formation. H_2O_2 formation was measured by colorimetry at 540 nm. Results were converted using the standard curve for a known concentration of H_2O_2.

Quantification of Tissue Nitric Oxide

The concentration of NO (n = 8–10 samples) was assessed by means of a colorimetric assay kit (BioVision Inc., Milpitas, CA, United States). This assay quantitates NO production by providing a measure of total nitrate/nitrite. NO production was measured in tissue homogenates. Briefly, LV tissue samples (n = 8–10/group) were treated with trichloroacetic acid (8 g in 80 ml acetone; Sigma-Aldrich) and washed with 1 ml 0.2% DTT. Tissue samples were homogenized in 1% SDS sample buffer [Tri-distilled water: 8.47 ml; glycerol: 2.1 ml; 10% SDS: 1.4 ml; 0.5 M Tris-HCl (pH 6.8): 1.75 ml; brome-phenol blue: 0.28 ml; DTT: 32.4 mg; all from Sigma-Aldrich]. These tissue samples underwent sonication and were subsequently centrifuged at 14,000 g for 15 min at 5°C. Supernatants

containing equal amounts of total protein were analyzed for NO concentration.

In the first step, nitrate was converted to nitrite using nitrate reductase. In the second step, Griess reagents convert nitrite to an azochromophore reflecting NO concentration in the tissue samples. Nitrite levels could be measured independently from nitrate by omitting the first step. The absorbance of samples was measured at 540 nm using a plate reader. An assay buffer was used to generate a standard curve from which the absorbances of the samples could be translated into the nitrite and nitrate concentrations.

Statistical Analysis

Descriptive statistics for data location and variability was based on arithmetic mean and standard error of the mean (SEM), respectively. Groups defined by disease status and levels of SL, or a combination of these factors, were compared in terms of continuous variables using Student's two-sample t test (if distributional assumptions were satisfied) or Wilcoxon's rank-sum test (otherwise). All such tests were unpaired (the effect of all factors including stimulation length was assessed on independent samples) and stratified for equivalence on other factors, if any. Differences were considered to be statistically significant at $P < 0.05$.

RESULTS

Improved Diastolic Function Upon Soluble Guanylyl Cyclase Activator Treatment in Dahl Salt-Sensitive Rats

Transthoracic echocardiography was performed, and EF and fractional shortening were measured (parasternal long-axis view in M-mode) in anesthetized DAHL rats (n = 4) and controls (n = 4). Peak early (E), late (A) diastolic filling velocities and isovolumetric relaxation time (IVRT) were measured by pulsed wave Doppler. Tissue Doppler mode was applied to measure peak early diastolic (e′) and late diastolic (a′) mitral annular velocities. Echocardiographic measurements were performed at baseline conditions and after the treatment. Overall and despite the low n numbers, DAHL rats displayed a diastolic dysfunction indicated by prolonged IVRT, reduced E/A ratio. sGC activator significantly shortened IVRT and increased E/A ratio, indicating an improved diastolic function (**Table 2**).

Improved Cardiomyocyte Function Upon Soluble Guanylyl Cyclase Activator Treatment in Dahl Salt-Sensitive Rats

To assess the functional effects of sGC activator, we measured cardiomyocyte stiffness ($F_{passive}$). **Figure 1A** shows a representative elasticity test protocol and force recording for both DSS rats and controls. DSS rats showed a steeper $F_{passive}$ compared to controls (**Figure 1B**). Acute *in vivo* treatment with sGC activator significantly reduced cardiomyocyte $F_{passive}$ at SLs 2.1–2.4 μm (**Figures 1D,F**), but did not affect controls. We then treated cardiomyocytes with either PKG or PKA to determine whether these two kinases have an effect additional to sGC activator. Supplementary PKG (**Figures 1C,D**) and PKA (**Figures 1E,F**) had no significant effect on $F_{passive}$ in sGC activator-treated DSS rats as was also the case for the sGC activator-treated control group. PKG and PKA activity was significantly reduced in DSS rats and was restored to control levels after treatment with sGC activator (**Figures 1G,H**).

Improved Titin Phosphorylation After Soluble Guanylyl Cyclase Activator Treatment

Cardiomyocyte $F_{passive}$ is partially determined by titin phosphorylation, an important downstream target of the cGMP-PKG and cAMP-PKA pathways. We therefore studied whether improved cardiomyocyte stiffness is due to changes in titin phosphorylation. We assessed total titin using a Ser/Thr antibody and measured conserved phosphoserines within the I-band region, including three serines within the N2Bus (Ser3991, Ser4043, and Ser4080 of full-length mouse titin) and conserved serines in the PEVK segment (Ser12742 and Ser12884). Total titin phosphorylation was significantly reduced

TABLE 2 | *In vivo* data before and after treatment with sGC activator in control and DSS groups.

	Control	Control + sGC	DAHL	DAHL + sGC
IVRT (ms)	28.25 ± 0.1	28.32 ± 0.1	34.44 ± 0.7***	28.46 ± 0.4†††
E/A	2.0 ± 0.1	2.0 ± 0.02	1.2 ± 0.02***	1.44 ± 0.03†††
e′/a′	1.6 ± 0.1	1.8 ± 0.05	1.24 ± 0.04	1.34 ± 0.03
EF	55.11 ± 1.1	54.8 ± 0.1	56.14 ± 3.61	53.5 ± 1.2
dP/dtmax (mmHg/s)	8.610 ± 211.6	8.334 ± 55.5	9.772 ± 122.0*	8.538 ± 163.7†
dP/dtmin (mmHg/s)	−10.578 ± 138.6	−10.201 ± 185	−8.423.25 ± 180*	−10.203 ± 357†
Tau (ms)	9.94 ± 1.8	10.17 ± 0.1	11.55 ± 0.7	9.8 ± 0.21(p = 0.06)
TD (ms)	28.90 ± 1.2	27.30 ± 1.0	37.70 ± 1.0**	26.95 ± 0.96††

*LV, left ventricular; IVRT, isovolumetric relaxation time; A, peak trans-mitral late left LV diastolic filling velocity; E, peak trans-mitral early LV diastolic filling velocity; a', peak late diastolic mitral annular velocity by tissue Doppler; e', peak early diastolic mitral annular velocity by tissue Doppler; EF, ejection fraction; dP/dtmax, the maximal slope of LV systolic pressure increment; dP/dtmin, the maximal slope of LV diastolic pressure decrement; Tau (τ), the time constant for isovolumic relaxation; DT, E wave deceleration time; sGC, soluble guanylyl cyclase. Data are shown as mean ± SEM; *P < 0.05, **P < 0.001,***P < 0.0001 control untreated versus DSS untreated and †P < 0.05, ††P < 0.001, †††P < 0.0001 before versus after sGC activator treatment.*

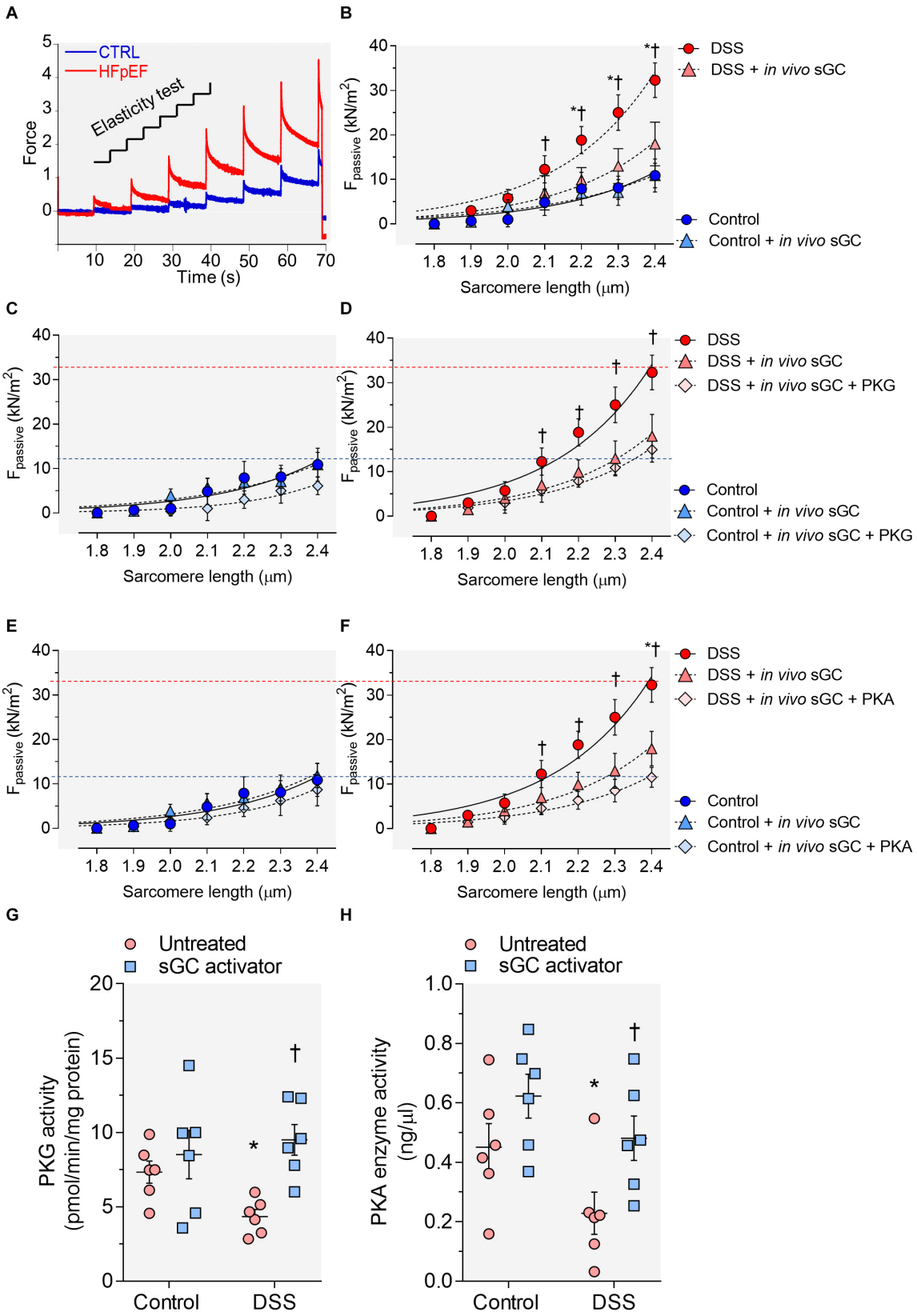

FIGURE 1 | Continued

FIGURE 1 | Cardiomyocyte passive stiffness and protein kinase (PK)G and PKA activity in the rat model. **(A)** Original recording of the force response to stepwise cell stretching of isolated skinned cardiomyocytes. **(B)** Control and Dahl salt-sensitive (DSS) passive force ($F_{passive}$) at sarcomere length (SL) 1.8–2.4 μm in the presence or absence of *in vivo* soluble guanylyl cyclase (sGC) activator. **(C,D)** Control and DSS $F_{passive}$ at SL 1.8–2.4 μm in the presence or absence of *in vivo* sGC activator and subsequently added PKG. **(E,F)** Control and DSS $F_{passive}$ at SL 1.8–2.4 μm in the presence or absence of *in vivo* sGC activator and subsequently added PKG. Curves are second-order polynomial fits to the means (± SEM; n = 4–5 cardiomyocytes/heart). For **(B)**, $^{*}P < 0.05$ control baseline versus DSS baseline, $^{\dagger}P < 0.05$ DSS baseline versus DSS after sGC activator treatment. **(D)** $^{*}P < 0.05$ DSS baseline versus DSS after sGC activator treatment, $^{\dagger}P < 0.05$ DSS after sGC activator treatment versus DSS after sGC activator treatment followed by PKG treatment. **(F)** $^{*}P < 0.05$ DSS baseline versus DSS after sGC activator treatment followed by PKA in Student's *t*-test. **(G)** PKG activity. **(H)** PKA activity. Data are shown as mean ± SEM; n = 7–8 left ventricular (LV) samples/group. $^{*}P < 0.05$ control untreated versus DSS untreated and $^{\dagger}P < 0.05$ before versus after sGC activator treatment.

in DSS animals and restored upon sGC activator treatment (**Figure 2A**). Phosphoserines located within the I-band region (Ser3991, Ser4043, Ser4080), together with Ser12884 in the PEVK segment, were hypo-phosphorylated (**Figures 2B–D,F**), while Ser12742 of the PEVK domain was hyperphosphorylated, in DSS rats. sGC activator significantly increased the phosphorylation of Ser4043, Ser4080, and Ser12884 but did not affect the phosphorylation of Ser3991 (**Figures 2B–D,F**) and significantly reduced Ser12742 phosphorylation (**Figure 2E**).

Kinases Activity Upon Treatment With Soluble Guanylyl Cyclase Activator in Dahl Salt-Sensitive Rats

Bioavailability of NO is reduced by oxidative stress and impacts both the activity and concentration of the downstream targets sGC and cGMP (Franssen et al., 2016). In DSS rats, NO bioavailability, sGC activity, and cGMP concentration were reduced at baseline and restored after sGC treatment (**Figures 3A–C**). To understand the beneficial effect of sGC on signaling pathways and thereby on cardiomyocyte function, we assessed protein kinases, including CaMKII, PKC, and ERK2, that play a role in maladaptive remodeling of HFpEF myocardium. The activities of CaMKII and PKC were significantly high in DSS rats and reduced upon treatment with sGC activator, whereas ERK2 activity did not differ between DSS rats and controls and remained unaltered after the treatment (**Figures 3D–F**). Kinase activities did not show any changes between controls and controls treated with sGC activator.

Soluble Guanylyl Cyclase Activator Promotes Translocation of Soluble Guanylyl Cyclase Toward the Intercalated Disc Region

Using confocal microscopy, we found that sGC is distributed throughout the cytosol and intercalated disc in control rats (**Figure 4A**), whereas sGC appeared to be more concentrated in the myofilaments and almost absent around the intercalated disc in DSS rats (**Figure 4C**). Treatment with sGC activator promoted the translocation of sGC from the cytosol to the intercalated disc, as seen in **Figures 4B,D**. We confirmed translocation to the intercalated disc by staining for connexin 43, an integral gap junction protein that is part of the intercalated disc and t-tubuli. Furthermore, a disrupted pattern and reduced level of connexin 43 was noted in DSS rats, and the pattern partially improved after sGC activator treatment in both control treated and DSS treated rats (**Figures 4E–H**). We also performed a dual staining of connexion 43 and sGC to show the translocation of sGC toward the intercalated disc region (**Figures 4I–L**). As shown, there is a localization of connexion 43 and sGC in all groups. However, in the treated groups control and DSS clearly show enhanced presence of sGC in the intercalated disc region, confirming the previous suggested translocation of the sGC toward the intercalated disc region. Electron microscopy showed lower expression of PKGIα and sGC proteins in DSS rats, and specifically in cardiomyocytes, while expression was enhanced in cardiomyocytes after sGC treatment (**Figures 5A,B**).

Pro-Inflammatory Cytokines and Oxidative Stress Are Reduced in Dahl Salt-Sensitive Rats

We used ELISA to assess LV myocardial pro-inflammatory cytokines including interleukin-6 (IL6), intercellular cell adhesion molecule-1 (ICAM1), vascular cell adhesion molecule-1 (VCAM1), and tumor necrosis factor alpha (TNFα), which were all found to be elevated in DSS rats compared to the control group (**Figures 6A–D**). This upregulation was reduced to control group levels upon treatment with sGC activator, but no effect was found in the control group after treatment with sGC (**Figures 6A–D**). To determine oxidative stress levels, we measured 3-nitrotyrosine, lipid peroxide (LPO), H_2O_2, and reduced glutathione (GSH), all of which were found to be significantly upregulated in DSS rats compared to the control group. Treatment with sGC activator reduced oxidative stress parameters to control group levels (**Figures 6E–H**).

Improved Passive Force Upon Treatment With Soluble Guanylyl Cyclase Activator in Human Heart Failure With Preserved Ejection Fraction

To study the functional effect of sGC activator in human myocardial biopsies (**Table 1**) from HFpEF patients we measured cardiomyocyte $F_{passive}$ before and after acute *in vitro* treatment. **Figure 7A** shows a representative elasticity test protocol and force recording for HFpEF myocardium biopsies and controls. Human HFpEF myocardium biopsies showed increased cardiomyocyte $F_{passive}$ compared to controls, which confirmed previous findings (**Figure 7B**) (Borbely et al., 2005; Franssen et al., 2016). This increase could be reduced upon *in vitro* treatment with sGC activator (**Figure 7D**), while no changes were observed in control non-failing donor hearts after treatment (**Figure 7C**). Additional treatment with PKGIα further significantly reduced $F_{passive}$ at SL 2.3 and 2.4 μm, indicating that the sGC activator did not

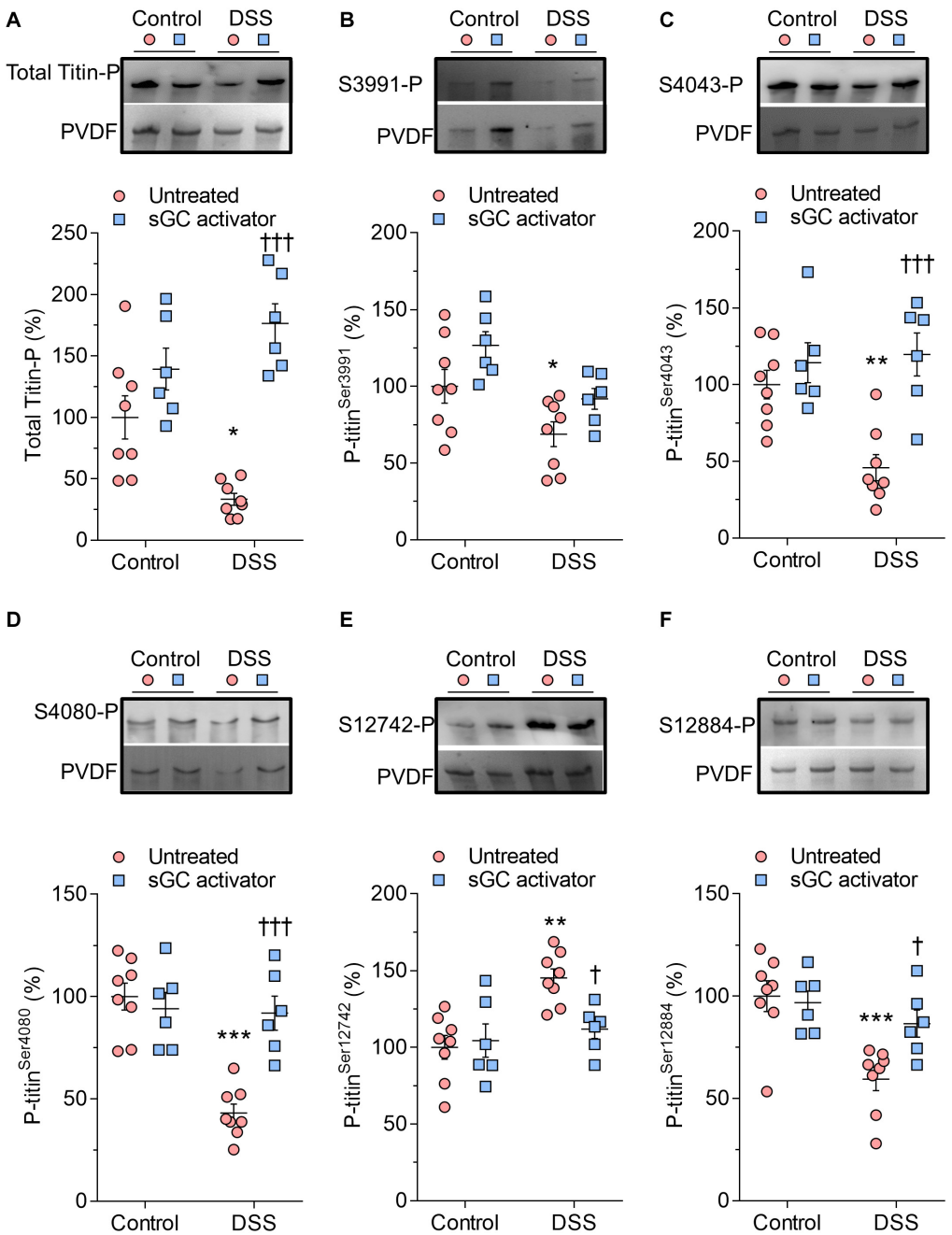

FIGURE 2 | Titin phosphorylation in Dahl salt-sensitive (DSS) and control rats. **(A)** Total titin phosphorylation. **(B)** Phospho (P) site-specific within titin-N2Bus at Ser3991. **(C)** P site-specific within titin-N2Bus at Ser4043. **(D)** P site-specific within titin-N2Bus at Ser4080. **(E)** P site-specific within titin PEVK segment at Ser-12742. **(F)** P site-specific within titin PEVK segment at Ser-12884. Data are shown as mean ± SEM; n = 7–8 left ventricular (LV) samples/group. $^{*}P < 0.05$, $^{**}P < 0.001$, $^{***}P < 0.0001$ control untreated versus DSS untreated and $^{\dagger}P < 0.05$, $^{\dagger\dagger\dagger}P < 0.0001$ before versus after soluble guanylyl cyclase (sGC) activator treatment.

fully correct the increased cardiomyocyte Fpassive observed in HFpEF myocardium biopsies, perhaps due to the fact that PKGIα did not fully phosphorylate titin-mediated PKG phosphorylation, while PKA had no further significant effect after sGC treatment (**Figures 7E,F**). To assess whether these functional changes could be due to the level of PKG and PKA activity, we measured the activity of these kinases and found both to be significantly depressed in HFpEF myocardium biopsies. sGC significantly restored activity (**Figures 7G,H**). Improved cardiomyocyte function was related to improved total titin phosphorylation, which was originally reduced in these biopsies (**Figure 7I**), in addition to increased phosphorylation of the specific serine

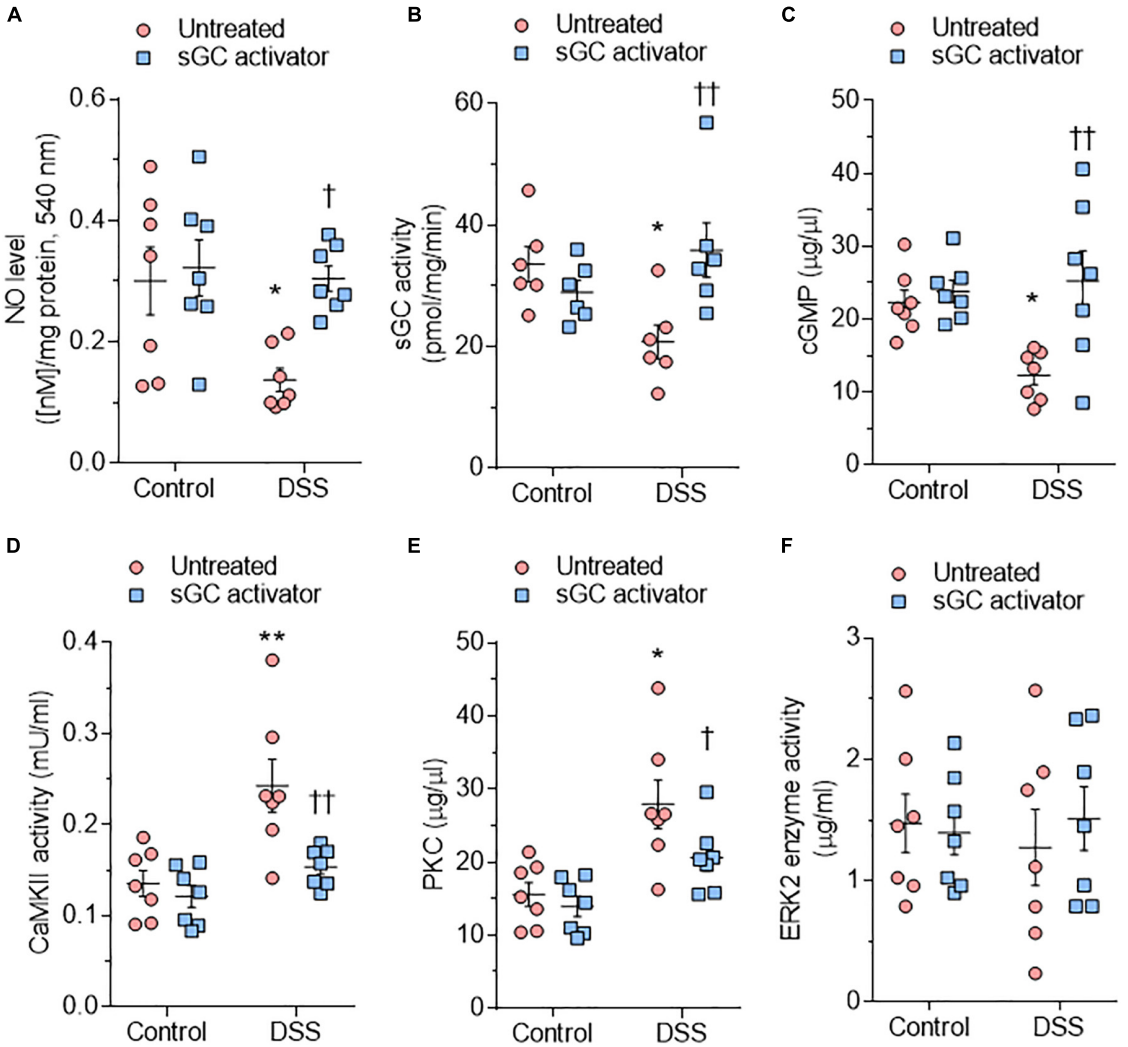

FIGURE 3 | Soluble guanylyl cyclase (sGC)–cyclic guanosine monophosphate (cGMP) pathway components and activities of major kinases in the rat model. **(A)** Nitric oxide (NO) bioavailability. **(B)** sGC activity. **(C)** Myocardial cGMP-dependent protein kinase (PK) concentration. **(D)** Calcium/calmodulin-dependent kinase II (CaMKII) activity. **(E)** PKC activity. **(F)** Extracellular signal-regulated kinase 2 (ERK2) activity. Data are shown as mean ± SEM; n = 6–7 left ventricular (LV) samples/group. $^{*}P < 0.05$, $^{**}P < 0.001$, $^{***}P < 0.0001$ control untreated versus Dahl salt-sensitive (DSS) untreated and $^{\dagger}P < 0.05$, $^{\dagger\dagger}P < 0.001$ before versus after sGC activator treatment.

phospho-sites Ser4010 (PKA-dependent) and Ser4099 (PKG-dependent) of full-length human titin in DSS rats after sGC treatment. Both phosphosites were significantly downregulated at the baseline before the treatment. (**Figures 7J,K**)

Soluble Guanylyl Cyclase Activator Improves Kinases Involved in Hypertrophic Pathways and Reduces Pro-Inflammatory Cytokines and Oxidative Stress in Human Heart Failure With Preserved Ejection Fraction

Human HFpEF myocardium biopsies showed a trend similar to that observed in DSS rats, with a significant reduction of the sGC–cGMP–PKG pathway that could be attenuated upon treatment with sGC activator (**Figures 8A–C**). CaMKII, PKC, and ERK2 were significantly upregulated in HFpEF myocardium biopsies compared to non-failing donor hearts and were lowered by treatment with sGC activator (**Figures 8D–F**). We then assessed whether pro-inflammatory cytokines (IL-6, ICAM1, VCAM1, TNFα) and oxidative stress (3-nitrotyrosine, LPO, H_2O_2, GSH) were higher in HFpEF human myocardium biopsies and studied the effect of *in vitro* sGC activator treatment on these parameters. As expected, *in vitro* treatment with sGC activator significantly reduced inflammatory cytokines and oxidative stress to the levels observed in control non-failing donor hearts (**Figures 9A–H**). The non-failing donor hearts showed no changes in inflammatory cytokines or oxidative stress after sGC treatment (**Figures 9A–H**).

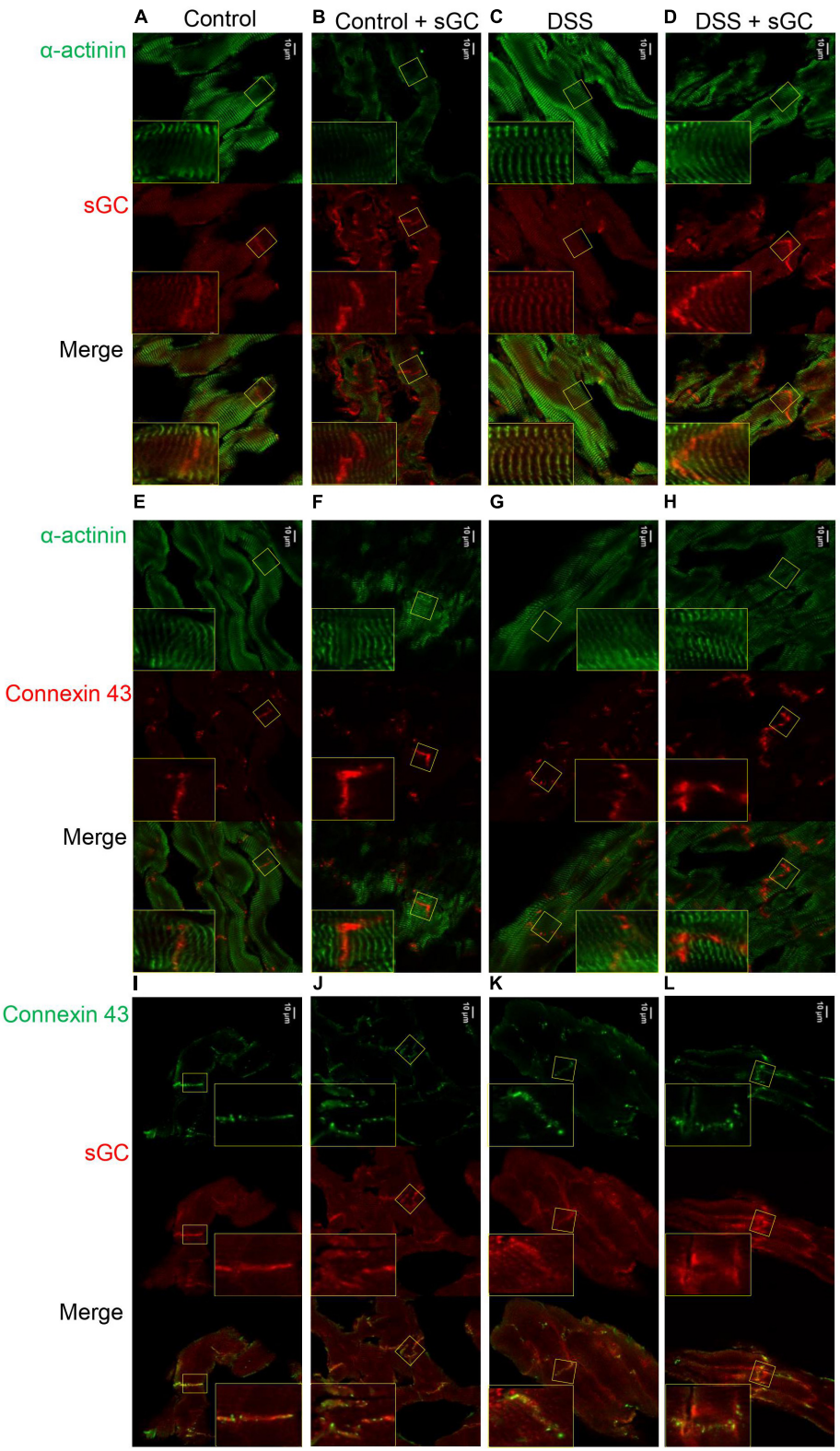

FIGURE 4 | cLSM images of control and DSS rat cardiomyocytes before and after sGC activator treatment demonstrating sGC translocation to the intercalated disc **(A–D)**. Representative immunofluorescence images of cardiomyocytes stained for cardiac sGC (red) and counterstained for α-actinin (green). **(E–H)** Immunofluorescence images of cardiomyocytes stained for connexin 43 (red) and counterstained for α-actinin (green). **(I–L)** Representative immunofluorecence images of cardiomyocytes stained for connexin 43 (green) and sGC (red).

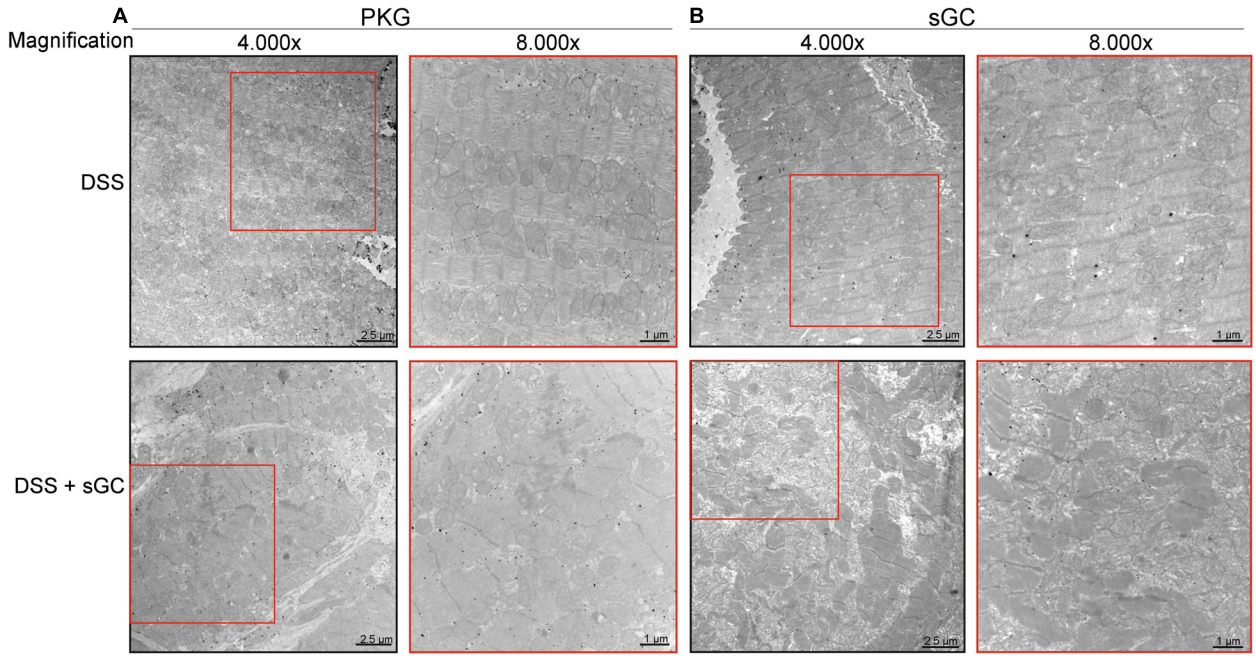

FIGURE 5 | Immunoelectron micrographs of Dahl salt-sensitive (DSS) rat cardiomyocytes before and after soluble guanylyl cyclase (sGC) activator treatment stained for protein kinase (PK)G or sGC. **(A)** Representative immunoelectron micrographs of cardiomyocytes from DSS + DSS-treated rat hearts stained for PKG. **(B)** Immunoelectron micrographs of cardiomyocytes from DSS + DSS-treated rat hearts stained for sGC.

DISCUSSION

Currently, limited understanding of HF with LV diastolic dysfunction is one of the major reasons for the inability to develop effective treatment options for patients with this life-threatening condition. A more modern updated view considers a complex interaction of structural, functional, molecular, and organismal alterations that account for the progressive nature of this HF type. Metabolic disorders such as obesity, metabolic syndrome, and diabetes mellitus are major cardiovascular risk factors, are accompanied by diastolic dysfunction and an increased risk of mortality, and are often associated with oxidative stress (Paulus and Tschope, 2013; Franssen et al., 2016). Recent evidence by us and others has suggested that oxidative stress may be the mechanistic link between obesity, diabetes mellitus, and related complications (Borlaug and Paulus, 2011; Paulus and Tschope, 2013; Franssen et al., 2016). Earlier failures to identify the underlying causes of the syndrome may explain the disappointing clinical trial results and indicate that progress will not be possible until we disentangle symptoms from causes. Our current findings show that the sGC activator BAY 58-2667 improves cardiomyocyte function *via* improved titin phosphorylation, an effect likely due to improved signaling pathways including the pathway NO–sGC–cGMP–PKG and the hypertrophic pathways mediated by CaMKII, PKC, and ERK2, in addition to the PKA pathway. Moreover, the improvement mediated by sGC activation also seems to be related to the reorganization and increased expression of connexin 43 at the gap junctions in both control and DSS rats. Interestingly, translocation of sGC toward the intercalated disk was observed in controls and DSS rats after the treatment. Finally, improved cardiomyocyte function after sGC treatment appears to be associated with reduced pro-inflammatory cytokines and oxidative stress parameters.

An earlier study showed that in the myocardium of HFpEF patients and ZSF1-HFpEF rats, E-selectin, ICAM, and VCAM expression levels were upregulated, in addition to raised expression of nicotinamide adenine dinucleotide phosphate (NADPH) oxidase 2 in macrophages and endothelial cells but not in cardiomyocytes (Franssen et al., 2016). In addition, the uncoupling of endothelial NO synthase was associated with reduced myocardial nitrite/nitrate concentration, cGMP content, and PKG activity. Taken together, these findings indicate that increased inflammation and oxidative stress contribute to the reduced NO-dependent signaling from endothelial cells to cardiomyocytes and to the high cardiomyocyte stiffness and hypertrophy observed in HFpEF (Franssen et al., 2016) and in the current study. TNFα and IL-1β further promote cardiomyocyte hypertrophy (Yokoyama et al., 1997), and the cytokine IL-6 can increase cardiomyocyte stiffness *via* a reduction in titin phosphorylation (Savvatis et al., 2014).

Reduced NO signaling is resulting from increased generation of reactive oxygen species (ROS), endothelial damage, and NO synthase impairment but also reduced NO binding to sGC due to oxidative stress. This interruption of NO signaling can lead to endothelial dysfunction, cardiomyocyte dysfunction, fibrosis, and inflammation (Franssen et al., 2016). sGC is a key signal transduction enzyme in the cardiovascular system and is not

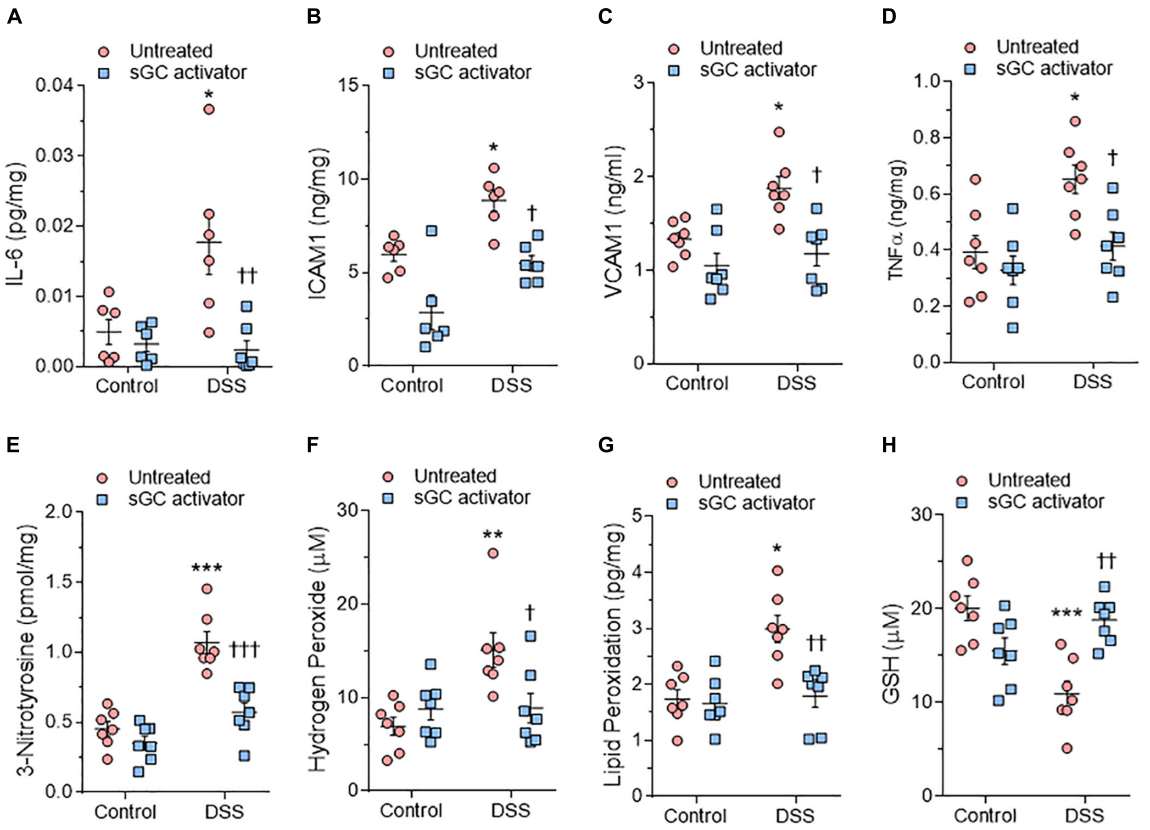

FIGURE 6 | Myocardial inflammation and oxidative stress in heart tissue from the rat model. **(A)** Interleukin 6 (IL-6). **(B)** Intercellular adhesion molecule 1 (ICAM1). **(C)** Vascular cell adhesion molecule 1 (VCAM1). **(D)** Tumor necrosis factor alpha (TNFα). **(E)** 3-nitrotyrosine. **(F)** Hydrogen peroxide (H_2O_2). **(G)** Lipid peroxide (LPO). **(H)** Reduced glutathione (GSH). Data are shown as mean ± SEM; n = 7–8 left ventricular (LV) samples/group. $^{*}P < 0.05$, $^{**}P < 0.001$, $^{***}P < 0.0001$ control untreated versus Dahl salt-sensitive (DSS) untreated and $^{\dagger}P < 0.05$, $^{\dagger\dagger}P < 0.001$, $^{\dagger\dagger\dagger}P < 0.0001$ before versus after sGC activator treatment.

only impaired in HFpEF but also in a variety of diseases such as hypertension, pulmonary hypertension, chronic kidney disease, and erectile dysfunction, all of which are associated with impaired NO–sGC–cGMP signaling (Kemp-Harper and Feil, 2008; Schulz et al., 2008; Stasch et al., 2011; Klinger and Kadowitz, 2017). sGC activators have a beneficial effect on cardiomyocyte function in DSS rats and HFpEF myocardium biopsies, which could be beneficial for diastolic dysfunction, as observed in a study by Esposito et al. (2017), and could therefore represent a potential HFpEF treatment. Cardiomyocyte improvement in both DSS rats and HFpEF human myocardium appears to be associated with an improved NO–sGC–cGMP–PKG pathway, in addition to the PKA pathway and hypertrophic pathways such as CaMKII, ERK2, and PKC. Therefore, an improved NO–sGC–cGMP–PKG pathway could be the result of improved sGC bioavailability due to activation of sGC or the result of reduced oxidative stress and inflammation, which may have affected endothelial function and cardiomyocyte function *via* the increased NO bioavailability observed in DSS rats and HFpEF myocardium biopsies.

Cardiomyocyte stiffness is mainly determined by titin isoform switching, titin phosphorylation, and titin oxidation (Alegre-Cebollada et al., 2014; Linke and Hamdani, 2014). Previously, it was shown that titin is phosphorylated by different kinases, with distinct effects on cardiomyocyte $F_{passive}$ (Yamasaki et al., 2002; Fukuda et al., 2005; Kruger and Linke, 2006; Borbely et al., 2009; Hidalgo et al., 2009; Kruger et al., 2009; Raskin et al., 2012). The cardiac titin N2Bus spring element is phosphorylated by PKA (Yamasaki et al., 2002; Fukuda et al., 2005; Kruger and Linke, 2006), PKG (Kruger et al., 2009), ERK2 (Raskin et al., 2012), and CaMKIIδ (Hamdani et al., 2013b). All of these kinases reduce $F_{passive}$ (Yamasaki et al., 2002; van Heerebeek et al., 2006; Borbely et al., 2009; Kruger et al., 2009; Raskin et al., 2012). By contrast, a PEVK region constitutively expressed in full-length titin is phosphorylated by PKCα, and this modification increases cardiomyocyte $F_{passive}$ (Hidalgo et al., 2009). Thus, acute changes in titin-based stiffness *via* titin phosphorylation can occur in opposite directions, depending on which signaling pathway is activated (Linke and Hamdani, 2014). The current study shows that acute treatment with sGC activator increases total titin phosphorylation and site-specific phosphorylation of titin, specifically at the elastic regions N2Bus and PEVK, in turn decreasing titin-based cardiomyocyte passive stiffness in both DSS rats and HFpEF myocardium biopsies. We also showed improved site-specific phosphorylation at the elastic

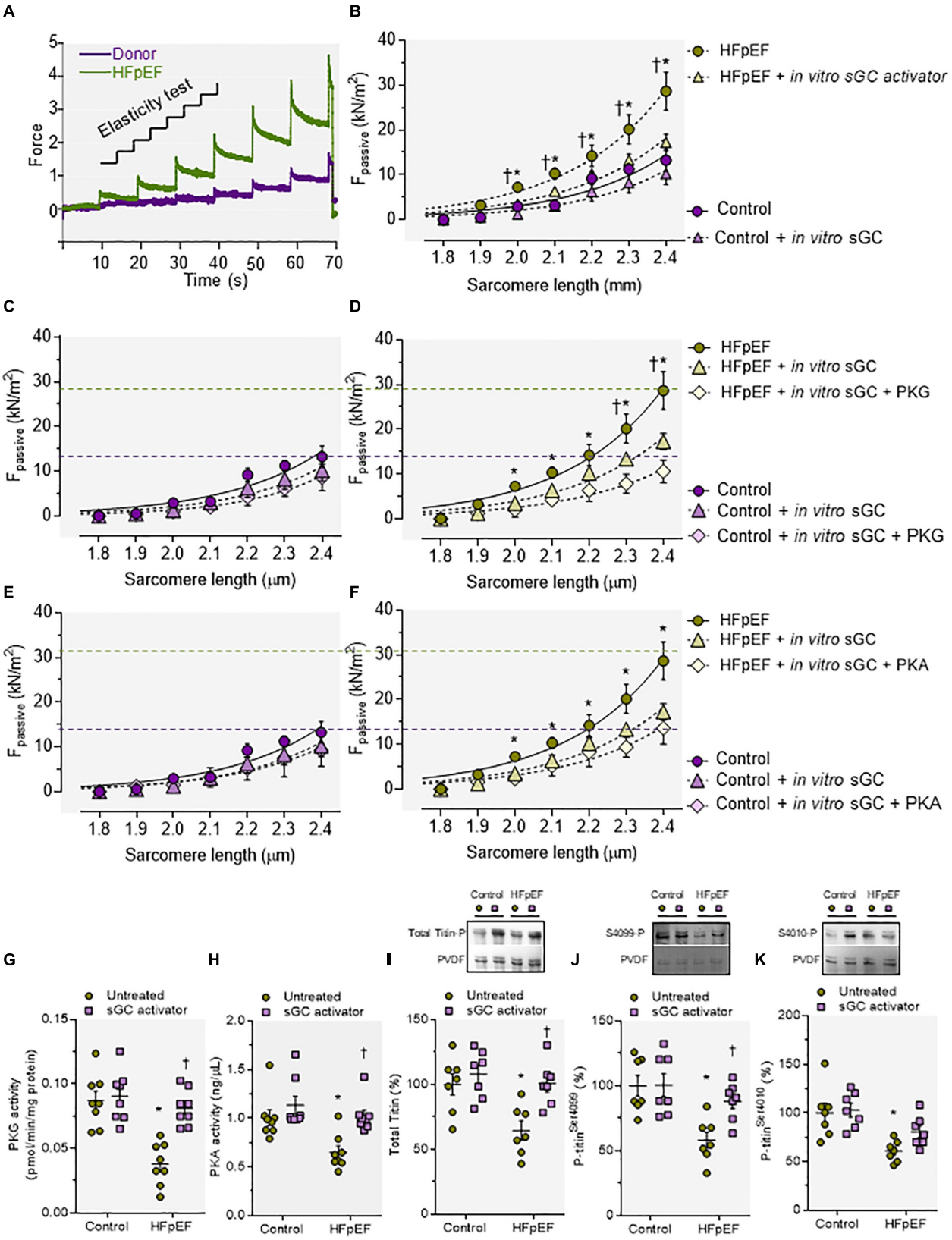

FIGURE 7 | Continued

FIGURE 7 | Cardiomyocyte passive stiffness; protein kinase (PK)G and PKA activities and titin phosphorylation of myocardial biopsies of human heart failure with preserved ejection fraction (HFpEF) patients before and after *in vitro* incubation with soluble guanylyl cyclase (sGC) activator. **(A)** Original recording of the force response to stepwise cell stretching of isolated skinned cardiomyocytes. **(B)** Control and Dahl salt-sensitive (DSS) passive force ($F_{passive}$) at sarcomere length (SL) 1.8–2.4 μm in the presence or absence of sGC activator. **(C,D)** Control and DSS $F_{passive}$ at SL 1.8–2.4 μm in the presence or absence of sGC activator and subsequently added PKG. **(E,F)** Control and DSS $F_{passive}$ at SL 1.8–2.4 μm in the presence or absence of sGC activator and subsequently added PKA. Fit curves are two-order polynomials to the means. Data are mean ± SEM; n = 4–5/heart. For **(B)**, $^{*}P < 0.05$ control baseline versus HFpEF baseline, $^{\dagger}P < 0.05$ HFpEF baseline versus after sGC activator treatment. **(D)** $^{*}P < 0.05$ HFpEF baseline versus HFpEF after sGC activator treatment, $^{\dagger}P < 0.05$ HFpEF after sGC activator treatment versus HFpEF after sGC activator treatment followed by PKG treatment. **(F)** $^{*}P < 0.05$ HFpEF baseline versus HFpEF after sGC activator treatment in Student's *t*-test. **(G)** PKG activity. **(H)** PKA activity. **(I)** Total titin phosphorylation. **(J)** Site-specific phosphorylation of titin-N2Bus at Ser4099. **(K)** Site-specific phosphorylation of titin-N2Bus at Ser4010. Data are shown as mean ± SEM; n = 7–8 left ventricular (LV) samples/group. $^{*}P < 0.05$ control untreated versus HFpEF untreated and $^{\dagger}P < 0.05$ before versus after sGC activator treatment.

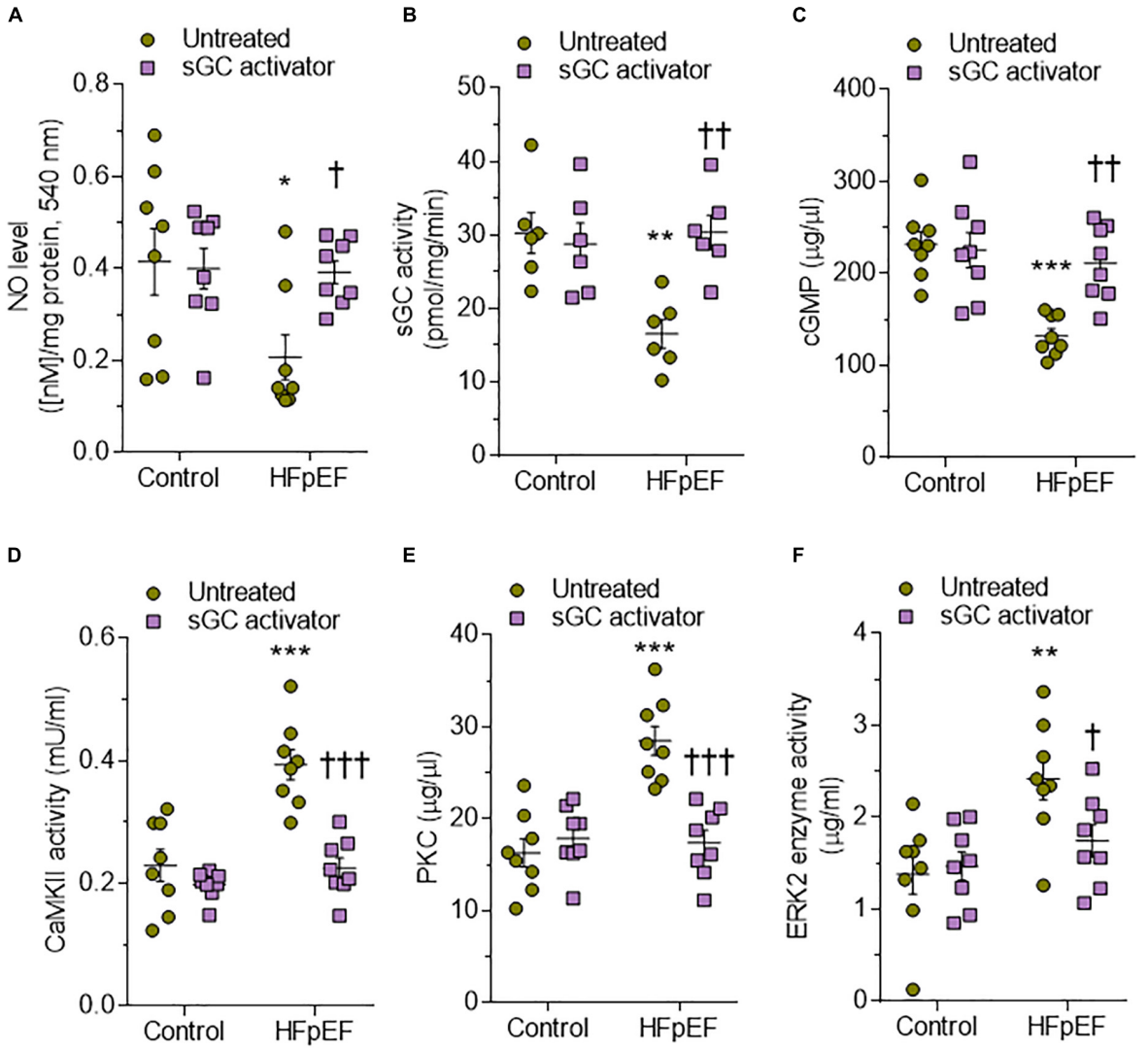

FIGURE 8 | Soluble guanylyl cyclase (sGC)–cyclic guanosine monophosphate (cGMP) pathway components and activities of major kinases in human heart failure with preserved ejection fraction (HFpEF) hearts. **(A)** Nitric oxide (NO) bioavailability. **(B)** sGC activity. **(C)** Myocardial cGMP-dependent protein kinase levels. **(D)** Calcium/calmodulin-dependent kinase II (CaMKII) activity. **(E)** Protein kinase C (PKC) activity. **(F)** Extracellular signal-regulated kinase 2 (ERK2) activity. Data are shown as mean ± SEM; n = 7–8 left ventricular (LV) samples/group. $^{*}P < 0.05$ control untreated versus HFpEF untreated and $^{\dagger}P < 0.05$ before versus after sGC activator treatment.

N2Bus titin site, indicating that improved titin phosphorylation results from improvements in signaling pathways involving PKA, PKG, CaMKII, and/or ERK2. We previously reported evidence that activation of cGMP–PKG in a large animal model of HFpEF treated acutely with sildenafil followed by BNP led to increased titin phosphorylation, lower cardiomyocyte

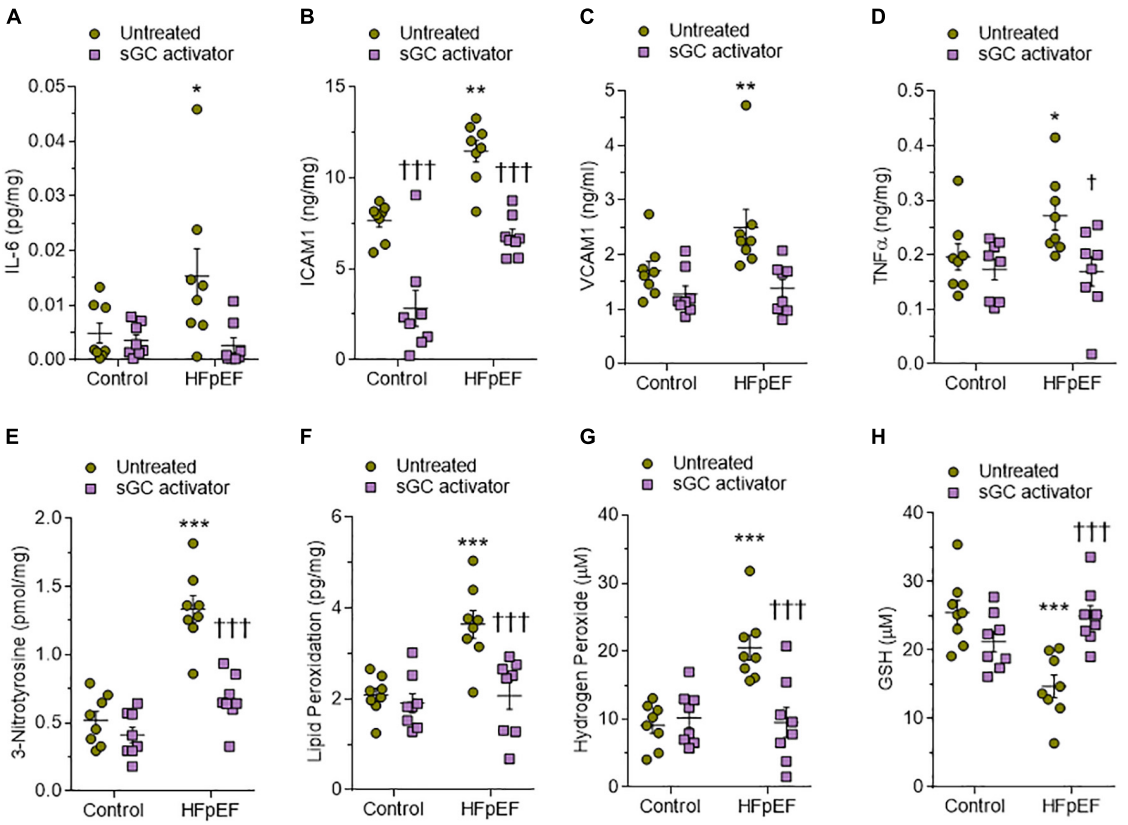

FIGURE 9 | Expression of markers of myocardial inflammation and oxidative stress in non-failing and heart failure with preserved ejection fraction (HFpEF) patient hearts. **(A)** Interleukin 6 (IL6). **(B)** Intercellular adhesion molecule 1 (ICAM1). **(C)** Vascular cell adhesion molecule 1 (VCAM1). **(D)** Tumor necrosis factor alpha (TNFα). **(E)** 3-nitrotyrosine. **(F)** Hydrogen peroxide (H_2O_2). **(G)** Lipid peroxide (LPO). **(H)** Reduced glutathione (GSH). Data are shown as mean ± SEM; n = 7–8 left ventricular (LV) samples/group. *$P < 0.05$ control untreated versus HFpEF untreated and †$P < 0.05$ before versus after soluble guanylyl cyclase (sGC) activator treatment.

$F_{passive}$, and improved diastolic function (Bishu et al., 2011). However, in other large animal models, acute stimulation of sGC did not impact LV capacitance, for example, in normal and hypertrophied porcine hearts *in vivo* (Alogna et al., 2018). Nevertheless, titin phosphorylation was increased, suggesting that in this model, increased titin phosphorylation is perhaps not indicative of increased *in vivo* LV capacitance (Alogna et al., 2018). Similarly, an improved cGMP–PKG signaling pathway has been demonstrated in a small animal model with diastolic dysfunction treated chronically with DPP4 inhibitor (an enzyme involved in cGMP degradation). This model showed improved diastolic stiffness and cardiomyocyte function through increased titin phosphorylation and reduced fibrosis (Hamdani et al., 2014).

In the present study, we found reduced PKC activity and improved titin–PEVK site-specific phosphorylation after treatment with the sGC activator, both of which may have contributed to the reduced cardiomyocyte stiffness. Additional posttranslational modifications that alter the stiffness of titin include arginylation (Leite Fde et al., 2016) and various oxidative modifications, such as disulfide bonding (Grutzner et al., 2009; Giganti et al., 2018), S-glutathionylation (Alegre-Cebollada et al., 2014), and sulphenylation (Beedle et al., 2016). Therefore, since the sGC activator reduces oxidative stress, improved cardiomyocyte stiffness could be related, in part, to reduced titin oxidation. The reversible oxidative modifications previously found in the various I-band titin regions have been shown to modify titin-based stiffness also in isolated human cardiomyocytes (Linke and Hamdani, 2014; Beckendorf and Linke, 2015; Breitkreuz and Hamdani, 2015). Disulfide bond formation in the cardiac-specific N2-Bus region appeared to decrease N2B extensibility, stiffen the titin molecule, and increase cardiomyocyte $F_{passive}$ (Grutzner et al., 2009). In contrast, cysteine S-glutathionylation in the Ig domains of the elastic I-band region affects cardiomyocyte $F_{passive}$ in the opposite direction (Alegre-Cebollada et al., 2014). Explanation of this effect considers that cryptic cysteines in titin Ig domains become available for redox modification when they unfold. Upon stretching of cardiac sarcomeres, Ig domain unfolding increases and cryptic cysteines becoming exposed to oxidized glutathione will be S-glutathionylated, which greatly weakens the mechanical stability of the Ig domains and their ability to refold, leading to a reduced cardiomyocyte $F_{passive}$ (Alegre-Cebollada et al., 2014). This effect can be reversed by adding reduced glutathione (Alegre-Cebollada et al., 2014). Conversely, S-sulphenylation of cryptic cysteines in Ig domains can cause titin

stiffening by promoting S-S bonding in titin Ig domains (Beedle et al., 2016). Taken together, the contribution of titin oxidation to cardiomyocyte $F_{passive}$ modulation cannot be discounted in the current study. In addition to titin, we also checked the phosphorylation status of calcium handling proteins including ryonidine receptor (RYR) and phospholamban (PLN) at serines Ser2808 and Ser4080, respectively. RyR phosphorylation was unaltered in DSS rats and was comparable to the controls. sGC activator did not further affect both groups. Phosphorylation of PLN was not significantly changed in DSS rats compared to controls, and sGC activator significantly increased the baseline phosphorylation level in both control and DSS groups. This suggested perhaps also the contribution of PLN in improved cardiac function.

In addition, NO may also promote protein modification through nitration of tyrosines to form the stable 3-nitrotyrosine. Accumulation of 3-nitrotyrosine in proteins is indicative of ROS and reactive nitrogen species (RNS) stress (Ischiropoulos, 2003). When redox-active thiols are combined with RNS in our system, it forms S-nitrosothiols, which then alters protein function. The protein thiol redox state of cells is maintained by the mitochondria, which are a major source of cellular oxidants, and the basal production of oxidants. This in turn affects both global S-nitrosation and disulfide formation of proteins (Ischiropoulos, 2003). Therefore, we cannot exclude that the sGC activator in our model might have an effect on the mitochondrial function and might also contribute to pathway improved function seen in the DSS treated rats.

The sGC activator induced a reversible shift toward pro-inflammatory cytokines and reduced oxidative stress, influencing cardiomyocyte function *via* improved signaling pathways and thereby titin phosphorylation. Cardiac fibrosis is also involved in the modulation of diastolic function and is an important contributor to diastolic impairment in HFpEF as it increases LV and peripheral vascular stiffness (Borbely et al., 2005; van Heerebeek et al., 2008; Zile et al., 2015), an impairment due to the migration of leukocytes and macrophages in humans (Kai et al., 2005) and experimental HF models (Luft et al., 1999; Fischer et al., 2008; Haase et al., 2014). BAY 58-2667 has been shown to reduce monocyte/macrophage infiltration into cardiac tissue and to reverse inflammatory gene expression patterns in failing rat hearts (Wilck et al., 2018), in addition to its role in reducing interstitial fibrosis and blood pressure (Masuyama et al., 2006); these combined actions likely result in improved diastolic function.

Strikingly, improved cardiomyocyte function could be attributed, in part, to sGC translocation, as immunohistochemistry found sGC preferentially at the intercalated disk after treatment of DSS rats with sGC activator, whereas the sGC signal was almost absent from the intercalated disk in DSS rats before treatment. In addition, sGC appeared to have translocated somewhat more to the sarcomere after treatment of DSS cardiomyocytes with the activator. Interestingly, connexin 43 appeared to be reduced and disrupted at the intercalated disk in DSS rats, an effect partially reversed after treatment. Taken together, these findings suggest that a functional NO–sGC–cGMP pathway preserves the intercalated disk, the site of mechanical and electrical conduction between cardiomyocytes and perhaps also fibroblasts (Menges et al., 2019) and endothelial cells (Yuan et al., 2015; Johnson and Camelliti, 2018). Connexin 43 expressed in endothelial cells modulates monocyte–endothelial adhesion by regulating cell adhesion proteins, an interaction that is decreased upon reduced connexin 43 (Yuan et al., 2015). Furthermore, in connexin 43-knockout mice, ischemia leads to an increased frequency and duration of ventricular tachycardia as well as spontaneous ventricular arrhythmia, which results in higher rates of sudden cardiac death (Johnson and Camelliti, 2018). Formation of connexin 43-containing gap junctions at the intercalated disk involves trafficking from the endoplasmic reticulum to the Golgi to stabilize the intercalated disk (Thevenin et al., 2013). This process may be controlled by kinase activation that leads to connexin 43 phosphorylation, in addition to interaction with several additional binding partners. As it has been proposed that PKA may be involved in connexin 43–gap junction assembly (Solan and Lampe, 2007, 2014), we speculate that PKG may also be involved. cAMP and cGMP are ubiquitous second messengers with a similar range of functions in vascular homeostasis and disease. However, the exact roles of both molecules in the regulation of connexins and gap junction intercellular communication are still unclear, although it is known that activation of the NO–sGC–cGMP induces connexin 43 expression and increases intercellular communication *via* gap junctions (Yao et al., 2005). Our observation that sGC is located at the intercalated disk and that this localization is disrupted in DSS rats, together with the novel finding that connexin 43 is also disrupted and reduced at the intercalated disk in DSS rats suggests that further investigation of the potential function of the NO–sGC–cGMP pathway in relation to connexin 43 function is warranted in HFpEF patients.

Numerous studies have demonstrated the cardioprotective effects of NO–sGC–cGMP–PKG signaling. sGC stimulation can attenuate LV remodeling after myocardial infarction in mice (Frankenreiter et al., 2018; Berg et al., 2019), decrease extracellular matrix protein production in human cardiac fibroblasts following TGF-β stimulation, and attenuate vascular dysfunction in diabetic rats (Grontved et al., 2014). The eNOS transcriptional enhancer (AVE9488) improves cardiac remodeling after myocardial infarction (Fraccarollo et al., 2008) and platelet NO availability and hyperactivity in HF. Our studies indicate that the sGC activator can act in a similar fashion under oxidative stress, and inflammation was reduced in our animal model and in HFpEF myocardium biopsies after treatment. We have shown that sGC activator can positively impact the pathology of DSS rats with diastolic dysfunction and in HFpEF myocardium human biopsies *via* improved cardiomyocyte function.

CONCLUSION

Our data show that an sGC activator improves cardiomyocyte function, reduces inflammation and oxidative stress, and improves NO–sGC–cGMP–PKG signaling and hypertrophic

signaling pathways including CaMKII, ERK2, and PKCα. These findings suggest that upstream reduction of inflammation and oxidative stress, together with the enhancement of signaling pathways by sGC activators, may provide new opportunities for improving diastolic function in HFpEF patients.

DATA AVAILABILITY STATEMENT

All datasets generated for this study are included in the article/supplementary material.

ETHICS STATEMENT

The studies involving human participants were reviewed and approved by Berlin, Germany Ethics Committee approval (EA2/140/16). The patients/participants provided their written informed consent to participate in this study. The animal study was reviewed and approved by Ruhr University Bochum (Germany; ethical statement number: 84-02.04.2015.A449).

AUTHOR CONTRIBUTIONS

DK has performed all experiments, analyzed all data, and wrote the manuscript. ÁK performed mechanics experiments and *in vivo* study with sGC activator. MH performed biochemistry experiments and wrote the manuscript. ML performed electron microscopy. MS performed biochemistry experiments. AA performed electron microscopy. PS provided the drug and revised the manuscript. ZP helped with the mechanic experiments. PR revised the manuscript. PH provided tissues and revised the manuscript. IF-P supervised *in vivo* study. WL helped with interpretation of the data and rewrote the manuscript. KJ supervised the biochemistry experiments. SV and CT provided tissues, analyzed all clinical data, and revised the manuscript. AM revised the manuscript. NH designed the study, supervised all experiments, performed mechanics, analyzed all data, and wrote the manuscript.

FUNDING

This work was supported by Bayer AG (Wuppertal, Germany) by a restricted Research Grant and DFG (HA 7512/2-1).

ACKNOWLEDGMENTS

We gratefully acknowledge the technical assistance of Anja Vöge and Frauke De Pasquale. Also we acknowledge support by the DFG Open Access Publication Funds of the Ruhr-Universität Bochum.

REFERENCES

Alegre-Cebollada, J., Kosuri, P., Giganti, D., Eckels, E., Rivas-Pardo, J. A., Hamdani, N., et al. (2014). S-glutathionylation of cryptic cysteines enhances titin elasticity by blocking protein folding. Cell 156, 1235–1246. doi: 10.1016/j.cell.2014.01.056

Alogna, A., Schwarzl, M., Manninger, M., Hamdani, N., Zirngast, B., Kloth, B., et al. (2018). Acute stimulation of the soluble guanylate cyclase does not impact on left ventricular capacitance in normal and hypertrophied porcine hearts in vivo. Am. J. Physiol. Heart Circ. Physiol. 315, H669–H680. doi: 10.1152/ajpheart.00510.2017

Beckendorf, L., and Linke, W. A. (2015). Emerging importance of oxidative stress in regulating striated muscle elasticity. J. Muscle Res. Cell Motil. 36, 25–36. doi: 10.1007/s10974-014-9392-y

Beedle, A. E., Lynham, S., and Garcia-Manyes, S. (2016). Protein S-sulfenylation is a fleeting molecular switch that regulates non-enzymatic oxidative folding. Nat. Commun. 7:12490. doi: 10.1038/ncomms12490

Berg, D. D., Wiviott, S. D., Scirica, B. M., Gurmu, Y., Mosenzon, O., Murphy, S. A., et al. (2019). Heart failure risk stratification and efficacy of Sodium-Glucose cotransporter-2 inhibitors in patients with type 2 diabetes mellitus. Circulation 140, 1569–1577. doi: 10.1161/CIRCULATIONAHA.119.042685

Bishu, K., Hamdani, N., Mohammed, S. F., Kruger, M., Ohtani, T., Ogut, O., et al. (2011). Sildenafil and B-type natriuretic peptide acutely phosphorylate titin and improve diastolic distensibility in vivo. Circulation 124, 2882–2891. doi: 10.1161/CIRCULATIONAHA.111.048520

Borbely, A., Falcao-Pires, I., van Heerebeek, L., Hamdani, N., Edes, I., Gavina, C., et al. (2009). Hypophosphorylation of the Stiff N2B titin isoform raises cardiomyocyte resting tension in failing human myocardium. Circ. Res. 104, 780–786. doi: 10.1161/CIRCRESAHA.108.193326

Borbely, A., van der Velden, J., Papp, Z., Bronzwaer, J. G., Edes, I., Stienen, G. J., et al. (2005). Cardiomyocyte stiffness in diastolic heart failure. Circulation 111, 774–781. doi: 10.1161/01.CIR.0000155257.33485.6D

Borlaug, B. A., and Paulus, W. J. (2011). Heart failure with preserved ejection fraction: pathophysiology, diagnosis, and treatment. Eur. Heart J. 32, 670–679. doi: 10.1093/eurheartj/ehq426

Breitkreuz, M., and Hamdani, N. (2015). A change of heart: oxidative stress in governing muscle function? Biophys. Rev. 7, 321–341. doi: 10.1007/s12551-015-0175-5

Degen, C. V., Bishu, K., Zakeri, R., Ogut, O., Redfield, M. M., and Brozovich, F. V. (2015). The emperor's new clothes: PDE5 and the heart. PLoS One 10:e0118664. doi: 10.1371/journal.pone.0118664

Lee, D. I., Zhu, G., Sasaki, T., Cho, G. S., Hamdani, N., Holewinski, R., et al. (2015). Phosphodiesterase 9A controls nitric-oxide-independent cGMP and hypertrophic heart disease. Nature 519, 472–476. doi: 10.1038/nature14332

Esposito, G., Cappetta, D., Russo, R., Rivellino, A., Ciuffreda, L. P., Roviezzo, F., et al. (2017). Sitagliptin reduces inflammation, fibrosis and preserves diastolic function in a rat model of heart failure with preserved ejection fraction. Br. J. Pharmacol. 174, 4070–4086. doi: 10.1111/bph.13686

Evgenov, O. V., Pacher, P., Schmidt, P. M., Hasko, G., Schmidt, H. H., and Stasch, J. P. (2006). NO-independent stimulators and activators of soluble guanylate cyclase: discovery and therapeutic potential. Nat. Rev. Drug Discov. 5, 755–768. doi: 10.1038/nrd2038

Fischer, R., Dechend, R., Qadri, F., Markovic, M., Feldt, S., Herse, F., et al. (2008). Dietary n-3 polyunsaturated fatty acids and direct renin inhibition improve electrical remodeling in a model of high human renin hypertension. Hypertension 51, 540–546. doi: 10.1161/HYPERTENSIONAHA.107.103143

Fraccarollo, D., Widder, J. D., Galuppo, P., Thum, T., Tsikas, D., Hoffmann, M., et al. (2008). Improvement in left ventricular remodeling by the endothelial nitric oxide synthase enhancer AVE9488 after experimental myocardial infarction. Circulation 118, 818–827. doi: 10.1161/CIRCULATIONAHA.107.717702

Frankenreiter, S., Groneberg, D., Kuret, A., Krieg, T., Ruth, P., Friebe, A., et al. (2018). Cardioprotection by ischemic postconditioning and cyclic guanosine

monophosphate-elevating agents involves cardiomyocyte nitric oxide-sensitive guanylyl cyclase. Cardiovasc. Res. 114, 822–829. doi: 10.1093/cvr/cvy039

Franssen, C., Chen, S., Unger, A., Korkmaz, H. I., De Keulenaer, G. W., Tschope, C., et al. (2016). Myocardial microvascular inflammatory endothelial activation in heart failure with preserved ejection fraction. JACC Heart Fail 4, 312–324. doi: 10.1016/j.jchf.2015.10.007

Fukuda, N., Wu, Y., Nair, P., and Granzier, H. L. (2005). Phosphorylation of titin modulates passive stiffness of cardiac muscle in a titin isoform-dependent manner. J. Gen. Physiol. 125, 257–271. doi: 10.1085/jgp.200409177

Gheorghiade, M., Larson, C. J., Shah, S. J., Greene, S. J., Cleland, J. G., Colucci, W. S., et al. (2016). Developing new treatments for heart failure: focus on the heart. Circ. Heart Fail 9:e002727. doi: 10.1161/CIRCHEARTFAILURE.115.002727

Giganti, D., Yan, K., Badilla, C. L., Fernandez, J. M., and Alegre-Cebollada, J. (2018). Disulfide isomerization reactions in titin immunoglobulin domains enable a mode of protein elasticity. Nat. Commun. 9:185. doi: 10.1038/s41467-017-02528-7

Grontved, A., Pan, A., Mekary, R. A., Stampfer, M., Willett, W. C., Manson, J. E., et al. (2014). Muscle-strengthening and conditioning activities and risk of type 2 diabetes: a prospective study in two cohorts of US women. PLoS Med. 11:e1001587. doi: 10.1371/journal.pmed.1001587

Grutzner, A., Garcia-Manyes, S., Kotter, S., Badilla, C. L., Fernandez, J. M., and Linke, W. A. (2009). Modulation of titin-based stiffness by disulfide bonding in the cardiac titin N2-B unique sequence. Biophys. J. 97, 825–834. doi: 10.1016/j.bpj.2009.05.037

Haase, N., Rugor, J., Przybyl, L., Qadri, F., Muller, D. N., and Dechend, R. (2014). Relaxin does not improve Angiotensin II-induced target-organ damage. PLoS One 9:e93743. doi: 10.1371/journal.pone.0093743

Hamdani, N., Bishu, K. G., von Frieling-Salewsky, M., Redfield, M. M., and Linke, W. A. (2013a). Deranged myofilament phosphorylation and function in experimental heart failure with preserved ejection fraction. Cardiovasc. Res. 97, 464–471. doi: 10.1093/cvr/cvs353

Hamdani, N., Krysiak, J., Kreusser, M. M., Neef, S., Dos Remedios, C. G., Maier, L. S., et al. (2013b). Crucial role for Ca2(+)/calmodulin-dependent protein kinase-II in regulating diastolic stress of normal and failing hearts via titin phosphorylation. Circ. Res. 112, 664–674. doi: 10.1161/CIRCRESAHA.111.300105

Hamdani, N., Hervent, A.-S., Vandekerckhove, L., Matheeussen, V., Demolder, M., Baerts, L., et al. (2014). Left ventricular diastolic dysfunction and myocardial stiffness in diabetic mice is attenuated by inhibition of dipeptidyl peptidase 4. Cardiovasc. Res. 104, 423–431. doi: 10.1093/cvr/cvu223

Hidalgo, C., Hudson, B., Bogomolovas, J., Zhu, Y., Anderson, B., Greaser, M., et al. (2009). PKC phosphorylation of titin's PEVK element: a novel and conserved pathway for modulating myocardial stiffness. Circ. Res. 105, 631–638. doi: 10.1161/CIRCRESAHA.109.198465

Ischiropoulos, H. (2003). Biological selectivity and functional aspects of protein tyrosine nitration. Biochem. Biophys. Res. Commun. 305, 776–783. doi: 10.1016/s0006-291x00814-3

Johnson, R. D., and Camelliti, P. (2018). Role of Non-myocyte gap junctions and connexin hemichannels in cardiovascular health and disease: novel therapeutic targets? Int. J. Mol. Sci. 19:866. doi: 10.3390/ijms19030866

Kai, H., Kuwahara, F., Tokuda, K., and Imaizumi, T. (2005). Diastolic dysfunction in hypertensive hearts: roles of perivascular inflammation and reactive myocardial fibrosis. Hypertens. Res. 28, 483–490. doi: 10.1291/hypres.28.483

Kemp-Harper, B., and Feil, R. (2008). Meeting report: cGMP matters. Sci. Signal. 1:e12. doi: 10.1126/stke.19pe12

Klinger, J. R., and Kadowitz, P. J. (2017). The nitric oxide pathway in pulmonary vascular disease. Am. J. Cardiol. 120, S71–S79. doi: 10.1016/j.amjcard.2017.06.012

Kruger, M., Kotter, S., Grutzner, A., Lang, P., Andresen, C., Redfield, M. M., et al. (2009). Protein kinase G modulates human myocardial passive stiffness by phosphorylation of the titin springs. Circ. Res. 104, 87–94. doi: 10.1161/CIRCRESAHA.108.184408

Kruger, M., and Linke, W. A. (2006). Protein kinase-A phosphorylates titin in human heart muscle and reduces myofibrillar passive tension. J. Muscle Res. Cell Motil. 27, 435–444. doi: 10.1007/s10974-006-9090-5

Leite Fde, S., Kashina, A., and Rassier, D. E. (2016). Posttranslational arginylation regulates striated muscle function. Exerc. Sport Sci. Rev. 44, 98–103. doi: 10.1249/JES.0000000000000079

Linke, W. A., and Hamdani, N. (2014). Gigantic business: titin properties and function through thick and thin. Circ. Res. 114, 1052–1068. doi: 10.1161/CIRCRESAHA.114.301286

Luft, F. C., Mervaala, E., Muller, D. N., Gross, V., Schmidt, F., Park, J. K., et al. (1999). Hypertension-induced end-organ damage : a new transgenic approach to an old problem. Hypertension 33(1 Pt 2), 212–218. doi: 10.1161/01.hyp.33.1.212

Masuyama, H., Tsuruda, T., Kato, J., Imamura, T., Asada, Y., Stasch, J. P., et al. (2006). Soluble guanylate cyclase stimulation on cardiovascular remodeling in angiotensin II-induced hypertensive rats. Hypertension 48, 972–978. doi: 10.1161/01.HYP.0000241087.12492.47

Menges, L., Krawutschke, C., Fuchtbauer, E. M., Fuchtbauer, A., Sandner, P., Koesling, D., et al. (2019). Mind the gap [junction]: NO-induced cGMP in cardiac myocytes originates from fibroblasts. Br. J. Pharmacol. 176, 4696–4707. doi: 10.1111/bph.14835

Mittendorf, J., Weigand, S., Alonso-Alija, C., Bischoff, E., Feurer, A., Gerisch, M., et al. (2009). Discovery of riociguat (BAY 63-2521): a potent, oral stimulator of soluble guanylate cyclase for the treatment of pulmonary hypertension. ChemMedChem 4, 853–865. doi: 10.1002/cmdc.200900014

Paulus, W. J., and Tschope, C. (2013). A novel paradigm for heart failure with preserved ejection fraction: comorbidities drive myocardial dysfunction and remodeling through coronary microvascular endothelial inflammation. J. Am. Coll. Cardiol. 62, 263–271. doi: 10.1016/j.jacc.2013.02.092

Pieske, B., Maggioni, A. P., Lam, C. S. P., Pieske-Kraigher, E., Filippatos, G., Butler, J., et al. (2017). Vericiguat in patients with worsening chronic heart failure and preserved ejection fraction: results of the SOluble guanylate Cyclase stimulatoR in heArT failurE patientS with PRESERVED EF (SOCRATES-PRESERVED) study. Eur. Heart J. 38, 1119–1127. doi: 10.1093/eurheartj/ehw593

Raskin, A., Lange, S., Banares, K., Lyon, R. C., Zieseniss, A., Lee, L. K., et al. (2012). A novel mechanism involving four-and-a-half LIM domain protein-1 and extracellular signal-regulated kinase-2 regulates titin phosphorylation and mechanics. J. Biol. Chem. 287, 29273–29284. doi: 10.1074/jbc.M112.372839

Redfield, M. M., Chen, H. H., Borlaug, B. A., Semigran, M. J., Lee, K. L., Lewis, G., et al. (2013). Effect of phosphodiesterase-5 inhibition on exercise capacity and clinical status in heart failure with preserved ejection fraction: a randomized clinical trial. JAMA 309, 1268–1277. doi: 10.1001/jama.2013.2024

Sandner, P., Zimmer, D. P., Milne, G. T., Follmann, M., Hobbs, A., and Stasch, J. P. (2019). Correction to: soluble guanylate cyclase stimulators and activators. Handb. Exp. Pharmacol. doi: 10.1007/164_2019_249 [Online ahead of print]

Savvatis, K., Muller, I., Frohlich, M., Pappritz, K., Zietsch, C., Hamdani, N., et al. (2014). Interleukin-6 receptor inhibition modulates the immune reaction and restores titin phosphorylation in experimental myocarditis. Basic Res. Cardiol. 109:449. doi: 10.1007/s00395-014-0449-2

Schulz, E., Jansen, T., Wenzel, P., Daiber, A., and Munzel, T. (2008). Nitric oxide, tetrahydrobiopterin, oxidative stress, and endothelial dysfunction in hypertension. Antioxid. Redox Signal. 10, 1115–1126. doi: 10.1089/ars.2007.1989

Solan, J. L., and Lampe, P. D. (2007). Key connexin 43 phosphorylation events regulate the gap junction life cycle. J. Membr. Biol. 217, 35–41. doi: 10.1007/s00232-007-9035-y

Solan, J. L., and Lampe, P. D. (2014). Specific Cx43 phosphorylation events regulate gap junction turnover in vivo. FEBS Lett. 588, 1423–1429. doi: 10.1016/j.febslet.2014.01.049

Stasch, J. P., Becker, E. M., Alonso-Alija, C., Apeler, H., Dembowsky, K., Feurer, A., et al. (2001). NO-independent regulatory site on soluble guanylate cyclase. Nature 410, 212–215. doi: 10.1038/35065611

Stasch, J. P., and Hobbs, A. J. (2009). NO-independent, haem-dependent soluble guanylate cyclase stimulators. Handb. Exp. Pharmacol. 191, 277–308. doi: 10.1007/978-3-540-68964-5_13

Stasch, J. P., Pacher, P., and Evgenov, O. V. (2011). Soluble guanylate cyclase as an emerging therapeutic target in cardiopulmonary disease. Circulation 123, 2263–2273. doi: 10.1161/CIRCULATIONAHA.110.981738

Stasch, J. P., Schmidt, P. M., Nedvetsky, P. I., Nedvetskaya, T. Y., Arun Kumar, H. S., Meurer, S., et al. (2006). Targeting the heme-oxidized nitric oxide

receptor for selective vasodilatation of diseased blood vessels. J. Clin. Invest. 116, 2552–2561. doi: 10.1172/JCI28371

Thevenin, A. F., Kowal, T. J., Fong, J. T., Kells, R. M., Fisher, C. G., and Falk, M. M. (2013). Proteins and mechanisms regulating gap-junction assembly, internalization, and degradation. Physiology 28, 93–116. doi: 10.1152/physiol.00038.2012

van Heerebeek, L., Borbely, A., Niessen, H. W., Bronzwaer, J. G., van der Velden, J., Stienen, G. J., et al. (2006). Myocardial structure and function differ in systolic and diastolic heart failure. Circulation 113, 1966–1973. doi: 10.1161/CIRCULATIONAHA.105.587519

van Heerebeek, L., Franssen, C. P., Hamdani, N., Verheugt, F. W., Somsen, G. A., and Paulus, W. J. (2012). Molecular and cellular basis for diastolic dysfunction. Curr. Heart Fail Rep. 9, 293–302. doi: 10.1007/s11897-012-0109-5

van Heerebeek, L., Hamdani, N., Handoko, M. L., Falcao-Pires, I., Musters, R. J., Kupreishvili, K., et al. (2008). Diastolic stiffness of the failing diabetic heart: importance of fibrosis, advanced glycation end products, and myocyte resting tension. Circulation 117, 43–51. doi: 10.1161/CIRCULATIONAHA.107.728550

Wilck, N., Marko, L., Balogh, A., Kraker, K., Herse, F., Bartolomaeus, H., et al. (2018). Nitric oxide-sensitive guanylyl cyclase stimulation improves experimental heart failure with preserved ejection fraction. JCI Insight 3:e96006. doi: 10.1172/jci.insight.96006

Yamasaki, R., Wu, Y., McNabb, M., Greaser, M., Labeit, S., and Granzier, H. (2002). Protein kinase A phosphorylates titin's cardiac-specific N2B domain and reduces passive tension in rat cardiac myocytes. Circ. Res. 90, 1181–1188. doi: 10.1161/01.res.0000021115.24712.99

Yao, J., Hiramatsu, N., Zhu, Y., Morioka, T., Takeda, M., Oite, T., et al. (2005). Nitric oxide-mediated regulation of connexin43 expression and gap junctional intercellular communication in mesangial cells. J. Am. Soc. Nephrol. 16, 58–67. doi: 10.1681/ASN.2004060453

Yokoyama, T., Nakano, M., Bednarczyk, J. L., McIntyre, B. W., Entman, M., and Mann, D. L. (1997). Tumor necrosis factor-alpha provokes a hypertrophic growth response in adult cardiac myocytes. Circulation 95, 1247–1252. doi: 10.1161/01.cir.95.5.1247

Yuan, D., Sun, G., Zhang, R., Luo, C., Ge, M., Luo, G., et al. (2015). Connexin 43 expressed in endothelial cells modulates monocyteendothelial adhesion by regulating cell adhesion proteins. Mol. Med. Rep. 12, 7146–7152. doi: 10.3892/mmr.2015.4273

Zile, M. R., Baicu, C. F., Ikonomidis, J. S., Stroud, R. E., Nietert, P. J., Bradshaw, A. D., et al. (2015). Myocardial stiffness in patients with heart failure and a preserved ejection fraction: contributions of collagen and titin. Circulation 131, 1247–1259. doi: 10.1161/CIRCULATIONAHA.114.013215

Conflict of Interest: The authors declare that this study received funding from Bayer AG. The funder was not involved in the study design, collection, analysis, interpretation of data, the writing of this article or the decision to submit it for publication. Howere, the funder had the following involvement with the study "Approval of the manuscript."

frontiers in Physiology

BRIEF RESEARCH REPORT
published: 03 June 2020
doi: 10.3389/fphys.2020.00516

Hypertrophic and Dilated Cardiomyopathy-Associated Troponin T Mutations R130C and ΔK210 Oppositely Affect Length-Dependent Calcium Sensitivity of Force Generation

*Marcel Groen[1], Alfredo Jesus López-Dávila[2], Stefan Zittrich[3], Gabriele Pfitzer[4] and Robert Stehle[3]**

[1] Department of Neurology and Neurogeriatry, Johannes Wesling Medical Center, Ruhr-University Bochum, Bochum, Germany, [2] Department of Molecular and Cell Physiology, Hannover Medical School, Hanover, Germany, [3] Institute of Vegetative Physiology, University of Cologne, Cologne, Germany, [4] Institute of Neurophysiology, University of Cologne, Cologne, Germany

OPEN ACCESS

Edited by:
Sachio Morimoto, International University of Health and Welfare (IUHW), Japan

Reviewed by:
Vasco Sequeira, VU University Medical Center, Netherlands
Steven Baxter Marston, Imperial College London, United Kingdom

***Correspondence:**
Robert Stehle
robert.stehle@uni-koeln.de

Specialty section:
This article was submitted to Striated Muscle Physiology, a section of the journal Frontiers in Physiology

Received: *17 January 2020*
Accepted: *27 April 2020*
Published: *03 June 2020*

Citation:
Groen M, López-Dávila AJ, Zittrich S, Pfitzer G and Stehle R (2020) Hypertrophic and Dilated Cardiomyopathy-Associated Troponin T Mutations R130C and ΔK210 Oppositely Affect Length-Dependent Calcium Sensitivity of Force Generation. Front. Physiol. 11:516. doi: 10.3389/fphys.2020.00516

Length-dependent activation of calcium-dependent myocardial force generation provides the basis for the Frank-Starling mechanism. To directly compare the effects of mutations associated with hypertrophic cardiomyopathy and dilated cardiomyopathy, the native troponin complex in skinned trabecular fibers of guinea pigs was exchanged with recombinant heterotrimeric, human, cardiac troponin complexes containing different human cardiac troponin T subunits (hcTnT): hypertrophic cardiomyopathy-associated hcTnT^{R130C}, dilated cardiomyopathy-associated hcTnT$^{\Delta K210}$ or the wild type hcTnT (hcTnT^{WT}) serving as control. Force-calcium relations of exchanged fibers were explored at short fiber length defined as 110% of slack length (L_0) and long fiber length defined as 125% of L_0 (1.25 L_0). At short fiber length (1.1 L_0), calcium sensitivity of force generation expressed by $-\log [Ca^{2+}]$ required for half-maximum force generation (pCa_{50}) was highest for the hypertrophic cardiomyopathy-associated mutation R130C (5.657 ± 0.019), intermediate for the wild type control (5.580 ± 0.028) and lowest for the dilated cardiomyopathy-associated mutation ΔK210 (5.325 ± 0.038). Lengthening fibers from 1.1 L_0 to 1.25 L_0 increased calcium sensitivity in fibers containing hcTnT^{R130C} (delta-pCa_{50} = +0.030 ± 0.010), did not alter calcium sensitivity in the wild type control (delta-pCa_{50} = −0.001 ± 0.010), and decreased calcium sensitivity in fibers containing hcTnT$^{\Delta K210}$ (delta-pCa_{50} = −0.034 ± 0.013). Length-dependent activation indicated by the delta-pCa_{50} was highly significantly ($P < 0.001$) different between the two mutations. We hypothesize that primary effects of mutations on length-dependent activation contribute to the development of the diverging phenotypes in hypertrophic and dilated cardiomyopathy.

Keywords: contractility, length dependent activation, thin filament regulation, cardiomyopathy, sarcomere length, force generation, troponin, calcium sensitivity

INTRODUCTION

The Frank-Starling law describes the intrinsic ability of the heart ventricle to adapt the systolic stroke volume to the previous diastolic filling. One main reason for this ability is the increased calcium sensitivity of the stretched myocardium, reviewed in Hanft et al. (2008), de Tombe et al. (2010) and Ait Mou et al. (2015) and also termed length-dependent activation (LDA). LDA has been attributed to different mechanisms intrinsic to the sarcomere, involving changes in filament lattice spacing (Hanft et al., 2008), stretch-dependent Ca^{2+} regulation of troponin (Arteaga et al., 2000; Konhilas et al., 2003; Korte et al., 2012; Zhang et al., 2017), ordering of myosin head orientation (Farman et al., 2011), strain-sensing in titin (Millman and Irving, 1988; Ait Mou et al., 2015; Ait-Mou et al., 2016; Linke, 2018), and the communication between these mechanisms (Ait-Mou et al., 2016; Zhang et al., 2017).

Mutations in proteins of the sarcomere are associated with hypertrophic cardiomyopathy (HCM) and dilated cardiomyopathy (DCM). HCM and DCM mutations can occur in the same protein like in human cardiac troponin T (hcTnT) (Kamisago et al., 2000; Marston and Hodgkinson, 2001; Song et al., 2005; Lu et al., 2013). Cardiac troponin T (cTnT) transfers the Ca^{2+} binding event from cardiac troponin C (cTnC) to troponin I (cTnI) and tropomyosin (Tm) [recently reviewed in (Marston and Zamora, 2020)]. Previous studies investigating individual mutations in these regulatory proteins associated with HCM and DCM either mostly reported negative or no consequence of mutations on LDA (Li et al., 2013; Sequeira et al., 2013; Mickelson and Chandra, 2017; Reda and Chandra, 2018, 2019).

Hypertrophic cardiomyopathy and DCM differ not only as to heart morphology but also to the type of cardiac dysfunction and histology. Diastolic dysfunction and cardiomyocyte disarray is typical for HCM whereas systolic function and shape of cardiomyocytes are often normal in HCM. In contrast, severe systolic dysfunction and thinned cardiomyocytes are typical features of DCM. HCM mutations mostly increase calcium sensitivity of contraction while DCM mutations mostly decrease it (Robinson et al., 2002, 2007; Mirza et al., 2005; Willott et al., 2010; Kalyva et al., 2014). Besides the direct effect of mutations on calcium sensitivity, also their effect on posttranslational modification of regulatory proteins correlates with the type of cardiomyopathy (Sfichi-Duke et al., 2010; Lu et al., 2013; Memo et al., 2013; Messer et al., 2016). However, to the best of our knowledge, no study so far examined the effects of HCM and DCM-associated mutations on LDA within the same experiment, keeping identical conditions among control, HCM and DCM mutant.

To test if there is any difference in the effects of HCM- and DCM-associated mutations on mechanical parameters, in particular on LDA, we exchanged the native troponin complex in skinned fibers dissected from papillary muscle of the left ventricle of the guinea pig by recombinant human heterotrimeric troponin complexes (hcTn) containing different recombinant hcTnT: either hcTnT with the HCM-associated exchange of arginine-130 to cysteine ($hcTnT^{R130C}$), hcTnT with the DCM-associated deletion of lysine-210 ($hcTnT^{\Delta K210}$), or wild type hcTnT as control. Fibers incorporated with the two mutations exhibited highly significant different and opposite response of calcium sensitivity to lengthening, i.e., calcium sensitization for the HCM and calcium desensitization for the DCM mutation. These findings suggest that the HCM and DCM mutation might exert opposite primary effects on the Frank-Starling mechanism.

MATERIALS AND METHODS

Skinned Fiber Preparation and Mechanical Setup

Skinned fibers were dissected from the left ventricular papillary muscles of the guinea pig (Stehle et al., 2002) and stored for up to 60 h at 0°C in skinning solution containing 5 mM KH_2PO_4, 5 mM Na-acide, 3 mM magnesium acetate, 5 mM K_2EGTA, 3 mM Na_2MgATP, 47 mM sodium creatine phosphate, 2 mM dithiothreitol (DTT), 0.2 mM 4-(2-aminoethyl)benzenesulfonyl-fluoride (AEBSF), 10 μM leupeptin, 10 μM antipain, 5 mg/l aprotinin. Skinned fibers were mounted in skinning solution in the mechanical setup between a force transducer (KG7A) with bridge-amplifier DUBAM 7C (Scientific Instruments, Heidelberg, Germany) and a fixed clamp. After mounting, fibers were stretched by 10% of their slack length L_0 to 1.1 L_0.

Troponin Exchange

The three subunits of hcTn, i.e., hcTnC, hcTnT, and hcTnI were separately expressed in *Escherichia coli* and isolated as described previously (Kruger et al., 2003). For the exchange of the endogenous guinea pig cTn for the exogenous recombinant human cTn, the fibers were incubated in the mechanical setup at 10°C for 15 min in exchange buffer (in mmol/L): 132 NaCl, 5 KCl, 1 $MgCl_2$, 10 Tris, 5 EGTA, 1 NaN_3, pH 7.1 (20°C) followed by incubation in the same buffer containing in addition 3 mg/ml hcTn for 180 min at 20°C (Neulen et al., 2007).

The exchange of the endogenous guinea pig cTn (gcTn) for the exogenous hcTn was probed by 12.5% SDS-PAGE and visualizing proteins by Commassie-R250-staining (Solzin et al., 2007). Guinea pig cTnI (gcTnI) contains one more amino acid and migrates less than hcTnI on the gel (**Supplementary Figure S1** in **Supplementary Material**). Exchange efficiency was defined by the ratio of hcTnI intensity per total intensity of hcTnI and gcTnI and quantified using Phoretix-1 as illustrated in **Supplementary Figure S1**.

Force-pCa Relations

Force-pCa relations were measured using mixtures of Ca^{2+}-buffered activating and relaxing solutions containing 3 mM $(CaCl_2)K_2EGTA$ (activating solution, pCa 4.7) or 3 mM K_4Cl_2EGTA (relaxing solution, pCa 7), 10 mM imidazole, 10 mM Na_2MgATP, 3 mM $MgCl_2$, 32.7 mM sodium creatine phosphate, 2 mM DTT, pH 7.0, μ = 178 mM. To ensure saturation of free Ca^{2+} concentration at all conditions, an extra activation solution (pCa 4.28) was prepared by adding 3 mL 60 mM $CaCl_2$ per 100 mL activating solution. Experimental temperature was 10°C.

Force–pCa relations were fitted by sigmoidal Hill equation: $F_{norm} = 1 + 10^{(pCa50 - pCa)nH}$, where F_{norm} is the force at pCa = −log [Ca^{2+}]/M normalized to maximum force at pCa 4.28, pCa_{50} is the pCa at which $F_{norm} = 0.5$, and n_H is the Hill coefficient indicating the slope of the force–pCa relation.

Statistical Analysis

Two-way repeated measures analysis of variance (Two-way RM ANOVA) was performed under GraphPad Prism 4 to test the effects of two factors, the effect of hcTnT-type ($hcTnT^{R130C}$, $hcTnT^{WT}$, and $hcTnT^{\Delta K210}$) and the effect of fiber length (1.1 L_0 and 1.25 L_0) on each analyzed parameter. Data was subject-matched (fiber-matched) for analyzing the effect of fiber length on parameters that were measured in each individual fiber first at 1.1 L_0 and then at 1.25 L_0. Subject matching was highly indicated by $P < 0.0001$ for each parameter. Significant hcTnT-type-fiber length interaction ($P < 0.05$) in the two-way RM ANOVA indicated dissimilar length change of the parameter among the three hcTnT-types. To probe the cause for significant interaction, *post hoc* analysis was performed using Tukey's multiple comparison test yielding the *P*-values indicated in the results by * for $P < 0.05$, ** for $P < 0.01$, and *** for $P < 0.001$. When length affected the parameter with no significant interaction, the significance for length changing the parameter indicated by the subject-matched delta values of the parameter being significantly different from zero was analyzed by Bonferroni post-tests and indicated by # for $P < 0.05$, ## for $P < 0.01$, and ### for $P < 0.001$. All parameter values are given as mean ± SEM (standard error of the mean) of *n* fibers exchanged for each hcTnT-type.

RESULTS

Control of Troponin Exchange

The endogenous troponin complex in the left ventricular skinned fibers from guinea pigs was exchanged by exogenous recombinant human cardiac heterotrimeric troponin complex (hcTn) containing the hcTnC and hcTnI wild type subunits and either $hcTnT^{WT}$, $hcTnT^{R130C}$ or $hcTnT^{\Delta K210}$. The exchange in the fibers of the exogenous hcTn complexes for the endogenous cTn was tested by preparing three samples for each type of recombinant hcTn exchange. Each sample contained two fibers that were subjected to the exchange protocol in the chamber of the mechanical setup under the same conditions as performed for the mechanical measurements and each sample was then quantified for the relative amounts of endogenous and exogenous hcTn (**Supplementary Figure S1**). The exchange efficiency defined by the ratio of hcTnI per total cTnI (sum of endogenous gcTnI and exogenous hcTnI) was 46 ± 2% for the exchange done with hcTn containing the $hcTnT^{WT}$, 44 ± 1% for the one containing the $hcTnT^{R130C}$ and 48 ± 2% for the one containing the $hcTnT^{\Delta K210}$ (mean ± SEM of each $n = 3$). There were no significant differences in the efficiencies for the three exchanges. Similar exchange efficiencies have been reported in a previous *in vitro* study of the $hcTnT^{\Delta K210}$ mutation using exchange of recombinant hcTn for endogenous cTn in permeabilized rabbit cardiac muscle fibers (Morimoto et al., 2002).

Biomechanical Measurements

For the force measurements, fibers were prepared from 7 guinea pig hearts. 18 fibers were exchanged for hcTn containing HCM-associated $hcTnT^{R130C}$, 19 fibers contained the $hcTnT^{WT}$ control and 19 fibers contained the DCM-associated $hcTnT^{\Delta K210}$. **Figure 1A** shows the resting tension (F_{REST}) of fibers exchanged with the three different hcTnT at short fiber length (110% of slack length, 1.1 L_0) and after stretching them to long fiber length (125% of slack length, 1.25 L_0). Although the statistical analysis by two-way RM ANOVA indicated strong significant increase of F_{PASS} by stretch ($P < 0.0001$) confirmed for each hcTnT-type by Bonferroni post-test (see ### in **Figure 1A**), there was no significant interaction ($P = 0.37$) between the effects of fiber length and hcTnT-type on F_{PASS} (**Figure 1A** and **Table 1**). No interaction indicates similar passive mechanical properties of fibers containing the three different types of hcTnT. Similarly to passive tension, two-way RM ANOVA revealed no interaction between the effects of fiber length and hcTnT-type on the maximum tension (F_{MAX}) during contraction (**Figure 1B** and **Table 1**). F_{MAX} was strongly significantly increased ($P < 0.0001$) by stretching the fibers. Bonferroni post-tests confirmed the significant effect of stretch on F_{MAX} for each hcTnT-type. The results for F_{MAX} indicate that the mutations do not alter the maximum force-generating capacity or its length dependence. The values of F_{PASS} and F_{MAX} are summarized in **Supplementary Table S1** (see **Supplementary Material**) and their statistical analysis in **Table 2**.

Along with resting tension and maximum tension, the full force-pCa relations were determined before and after lengthening fibers from 1.1 L_0 to 1.25 L_0. **Figure 1C** illustrates the average force-pCa relations of the three groups of different hcTn-exchanged fibers at short (1.1 L_0, circles) and long fiber length (1.25 L_0, triangles). At short fiber length, the relation of $hcTnT^{R130C}$-exchanged fibers is shifted to the left compared to the relation of the $hcTnT^{WT}$ control, i.e., to higher pCa values or lower [Ca^{2+}]. This leftward shift is slightly enhanced upon lengthening the fibers from 1.1 L_0 to 1.25 L_0. Opposite to the HCM mutation, the relation of the fibers containing the DCM-associated $hcTnT^{\Delta K210}$ is slightly shifted to the right compared to the relation of the control fibers containing the $hcTnT^{WT}$ (**Figure 1C**). The basal calcium desensitization by the DCM mutation observed at short fiber length is further enhanced by lengthening the fibers to 1.25 L_0.

To test for statistical significant differences in calcium-dependent force generation among the three types of hcTn exchange and among the two lengths, the force-pCa relation plotted for each individual fiber at each length was fitted by the sigmoidal Hill function (see section "Materials and Methods") to quantify the mean and variation of pCa_{50} and n_H as indicators for calcium sensitivity and cooperativity of the calcium-dependent force generation, respectively. Two-way RM ANOVA revealed a highly significant effect ($P < 0.0001$) of the hcTnT-type on the pCa_{50} (**Figure 2A**, **Table 2**, and **Supplementary Table S1**). Most important, there was high interaction ($P = 0.0009$) of the

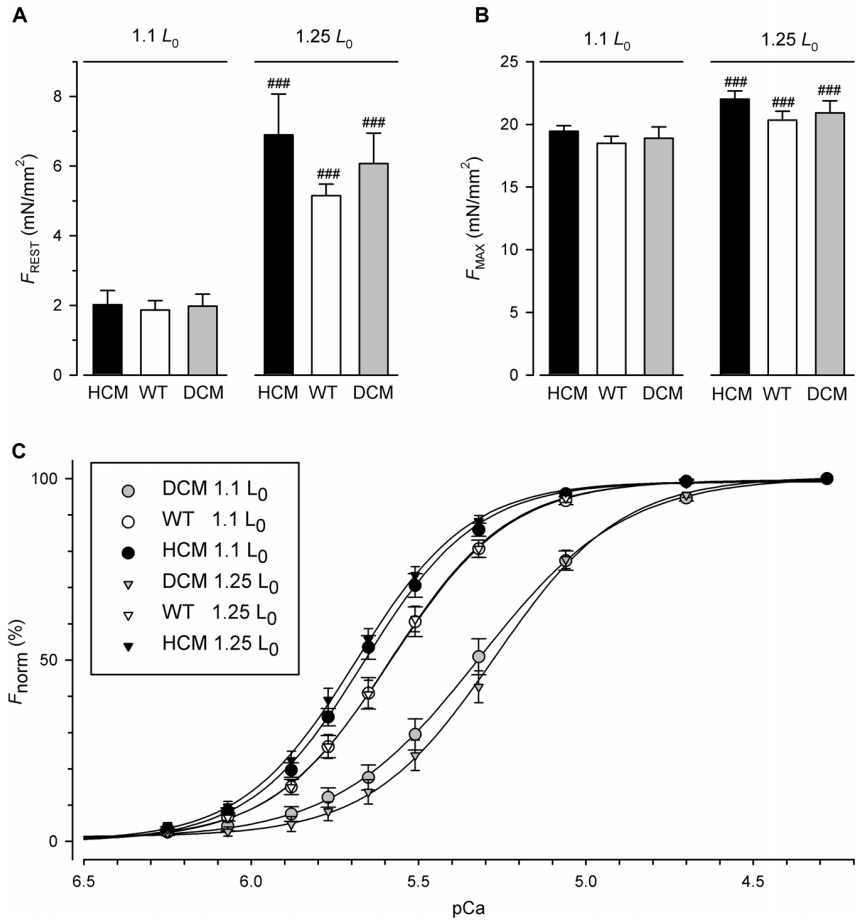

FIGURE 1 | Resting, maximum and calcium-dependent force generation of skinned fibers exchanged for human hcTn containing HCM-associated hcTnT^{R130C} (n = 18 fibers), hcTnT^{WT} (n = 19 fibers), or DCM-associated hcTnT$^{\Delta K210}$ (n = 19 fibers). **(A)** Resting tension measured in relaxing solution (pCa 7) at short (1.1 L_0) and long (1.25 L_0) fiber length. **(B)** Maximum tension measured at pCa 4.28. **(C)** Force-pCa relations at short fiber length (1.1 L_0) and long fiber length (1.25 L_0). Normalized force is scaled as percentage from 0% for resting tension to 100% for maximum tension. $^{###}$Indicates highly significant different to 1.1 L0 in paired Bonferroni post tests.

TABLE 1 | Changes in resting tension, maximum tension, pCa_{50} and n_H induced by lengthening fibers from 1.1 to 1.25 L_0.

	hcTnT^{R130C}	hcTnT^{WT}	hcTnT$^{\Delta K210}$
Delta-F_{REST} (mN/mm^2)	+4.89 ± 0.94$^{###}$	+3.28 ± 0.39$^{###}$	+4.09 ± 0.70$^{###}$
Delta-F_{MAX} (mN/mm^2)	+2.56 ± 0.56$^{###}$	+1.85 ± 0.35$^{###}$	+2.01 ± 0.50$^{###}$
Delta-pCa_{50}	+0.030 ± 0.010$^{\#***}$	−0.001 ± 0.010	−0.034 ± 0.013$^{\#}$
Delta-n_H	−0.06 ± 0.12	−0.02 ± 0.07	+0.22 ± 0.14

Values present mean ± SEM of subject-matched parameter changes, i.e., the parameter changes of the individual fibers exchanged for hcTn containing different hcTnT (hcTnT^{R130C} n = 18, hcTnT^{WT}: n = 19, hcTnT$^{\Delta K210}$: n = 19). Significant change by lengthening: $^{\#}P < 0.05$, $^{\#\#}P < 0.01$, $^{\#\#\#}P < 0.001$. Significant different to hcTnT$^{\Delta K210}$: $^{***}P < 0.001$.

effects of hcTnT-type and fiber length on the pCa_{50} indicating dissimilar lengthening-induced change of pCa_{50} (delta-pCa_{50}) among the fibers containing the three different hcTnT-types. In contrast to the strong interaction found for the pCa_{50}, there is no interaction (P = 0.18), no effect of fiber length (P = 0.37) and no effect of hcTnT-type (P = 0.47) on the Hill coefficient n_H in the two-way RM ANOVA (**Figure 2B**, **Table 2**, and **Supplementary Table S1**).

For further analysis of the effect of hcTnT-type on the pCa_{50}, the data sets were separated for either short (1.1 L_0) or long (1.25 L_0) fiber length and *post hoc* tested by one-way ANOVA which confirmed the significant effect of hcTnT-type on the pCa_{50} for each of the two lengths ($P < 0.001$). Tukey's multiple comparison revealed that the DCM mutant highly significantly ($P < 0.001$) decreases Ca sensitivity at both lengths when either compared to the wild type or to the HCM mutant, whereas the HCM mutant increases Ca sensitivity only at long ($P < 0.05$) but not at short fiber length compared to the wild type (**Figure 2A** and **Supplementary Table S1**), thus lengthening manifested in an effect of the HCM mutant compared to wild type.

Post hoc analysis for searching the reason of the high interaction of hcTnT-type and length effects on the pCa_{50}

TABLE 2 | *P*-values obtained in statistical analysis of the parameters. $F_{pCa's}$ correspond to the normalized force values at the respective pCa.

Parameter	Two-way RM ANOVA				Tukey's multiple comparison			Bonferroni post-test		
	Interaction	hcTnT-type	Fiber length	Subject match	HCM vs. WT	HCM vs. DCM	DCM vs. WT	HCM	WT	DCM
F_{REST}	0.37	0.78	***	***	n.d.	n.d.	n.d.	$\uparrow^{\#\#\#}$	$\uparrow^{\#\#\#}$	$\uparrow^{\#\#\#}$
F_{ACT}	0.55	0.41	***	***	n.d.	n.d.	n.d.	$\uparrow^{\#\#\#}$	$\uparrow^{\#\#\#}$	$\uparrow^{\#\#\#}$
pCa_{50}	***	***	0.81	***	–	***	–	$\uparrow^{\#}$	–	$\downarrow^{\#}$
n_H	0.18	0.37	0.47	***	n.d.	n.d.	n.d.	–	–	–
$F_{pCa6.25}$	0.44	0.35	0.25	***	n.d.	n.d.	n.d.	–	–	–
$F_{Ca6.07}$	***	**	0.67	***	*	***	–	$\uparrow^{\#\#}$	–	$\downarrow^{\#}$
$F_{pCa5.88}$	***	***	0.68	***	**	***	*	$\uparrow^{\#\#\#}$	–	$\downarrow^{\#\#\#}$
$F_{pCa5.77}$	***	***	0.53	***	–	***	–	$\uparrow^{\#\#}$	–	–
$F_{pCa5.65}$	**	***	0.50	***	–	**	–	–	–	$\downarrow^{\#\#}$
$F_{pCa5.51}$	**	***	0.63	***	–	**	–	–	–	$\downarrow^{\#\#}$
$F_{pCa5.32}$	***	***	0.11	***	–	***	*	–	–	$\downarrow^{\#\#\#}$
$F_{pCa5.06}$	0.97	***	0.33	***	n.d.	n.d.	n.d.	–	–	–
$F_{pCa4.7}$	0.27	***	0.86	***	n.d.	n.d.	n.d.	–	–	–

*Two-way RM ANOVA and Tukey's multiple comparison post-tests were used to test for significant differences among hcTnT-types: *P < 0.05, **P < 0.01, ***P < 0.001. n.d., not determined because of insignificant interaction (P > 0.05). Bonferroni post-tests indicate significant length-dependent changes of parameters for the hcTnT-type: #P < 0.05, ##P < 0.01, ###P < 0.001; ↑ marks increase, ↓ marks decrease of parameter; – indicates not significant (P > 0.05).*

by Tukey's multiple comparison yielded highly significant ($P < 0.001$) different delta-pCa_{50} of fibers containing HCM-associated $hcTnT^{R130C}$ compared to fibers containing DCM-associated $hcTnT^{\Delta K210}$ (**Figure 2C** and **Tables 1**, **2**). The 95% confidence interval of the delta-pCa_{50} of fibers containing $hcTnT^{R130C}$ was fully positive (+0.002 to +0.058) whereas that of fibers containing $hcTnT^{\Delta K210}$ was fully negative (−0.062 to −0.007). The significant difference ($P < 0.05$) of the intervals from zero is also reflected by the corresponding Bonferroni post-tests (#-marks in **Figure 2C**) and indicates that lengthening induced calcium sensitization in fibers containing the HCM mutation whereas lengthening caused calcium desensitization in fibers containing the DCM mutation. The delta-pCa_{50} of fibers containing wild type hcTnT is in-between the delta-pCa_{50} of the fibers containing the mutants and not significantly different to each mutant.

To analyze the effects of hcTnT and length on the calcium-dependent force at sub-maximally activating [Ca^{2+}], the normalized force at each pCa was tested by two-way RM ANOVA. Strong significant interaction of hcTnT-type and fiber length effects on normalized force were found for pCa 6.07 ($P = 0.0002$), pCa 5.88 ($P < 0.0001$), pCa 5.77 ($P = 0.0006$), pCa 5.65 ($P = 0.0022$), pCa 5.51 ($P = 0016$), and pCa 5.32 ($P = 0.006$) indicating dissimilarity of lengthening-induced change of normalized force (delta-F_{norm}) for at least one hcTnT-type at the respective pCa (**Table 2**). The delta-F_{norm} values at submaximal activating pCa are plotted in **Figure 2D**. Post-tests confirmed that at each of the above pCa, fibers containing the HCM and the DCM mutation differ significantly by at least $P < 0.01$ in their delta-F_{norm} (**Table 2**). At pCa 5.88, all three hcTnT-types differed significantly in delta-F_{norm} ($P < 0.01$ for HCM versus WT, $P < 0.05$ for DCM versus WT, and $P < 0.001$ for HCM versus DCM) (**Figure 2D** and **Table 2**). In summary, stretching fibers containing the HCM mutation increased calcium sensitivity (pCa_{50}) and F_{norm} whereas stretching fibers containing the DCM mutation decreased calcium sensitivity and F_{norm}.

DISCUSSION

Basic Effects of the hcTnT Mutations on Calcium Sensitivity

The two mutations R130C and ΔK210 in hcTnT have been associated with autosomal dominant inherited hypertrophic or dilated cardiomyopathy, respectively (Kamisago et al., 2000; Song et al., 2005; Wang et al., 2007). The basal effects of the HCM-associated mutation R130C and of the DCM-associated mutation ΔK210 on calcium sensitivity found in this study resemble the most common phenotype of HCM-mutations and DCM-associated mutations on calcium sensitivity. They are in general agreement with numerous previous studies of HCM- and DCM-associated mutations in hcTnT reporting increase of calcium sensitivity by HCM- and decrease of calcium sensitivity by DCM-associated mutations (Morimoto et al., 2002; Lu et al., 2003, 2013; Venkatraman et al., 2003; Mirza et al., 2005; Robinson et al., 2007; Messer et al., 2016).

The functional consequences of the ΔK210 mutation in hcTnT have been extensively analyzed using *in vitro*, *ex vivo,* and *in vivo* models (Morimoto et al., 2002; Robinson et al., 2002; Venkatraman et al., 2003; Mirza et al., 2005; Du et al., 2007; Robinson et al., 2007; Sfichi-Duke et al., 2010) whereas to the best of our knowledge, there is no functional study for the R130C mutation. A study of knock-in mice expressing $cTnT^{\Delta K210}$ showed that the decrease of calcium sensitivity was higher in homozygous than in heterozygous $cTnT^{\Delta K210}$ mice indicating that the calcium desensitization by this mutation increased with the relative amount of mutant protein (Du et al., 2007). The exchange efficiencies in this study of 44–48% are in a good range to mimic the typical co-expression of mutant

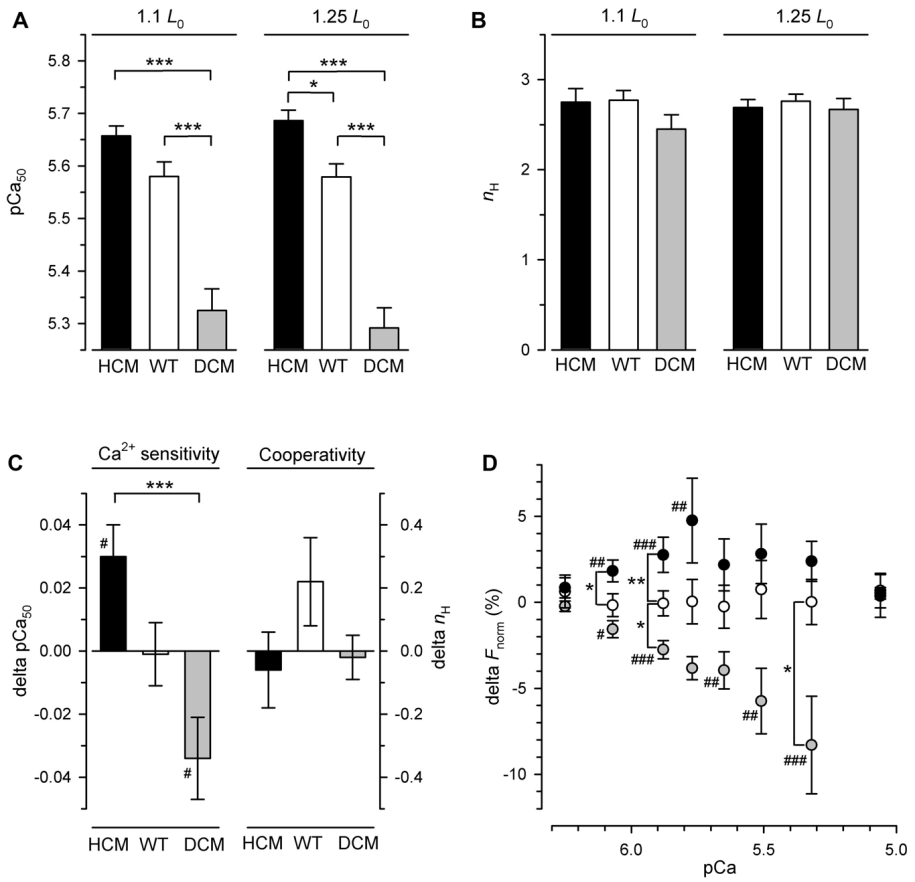

FIGURE 2 | Length-dependent parameters and parameter changes of calcium-dependent force generation of hcTn-exchanged skinned fibers. HCM: fibers containing $hcTnT^{R130C}$ (black circles and bars), WT: fibers containing $hcTnT^{WT}$ (white circles and bars), DCM: fibers containing $hcTnT^{\Delta K210}$ (gray circles and bars). **(A)** Calcium sensitivity is expressed by the pCa_{50} required for half-maximum increase of calcium-dependent force generation. **(B)** Cooperativity of calcium-dependent force generation is expressed by the Hill coefficient n_H of force-pCa relations. **(C)** Change of pCa_{50} and Hill coefficient n_H induced by lengthening the fiber from 1.1 L_0 to 1.25 L_0. **(D)** Change of normalized force at the respective pCa induced by lengthening the fiber from 1.1 L_0 to 1.25 L_0. Change (delta) of parameters in **(C,D)** are calculated by subtracting for each fiber the parameter value at 1.1 L_0 from the parameter value at 1.25 L_0. Significant change of parameter (delta different from zero) is indicated by $^{\#}P < 0.05$, $^{\#\#}P < 0.01$, $^{\#\#\#}(P < 0.001)$. Asterisks indicate significant differences $^{*}P < 0.05$, $^{**}P < 0.01$, $^{***}P < 0.001$ between the hcTnT-types in Tukey's multiple comparison post-tests. For sake of clarity, only the *P*-values for comparisons between mutants and wild type but not the ones comparing the two mutants were plotted in the subfigure **(D)** (for complete list of *P*-values see **Table 2**).

and wild type hcTnT protein in the heterozygous allelic patients albeit the relative amount of the expression of mutant protein in patients can substantially differ from the theoretical value of 50% (Tripathi et al., 2011). The significant lower calcium sensitivity in absence of significant differences of maximum force and cooperativity of calcium-dependent force generation of fibers containing $hcTnT^{\Delta K210}$ compared to $hcTnT^{WT}$ found in this study resemble the previously reported effects on these parameters found between fibers isolated from heterozygous $cTnT^{\Delta K210}$ knock-in and wild type mice (Du et al., 2007). Thus, the *in vitro* exchange of hcTn in cardiac fibers performed in this study qualitatively reproduces the basic functional phenotype found in the *ex vivo* fiber approach (Du et al., 2007). The suitability of the *in vitro* approach to mimic primary effects of mutations on calcium sensitivity together with their diverging basal effects on calcium sensitivity at short fiber length provides a promising starting point for studying their effects on LDA.

Limitations of the Present Study

An unexpected result in our study was the lack of lengthening-induced change of calcium sensitivity (delta-pCa_{50} = 0) and the low increase of F_{MAX} (+10%) in fibers exchanged with hcTn wild type. Most likely the exchange for the recombinant human cardiac troponin complex in the fibers does not restore the LDA of the native cTn. Low LDA might partly result from the dephosphorylated state of cTnI in recombinant cTn (Konhilas et al., 2003). However, previous studies examining effects of cTnT mutation on LDA by exchange of recombinant gcTn into guinea pig cardiac fibers reported delta-pCa_{50} values of +0.1 and increase of F_{MAX} by 62–65% after wild type exchange (Reda and Chandra, 2018, 2019). Reda and Chandra (2018, 2019) used recombinant cTn consisting of the guinea pig isoforms while we used recombinant cTn consisting of the human isoforms. Thus, the lacking length-dependent change of pCa_{50} and the low increase of F_{MAX} for the wild type control in our study might

result from the species-specific difference in the cTn. We chose the human isoforms because the aim of our study was to compare the effects of cTnT mutations related to human cardiomyopathy.

To the best of our knowledge, no functional study of the HCM-associated mutation hcTnT^{R130C} exists so far. We found no difference in calcium sensitivity compared to wild type at short fiber length for this mutation but significant higher calcium sensitivity at long fiber length. Thus, screening the effect of this mutation on calcium sensitivity under basal conditions only would have been negative because the calcium sensitization only became evident under stretch. However, this finding underlines the positive effect of this HCM mutation on LDA.

Finally, we choose rather simple protocol for working at same relative fiber length instead of measuring and adjusting sarcomere length prior activation. Slack length (L_0) were measured prior to hcTn exchange, and biomechanical parameters determined after hcTn exchange at 1.1- and 1.25-fold of that L_0 measured prior exchange. Therefore, all fibers should have similar sarcomere length at L_0 independent of the type of hcTnT. Furthermore, the three different types of hcTnT-exchanged fibers exhibited similar passive and maximum tension and therefore likely adopted similar sarcomere lengths before and during calcium activation in the mechanical experiments.

Effect of hcTnT Mutations on LDA

The primary aim of the study was to test if HCM and DCM-associated mutations in the human troponin complex exert different effects on the length dependence of mechanical parameters, in particular of calcium sensitivity reflecting LDA. As two-way RM ANOVA analysis indicated no difference in the effects of lengthening on resting and maximum tension for the three type of hcTnT, the HCM-associated R130C and the DCM-associated ΔK210 mutation seem not to alter the basal inhibitory and the maximum regulatory capacity of hcTn. Lengthening changed calcium sensitivity in opposite direction for the two mutations as indicated by the opposite signs of their 95% confidence intervals and the highly significant difference ($P < 0.001$) for their delta-pCa_{50}, indicating calcium sensitization by the HCM-associated and calcium desensitization by the DCM-associated mutation. LDA has been also associated to changes in the lattice spacing (McDonald and Moss, 1995; Fuchs and Smith, 2001) and lattice spacing depends on filament charge according to the Donnan potential (Millman and Irving, 1988). Since R130C and ΔK210 both lead to loss of a positive charge in hcTnT, their opposite effects on LDA cannot be explained by filament charge. Instead they likely reflect specific effects of the two sites, 130 and 210 on hcTnT, in the modulation of LDA.

Consistent with our finding of calcium desensitization by the DCM-associated ΔK210 mutation being augmented under stretch, the DCM-associated mutation R174W decreases calcium sensitivity and attenuates the sarcomere length-dependent increase of calcium sensitivity in guinea pig cardiac fibers (Reda and Chandra, 2019). Whether this applies for all DCM-associated mutations in hcTnT needs to be tested in future studies. In any case, it is definitive from previous studies that the mechanism does not apply for all HCM-associated mutations in thin filament proteins and that not all mutations increasing calcium sensitivity enhance LDA. The hypertrophic cardiomyopathy-associated mutation F87L in the central region of cTnT enhances calcium sensitivity but attenuates LDA (Reda and Chandra, 2018) and the RCM-associated mutation hcTnI^{R145W} does not affect LDA although it strongly increases calcium sensitivity (Dvornikov et al., 2016). Thus, modifications of different sites in cTn might exert either positive or negative effects on LDA. Probing the effects of further mutations in Tm and cTn subunits on LDA provides a promising approach to map protein domains involved in LDA for understanding how these proteins integrate the length and the calcium signal for modulating myocardial contraction.

Possible Contribution of LDA in the Diverging Phenotype of DCM and HCM

Several hypotheses have been formulated to explain the diverging heart phenotypes in HCM versus DCM manifesting from specific mutations within the same protein like cTnT: (1) mutations directly affecting calcium sensitivity (Robinson et al., 2002, 2007), (2) mutations affecting EC coupling or Ca^{2+} homeostasis (Tardiff et al., 2015; Crocini et al., 2016), and (3) mutations interfering with the effect of posttranslational modifications on calcium sensitivity (Sfichi-Duke et al., 2010; Memo et al., 2013; Messer et al., 2016). The systemic development of each of the two diseases in the human is even more complex and highly variable (Maron et al., 2012; Deranek et al., 2019). Studies of human samples revealed that hcTnI is hypo-phosphorylated in myocardial samples from HCM and DCM patients compared to control samples from donor hearts (Hamdani et al., 2008; Sequeira et al., 2013, 2015). It is known that phosphorylation of cTnI by PKA increases lengthening-induced calcium sensitization by increasing the delta-pCa (Konhilas et al., 2003). The lower phosphorylation of cTnI in human patients and animal models for cardiomyopathies compared to control samples could therefore complicate the elucidation of the direct effect of the mutation on LDA. For example, low phosphorylation of hcTnI in HCM-associated patients might reduce LDA and prevent detection of possible increase of LDA by the mutation itself. The simple approach of exchanging recombinant cTn in guinea pig cardiac fibers, like in previous (Mickelson and Chandra, 2017; Reda and Chandra, 2018, 2019) and this study does not include this complication. The direct comparison of HCM and DCM mutant hcTnT found in our study supports the hypothesis that if one excludes posttranslational modulation of myofilaments proteins, HCM- and DCM-associated mutations can increase and decrease LDA, respectively.

Although, our study is in agreement with previous functional studies of the ΔK210 mutation and the prevalent disposition of HCM mutations increasing and DCM mutations decreasing calcium sensitivity, the definite reasons why the ΔK210 mutation results in DCM and the R130C mutation in HCM remain elusive. While typical features of HCM are increased wall thickness, cardiomyocyte disarray, fibrosis and impaired diastolic filling, DCM is characterized by enlarged ventricles, reduced ventricular wall thickness to volume ratio and impaired systolic contraction, i.e., reduced ejection fraction (Garfinkel et al., 2018;

Deranek et al., 2019). An interesting hypothesis is that the primary, acute effects of mutations on LDA, in the long term, might contribute to the directionality of the diverging histological and morphological phenotypes of HCM and DCM. Chronically enhanced response to stretch could contribute to strain imbalance of cardiomyocytes, cardiomyocyte disarray and wall thickening in HCM, while impaired contractile response to stretch might lead to overstretched thin cardiomyocytes and enlarged ventricles in DCM. Certainly, the primary effects of the mutations on LDA found in this study are counteractive and not compensatory mechanisms for the primary diastolic dysfunction in HCM and systolic dysfunction in DCM. Regarding the finding that the Frank–Starling mechanism is also impaired in the late-stage heart failure (Schwinger et al., 1994), the effect of the DCM mutation on impairing LDA is expected to be detrimental.

DATA AVAILABILITY STATEMENT

The datasets generated for this study are available on request to the corresponding author.

ETHICS STATEMENT

Guinea pig were killed for subsequent removal of the heart according to the guidelines approved by the ethical committee of the Landesamt für Natur, Umwelt und Verbraucherschutz Nordrhein-Westfalen (LANUV NRW Leibnizstrasse 10 D-45659 Recklinghausen Germany).

AUTHOR CONTRIBUTIONS

MG performed the biomechanical and biochemical experiments and data analysis. AL-D instructed MG in the fiber preparation and the biomechanical experiments. SZ prepared the recombinant protein and instructed MG in the biochemical analysis. GP contributed to the clinical aspects of the discussion. RS designed the study, supervised the experiments, data analysis, and wrote the manuscript.

FUNDING

This work was supported by Köln Fortune (Faculty of Medicine, Cologne) to RS.

SUPPLEMENTARY MATERIAL

The Supplementary Material for this article can be found online at: https://www.frontiersin.org/articles/10.3389/fphys.2020.00516/full#supplementary-material

REFERENCES

Ait Mou, Y., Bollensdorff, C., Cazorla, O., Magdi, Y., and de Tombe, P. P. (2015). Exploring cardiac biophysical properties. *Glob. Cardiol. Sci. Pract.* 2015:10. doi: 10.5339/gcsp.2015.10

Ait-Mou, Y., Hsu, K., Farman, G. P., Kumar, M., Greaser, M. L., Irving, T. C., et al. (2016). Titin strain contributes to the Frank-Starling law of the heart by structural rearrangements of both thin- and thick-filament proteins. *Proc. Natl. Acad. Sci. U.S.A.* 113, 2306–2311. doi: 10.1073/pnas.1516732113

Arteaga, G. M., Palmiter, K. A., Leiden, J. M., and Solaro, R. J. (2000). Attenuation of length dependence of calcium activation in myofilaments of transgenic mouse hearts expressing slow skeletal troponin I. *J. Physiol.* 526(Pt 3), 541–549.

Crocini, C., Ferrantini, C., Scardigli, M., Coppini, R., Mazzoni, L., Lazzeri, E., et al. (2016). Novel insights on the relationship between T-tubular defects and contractile dysfunction in a mouse model of hypertrophic cardiomyopathy. *J. Mol. Cell. Cardiol.* 91, 42–51. doi: 10.1016/j.yjmcc.2015.12.013

de Tombe, P. P., Mateja, R. D., Tachampa, K., Ait Mou, Y., Farman, G. P., and Irving, T. C. (2010). Myofilament length dependent activation. *J. Mol. Cell. Cardiol.* 48, 851–858. doi: 10.1016/j.yjmcc.2009.12.017

Deranek, A. E., Klass, M. M., and Tardiff, J. C. (2019). Moving beyond simple answers to complex disorders in sarcomeric cardiomyopathies: the role of integrated systems. *Pflugers Arch.* 471, 661–671. doi: 10.1007/s00424-019-02269-0

Du, C.-K., Morimoto, S., Nishii, K., Minakami, R., Ohta, M., Tadano, N., et al. (2007). Knock-in mouse model of dilated cardiomyopathy caused by troponin mutation. *Circ. Res.* 101, 185–194.

Dvornikov, A. V., Smolin, N., Zhang, M., Martin, J. L., Robia, S. L., and de Tombe, P. P. (2016). Restrictive cardiomyopathy troponin I R145W mutation does not perturb myofilament length-dependent activation in human cardiac sarcomeres. *J. Biol. Chem.* 291, 21817–21828.

Farman, G. P., Gore, D., Allen, E., Schoenfelt, K., Irving, T. C., and de Tombe, P. P. (2011). Myosin head orientation: a structural determinant for the Frank-Starling relationship. *Am. J. Physiol. Heart Circ. Physiol.* 300, H2155–H2160. doi: 10.1152/ajpheart.01221.2010

Fuchs, F., and Smith, S. H. (2001). Calcium, cross-bridges, and the Frank-Starling relationship. *News Physiol. Sci.* 16, 5–10.

Garfinkel, A. C., Seidman, J. G., and Seidman, C. E. (2018). Genetic pathogenesis of hypertrophic and dilated cardiomyopathy. *Heart Fail. Clin.* 14, 139–146. doi: 10.1016/j.hfc.2017.12.004

Hamdani, N., Kooij, V., van Dijk, S., Merkus, D., Paulus, W. J., Remedios, C. D., et al. (2008). Sarcomeric dysfunction in heart failure. *Cardiovasc. Res.* 77, 649–658.

Hanft, L. M., Korte, F. S., and McDonald, K. S. (2008). Cardiac function and modulation of sarcomeric function by length. *Cardiovasc. Res.* 77, 627–636.

Kalyva, A., Parthenakis, F. I., Marketou, M. E., Kontaraki, J. E., and Vardas, P. E. (2014). Biochemical characterisation of Troponin C mutations causing hypertrophic and dilated cardiomyopathies. *J. Muscle Res. Cell Motil.* 35, 161–178. doi: 10.1007/s10974-014-9382-0

Kamisago, M., Sharma, S. D., DePalma, S. R., Solomon, S., Sharma, P., McDonough, B., et al. (2000). Mutations in sarcomere protein genes as a cause of dilated cardiomyopathy. *N. Engl. J. Med.* 343, 1688–1696.

Konhilas, J. P., Irving, T. C., Wolska, B. M., Jweied, E. E., Martin, A. F., Solaro, R. J., et al. (2003). Troponin I in the murine myocardium: influence on length-dependent activation and interfilament spacing. *J. Physiol.* 547, 951–961.

Korte, F. S., Feest, E. R., Razumova, M. V., Tu, A.-Y., and Regnier, M. (2012). Enhanced Ca^{2+} binding of cardiac troponin reduces sarcomere length dependence of contractile activation independently of strong crossbridges. *Am. J. Physiol. Heart Circ. Physiol.* 303, H863–H870. doi: 10.1152/ajpheart.00395.2012

Kruger, M., Pfitzer, G., and Stehle, R. (2003). Expression and purification of human cardiac troponin subunits and their functional incorporation into isolated cardiac mouse myofibrils. *J. Chromatogr. B Analyt. Technol. Biomed. Life Sci.* 786, 287–296.

Li, A. Y., Stevens, C. M., Liang, B., Rayani, K., Little, S., Davis, J., et al. (2013). Familial hypertrophic cardiomyopathy related cardiac troponin C L29Q mutation alters length-dependent activation and functional effects of phosphomimetic troponin I*. *PLoS One* 8:e79363. doi: 10.1371/journal.pone.0079363

Linke, W. A. (2018). Titin gene and protein functions in passive and active muscle. *Annu. Rev. Physiol.* 80, 389–411. doi: 10.1146/annurev-physiol-021317-121234

Lu, Q.-W., Morimoto, S., Harada, K., Du, C.-K., Takahashi-Yanaga, F., Miwa, Y., et al. (2003). Cardiac troponin T mutation R141W found in dilated cardiomyopathy stabilizes the troponin T-tropomyosin interaction and causes a Ca^{2+} desensitization. *J. Mol. Cell. Cardiol.* 35, 1421–1427.

Lu, Q.-W., Wu, X.-Y., and Morimoto, S. (2013). Inherited cardiomyopathies caused by troponin mutations. *J. Geriatr. Cardiol.* 10, 91–101. doi: 10.3969/j.issn.1671-5411.2013.01.014

Maron, B. J., Maron, M. S., and Semsarian, C. (2012). Genetics of hypertrophic cardiomyopathy after 20 years: clinical perspectives. *J. Am. Coll. Cardiol.* 60, 705–715. doi: 10.1016/j.jacc.2012.02.068

Marston, S., and Zamora, J. E. (2020). Troponin structure and function: a view of recent progress. *J. Muscle Res. Cell Motil.* 41, 71–89. doi: 10.1007/s10974-019-09513-1

Marston, S. B., and Hodgkinson, J. L. (2001). Cardiac and skeletal myopathies: can genotype explain phenotype? *J. Muscle Res. Cell Motil.* 22, 1–4.

McDonald, K. S., and Moss, R. L. (1995). Osmotic compression of single cardiac myocytes eliminates the reduction in Ca^{2+} sensitivity of tension at short sarcomere length. *Circ. Res.* 77, 199–205.

Memo, M., Leung, M.-C., Ward, D. G., dos Remedios, C., Morimoto, S., Zhang, L., et al. (2013). Familial dilated cardiomyopathy mutations uncouple troponin I phosphorylation from changes in myofibrillar Ca^{+} sensitivity. *Cardiovasc. Res.* 99, 65–73.

Messer, A. E., Bayliss, C. R., El-Mezgueldi, M., Redwood, C. S., Ward, D. G., Leung, M.-C., et al. (2016). Mutations in troponin T associated with Hypertrophic Cardiomyopathy increase Ca^{2+}-sensitivity and suppress the modulation of Ca^{2+}-sensitivity by troponin I phosphorylation. *Arch. Biochem. Biophys.* 601, 113–120.

Mickelson, A. V., and Chandra, M. (2017). Hypertrophic cardiomyopathy mutation in cardiac troponin T (R95H) attenuates length-dependent activation in guinea pig cardiac muscle fibers. *Am. J. Physiol. Heart Circ. Physiol.* 313, H1180–H1189. doi: 10.1152/ajpheart.00369.2017

Millman, B. M., and Irving, T. C. (1988). Filament lattice of frog striated muscle. Radial forces, lattice stability, and filament compression in the A-band of relaxed and rigor muscle. *Biophys. J.* 54, 437–447.

Mirza, M., Marston, S., Willott, R., Ashley, C., Mogensen, J., McKenna, W., et al. (2005). Dilated cardiomyopathy mutations in three thin filament regulatory proteins result in a common functional phenotype. *J. Biol. Chem.* 280, 28498–28506.

Morimoto, S., Lu, Q. W., Harada, K., Takahashi-Yanaga, F., Minakami, R., Ohta, M., et al. (2002). Ca^{2+}-desensitizing effect of a deletion mutation Delta K210 in cardiac troponin T that causes familial dilated cardiomyopathy. *Proc. Natl. Acad. Sci. U.S.A.* 99, 913–918.

Neulen, A., Blaudeck, N., Zittrich, S., Metzler, D., Pfitzer, G., and Stehle, R. (2007). Mn2+-dependent protein phosphatase 1 enhances protein kinase A-induced Ca^{2+} desensitisation in skinned murine myocardium. *Cardiovasc. Res.* 74, 124–132.

Reda, S. M., and Chandra, M. (2018). Cardiomyopathy mutation (F88L) in troponin T abolishes length dependency of myofilament Ca^{2+} sensitivity. *J. Gen. Physiol.* 150, 809–819. doi: 10.1085/jgp.201711974

Reda, S. M., and Chandra, M. (2019). Dilated cardiomyopathy mutation (R174W) in troponin T attenuates the length-mediated increase in crossbridge recruitment and myofilament Ca^{2+} sensitivity. *Am. J. Physiol. Heart Circ. Physiol.* 317, H648–H657. doi: 10.1152/ajpheart.00171.2019

Robinson, P., Griffiths, P. J., Watkins, H., and Redwood, C. S. (2007). Dilated and hypertrophic cardiomyopathy mutations in troponin and alpha-tropomyosin have opposing effects on the calcium affinity of cardiac thin filaments. *Circ. Res.* 101, 1266–1273.

Robinson, P., Mirza, M., Knott, A., Abdulrazzak, H., Willott, R., Marston, S., et al. (2002). Alterations in thin filament regulation induced by a human cardiac troponin T mutant that causes dilated cardiomyopathy are distinct from those induced by troponin T mutants that cause hypertrophic cardiomyopathy. *J. Biol. Chem.* 277, 40710–40716.

Schwinger, R. H., Bohm, M., Koch, A., Schmidt, U., Morano, I., Eissner, H. J., et al. (1994). The failing human heart is unable to use the Frank-Starling mechanism. *Circ. Res.* 74, 959–969.

Sequeira, V., Najafi, A., Wijnker, P. J. M., Dos Remedios, C. G., Michels, M., Kuster, D. W. D., et al. (2015). ADP-stimulated contraction: a predictor of thin-filament activation in cardiac disease. *Proc. Natl. Acad. Sci. U.S.A.* 112, E7003–E7012. doi: 10.1073/pnas.1513843112

Sequeira, V., Wijnker, P. J. M., Nijenkamp, L. L. A. M., Kuster, D. W. D., Najafi, A., Witjas-Paalberends, E. R., et al. (2013). Perturbed length-dependent activation in human hypertrophic cardiomyopathy with missense sarcomeric gene mutations. *Circ. Res.* 112, 1491–1505. doi: 10.1161/CIRCRESAHA.111.300436

Sfichi-Duke, L., Garcia-Cazarin, M. L., Sumandea, C. A., Sievert, G. A., Balke, C. W., Zhan, D.-Y., et al. (2010). Cardiomyopathy-causing deletion K210 in cardiac troponin T alters phosphorylation propensity of sarcomeric proteins. *J. Mol. Cell. Cardiol.* 48, 934–942. doi: 10.1016/j.yjmcc.2010.01.005

Solzin, J., Iorga, B., Sierakowski, E., Gomez Alcazar, D. P., Ruess, D. F., Kubacki, T., et al. (2007). Kinetic mechanism of the Ca^{2+}-dependent switch-on and switch-off of cardiac troponin in myofibrils. *Biophys. J.* 93, 3917–3931.

Song, L., Zou, Y., Wang, J., Wang, Z., Zhen, Y., Lou, K., et al. (2005). Mutations profile in Chinese patients with hypertrophic cardiomyopathy. *Clin. Chim. Acta* 351, 209–216.

Stehle, R., Kruger, M., Scherer, P., Brixius, K., Schwinger, R. H. G., and Pfitzer, G. (2002). Isometric force kinetics upon rapid activation and relaxation of mouse, guinea pig and human heart muscle studied on the subcellular myofibrillar level. *Basic Res. Cardiol.* 97(Suppl. 1), I127–I135.

Tardiff, J. C., Carrier, L., Bers, D. M., Poggesi, C., Ferrantini, C., Coppini, R., et al. (2015). Targets for therapy in sarcomeric cardiomyopathies. *Cardiovasc. Res.* 105, 457–470. doi: 10.1093/cvr/cvv023

Tripathi, S., Schultz, I., Becker, E., Montag, J., Borchert, B., Francino, A., et al. (2011). Unequal allelic expression of wild-type and mutated beta-myosin in familial hypertrophic cardiomyopathy. *Basic Res. Cardiol.* 106, 1041–1055. doi: 10.1007/s00395-011-0205-9

Venkatraman, G., Harada, K., Gomes, A. V., Kerrick, W. G. L., and Potter, J. D. (2003). Different functional properties of troponin T mutants that cause dilated cardiomyopathy. *J. Biol. Chem.* 278, 41670–41676.

Wang, S.-X., Zou, Y.-B., Fu, C.-Y., Song, L., Wang, H., Wang, J.-Z., et al. (2007). [Family hypertrophic cardiomyopathy caused by a 14035c > t mutation in cardiac troponin T gene]. *Zhonghua Yi Xue Za Zhi* 87, 371–374.

Willott, R. H., Gomes, A. V., Chang, A. N., Parvatiyar, M. S., Pinto, J. R., and Potter, J. D. (2010). Mutations in Troponin that cause HCM, DCM AND RCM: what can we learn about thin filament function? *J. Mol. Cell. Cardiol.* 48, 882–892. doi: 10.1016/j.yjmcc.2009.10.031

Zhang, X., Kampourakis, T., Yan, Z., Sevrieva, I., Irving, M., and Sun, Y.-B. (2017). Distinct contributions of the thin and thick filaments to length-dependent activation in heart muscle. *eLife* 6:e24081. doi: 10.7554/eLife.24081

Conflict of Interest: The authors declare that the research was conducted in the absence of any commercial or financial relationships that could be construed as a potential conflict of interest.

frontiers in Physiology

ORIGINAL RESEARCH
published: 09 June 2020
doi: 10.3389/fphys.2020.00467

Using Systolic Local Mechanical Load to Predict Fiber Orientation in Ventricles

Takumi Washio[1,2], Seiryo Sugiura[1], Jun-ichi Okada[1,2] and Toshiaki Hisada[1]*

[1] UT-Heart Inc., Kashiwanoha Campus Satellite, Kashiwa, Japan, [2] Future Center Initiative, Kashiwanoha Campus Satellite, University of Tokyo, Kashiwa, Japan

A simple rule adopted for myofiber reorientation in the ventricles is pursued by taking the microscopic branching network of myocytes into account. The macroscopic active tension generated on the microscopic branching structure is modeled by a multidirectional active stress tensor, which is defined as a function of the strains in the branching directions. In our reorientation algorithm, the principal direction of the branching network is updated so that it turns in the direction of greater active tension in the isovolumetric systole. Updates are performed step-by-step after the mechanical equilibrium has been attained with the current fiber structure. Starting from a nearly flat distribution of the principal fiber orientation along the circumferential direction, the reoriented fiber helix angles range from 70 to 40° at epicardium and from 60 to 80° at endocardium, in agreement with experimental observations. The helical ventricular myocardial band of Torrent-Guasp's model and the apical spiral structure of Rushmer's model are also reconstructed by our algorithm. Applying our algorithm to the infarcted ventricle model, the fiber structure near the infarcted site is remodeled so that the helix angle becomes steeper with respect to the circumferential direction near the epicardial surface. Based on our numerical analysis, we draw the following conclusions. (i) The multidirectional active tension based on the microscopic branching network is potentially used to seek tighter connection with neighboring aggregates. (ii) The thickening and thinning transitions in response to active tension in each myocyte allow the macroscopic principal fiber orientation of the microscopic branching network to move toward the direction of greater active tension. (iii) The force–velocity relationship is the key factor in transferring the fiber shortening strain to the magnitude of active tensions used in the myofiber reorientation. (iv) The algorithm naturally leads to homogeneity in the macroscopic active tension and the fiber shortening strain, and results in near-optimal pumping performance. (v) However, the reorientation mechanism may degrade the pumping performance if there is severely inhomogeneous contractility resulting from infarction. Our goal is to provide a tool to predict the fiber architecture of various heart disease patients for numerical simulations of their treatment plans.

Keywords: fiber orientation, ventricle, active stress, branching structure, mechanical load, remodeling, infarction

OPEN ACCESS

Edited by:
Henk Granzier,
The University of Arizona,
United States

Reviewed by:
Margaret Westfall,
University of Michigan, United States
Laurin Michelle Hanft,
University of Missouri, United States

****Correspondence:***
Takumi Washio
washio@ut-heart.com;
washio@sml.k.u-tokyo.ac.jp

Specialty section:
This article was submitted to Striated Muscle Physiology, a section of the journal Frontiers in Physiology

Received: *12 February 2020*
Accepted: *16 April 2020*
Published: *09 June 2020*

Citation:
Washio T, Sugiura S, Okada J and Hisada T (2020) Using Systolic Local Mechanical Load to Predict Fiber Orientation in Ventricles. Front. Physiol. 11:467. doi: 10.3389/fphys.2020.00467

INTRODUCTION

The distribution of fiber orientation in the ventricle wall is a key factor in determining the volume of blood ejected, local mechanical load, and energy consumption. Ideally, the fiber structure should maximize the ejection fraction while minimizing the mechanical load and energy consumption. However, such optimization is difficult to attain because of the complicated relationship between the active tension, energy consumption, and muscle deformation. In particular, the active tension is not determined by the strain alone, but also by the shortening velocity along the fiber orientation. Nevertheless, in our previous work (Washio et al., 2016) we showed that such optimization can be performed by sensing the multidirectional impulses in the microscopic branching myofibril structure during the systolic phase and shifting the center of the branches toward the direction of greatest impulse (**Figure 1**). Surprisingly, we found that this process constructed a realistic fiber structure of the left ventricle, starting from an almost flat distribution of fiber orientations along the circumferential direction. Furthermore, we saw that the distributions of active tension, sarcomere shortening velocity, and energy consumption were much more uniform than that of the artificial fiber structure with a linearly interpolated transmural helical fiber angle arrangement. The active tension decreases as the fiber shortening velocity increases (the force–velocity relationship, Hunter et al., 1998). Therefore, the strain and stress along the fiber orientation are strongly correlated. Our previous work suggests that the uniformity of the fiber shortening velocity could be naturally realized by examining the fiber structure in terms of the uniform active stress. In addition, the uniformity of the fiber active stress could be realized by using the microscopic branching fiber architecture. This macroscopic reorientation mechanism can be understood microscopically, as depicted in **Figure 1**. Under the force–velocity relationship in myofibrils, myocytes that are strongly pulled by their neighboring myocytes generate greater active tension, because they are shortened slower than other myocytes. If the myocytes that sense greater tension along their longitudinal direction become thicker, the principal fiber direction in the local aggregate can be reoriented to the new direction, strengthening the connections with the neighboring aggregates.

In this paper, to predict the fiber orientation in the ventricle, we propose a reorientation algorithm in which a simple active stress model that refers only to the strains in the multidirectional fibers around the principal fiber orientation is used instead of the sophisticated model that refers also to the fiber shortening velocities. In the simple model, the strains in the multidirectional fibers are referenced to compute the active stresses in the associated directions, and the obtained stresses are superposed to reproduce the macroscopic active stress on the branching network. Furthermore, the static equilibrium under isovolumetric condition is computed instead of the equilibrium in the whole dynamical systole. This contrasts with the sophisticated cross-bridge model used to compute dozens of heartbeats in our previous work. In the previous approach, the fiber structure was updated by referring to the active tension impulses in the branching directions after each heartbeat. Thus,

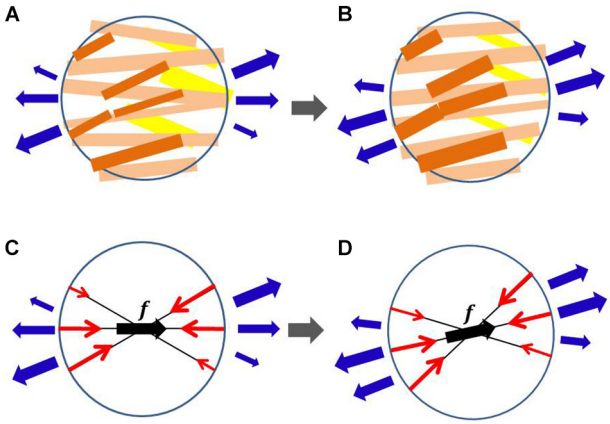

FIGURE 1 | Myofiber reorientation process in the microscopic branching network of myocytes **(A,B)** and the associated macroscopic representation by the multidirectional branching active stress **(C,D)**. The myocytes with greater active tension are colored dark orange, whereas those with smaller active tension are colored yellow in **(A,B)**. The macroscopic representations of the multidirectional active stresses are given in **(C,D)**, in which ***f*** denotes the principal fiber direction, and the length of the red arrows represents the aggregated magnitude of active tension in each direction. The external tensions imposed by the neighboring aggregates are represented by blue arrows. In the reorientation process, we assume that the myocytes that sense greater tension in **(A)** become thicker in **(B)** and those that sense smaller tension in **(A)** become thinner in **(B)**. The microscopic thickening and thinning process is macroscopically modeled so that the eccentricity of active tensions from the principal fiber direction is diminished. The changes in external tensions (blue arrows) from **(A,C)** to **(B,D)** represent the reorientation in neighboring aggregates.

dozens of heartbeats were needed to identify the final structure. In this study, we simulate only the isovolumetric contraction phase, and update the fiber structure step-by-step after finding the mechanical equilibrium for the updated fiber structure. Thus, the computational cost is considerably less than that of the previous approach. The reason for using the isovolumetric phase is that we can limit the range of overall fiber shortening strain because of the constraint on the cavity volume. Thus, the force–velocity relationship in the dynamic condition can be approximately simulated by a simple linear relationship between the active tension and the fiber shortening strain under small deformations in the static condition. This simplified active stress model highlights the essential factors involved in the myofiber reorientation mechanism.

Rijcken et al. (1997) showed that the physiological fiber helix angle can be predicted by minimizing the integrated variance of fiber stain at the beginning of the ejection stage. Their work was later extended to consider the whole ejection process (Rijcken et al., 1999). The design space of the fiber helix angle is limited to two parameters that characterize the linear function which approximates the transmural change in the fiber helix angle in the rotationally symmetric left ventricular model, whereas our reorientation process allows changes at each individual location in the three-dimensional biventricular model. Rijcken et al. considered an objective function given by integrating the variance of fiber strains, and optimized this function for three

parameters that characterize the fiber structure; in contrast, we do not have any specific objective function, instead using only local information about the mechanical loads. Kroon et al. (2009) hypothesized that myofibers adapt their local orientation to achieve minimal fiber–cross-fiber shear strain during the cardiac cycle, and proposed a simple reorientation process that uses only the local deformation gradient tensor to update the fiber orientation. Their idea is based on breaking and forming connections between the extra-cellular matrix and myofibers, whereas our method is based on the thickening and thinning of myocytes in the microscopic branching network. In this paper, we show that our reorientation process attains a physiologically reasonable fiber structure, even when starting from a nearly flat distribution of fiber orientation along the circumferential direction; such a large reorientation of helix angles was not tested by Kroon et al. (2009) or in subsequent studies (Pluijmert et al., 2012, 2017).

Regarding the possibility of personalized fiber structure modeling, a quite different approach was proposed by Lekadir et al. (2014) who used statistical data to predict the fiber structure. This takes inter-subject variability in the ventricular shape into account, and estimates the fiber orientation at each individual myocardial location. Because our algorithm allows any initial fiber orientation distribution, and also permits inhomogeneous contractility, it can be used to modify the fiber structure obtained by an existing prediction tool toward a more mechanically reasonable form.

MATERIALS AND METHODS

Active Stress of Multidirectional Fibers

We represent the configuration of the unloaded ventricle by Ω, and call this the reference configuration. The current position of the material point $\boldsymbol{X} \in \Omega$ is represented as $\boldsymbol{x} = \boldsymbol{x}(\boldsymbol{X})$ (see **Supplementary Material S1** for Mathematical notations and the derivation of active stress tensor). The local infinitesimal deformation from the reference configuration is represented by the deformation gradient tensor $\boldsymbol{F} = \partial \boldsymbol{x}/\partial \boldsymbol{X}$. The active stress along the fiber direction, represented by the unit vector $\boldsymbol{f}$ in the reference configuration, is given by the second Piola–Kirchhoff stress tensor as

$$\boldsymbol{S}_{act} = \frac{T_f}{||\boldsymbol{Ff}||}\boldsymbol{f} \otimes \boldsymbol{f}, \tag{1}$$

where T_f is the active tension (contraction force per unit area in the reference configuration). The above definition of the second Piola–Kirchhoff stress tensor means that the traction force $\boldsymbol{dt}$ in the current configuration acting on an area element $\boldsymbol{N}dA$ in the reference configuration, in which the normal vector $\boldsymbol{N}$ points outward from the area, is given as follows:

$$\boldsymbol{dt} = \boldsymbol{F}\boldsymbol{S}_{act}\boldsymbol{N}dA = T_f \frac{\boldsymbol{Ff}}{||\boldsymbol{Ff}||}(\boldsymbol{f} \cdot \boldsymbol{N})dA, \tag{2}$$

where $\frac{\boldsymbol{Ff}}{||\boldsymbol{Ff}||}$ is the unit vector directed along the fiber orientation direction in the current configuration and $(\boldsymbol{f} \cdot \boldsymbol{N})$ is proportional to the number of myofibrils that pass through the unit area perpendicular to $\boldsymbol{N}$. This interpretation justifies the definition of $\boldsymbol{S}_{act}$. Note that $\boldsymbol{S}_{act}\boldsymbol{N}dA$ itself represents $\boldsymbol{F}^{-1}\boldsymbol{dt}$ from the definition of the second Piola–Kirchhoff stress tensor.

To use the reorientation process based on the mechanical equilibrium condition in the steady state, we define the multidirectional active stress tensor $\boldsymbol{S}_{act,MD}$ of the branching fiber orientations $(\boldsymbol{f}_i)_{i=0}^n$ as

$$\boldsymbol{S}_{act,MD} = T_{ref} \sum_{i=0}^{n} \frac{w_i \Psi(\in_i)}{||\boldsymbol{Ff}_i||}\boldsymbol{f}_i \otimes \boldsymbol{f}_i, \tag{3}$$

where T_{ref} is the reference value of the active tension and w_i is the weight assigned to the i-th direction. A value of T_{ref} = 40 kPa was adopted in our numerical experiments. In our pervious simulation work of beating ventricle (Washio et al., 2016) the active tension raised approximately up to 80 kPa. Therefore, we took the averaged value of active tension. The feedback from the deformation to the active stress is given by $\Psi(\in_i)$, which is a function of the contraction ratio from the end diastolic configuration given by

$$\in_i = 1 - \frac{||\boldsymbol{Ff}_i||}{||\boldsymbol{F}_{ED}\boldsymbol{f}_i||}, i = 0, \ldots, n, \tag{4}$$

where $\boldsymbol{F}_{ED}$ is the deformation gradient tensor at the end diastole. Ψ is defined such that the active tension decreases linearly to zero until the contraction ratio $\in_i$ reaches $\in_Z$, i.e.,

$$\Psi(\in_i) = \begin{cases} 1, & \in_i < 0 \\ 1 - \in_i / \in_Z, & 0 \leq \in_i \leq \in_Z \\ 0, & \in_i > \in_Z \end{cases} \tag{5}$$

In the numerical experiments, $\in_Z$ was set to 0.1 unless specified. As $\in_Z$ becomes smaller, the sensitivity of the stress to the strain increases. The function Ψ is defined so that it approximates the force–velocity relationship under the dynamic condition by the stress–strain relationship under the static condition. We do not focus on the actual magnitude of force and velocity, but rather the response of the force to small changes in velocity. Later, the validity of the simplification from the dynamic condition to the static condition will be confirmed by the insensitivity of the reoriented fiber structures to the parameters T_{ref} and $\in_Z$. Ψ is set to be one in the case of stretching ($\in_i < 0$) because the increase of active stress due to stretching may mislead the reorientation.

The branching fiber orientations are based on the orthonormal frame $\{\boldsymbol{f},\boldsymbol{s},\boldsymbol{n}\}$ as follows:

$$\boldsymbol{f}_0 = \boldsymbol{f}, \tag{6}$$

$$\boldsymbol{f}_i = \cos\theta \boldsymbol{f} + \sin\theta \left(\cos\frac{2\pi(i-1)}{n}\boldsymbol{s} + \sin\frac{2\pi(i-1)}{n}\boldsymbol{n} \right), \tag{7}$$

where $\boldsymbol{s}$ is the sheet orientation vector, which usually indicates the laminar plane together with the principal fiber orientation $\boldsymbol{f}$. However, the orientation of $\boldsymbol{s}$ is not essential in this study, because the sheet direction is only used to determine the branching directions in Eq. (7). The parameter θ is associated

with the dispersion degree of the branching structure. In the numerical experiments, the branching angle θ was set to 45° unless specified, and the weights $\{w_i\}$ were determined for the principal orientation as $w_0 = 1/2$ and for the eight peripheral orientations as $w_i = 1/16 (1 \leq i \leq 8)$. Note that these parameters do not necessarily reflect the physiological microscopic structure of the branching network, because our purpose is not to predict the pumping performance, but to predict the fiber structure. As we will see in the numerical experiments, the parameters have little effect on the obtained fiber structure.

Mechanical Equilibrium Condition

In the proposed method, the fiber structure is updated under the mechanical equilibrium in the isovolumetric contraction phase. The equilibrium equation is represented as follows:

$$\int_\Omega \delta \boldsymbol{E} : (\boldsymbol{S}_{act,MD} + \boldsymbol{S}_{pas} + 2pJ\boldsymbol{I}) d\Omega$$

$$= P_L \int_{\Gamma L} \delta \boldsymbol{u} \cdot \boldsymbol{n}_\Gamma \cdot d\Gamma_L + P_R \int_{\Gamma R} \delta \boldsymbol{u} \cdot \boldsymbol{n}_\Gamma \cdot d\Gamma_R, \quad (8)$$

$$\int_\Omega \delta p \left(2(J-1) - \frac{p}{k} \right) d\Omega = 0, \quad (9)$$

$$\begin{cases} V_L = V_{L,ED} \\ V_R = V_{R,ED} \end{cases}, \quad (10)$$

where $\boldsymbol{u} = \boldsymbol{u}(\boldsymbol{X}) = \boldsymbol{x}(\boldsymbol{X}) - \boldsymbol{X}$ is the displacement of material point $\boldsymbol{X} \in \Omega$, $\boldsymbol{E} = \frac{1}{2}(\boldsymbol{F}^T\boldsymbol{F} - \boldsymbol{I})$ is the Green–Lagrange strain tensor, $J = \det \boldsymbol{F}$ is the Jacobian, p is the hydrostatic pressure, k = 200 kPa is the bulk modulus, and P_L and P_R are the blood pressures in the left and right ventricles, respectively. Γ_L and Γ_R are the intracavity boundaries of the left and right ventricles, respectively, in the current configuration, and n_Γ is the outward normal unit vector from these surfaces. The Dirichlet boundary condition $\boldsymbol{u(X)} = 0$ is imposed on the boundary nodes around the valve rings. The last condition is the isovolumetric constraint, in which $V_{L,ED}$ and $V_{R,ED}$ are the cavity volumes, respectively, of the left and right ventricles at the end diastole. $\boldsymbol{S}_{pas}$ is the passive second Piola–Kirchhoff stress tensor, defined from the deformation potential W as

$$\boldsymbol{S}_{pas} = \frac{\partial W}{\partial \boldsymbol{E}} \quad (11)$$

In this study, the deformation potential W is given by

$$W = c_1(\tilde{I}_1 - 3) + c_2 \frac{\exp(q_2 \boldsymbol{E} : \boldsymbol{E}) - 1}{2} \quad (12)$$

Here, $\tilde{I}_1$ is the reduced invariant, defined as

$$\tilde{I}_1 = \det(\boldsymbol{C})^{-\frac{1}{3}} Tr(\boldsymbol{C}) \quad (13)$$

with the right Cauchy–Green deformation tensor $\boldsymbol{C} = \boldsymbol{F}^T\boldsymbol{F}$. We set c_1 = 25 Pa, c_2 = 800 Pa, and q_2 = 4. Applying the second term alone is unstable for small deformations, and so the first term was added. Because our focus is the impact of the fiber structure on the active stress, we did not introduce the anisotropy in the passive deformation energy caused by the fiber–laminar structure, which is specified by the distribution of fiber-sheet vectors (Usyk et al., 2000).

Myofiber Reorientation Algorithm

Given the initial frame distribution $\{\boldsymbol{f},\boldsymbol{s},\boldsymbol{n}\}$, the internal left and right ventricle cavity pressures are linearly increased up to the prescribed end diastolic pressures $P_{L,ED}$ and $P_{R,ED}$, respectively. In our simulations, values of $P_{L,ED}$ = 12 mmHg and $P_{R,ED}$ = 4 mmHg were adopted. During the expansion process of the cavity volumes, the active stress tensor is set to zero. Once the mechanical equilibrium at the end diastole has been established, the stretching along the branching directions $||\boldsymbol{F}_{ED}\boldsymbol{f}_i||$ is recorded for all elements in the ventricle. The mechanical equilibrium is then computed in the isovolumetric contraction phase, where the reference value T_{ref} of active stress is gradually increased to the prescribed reference value. During this process, the cavity volumes of the left and right ventricles are constrained to the end diastolic volumes, $V_{L,ED}$ and $V_{R,ED}$, respectively. Once the mechanical equilibrium has been attained with the prescribed reference value T_{ref}, the reorientation process starts. In this process, the frames $\{\boldsymbol{f},\boldsymbol{s},\boldsymbol{n}\}$ of all elements are updated by the following procedure. First, the candidate new principal direction $\boldsymbol{e} = \tilde{\boldsymbol{e}}/||\tilde{\boldsymbol{e}}||$ of the multidirectional active tensor $\boldsymbol{S}_{act,MD}$ in Eq. (3) is computed by summing the weighted vectors:

$$\tilde{\boldsymbol{e}} = \sum_{i=0}^{n} w_i \Psi(\in_i) \boldsymbol{f}_i. \quad (14)$$

The angle $\tilde{\eta}$ between the principal fiber orientation vector $\boldsymbol{f}$ and the vector $\boldsymbol{e}$ is then computed as

$$\cos \tilde{\eta} = \boldsymbol{f} \cdot \boldsymbol{e}. \quad (15)$$

As the rotation angle from $\boldsymbol{f}$ to $\boldsymbol{e}$ in determining the new fiber orientation, a small angle is taken by multiplying the weight ω by $\tilde{\eta}$:

$$\eta = \omega \tilde{\eta}, \quad (16)$$

because the application of $\tilde{\eta}$ itself to the rotation of the frame $\{\boldsymbol{f},\boldsymbol{s},\boldsymbol{n}\}$ may cause the Newton iterations to break down while computing the mechanical equilibrium after updating the frame. In this study, a value of $\omega = 0.05$ was adopted. The axis of rotation $\boldsymbol{r}_f$ is determined so that it is perpendicular to $\boldsymbol{f}$ and $\boldsymbol{e}$. Namely, the unit vector $\boldsymbol{g} = \tilde{\boldsymbol{g}}/||\tilde{\boldsymbol{g}}||$ is computed from $\tilde{\boldsymbol{g}} = \boldsymbol{e} - (\boldsymbol{e} \cdot \boldsymbol{f})\boldsymbol{f}$, and then the axis is computed from $\boldsymbol{r}_f = \boldsymbol{f} \times \boldsymbol{g}$. The rotation $\boldsymbol{R}(\eta)$, represented as

$$\boldsymbol{R}(\eta) = \begin{bmatrix} \cos\eta & -\sin\eta & 0 \\ \sin\eta & \cos\eta & 0 \\ 0 & 0 & 1 \end{bmatrix}, \quad (17)$$

with respect to the orthonormal basis $\{\boldsymbol{f},\boldsymbol{g},\boldsymbol{r}_f\}$ is applied to update each basis in the frame $\{\boldsymbol{f},\boldsymbol{s},\boldsymbol{n}\}$. After updating the frame, the stretch ratios along the branching directions $\{||\boldsymbol{F}_{ED}\boldsymbol{f}_i||\}$ in Eq. (4) are recomputed for the end diastolic deformation. The mechanical equilibrium is computed again for the next update.

It is not clear whether there is a stationary fiber structure in this reorientation process. Though we expect a monotonic increase in the intracavitary pressures P_L and P_R, it is possible that they could decrease during the reorientation process. To avoid such a case, we also introduce a modified reorientation process that is insensitive to small eccentricity in the vector $\tilde{\boldsymbol{e}}$ in Eq. (14). Namely, we introduce a threshold value $\tilde{\eta}_T$, and do not update the frame if the following condition is satisfied:

$$\tilde{\eta} \leq \tilde{\eta}_T. \tag{18}$$

Using this strategy to ensure insensitivity to small eccentricity, we could expect the evolution of the fiber structure to stop at some point. In the numerical experiments, this insensitivity mechanism was applied with the threshold $\tilde{\eta}_T = 1^\circ$ unless otherwise specified.

Finite Element Ventricular Model and Computation Resource

In the finite element modeling, the ventricular walls were discretized with 45,000 tetrahedral elements, where the

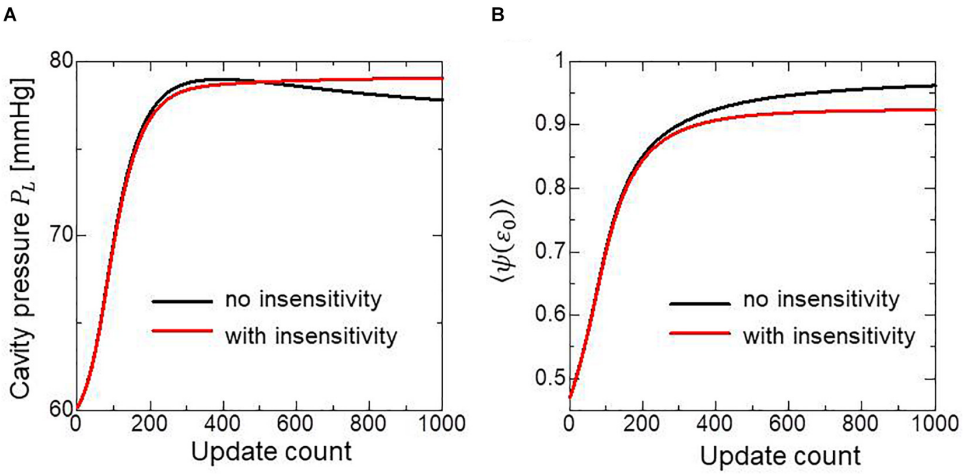

FIGURE 2 | Changes in the left ventricular intracavitary pressure **(A)** and the averaged active stress factors in the principal fiber direction **(B)** during the reorientation process with (red lines) and without (black lines) the insensitivity mechanism. When the insensitivity mechanism was not adopted, the intracavitary pressure gently decreased after reaching the maximum (**A:** black line), though the active stress factor monotonically increased (**B:** black line).

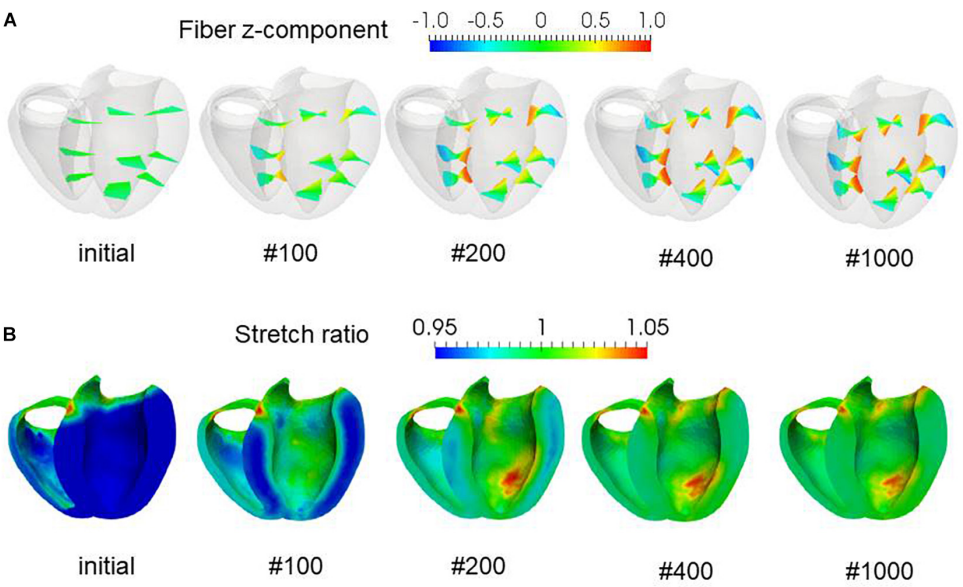

FIGURE 3 | Evolution of fiber helix angles **(A)** and stretch ratio from the end diastolic configuration **(B)** during the reorientation process. The fiber helix angles are shown for the anteroseptal, anterior, and anterolateral zones in **(A)**. The colors indicate the z (longitudinal direction) component of the fiber orientation vector ***f***. The distribution of stretch ratio in the principal fiber direction ($1-\epsilon_0$) on the infero-endocardial surface and the septal and lateral cross-sections are shown in **(B)**. The numbers below each figure indicate the number of updates. The fiber structure remained stationary after 400 updates.

MINI(5/4c) element (Brezzi and Fortin, 1991) was adopted to avoid the instability caused by the nearly incompressible condition in Eq. (9). Though the higher-order interpolation of MINI elements was applied to the displacement $\boldsymbol{u}$ to evaluate the integration associated with the passive stress tensor, standard linear interpolation ignoring the central node was adopted for the active stress. Thus, it was sufficient to assign one basis $\{\boldsymbol{f},\boldsymbol{s},\boldsymbol{n}\}$ for each element. Therefore, reorientation based on Eq. (14) was performed by referencing the contraction ratio $\in_i$, which was computed at the central integration point of each tetrahedral element. The computations were performed using a parallel computer system (Intel Xeon E-2670 [2.6 GHz], 16 cores; Intel, Santa Clara, CA, United States) with a computation time of 14 s for a single update.

RESULTS

Evolution of Fiber Structure From a Nearly No-Twisting Structure

To examine the effectiveness of the reorientation process, we set the initial configuration of the principal unit vector distribution $\{\boldsymbol{f}\}$ of the left ventricle to be nearly circumferential by interpolating the fiber helix angle linearly according to the transmural depth from −10° at the epicardium to +10° at the endocardium. Such a small twisting in the transmural direction, leaning a little to the physiological fiber structure (−60°at the epicardium to +60° at the endocardium), was assigned to prevent the reorientation process from heading toward the opposite twisting structure (+60° at the epicardium to −60° at the endocardium). The sheet vector distribution $\{\boldsymbol{s}\}$ was set to be perpendicular to the tangential plane at the nearest point on the epicardial surface. The left ventricular intracavitary pressure monotonically increased until it reached a stationary value under the insensitivity mechanism, whereas a gradual decline was observed in the case of the reorientation without the insensitivity mechanism (**Figure 2A**). Remarkably, the averaged value of $\Psi(\in_0)$ (Eq. 5) increased monotonically throughout the iterative process, even in the latter case (**Figure 2B**). Namely, without the insensitivity mechanism, the reduction in cavity pressure was accompanied by an increase in the averaged active stress. This suggests that maximizing the local stress does not necessarily maximize the intracavitary pressure. The evolution of the fiber helix angle (**Figure 3A**) shows that the reorientation process

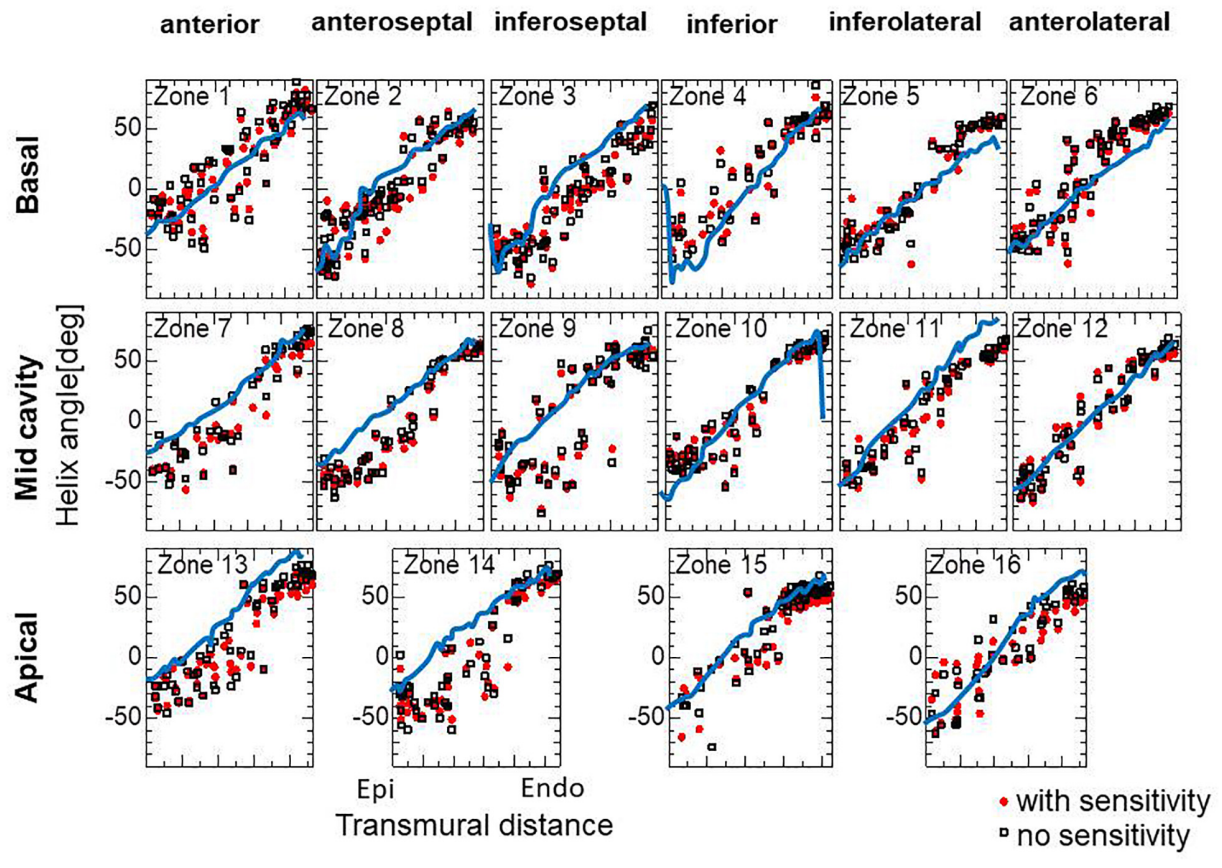

FIGURE 4 | Transmural helical angle arrangement of the optimized fiber structure in American Heart Association segments (The zones 1–16 are shown in **Supplementary Material S2**). The red dots and black squares were obtained by the reorientation processes with and without the insensitivity mechanism, respectively, and the blue lines were digitized from the diffusion tensor magnetic resonance imaging study reported by Lombaert et al. (2012), which averaged the data obtained from 10 healthy human hearts.

effectively stops after the fiber strain has been homogenized (**Figure 3B**). A detailed comparison of the fiber helix angle with experimental data obtained by a diffusion tensor magnetic resonance imaging study (Lombaert et al., 2012) shows good agreement with the fiber structure of real healthy human ventricles (**Figure 4**). Note that the helix angles were evaluated with respect to the end diastolic configuration.

Influence of Inhomogeneity in the Contractility

To examine whether the proposed approach can predict the remodeling after infarction, we applied our reorientation algorithm to the finite element ventricular model with degenerated active stress in specific regions. In this simulation, we started the reorientation from the fiber structure that had been optimized by the procedure described in the previous section to simulate the remodeling from the healthy condition. The region of infarction was as shown in **Figure 5A**, assuming left anterior descending artery stenosis. In the infarcted region, the reference active tension T_{ref} was reduced to 10% of the healthy remaining part. In the reorientation process, the left ventricular intracavitary pressure P_L decreases, though the homogeneity of strain is improved (**Figure 5B**). Near the infarction boundary in the anterior healthy region, the helix angles at the epicardium become sharper, whereas they become gentler at the endocardium (**Figures 5C–F**). In particular, the fiber integral curves run along the boundary of the infarction, as observed by Sosnovik et al. (2009). In **Figure 6**, the fiber helix angles are plotted along with those of the initial fiber structure. The distributions have shifted downward slightly at the inferoseptal (Zones 3, 9, and 14) and anterolateral walls (Zones 6, 12, and 16), but are unchanged in the anterior (Zones 1, 7, and 13), which is remote from the site of infarction. This agrees well with the results of experimental studies by Wu et al. (2007, 2011).

Sensitivity Analysis

The choice of branching angle θ appears to be essential. In our experience, taking a value of around 45° gives optimal performance. A smaller branching angle enlarged the deviation in helix angle around the middle layer, and made the helix angle at the endocardium slightly smaller, whereas a larger angle diminished the sensitivity to eccentricity in the active tension (**Figure 7A**). Regarding the choice of the parameter $\in_Z$ in defining the gradient in the stress–strain relationship (Eq. 5), the adoption of a higher value again diminished the sensitivity to eccentricity in the active tension (**Figure 7B**). In terms of the

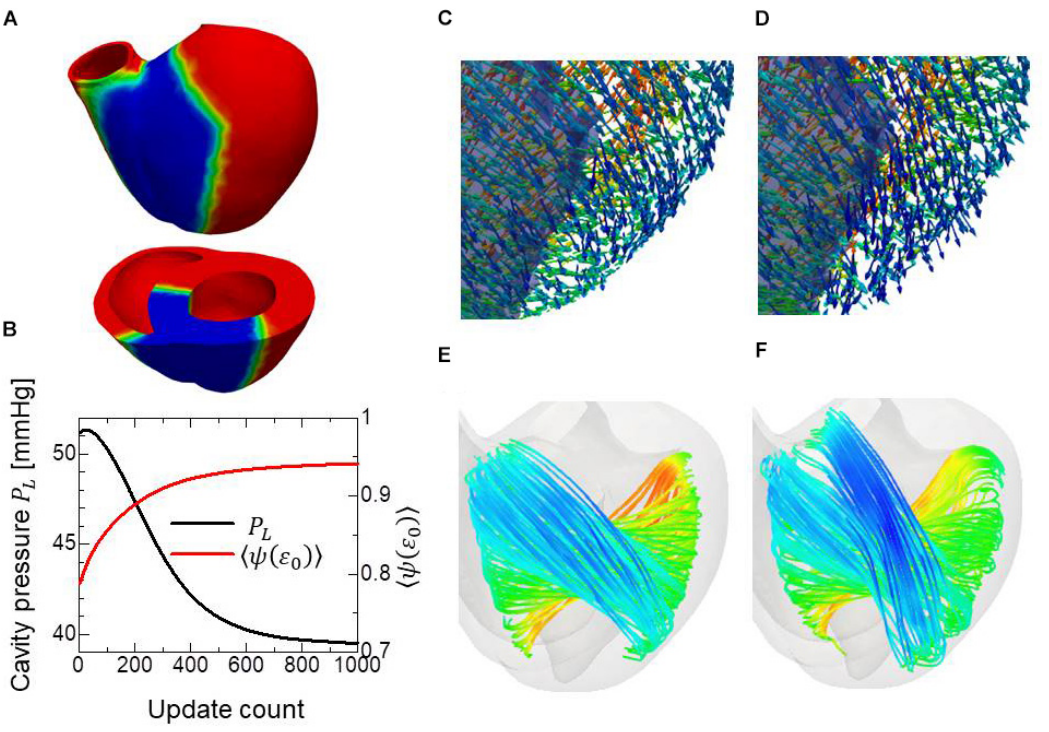

FIGURE 5 | Remodeling of the infarcted ventricle. The remodeling process started from the optimized fiber structure with homogeneous contractility. The region colored blue is the site of infarction, where only 10% of contractility compared to the healthy part was assumed **(A)**. Changes in the left ventricular intracavitary pressure (black line) and the averaged active tension factor (red line) during the remodeling process **(B)**. The distribution of the principal fiber direction ***f*** in the apical anterior region is shown before the remodeling process **(C)** and after the remodeling process with 1000 updates. The infarcted region is shaded **(D)**. The stream lines of the principal fiber direction are shown before the remodeling process **(E)** and after the remodeling process with 1000 updates **(F)**. Here, the colors on the curves indicate the z-component (longitudinal direction) of the principal fiber direction ***f***. The streamlines were constructed by the software PARAVIEW, where the Runge–Kutta 4–5 integrator was adopted.

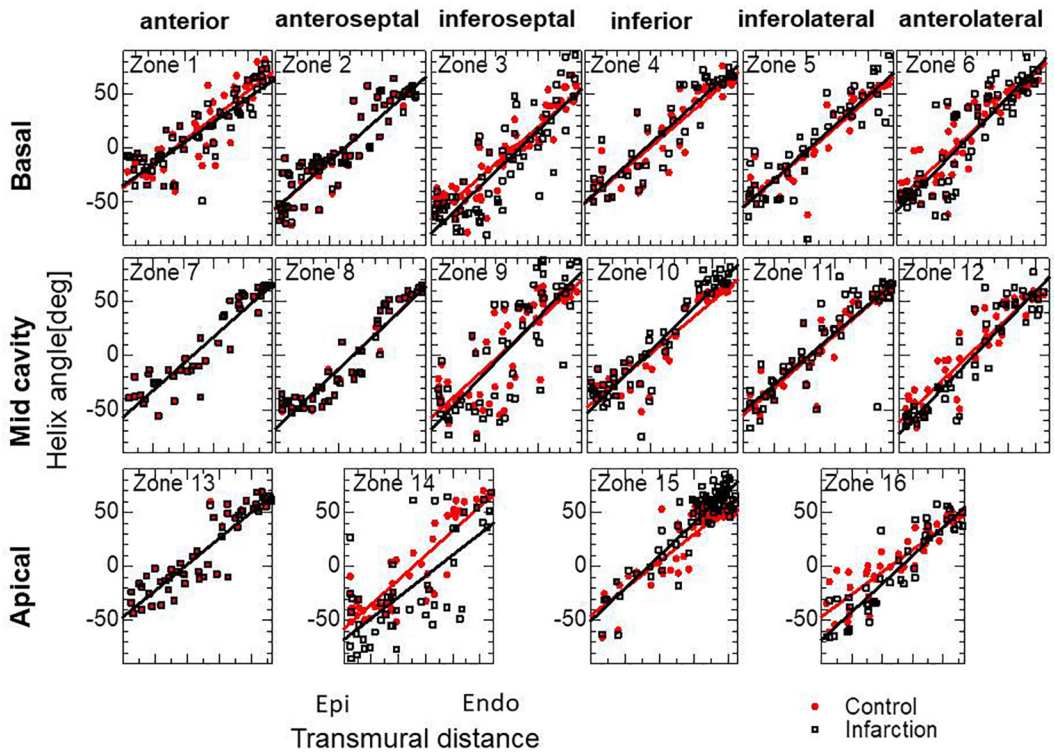

FIGURE 6 | Transmural helical angle arrangement of the optimized fiber structure of the infarcted ventricle model. The black squares dots were obtained by the remodeling processes for the infarcted ventricle model. The red dots indicate the initial arrangement obtained by the optimization for the standard ventricle model. The lines indicate the least-squares approximation of dots with the linear functions.

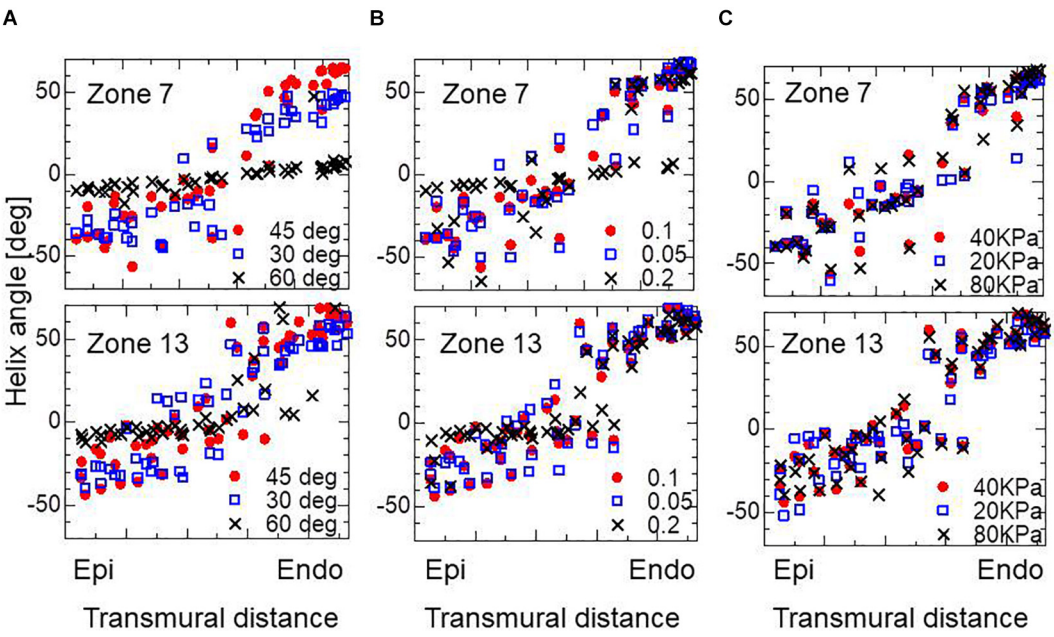

FIGURE 7 | Impacts on the transmural helical angle arrangement of the optimized fiber structure of the variation of dispersion degree of the branching structure θ = 30, 45, and 60° **(A)**, the gradient ϵ_Z = 0.1, 0.05, and 0.2 in defining the stress–strain relationship in the active tension factor **(B)**, and the reference value of the active tension T_{ref} = 20, 40, and 80 kPa **(C)**. The plots for Zone 7: mid cavity-anterior and Zone 13: apical-anterior are shown.

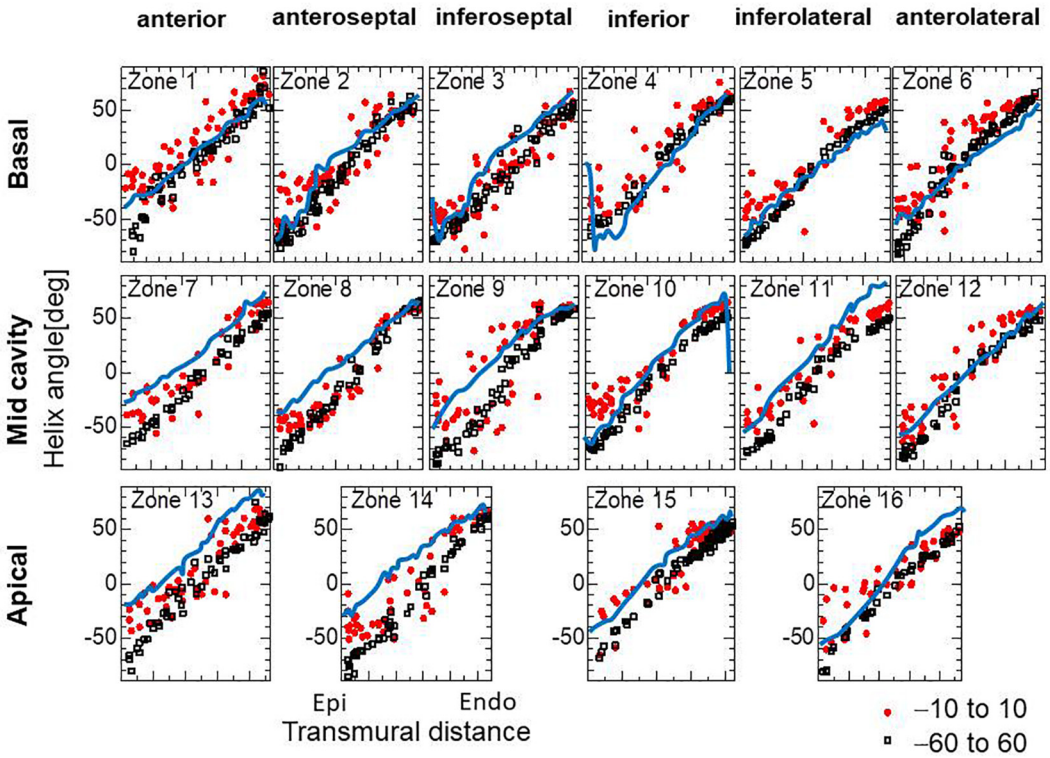

FIGURE 8 | Helical angle arrangement of the optimized fiber structure in American Heart Association segments. The red dots and black squares were obtained by the reorientation processes (1000 updates) starting from the linear transmural distribution from –10° (Epi) to 10° (Endo), and from –60° (Epi) to 60° (Endo), respectively, and the blue lines were digitized from the diffusion tensor magnetic resonance imaging study reported by Lombaert et al. (2012), which averaged the data obtained from 10 healthy human hearts.

magnitude of active stress, the impact of the reference value T_{ref} (Eq. 3) on the optimized fiber structure was small (**Figure 7C**).

For the practical use of our approach, it seems more efficient to start the reorientation process from the standard twisting fiber structure. In **Figure 8**, the optimized fiber structure obtained after 1000 updates starting from an artificial standard structure (linear transmural change from −60° [Epi] to 60° [Endo]) is compared with that starting from a flat distribution (linear transmural change from −10° [Epi] to 10° [Endo]). The resulting structures appear, on average, quite similar for the mid and endocardium layers, although the deviations in the former distributions are much smaller than in the latter. Though the transmural twisting was not markedly different before and after the optimization (**Figure 9A**), the inhomogeneity of the strain was considerably improved (**Figure 9B**).

Reconstruction of Helical Ventricular Myocardial Band

Remarkably, our reorientation process was able to construct the helical ventricular myocardial band running from the apical epicardium to the basal epicardium via the septal endocardium (**Figure 10A**), as found by Torrent-Guasp (Buckberg et al., 2008). Such stream lines cannot be generated from artificial fiber direction vectors that run perpendicular to the transmural direction everywhere. The spiral structure at the apex (Rushmer et al., 1953; Grant, 1965; Buckberg, 2002) was also accurately reproduced by our reorientation algorithm (**Figure 10B**). The success of our numerical model in reconstructing these sophisticated structures further validates the applicability of our simple rule in real physiological tissue.

Pumping Performance

We applied the artificial standard fiber structure (linear transmural change from −60° [Epi] to 60° [Endo]) and the resulting optimized fiber structure to the beating simulation code used in our previous work (Washio et al., 2016). The aim was to confirm that the optimized fiber structure with the simple active stress model in the isovolumetric contraction phase is effective for the whole beating simulation with a physiologically realistic cross-bridge model. In this simulation, the same parameter set of passive material properties as in the reorientation process was applied to eliminate the effect of the laminar structure determined by the sheet direction vector $\boldsymbol{s}$, and the single-directional active stress (Eq. 1) was adopted with the active tension T_f computed by 32 filament pairs in the cross-bridge model for each element. The heart rate was set to 60 beats per minute, and the Ca^{2+}-transient generated by the midmyocardial cell model proposed by ten Tusscher and Panfilov (2006) was applied. We used transmural delays determined by the distances from the endocardial surfaces of the left and right

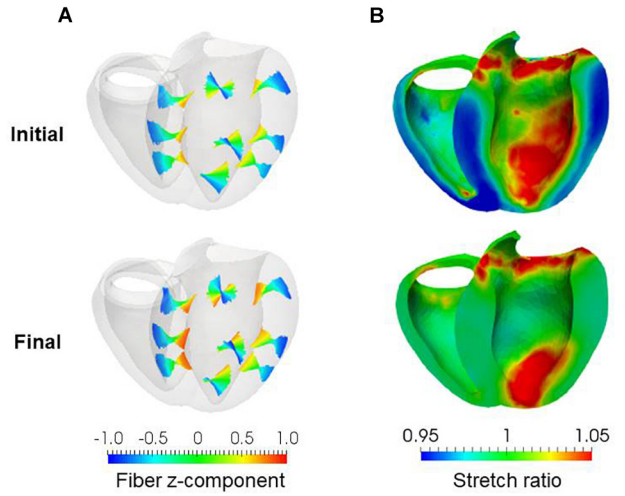

FIGURE 9 | Results of reorientation starting from the linear distribution of fiber helix angle from –60° (Epi) to 60° (Endo). The fiber helix angles are shown for the anteroseptal, anterior, and anterolateral zones in **(A)**. The colors indicate the z (longitudinal direction) component of the fiber orientation vector ***f***. The distribution of stretch ratio in the principal fiber direction ($1-\epsilon_0$) on the infero-endocardial surface and the septal and lateral cross-sections are shown in **(B)**. The upper figures show them for the initial fiber structure, and the lower figures show them for the final structure obtained after 1000 updates.

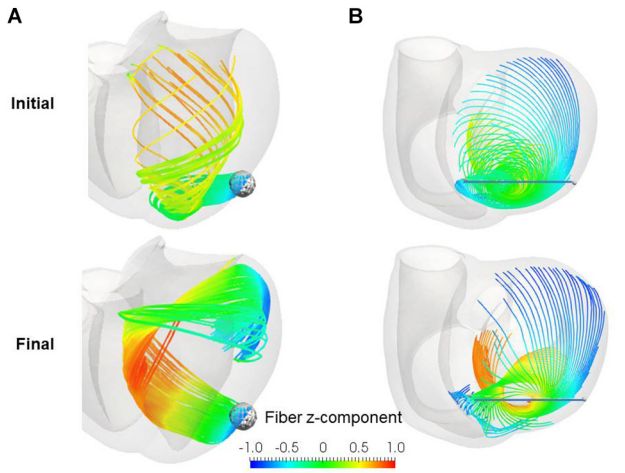

FIGURE 10 | Stream lines before (upper) and after (lower) the reorientation starting from the linear distribution of fiber helix angle from –60° (Epi) to 60° (Endo). **(A)** Stream lines integrated along the principal fiber direction ***f*** from the ball placed at the epicardial apical anterolateral portion. **(B)** Stream lines integrated from the points distributed on the line running through the apex. The colors indicate the z (longitudinal direction) component of the fiber orientation vector ***f***. The streamlines were constructed by the software PARAVIEW, where the Runge–Kutta 4–5 integrator was adopted.

ventricles under a transmural condition velocity of 52 cm/s, as measured by Taggart et al. (2000).

Comparisons of the pumping performance show considerable improvements in the blood ejection [65 vs. 58 ml], rise of blood pressure (122 vs. 115 mmHg) (**Figure 11A**), and amount of work (1.00 vs. 0.85 J) (**Figure 11B**) under our reorientation process, which was applied using the simple active stress model in the isovolumetric phase. In comparing the active tension distribution (**Figure 11C**), the homogenization effects produced by the reorientation mechanism are clearly apparent in both the isovolumetric phase and the blood ejection phase. The correlation in the contours between the active tension (**Figure 11C**) and the fiber shortening velocity (**Figure 11D**) indicates the impact of the force–velocity relationship on the contractility. Namely, the active tension is small where the fiber shortening velocity is high.

Computational Efficiency

Because the mechanical equilibrium must be attained for the highly non-linear finite element problem, the reorientation process should be performed carefully to avoid the Newton iterations breaking down. This is the reason for the factor $\omega = 0.05$ in Eq. (16) when modifying the rotation angle $\tilde{\eta}$ to the angle η between ***f*** and ***e***. For practical use in the personalized modeling of fiber structure, it is preferable to reduce the number of updates required to obtain the final structure by using a larger value of ω. Here, we examine whether we can improve the computational efficiency by applying a smaller reference value of the active tension T_{ref} without degrading the quality of the obtained fiber structure. To maintain computational stability with a larger coefficient value of $\omega = 0.2$, we reduced the reference value T_{ref} from 40 to 10 kPa (Eq. 3). Because this reduces the strain, we also decreased $\in_Z$ from 0.1 to 0.05 to increase the sensitivity of stress to strain. As shown in **Figures 12A,B**, the convergence was accelerated by a factor of about four by this strategy. The good agreement in the transmural changes of helix angles everywhere in the left ventricle between the fiber structure after 400 updates with the previous process and after 100 updates with the accelerated process demonstrate the reliability of the acceleration technique (**Figure 13**). With this acceleration, the computation time was reduced to 0.4 h (100 updates) from 1.6 h (400 updates). This result clearly indicates that the optimized fiber structure is insensitive to the magnitude of the contractile tension, suggesting that large deformation analysis is not always necessary for predicting the fiber orientation.

DISCUSSION

In this study, a simple stress–strain relationship (Eq. 5) under static equilibrium was used for myofiber reorientation of the biventricular finite element model. This relationship was introduced as a replacement for the force–velocity relationship in the whole dynamical systole. The simplification provided an insight into the reorientation mechanism using the microscopic branching fiber architecture. Namely, the force–velocity relationship implies less active tension for faster shortening. This corresponds to the property of the stress–strain relationship that represents lower stress with greater shortening strain. Our approach using the association of the two relationships under the dynamic and static conditions was verified by the unaffected fiber structures for the magnitudes of active tension (**Figures 7C**, **12**, **13**) and the beating ventricle simulation results (**Figure 11**).

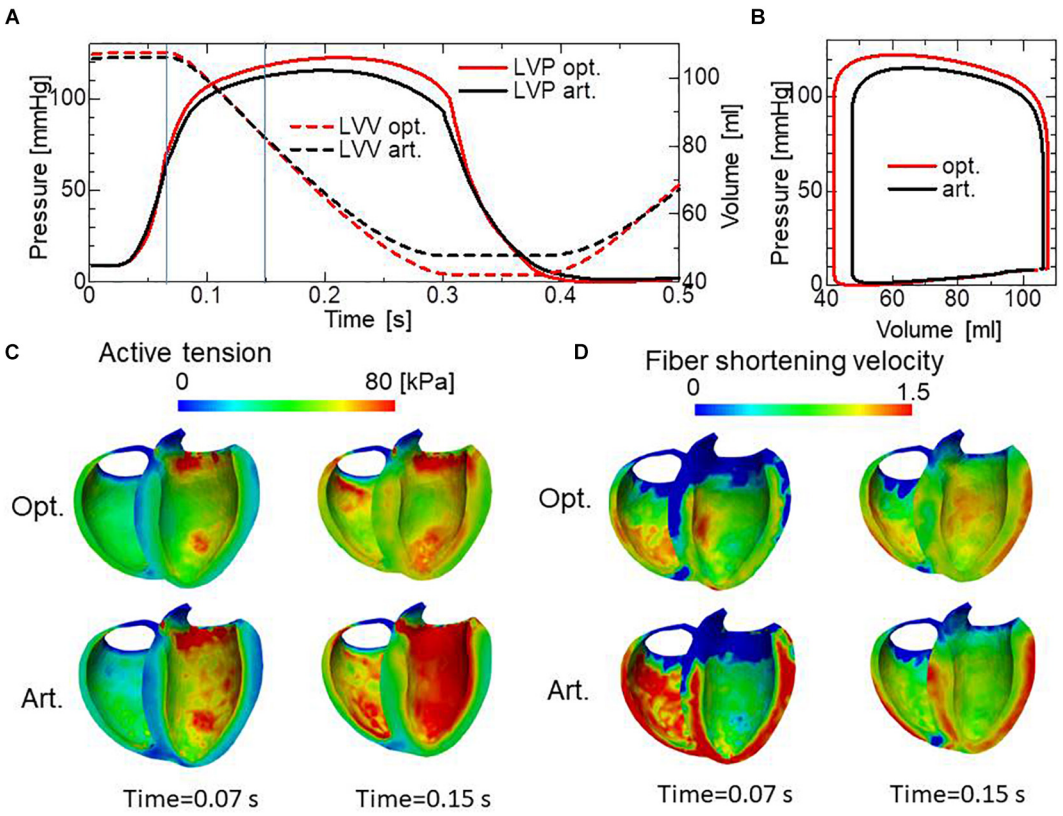

FIGURE 11 | Comparison of pumping performance for the optimized fiber structure and the artificial fiber structure. **(A)** Time courses of left ventricular intracavitary pressures for the optimized fiber structure (red solid line) and the artificial fiber structure (black solid line), and time courses of left ventricular volumes for the optimized fiber structure (red broken line) and the artificial fiber structure (black broken line). **(B)** Pressure–volume loops for the optimized fiber structure (red) and the artificial fiber structure (black). **(C)** Distribution of active tension for the optimized fiber structure (upper) and the artificial fiber structure (lower) at the end of the isovolumetric contraction phase (Time = 0.07 s) and at the middle of the blood ejection phase (Time = 0.15 s). These timings are indicated by the vertical line in **(A)**. **(D)** Distribution of fiber shortening velocity for the optimized fiber structure (upper) and the artificial fiber structure (lower) at the end of the isovolumetric contraction phase (Time = 0.07 s) and at the middle of the blood ejection phase (Time = 0.15 s).

While the reorientation mechanism worked well in terms of improving the pumping performance when the muscle contractility was homogeneous (**Figure 3**), it was also shown that the same mechanism may negatively affect the pumping performance for the ventricles that contain regions severely damaged by infarction. In our numerical model, the mechanism modified the fiber structure in the healthy region near the site of infarction such that the fiber stream lines run along that boundary (**Figures 5D,F**). As a result, the connections between the healthy region and the site of infarction are weakened, which results in the region around the boundary becoming elongated in the cross-fiber direction and a decrease in intracavitary pressure (**Figure 5B**).

The successful reconstruction of the helical ventricular myocardial band of Torrent-Guasp's model and the apical spiral structure of Rushmer's model indicate that these interesting structures should be inevitable results of the simple reorientation mechanism, regardless of their roles in pumping. Our analysis suggests that these structures make the myocytes support each other along their longitudinal direction, thus minimizing the overall fiber shortening strains.

Our macroscopic multidirectional active tensor was shown to be useful for predicting the fiber structure, and also for understanding the reorientation mechanism using the microscopic branching structure. However, we must be careful in applying this tensor to beating heart dynamical simulations, because such multidirectional stress degrades the pumping performance, with the degradation becoming worse as the dispersion angle θ in Eq. 7 increases. Actually, in our model with the common reference active tension T_{ref} = 40 kPa, the left ventricular intracavitary pressures for the optimized structure were 89.7 mmHg and 79.0 mmHg, respectively, for $\theta = 30°$ and $\theta = 45°$. Because we assumed a nearly incompressible property for the muscle, the active tension in one direction imposes expansions in orthogonal directions. Therefore, the active tensions in the branching directions interfere with each other. However, it is not known whether the real microscopic branching architecture has the same disadvantage, because our macroscopic model may be too simple to reproduce the sophisticated characteristics of the branching architecture. Another point of concern is the disorder of the fiber helix angle—it is not certain whether the disorder was generated by some

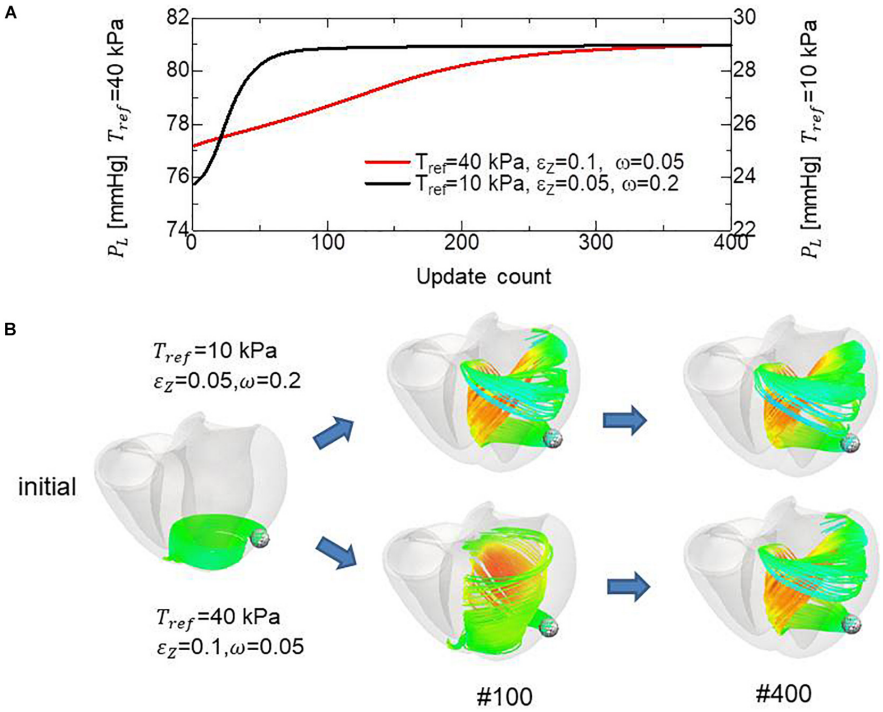

FIGURE 12 | Comparison of remodeling process with the standard parameter set (T_{ref} = 40 kPa, ϵ_Z = 0.1, ω = 0.05) and the variant (T_{ref} = 10 kPa, ϵ_Z = 0.05, ω = 0.2) for acceleration. **(A)** Transients of the left ventricular intracavitary pressures. **(B)** Evolution of fiber structures are compared by the stream lines starting from the ball placed at the epicardial apical anterolateral portion. The numbers indicate the number of updates. The streamlines were constructed by the software PARAVIEW, where the Runge–Kutta 4–5 integrator was adopted. With the accelerated reorientation process, the increase in cavity pressure and evolution of fiber structure remain almost unchanged after 100 updates.

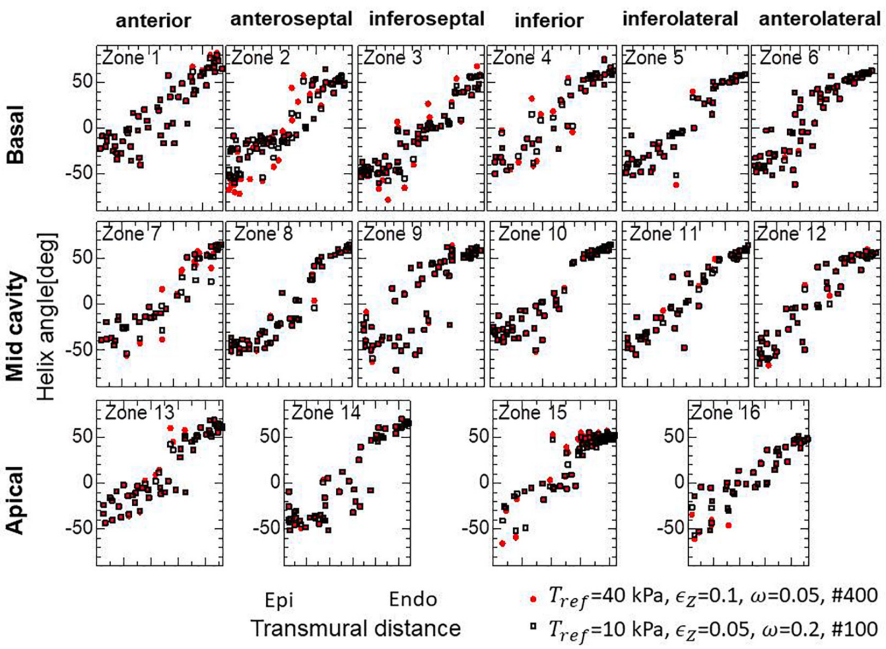

FIGURE 13 | Unchanged transmural helical angle arrangement of the optimized fiber structure in overall left ventricular wall given by the acceleration technique. The red dots and black squares were obtained by 400 updates of the reorientation processes with the standard parameter set (T_{ref} = 40 kPa, ϵ_Z = 0.1, ω = 0.05) and by 100 updates with the variant (T_{ref} = 10 kPa, ϵ_Z = 0.05, ω = 0.2) for acceleration, respectively. The two distributions are almost the same everywhere in the left ventricle wall.

characteristic errors of finite element discretization. Apparently, the disorder is not improved after being generated during the reorientation process. Indeed, when the initial structure was closer to the optimal structure, the disorder became considerably smaller, even after the same number of iterations (**Figure 9A**). Note that the intracavitary pressure also increased from 79.0 to 82.3 mmHg when the initial structure was changed. Thus, the question arises as to whether there is some mechanism for diminishing the disorder. The numerical smoothing of disorder is not so simple, because $\boldsymbol{f}$ and $-\boldsymbol{f}$ are equivalent in terms of defining the active stress tensor, but not for smoothing the distribution of $\boldsymbol{f}$.

Our main goal of this study is to construct a tool to predict the fiber structure for individual heart disease patients, and use the obtained data as the input for computer simulations to optimize the treatments. Though the validation for the healthy ventricle in **Figure 4** and the infarcted ventricle in **Figures 5**, **6** show the potential of our algorithm as such a tool, we must further validate it with animal models of regional infarct, pressure overload, and volume overload. Because our algorithm is based on the static mechanical equilibrium in the isovolumetric systole, it can't be directly applied to cases of dyssynchrony or diastolic dysfunction. In case of dyssynchrony, some regional weighting to the active stress according to the excitation timing (smaller weight to latterly excited region) may be effective. In case of diastolic dysfunction in which smooth relaxation of sarcomeres is hindered due to residual cross-bridges of actomyosin complex, our algorithm may be valid by properly reproducing the end diastolic configuration as the starting point of our optimization. Further investigations by comparisons with experimental facts are needed for these issues.

In this study, we did not consider the role of the laminar structure indicated by the sheet orientation vector $\boldsymbol{s}$. We have tested the reorientation process with non-symmetric weights such as $w_0 = 1/2$, $w_1 = w_5 = 1/8$, $w_2 = w_4 = w_6 = w_8 = 1/16$, $w_3 = w_7 = 0$ in Eq. (7), and updated the frame $\{\boldsymbol{f},\boldsymbol{s},\boldsymbol{n}\}$ using the two eigenvectors associated with the first- and second-largest eigenvalues of the tensor: $\boldsymbol{D} = \sum_{i=0}^{8} w_i \psi_i(\in_i) \boldsymbol{f}_i \otimes \boldsymbol{f}_i$. However, the intracavity pressure decreased by 19 mmHg compared with the fiber structure obtained by the reorientation process using symmetric weights, and the disorder in helix angles increased considerably. Therefore, further studies are needed to identify the role of the laminar structure, including its impact on the passive properties.

In the ventricular model used in this study, the papillary muscles were neglected. Thus, the mechanical loads imposed by pulling forces via chordae tendineae were ignored. Because the total pulling force via chordae tendineae is about the same as the product of valve area and intracavitary pressure, it may give considerable impact on the fiber architecture around the roots of the papillary muscles. In fact, the gaps at the epicardial region in zones 9 and 14 around the apical and mid septal segments (see also **Supplementary Material S2**) between the numerical results and the experimental data in **Figure 4** may be caused by the removal of a right ventricular papillary muscle attached to the septal inner wall. The inclusion of papillary muscles in the numerical ventricle model along with their appropriate mechanical treatment is our future work.

DATA AVAILABILITY STATEMENT

The datasets generated for this study are available on request to the corresponding author.

AUTHOR CONTRIBUTIONS

SS and TH designed the project. TW designed and conceived the numerical algorithm of reorientation. TW and JO constructed the simulation code and the input data. TW wrote the manuscript with inputs from SS and TH.

FUNDING

This work was supported in part by the Ministry of Education, Culture, Sports, Science, and Technology of Japan (MEXT) as a Priority Issue on Post-K computing (Integrated Computational Life Science to Support Personalized and Preventive Medicine) (Project ID: hp180210 and hp190179).

ACKNOWLEDGMENTS

We thank Edanz Group (www.edanzediting.com/ac) for editing a draft of this manuscript.

SUPPLEMENTARY MATERIAL

The Supplementary Material for this article can be found online at: https://www.frontiersin.org/articles/10.3389/fphys.2020.00467/full#supplementary-material

REFERENCES

Brezzi, F., and Fortin, M. (1991). *Mixed and Hybrid Finite Element Methods. (Springer Series in Computational Mathematics).* New York, NY: Springer, 15, 200–273.

Buckberg, G. (2002). Basic science review: the helix and the heart. *J. Thorac. Cardiovasc. Surg.* 124, 863–883. doi: 10.1067/mtc.2002.122439

Buckberg, G., Mahajan, A., Saleh, S., Hoffman, J. I., and Coghlan, C. (2008). Structure and function relationships of the helical ventricular myocardial band. *J. Thorac. Cardiovasc. Surg.* 1, 578–589. doi: 10.1016/j.jtcvs.2007.10.088

Grant, R. P. (1965). Notes on the muscular architecture of the left ventricle. *Circulation* 32, 301–308. doi: 10.1161/01.CIR.32.2.301

Hunter, P. J., MaCulloch, A. D., and ter Keurs, H. E. D. J. (1998). Modelling the mechanical properties of cardiac muscle. *Prog. Biophys. Mol. Biol.* 69, 289–331. doi: 10.1016/s0079-6107(98)00013-3

Kroon, W., Delhaas, T., Bovendeerd, P., and Arts, T. (2009). Computational analysis of the myocardial structure: adaptation of cardiac myofiber orientations through deformation. *Med. Image Anal.* 13, 346–353. doi: 10.1016/j.media.2008.06.015

Lekadir, K., Hoogendoorn, C., Pereanez, M., Albà, X., Pashaei, A., and Frangi, A. F. (2014). Statistical personalization of ventricular fiber orientation using shape predictors. *EEE Trans Med Imaging* 33, 882–890. doi: 10.1109/TMI.2013.2297333

Lombaert, H., Peyrat, J. M., Croisille, P., Rapacchi, S., Fanton, L., Cheriet, F., et al. (2012). Human atlas of the cardiac fiber architecture: study on a healthy population. *IEEE Trans. Med. Imaging* 31, 1436–1447. doi: 10.1109/TMI.2012.2192743

Pluijmert, M., Delhaas, T., de la Parra, A. F., Kroon, W., Prinzen, F. W., and Bovendeerd, P. H. M. (2017). Determinants of biventricular cardiac function: a mathematical model study on geometry and myofiber orientation. *Biomech. Model. Mechanobiol.* 16, 721–729. doi: 10.1007/s10237-016-0825-y

Pluijmert, M., Kroon, W., Rossi, A. C., Bovendeerd, P. H. M., and Delhaas, T. (2012). Why SIT works: normal function despite typical myofiber pattern in situs inversus totalis (SIT) hearts derived by shear-induced myofiber reorientation. *PLoS Comput. Biol.* 8:e1002611. doi: 10.1371/journal.pcbi.1002611

Rijcken, J., Bovendeerd, P. H., Schoofs, A. J., van Campen, D. H., and Arts, T. (1999). Optimization of cardiac fiber orientation for homogeneous fiber strain during ejection. *Ann. Biomed. Eng.* 27, 289–297. doi: 10.1114/1.147

Rijcken, J., Bovendeerd, P. H. M., Schoofs, A. J., van Campen, D. H., and Arts, T. (1997). Optimization of cardiac fiber orientation for homogeneous fiber strain at beginning of ejection. *J. Biomech.* 30, 1041–1049. doi: 10.1016/S0021-9290(97)00064-X

Rushmer, R. F., Crystal, D. K., and Wagner, C. (1953). The functional anatomy of ventricular contraction. *Circ. Res.* 1, 162–170. doi: 10.1161/01.RES.1.2.162

Sosnovik, D. E., Wang, R., Dai, G., Wang, T., Aikawa, E., Novikov, M., et al. (2009). Diffusion spectrum MRI tractography reveals the presence of a complex network of residual myofibers in infarcted myocardium. *Circ. Cardiovasc. Imaging* 2, 206–212. doi: 10.1161/CIRCIMAGING.108.815050

Taggart, P., Sutton, P. M., Opthof, T., Coronel, R., Trimlett, R., Pugsley, W., et al. (2000). Inhomogeneous transmural conduction during early ischaemia in patients with coronary artery disease. *J. Mol. Cell Cardiol.* 32, 621–630. doi: 10.1006/jmcc.2000.1105

ten Tusscher, K. H., and Panfilov, A. V. (2006). Alternans and spiral breakup in a human ventricular tissue model. *Am. J. Physiol. Heart Circ. Physiol.* 291, H1088–H1100. doi: 10.1152/ajpheart.00109.2006

Usyk, T. P., Mazhari, R., and McCulloch, A. D. (2000). Effect of laminar orthotrophic myofiber architecture on regional stress and strain in the canine left ventricle. *J. Elasticity* 61, 143–164. doi: 10.1023/A:1010883920374

Washio, T., Yoneda, K., Okada, J., Kariya, T., Sugiura, S., and Hisada, T. (2016). Ventricular fiber optimization utilizing the branching structure. *Int. J. Numer. Method Biomed. Eng.* 32:e02753. doi: 10.1002/cnm.2753

Wu, E. X., Wu, Y., Nicholls, J. M., Wang, J., Liao, S., Zhu, S., et al. (2007). MR diffusion tensor imaging study of postinfarct myocardium structural remodeling in a porcine model. *Magn. Reson. Med.* 58, 687–695. doi: 10.1002/mrm.21350

Wu, Y., Zhang, L. J., Zou, C., Tse, H. F., and Wu, E. X. (2011). Transmural heterogeneity of left ventricular myocardium remodeling in postinfarct porcine model revealed by MR diffusion tensor imaging. *J. Magn. Reson. Imaging* 34, 43–49. doi: 10.1002/jmri.22589

Conflict of Interest: TW, SS, JO, and TH were employed by the company UT-Heart Inc.

frontiers in Physiology

METHODS
published: 08 July 2020
doi: 10.3389/fphys.2020.00612

Approaches to High-Throughput Analysis of Cardiomyocyte Contractility

Peter T. Wright, Sharmane F. Tsui, Alice J. Francis, Kenneth T. MacLeod and Steven B. Marston**

Myocardial Function, National Heart and Lung Institute, Imperial College London, London, United Kingdom

OPEN ACCESS

Edited by:
Norio Fukuda, Jikei University School of Medicine, Japan

Reviewed by:
Kenneth Scott Campbell, University of Kentucky, United States
Kerry S. McDonald, University of Missouri, United States

***Correspondence:**
Peter T. Wright
pw1309@ic.ac.uk
Steven B. Marston
s.marston@imperial.ac.uk

Specialty section:
This article was submitted to Striated Muscle Physiology, a section of the journal Frontiers in Physiology

Received: *20 January 2020*
Accepted: *15 May 2020*
Published: *08 July 2020*

Citation:
Wright PT, Tsui SF, Francis AJ, MacLeod KT and Marston SB (2020) Approaches to High-Throughput Analysis of Cardiomyocyte Contractility. Front. Physiol. 11:612. doi: 10.3389/fphys.2020.00612

The measurement of the contractile behavior of single cardiomyocytes has made a significant contribution to our understanding of the physiology and pathophysiology of the myocardium. However, the isolation of cardiomyocytes introduces various technical and statistical issues. Traditional video and fluorescence microscopy techniques based around conventional microscopy systems result in low-throughput experimental studies, in which single cells are studied over the course of a pharmacological or physiological intervention. We describe a new approach to these experiments made possible with a new piece of instrumentation, the CytoCypher High-Throughput System (CC-HTS). We can assess the shortening of sarcomeres, cell length, Ca^{2+} handling, and cellular morphology of almost 4 cells per minute. This increase in productivity means that batch-to-batch variation can be identified as a major source of variability. The speed of acquisition means that sufficient numbers of cells in each preparation can be assessed for multiple conditions reducing these batch effects. We demonstrate the different temporal scales over which the CC-HTS can acquire data. We use statistical analysis methods that compensate for the hierarchical effects of clustering within heart preparations and demonstrate a significant false-positive rate, which is potentially present in conventional studies. We demonstrate a more stringent way to perform these tests. The baseline morphological and functional characteristics of rat, mouse, guinea pig, and human cells are explored. Finally, we show data from concentration response experiments revealing the usefulness of the CC-HTS in such studies. We specifically focus on the effects of agents that directly or indirectly affect the activity of the motor proteins involved in the production of cardiomyocyte contraction. A variety of myocardial preparations with differing levels of complexity are in use (e.g., isolated muscle bundles, thin slices, perfused dual innervated isolated heart, and perfused ventricular wedge). All suffer from low throughput but can be regarded as providing independent data points

in contrast to the clustering problems associated with isolated cell studies. The greater productivity and sampling power provided by CC-HTS may help to reestablish the utility of isolated cell studies, while preserving the unique insights provided by studying the contribution of the fundamental, cellular unit of myocardial contractility.

Keywords: cardiomyocytes, high-throughput, sarcomere, calcium, contractility

INTRODUCTION

The isolation and study of cardiomyocytes have made a remarkable contribution to our understanding of myocardial physiology and pathophysiology. Cardiomyocytes are the elementary units responsible for the contraction of the myocardial tissue. They contain the complete excitation–contraction coupling system and an intact sarcomeric contractile apparatus involved in cellular contraction (Bers, 2002). The isolation of cardiomyocytes makes the study of these processes possible by virtue of extracting the cells from their integrated multi-cellular environment (Harding et al., 1992). The separation of cells from their contractile, vascular, and neurohormonal milieu means that the effects of specific pharmacologic, genetic, or surgical manipulation on cellular physiology can be observed (Davia et al., 1999; Stark et al., 2004; Lyon et al., 2011). From a technical perspective, a single cell is amenable to microscopic analysis. In the case of fluorescent or super-resolution approaches, isolation of cells allows the visualization of cells and sub-cellular/organellar compartments without unwanted effects from the tissue level (Nikolaev et al., 2010; Brandenburg et al., 2016). In recent decades, the genetic manipulation of cells in culture, the introduction of dyes (for Ca^{2+} in particular), and Förster resonance energy transfer (FRET)-based biosensors have become conventional in the isolated cellular preparation (Glukhov et al., 2015; Miragoli et al., 2016; Sanchez-Alonso et al., 2016; Wright et al., 2018a,b).

The very strengths of the isolated cardiomyocyte preparation are unfortunately also a source of weakness. The enzymatic digestion of the heart is not always consistent and batch effects will be observable even if the protocol is run by an experienced operator. From a scientific perspective, this injects variability into datasets, which makes physiologically important effects harder to detect. The separation of cells from their integrated conformation within tissue denies them the support system to which they are evolutionarily adapted. Prolonging the lifetime of acutely dissociated cardiomyocytes by cell culture is artificial and produces time-sensitive preparations in which cells rapidly remodel and de-differentiate even under optimal conditions (Pavlović et al., 2010; Abi-Gerges et al., 2013). The mechano-electric environment is intrinsic to the control of single-cell behavior, and this is technically difficult to replicate for a single-cell preparation. From a statistical perspective, these preparations are "hierarchically clustered" whereby cells from one heart isolation are innately more similar than those isolated from another. Inappropriate analyses that ignore the dependence or "nesting" of measurements of cells from a single preparation are conventionally employed and can lead to "pseudoreplication," increasing the chance of false positives (Sikkel et al., 2017).

Latent cardiomyocyte heterogeneity (in healthy and failing organs) is an important limitation of single-cell approaches (Paur et al., 2012; Molina et al., 2014; Yue et al., 2017; Wright et al., 2018a). Moreover, the innate electrophysiological differences between myocardial chambers and layers are detailed in the most basic cardiovascular textbook (Szentadrassy et al., 2005) but are usually overlooked as an inconvenient truth by most of those who perform isolated cardiomyocyte studies. In the case of the single-cell preparation, the sampling power of most myocardial techniques are simply too low to make full description of the diversity of cardiomyocyte phenotypes feasible. A view of cardiomyocytes as a monolithic population of cells of a single phenotype persists.

It is evident that the key problem is that current techniques for studying cardiomyocytes are extremely time-consuming while viable cells have a lifetime of hours. Consequently, only a few cells can be studied from each preparation and most remaining cells are wasted. With a small number of cells assayed and the necessity (from ethical, financial, and personnel considerations) to combine measurements from multiple myocyte preparations, this technique may justifiably be challenged as lacking the necessary statistical power to test hypotheses. If it was possible to speed up measurements by assessing in parallel many cells it may be possible to rehabilitate single-cell studies.

Increased throughput measurements can be made possible by reorganizing the microscopy system so that a computer-controlled scanning microscope makes measurements on many myocytes in a stationary sample. In this paper, we report our experiences using the CytoCypher/IonOptix MultiCell System^{TM} to measure myocyte contractility and Ca^{2+} transients. Using this system, operators can expect to measure 30 cells in less than 8 min, with optimal cell function and environmental conditions. With the automated cell finding system, still higher measurement rates are possible and selection bias is reduced (Helmes, 2017). We show how this instrument enables far richer datasets to be collected from a single animal in a short time while cells remain viable. These are more representative of the entire population of cells present in the native myocardial sample enabling us to analyze in depth the statistics and power of the myocyte contraction measurement. In addition, we demonstrate high-throughput routines to investigate the pharmacological profiles of known drugs that act upon the contractile apparatus.

METHODS AND EQUIPMENT

Animal Care and Procedures

Animal experiments met the criteria of Imperial College London and Animals in Scientific Procedures Act (ASPA) 1986 as well as the 2010/63/EU Directive.

Instrumentation

Module	Manufacturer
CytoCypher Microscope Module with 35 mm Dish Insert	CytoCypher BV, Netherlands
CytoCypher System Control Module	CytoCypher BV, Netherlands
IonOptix MyoCam S3 Video Camera	IonOptix LLC, United States
Myopacer with 35 mm Dish Field Stimulation Element	IonOptix LLC, United States
UV LED Fluorescent Source	Cairn Research, United Kingdom
UV Filter Set	Cairn Research, United Kingdom
IonOptix Fluorescence System Interface	IonOptix LLC, United States
Cell Framing Adaptor Desktop PC	IonOptix LLC, United States
CytoCypher Perfusion Module (optional)	CytoCypher BV, Netherlands

Software

Software	Developer
IonOptix IonWizard	IonOptix LLC, United States
CytoCypher TAT	CytoCypher BV, Netherlands
CytoCypher Cytosolver	CytoCypher BV, Netherlands
Cytospectre	University of Tampere, Finland

Myocyte Isolation Protocols

Rat Isolation

Rats are sacrificed by cervical dislocation after the induction of a brief anesthesia in an atmosphere of 5% isoflurane. An incision is made across the base of the rib cage and on either side of the thorax to fully expose the thoracic cavity. The entire contents of the cavity are removed and placed in ice-cold Krebs–Henseleit (KH) Buffer (119 mM NaCl, 4.7 mM KCl, 0.94 mM $MgSO_4$, 1 mM $CaCl_2$, 1.2 mM KH_2PO_4, 25 mM $NaHCO_3$, and 11.5 mM glucose; 95% O2, 5% CO_2). The tissue is placed in clean ice-cold KH. The lungs, thyroid, and superfluous pericardial fat are dissected away from the heart, leaving the aorta and atria intact. The heart is then rapidly cannulated via the aorta, connected to a Langendorff apparatus and retrogradely perfused with KH at 37°C. After 1–1½ min, the KH buffer is switched to a low Ca^{2+} ($LoCa^{2+}$) buffer [12–15 μM $CaCl_2$, 120 mM NaCl, 5.4 mM KCl, 5 mM $MgSO_4$, 5 mM pyruvate, 20 mM glucose, 20 mM taurine, 10 mM HEPES, and 5 mM nitrilotriacetic acid (NTA); 100% O_2] for 5 min. Subsequently, a solution of 1 mg/ml Collagenase II and 0.6 mg/ml Hyaluronidase (C + H) in enzyme (Enz) buffer (120 mM NaCl, 5.4 mM KCl, 5 mM $MgSO_4$, 5 mM pyruvate, 20 mM glucose, 20 mM taurine, 10 mM HEPES, and 150 μM $CaCl_2$) is perfused into the heart for 10 min. After 10 min of enzymic digestion, the Langendorff perfusion is switched off and the heart is cut down. The heart is then placed in fresh C + H and dissected and minced. The samples are gently shaken mechanically at 35°C for 5 min and filtered through gauze. If necessary, the right and left ventricles are separated and processed separately. The undigested tissue is placed back in the tube with fresh C + H and shaken for a further 30 min. The solution is then strained through gauze and the resulting filtrate is centrifuged for 1 min at 700 rpm to yield a pellet of cells. These isolations yield between 80 and 95% rod-shaped cardiomyocytes.

Mouse Isolation Procedure 1

Mouse cells are isolated using one of two different procedures. The first is similar to that described for rat with several modifications. The mouse heart is extracted using the same procedure as for rat and placed in cold KH buffer. The heart is dissected and retrogradely perfused on a modified Langendorff apparatus with KH for 1–1½ min. Subsequently, the heart is perfused with the $LoCa^{2+}$ buffer for 5 min. Following this stage, protease solution (0.36 mg/ml) is perfused for 1 min before switching to C + H for 5 min. The heart is then dissected in Enz and passed through a pipette to break up the tissue and yield single cells.

Mouse Isolation Procedure 2

In the second procedure, the mouse heart is initially placed into ice-cold HEPES buffer (NaCl 113 mM, KCl 4.7 mM, KH_2PO_4 0.6 mM, Na_2HPO_4 0.6 mM, $MgSO_4$ 1.2 mM, $NaHCO_3$ 12 mM, $KHCO_3$ 10 mM, HEPES 10 mM, and Taurine 30 mM). It is then perfused with the HEPES buffer at 37°C, after the fluid exiting the heart becomes clear, trypsin/Liberase solution is added to the perfusate (Solution composition as detailed above plus 13 μM $CaCl_2$, Liberase 0.05 mg/ml, and 0.3 mg/ml Trypsin). The heart is then dissected in perfusion buffer and passed through a pipette to break up the tissue and yield single cells.

These isolations yield between 60 and 80% rod-shaped cardiomyocytes.

Guinea Pig Isolation Procedure

The guinea pig heart is placed in ice-cold heparinized KH buffer (NaCl 120 mM, KCl 4.7 mM, $MgSO_4$ 0.94 mM, KH_2PO_4 1.2 mM, $NaHCO_3$ 25 mM, Glucose 11.5 mM, and $CaCl_2$ 1 mM, pH 7.4). The heart is perfused with KH 1–2 min at a rate of 6–8 ml/min. A low-Ca^{2+} ($LoCa^{2+}$ NaCl 120 mM, KCl 5.4 mM, $MgSO_4$ 5 mM, Na Pyruvate 5 mM, Glucose 20 mM, Taurine 20 mM, HEPES 10 mM, $CaCl_2$ 12–15 μM, NTA 5 mM, and pH 6.96) is perfused for 4–5 min; all cardiac contraction ceases. An enzyme solution containing Liberase TL is perfused for 6–10 min [NaCl 120 mM, KCl 5.4 mM, $MgSO_4$ 5 mM, Na Pyruvate 5 mM, Glucose 20 mM, Taurine 20 mM, HEPEs 10 mM, $CaCl_2$ 0.2 mM, and Liberase TL (Gibco) 0.1 mg/ml]. The left ventricle is then dissected into 2-mm^3 cubes. The chunks are added to the same enzyme solution, shaken, oxygenated, and triturated. The solution is filtered every 3 min until digestion complete. The suspension is centrifuged at 400 rpm for 1 min and the resulting cell pellet is resuspended in fresh enzyme solution without Liberase TL. Myocytes are

stored in DMEM solution at room temperature and ready for experimental use.

These isolations yield between 70 and 85% rod-shaped cardiomyocytes.

Human Cardiomyocyte Isolation Procedure

Samples of human atria or ventricles are obtained from consenting patients within the Imperial College Healthcare Trust heart transplant program in accordance with the Declaration of Helsinki and local ethical review. Biopsies of human tissue are acquired and placed in ice-cold Low Ca^{2+} solution [NaCl 120 mM, KCl 5.4 mM, $MgSO_4$ 5 mM, Pyruvate 5 mM, Glucose 20 mM, Taurine 20 mM, HEPES 10 mM, and NTA 5 mM, bubbled with 100% O_2. pH was adjusted to 6.95, free $[Ca^{2+}]$ was 1 to 3 μM]. The tissue is diced into 1-mm^3 chunks in ice-cold $LoCa^{2+}$. It is then washed for 3 min in warmed, oxygenated $LoCa^{2+}$ by manually shaking in a water bath; after the first step, the supernatant is removed and replaced with fresh $LoCa^{2+}$ and shaken again.

Ventricular tissue

Subsequently, the tissue is shaken for 45 min in enzyme solution containing protease XXIV (NaCl 120 mM, KCl 5.4 mM, $MgSO_4$ 5 mM, pyruvate 5 mM, glucose 20 mM, taurine 20 mM, HEPES 10 mM, 150 μM $CaCl_2$, and protease 4 U/ml–0.36 mg/ml). The supernatant is removed by filtering through gauze, and the undigested tissue is then shaken for 10–15 min in solution containing collagenase Type V (NaCl 120 mM, KCl 5.4 mM, $MgSO_4$ 5 mM, pyruvate 5 mM, glucose 20 mM, taurine 20 mM, HEPES 10 mM, 150 μM $CaCl_2$, and collagenase 1 mg/ml). This step is repeated multiple times. After each stage, the supernatant is filtered through gauze and the undigested tissue is returned to the shaker bath. Supernatants are centrifuged at 700 rpm for 2 min. Cell pellets are resuspended in enzyme solution without enzymes.

Atrial tissue

This procedure is analogous to the isolation of ventricular tissue except that the protease containing solution is supplemented with type V collagenase (collagenase, 0.5 mg/ml).

These isolations yield between 10 and 25% rod-shaped cardiomyocytes.

Cell Culture

Laminin Attachment

Isolated cells are plated on laminin-coated coverslips or Matek™ (Matek Corp, United States) dishes, in culture media containing FBS (MEM salts 10.74 g/L, $NaHCO_3$ 9 mM, L-Glutamine 1%, and Penicillin/Streptomycin 1%). Cells are incubated for 1 h to allow attachment (5% CO_2, 37°C). The dishes are then supplemented with 1 ml of MEM to prevent drying.

Free Solution

Isolated cells are resuspended in MEM solution and plated in 35-mm petri dishes with 13-mm glass inserts and placed in the incubator (5% CO_2, 37°C) until use.

Fura-2 or Fura-4f AM Loading

Fura-2AM or Fura-4fAM are resuspended in DMSO to produce 1 mM solutions. Cells attached to laminin are loaded by applying perfusion solutions containing 1 μM or 5 μM Ca^{2+}-sensitive dye to Matek and incubated in the dark at room temperature for 10–15 min or 25 min for guinea pig cells. Cells in solution are aspirated, spun gently, and resuspended in perfusion solutions containing 1 μM Fura-2/Fura-4fAM. The solutions are spun again and the dye containing solution is removed. The cells plated on Matek or in solution are washed once with clean perfusion buffer before analysis on the CytoCypher system.

Measurements With CytoCypher HTS

Isolated cardiomyocytes are paced using a field stimulator at a frequency of between 0.2 and 2 Hz (20–50 V, 10-ms pulse width). The CytoCypher HTS is based on a static observation platform for the cells and a static high-resolution camera with a scanning microscope taking advantage of the infinity corrected optics present in most modern microscope lenses. This allows for rapid scanning without disturbing the cells. The area that can be scanned is 15 mm^2. A mosaic field approximately 3500 × 1600 μm is presented from which a region of interest can be selected (**Figure 1**), and individual cells were located and orientated. The selected cell is optimized for sarcomere length detection and then the recording can be made. The cell is marked for re-assay by the software with the coordinates of where the measurement was taken marked out with a green rectangle. The next cell is subsequently selected. Microscope movements are virtually instantaneous, and position can be refined by mouse or keyboard control, taking just a few seconds. Experienced operators can expect to measure up to 30 cells in <8 min. An automated cell finding system enables automatic detection and measurement of myocytes (**Supplementary Video 1**). In favorable conditions, this is quicker than the best manual selection. Since selection is based on pre-defined criteria, results obtained by the system itself cannot be influenced by operator bias, for instance, by selecting the most obviously contractile cells (**Table 1**). For Fura-dye measurements, the microscope is supplemented by a dual excitation LED light source and photomultiplier detector for simultaneous ratiometric Ca^{2+} measurements (this solid-state solution is a considerable advance on current rotating filter methodology). Data are analyzed using the Cytosolver or Transient Analysis Tool (IonOptix LLC, United States) software environments; these packages are a development of the well-established IonWizard software with much greater speed and a user-friendly interface. For the purposes of this study, we have analyzed three key parameters of contraction magnitude and speed: percentage shortening of sarcomeres, time to peak from 10% of peak (TTP90), and time from peak to 10% above baseline (TTB90).

Morphological Analysis of Cardiomyocytes

As well as functional data, the CytoCypher HTS acquires thumbnail images of each cell it investigates (**Figure 2A**).

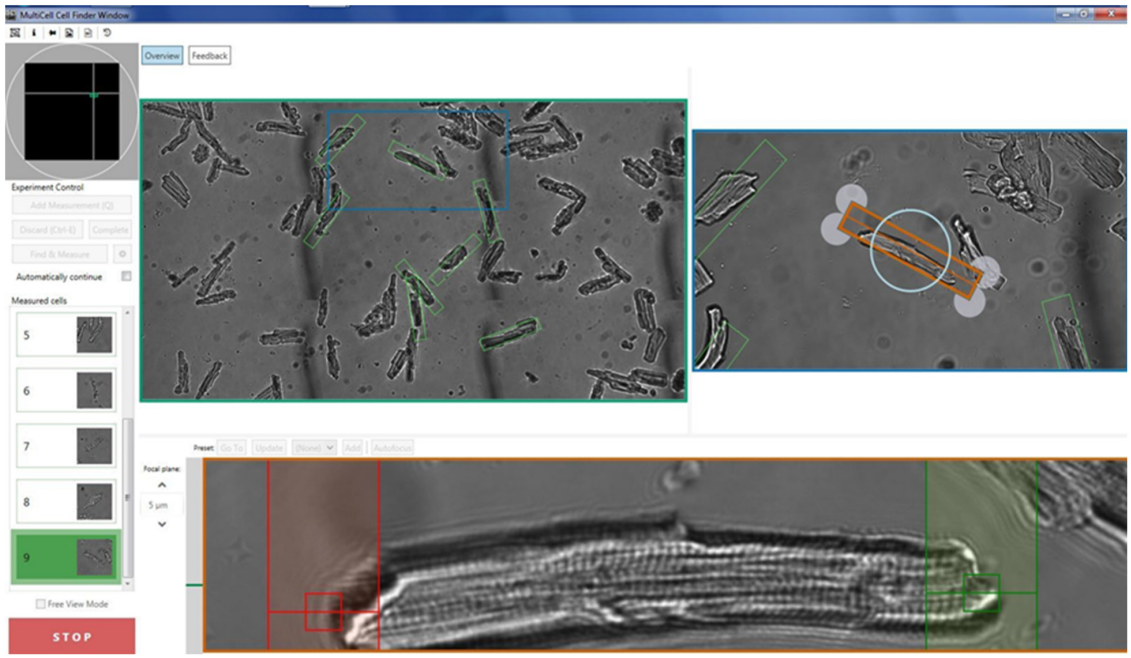

FIGURE 1 | Illustration of the acquisition screen of the CytoCypher High-Throughput System for the analysis of cardiomyocyte contractility. See also **Supplementary Video**.

This allows one to derive 2D morphological information. We create a segmentation mask using a self-produced macro in FIJI (**Figure 2B**) and use this in conjunction with the freeware image analysis program Cytospectre (University of Tampere, Finland; Kartasalo et al., 2015). As well as measuring normal geometric parameters from the segmentation mask, this program performs a spectral analysis of the region of interest and can give an indication of the dominant frequencies within the entire cardiomyocyte. **Figure 2C** shows the mixed coarse frequency component of the image of a cardiomyocyte; the repeating sarcomere structures within the cell dominate and give a large peak at around 1.8 µm. A more organized cell with a stronger sarcomere pattern will have a taller, sharper peak at the mode frequency relating to the average sarcomere length. Therefore, one can analyze the nature of the distribution of these geometric and spectral parameters alongside functional ones within a given cell sample and adapt statistical methodology accordingly.

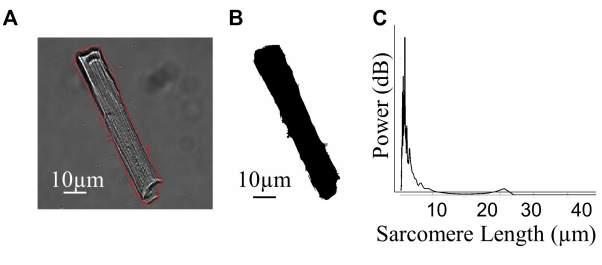

FIGURE 2 | Morphological investigation of cardiomyocytes. **(A)** Example image of a rat cardiomyocyte acquired by the CytoCypher HTS during the measurement of contraction; the red line indicates the application of a segmentation mask. **(B)** Segmentation mask generated automatically by Fiji software using our semi-automated analysis. **(C)** Plot demonstrating the relative "power" of different frequencies within the cell, generated by the Cytospectre program.

TABLE 1 | Standard cellular morphological parameters utilized for manual and automated cell finding by the CytoCypher system.

Manual acquisition criteria	
1. Rod shaped morphology with clear and well-organized sarcomere striations throughout the cell body. Cell bodies with artifacts or abnormal bulges were avoided.	
2. Regular contractions upon electrical stimulation. Exclude myocytes with extra or escaped beats	
Automatic acquisition criteria	
Area	
Maximum area (μm^2)	6000
Minimum area (μm^2)	1000
Aspect ratio	
Maximum ratio	0.5
Minimum ratio	0.1
Misc.	
Cell Overlap Parameter (µm; i.e., avoids two cells together)	40
Number of cells	50
Well scanning	Spiral motion
Operations on full field	Static cell finding with autofocus

Statistics

As discussed in the Introduction section, we believe that conventional analyses that utilize single-cell recordings as independent samples commit the error of "pseudoreplication," introducing a significant false-positive rate in studies of isolated cells (Sikkel et al., 2017). Conventional *t* tests and analysis of variance assume that each sample is independent and combine data from many preps, but in reality, cells from one preparation are more like each other than cells from other preparations. As a result, individual cell recordings taken from the same preparation can be nested within that preparation, meaning that a hierarchical structure is present within the dataset. In this paper, we use GraphPad Prism 6.0 to compute conventional column statistics from datasets without introducing hierarchical structure (mean, standard deviation). When comparing two independent conditions, we used unpaired Students' *t* test assuming statistical significance if $p < 0.05$. Where pharmacological stimuli were applied to a preparation of cells after baseline measurements were taken, we used a paired *t* test assuming statistical significance of $p < 0.05$. If data were not normally distributed, we applied Wilcoxon's test. To perform an analysis of the datasets with hierarchical structure preserved, we used a pre-published methodology using RStudio (Sikkel et al., 2017). Sikkel et al. provide a full explanation of the theoretical issues of this area and the practical implementation of hierarchical techniques. Their method produces a theoretical mean and standard error based on the relative contribution of individual preparations to the totality of the data. It also gives an intra-class correlation (ICC) statistic that indicates the similarity of preparations also known as "clustering." If the mean value of samples is very different between preparations with little overlap in the distributions of values, then the data are considered highly clustered with a high ICC. Complete overlap of the distributions of all preparations and identical means will yield an ICC of 0%. Based on these statistics, this analysis produces a *t* test (plus a relevant *p* value) between condition A and B using the theoretical means, errors, and idealized degrees of freedom and indicates whether a hierarchical or conventional statistical approach is most suitable. All statistical tests are indicated in Figure legends $*p < 0.05$, $**p < 0.001$, $***p < 0.001$, and $****p < 0.0001$.

RESULTS

A New Paradigm for Measuring Myocyte Contractility

The principles for high-throughput myocyte measurements differ radically from previous methods. We study many cells, each for a short period rather than a few cells over extended periods. Myocytes are plated onto laminin-coated 35-mm dishes and mounted in the CytoCypher apparatus (**Figure 1** and **Supplementary Video 1**). Measurements are made on as many of the myocytes in a field of view as necessary. In practice, this can be between 10 and 50 myocytes. Measurements are made by sarcomere length detection using the Fast Fourier Transform method or by cell length based on edge detection if the sarcomere pattern is not sufficiently clear. Myocytes may be selected manually using mouse and keyboard controls to locate, focus, and orientate the myocyte in about 4 s. A short recording of contractions, usually over a period of ∼5–10 s (depending on stimulation frequency) is made before moving on to the next cell.

In automatic mode, the microscope searches for objects that meet the preset criteria (**Table 1**). This mode is preferable since it avoids operator bias. It is optimal with about 20 viable myocytes in a field of view; sparse fields of myocytes can be detected more quickly manually. The data are then saved and may be analyzed online using Cytosolver software or offline using the Transient Analysis Tool, yielding the same contractility parameters as the well-known IonWizard software but much more rapidly. This avoids moving the bottleneck from the acquisition to the analysis phase. The myocyte positions are saved so that the myocytes may be remeasured; in this way, it is possible to build up a time course of parameters for individual cells (see **Figure 1**).

Although changing solution in a flow cell is possible, this would slow down the measurements in the CytoCypher. Our usual protocol is to aspirate the fluid from the dish of myocytes and replace it with a new solution, an operation that takes just a few seconds. It is possible to make up to four solution changes this way before the cell population becomes too sparse. Alternatively, one could use a fresh dish of myocytes for each solution change.

For example, we measured the sarcomere contraction response of three dishes of cells, one untreated, one treated with the β-adrenoceptor agonist dobutamine, and one treated with the myosin modulator Omecamtiv Mecarbil (OM; **Figure 3A**). The dobutamine increases the amplitude of contraction and shortens the relaxation, whereas OM has the opposing effect. **Figure 3B** presents scatter plots of the recordings of percentage sarcomere shortening, time taken to 90% peak contraction from baseline (TTP90), and time taken to 90% relaxation (TTB90) following treatment with OM (2.4 μM). **Figure 3C** presents time course data for the three parameters following individual cells over the course of their treatment with resampling at 2.5-min intervals.

Does Fura-4f Treatment Affect Myocyte Contractility?

Analysis of Hierarchical Clustering in Parameters Relating to Cardiomyocyte Function

Researchers may desire data concerning Ca^{2+} handling from cells that have been labeled with a Ca^{2+} dye such as Fura-2. Unfortunately, high-affinity Ca^{2+}dyes have been reported to buffer Ca^{2+} within the cell and alter their physiological behavior (Wokosin et al., 2004; Fast, 2005). Here, we demonstrate baseline contraction data for cells with and without loading with Ca^{2+} dye Fura-4f. In populations of cells that are not loaded with Fura-4f, about 20–30% appear to be non-contractile (**Supplementary Figure 2A**). By contrast, in sets of cells labeled with Fura-4f, 10–15% are not contractile (**Supplementary Figure 2B**).

As stated earlier, many indices of cardiomyocyte function are not truly independent measurements but are "nested" within a population derived from a specific animal. Cells from the same isolation are more alike and "cluster" around a specific mean for that preparation. In **Figure 4**, we present the baseline data for a

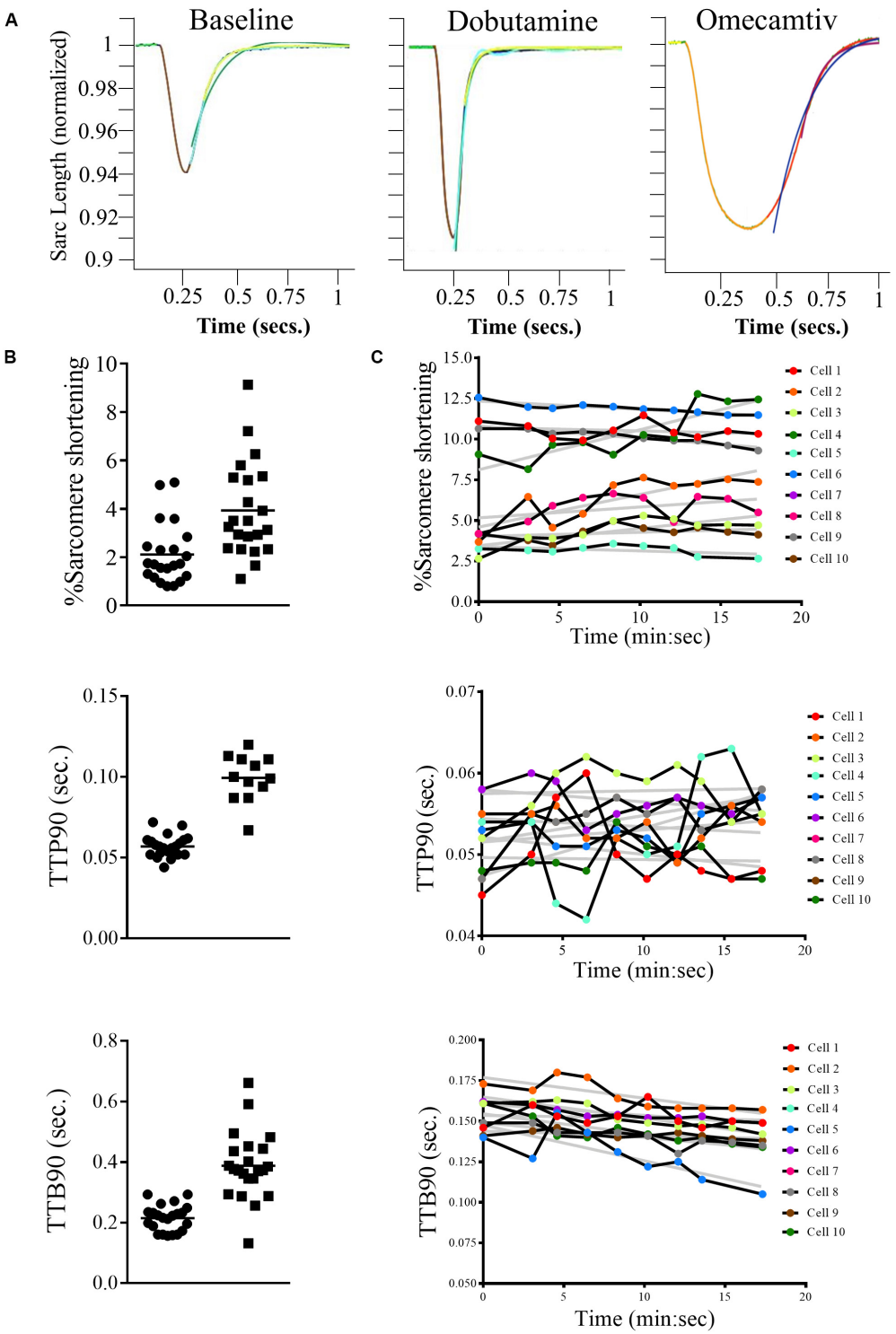

FIGURE 3 | Examples of measurements made using the CytoCypher HTS. **(A)** Average rat sarcomere length transients, 1 Hz, 20 V stimulation; baseline, 3 μM dobutamine (note larger peak and faster transients), and 2.4 μM Omecamtiv Mecarbil (note slower transients). The traces are averages of 10 contractions collected over 10 s. The colored segments represent green original average trace; yellow, baseline fit; orange, peak fit; red, recovery fit; purple, single exponential fit (Tau); and blue, double exponential fit. **(B)** The calculated parameters,% shortening, TTP90, secs and TTB90, secs from approximately 20 myocytes at baseline and in the presence of 2.4 μM Omecamtiv Mecarbil are shown with mean value indicated. Automatic cell finding; the two measurements took about 4 min each. Distribution of values is not normal, so significance is tested by Wilcoxon method. **(C)** Time course of the calculated parameters (% shortening, TTP90, secs and TTB90, secs) in the presence of 3 μM dobutamine + 0.05 μM ICI 118,551 for 10 myocytes in a field of view over 20 min. The gray lines are linear regression fits to the data. This plot shows the variability, both between myocytes and its change over time. The values in individual myocytes may increase or decrease slightly with time but on average% shortening and TTP90 are stable while TTB90 declines slightly over time.

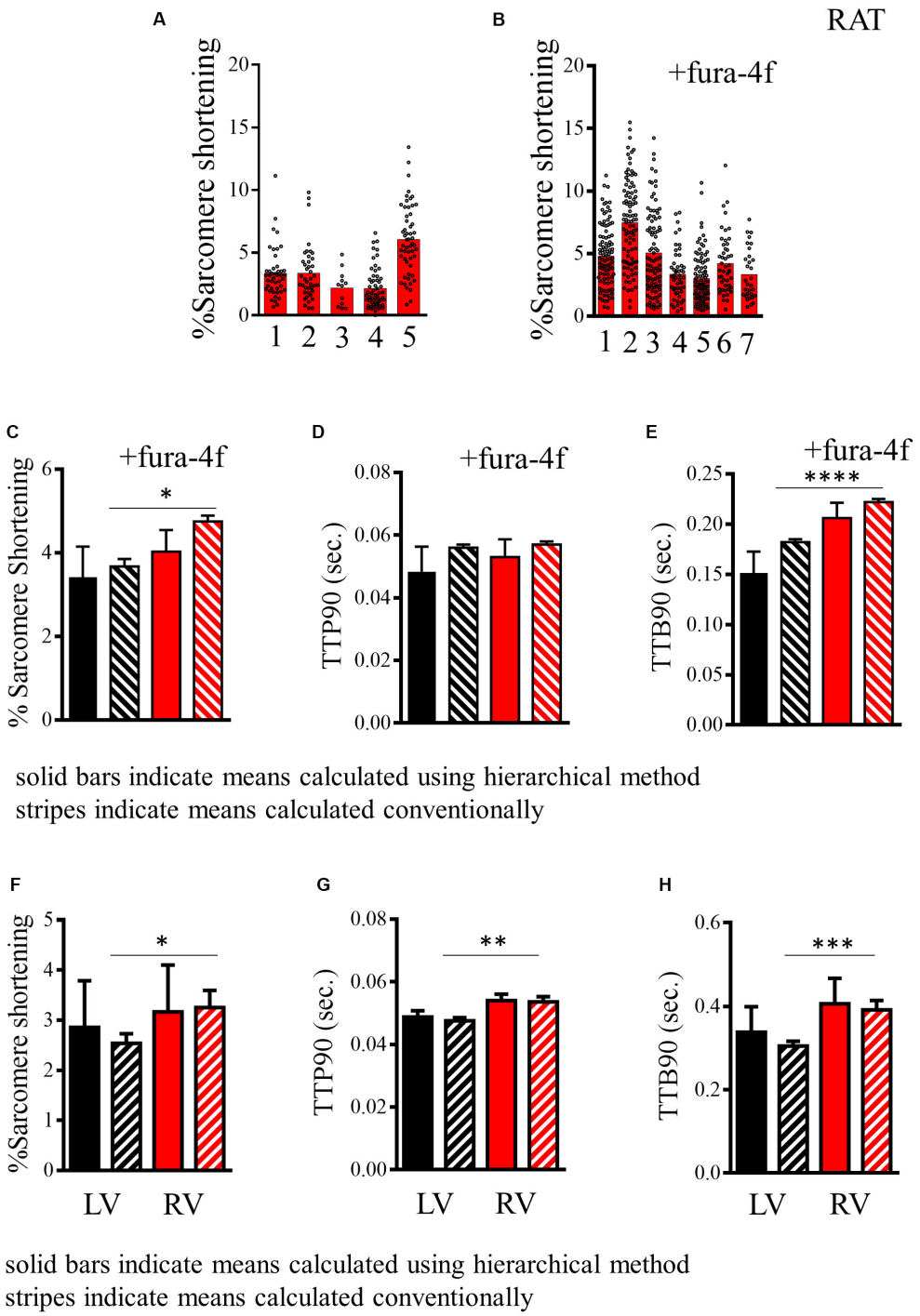

FIGURE 4 | Analysis of contractility of rat cardiomyocytes. **(A,B)** Histogram displaying measurements of the baseline sarcomere shortening of multiple individual preparations of rat cardiomyocytes without and with fura-4f loading. **(C)** Histogram comparing estimated mean and standard deviation of sarcomere shortening in the populations of rat cardiomyocytes presented in A (–Fura-4f black) and B (+Fura-4f red) with hierarchical structure included (solid bars) and assuming all measurements are independent samples (striped bars). **(D)** Histogram comparing estimated mean and standard deviation of TTP90 in populations of rat cardiomyocytes presented in **Supplementary Figure 2C** (–Fura-4f black) and D (+Fura-4f red) with hierarchical structure included (solid bars) and assuming all measurements are independent samples (striped bars). **(E)** Histogram comparing estimated mean and standard deviation of TTP90 in populations of rat cardiomyocytes presented in **Supplementary Figure 2E** (–Fura-4f black) and F (+Fura-4f red) with hierarchical structure included (solid bars) and assuming all measurements are independent samples (striped bars). **(F)** A representation of the estimated mean and standard error of sarcomere shortening of left and right ventricular cardiomyocytes isolated from mice. Datasets assuming a hierarchical structure (solid bars) and assuming no structure (striped bars). **(G)** Representations of the means and standard error of TTP90 of left and right ventricular cardiomyocytes isolated from mice with hierarchical structure (solid) and without (striped). **(H)** Representation of the means and standard error of TTB90 of left and right ventricular cardiomyocytes isolated from mice with hierarchical structure (solid) and without (striped).

group of five to seven independent rat cardiomyocyte isolations derived from measures of sarcomere shortening recorded in the presence of 2 mM Ca^{2+} and stimulated at 1 Hz. As can be seen from the histograms in **Figures 4A,B** plotting results from different preparations, average sarcomere shortening for each preparation shows significant variation in addition to the variable distribution of the individual myocyte measurements around the preparation mean. We present the mean and standard error for these data computed by conventional methods with each measurement assumed to be independent or with correction for hierarchical effects, for rat cells with or without Fura-4f labeling (**Figure 4C**). **Table 2** displays numeric data with relevant statistics allowing comparison of the two datasets. Our analysis indicates an ICC score of 18.5% for % sarcomere shortening for our populations of cells. This suggests a moderate level of clustering, which is observable in the histograms. The common unpaired *t*-test indicates that the difference between the two groups is statistically significant ($p < 0.016$). In **Figure 4F**, we indicate the hierarchical estimate mean and standard error of the two cell populations. Such statistical treatment reveals that there is no difference in the means of the two groups ($p = 0.51$; **Table 2**). The effective degrees of freedom due to hierarchical effects computed by our analysis are 12.1 and 12.3 for the respective samples, indicating that the statistical significance suggested by the common test is the result of significant "pseudo-replication." This analysis indicates that statistical methods acknowledging "hierarchy" are required to firmly test any hypothesized difference between Fura-4f loaded cells and control.

Similar clustering can be observed for the time taken to reach 90% of the peak from baseline (ICC, 28.2% TTP90; **Supplementary Figures 2C,D**). There is no difference between the means estimated for cells with and without Fura-4f loading (**Figure 4D** and **Table 2**). For this parameter, both the common test and the hierarchical test indicate no significant difference ($p = 0.11$ and 0.64, respectively).

Loading cells with Fura-4f appears to lengthen the time taken to reach 90% of the baseline (TTB90), indicating slower relaxation. Clustering can be seen within the different batches of cells (ICC, 16.7%; **Supplementary Figures 2E,F**). The common test suggests that the increase in TTB90 is statistically significant ($p < 0.0001$). The hierarchical estimate means also indicate a longer TTB90 for Fura-4f-loaded cells, but this difference just falls short of statistical significance ($p = 0.06$, df 11.1–10.9; **Figure 4E** and **Table 2**). Once again, the difference indicated by the common test is the result of a large amount of pseudo-replication, with each measurement from a single preparation only accounting for around two theoretical degrees of freedom.

Comparisons of Mouse, Guinea Pig, and Human Myocytes With Rat

Mouse Cardiomyocytes

The mouse is a common model species employed in cardiovascular biology, but the isolation of cardiomyocytes from this animal is more technically challenging than from the rat. Here, we present baseline data derived from measurements of changes in sarcomere length of cells from the left and right ventricles of three individual mice. Greater clustering can be observed for each of the parameters reflecting greater batch-to-batch variability in the cells. This appears to account for most of the variation because cells from left and right ventricles from the same heart seem to be more similar than cells from the same region of different hearts (**Supplementary Figures 3A–C**). Measurements of % sarcomere shortening are moderately clustered (ICC, 30.9%) for left and right ventricular cells, meaning hierarchical statistical methods must be employed (**Table 2**). The analysis we perform applies a test to determine whether hierarchical or common statistical approaches should be employed. Cardiomyocytes derived from right ventricle seem to have a slightly greater mean baseline contractility. The common unpaired *t*-test suggests that this is statistically significant ($p < 0.05$). However, this is not the case for the estimated means due to the correction for pseudoreplication ($p = 0.822$, df < 6; **Figure 4F** and **Table 2**).

Measurements of TTP90 display very little clustering (ICC, 3.4%), the hierarchical analysis is not strictly necessary here. Population and estimated means suggest a longer TTP90 in right ventricular cells. An unpaired *t*-test indicates that this is statistically significant ($p < 0.01$), but this disappears after hierarchical correction ($p = 0.15$, df < 3–5; **Supplementary Figure 3B**).

TTB90 measurements are moderately clustered (ICC, 30.3%; **Table 2** and **Supplementary Figure 3C**). Population and estimated means seem to suggest a slightly longer TTB90 in right ventricular cells on average. The common *t* test indicates that this difference is statistically significant ($p < 0.001$) but again this disappears with correction of clustering and psuedoreplication ($p < 0.4599$, df < 5; **Figure 4H**). We also present a small amount of data for cells isolated from entire mouse hearts, without dissection and loaded with the Ca^{2+} dye Fura-4f in two isolations. Apparently, Fura-4f slightly reduces contractility and lengthens TTB90. This is of course slightly different from the rat data that utilized Fura-4f (**Supplementary Figures 3D–F**).

Human Cardiomyocytes

The CytoCypher HTS system was able to collect significant amounts of data from myocytes prepared from small human heart biopsies due to its speed and ability to analyze all the cells in a dish. **Figure 5** presents measurements from cardiomyocytes isolated from human ventricles and atria explanted from patients with hypertrophic cardiomyopathy. **Figures 5A–E** show results with a ventricular sample: **Figure 5A** shows the morphology of the ventricular myocyte in a bright-field thumbnail image acquired by the CytoCypher system. **Figure 5B** presents plots of sarcomere length over the contraction cycle at different pacing frequencies. For this cell, the largest contraction was observed at 1 Hz. Variation in the baseline contraction can be observed at different pacing frequencies, indicating the sensitivity of this parameter to the experimental conditions. At 2 Hz, the cell became arrhythmic and a transient could not be recorded. Histograms present the average % sarcomere shortening, TTP90, and TTB90 over a range of stimulation frequencies in **Figures 5C–E**.

TABLE 2 | Table describing the mean and standard error of baseline measurements of myocytes from mouse, rat, guinea pig, and human hearts measurements of functional parameters.

			Simple statistics			Hierarchical statistics				*p* values		
Sample	**Prep.**	***n***	**%**	**TTP90**	**TTB90**	**% (ICC)**	**TTP90 (ICC)**	**TTB90 (ICC)**	**Suit.**	***p* values**		
Rat	5	226	3.670 ± 0.180	0.056 ± 0.001	0.182 ± 0.003	3.148 ± 0.730 (18.5)	0.048 ± 0.008 (28.2)	0.151 ± 0.021 (16.7)	YYY	Rat vs. rat + fura		
Rat + Fura	7	510	4.751 ± 0.137	0.057 ± 0.001	0.222 ± 0.003	4.026 ± 0.518	0.053 ± 0.006	0.206 ± 0.015		parameter	Simple	Hierarchical
										%	< 0.0001	0.051
										TTP90	0.55	0.64
										TTB90	< 0.0001	0.06
Mouse LV	3	165	2.539 ± 0.191	0.048 ± 0.001	0.305 ± 0.012	2.854 ± 0.930 (30.9)	0.049 ± 0.002 (3.4)	0.338 ± 0.006 (30.3)	YNY	Mouse LV vs. mouse RV		
Mouse RV	3	84	3.250 ± 0.346	0.054 ± 0.002	0.391 ± 0.023	3.164 ± 0.937	0.054 ± 0.002	0.406 ± 0.061		parameter	Simple	Hierarchical
										%	0.0519	0.82
										TTP90	0.0013	0.15
										TTB90	0.0002	0.46
Guinea Pig	1	71	5.213 ± 0.360	0.228 ± 0.010	0.627 ± 0.021	–	–	–	–	–		
Human LV	1	4	3.202 ± 0.994	0.244 ± 0.040	0.687 ± 0.074	–	–	–	–	–		
Human LA	1	14	0.430 ± 0.161	0.062 ± 0.016	0.446 ± 0.153	–	–	–	–	–		
Human RA	1	5	2.500 ± 0.832	0.218 ± 0.121	0.637 ± 0.131	–	–	–	–	–		

The table describes the statistics generated by conventional and advanced (hierarchical) approaches and includes the results of statistical significance between appropriate samples. The column (suit.) describes whether the advanced test (Y) or the conventional test (N) is sufficient in each case. Results from several preparations are presented using simple statistics (mean ± standard deviation) and using hierarchical statistics (mean ± standard deviation and ICC). The p values column presents the calculations of p using Student's t test or the hierarchical method. Significance is commonly reduced using hierarchical statistics.

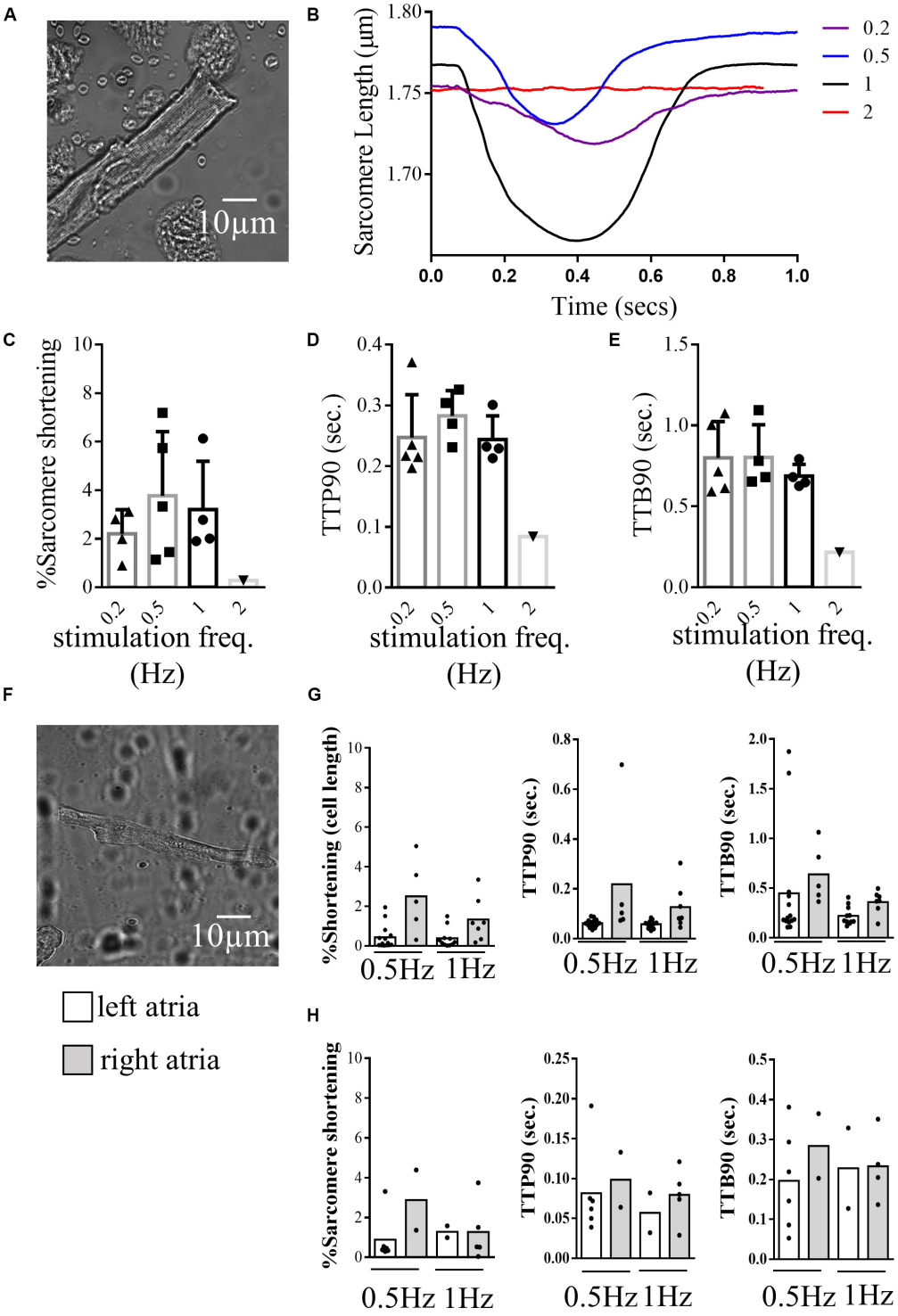

FIGURE 5 | Contractility of human cardiomyocytes. **(A)** Example image of a human ventricular cardiomyocyte isolated from the left ventricle of a patient with hypertrophic cardiomyopathy recorded during contraction analysis by the CytoCypher HTS. **(B)** Example traces of sarcomere shortening during the contraction cycle in the same cell paced at different frequencies. **(C)** Histogram and dot plots demonstrating the percentage sarcomere shortening of ventricular cells at different pacing frequencies. triangle = 0.2 Hz, square = 0.5 Hz, circle (line in bold) = 1 Hz inverted triangle = 2 Hz. **(D)** Histogram and dot plots demonstrating the TTP90 of sarcomere shortening of ventricular cells at different pacing frequencies. **(E)** Histogram and dot plots demonstrating the TTB90 of sarcomere shortening of ventricular cells at different pacing frequencies. **(F)** Example image of a human cardiomyocyte isolated from the left atrial chamber of a patient with hypertrophic cardiomyopathy. **(G)** Histogram and dot plots representing the cell shortening behaviors of cardiomyocytes isolated from the left and right atrial chambers of the same patient, paced at 0.5, and 1 Hz (% cell shortening, TTP90, and TTB90). clear bar = left atria and gray bar = right atria **(H)** Histogram and dot plots representing the sarcomere shortening behaviors of left and right atrial cardiomyocytes isolated from the left and right atria paced at 0.5 and 1 Hz (% sarcomere shortening, TTP90, and TTB90). clear bar = left atria and gray bar = right atria.

Figures 5F–H show results obtained with atrial samples. **Figure 5F** shows the morphology of a cardiomyocyte from the left atria of a patient with hypertrophic cardiomyopathy. The sarcomeric structure of these cells is less well defined than those from rodent or human ventricle. As a result, cell length measurements were more readily visualized by the CytoCypher than measurements from the sarcomere pattern. **Figure 5G** shows results using cell length detection and **Figure 5H** shows the same cells with sarcomere length detection for left and right atria at two stimulation frequencies.

Guinea Pig Cardiomyocytes

The guinea pig is a common model animal in fundamental cardiovascular biology. It is particularly useful for electrophysiological studies due to a closer relationship between the guinea pig and human action potential morphology (ion channel complement) than the rat or mouse. In **Supplementary Figure 4**, we present baseline data for contractility and Ca^{2+} handling in control Dunkin-Hartley guinea pig cardiomyocytes paced at 0.5 Hz. **Supplementary Figure 5A** presents example traces of guinea pig sarcomere shortening and Ca^{2+} transients in Fura-4f-loaded cells. Percentage shortening, TTP90, and TTB 90 were measured by both sarcomere length and cell length procedures (B–G). These measurements reveal the intimate connection between cell shortening and sarcomere shortening. Although the percentage shortening is similar to the rat and mouse, the guinea pig shows slower contraction kinetics, especially contraction onset as indicated by TTP90 (**Table 2**).

Hierarchical Statistics of Ca^{2+} Transients

Ca^{2+} transients may be measured simultaneously with contractility. In **Figure 6**, we present data from measurements of changes in Ca^{2+} activity within mouse and rat cardiomyocytes loaded with Fura-4F. Example Ca^{2+} transients for rat and mouse are presented in **Figures 6A,B**, respectively. The peak heights of the Ca^{2+} transients (delta F/F0) are moderately clustered in mouse and rat cells (ICC, 26.6%; **Supplementary Figures 5A,D**). Population and hierarchical estimated means indicate little difference between the F/F0 values for rat and mouse. Neither the population nor hierarchically estimated means are statistically different (population, $p = 0.23$; estimate, $p = 0.8$ df $14.9 + 13.5$; **Figure 6C**). Intriguingly, the TTP90 is once again the least clustered parameter (ICC, 2.7%), but it is still suggested to require a hierarchical approach (**Supplementary Figures 5B,E**). The TTP90 is longer in mouse than in rat; this is statistically significant according to common ($p < 0.0001$) and hierarchical methods ($p < 0.0001$, df $14 + 10$; **Figure 6D**). The data for the TTB90 parameter are moderately clustered (ICC, 13.4%; **Supplementary Figures 5C,F**). Like TTP90, TTB90 is longer in mouse than in rat. This is suggested to be significantly different by the common ($p < 0.0001$) and hierarchical methodologies ($p < 0.0001$, df $14 + 12$; **Figure 5E**). In the guinea pig, the height of the Ca^{2+} transient (delta F/F0) is similar to mouse and rat, but the onset of Ca^{2+} release is slower, and the decline of Ca^{2+} is slower (**Supplementary Figures 4H–J**) in common with the contractile transients (**Table 3**).

Morphological Analysis

A morphological analysis of the entire cell can be performed using the thumbnails acquired in the course of the analysis runs, allowing the derivation of several morphological parameters of interest. We present the values acquired for a population of control rat cells (**Table 4**). In **Supplementary Figure 1**, we present a comparison of rat and guinea pig cardiomyocyte morphologies. Between 50 and 100 cells from a single rat and a single guinea pig isolation were assessed. Although visually similar (**Supplementary Figures 1A,B**), the two cell types diverge in several respects. The sarcomere length of guinea pig cells is shorter than the rat (**Supplementary Figure 1C**). Guinea pig cells have a greater area (**Supplementary Figure 1D**) and perimeter length (**Supplementary Figure 1E**) than rat cells. They are also longer (**Supplementary Figure 1F**) and wider (**Supplementary Figure 1G**). Interestingly, it appears that rat cells are more linear (higher eccentricity) and less lobular (higher solidity) than guinea pig cells (**Supplementary Figures 1H,I** and **Table 4**). The higher linearity of rat cells may suggest that there is some evolutionary benefit to a higher aspect ratio for this species. From the perspective of solidity, these data suggest that rat cells form fewer branching contacts with their neighboring cells or disaggregate more fully upon isolation.

Assessment of Small Molecules That Act on Myocyte Contractility

Using the CytoCypher HTS, it is now possible to dramatically speed up the measurement of the effects of agonists and antagonists on contractility and Ca^{2+} transients. Many measurements may be made on a single preparation of myocytes and so the confounding effects of inter-sample variability are reduced by performing a larger number of tests on the same preps, giving individual runs internal consistency. If technical replicates are performed, the aggregate data can be analyzed with hierarchical statistics; this improves the statistical power of the experiments by reducing the intrinsic variability of the samples, introduced mainly by preparation effects. As shown above, this dramatically improves the statistical power of measurements. **Figure 7** shows an example of a simple drug screening protocol using a single rat myocyte preparation with several established β-agonists and antagonists, recently developed drugs that act on myocyte contractility and novel compounds that are proposed to have "recoupling" activity (Tadano et al., 2010; Papadaki et al., 2015; Sheehan et al., 2018). The 13 compounds were tested in about 5 h. Myocytes are kept at 4°C and plated onto laminin-coated dishes in three batches at approximately 2-h intervals to avoid run down in older preparations of cardiomyocytes. For each dish, a baseline is measured and then the solution is changed to one containing the drug. Most of the time is taken up with equilibration periods: if the compounds could be loaded in parallel in multi-well dishes, recording could be speeded up a further 5- to 10-fold (Juni et al., 2019).

In our analysis, myocytes with zero% shortening are included in the average to avoid bias (**Figure 7A**); however, they are excluded from the TTP90 and TTB90 averages since rate processes are only relevant when contraction occurs

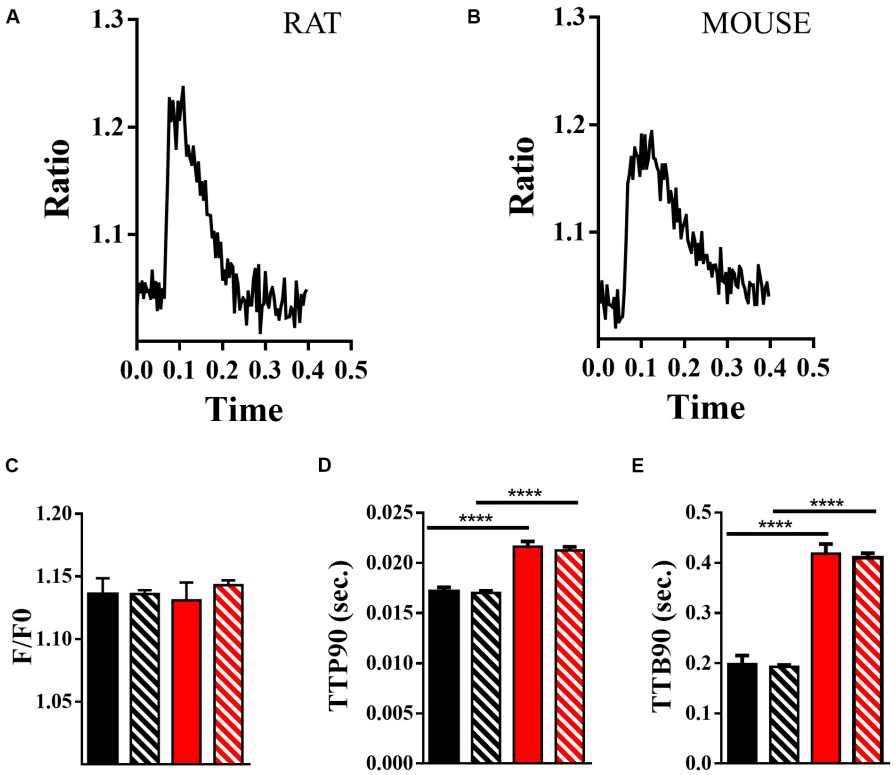

FIGURE 6 | Measurement of Ca^{2+} transients using Fura-4f. **(A)** Example Ca^{2+} transient from a rat ventricular cardiomyocyte loaded with fura-4f. **(B)** Example Ca^{2+} transient of a mouse ventricular cardiomyocyte loaded with fura-4f. **(C)** Comparison of F/F0 of rat (black) and mouse (red) Ca^{2+} transients, means and standard error with hierarchical effects included (solid) and without (striped). **(D)** Comparison of TTP90 of Ca^{2+} transients of rat (black) and mouse (red) Ca^{2+} transients, means and standard error with hierarchical effects included (solid) and without (striped; $^{****}p < 0.0001$). **(E)** Comparison of TTB90 of Ca^{2+} transients of rat (black) and mouse (red) Ca^{2+} transients, means and standard error with hierarchical effects included (solid) and without (striped; $^{****}p < 0.0001$).

(**Figures 7B,C**). The results for individual cells are also presented in **Supplementary Figure 6** for each of the three parameters. The result for dobutamine is as expected. Inotropic and lusitropic changes are evident with an increase in shortening amplitude accompanied by faster contraction (TTP90 less) and relaxation (TTB90 less). The myosin activator OM in contrast produces an increased mean contraction amplitude accompanied by slowing of both contraction and relaxation, as found previously, indicating that it enhances contractility by prolonging the contractile event (Woody et al., 2018; Juni et al., 2019). The myosin inhibitor Mavacamten reduces contractile amplitude to the point where so few myocytes are contracting that TTP90 and TTB90 cannot be measured as previously shown (Green et al., 2016). The effects of the other compounds were not particularly distinctive. Atenolol increased the% shortening and decreased TTB90 similar to dobutamine; this effect was observed in two further screens (see **Supplementary Figure 7**). Nebivolol and EGCG both increased TTB90 by about 20% but only the Nebivolol effect was consistently found. Nebivolol, ECG, and EGCG have been proposed as desensitizers, but may also have additional actions (Nebivolol as a beta blocker and EGCG as an inotrope; Feng et al., 2012; Stücker et al., 2017). None of these compounds showed a reduction of% shortening or reduction of TTB90 indicative of enhanced relaxation in our study. Most of the compounds proposed to affect the dobutamine response of mutant myocytes ("recouplers": Silybin A and B, dehydrosilybin A and B, resveratrol, and novobiocin) had little effect on the baseline response in wild type as predicted (Papadaki et al., 2015; Wilkinson et al., 2015; Sheehan et al., 2018).

To test for reproducibility of the drug screening experiment, we repeated it three times and analyzed the data with hierarchical statistics as well as simple statistics (**Supplementary Figure 7A**). In comparison to the conventional approach, the SEM adjusted with hierarchical statistics were much larger, reducing the chances of false-positive results. Dobutamine, OM, and Mavacamten effects remained significant, and significant changes were uncovered in SilybinB, SilybinA, ECG, Atenolol, DHSA, and EGCG. Moreover, drugs such as Resveratrol and EGCG demonstrated opposing relationships in the change of contractile force relative to baseline conditions before and after adjusting with hierarchical statistics. **Supplementary Figure 7B** illustrates the ratio change between treatment and baseline contractility values and were subsequently expressed as a percentage.

We conclude that this type of screen can identify effects of small molecules upon the relevant parameters of myocyte contractility rapidly and does not produce false positives, as is evident when repeats of the screen are compared

TABLE 3 | Baseline measurements of calcium in myocytes from mouse, rat, and guinea pig using Fura-4f.

			Simple			Hierarchical				
	Prep.	*n*	F/F0	TTP90	TTB90	F/F0	TTP90	TTB90	Suit.	*p* values
Rat	6	505	1.136 ± 0.003	0.017 ± 0.0002	0.193 ± 0.004	1.134 ± 0.013	0.017 ± 0.0004	0.198 ± 0.019	YYY	Rat vs. Mouse
										F/F0
										Simple 0.157
										Hierarchical 0.802
Mouse	7	311	1.143 ± 0.004	0.021 ± 0.0004	0.411 ± 0.009	1.131 ± 0.014	0.022 ± 0.0005	0.418 ± 0.017	–	Mouse vs. Guinea Pig
										F/F0
										Simple <0.0001
										Hierarchical –
Guinea Pig	1	75	1.196 ± 0.001	0.083 ± 0.006	0.564 ± 0.016	–	–	–	–	Guinea Pig vs. Rat
										F/F0
										Simple <0.0001
										Hierarchical –

				TTP90	TTB90
				<0.0001	<0.0001
				<0.0001	<0.0001
				<0.0001	<0.0001
				–	–
				<0.0001	<0.0001
				–	–

Comparison of the mean and standard error of parameters of calcium handling measured by Fura-4f dye labeling of rat, mouse, and guinea pig cardiomyocytes. Advanced statistical tests are applied to mouse and rat populations to indicate statistically significant differences between the kinetic parameters. Results from a number of preparations are presented using simple statistics (mean ± standard deviation) and using hierarchical statistics (mean ± standard deviation and (ICC)]. The p values column presents the calculations of p using Student's t test or the hierarchical method.

TABLE 4 | Comparison of morphology of rat and guinea pig cells.

		Mean	SEM	*n*	*p* value
Sarcomere	Rat	1.826	0.005	101	0.0001
	Guinea Pig	1.776	0.01	50	
Area	Rat	3687	85.96	101	0.0001
	Guinea Pig	4991	168.2	50	
Length	Rat	133.3	1.855	101	0.0001
	Guinea Pig	161.0	3.432	50	
Width	Rat	37.39	0.64	101	0.0002
	Guinea Pig	42.69	1.22	50	
Perimeter	Rat	386.9	6.91	101	0.0001
	Guinea Pig	498.9	10.64	50	
Eccentricity	Rat	0.956	0.002	101	0.5
	Guinea Pig	0.959	0.004	50	
Solidity	Rat	0.859	0.005	101	0.0001
	Guinea Pig	0.815	0.007	50	

Comparison of basic morphological parameters of cardiomyocytes isolated from Rat and Guinea Pig acquired in the process of generating functional measurements on the CytoCypher and analyzed by our automated script and the CytoSpectre program. Analysis was performed with conventional statistical tests as only single preparations were used.

(**Supplementary Figures 7A,B**). An initial screen could be performed this way, followed up by more extensive tests of the compounds that can be followed up by more extensive tests of the compounds that show promise; moreover, the screen uses only a small amount of solution (2.5 ml), but a much smaller volume is possible, enabling rare or expensive compounds to be assessed.

Dose–response curves are readily constructed using the CC-HTS. With a single preparation of cells, we can obtain two dose–response curves in 5 h, tracking 10–20 cells per condition. We demonstrate here dose–response curves for three contrasting drugs that act upon myocyte contractility. **Figures 8A–C** show the dose–response curve for dobutamine in the presence of 50 nM ICI 118,551. The increase in% shortening was almost linear and did not satisfactorily fit a simple binding equation (**Figure 8A**); however, TTP90 (**Figure 8B**); and TTB90 (**Figure 8C**) showed simple saturation kinetics with EC50 of 0.14 ± 0.06 μM and 0.21 ± 0.09 μM, respectively. Scatter plots showing values of individual myocytes can be found in **Supplementary Figures 8A–C**.

Figures 8D–F show the inhibition of contractility by Mavacamten. Percent shortening was well fitted to a simple binding equation with EC50 of 0.8 ± 0.16 μM (**Figure 8D**). TTP90 was reduced by 18% with an EC50 of 0.37 ± 0.20 μM; the significance of the fit is reduced since the number of contracting myocytes diminished rapidly at the higher concentrations (**Figure 8E**). For TTB90, an EC50 of 0.9 ± 0.9 μM was estimated from the small number of data points available (**Figure 8F**). Scatter plots showing values of individual samples can be found in **Supplementary Figure 8**.

All three parameters were increased by OM (**Figures 8G–I**); however, at concentrations above 3 μM, we found that the majority of cells became hypercontractile and rapidly rounded up. Although the concentration range was lower than ideal, the data fits to a simple binding equation were obtained. The

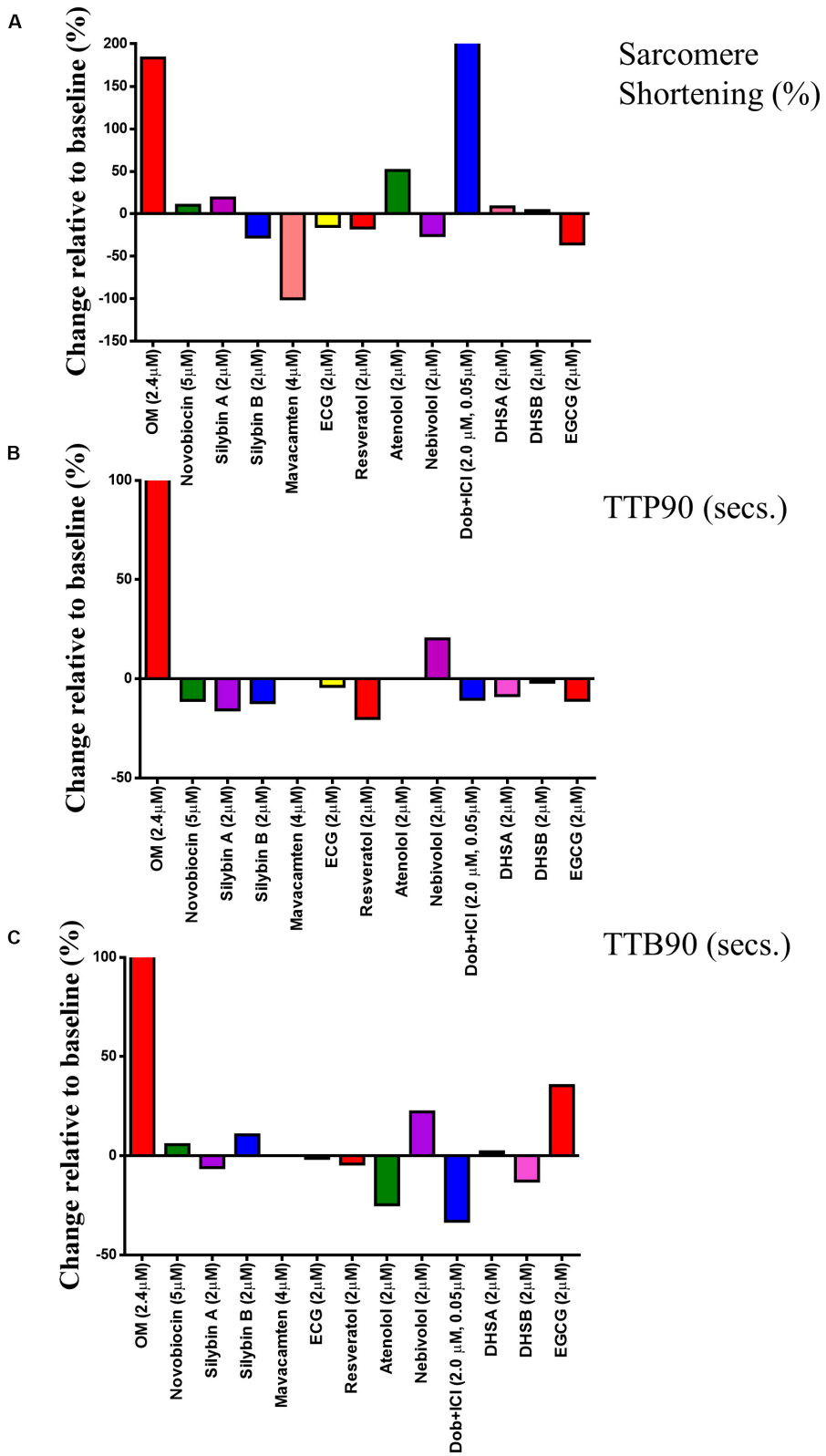

FIGURE 7 | Single concentration screen for compounds with potential to affect myocyte contractility. The effects of 13 compounds were tested using a single preparation of rat myocytes. **(A–C)** show the fractional change in each parameter due to the compound: $y = 100 \times$ (mean with compound/mean baseline)-100. For original data, see **Supplementary Figure 6**. These data are constructed from a dataset of between 25 and 30 cardiomyocytes.

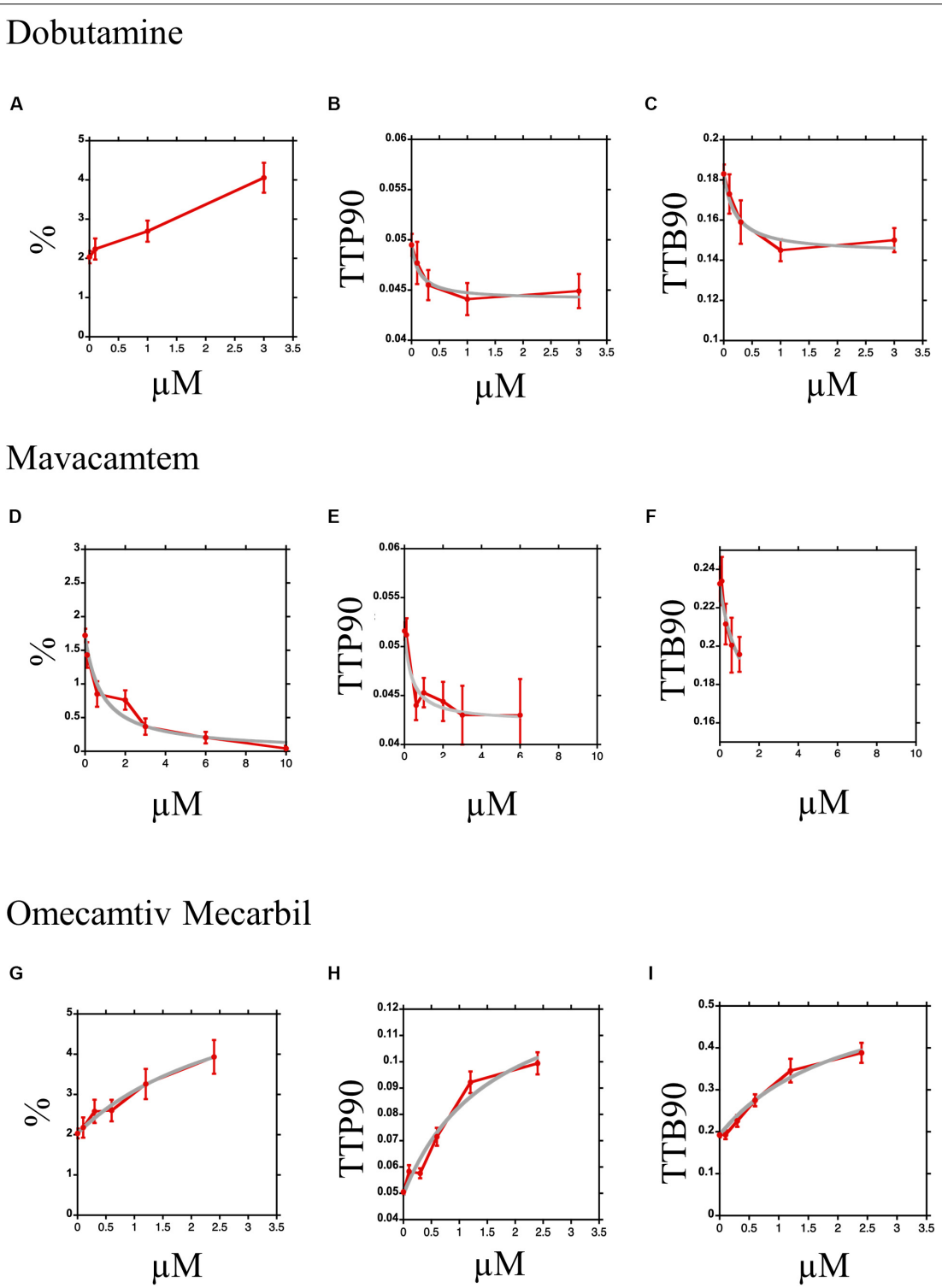

FIGURE 8 | Dose–response curves for Dobutamine, Omecamtiv Mecarbil, and Mavacamten. **(A–C)** Dose–response curve for myocyte contraction in the presence of Dobutamine and 0.05 μM ICI 118,551. The mean and standard error are plotted in red; the data for TTP90 and TTB90 are fitted to the equation $y = y0–[Bm.(dobu)/(EC50 + (dobu))]$ in gray. The % shortening parameter could not be fitted. **(D,E)** Dose–response curve for myocyte contraction in the presence of Omecamtiv Mecarbil. The mean and standard error are plotted in red; the data for all three parameters are fitted to the equation $y = y0 + [Bm.(OM)/(EC50 + (OM))]$ in gray. **(G–I)** Dose–response curves for myocyte contraction in the presence of Mavacamten. The mean and standard error are plotted in red; the data for all three parameters are fitted to the equation $y = y0–[y0.(mava)/(EC50 + (mava))]$ in gray.

curve fitting indicated that OM increased% shortening by 216% (**Figure 8G**), TTP90 by 175% (**Figure 8H**), and TTB90 by 202% (**Figure 8I**) with EC50 of 3.1 ± 1.3 μM, 1.8 ± 0.9 μM, and 2.2 ± 0.9 μM respectively. Scatter plots showing values of individual samples can be found in **Supplementary Figure 8**.

DISCUSSION

The introduction of a high-throughput method for measuring myocyte contractility and Ca^{2+} transients has the potential to revolutionize the study of cardiomyocyte pharmacology, physiology, and pathophysiology. We have shown that it is now possible to collect rapidly large amounts of data from a single myocyte preparation enabling comparisons to be made using simple statistics. This is ideal for drug screens and dose–response studies. The quantity of data collected allows robust hierarchical statistical analysis that is of value when comparing different cell preparations. The speed of data collection means unstable myocyte preparations can now be more fully exploited.

Other researchers, for example, Harmer et al. (2012), have attempted to increase the productivity of analyses of adult cardiomyocytes, but the CytoCypher represents a comprehensive system for this. Myocardial preparations of intermediate complexity have existed for longer than the isolated cardiomyocyte approach; each has advantages and disadvantages. Papillary muscles and ventricular strips have been employed in organ bath experiments for decades and have allowed researchers to assess the effect of pathological and pharmacological interventions on mechanically loaded preparations (Frisk et al., 2016). However, these preparations are not illustrative of specific layers of the compacted working, ventricular myocardium. More recently, researchers have tried to produce engineered heart tissue constructs from induced pluripotent stem cells (Hirt et al., 2014). Despite being contractile and capable of producing physiologically relevant force, the phenotype of the cells is not consistent with preparations from native hearts. The preparation of ultra-thin myocardial slices using microtomy offers a useful approach to assess single cells and their conduction properties from bona fide ventricular myocardial tissue (Watson et al., 2019a,b). Slice preparations preserve the multi-cellularity, architecture, and physiological environment of the ventricular tissue. These preparations can be manipulated mechanically and survive well in culture. As these preparations are only a few cells thick, the observer is still able to interrogate the structural phenotype of individual cells within a layer using conventional confocal microscopy techniques. Currently, this methodology is limited to larger rodents, obviating the analysis of tissue from mouse models and so precluding the acquisition of important data from hearts manipulated with genetic approaches and tools.

Until now, myocyte contraction measurements have been low-throughput assays. They require multiple heart isolations to collect sufficient data that generate well-powered experiments to distinguish changes due to treatments from inter-prep variability. The CC-HTS system avoids most of these problems by measuring contractility (and Ca^{2+}) in large numbers of myocytes from a single animal in a short time while cells are viable. Richer datasets are produced that are more representative of the entire population of cells present in the native myocardial sample.

This has enabled us to address the question of how to handle the statistics of inter-preparation and within-preparation variability. By analysis of many hundreds of myocytes, the problem of psuedoreplication leading to false-positive results when data from different preparations are combined is laid bare. This clearly has implications for many current studies that do not take this into account. HTS allows us to collect enough data to confirm or deny differences between treatments or between cell types with the appropriate statistical routine to ensure the statistical power is adequate.

High-throughput systems reduce the pseudoreplication problem since all measurements can be made on one preparation within a short period of time, thus legitimizing the use of simple statistics (Juni et al., 2019). Examples of such measurements are shown for single concentration drug screens and dose–response curves. The HTS method also allows us to study rare or unstable myocytes, such as myocytes derived from human heart material that may have been impossible to measure previously. From a practical point of view, with increased measurement speed, it now becomes possible (in some species/conditions) to study almost all the myocytes in a single preparation, which is a major advantage when myocytes come from rare or expensive sources, such as transgenic mice.

We propose two experimental areas in which the deployment of high-throughput analyses of isolated cardiomyocytes will be advantageous. Firstly, in drug screening where the inter-sample variation is extremely problematic, we propose that the increase in productivity should be used to screen multiple drugs. Secondly, where the baseline characteristics of populations of animals, such as those used for disease modeling or genetic mutants where inter-preparation effects are unavoidable, the high-throughput approach can be used in tandem with advanced statistical approaches to eliminate false-positive effects.

CONCLUSION

The introduction of HTS methodology for myocytes has increased the speed of measurement dramatically and improved statistical power while reducing the number of myocyte preparations needed for a study.

DATA AVAILABILITY STATEMENT

The datasets generated for this study are available on request to the corresponding author.

ETHICS STATEMENT

The studies involving human participants were reviewed and approved by United Kingdom Human Tissue Authority and Research Ethics Committees. The patients/participants provided

their written informed consent to participate in this study. The animal study was reviewed and approved by Imperial College AWERB – Imperial College London, United Kingdom.

AUTHOR CONTRIBUTIONS

PW and SM conceived the study, performed experiments, and authored the manuscript. ST and AF performed experiments. KM assisted in the preparation of the manuscript. All authors contributed to the article and approved the submitted version.

FUNDING

This study was supported by British Heart Foundation RG/17/13/33173 and PG/17/3/32722 (PW), and the purchase of the CytoCypher HTS was made possible by BHF IG/33974 (SM, PW, and KM).

ACKNOWLEDGMENTS

We would like to acknowledge Mr. Peter O'Gara for his isolation of cardiomyocytes and Mr. Stephen Rothery for producing our image segmentation macro to be used in conjunction with the Cytospectre^{TM} program.

SUPPLEMENTARY MATERIAL

The Supplementary Material for this article can be found online at: https://www.frontiersin.org/articles/10.3389/fphys.2020.00612/full#supplementary-material

REFERENCES

Abi-Gerges, N., Pointon, A., Pullen, G. F., Morton, M. J., Oldman, K. L., Armstrong, D., et al. (2013). Preservation of cardiomyocytes from the adult heart. *J. Mol. Cell. Cardiol.* 64, 108–119. doi: 10.1016/j.yjmcc.2013.09.004

Bers, D. M. (2002). Cardiac excitation-contraction coupling. *Nature* 415, 198–205. doi: 10.1038/415198a

Brandenburg, S., Kohl, T., Williams, G. S. B., Gusev, K., Wagner, E., Rog-Zielinska, E. A., et al. (2016). Axial tubule junctions control rapid calcium signaling in atria. *J. Clin. Invest.* 126, 3999–4015. doi: 10.1172/JCI88241

Davia, K., Hajjar, R. J., Terracciano, C. M., Kent, N. S., Ranu, H. K., O'Gara, P., et al. (1999). Functional alterations in adult rat myocytes after overexpression of phospholamban with use of adenovirus. *Physiol. Genomics* 1, 41–50. doi: 10.1152/physiolgenomics.1999.1.2.41

Fast, V. G. (2005). Simultaneous optical imaging of membrane potential and intracellular calcium. *J. Electrocardiol.* 38, 107–112. doi: 10.1016/j.jelectrocard.2005.06.023

Feng, W., Hwang, H. S., Kryshtal, D. O., Yang, T., Padilla, I. T., Tiwary, A. K., et al. (2012). Coordinated regulation of murine cardiomyocyte contractility by nanomolar (-)-epigallocatechin-3-gallate, the major green tea catechin. *Mol. Pharmacol.* 82, 993–1000. doi: 10.1124/mol.112.079707

Frisk, M., Ruud, M., Espe, E. K. S., Aronsen, J. M., Røe, ÅT., Zhang, L., et al. (2016). Elevated ventricular wall stress disrupts cardiomyocyte t-tubule structure and calcium homeostasis. *Cardiovasc. Res* 112, 443–451. doi: 10.1093/cvr/cvw111

Glukhov, A. V., Balycheva, M., Sanchez-Alonso, J. L., Ilkan, Z., Alvarez-Laviada, A., Bhogal, N., et al. (2015). direct evidence for microdomain-specific localization and remodeling of functional L-Type calcium channels in rat and human atrial myocytes. *Circulation* 132, 2372–2384. doi: 10.1161/CIRCULATIONAHA.115.018131

Green, E. M., Wakimoto, H., Anderson, R. L., Evanchik, M. J., Gorham, J. M., Harrison, B. C., et al. (2016). A small-molecule inhibitor of sarcomere contractility suppresses hypertrophic cardiomyopathy in mice. *Science* 351, 617–621. doi: 10.1126/science.aad3456

Harding, S. E., Jones, S. M., O'Gara, P., del Monte, F., Vescovo, G., and Poole-Wilson, P. A. (1992). Isolated ventricular myocytes from failing and non-failing human heart; the relation of age and clinical status of patients to isoproterenol response. *J. Mol. Cell. Cardiol.* 24, 549–564. doi: 10.1016/0022-2828(92)91843-T

Harmer, A. R., Abi-Gerges, N., Morton, M. J., Pullen, G. F., Valentin, J. P., and Pollard, C. E. (2012). Validation of an in vitro contractility assay using canine ventricular myocytes. *Toxicol. Appl. Pharmacol.* 260, 162–172. doi: 10.1016/j.taap.2012.02.007

Helmes, M. (2017). *High Throughput Investigation of EC Coupling in Isolated Cardiac Myocytes. YouTube*. Available online at: http://www.youtube.com/watch?v=ytmXaOj7jss (accessed December 8, 2019).

Hirt, M. N., Boeddinghaus, J., Mitchell, A., Schaaf, S., Bornchen, C., Muller, C., et al. (2014). Functional improvement and maturation of rat and human engineered heart tissue by chronic electrical stimulation. *J. Mol. Cell. Cardiol.* 74, 151–161. doi: 10.1016/j.yjmcc.2014.05.009

Juni, R. P., Kuster, D. W. D., Goebel, M., Helmes, M., Musters, R. J. P., van der Velden, J., et al. (2019). Cardiac microvascular endothelial enhancement of cardiomyocyte function is impaired by inflammation and restored by empagliflozin. *JACC. Basic to Transl. Sci.* 4, 575–591. doi: 10.1016/j.jacbts.2019.04.003

Kartasalo, K., Pölönen, R.-P., Ojala, M., Rasku, J., Lekkala, J., Aalto-Setälä, K., et al. (2015). CytoSpectre: a tool for spectral analysis of oriented structures on cellular and subcellular levels. *BMC Bioinformatics* 16:344. doi: 10.1186/s12859-015-0782-y

Lyon, A. R., Bannister, M. L., Collins, T., Pearce, E., Sepehripour, A. H., Dubb, S. S., et al. (2011). SERCA2a gene transfer decreases sarcoplasmic reticulum calcium leak and reduces ventricular arrhythmias in a model of chronic heart failure. *Circ. Arrhythm. Electrophysiol.* 4, 362–372. doi: 10.1161/CIRCEP.110.961615

Miragoli, M., Sanchez-Alonso, J. L., Bhargava, A., Wright, P. T., Sikkel, M., Schobesberger, S., et al. (2016). Microtubule-dependent mitochondria alignment regulates calcium release in response to nanomechanical stimulus in heart myocytes. *Cell Rep.* 14, 140–151. doi: 10.1016/j.celrep.2015.12.014

Molina, C. E., Johnson, D. M., Mehel, H., Spätjens, R. L. H. M. G., Mika, D., Algalarrondo, V., et al. (2014). Interventricular differences in β-adrenergic responses in the canine heart: role of phosphodiesterases. *J. Am. Hear. Assoc. Cardiovasc. Cerebrovasc. Dis.* 3:e000858. doi: 10.1161/JAHA.114.000858

Nikolaev, V. O., Moshkov, A., Lyon, A. R., Miragoli, M., Novak, P., Paur, H., et al. (2010). β2-adrenergic receptor redistribution in heart failure changes cAMP compartmentation. *Science* 327, 1653–1657. doi: 10.1126/science.1185988

Papadaki, M., Vikhorev, P. G., Marston, S. B., and Messer, A. E. (2015). Uncoupling of myofilament Ca2+-sensitivity from troponin I phosphorylation by mutations can be reversed by Epigallocatechin-3-Gallate. *Cardiovasc. Res.* 108, 99–110. doi: 10.1093/cvr/cvv181

Paur, H., Wright, P. T., Sikkel, M. B., Tranter, M. H., Mansfield, C., O'Gara, P., et al. (2012). High levels of circulating epinephrine trigger apical cardiodepression in a β(2)-Adrenoceptor/Gi-Dependent manner: a new model of takotsubo cardiomyopathy. *Circulation* 126, 697–706. doi: 10.1161/CIRCULATIONAHA.112.111591

Pavlović, D., McLatchie, L. M., and Shattock, M. J. (2010). The rate of loss of T-tubules in cultured adult ventricular myocytes is species dependent. *Exp. Physiol.* 95, 518–527. doi: 10.1113/expphysiol.2009.052126

Sanchez-Alonso, J. L., Bhargava, A., O'Hara, T., Glukhov, A. V., Schobesberger, S., Bhogal, N. K., et al. (2016). Microdomain-specific modulation of L-Type calcium channels leads to triggered ventricular arrhythmia in heart failure. *Circ. Res.* 119, 944–955. doi: 10.1161/circresaha.116.308698

Sheehan, A., Messer, A., Papadaki, M., Choudhry, A., Kren, V., Biedermann, D., et al. (2018). Molecular defects in cardiac myofilament Ca2+- regulation due

to cardiomyopathy-linked mutations can be reversed by small molecules binding to troponin. *Front. Physiol.* 9:243. doi: 10.3389/fphys.2018.00243

Sikkel, M. B., Francis, D. P., Howard, J., Gordon, F., Rowlands, C., Peters, N. S., et al. (2017). Hierarchical statistical techniques are necessary to draw reliable conclusions from analysis of isolated cardiomyocyte studies. *Cardiovasc. Res.* 113, 1743–1752. doi: 10.1093/cvr/cvx151

Stark, J. C. C., Haydock, S. F., Foo, R., Brown, M. J., and Harding, S. E. (2004). Effect of overexpressed adenylyl cyclase VI on beta 1- and beta 2-adrenoceptor responses in adult rat ventricular myocytes. *Br. J. Pharmacol.* 143, 465–476. doi: 10.1038/sj.bjp.0705976

Stücker, S., Kresin, N., Carrier, L., and Friedrich, F. W. (2017). Nebivolol desensitizes myofilaments of a hypertrophic cardiomyopathy mouse model. *Front. Physiol.* 8:558. doi: 10.3389/fphys.2017.00558

Szentadrassy, N., Banyasz, T., Biro, T., Szabo, G., Toth, B. I., Magyar, J., et al. (2005). Apico–basal inhomogeneity in distribution of ion channels in canine and human ventricular myocardium. *Cardiovasc. Res.* 65, 851–860. doi: 10.1016/j.cardiores.2004.11.022

Tadano, N., Du, C.-K., Yumoto, F., Morimoto, S., Ohta, M., Xie, M.-F., et al. (2010). Biological actions of green tea catechins on cardiac troponin C. *Br. J. Pharmacol.* 161, 1034–1043. doi: 10.1111/j.1476-5381.2010.00942.x

Watson, S. A., Terracciano, C. M., and Perbellini, F. (2019a). Myocardial sices: an intermediate complexity platform for translational cardiovascular research. *Cardiovasc. Drugs Ther.* 33, 239–244. doi: 10.1007/s10557-019-06853-5

Watson, S., Duff, J., Bardi, I., Zabielska, M., Atanur, S., Jabbour, R., et al. (2019b). Biomimetic electromechanical stimulation to maintain adult myocardial slices in vitro. *Nat. Commun.* 10:2168. doi: 10.1038/s41467-019-10175-3

Wilkinson, R., Song, W., Smoktunowicz, N., and Marston, S. (2015). A dilated cardiomyopathy mutation blunts adrenergic response and induces contractile dysfunction under chronic angiotensin II stress. *Am. J. Physiol. Heart Circ. Physiol.* 309, H1936–H1946. doi: 10.1152/ajpheart.00327.2015

Wokosin, D. L., Loughrey, C. M., and Smith, G. L. (2004). Characterization of a range of fura dyes with two-photon excitation. *Biophys. J.* 86, 1726–1738. doi: 10.1016/s0006-3495(04)74241-1

Woody, M. S., Greenberg, M. J., Barua, B., Winkelmann, D. A., Goldman, Y. E., and Ostap, E. M. (2018). Positive cardiac inotrope omecamtiv mecarbil activates muscle despite suppressing the myosin working stroke. *Nat. Commun.* 9:3838.

Wright, P. T., Bhogal, N. K., Diakonov, I., Pannell, L. M. K., Perera, R. K., Bork, N. I., et al. (2018a). Cardiomyocyte membrane structure and cAMP compartmentation produce anatomical variation in β2AR-cAMP Responsiveness in murine hearts. *Cell Rep.* 23, 459–469. doi: 10.1016/j.celrep.2018.03.053

Wright, P. T., Sanchez-Alonso, J. L., Lucarelli, C., Alvarez-Laviada, A., Poulet, C. E., Bello, S. O., et al. (2018b). Partial mechanical unloading of the heart disrupts L-Type calcium channel and beta-adrenoceptor signaling microdomains. *Front. Physiol.* 9:1302. doi: 10.3389/fphys.2018.01302

Yue, X., Zhang, R., Kim, B., Ma, A., Philipson, K. D., and Goldhaber, J. I. (2017). Heterogeneity of transverse-axial tubule system in mouse atria: remodeling in atrial-specific Na+–Ca2 + exchanger knockout mice. *J. Mol. Cell. Cardiol.* 108, 50–60. doi: 10.1016/J.YJMCC.2017.05.008

Conflict of Interest: The authors declare that the research was conducted in the absence of any commercial or financial relationships that could be construed as a potential conflict of interest.

frontiers in Physiology

ORIGINAL RESEARCH
published: 21 July 2020
doi: 10.3389/fphys.2020.00815

Large-Scale Contractility Measurements Reveal Large Atrioventricular and Subtle Interventricular Differences in Cultured Unloaded Rat Cardiomyocytes

*Edgar E. Nollet[1], Emmy M. Manders[2], Max Goebel[1], Valentijn Jansen[1], Cord Brockmann[1], Jorrit Osinga[1], Jolanda van der Velden[1], Michiel Helmes[1,2] and Diederik W. D. Kuster[1]**

[1] Department of Physiology, Amsterdam UMC, Vrije Universiteit Amsterdam, Amsterdam Cardiovascular Sciences, Amsterdam, Netherlands, [2] CytoCypher BV, Wageningen, Netherlands

OPEN ACCESS

Edited by:
Henk Granzier, The University of Arizona, United States

Reviewed by:
Mei Methawasin, The University of Arizona, United States
Olivier Cazorla, Université de Montpellier, France

***Correspondence:**
Diederik W. D. Kuster
d.kuster@amsterdamumc.nl

Specialty section:
This article was submitted to Striated Muscle Physiology, a section of the journal Frontiers in Physiology

Received: *20 December 2019*
Accepted: *18 June 2020*
Published: *21 July 2020*

Citation:
Nollet EE, Manders EM, Goebel M, Jansen V, Brockmann C, Osinga J, van der Velden J, Helmes M and Kuster DWD (2020) Large-Scale Contractility Measurements Reveal Large Atrioventricular and Subtle Interventricular Differences in Cultured Unloaded Rat Cardiomyocytes. Front. Physiol. 11:815. doi: 10.3389/fphys.2020.00815

The chambers of the heart fulfill different hemodynamic functions, which are reflected in their structural and contractile properties. While the atria are highly elastic to allow filling from the venous system, the ventricles need to be able to produce sufficiently high pressures to eject blood into the circulation. The right ventricle (RV) pumps into the low pressure pulmonary circulation, while the left ventricle (LV) needs to overcome the high pressure of the systemic circulation. It is incompletely understood whether these differences can be explained by the contractile differences at the level of the individual cardiomyocytes of the chambers. We addressed this by isolating cardiomyocytes from atria, RV, LV, and interventricular septum (IVS) of five healthy wild-type rats. Using a high-throughput contractility set-up, we measured contractile function of 2,043 cells after overnight culture. Compared to ventricular cardiomyocytes, atrial cells showed a twofold lower contraction amplitude and 1.4- to 1.7-fold slower kinetics of contraction and relaxation. The interventricular differences in contractile function were much smaller; RV cells displayed 12–13% less fractional shortening and 5–9% slower contraction and 3–15% slower relaxation kinetics relative to their LV and IVS counterparts. Aided by a large dataset, we established relationships between contractile parameters and found contraction velocity, fractional shortening and relaxation velocity to be highly correlated. In conclusion, our findings are in line with contractile differences observed at the atrioventricular level, but can only partly explain the interventricular differences that exist at the organ level.

Keywords: cardiomyocyte, contractility, large-scale, atria, ventricles, regional differences

INTRODUCTION

The heart consists of atria and ventricles which at a cellular level are activated through excitation–contraction coupling in a highly coordinated fashion to provide sufficient pressure to maintain perfusion of the body. The structural and contractile properties of each compartment are linked to the hemodynamic function it fulfills. The right ventricle (RV) ejects blood into the low pressure pulmonary vasculature, whereas the left ventricle (LV) pumps blood into the high pressure systemic circulation. As a result, the wall of the RV is considerably thinner and more compliant than the LV wall (Voelkel et al., 2006). The atria function predominantly as a reservoir for venous return and under normal circumstances does not have to overcome high pressures during contraction, which is reflected by highly elastic properties of the atrial myocardium (Blume et al., 2011). Functional differences between the chambers of the heart are also apparent in the differential response to changes in hemodynamics, such as chronic pressure overload (Belin et al., 2011; Rain et al., 2014).

The structural and functional differences between the chambers of the heart may be explained by distinct functional properties of individual cardiomyocytes from each region. Up to date, the contractile function of cardiomyocytes from different regions has not been subject of intensive study. The limited number of studies covering this topic reports inconclusive findings (McMahon et al., 1996; Tanaami et al., 2005; Kondo et al., 2006; Sathish et al., 2006; Belin et al., 2011; Chu et al., 2013), which may be attributed to species differences, methodological differences, selection bias, and small sample sizes (Chung and Campbell, 2013; Sikkel et al., 2017; Clark and Campbell, 2019; Kuster, 2019). Furthermore, regional differences may be small and can therefore only be studied through unbiased, extensive sampling.

We performed large-scale contractility measurements on intact unloaded rat cardiomyocytes isolated from atrial (AT), LV, RV, and interventricular septal (IVS) tissue to assess whether differences in contractile properties exist at the level of single cardiomyocytes.

MATERIALS AND METHODS

Ethical Approval

The animal experiments were performed in accordance with the guidelines from Directive 2010/63/EU of the European Parliament on the protection of animals used for scientific purposes and were approved by the ethics committees of VU University Medical Center, Amsterdam, Netherlands.

Adult Rat Cardiomyocyte Isolation and Culturing

Cardiomyocytes were isolated from adult Wistar rats (n = 5) weighing 200–250 g. Intact AT (left and right atrium were combined), LV, RV, and IVS rat cardiomyocytes were isolated through collagenase digestion of hearts essentially as described previously (Sequeira et al., 2015; van Deel et al., 2017). In brief, rats were euthanized via isoflurane inhalation, after which hearts were quickly harvested and washed in cold isolation Tyrode solution (130 mM NaCl, 5.4 mM KCl, 3 mM sodium pyruvate, 25 mM HEPES, 0.5 mM $MgCl_2$, 0.33 mM NaH_2PO_4, 22 mM glucose, pH 7.4) containing 0.2 mM EGTA (Tyrode–EGTA). Hearts were subsequently cannulated to a Langendorff set-up via the aorta and perfused with Tyrode-EGTA for 2 min at 37°C. Next, hearts were perfused for 25–35 min (depending on the integrity of the tissue) with enzyme Tyrode solution composed of Tyrode solution, 50 μM $CaCl_2$, and 1.2 mg/mL collagenase (Type II, 265 U/mg; Worthington Biochemical, NJ, United States). The heart was removed from the cannula and separated into AT, LV, RV, and IVS. Each part was cut into fine pieces, followed by trituration for 3 min with a plastic Pasteur pipette in stopping buffer solution 1 [SB-1; Tyrode solution, 0.6 mg/mL collagenase, 100 μM $CaCl_2$, and 10 mg/mL bovine serum albumin (BSA)]. Cell suspensions were filtered through a 300 μm nylon mesh filter and collected in 50 mL Falcon tubes, followed by centrifugation for 1 min at 27 × g at room temperature. Pellets containing cardiomyocytes were resuspended in SB solution 2 (SB-2; Tyrode solution, 250 μM $CaCl_2$ and 10 mg/mL BSA) and incubated for 10 min at 37°C in order for the cells to settle. After the removal of supernatants, cardiomyocytes were resuspended in SB solution 3 (SB-3; Tyrode solution, 500 μM $CaCl_2$ and 10 mg/mL BSA) and incubated for 10 min at 37°C. Hereafter, cardiomyocytes were suspended in plating medium [Medium 199 (Lonza, Basel, Switzerland), 1% penicillin/streptomycin and 5% fetal bovine serum (FBS)] and transferred to laminin-coated 35 mm^2 glass-bottomed dishes (MatTek, Ashland, MA, United States). Following 1 h of incubation at 37°C in humidified air with 5% CO_2, unattached cells were washed away by replacing plating medium with culture medium [Medium 199, 1% penicillin/streptomycin, insulin transferrin selenium (ITS; Sigma-Aldrich, composition: insulin, 10 mg/L; transferrin, 5.5 mg/L; selenium 5 μg/L) and 0.5 μM cytochalasin D (Life Technologies)]. The latter two compounds were added in order to prevent dedifferentiation and optimize cell viability (Viero et al., 2008; Tian et al., 2012). Cardiomyocytes were cultured overnight in an incubator at 37°C in humidified air with 5% CO_2.

Cardiomyocyte Contractility

Cardiomyocyte contractility measurements were performed using the CytoCypher Multicell High Throughput System (CytoCypher BV, Wageningen, Netherlands). To measure contractility, culture medium was replaced by experimental Tyrode solution (137 mM NaCl, 5.4 mM KCl, 3 mM sodium pyruvate, 5 mM HEPES, 0.57 mM $MgCl_2$, 0.33 mM NaH_2PO_4, 1.8 mM $CaCl_2$ and 5.6 mM glucose, pH 7.4). Dishes were placed on a fast x–y–z position programmable scanning microscope, allowing rapid identification and measurements of contracting cardiomyocytes. Cell shortening experiments were performed as described previously (Juni et al., 2019). Contraction was evoked via electrical field stimulation (2 Hz, 4 ms pulse duration, 25 V) at 37°C. Sarcomere shortening and relaxation kinetics were quantified via a video-based sarcomere length (SL) detection system (IonOptix corporation, Milton, MA, United States) at 250 Hz sampling frequency. Each cell was measured for 5 s, in

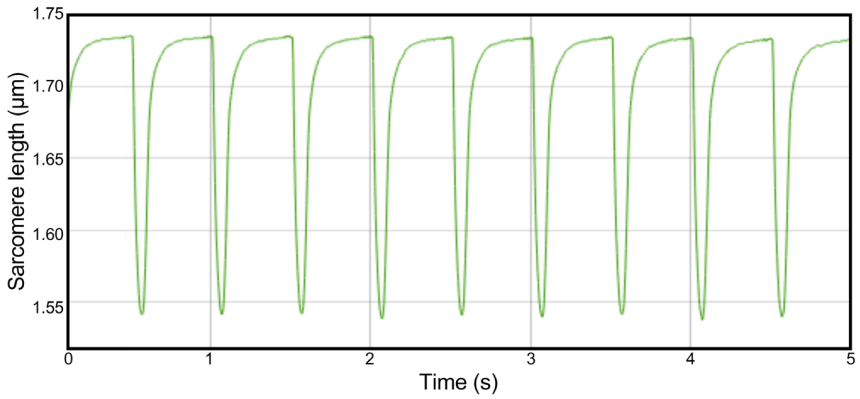

FIGURE 1 | Example trace of a full-length recording in a single cell. Cells were paced with a frequency of 2 Hz. Sarcomere length was measured for 5 s, in which 8 or 9 contractions could be recorded.

which 8–9 contraction traces could be recorded (see **Figure 1** for an example of a full-length trace of a single cell). All contracting cardiomyocytes that could be measured within a 20 min time frame per dish were measured. We observed no significant rundown in contractility during this period. In a subset of cells, cardiomyocyte width and length were assessed via edge detection. Width was measured at three locations along the length of the cell (at 25, 50, and 75%). Contractility assays were performed within 18–24 h after isolation. During this period, no decline in contractility was observed.

Data Analysis

A schematic overview of data analysis is depicted in **Figure 2**. The batch of raw contractility data was analyzed using the CytoSolver Transient Analysis Tools package from CytoCypher BV (Wageningen, Netherlands) to yield averaged contractile and kinetic parameters from each cell. With this software, the relaxation phase is fitted with a bi-exponential fit starting at 10% return time. Individual cells were excluded from further analysis if they did not meet all inclusion criteria (**Figure 2**). Data were subsequently tested for normality and transformed via log or square root transformation when appropriate. Hierarchical clustering analysis (Sikkel et al., 2017) was performed to quantify the amount of clustering for each rat and dish. If the data were tightly grouped, appropriate corrections to the statistical significance test were applied. A student's *t*-test or two-way analysis of variance (ANOVA) where appropriate was performed to test for differences between regions, followed by Bonferroni *post hoc* testing. The significance level was set at $p < 0.01$.

RESULTS

Contractility and Cell Dimension Differences Between Heart Regions

In total, 2,512 cardiomyocytes from five healthy rats were measured, of which 2,043 met the inclusion criteria for further analysis (**Figure 2**). Representative cells from each region are shown in **Figure 3**. Averaged contraction and velocity traces of each region are depicted in **Figures 4A–C**. These traces indicate markedly different contraction characteristics in AT cells compared to cells isolated from ventricular regions. A principal component analysis (PCA) was carried out to assess if cardiomyocytes from AT, LV, RV, and IVS display clustering based on their respective origin (**Figure 4D**). Hereto, redundant variables (e.g., "Time to Peak 10%," "Time to Peak 20%") were omitted to avoid overrepresentation of similar variables in the dimension axes. This confirmed that only cells from AT were clearly distinct from cells from the ventricular regions. To elucidate, the main purpose of a PCA is to reduce the number of variables in a dataset, especially when many variables are correlated with each other, while retaining the variation and differences in the dataset (Jolliffe and Cadima, 2016). Hence, the variables are "combined" mathematically into several dimensions that indicate the percentage of differences retained. In our case, Dim 1 represents 37% of the difference in the dataset, while Dim 2 represents 35%. In **Supplementary Figure S1**, the length of the arrow indicates how strongly the parameter affects the dimension. Thus, fractional shortening, relaxation velocity, contraction velocity, and time to peak all contribute substantially to the difference between AT and ventricular cells. Excluding the AT cells from the analysis showed that ventricular cells do not display clustering based on regional origin (**Figure 4E**).

To further address how contractility of AT cells differ from ventricular cells, data from LV, RV, and IVS cells were pooled (labeled "VT") and tested for significance against AT cells after correcting for normality and variation arising from rat and dish differences (**Table 1**). Cells from AT tissue were found to differ strongly from VT cells for every parameter tested except 80% relaxation time and relaxation coefficient tau. Most notably, fractional shortening in AT cells was twofold lower compared to VT cells. Velocities of contraction and relaxation were substantially lower in AT cells compared to values observed in VT cardiomyocytes. Despite lower contraction velocity, AT cells reached peak earlier than VT cells. Similarly, partial relaxation is achieved earlier in AT cells than VT cells, in spite of lower maximal relaxation velocity in AT cells. In terms of cell dimensions, AT cells were found to be both shorter and smaller

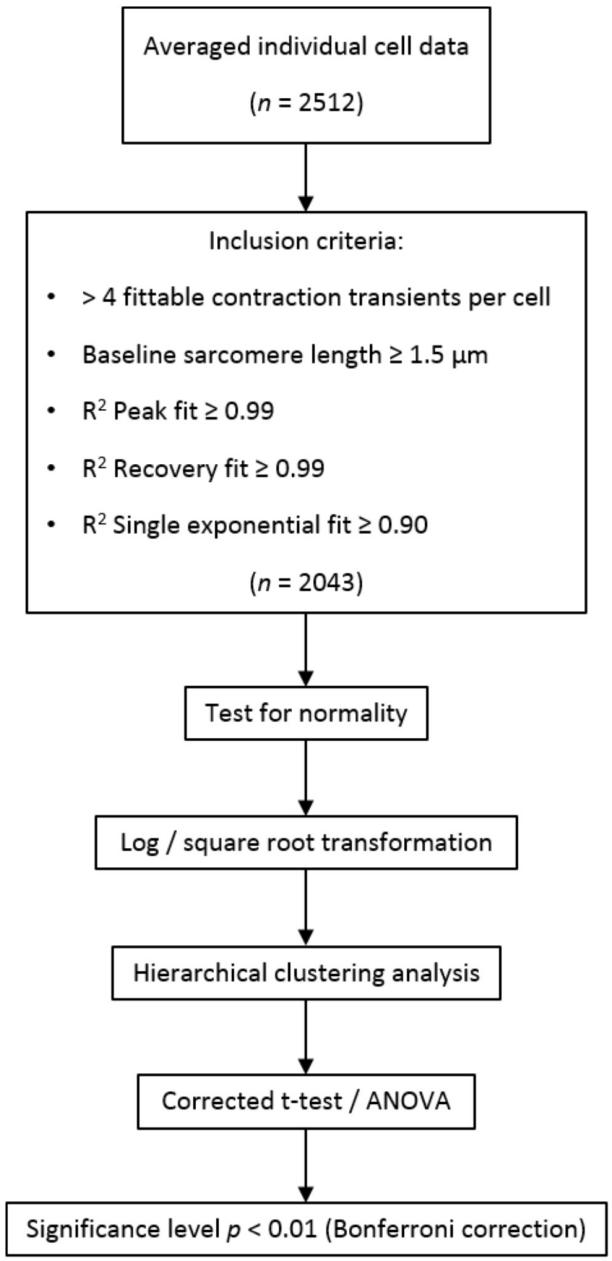

FIGURE 2 | Schematic overview of data processing and analysis. In total, 2,512 cells were measured, of which 2,043 were included in analysis. If no more than four contraction transients could be fitted by the transient analysis software (i.e., due to disturbances in the sarcomere length signal), cells were excluded from the analysis. Short resting sarcomere length and inaccurate fitting of the contraction transients were additional exclusion criteria.

compared to VT cells, indicating that, as anticipated, atrial cardiomyocytes are both structurally and functionally distinct from ventricular cardiomyocytes.

To define if differences between RV and LV structure and function arise from inherent changes in the cardiomyocytes that make up the ventricles, we compared dimensions and contractile properties of RV, LV, and IVS cardiomyocytes (**Table 2**). RV cells were found to have a lower amplitude of contraction than LV and IVS when expressed both in absolute terms (peak height) as well as relative terms (fractional shortening). With respect to contraction kinetics, RV cardiomyocytes showed a slightly lower velocity of shortening compared to LV and IVS. Relaxation velocity in IVS cells was higher compared to RV and LV cells. Compared to LV, a trend toward lower relaxation velocity was observed in RV ($p = 0.02$). RV cells moreover reached peak earlier than LV and IVS cells. Lastly, with respect to cell dimensions, LV cardiomyocytes were larger both in terms of width and length compared to RV. The analysis on regional differences in fractional shortening and contraction and relaxation velocities were performed on cardiomyocytes from five animals taken together, but can also be observed when looking at individual animals (**Supplementary Figure S2**).

Correlation Between Contractility Parameters

The size of our dataset allowed us to establish correlations between contractility parameters (**Figure 5**). Contraction velocity strongly correlates with relaxation velocity ($R^2 = 0.68$). Fractional shortening displays robust correlation with both contraction velocity ($R^2 = 0.55$) and relaxation velocity ($R^2 = 0.59$), but correlates poorly with time to peak ($R^2 = 0.06$). No regional differences were observed in correlations between these parameters when RV, LV, and IVS cells were analyzed separately (data not shown). Fractional shortening shows no correlation with relaxation time (50% relaxation time; $R^2 = 0.004$), and relaxation coefficient (tau; $R^2 = 0.06$). These findings imply that contraction velocity is the most important determinant of the degree of contraction and the velocity of subsequent relaxation.

Relation Between Effect Size and Sample Size

The large-scale dataset obtained in this study provides an accurate estimation of the variation that is present among ventricular cardiomyocytes. Therefore, the standard deviations of the parameters reported in this study (**Tables 1**, **2**) can be used to calculate the sample size that is needed to uncover an anticipated effect size. Calculating the sample size for a range of effect sizes generates an exponential function, which is exemplified in **Figure 6** for fractional shortening, contraction velocity, and relaxation velocity. When subtle differences are subject of study, such as the regional differences reported here, a large sample size is required, in particular when kinetics of contraction are addressed. To elucidate, fractional shortening in RV cells was 7.8%, and in IVS cells, it was 8.8%. Hence, this constitutes an effect size of 13% and requires a sample size of 140 per group in order to be detected with statistical significance at the level of $p < 0.01$. In contrast, β-adrenergic receptor stimulation with isoproterenol typically induces effect sizes of more than 50% (Harding et al., 1988; Najafi et al., 2016) and hence can be studied using relatively small sample sizes ($n = 10–20$). This may serve as guidance to future studies investigating contractility differences between (experimental) conditions.

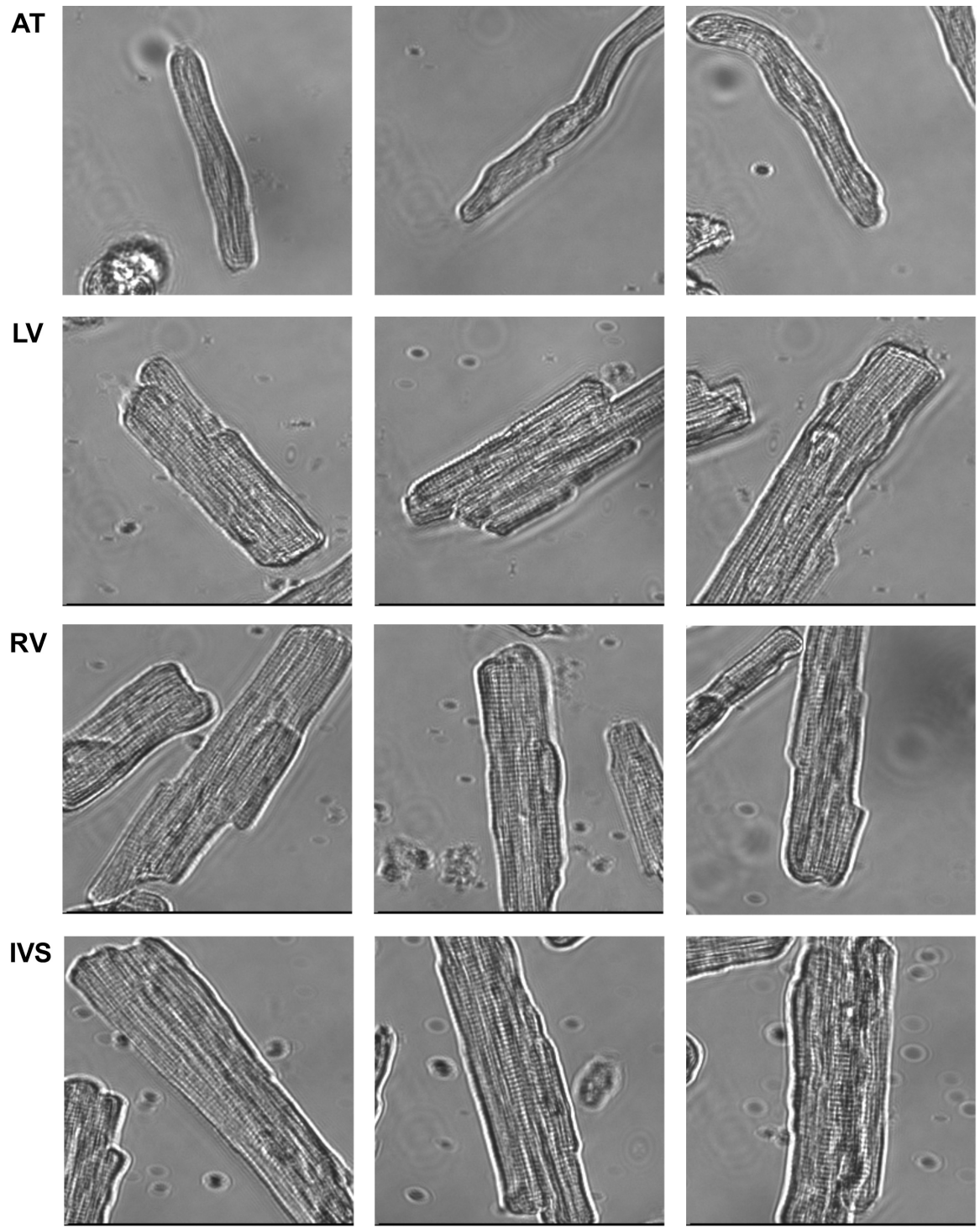

FIGURE 3 | Representative cells from each cardiac region. Cells from atrium (AT) were markedly thinner and shorter than cells from left ventricle (LV) and right ventricle (RV) and interventricular septum (IVS).

DISCUSSION

In the present study, we deployed a high-throughput system to measure contractile properties and cell dimensions in AT, LV, RV, and IVS cardiomyocytes isolated from healthy rats. We observed major differences between AT and ventricular cells. Moreover, we report relatively small, but significant contractile and dimensional differences between cardiomyocytes from

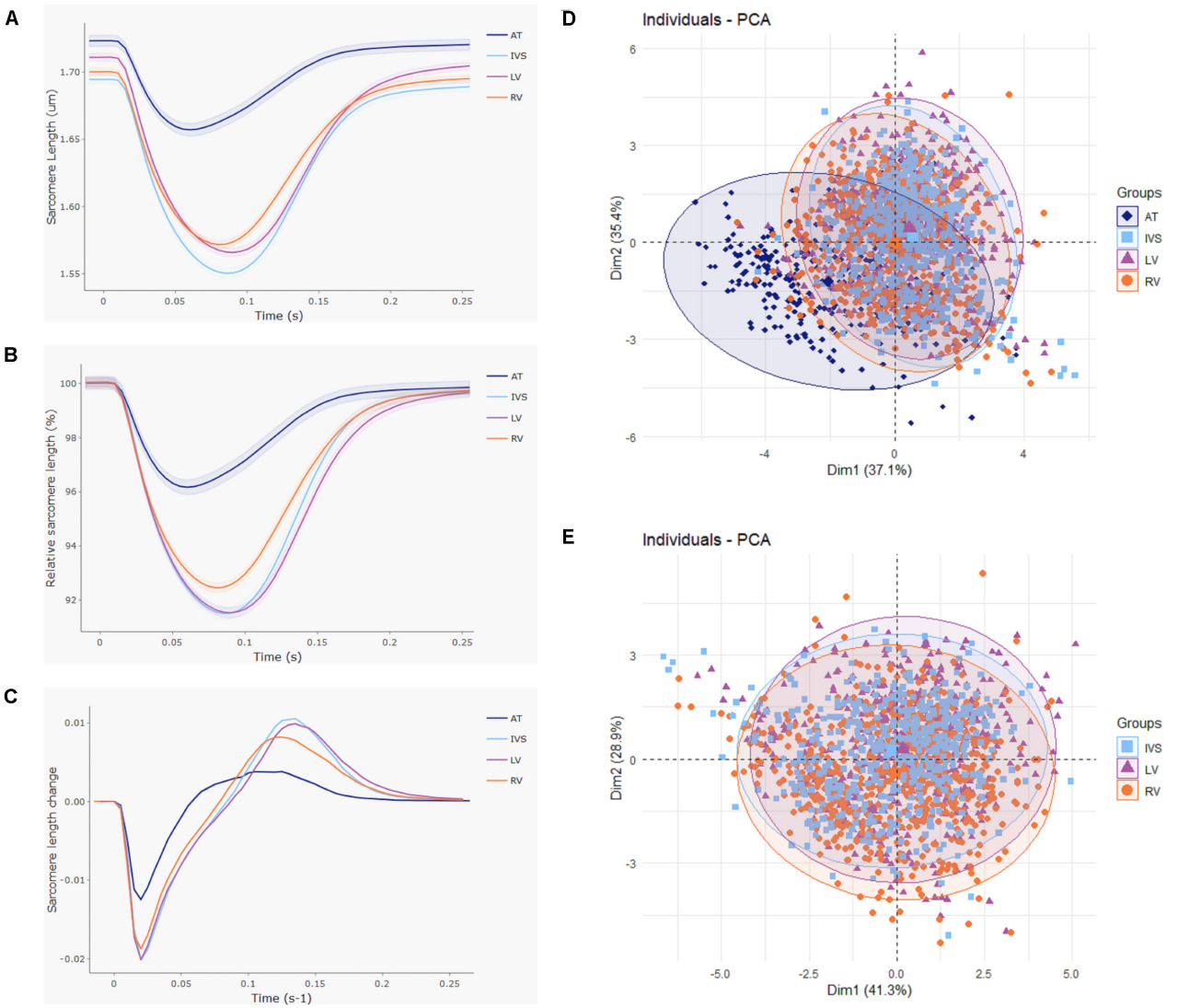

FIGURE 4 | Large atrioventricular and small interventricular differences in contractile function. Contractile function was compared between cardiomyocytes isolated from atria (AT; n = 272), left (LV; n = 553), and right ventricle (RV; n = 711) and interventricular septum (IVS; n = 507) from five rats. **(A)** Averaged and **(B)** normalized contraction traces and **(C)** averaged velocity traces for each cardiac region. Shading indicates SEM. **(D)** Principal component analysis displays clear clustering of AT cells. **(E)** Principal component analysis with AT cells omitted shows no separate clusters at the ventricular level.

ventricular regions, most notably lower contraction amplitude and kinetics in RV cardiomyocytes compared with LV and IVS. Differences between atrial and ventricular cardiomyocytes are in keeping with the respective functions of atria and ventricles. The much smaller differences between RV, IVS, and LV cardiomyocytes can only partly explain the differences between RV and LV that exist at the organ level. Our large dataset enabled us to detect small differences despite the remarkable heterogeneity we demonstrate to be present among cells. We could also correlate contractile parameters, revealing a strong correlation between contraction velocity, fractional shortening, and relaxation velocity. Taken together, our study highlights the importance of extensive, unbiased sampling when performing studies on cardiomyocyte contractility.

Contractile Differences Between AT and Ventricular Cardiomyocytes

To the best of our knowledge, unloaded shortening in AT cardiomyocytes relative to ventricular cells has not been comprehensively assessed. A study by Tanaami et al. (2005) reports no contractile differences between rat AT and VT cardiomyocytes in terms of fractional shortening. However, this was based on experiments in a small number of cardiomyocytes (n = 12–30) in which a large standard error was observed. Under loaded conditions, Luss et al. (1999) demonstrated AT cells to reach peak force development in a shorter time period than LV cells, which is in good agreement with our observation that AT cells achieve peak shortening earlier than ventricular cells (**Table 1**). This might in part be explained by higher

TABLE 1 | Contractile and cell dimension differences between AT and ventricular (VT) cells.

Contractility parameters	**AT** ***n* = 272**	**VT** ***n* = 1771**	
Baseline SL (μm)	1.72 ± 0.07	1.70 ± 0.07	*
Peak height (μm)	0.07 ± 0.05	0.14 ± 0.05	**
Fractional shortening (%)	4.3 ± 3.0	8.4 ± 2.6	**
Time to peak (ms)	55.0 ± 17.8	84.1 ± 20.1	**
Time to peak 80 (ms)	31.2 ± 8.7	44.2 ± 9.8	**
Time to peak 50 (ms)	20.7 ± 5.2	26.8 ± 6.2	**
Time to peak 20 (ms)	13.1 ± 3.2	15.8 ± 3.9	**
Contraction velocity (μm/s)	−3.4 ± 2.6	−4.6 ± 2.0	**
80% Relaxation time (ms)	61.0 ± 31.6	63.3 ± 18.9	
50% Relaxation time (ms)	34.0 ± 14.5	43.6 ± 13.8	**
20% Relaxation time (ms)	18.8 ± 8.6	28.4 ± 10.3	**
Relaxation velocity (μm/s)	2.1 ± 1.8	3.5 ± 1.7	**
Tau (ms^{-1})	37.1 ± 30.8	36.2 ± 23.8	
Cell dimensions	**AT** **Width: *n* = 106** **Length: *n* = 63**	**VT** **Width: *n* = 982** **Length: *n* = 633**	
Cell width (μm)	22.7 ± 7.9	32.2 ± 7.0	**
Cell length (μm)	80.8 ± 26.1	98.9 ± 17.7	**

*Data are illustrated as mean ± SD. Significant differences are indicated by **p < 0.001 or *p < 0.01 versus AT.*

TABLE 2 | Interventricular contractile and cell dimension differences.

Contractility parameters	**LV** ***n* = 553**		**RV** ***n* = 711**		**IVS** ***n* = 507**
Baseline SL (μm)	1.71 ± 0.07		1.70 ± 0.07		1.70 ± 0.08
Peak height (μm)	0.15 ± 0.04	**	0.13 ± 0.05	††	0.15 ± 0.04
Fractional shortening (%)	8.7 ± 2.6	**	7.8 ± 2.7	††	8.8 ± 2.5
Time to peak (ms)	88.4 ± 20.5	*	80.0 ± 20.0	††	85.2 ± 18.9
Time to peak 80 (ms)	45.6 ± 10.0	*	42.5 ± 9.5	††	45.1 ± 9.6
Time to peak 50 (ms)	27.4 ± 6.3	*#	25.7 ± 5.8	††	27.6 ± 6.4
Time to peak 20 (ms)	16.1 ± 4.0	#	15.0 ± 3.5	††	16.6 ± 4.2
Contraction velocity (μm/s)	−4.6 ± 1.9	*	−4.4 ± 2.1	†	−4.8 ± 2.0
80% Relaxation time (ms)	67.5 ± 18.9	#	62.7 ± 20.3		59.5 ± 16.0
50% Relaxation time (ms)	46.7 ± 13.9		42.8 ± 14.5		41.3 ± 12.2
20% Relaxation time (ms)	30.5 ± 10.3		27.7 ± 10.6		27.1 ± 9.4
Relaxation velocity (μm/s)	3.4 ± 1.6	#	3.3 ± 1.7	††	3.8 ± 1.7
Tau (ms^{-1})	38.2 ± 25.2		34.9 ± 21.4		35.9 ± 25.2
Cell dimensions	**LV** **Width: *n* = 337** **Length: *n* = 210**		**RV** **Width: *n* = 379** **Length: *n* = 259**		**IVS** **Width: *n* = 266** **Length: *n* = 164**
Cell width (μm)	33.5 ± 7.4	**	31.1 ± 6.6		32.3 ± 6.9
Cell length (μm)	102.0 ± 19.0	*	97.7 ± 18.0		97.0 ± 14.8

*Data are illustrated as mean ± SD. Significant differences are indicated by *p < 0.01 or **p < 0.001 for LV versus RV; #p < 0.01 or ##p < 0.001 for LV versus IVS; †p < 0.01 or ††p < 0.001 for RV versus IVS.*

expression of the fast α-isoform of cardiac myosin heavy chain (MHC) and faster cross-bridge kinetics in atrial relative to ventricular tissue (Reiser and Kline, 1998; Andruchov et al., 2006), although in the present study contraction velocity was lower in atrial than in ventricular cardiomyocytes. Relative to ventricular cells, AT cells display shorter action potentials, more heterogeneous intracellular Ca^{2+} transient propagation, and higher sarcoplasmic reticulum (SR) Ca^{2+}-ATPase (SERCA2) levels (Minajeva et al., 1997; Luss et al., 1999; Walden et al., 2009; Greiser et al., 2014); hence, Ca^{2+}-release from the SR and subsequent cross-bridge activation may be less uniformly orchestrated, which combined with faster Ca^{2+} re-uptake may give rise to short-lived, relatively slow contractions (Brandenburg et al., 2016). This would explain the low amplitude of fractional shortening and slow kinetics of contraction observed in our study. Faster Ca^{2+} re-uptake may also in part explain why in our study AT cells required less time to re-lengthen during the early phase of relaxation, although lower relaxation velocity indicates overall slower relengthening than ventricular cells.

Contractile Differences Between Ventricular Regions

Our findings predominantly suggest that RV cardiomyocytes show reduced contraction amplitude and kinetics of contraction and relaxation compared to LV and IVS. Hence, under unloaded conditions cardiomyocytes display similarity to RV and LV contraction *in vivo*, i.e., less shortening and slower relaxation as assessed by tricuspid and mitral valve inflow in RV versus LV (Zoghbi et al., 1990; Pela et al., 2004; Hudsmith et al., 2005). Comparing shortening velocity under unloaded conditions to tissue contraction velocity is complicated due to differences in fiber orientation, which is more longitudinal in the RV and more circular in the LV (Naito et al., 1995). Accordingly, in the RV, longitudinal shortening is the main contributor to contraction, as opposed to circumferential shortening in the LV.

Our general finding of lower contractility in the RV versus LV is consistent with other studies reporting interventricular differences in unloaded shortening in rodent cardiomyocytes (Kondo et al., 2006; Sathish et al., 2006; Chu et al., 2013). However, the percent difference in shortening between LV and RV cells in these studies is considerably larger (ranging from 25 to 80%) than the difference we report here (12%). A similar trend is seen for kinetics of contraction, where we measured a 5% difference in contraction velocity between RV and LV, compared to 44% in the study by Kondo et al. (2006). Importantly, we measured shortening at a tightly controlled physiological temperature (37°C), whereas comparable experiments were carried out at less optimally controlled room temperature (19–22°C) (Kondo et al., 2006; Sathish et al., 2006; Chu et al., 2013). Cross-bridge cycling and concomitant cardiomyocyte shortening are highly temperature sensitive (de Tombe and Stienen, 2007; Chung and Campbell, 2013); thus, any differences that may exist between RV and LV cells could be magnified when measuring at non-physiological temperatures. Also, we detected no LV versus RV difference in relaxation as defined by the time constant tau, dissimilarly to Chu et al. (2013) who report a twofold higher value in RV versus LV. This discrepancy might be explained by different experimental temperatures, as this heavily influences cardiomyocyte relaxation (Chung and Campbell, 2013). A study by McMahon et al. (1996) addressing unloaded shortening

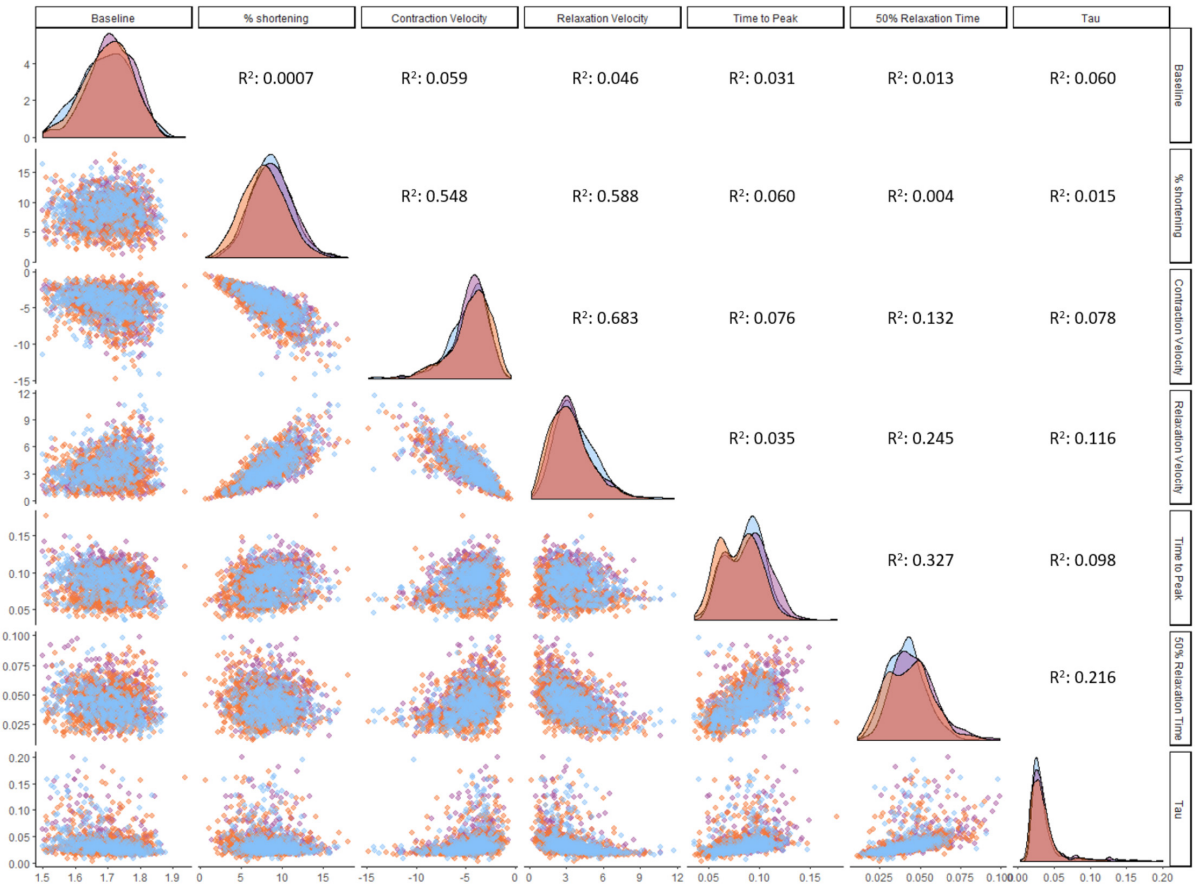

FIGURE 5 | Correlations between contractility parameters. Correlation analysis was performed on ventricular cardiomyocytes (n = 1,771). Distribution plots and individual cardiomyocytes are colored based on their origin: RV (orange), LV (purple), and IVS (blue). All correlations with an R^2 larger than 0.01 are statistically significant at the level of $p < 0.001$.

in large numbers of porcine cardiomyocytes reported higher contractility in RV compared to LV cells, which is in contrast to findings in rodents. As these data were gathered under experimental conditions identical to our study, their findings likely reflect a species difference.

The exact mechanisms underlying the interventricular differences reported here remain largely enigmatic. The RV has a different embryological origin than the LV (Cai et al., 2003); hence, contractile differences may simply be a reflection thereof. Additionally, the LV and RV may adapt to loading conditions not only structurally via cardiomyocyte count but also at the level of individual cells. The latter is also reflected in the cell dimension difference we observed, with LV cells being on average larger than RV cells. Findings from proteomic studies indicate LV versus RV differences in protein expression levels of sarcomere proteins such as myosin light chain 2, α-MHC and cardiac myosin binding protein C, and tropomyosin- and titin isoforms, i.e., more stiff titin in the LV (Comunian et al., 2011; Cadete et al., 2012; Peng et al., 2013). These differences may partly contribute to the contraction properties of LV and RV myofilaments described by Belin et al. (2011), in addition to the differences in myofilament phosphorylation they observed. Titin isoform composition could play a role in the kinetics and extent of contraction, as we recently showed (Najafi et al., 2019). Furthermore, LV versus RV differences have been found in terms of ion channel make-up and regulation (Gaborit et al., 2007; Molina et al., 2016; Zaitsev et al., 2019). As the IVS separates the LV and RV and is formed from the cell populations of both LV and RV embryological origin in rodents (Franco et al., 2006), we expected IVS cells to have contractile parameters intermediate between RV and LV. However, there were very few significant differences between LV and IVS, but almost all measured parameters were different between IVS and RV. This indicates that with respect to contraction/relaxation, IVS and LV are more similar to each other than the RV. Taken together, LV and RV are distinct from one another in multiple cellular aspects, which may provide a substrate for contractile differences and represents an interesting avenue for future research.

Intraregional Variability

We observed remarkable intraregional variation in cardiomyocyte contractility, which may stem from several factors. For example, Clark and Campbell (2019) recently

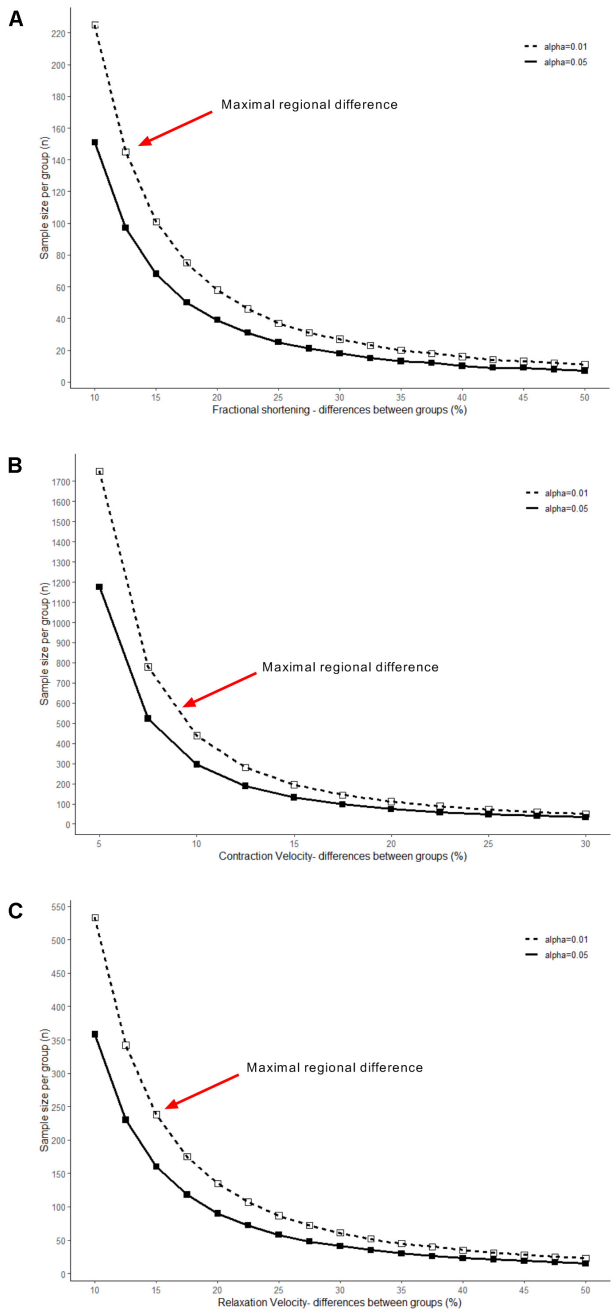

FIGURE 6 | Relationships between effect and sample size. Sample sizes needed to detect a range of effect sizes were calculated and plotted, using the variability of ventricular cells in: **(A)** fractional shortening, **(B)** contraction velocity, and **(C)** relaxation velocity. Solid line shows effect size at significance level of $p < 0.05$, dashed line of $p < 0.01$. Red arrows indicate sample size required for uncovering effect sizes at the magnitude of the regional differences identified in this study.

demonstrated that variation in unloaded rat cardiomyocytes decreases if cells are sampled from a smaller area, implying that local stretch and strain and paracrine signaling impact on cellular contractility (Kuster, 2019). Heterogeneity may also arise from differences between transmural regions. Transmural differences have been described for numerous properties, such as length-dependent activation, action potential waveforms, calcium homeostasis, mitochondrial respiration, ion channel make-up, and myofilament protein phosphorylation (Gaborit et al., 2007; Cazorla and Lacampagne, 2011; Gregorich et al., 2015; Kindo et al., 2016), which may all influence contractility. Experiments in a limited number of unloaded cardiomyocytes from subepicardial, midmyocardial and subendocardial regions suggest the existence of subtle contractile differences (Chung and Campbell, 2013), which would be an interesting subject for more extensive study.

Correlations Between Contractile Parameters

The large scale of our dataset enabled us to look for correlations between different parameters. We found a strong correlation between contraction velocity, fractional shortening, and relaxation velocity. The correlation between relaxation velocity and amplitude of shortening was previously described to occur in canine (Tsutsui et al., 1993) and porcine cardiomyocytes (McMahon et al., 1996). Also in a recent paper by Clark and Campbell (2019), a correlation was observed between cell shortening and time to 50% relaxation in rat cardiomyocytes. Cells that showed a greater amplitude of cell shortening had a shorter relaxation time. In the current study, the velocity of relaxation correlated much better to shortening than time to 50% relaxation. This might be expected as relaxation time is more dependent on the amplitude of contraction than velocity. The observation that there is a robust correlation between contraction and relaxation velocity was shown in an elegant paper by Janssen (2010). Here he compiled data from isometric contractions of mouse trabeculae that his group had gathered over the years and showed that under a wide variety of conditions, contraction and relaxation velocities correlated very strongly. The relationship between kinetics of contraction and relaxation seemed to be a property of the myofilaments, as perturbations to calcium transients did not influence the correlation (Janssen, 2010). The exact mechanism that determines this relationship is not well understood, but could involve cardiac myosin binding protein C (Janssen, 2010), which is an important mediator of cross-bridge cycling (Previs et al., 2014; Sequeira et al., 2014).

Limitations

We acknowledge several methodological limitations in this study. We combined cardiomyocytes from the left and right atrium in order to obtain a sufficient number of atrial cells, thus obscuring contractile differences that may exist between cardiomyocytes from these two regions. Furthermore, measurements were performed after overnight culture, allowing cells to recover from stress and damage induced during isolation (Mitcheson et al., 1998) and enabling us to perform all individual animal measurements on a single day. However, during this culturing period, regional contractile differences may become less pronounced compared to that directly after isolation.

CONCLUSION

Here, we report large atrioventricular contractile differences that are in line with differences at the organ level. The interventricular differences we found are more subtle and reflect only in part the differences observed *in vivo*. Through extensive sampling we furthermore identified strong correlations between contraction velocity, fractional shortening and relaxation velocity. Lastly, our large-scale dataset demonstrates notable intraregional heterogeneity, providing valuable methodological insights for future cardiomyocyte shortening studies.

DATA AVAILABILITY STATEMENT

All datasets generated for this study are available upon request.

ETHICS STATEMENT

The animal study was reviewed and approved by the ethics committees of the VU University Medical Center, Amsterdam, Netherlands.

AUTHOR CONTRIBUTIONS

EN, EM, MH, and DK designed the study, wrote the manuscript, and performed the experiments and data analysis. MG, VJ, CB, and JO helped performing the experiments and edited the manuscript. JV helped drafting and revising the manuscript. All authors contributed to the article and approved the submitted version.

FUNDING

We acknowledge support from the Netherlands Cardiovascular Research Initiative, an initiative with support from the Dutch Heart Foundation, CVON2014-40 DOSIS & CVON2017−18 ARENA−PRIME, and NWO (NWO-ZonMW; 91818602 VICI) grant to JV. The project is co-funded by the PPP Allowance made available by Health∼Holland, Top Sector Life Sciences & Health, to stimulate public–private partnerships, DK and MH.

SUPPLEMENTARY MATERIAL

The Supplementary Material for this article can be found online at: https://www.frontiersin.org/articles/10.3389/fphys.2020.00815/full#supplementary-material

REFERENCES

Andruchov, O., Andruchova, O., and Galler, S. (2006). Fine-tuning of cross-bridge kinetics in cardiac muscle of rat and mouse by myosin light chain isoforms. *Pflugers Arch.* 452, 667–673. doi: 10.1007/s00424-006-0080-7

Belin, R. J., Sumandea, M. P., Sievert, G. A., Harvey, L. A., Geenen, D. L., Solaro, R. J., et al. (2011). Interventricular differences in myofilament function in experimental congestive heart failure. *Pflugers Arch.* 462, 795–809. doi: 10.1007/s00424-011-1024-4

Blume, G. G., McLeod, C. J., Barnes, M. E., Seward, J. B., Pellikka, P. A., Bastiansen, P. M., et al. (2011). Left atrial function: physiology, assessment, and clinical implications. *Eur. J. Echocardiogr.* 12, 421–430. doi: 10.1093/ejechocard/jeq175

Brandenburg, S., Arakel, E. C., Schwappach, B., and Lehnart, S. E. (2016). The molecular and functional identities of atrial cardiomyocytes in health and disease. *Biochim. Biophys. Acta* 1863(7 Pt B), 1882–1893. doi: 10.1016/j.bbamcr.2015.11.025

Cadete, V. J., Lin, H. B., Sawicka, J., Wozniak, M., and Sawicki, G. (2012). Proteomic analysis of right and left cardiac ventricles under aerobic conditions and after ischemia/reperfusion. *Proteomics* 12, 2366–2377. doi: 10.1002/pmic.201100604

Cai, C. L., Liang, X., Shi, Y., Chu, P. H., Pfaff, S. L., Chen, J., et al. (2003). Isl1 identifies a cardiac progenitor population that proliferates prior to differentiation and contributes a majority of cells to the heart. *Dev. Cell* 5, 877–889. doi: 10.1016/s1534-5807(03)00363-0

Cazorla, O., and Lacampagne, A. (2011). Regional variation in myofilament length-dependent activation. *Pflugers Arch.* 462, 15–28. doi: 10.1007/s00424-011-0933-6

Chu, C., Thai, K., Park, K. W., Wang, P., Makwana, O., Lovett, D. H., et al. (2013). Intraventricular and interventricular cellular heterogeneity of inotropic responses to alpha(1)-adrenergic stimulation. *Am. J. Physiol. Heart Circ. Physiol.* 304, H946–H953.

Chung, C. S., and Campbell, K. S. (2013). Temperature and transmural region influence functional measurements in unloaded left ventricular cardiomyocytes. *Physiol. Rep.* 1:e00158. doi: 10.1002/phy2.158

Clark, J. A., and Campbell, S. G. (2019). Diverse relaxation rates exist among rat cardiomyocytes isolated from a single myocardial region. *J. Physiol.* 597, 711–722. doi: 10.1113/jp276718

Comunian, C., Rusconi, F., De Palma, A., Brunetti, P., Catalucci, D., and Mauri, P. L. (2011). A comparative MudPIT analysis identifies different expression profiles in heart compartments. *Proteomics* 11, 2320–2328. doi: 10.1002/pmic.201000479

de Tombe, P. P., and Stienen, G. J. (2007). Impact of temperature on cross-bridge cycling kinetics in rat myocardium. *J. Physiol.* 584(Pt 2), 591–600. doi: 10.1113/jphysiol.2007.138693

Franco, D., Meilhac, S. M., Christoffels, V. M., Kispert, A., Buckingham, M., and Kelly, R. G. (2006). Left and right ventricular contributions to the formation of the interventricular septum in the mouse heart. *Dev. Biol.* 294, 366–375. doi: 10.1016/j.ydbio.2006.02.045

Gaborit, N., Le Bouter, S., Szuts, V., Varro, A., Escande, D., Nattel, S., et al. (2007). Regional and tissue specific transcript signatures of ion channel genes in the non-diseased human heart. *J. Physiol.* 582(Pt 2), 675–693. doi: 10.1113/jphysiol.2006.126714

Gregorich, Z. R., Peng, Y., Lane, N. M., Wolff, J. J., Wang, S., Guo, W., et al. (2015). Comprehensive assessment of chamber-specific and transmural heterogeneity in myofilament protein phosphorylation by top-down mass spectrometry. *J. Mol. Cell Cardiol.* 87, 102–112. doi: 10.1016/j.yjmcc.2015.08.007

Greiser, M., Kerfant, B. G., Williams, G. S., Voigt, N., Harks, E., Dibb, K. M., et al. (2014). Tachycardia-induced silencing of subcellular Ca2+ signaling in atrial myocytes. *J. Clin. Invest.* 124, 4759–4772. doi: 10.1172/jci70102

Harding, S. E., Vescovo, G., Kirby, M., Jones, S. M., Gurden, J., and Poole-Wilson, P. A. (1988). Contractile responses of isolated adult rat and rabbit cardiac myocytes to isoproterenol and calcium. *J. Mol. Cell Cardiol.* 20, 635–647. doi: 10.1016/s0022-2828(88)80121-4

Hudsmith, L. E., Petersen, S. E., Francis, J. M., Robson, M. D., and Neubauer, S. (2005). Normal human left and right ventricular and left atrial dimensions using steady state free precession magnetic resonance imaging. *J Cardiovasc. Magn. Reson.* 7, 775–782. doi: 10.1080/10976640500295516

Janssen, P. M. (2010). Kinetics of cardiac muscle contraction and relaxation are linked and determined by properties of the cardiac sarcomere. *Am. J. Physiol. Heart Circ. Physiol.* 299, H1092–H1099.

Jolliffe, I. T., and Cadima, J. (2016). Principal component analysis: a review and recent developments. *Philos. Trans. A Math. Phys. Eng. Sci.* 374:20150202. doi: 10.1098/rsta.2015.0202

Juni, R. P., Kuster, D. W. D., Goebel, M., Helmes, M., Musters, R. J. P., van der Velden, J., et al. (2019). Cardiac microvascular endothelial enhancement of cardiomyocyte function is impaired by inflammation and restored by empagliflozin. *JACC Basic Transl. Sci.* 4, 575–591. doi: 10.1016/j.jacbts.2019.04.003

Kindo, M., Gerelli, S., Bouitbir, J., Hoang Minh, T., Charles, A. L., Mazzucotelli, J. P., et al. (2016). Left ventricular transmural gradient in mitochondrial respiration is associated with increased sub-endocardium nitric oxide and reactive oxygen species productions. *Front. Physiol.* 7:331. doi: 10.3389/fphys.2016.00331

Kondo, R. P., Dederko, D. A., Teutsch, C., Chrast, J., Catalucci, D., Chien, K. R., et al. (2006). Comparison of contraction and calcium handling between right and left ventricular myocytes from adult mouse heart: a role for repolarization waveform. *J. Physiol.* 571(Pt 1), 131–146. doi: 10.1113/jphysiol.2005.101428

Kuster, D. W. D. (2019). What grows together, goes together: assessing variability in cardiomyocyte function. *J. Physiol.* 597, 665–666. doi: 10.1113/jp277287

Luss, I., Boknik, P., Jones, L. R., Kirchhefer, U., Knapp, J., Linck, B., et al. (1999). Expression of cardiac calcium regulatory proteins in atrium v ventricle in different species. *J. Mol. Cell Cardiol.* 31, 1299–1314. doi: 10.1006/jmcc.1999.0962

McMahon, W. S., Mukherjee, R., Gillette, P. C., Crawford, F. A., and Spinale, F. G. (1996). Right and left ventricular geometry and myocyte contractile processes with dilated cardiomyopathy: myocyte growth and beta-adrenergic responsiveness. *Cardiovasc. Res.* 31, 314–323. doi: 10.1016/0008-6363(95)00212-x

Minajeva, A., Kaasik, A., Paju, K., Seppet, E., Lompre, A. M., Veksler, V., et al. (1997). Sarcoplasmic reticulum function in determining atrioventricular contractile differences in rat heart. *Am. J. Physiol.* 273, H2498–H2507.

Mitcheson, J. S., Hancox, J. C., and Levi, A. J. (1998). Cultured adult cardiac myocytes: future applications, culture methods, morphological and electrophysiological properties. *Cardiovasc. Res.* 39, 280–300. doi: 10.1016/s0008-6363(98)00128-x

Molina, C. E., Heijman, J., and Dobrev, D. (2016). Differences in left versus right ventricular electrophysiological properties in cardiac dysfunction and arrhythmogenesis. *Arrhythm. Electrophysiol. Rev.* 5, 14–19.

Naito, H., Arisawa, J., Harada, K., Yamagami, H., Kozuka, T., and Tamura, S. (1995). Assessment of right ventricular regional contraction and comparison with the left ventricle in normal humans: a cine magnetic resonance study with presaturation myocardial tagging. *Br. Heart J.* 74, 186–191. doi: 10.1136/hrt.74.2.186

Najafi, A., Sequeira, V., Helmes, M., Bollen, I. A., Goebel, M., Regan, J. A., et al. (2016). Selective phosphorylation of PKA targets after beta-adrenergic receptor stimulation impairs myofilament function in Mybpc3-targeted HCM mouse model. *Cardiovasc. Res.* 110, 200–214. doi: 10.1093/cvr/cvw026

Najafi, A., van de Locht, M., Schuldt, M., Schonleitner, P., van Willigenburg, M., Bollen, I., et al. (2019). End-diastolic force pre-activates cardiomyocytes and determines contractile force: role of titin and calcium. *J. Physiol.* 597, 4521–4531. doi: 10.1113/jp277985

Pela, G., Regolisti, G., Coghi, P., Cabassi, A., Basile, A., Cavatorta, A., et al. (2004). Effects of the reduction of preload on left and right ventricular myocardial velocities analyzed by dopplzer tissue echocardiography in healthy subjects. *Eur. J. Echocardiogr.* 5, 262–271. doi: 10.1016/j.euje.2003.10.001

Peng, Y., Yu, D., Gregorich, Z., Chen, X., Beyer, A. M., Gutterman, D. D., et al. (2013). In-depth proteomic analysis of human tropomyosin by top-down mass spectrometry. *J. Muscle Res. Cell Motil.* 34, 199–210. doi: 10.1007/s10974-013-9352-y

Previs, M. J., Michalek, A. J., and Warshaw, D. M. (2014). Molecular modulation of actomyosin function by cardiac myosin-binding protein C. *Pflugers Arch.* 466, 439–444. doi: 10.1007/s00424-013-1433-7

Rain, S., Handoko, M. L., Vonk Noordegraaf, A., Bogaard, H. J., van der Velden, J., and de Man, F. S. (2014). Pressure-overload-induced right heart failure. *Pflugers Arch.* 466, 1055–1063.

Reiser, P. J., and Kline, W. O. (1998). Electrophoretic separation and quantitation of cardiac myosin heavy chain isoforms in eight mammalian species. *Am. J. Physiol.* 274, H1048–H1053.

Sathish, V., Xu, A., Karmazyn, M., Sims, S. M., and Narayanan, N. (2006). Mechanistic basis of differences in Ca2+ -handling properties of sarcoplasmic reticulum in right and left ventricles of normal rat myocardium. *Am. J. Physiol. Heart Circ. Physiol.* 291, H88–H96.

Sequeira, V., Najafi, A., McConnell, M., Fowler, E. D., Bollen, I. A., Wust, R. C., et al. (2015). Synergistic role of ADP and Ca(2+) in diastolic myocardial stiffness. *J. Physiol.* 593, 3899–3916. doi: 10.1113/jp270354

Sequeira, V., Witjas-Paalberends, E. R., Kuster, D. W., and van der Velden, J. (2014). Cardiac myosin-binding protein C: hypertrophic cardiomyopathy mutations and structure-function relationships. *Pflugers Arch.* 466, 201–206. doi: 10.1007/s00424-013-1400-3

Sikkel, M. B., Francis, D. P., Howard, J., Gordon, F., Rowlands, C., Peters, N. S., et al. (2017). Hierarchical statistical techniques are necessary to draw reliable conclusions from analysis of isolated cardiomyocyte studies. *Cardiovasc. Res.* 113, 1743–1752. doi: 10.1093/cvr/cvx151

Tanaami, T., Ishida, H., Seguchi, H., Hirota, Y., Kadono, T., Genka, C., et al. (2005). Difference in propagation of Ca2+ release in atrial and ventricular myocytes. *JPN J. Physiol.* 55, 81–91. doi: 10.2170/jjphysiol.r2077

Tian, Q., Pahlavan, S., Oleinikow, K., Jung, J., Ruppenthal, S., Scholz, A., et al. (2012). Functional and morphological preservation of adult ventricular myocytes in culture by sub-micromolar cytochalasin D supplement. *J. Mol. Cell Cardiol.* 52, 113–124. doi: 10.1016/j.yjmcc.2011.09.001

Tsutsui, H., Urabe, Y., Mann, D. L., Tagawa, H., Carabello, B. A., Cooper, G. T., et al. (1993). Effects of chronic mitral regurgitation on diastolic function in isolated cardiocytes. *Circ. Res.* 72, 1110–1123. doi: 10.1161/01.res.72.5.1110

van Deel, E. D., Najafi, A., Fontoura, D., Valent, E., Goebel, M., Kardux, K., et al. (2017). In vitro model to study the effects of matrix stiffening on Ca(2+) handling and myofilament function in isolated adult rat cardiomyocytes. *J. Physiol.* 595, 4597–4610. doi: 10.1113/jp274460

Viero, C., Kraushaar, U., Ruppenthal, S., Kaestner, L., and Lipp, P. (2008). A primary culture system for sustained expression of a calcium sensor in preserved adult rat ventricular myocytes. *Cell Calcium.* 43, 59–71. doi: 10.1016/j.ceca.2007.04.001

Voelkel, N. F., Quaife, R. A., Leinwand, L. A., Barst, R. J., McGoon, M. D., Meldrum, D. R., et al. (2006). Right ventricular function and failure: report of a National Heart, Lung, and Blood Institute working group on cellular and molecular mechanisms of right heart failure. *Circulation* 114, 1883–1891. doi: 10.1161/circulationaha.106.632208

Walden, A. P., Dibb, K. M., and Trafford, A. W. (2009). Differences in intracellular calcium homeostasis between atrial and ventricular myocytes. *J. Mol. Cell Cardiol.* 46, 463–473. doi: 10.1016/j.yjmcc.2008.11.003

Zaitsev, A. V., Torres, N. S., Cawley, K. M., Sabry, A. D., Warren, J. S., and Warren, M. (2019). Conduction in the right and left ventricle is differentially regulated by protein kinases and phosphatases: implications for arrhythmogenesis. *Am. J. Physiol. Heart Circ. Physiol.* 316, H1507–H1527.

Zoghbi, W. A., Habib, G. B., and Quinones, M. A. (1990). Doppler assessment of right ventricular filling in a normal population. Comparison with left ventricular filling dynamics. *Circulation* 82, 1316–1324. doi: 10.1161/01.cir.82.4.1316

Conflict of Interest: EM is an employee of CytoCypher BV. MH is CEO of CytoCypher BV.

The remaining authors declare that the research was conducted in the absence of any commercial or financial relationships that could be construed as a potential conflict of interest.

Advantages of publishing in Frontiers

OPEN ACCESS
Articles are free to read for greatest visibility and readership

FAST PUBLICATION
Around 90 days from submission to decision

HIGH QUALITY PEER-REVIEW
Rigorous, collaborative, and constructive peer-review

TRANSPARENT PEER-REVIEW
Editors and reviewers acknowledged by name on published articles

Frontiers
Avenue du Tribunal-Fédéral 34
1005 Lausanne | Switzerland

Visit us: www.frontiersin.org
Contact us: frontiersin.org/about/contact

REPRODUCIBILITY OF RESEARCH
Support open data and methods to enhance research reproducibility

DIGITAL PUBLISHING
Articles designed for optimal readership across devices

FOLLOW US
@frontiersin

IMPACT METRICS
Advanced article metrics track visibility across digital media

EXTENSIVE PROMOTION
Marketing and promotion of impactful research

LOOP RESEARCH NETWORK
Our network increases your article's readership